Physik Department

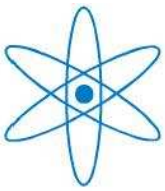

Towards the detection of low energy solar neutrinos in BOREXino: data readout, data reconstruction and background identification

Dissertation
von

Davide D'Angelo

Technische Universität München

Technische Universität München
Physik Department
Lehrstuhl für Experimentalphysik-Astroteilchenphysik E15
Univ.-Prof. Dr. Franz von Feilitzsch

Towards the detection of low energy solar neutrinos in BOREXino:
data readout, data reconstruction and background identification

Davide D'Angelo

Vollständiger Abdruck der von der Fakultät für Physik der Technischen Universität München zur Erlangung des akademischen Grades eines

Doktors der Naturwissenschaften (Dr. rer. nat.)

genehmigten Dissertation.

Vorsitzender:	Univ.-Prof. Dr. Manfred Kleber
Prüfer der Dissertation:	1. Univ.-Prof. Dr. Franz von Feilitzsch
	2. Univ.-Prof. Dr. Stephan Paul

Die Dissertation wurde am 14.02.2006 bei der Technischen Universität München eingereicht und durch die Fakultät für Physik am 10.03.2006 angenommen.

Abstract

New challenging questions in astro-particle physics are opened with the discovery of neutrino mass and mixing. Low energy solar neutrino spectroscopy plays now a fundamental role in understanding the new physics and the nuclear fusion processes in the sun. A large scale scintillation detector BOREXino at the Gran Sasso Laboratories (Italy) will soon pursue this goal in real time. In this work, a custom data acquisition system (electronics and software) has been developed together with the offline data processing algorithms. A water Čerenkov detector has been installed for cosmogenic background identification, including the tagging of ^{11}C in the energy window of *pep* neutrinos. With a prototype detector, the *in-situ* ^{11}C production rate was measured for the first time, resulting in $0.135 \pm 0.024[stat] \pm 0.014[syst]/d/ton$. The detection of the weak spectral contribution of *pep* neutrinos in BOREXino was shown to be realistic and will determine uniquely the fundamental solar *pp* fusion rate.

Neue herausfordernde Fragen der Astroteilchenphysik eröffnen sich mit der Entdeckung der Neutrinomassen und -mischung. Die Spektroskopie niederenergetischer solarer Neutrinos, spielt dabei eine fundamentale Rolle für das Verständnis dieser neuen Physik und der solaren Fusionsprozesse. BOREXino, ein großvolumiger Szintillationsdetektor, wird eine Echtzeitmessung im Untergrundlabor am Grand Sasso ermöglichen. In dieser Arbeit wurde ein Datenaufnahmesystem (Elektronik & Software) sowie Algorithmen zur Datenanalyse entwickelt. Ein Wasser-Cherenkov Detektor wurde installiert um kosmogenen Untergrund zu erkennen, einschließlich der Identifikation von ^{11}C im Energiefenster der *pep*-Neutrinos. Mit einem Prototypen wurde erstmals die *in-situ* Produktionsrate von ^{11}C zu $0.135 \pm 0.024[stat] \pm 0.014[syst]/Tag/Tonne$ bestimmt. Durch die Detektionsmöglichkeit des spektralen Beitrags von *pep*-Neutrinos wird das BOREXino-Experiment eine einzigartige Bestimmung der solaren *pp*-Fusionsrate zulassen.

Introduction

After the discovery of flavor oscillations of atmospheric neutrinos by the Kamiokande and Super-Kamiokande experiments, the SNO and KamLAND projects have recently brought evidence of oscillations also in solar neutrinos and in anti-neutrinos generated by nuclear power reactors.

These extraordinary achievements mark a major step ahead in the history of particle physics implying a non-zero neutrino mass and proving the concept of neutrino mixing. At the same time, in astrophysics, the long standing *solar neutrino puzzle* is solved, with the MSW-LMA solution being the accepted scenario. Today (and even more in the years to come) the improved understanding of the neutrino properties allows a new role for these particles as probes in astro-particle physics.

However, the recent discoveries posed a whole new set of questions to be addressed, bringing the neutrino field into a possibly higher state of excitement. For what concerns the intrinsic properties of the neutrino, the absolute neutrino mass scale and its hierarchy are now to be determined. Moreover the nature of the particle (Dirac or Majorana) is still unknown as well as parameters of the flavor mixing matrix such as the angle θ_{13} and the CP-violating phases. A large experimental activity is being planned and developed to answer these questions.

The BOREXino experiment at the Gran Sasso National Laboratory (Italy) is a real time scintillation detector, sensitive to the elastic scattering reaction of neutrinos on electrons. The detector construction has just been completed and the project is approaching the phase of scintillator filling.

The physics goals of BOREXino regard *in primis* the low energy solar neutrino spectroscopy of the ^7Be, *pep* and CNO branches. This will allow testing of the transition between matter-dominated (prevailing at high energy) and vacuum oscillations (dominating at low energy) postulated by the MSW-LMA model, where possibly new physics is to be discovered. This will be the ultimate test of the model and a direct proof of the mass hierarchy between the two eigenstates m_1 and m_2.

In addition, the low energy neutrino spectroscopy performed by BOREXino can contribute to constrain the value of θ_{13} and is particularly important in probing the fundamental thermo-nuclear fusion reactions occurring in the core of the sun:

- The ^7Be flux is poorly determined by current experimental data and its measurement can significantly improve the knowledge on the fundamental *pp* flux, via the luminosity constraint. Moreover it will be an important step to test the SSM energy

production scheme by comparing the prompt luminosity measured in neutrinos with the delayed (10^5 to 10^6 years) photon luminosity.

- The ratio of the *pep* vs. *pp* reactions in the sun is almost model independent, therefore a measurement of the *pep* flux would be as important as a *pp* flux measurement.

- CNO fluxes are experimentally almost undetermined and their measurement would allow the fraction of the solar power generation that occurs due to the CNO-cycle reactions to be established. Moreover the CNO cycle dominates in heavy stars and plays a key role in the age determination of globular clusters.

BOREXino's potential to measure the *pep* monochromatic emission as well as the three CNO fluxes relies on the possibility of tagging the background from ^{11}C produced *in situ* by the residual muon flux with high efficiency. To achieve this goal the outer water Čerenkov detector of the experiment has been designed and constructed not only for a high muon veto performance but also with the aim to reconstruct the tracks of through-going muons, a very important improvement of the ^{11}C tagging strategy.

The broad physics program of the project involves also the detection of neutrinos from the possible explosion of a supernova within our galaxy and the measurement of anti-neutrinos from the earth natural radioactive elements which would give important hints on the geo-physical models of our planet.

The experimental activity

The Ph.D. work presented in this thesis started on 01.11.2001 and was carried out in the BOREXino project, first at the Gran Sasso National Laboratory until June 2003 and thereafter at the Technische Universität in Munich up to the end of 2005.

My main contribution throughout this period has been on the outer detector of the experiment, whose responsibility I shared with a fellow Ph.D student[241] until 2004. In this context it was possible for me to go through all the phases of the detector's construction:

1. Installation of the 208 photomultiplier tubes and Tyvek reflector sheets constituting the detector.

2. Development and commissioning of the custom front-end electronics for PMT signals acquisition.

3. Development and commissioning of the data acquisition software, both the on-crate data transfer functions and the remote event building process within the context of the main DAQ system.

4. Development and commissioning of two different trigger systems and their integration with the main trigger setup.

5. Commissioning of the calibration system and its calibration in Gran Sasso. This system matches the wide dynamic range of the PMTs as Čerenkov light detectors and will improve the track reconstruction of muons.

6. Development of the algorithms for electronics pre-calibration, low level data decoding, calibration tasks and their implementation in the offline reconstruction program.

A parallel involvement throughout the Ph.D studies has been on the data acquisition of the experiment within a small group of collaborators. In this context we put the detector's electronics to work, we developed the online software including the DAQ, the run control tools, the network database, the online monitor and the user interfaces. I am also in charge of the slow control system that manages the electronics of the experiment, which I developed in 2001.

We commissioned and tested the BOREXino detector through a series of *air runs* during the years 2002-2004. These were 9 data taking periods of a few weeks each, with the detector filled just with air, where the photomultipliers, the electronics, the trigger system and the online software could be debugged and brought to their final shape. Among the variety of run conditions explored, all the laser and calibration instruments of the experiment have been brought into operation. In addition small radon and polonium sources have been used for testing physical algorithms (position reconstruction, α/β separation, ...).

In 2004 I proposed the re-design of the offline reconstruction program of the experiment and I co-developed the infrastructure of the new program, named *echidna*. I then founded a working group that now consists of about twenty physicists from the collaboration in charge of different physics algorithms.

While the BOREXino detector was being completed, its reduced scale prototype CTF was constantly taking data to test the scintillator radiopurity levels and the purification strategies for BOREXino. Since 2001 the data analysis has been performed within a working group of collaborators, where I am in charge of the delayed coincidence analyses.

The last months of this work were dedicated to the study of signal and background issues in view of the *pep* and CNO neutrino measurement. In particular the ^{11}C tagging strategy has been investigated in view of BOREXino and proved on the available CTF data. This has led to a measurement of the *in situ* production rate of ^{11}C, currently in course of publication[224].

The thesis layout

Chap. 1 presents a review of the current status of neutrino physics. The experimental results on atmospheric, reactor, accelerator and especially solar neutrino experiments are discussed in the framework of the standard solar model predictions and of the flavor oscillation theory of massive neutrinos. Finally today's standing point and the open questions in particle and astrophysics are summarized in view of the forthcoming experimental projects.

Chap. 2 introduces the BOREXino detector, its design and its experimental setup, it explains in details the physics goals and covers the signal and background issues of the project. A review of the scintillation detection principles is also included.

The design and installation work of the BOREXino outer detector (muon veto system) are described in Chap. 3, after the issue of cosmogenic muons in underground sites and

their detection in BOREXino is introduced.

Chap. 4 reviews the BOREXino read-out electronics and the trigger setup of the experiment with particular emphasis to the outer detector part.

The data acquisition is covered in chap. 5, where the architectural design of the online software is presented.

Chap. 6 reports the complete history of the *air runs*, the analysis of the data sets taken and the results obtained in terms of detector performance and status.

The design principles, the architecture and the physics algorithms of the new offline program for data reconstruction are explained in chap. 7.

Chap. 8 is dedicated to the custom calibration system of the outer detector and especially to its calibration and commissioning in the Gran Sasso laboratory.

The BOREXino prototype detector (CTF) is presented in chap. 9 as well as the analysis of the data from the CTF-3 phase.

In Chap. 10 the *pep* and CNO neutrinos measurement in BOREXino and the strategy for ^{11}C background reduction are discussed. The method is then applied on data from the CTF-3 campaign and the analysis to measure the *in situ* ^{11}C production rate is reported in detail.

Contents

Chapter 1

Neutrino Physics in 2006

Since its first postulation by Pauli in 1930, neutrinos have been protagonists in modern particle physics and astrophysics, with a key role being played by solar neutrinos and the so called *Solar Neutrino Problem* (SNP). This extraordinary puzzle intrigued theoretical and experimental physicists from different countries for over 40 years.

Surely neutrino physics is living a period of exceptional excitement, with new results being published every year from different experimental collaborations. In particular, the recent proof of the leptonic flavor conversion from the SNO collaboration, constitutes at the same time the first piece of evidence of physics beyond the *Standard Model of the Electro-Weak Interactions* and a basic confirmation of the largely discussed *Standard Solar Model*, ultimately pointing out that a solution for the SNP is on the horizon. Instead of diminishing the interest in the field, these results thrilled physicists all over the world in the attempt to answer the many open questions on the nature of neutrinos and on the still unexplored regions of the solar neutrino spectrum.

In year 2002 Raymond Davis and Mastoshi Koshiba, proposers of the early Homestake and KamiokaNDE neutrino experiments respectively, were awarded with the Nobel Prize in Physics for "pioneering contributions to astrophysics, in particular for the detection of cosmic neutrinos", surely a reward to two brilliant personalities, but also an acknowledgement of the efforts of all physicists working in this interesting sector.

1.1 Early neutrino observations

At the beginning of the 20th century, the observation of the continuous electron energy spectrum in β-decays seemed to violate energy conservation as the kinematics of the apparently two bodies decay implied the emission of mono-energetic electrons. At that time, Wolfgang Pauli, unlike Niels Bohr, was refusing to contemplate the possibility of violation of the energy conservation principle[2]. In 1930, he suggested a third "invisible" particle could be produced in the β-decay and carry away the missing energy[1]. For the moment, the particle, still named "neutron", was believed to be a constituent of the nucleus, at that time modeled out of protons and electrons. In the following years, along with Chadwick's discovery of the neutron in 1932 [3], the particle was renamed "neutrino" by Enrico Fermi and its role was revised in his model of β-decay, now commonly

accepted[4]. But with Fermi's theory came also Bethe and Peierls calculations[5] of a neutrino cross-section smaller than $\sim 10^{-44} cm^2$ and the scientific community concluded that there was no practical way to detect neutrinos.

Until the 50s the "undetectable" neutrinos remained an intriguing idea, but after World War II, the initial skepticism of many physicists, slowly started to be abandoned as more and more experimental evidences (e.g. electron capture in Beryllium[7], pion decay[6]) could be explained by the presence of the neutrino.

Thanks to the nuclear chain reactions (1942), developed in the context of the Manhattan project, it seemed that a neutrino source could be available, intense enough to overcome the low cross-section problem.

So, after a few failed attempts, in 1956, at the Savannah River nuclear reactor, finally Cowan and Reines succeeded in measuring (anti)neutrinos[8] via $\overline{\nu}_e + p \rightarrow e^+ + n$ (sec. 1.8). They placed three tanks with organic liquid scintillator[1] at $11m$ from the reactor's core, each of them equipped with 110 photomultiplier tubes. Two inter-layed tanks with a $CdCl_2$ solution were enhancing neutron capture on Cadmium nucleus. Being shielded from cosmic background by a $12m$ cover[2], the detector was able to clearly see a signal of $\sim 3ev/h$. This result, along with Davis' failure to observe the reactors neutrino capture on ^{37}Cl, led also to the neutrino-antineutrino distinction.

Though much lighter than electrons, neutrinos were still postulated to be somewhat massive. In 1957 however, Lee and Yang [9] suggested they could be massless Dirac particles and thus violate parity maximally. This hypothesis was confirmed in 1958 by the experiment at Brookhaven National Laboratory performed by M.Goldhaber et al., that showed clearly how neutrinos were produced with negative helicity[10].

In 1961 Schwartz et al. installed a $10t$ spark chamber at the new Brookhaven Alternating Gradient Synchrotron and demonstrated the presence of muon tracks (rather than electrons) produced by neutrinos emitted in pion decay[11]. Due to its different nature, this particle was labeled "muon neutrino", as opposed to the "electron neutrino" emitted in β-decay.

In the 70s with the discovery of neutral current interactions and the development of the *Standard Model*, neutrinos were ascribed as capable of weak interaction along with other leptons and quarks. Moreover, Kobayashi and Maskawa postulated in their CP-violation theory (1972) one more lepton family[12]. Similarly the four quarks known at the time had to be enlarged to account for one more family. All these new particles have been detected in years with the "tau-neutrino" seen last by the DONUT experiment[13] at Fermilab (2001) in the τ-decay of charmed mesons.

The number of neutrinos able to undergo weak interactions N_ν is constrained by the decay width of the Z^0 boson. The Z^0 can decay into $l\overline{l}$ ($l = e,\mu,\tau$), $q\overline{q}$ ($q = u,d,c,s,b$), $\nu_x\overline{\nu}_x$. Its so-called "invisible width", the partial decay width into neutrino-antineutrino pairs, is given by:

$$\Gamma_{\nu\overline{\nu}} = \frac{1}{12\pi}\frac{G_F}{\sqrt{2}}M_Z^3 N_\nu \tag{1.1}$$

where G_F is the Fermi constant and M_Z is the mass of the Z_0 boson.

[1] A brand new detection technique at that time.

[2] Possibly one of the first *underground* physics experiments.

Parameter	Value
Mass ($M_\odot$)	$1.99 \cdot 10^{33} g$
Radius ($R_\odot$)	$6.96 \cdot 10^{10} cm$
Average Density	$1.41\ g/cm^3$
Core density	$1.52 \cdot 10^2 g/cm^3$
Luminosity ($L_\odot$)	$3.84 \cdot 10^{33} erg/s$
Lum. in ν's	$0.023 L_\odot$
Age	$4.57 \cdot 10^9 y$
Surface temperature	$5.78 \cdot 10^3 K$
Core temperature	$15.7 \cdot 10^6 K$
Heavy elem. mass ab.	0.02
Initial He mass ab.	0.27
Total ν flux on earth	$6.55 \cdot 10^{10} cm^{-2} s^{-1}$

Tab. 1.1: *Main solar parameters. In upright characters results of direct and indirect measurements. In italic parameters calculated by solar models[16].*

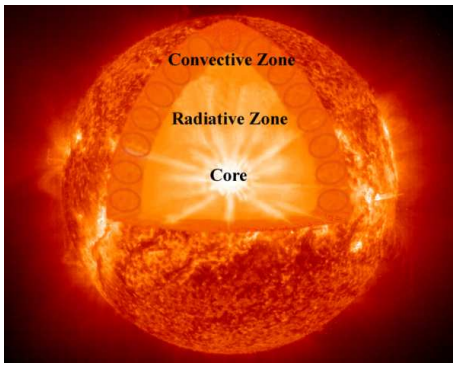

Fig. 1.1: *Sun Cross Section.*

From the measurements done at LEP it was possible to infer $\Gamma_{\nu\overline{\nu}}$ by subtracting from the total decay width the width into all the visible channels[14]. As a result:

$$N_\nu = 2.99 \pm 0.01$$

Cosmological considerations[15] agree on $N_\nu = 3$ for light neutrinos ($\ll 1 MeV$), however there could be a fourth interacting neutrino heavier than $M_Z/2 \sim 45 GeV$ that does not take part in the Z_0 decay.

Neutrinos capable of weak interactions are named *active*, while possible non interacting neutrinos postulated in a few models are named *sterile*[3].

Starting from theoretical studies in the 60s and with experimental activity in the 70s, the new era of solar neutrino physics opened up in the "standard" scenario described so far and, as it will be clear, it led to revolutionary ideas and discoveries.

1.2 The Standard Solar Model

All four fundamental interactions play a role in determining the structure of a star and its evolution along the different phases of its life. A solar model is a theory that models the functioning, in particular the energy production, and the evolution of a star similar to our sun, using knowledge coming from different physics sectors. The sun offers privileged observational evidences to our eyes and as a consequence many parameters are already known to a reasonable accuracy (tab. 1.1).

From geological studies on chondrites (objects as old as the solar system), the sun age could be estimated to $\sim 4.6 \cdot 10^9 y$[16]. Excluding a short initial phase, one can assume that since the entrance in the main sequence of the Herzsprung-Russel diagram, the star

[3]Sterile neutrinos, obviously, are not tied to the Z_0 decay width constraint.

has kept a luminosity approximately of the same order. This allowed the ruling out of the theories dominant until the late XIX century, enforcing chemical or gravitational energy production (the gravitational time scale is of only $3 \cdot 10^7 y$).

With the discovery of the nucleus and the mass-energy equivalence theories, the solar energy production started to be interpreted in terms of nuclear reactions[17]. In the following decades and especially in the last 30 or 40 years a great effort has been made to produce solar models, i.e. the iterative resolution of a set of state equations describing a few equilibrium assumptions within the boundary conditions of the measured sun parameters (tab. 1.1). The equilibrium conditions assumed are:

Hydrostatic Equilibrium: in a stable star the gravity force inside the star must be balanced by the outward pressure of the particle gas.

Thermal Equilibrium: the net energy flux must correspond to the energy produced in the nuclear reactions. Temporary violations of this equilibrium condition are allowed and are balanced by gravitational energy variations (contractions or expansions).

Radiative Equilibrium: the total luminosity of the star depends only on the radiative transport from core to surface with the radial temperature gradient and the medium opacity playing a major role in the model.

Convective Equilibrium: as a consequence of radiative instabilities, convective motions may be generated inside a layer which reduce its temperature gradient and mix the material. This is the only mechanism by which isotopic abundances may be varied, apart from nuclear reactions.

As it will be explained below, all reaction chains contributing to the energy balance imply fusion of 4 protons in a helium nucleus and therefore the conversion of 2 protons into 2 neutrons with consequent emission of 2 electron neutrinos.

The sun is very opaque with respect to electromagnetic radiation, allowing us to observe only the fraction coming from the surface layers. For this reason neutrino emission in nuclear reactions was initially considered of great astrophysical interest as it made possible:

> "... to look inside a star and probe directly the assumption on energy generation in stars" [J.Bahcall e R.Davis, 1964].

Since then, after the Homestake experiment (sec. 1.4.1) reported its first flux measurement visible on our planet, this perspective has reversed. On the one hand there was the confirmation of neutrino production in the sun, but on the other hand the experimental measurements indicated a clear deficit in comparison to the theoretical expectations, opening to what is commonly named as the *Solar Neutrino Problem* (SNP).

The latest model currently assumed as the reference work on the subject is dated 2005; it is due to J.N. Bahcall and A.M. Serenelli [23] and is named BS05(OP). However the previous version BP04 by J.N. Bahcall and M.H. Pinsonneault [22] dated 2004 is still widely referenced. In this chapter the term *Standard Solar Model* (SSM) will refer

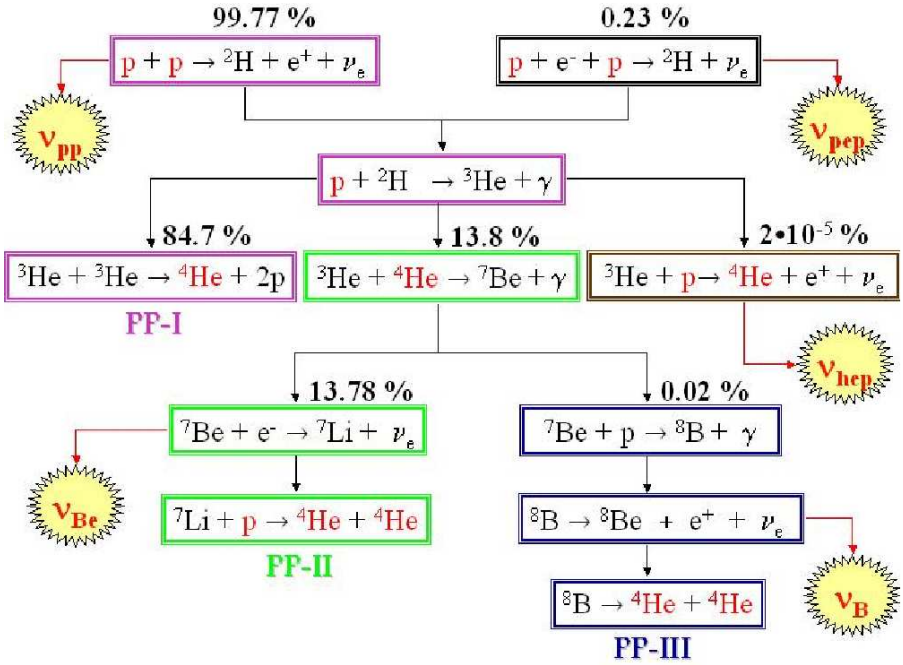

Fig. 1.2: *The* pp *chain reactions.*

indistinctly to either BS05(OP) or to BP04. The improvements in the BS05(OP) version are reviewed in [24] and will be mentioned in this chapter where they apply.

1.2.1 Nuclear Reactions in the sun

Those that combined the pioneer efforts of many astrophysicists, among which Atkinson and Houtermanns[18], in an organic theory of nuclear reactions in the sun core, were G.Gamow[19] and especially Hans Bethe [20]. Bethe, already at the end of the 30s understood the importance of weak interactions in hydrogen fusion processes.

Two reaction sequences sustain sun-like star luminosity, the *pp* chain and the CNO cycle and, as already mentioned above, they both in essence consist in a fusion $4p \longrightarrow {}^4He$. The CNO cycle is dominant in stars larger than a few solar masses where the core is a convective zone with a higher abundance of "heavy" elements. In stars like the sun or smaller the convective zone is at the surface (fig. 1.1) and the core is rather poor in elements like carbon. As a result the *pp* chain is largely dominating and accounts for 98.4% of the energy production. However the uncertainty is very large and experimental measurement of this ratio is one of the *desiderata* of today's solar astrophysics (sec. 1.11.2).

The *pp* chain

The first step of these weak interactions that fires the whole process, can be one of the following:

$$p + p \longrightarrow {}^2H + e^+ + \nu_e \tag{1.2}$$
$$p + e^- + p \longrightarrow {}^2H + \nu_e \tag{1.3}$$

where the latter, a three body interaction, is obviously disfavored to the level of 0.24% with respect to the former. This ratio, in spite of a minor model dependency, is approximately fixed.

This first step, as it is a weak interaction process, occurs at a lower rate compared to the following electromagnetic and strong reactions, constituting the bottleneck of the chain and determining its overall rate.

Deuterium resulting from eq. 1.2 (or eq. 1.3) quickly interacts with an additional proton:

$$p + {}^2H \longrightarrow {}^3He + \gamma \tag{1.4}$$

In this way deuterium equilibrium concentration remains low, making reactions like ${}^2H + {}^2H \longrightarrow {}^3He + p$ fully negligible.

At this point ${}^3He$ can undergo three different processes:

$${}^3He + p \longrightarrow {}^4He + e^+ + \nu_e \tag{1.5}$$
$${}^3He + {}^4He \longrightarrow {}^7Be + \gamma \tag{1.6}$$
$${}^3He + {}^3He \longrightarrow {}^4He + 2p \tag{1.7}$$

Reaction 1.5, yielding the rare *hep* neutrinos, is also a weak interaction and is strongly disfavored in competing with the other two.

Reaction 1.6 dominates in primordial star stages when the ${}^4He$ concentration is higher, but as soon as ${}^3He$ accumulates significantly reaction 1.7 takes over, thanks to its high cross section and this is the equilibrium condition of a star after entering main sequence. This is the first branch of the *pp* chain, named PP-I.

When, instead, we look at the fate of ${}^7Be$ produced in eq. 1.6, two new scenarios are possible:

Branch PP-II

$${}^7Be + e^- \longrightarrow {}^7Li + \nu_e \tag{1.8}$$
$${}^7Li + p \longrightarrow {}^4He + {}^4He \tag{1.9}$$

Branch PP-III

$${}^7Be + p \longrightarrow {}^8B + \gamma \tag{1.10}$$
$${}^8B \longrightarrow {}^8Be + e^+ + \nu_e \tag{1.11}$$
$${}^8Be \longrightarrow {}^4He + {}^4He \tag{1.12}$$

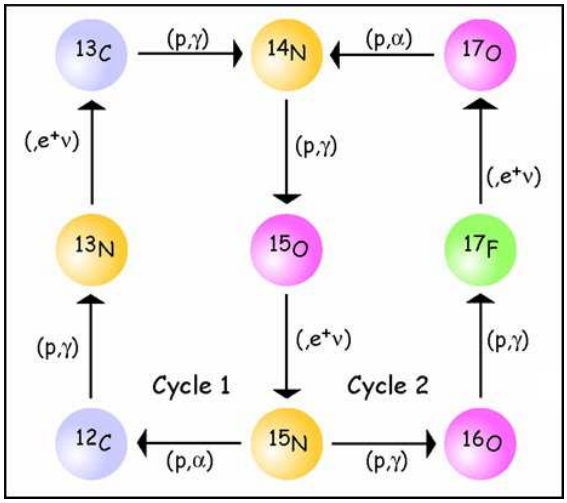

Fig. 1.3: *The CNO cycle reactions.*

In all three cases the net *pp* chain yield is identical:

$$p + p + p + p \longrightarrow {}^4He + 2e^+ + 2\nu_e \tag{1.13}$$

The Q($26.73MeV$) value of the net reaction is identical, however, the kinetic energy carried by neutrinos is different and therefore also the remaining fraction $Q^* = Q - \overline{q_\nu}$ contributing to sun energy balance.

The first neutrino produced in the *pp* chain is always[4] a ν_e^{pp} from eq. 1.2, while the second one is characteristic of the specific chain branch:

PP-I another neutrino from *pp* (eq. 1.2): ν_e^{pp}.

PP-II a neutrino from electron capture on ${}^7Be$ (eq. 1.8): ν_e^{Be}.

PP-III a neutrino from β^+ decay of ${}^8B$ (eq. 1.11): ν_e^{B}.

The branching ratios of the three terminations depend on solar parameters as well as on nuclear cross-sections which are not always well known in the relevant energy (sec. 1.2.1) region. In fig. 1.2 the most recent SSM predictions are shown.

The CNO cycle

The CNO cycle involves the three elements whose chemical symbols compose its name: Carbon, Nitrogen and Oxygen. As it can be seen in fig. 1.3 the cycle is actually composed by two sub-cycles, the CN cycle and the NO cycle sharing the reaction:

$${}^{14}N + p \longrightarrow {}^{15}O + \gamma \tag{1.14}$$

which is also the slowest reaction determining the overall cycle rate and its competitive behavior with the *pp* chain.

[4]With the exception of *pep* neutrinos (eq. 1.3) accounting for 0.23%.

The excited ^{16}O produced in proton capture on the ^{15}N has a higher branching ratio to decay into a ^{12}C and an α particle rather than to de-excite radiatively. For this reason the weight of the NO cycle is fixed to $4 \cdot 10^{-4}$ with respect to the CN counterpart.

The overall cycle balance for both CN and NO cycles can be written as:

$$^{12}C + 4p \longrightarrow {}^{12}C + {}^{4}He + 2e^{+} + 2\nu_e \tag{1.15}$$

that is the same as the *pp* chain (eq. 1.13), mediated by a ^{12}C.

Astrophysical S-factors calculations predict that CNO reactions are intrinsically very likely to occur but are inhibited by high Coulomb barriers. For this reason there exists a critical temperature above which the CNO cycle dominates on the *pp* chain. For a star with a chemical composition similar to the sun (*population-I* stars) this temperature would be $\sim 18 \cdot 10^6 K$, which exceeds the central solar temperature by $\sim 13\%$ (tab. 1.1). It is easy to imagine how slight model variations yielding a higher core temperature could easily change the interplay of the *pp* and CNO sequences.

1.2.2 Solar neutrino fluxes

The SSM has proven to be able to make reliable predictions in the frame of stellar evolution mechanism like the mass-luminosity relationship, the star evolution in the Herzsprung-Russel diagram and has shown a very good agreement with helioseismology measurements (sec. 1.2.4).

In terms of neutrino emissions the model calculates fluxes and spectra. Assuming the fraction of energy subtracted by neutrinos in the sun core is small[5] we can take $Q^* \simeq Q \simeq 26MeV$ as the approximate energy of a $4p \rightarrow {}^{4}He$ reaction, where two neutrinos are produced. It is immediately possible to predict roughly the overall neutrino flux on the earth:

$$\Phi_{tot} \simeq 2 \times \frac{L_\odot}{Q^*} \frac{1}{4\pi d^2} = 6.56 \times 10^{10} cm^{-2} s^{-1} \tag{1.16}$$

where d is the average sun-earth distance and $L_\odot$ is the measured solar luminosity. While many previsions of the model have large uncertainties or can be easily modified by playing with boundary conditions or model assumptions, the above relation is a constraint from which it is very difficult to escape and is known as *The Luminosity Constraint*[25].

The predicted fluxes for the single solar emissions are reported in tab. 1.2 together with the neutrino energies, while fig. 1.4 shows the calculated spectra. Obviously β^+ decays that have three particles in the final state yield a continuous spectrum up to $Q - 2m_{e^+}c^2$, while other weak two-bodies decays produce a monochromatic line. In the case of ^{7}Be, two lines are present as in 10% of the cases the ^{7}Li is produced in a $487keV$ excited state, rather than in the ground state.

Two are the main sources of theoretical uncertainties considered by authors in neutrino flux estimations:

1. Uncertainties on solar input parameters namely: radiative opacity, diffusion coefficient, luminosity and abundance of heavy elements at the surface.

[5] In fact at the level of $\sim 3\%$.

2. Uncertainties on the nuclear cross sections involved in the *pp* chain and the CNO cycle (sec. 1.2.3).

Experimental activity in both astrophysical observations and nuclear physics measurements has been very high in the last decades and has contributed significantly to the model evolution. Nuclear aspects will be considered in the next section, while among the astrophysical uncertainties the question related to heavy element abundance is clearly dominating (tab. 1.3). The reference abundances (1998) are reported in [26], but very recent (2005) measurements from the same group [27] show lower values. These latest measurements, in principle more accurate, if introduced in the model, produce inconsistencies with helioseismology results (sec. 1.2.4). Model BS05(OP) has therefore decided to stick to old values, but the controversy is open[24].

Looking at the spectrum of fig. 1.4, it is easy to see how the ^8B neutrinos are the easiest to observe, because of their high energy, but they are at the same time the ones whose predicted flux is less intense and most poorly determined. On the other hand, measuring *pp* neutrinos would probe the model to a much higher extent, as they make up for 98% of the overall flux with a 1% uncertainty, but their low energy poses the most critical experimental problems to their detection.

1.2.3 Nuclear cross sections

The knowledge of the nuclear cross sections involved in the *pp* and CNO chains[28] is an intriguing experimental challenge for nuclear physicists, as the result of their work heavily influences the SSM predictions.

Given two nuclear species Z_1, Z_2 in Maxwellian equilibrium with abundances n_1, n_2 and relative velocity v, the rate of their reaction is proportional to:

$$r_{12} \propto n_1 n_2 \langle \sigma v \rangle_{12} \propto n_1 n_2 T^{-\frac{3}{2}} f_0 \int_0^\infty S(E) e^{\left(-2\pi \frac{Z_1 Z_2 \alpha}{v}\right)} e^{\left(-\frac{E}{kT}\right)} dE \qquad (1.17)$$

where the first exponential is the Gamow factor for Coulomb barrier penetration and the second one reflects the Maxwell-Boltzmann velocity distribution (natural units assumed). f_0 is a correction for the electron screening effect which is different for laboratory measures compared to the solar plasma where atoms are mostly ionized. The energy dependence of the cross section has been left only in the so-called *astrophysical S-factor* $S(E)$, a quantity that for non-resonant reactions can more easily be modeled over an energy range that spans several orders of magnitude. The expansion of $S(E)$ in Taylor series yields the most probable energy for the reaction $E_0(Z_1, Z_2, T, \mu)$ [29], named the *Gamow Peak*.

In many cases, however, the Gamow Peak lies at energies which are too low for a direct laboratory measure, due to the high Coulomb barrier suppression. Therefore S-factors have often been extrapolated from higher energy measurements, often leaving the door open to speculative hypotheses on possible low energy resonant effects.

A large experimental activity has recently been carried out to measure the S-factors directly at Gamow Peak energies and to cover those reactions which are still poorly determined. Among the others, a special mention deserves the LUNA[6] project, an underground

[6]Laboratory for Underground Nuclear Astrophysics.

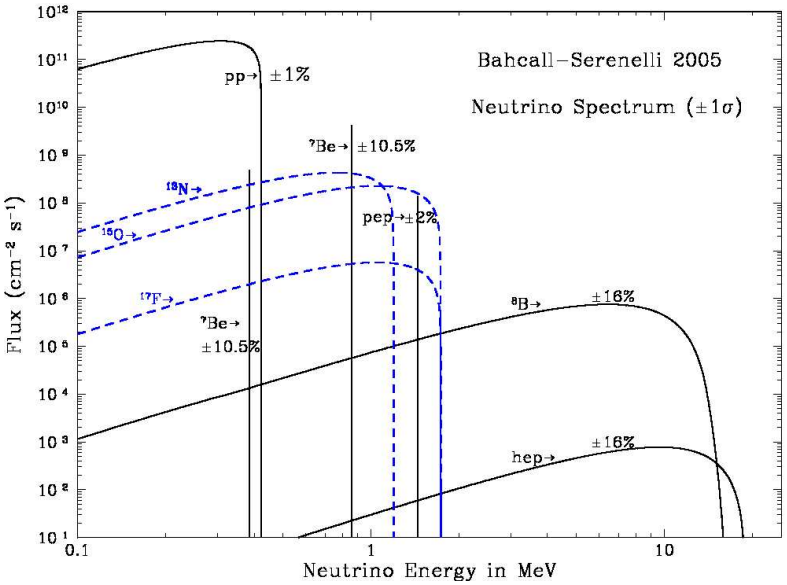

Fig. 1.4: *Solar neutrino spectrum predicted by* SSM *BS05(OP) [21].*

Source	$E_\nu(MeV)$	Flux $(10^{10}cm^{-2}s^{-1})$	err (%)
pp	$0 \rightarrow 0.42$	5.99×10^{0}	1.0
pep	1.44	1.42×10^{-2}	1.7
hep	$0 \rightarrow 18.8$	7.93×10^{-7}	15.5
^{7}Be	0.86(90%) 0.38(10%)	4.84×10^{-1}	10.5
^{8}B	$0 \rightarrow 14.06$	5.69×10^{-4}	16.3
^{13}N	$0 \rightarrow 1.2$	3.07×10^{-2}	$^{+31.2}_{-28.1}$
^{15}O	$0 \rightarrow 1.7$	2.33×10^{-2}	$^{+33.2}_{-28.8}$
^{17}F	$0 \rightarrow 1.7$	5.84×10^{-4}	52.2

Tab. 1.2: *Solar neutrino fluxes predicted by* SSM *BS05(OP) [23].*

Source	S_{33}	S_{34}	S_{17}	$S_{^{14}N}$	Opac	Diff	$L_\odot$	Z/X
pp	0.002	0.005	-	0.002	0.003	0.003	0.003	0.010
pep	0.003	0.007	-	0.002	0.005	0.004	0.003	0.020
hep	0.024	0.007	-	0.001	0.011	0.007	-	0.026
^{7}Be	0.023	0.080	-	-	0.028	0.018	0.014	0.080
^{8}B	0.021	0.075	0.038	0.001	0.052	0.040	0.028	0.200
^{13}N	0.001	0.004	-	0.118	0.033	0.051	0.021	0.332
^{15}O	0.001	0.004	-	0.143	0.041	0.055	0.024	0.375
^{17}F	0.001	0.004	-	0.001	0.043	0.043	0.057	0.026

Tab. 1.3: *Principal nuclear (columns 2-5) and astrophysical (columns 6-9) sources of uncertainties in the neutrino fluxes predicted by the model BP04[22]. Data for model BS05(OP) have not been released yet.*

facility with two accelerators which is performing especially the nuclear measurements of solar interest.

The main focuses of the experimental activity within the SSM are the following[29]:

pp* vs. *pep These reaction cross sections are too small to be measured in laboratory, but they are both well constrained by theoretical considerations.

$\boldsymbol{d(p,\gamma)He}$ (eq. 1.4).

Recently measured at LUNA[30] covering the Gamow peak ($2.5keV$). The reaction was confirmed to be so fast that any uncertainty in the cross section has no impact on the *pp* chain mechanism.

$\boldsymbol{S_{33}}$, $\boldsymbol{^3He(^3He,2p)^4He}$ **vs.** $\boldsymbol{S_{34}}$ $\boldsymbol{^3He(^4He,\gamma)^7Be}$ (eq. 1.7 and 1.6).

These two competing S-factors determine the branching ratios PPI vs. PPII+PPIII of the *pp* chain and are therefore of dramatic importance in flux predictions.

S_{33} was recently measured at the LUNA accelerator[31], with a good precision and down to the Gamow Peak energy ($\sim 21keV$)[7].

S_{34} is unfortunately one of the least known in the whole SSM[28]. Experiments based on direct γ capture and those based on ^7Be decay activity show different results, indicating possible non-understood systematics in at least one of the two methods. The result is a $\sim 20\%$ uncertainty that contributes 8% to both ^7Be and ^8B errors (tab. 1.3). Major activity is ongoing in the nuclear community to address this issue.

$\boldsymbol{S_{17}}$, $\boldsymbol{^7Be(p,\gamma)^8B}$ (eq. 1.10).

This S-factor determines alone the PPII vs. PPIII branching ratio, as the competing reaction is the well known weak process of electron capture on ^7Be[32]. S_{17} knowledge still relies on extrapolations and though it was improved considerably in years[33] it is still afflicted by a 3% systematics. Its contribution to the ^8B flux uncertainty is today decreased to 4%.

$\boldsymbol{S_{14}}$, $\boldsymbol{^{14}N(p,\gamma)^{15}O}$ (eq. 1.14).

It is the slowest reaction of the CNO cycle and therefore its rate determines the ratio CNO vs. *pp*-chain. Until recently, S_{14} was always inferred by extrapolations from measurements done at higher energies, but in 2004 the LUNA collaboration performed a direct measurement[34] and found a surprising result which is smaller by a factor ~ 2, cutting by half all CNO neutrino flux estimates[8].

The first four columns of tab. 1.3 show the impact of the S-factor knowledge on neutrino flux predictions.

[7] This allowed the resonance-based astrophysical solutions proposed to explain the Homestake result (sec. 1.4.4) to be ruled out.

[8] In addition to astrophysical consequences, like increasing the age of the globular clusters by $\sim 0.7Gy$.

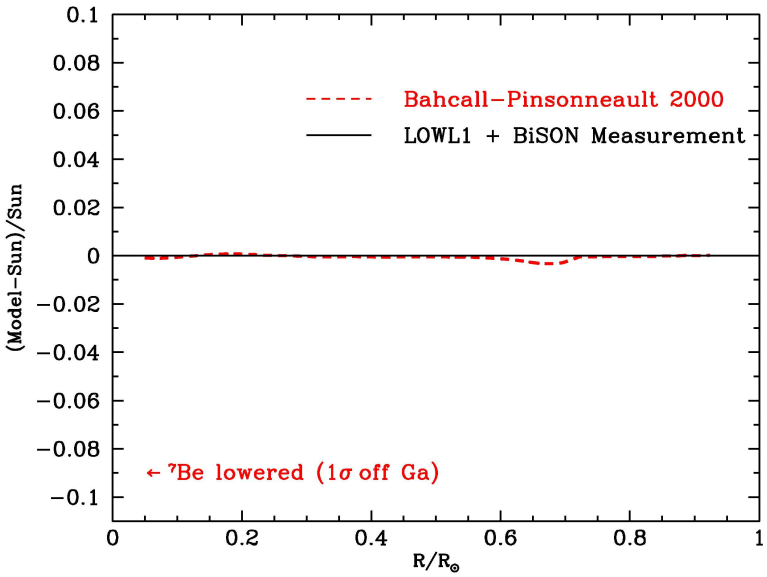

Fig. 1.5: *Relative discrepancy between sound speed foreseen by* SSM *and inferred by helioseismological observations[21]. The arrow shows the disagreement required to justify measured neutrino fluxes.*

1.2.4 Helioseismology

The hydrostatic equilibrium of the star is perturbed by pressure waves originating from the huge convective motions of the crust and propagating inward through a density gradient. The wave fronts, curved by continuous refraction, are trapped between a minimal radius and the surface and upon self-interference lead to stationary waves. These become visible at surface as modulations, whose frequency has been measured with a $1/10^5$ precision. The number of inferred solar parameters is quite large and the impact on solar models discrimination has been dramatic, leading to the general acceptance of the SSM. The best known is the calculated sound speed as a function of solar radius (fig. 1.5). As $c^2 \propto T_c$, a sound speed below predictions could have justified the apparent absence of the ^7Be flux in the Gallium experimental results (sec. 1.4.4), but, as it can be seen, this was clearly ruled out by data.

References [35, 36, 37] give a description of the principle, a complete recent review of the model and an update encompassing the latest experimental results.

1.3 Solar Neutrino Detectors

The very low cross section of neutrinos which is the precious characteristic that allows them to escape undisturbed from the sun core, also makes their detection a complex challenge. Different experimental designs are possible with different advantages and disadvantages. The main issues which have to be considered in the design of a neutrino detector are:

- *Large target mass.* To obtain a signal of at least a few events per day a target mass above ca. $100t$ must be considered.
- *Underground location.* The cosmic ray induced showers would be an unbearable background for a neutrino detector on the earth's surface. Deep underground sites insure the proper shelter. The coverage of a site is usually scaled for the specific rock density and expressed in *meters of water equivalent (m.w.e.)*.
- *High material radio-purity.* The target mass as well as any construction material must be carefully selected and/or purified to very high levels, to guarantee a low background from natural radioactivity. Shielding from site natural radioactivity must also be adequate.
- *High detection efficiency.* Dealing with low neutrino interaction rates inefficiencies must be absolutely minimized.
- *Signal characteristic tag.* The signal needs to be extracted from residual background events through some distinctive characteristic. A strong tagging, for example a coincidence with a subsequent event, allows privileged background rejection, while less efficient statistical subtraction from the energy spectrum has to be considered in the absence of a clear tag.

Keeping in mind the above considerations, the neutrino detectors can be approximately classified in two large categories: radiochemical experiments based on neutrino capture reactions on nuclei and real time detectors, often based on neutrino elastic scattering on electrons[9].

1.3.1 Radiochemical Detectors

Radiochemical experiments were proposed by Bruno Pontecorvo[41] in 1946 and are based on the reaction:

$$\nu_e + {}^{A}_{Z}Y \longrightarrow {}^{A}_{Z+1}Y + e^- \tag{1.18}$$

where the minimum required neutrino energy, given by the capture Q value, sets the detector energy threshold.

The expected signal rate per target nuclei can be predicted in the SSM as:

$$R = \sum_i \Phi_i \langle\sigma\rangle_i \tag{1.19}$$

where Φ_i are the neutrino fluxes and $\langle\sigma\rangle_i$ the relative averaged cross section for any neutrino emission of the spectrum above the energy threshold. A convenient unit has been defined for R, the SNU (*Solar Neutrino Unit*, $1SNU = 10^{-36}$ events per second per target nucleus).

[9] However in SNO (sec. 1.7.2) neutrino interactions on deuterium are exploited in a real time detector and the LENS project (sec. 1.12) is performing R&D for a real time detector using neutrino capture on ${}^{1}15In$.

The predicted rate has to be compared to its detected value:

$$R = \frac{n}{N} = \frac{n}{\frac{MX_A N_{Av}}{A}} \tag{1.20}$$

where n is the observed rate and where N, the number of target nuclei, is expressed in terms of the target mass M and X_A the relative isotopic abundance of ${}^A_Z Y$,

The detection is based on the fact that the nuclide ${}^A_{Z+1}Y$ will decay back to the stable ${}^A_Z Y$. The build up law of the ${}^A_{Z+1}Y$ will then be:

$$N(t) = n\tau(1 - exp(-t/\tau)) \tag{1.21}$$

Periodically a chemical extraction of the produced nuclei is performed with the help of some carrier gas. The decay activity of the extracted material is then measured in proportional counters for a few life times, yielding $N(t)$ at the time of extraction.

There are two possible background sources:

Exposure time background. Other reactions that compete with neutrino capture to the formation of the ${}^A_{Z+1}Y$ nuclide. These are mostly (p, n) reactions due to secondary protons originating from cosmic muons, fast fission neutrons or residual radioactive contaminants of the target ($(\alpha, p), (n, p)$ reactions).

Counting time background. Background from natural radioactive contaminants in or close to the proportional counters active volume as well as ${}^{222}Rn$ diffusing in it.

In radiochemical experiments all information about the neutrino interactions, like time, energy, position and direction, is lost. The only available information is the integral in the exposure time of the spectral portion above threshold.

In summary the parameters on which a good radiochemical detector is to be designed are:

1. High relative abundance of the sensitive isotope.
2. Relatively easy and fast extraction chemistry.
3. Mean life in the range $[1d, 1y]$ to have a clear signature without loosing much in the extraction operation.
4. Nuclear capture cross section known with a good accuracy.

In addition, of course, the availability at a reasonable cost of the target mass is required.

1.3.2 Electron Scattering Detectors

The most common alternative to the neutrino capture on nucleus for neutrino detection is the use of the signal due to the electron diffused in the elastic scattering reaction:

$$\nu_x + e^- \longrightarrow \nu_x + e^- \tag{1.22}$$

where x can be e, μ or τ.

The cross section of eq. 1.22 is known with great accuracy[39] from electroweak theory and is an advantage over the intrinsic indetermination of the nuclear matrix elements involved in the cross-section calculation for reactions 1.18.

The differential cross section can be written as[40]:

$$\frac{d\sigma_\nu}{dT_e}(T_\nu, T_e) = \frac{\sigma_e}{m_e}\left[g_l^2 + g_r^2\left(1 - \frac{T_e}{T_\nu}\right)^2 - g_l g_r \frac{m_e T_e}{T_\nu^2}\right] \tag{1.23}$$

with

$$g_l = \pm 0.5 + \sin^2\theta_w \qquad g_r = \sin^2\theta_w \qquad \sigma_e = \frac{2G_F^2 m_e^2}{\pi\hbar^4} = 88.1 \cdot 10^{-46} cm^2$$

where θ_w is the weak mixing angle.

In the g_l definition the positive and negative sign describe ν_e and ν_μ, ν_τ scattering respectively. The distinction arises from the fact that while ν_e scattering can occur for neutral current as well as charged current interaction, for ν_μ and ν_τ only the former is allowed.

Taking $\sin^2\theta_w \simeq \theta_w = 0.23$:

$$\frac{d\sigma_{\nu_e}(T_\nu, T_e)}{dT_e} = \quad 101 \quad \left[1 - 0.18\left(\frac{T_e}{T_\nu}\right) + 0.09\left(1 - \frac{1.62}{T_e}\right)\left(\frac{T_e}{T_\nu}\right)^2\right] \tag{1.24}$$

$$\frac{d\sigma_{\nu_\mu,\nu_\tau}(T_\nu, T_e)}{dT_e} = \quad 21.7 \quad \left[1 - 0.84\left(\frac{T_e}{T_\nu}\right) + 0.42\left(1 - \frac{1.60}{T_e}\right)\left(\frac{T_e}{T_\nu}\right)^2\right] \tag{1.25}$$

expressed in $10^{-46} cm^2 MeV^{-1}$. It's easy to see[39] how for example:

$$\left.\frac{\sigma_{\nu_\mu,\nu_\tau}}{\sigma_{\nu_e}}\right|_{E_{pp}} \simeq \frac{1}{3.7}, \qquad \left.\frac{\sigma_{\nu_\mu,\nu_\tau}}{\sigma_{\nu_e}}\right|_{E_{^7Be}} \simeq \frac{1}{4.7}, \qquad \left.\frac{\sigma_{\nu_\mu,\nu_\tau}}{\sigma_{\nu_e}}\right|_{E_{^8B}>5MeV} \simeq \frac{1}{6.6} \tag{1.26}$$

where $5MeV$ corresponds roughly to the threshold of Super-KamiokaNDE (sec. 1.7.1) and SNO detectors (sec. 1.7.2). As we will see, this ratio has important consequences in the determination of the signal visible to detectors enforcing reaction 1.22.

The electron recoil direction is closely related to the incoming neutrino track and, if the detection technique allows it to be observed, it can be a confirmation for the solar neutrino origin and can be used to reject isotropic background events. Information on the event time can allow the investigation of short-term signal modulations, like a possible day-night asymmetry (sec. 1.5).

In addition the neutrino energy can be inferred from the measured energy of the recoil electron. In this way real time experiments can perform neutrino spectroscopy and disentangle different flux contributions.

The recoil electron detection technique can be either of the following[10]:

[10]The upcoming ICARUS experiment [112] uses a third detector concept: a liquid argon *Time Projection Chamber* (TPC) (sec. 1.9.3).

Water Čerenkov detectors. The Čerenkov light emission occurs within a known angle to the electron path, allowing event track reconstruction. Due to the background conditions and the limited light yield, running experiments achieve a threshold of about $\sim 5MeV$, being therefore sensitive to ^8B ν's only.

Organic liquid scintillator detectors. They achieve ~ 50 times higher light yield and can therefore attempt sub-MeV spectroscopy. The energy threshold of the order of $\sim 200keV$ is determined by the intrinsic ^{14}C. No track reconstruction is possible as the scintillation process is isotropic.

1.4 First Generation Solar Neutrino Experiments

In this section the experiments that gave birth to the SNP are reviewed. Homestake, KamiokaNDE, GALLEX/GNO and SAGE can be regarded as *first generation experiments*, in the sense that they were conceived to understand whether the SNP was an astrophysical issue or a hint for new physics.

1.4.1 Homestake

Homestake was the pioneer experiment in the field of solar neutrino detection. The experiment was set up by Ray Davis and his collaborators[42] in 1970 in the Homestake mine (South Dakota, USA) and operated continuously until 1996. Ray Davis was awarded the Nobel Prize in physics in 2002 for opening the window of ν-astronomy.

The exploited nuclear capture reaction was:

$$\nu_e + {}^{37}Cl \longrightarrow {}^{37}Ar + e^- \tag{1.27}$$

with an $813keV$ energy threshold.

The target, $133t$ of ^{37}Cl was dissolved in $615t$ of C_2Cl_4.

The ^{37}Cl satisfies well all requirements of radiochemical experiments:

1. ^{37}Cl relative abundance is 24.2%.
2. Argon, as noble gas, can be easily separated.
3. ^{37}Ar mean life time is 50.5 days.
4. The emission of a $2.82keV$ auger electron after the decay, yields a clear signal and a 95% detection efficiency.
5. The cross section, in spite of being dominated by excited states transitions, is known to a good accuracy ($\sim 10\%$).

The expected signal made of ^8B, ^7Be and CNO neutrinos was:

$$R_{th} = (7.7^{+1.2}_{-1.0})SNU \tag{1.28}$$

The result of 26 years of data taking was instead[43]:

$$R_{exp} = (2.56 \pm 0.16[stat] \pm 0.15[syst])\, SNU = (2.56 \pm 0.22)\, SNU \tag{1.29}$$

This difference gave birth to the SNP.

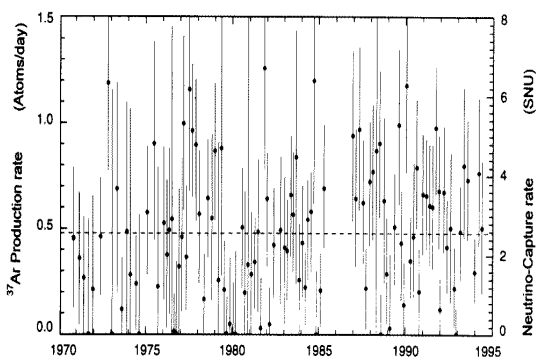

Fig. 1.6: *Homestake experimental results in 25 years of data taking[43]. Every point represents a run with a 1σ error. Interaction rate is given in daily produced ^{37}Ar nuclei (left) and in SNU (right). Dashed line is the overall average rate.*

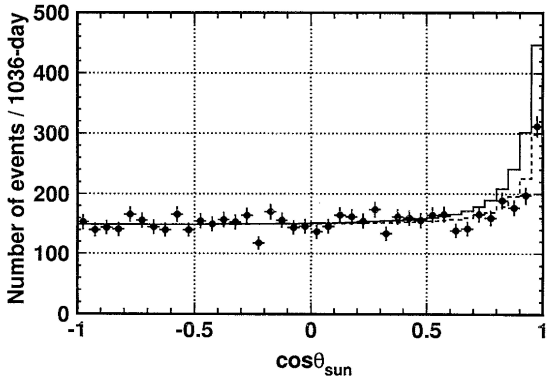

Fig. 1.7: *Angular distribution of KamiokaNDE neutrino events, the first evidence of neutrinos coming from the sun. The solid line is the SSM prediction, while the dashed line is the best fit to data[44].*

1.4.2 KamiokaNDE

KamiokaNDE (*Kamioka Nucleon Decay Experiment*) was the second experiment to measure solar neutrino fluxes and it was the first in real time and using Čerenkov light detection.

The detector was a cylindrical tank $15,6m$ in diameter and $16m$ high, holding $2142t$ of water watched by 948 large photomultiplier tubes. It was originally constructed and operated until 1985 as a nucleon decay experiment. Then it was converted into a neutrino detector purifying the water and adding an external tank acting as muon veto detector. It was operated in this frame from 1987 to 1995[11] with an energy threshold of $7.5MeV$ and a fiducial volume of $680t$.

The predicted flux, fully made of ^8B neutrinos was:

$$\Phi_{th}(\nu_e^{^8B}) = (5.15^{+0.98}_{-0.72}) \cdot 10^6 cm^{-2} s^{-1} \tag{1.30}$$

while in 2079 days of data taking, the measured rate was ~ 0.4 events/d [44] corresponding to a ν_e-flux::

$$\Phi_{exp}(\nu_e^{^8B}) = (2.82 \pm 0.19[stat] \pm 0.33[syst]) \cdot 10^6 cm^{-2} s^{-1} \tag{1.31}$$

KamiokaNDE's zenith angle distribution showed that the signal was clearly coming from the sun (fig. 1.7), giving the first direct evidence of a solar neutrino flux.

1.4.3 The Gallium experiments

After an idea of Kuz'min dated 1966[45] a few physicists of the Homestake experiment (one of them was Ray Davis), made the proposal[46] for a radiochemical experiment

[11] After the startup of its evolution Super-KamiokaNDE (sec. 1.7.1) in the middle 90s, the detector was de-commissioned and the cave now hosts the KamLAND experiment (sec. 1.8.3).

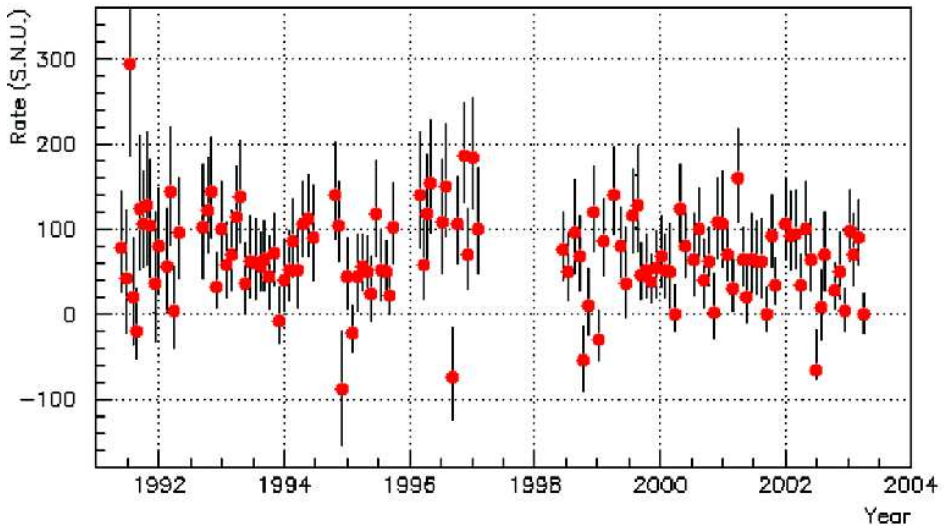

Fig. 1.8: *Final results for GALLEX and GNO experiments (1991 - 2003)[49].*

based on the nuclear capture reaction:

$$\nu_e + {}^{71}Ga \longrightarrow {}^{71}Ge + e^- \tag{1.32}$$

whose energy threshold of $233keV$ makes it sensitive to the most important and still undetected ν_e^{pp}.

Moreover the isotopic abundance of ${}^{71}Ga$ is relatively high (39.9%), ${}^{71}Ge$ decays with a mean life of $11.5d$ and can be chemically extracted within $1d$. All these advantages make gallium a valuable target for a radiochemical experiment. However the presence of transitions to excited states complicate the knowledge of the reaction cross-section and requires calibrations with neutrino sources.

GALLEX

GALLEX (*GALLium EXperiment*) construction started in 1988. The target mass was $30.3t$ of gallium in $100.9t$ 8-molar solution of $GaCl_3$ in HCl in a tank in the Gran Sasso National Laboratory (Italy).

The signal sought in the proportional counters after the monthly extraction (*solar run*) was, as in Homestake, made of de-excitation Auger electrons and X-rays of the product ${}^{71}Ga$ at $10.4keV$ (K-shell) and $\sim 1.2keV$ (L-shell). Background rejection was enforced with a maximum likelihood analysis on the pulse rise time and achieved an efficiency above 97%.

In 5 years of data taking (65 solar runs) between 1991 and 1997, GALLEX provided the following final result[47]:

$$R_{exp} = (77.5 \pm 6.2[stat]^{+4.3}_{-4.7}[syst])SNU \tag{1.33}$$

to be compared with the significantly higher rate foreseen by SSM:

$$R_{th} = (131^{+12}_{-10})SNU \tag{1.34}$$

In the years, different independent calibrations have been performed, including one with a neutrino source of ^{51}Cr of $\sim 65PBq$ and tests of the chemical extraction plant trying to spot possible inefficiencies. All calibrations attested the reliability of the measured rate[48].

GNO

After one year of transition with the renewal of the readout electronics, the GALLEX apparatus was restarted as the long term GNO (*Gallium Neutrino Observatory*) project[49].

The valuable idea was to reduce the systematic uncertainty of GALLEX and to monitor the *pp* flux for a full solar cycle, (i.e. 11 years) exploring possible long term (seasonal or cycle) time modulations.

The project was forced to shut down before schedule in April 2003 as a consequence of the emergency situation in the Gran Sasso laboratory (sec. 2.5).

The final result of GNO for the period 1998-2003 (58 solar runs) is:

$$R_{GNO} = (62.9 \pm 5.4[stat] \pm 2.5[syst])\ SNU \tag{1.35}$$

Combined with GALLEX yields for all 123 solar runs:

$$R_{Gallex+GNO} = (69.3 \pm 4.1[stat] \pm 3.6[syst])\ SNU \tag{1.36}$$

Fig. 1.8 shows the results of all GALLEX and GNO solar runs.

SAGE

SAGE (*Soviet-American Gallium Experiment*)[50] is a second experiment based on reaction eq. 1.32, situated in the underground laboratory of Baksan, in central Caucaso. Aside from different technical aspects the main difference is the target mass: $\sim 50t$ of metallic Gallium above the melting temperature of $30°C$.

Data taking started in 1990 and was planned until 2006, but after GNO shut down a prolongation is under discussion, due to the fundamental importance to run at least one experiment which is sensitive to solar *pp*-ν's.

The overall measured flux updated to 2003[51] is:

$$R_{exp} = (66.9 \pm 3.9[stat] \pm 3.6[syst])\ SNU \tag{1.37}$$

well in agreement with the GALLEX+GNO result of eq. 1.36.

Time modulation?

Both gallium detectors reported a decrease in the observed flux over their running time (1991-2003), amounting to $14 - 15SNU$ (i.e. $\sim -20\%$). The interpretation is under discussion: a statistical effect, a misinterpreted systematics or a real flux variation are being evaluated[52]. However a flat distribution yields also an acceptable *goodness-of-fit* in the 5-10% range and the central values of the two periods considered (1991-1997 and 1998-2003) are compatible at 2.4σ, so no strong evidence can be claimed.

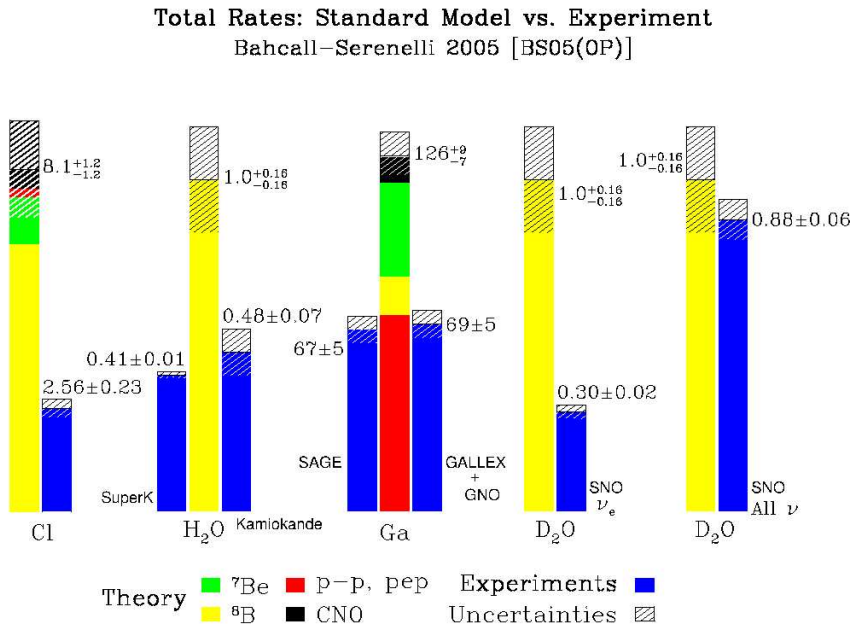

Fig. 1.9: *Prediction vs. Results of solar neutrino experiments[21].*

1.4.4 The (3) Solar Neutrino Problem(s)

As the signal predicted by the SSM for Homestake was made for 75% of ^8B neutrinos, whose flux is highly model dependent and even in the SSM is not predicted better than to a 16% accuracy, astrophysical solutions were originally favored to explain the observed flux discrepancy.

Two were the leading ideas[53]:

- *Non-standard solar models* were developed involving a lower core temperature of the sun of $\sim 14.8 \cdot 10^6 K$. This could be achieved postulating either a better radiative transport (reduced opacity, larger convective motions) or an additional pressure (centrifugal, magnetic) contributing to the star equilibrium.

- Without leaving the SSM, different astrophysical S-factors could justify different branching ratios in the *pp* chain and depress the ^8B flux in favor of other emissions.

These two kinds of astrophysical solutions were later ruled out respectively by helioseismology (sec. 1.2.4) and by nuclear cross section measurements (sec. 1.2.1).

At the beginning of the 90s the result of KamiokaNDE was also creating a second neutrino problem in terms of compatibility with the Homestake result[54]. The ^8B flux measured by KamiokaNDE is in agreement with Homestake only if the ^7Be branch is completely depressed. From the astrophysical point of view there was no convincing way to explain such suppression, therefore hypotheses about spectral distortions started to circulate and gave the first indications of a possible non standard neutrino physics.

Anyhow, as the neutrinos detected were mostly ^8B, astrophysical speculations could not be ruled out. The GALLEX and SAGE results changed this aspect.

Gallium experiments had a signal made for 57% of ν_e^{pp} and for 27% of $\nu_e^{^7Be}$. The measured $(78\pm8)SNU$ were barely enough to justify ν_e^{pp} flux which is tightly constrained by the solar luminosity (sec. 1.2) and known with excellent precision ($< 1\%$). Therefore no space at all was left for other emissions and speculations on a lower T_c could in no way justify a complete $\nu_e^{^7Be}$[55] absence.

In the middle 90s, even before helioseismological striking confirmation of the SSM, it was pretty clear that a solution to the SNP was requiring an enlargement of the *Standard Model of the Electro-Weak Interactions* to include new neutrino physics. So after starting as "probes" of astrophysical models, neutrinos have today risen to "protagonists" of a new possible physics.

1.5 Massive Neutrinos and Flavor Oscillations

The solution of the SNP resides in the attribution of non standard ν-properties: ν-mass and mixing. These arguments are covered extensively in literature, e.g. in [57, 58].

1.5.1 Possible neutrino masses

In the *Standard Model of the Electro-Weak Interactions* (SM) the neutrino is accounted for as a neutral stable particle with spin 1/2 and zero rest mass. In absence of a mass term, the Dirac's equation decouples in the two well known Weyl equations[56]. Similarly the γ_5 eigenstates, Dirac's 4-component spinors ψ, decouple into two 2-component Weyl spinors which are chirality eigenstates (with eigenvalues ±1):

$$\psi_L = P_L\psi \equiv \left(\frac{1-\gamma_5}{2}\right)\psi \ , \ \psi_R = P_R\psi \equiv \left(\frac{1+\gamma_5}{2}\right)\psi \tag{1.38}$$

where P_L and P_R are the usual projectors onto orthogonal components. The representation $\psi = \psi_L + \psi_R$ is Lorentz invariant because the two components transform independently. However parity (P) transforms them into each other and as ψ_R is not observed[12], P-violation is maximal. In other words, the neutrino is always in a pure chirality eigenstate (left-handed) and so is its antiparticle (right-handed).

We can accommodate in the Lagrangian a mass term for neutrinos in analogy to quarks and charged leptons:

$$-\mathcal{L}_D = m^D\left(\overline{\psi}_L\psi_R + \overline{\psi}_R\psi_L\right) \tag{1.39}$$

where m^D is a constant. As ψ_R does not exist in the SM, neutrinos are massless in this theory. If $\psi_R \neq 0$, this particle is not weakly interacting and is named *sterile* neutrino.

The mass term preserves the overall lepton number (L) conservation of the model and thus allows a neutrino mass eigenstate ν_i to be distinguished from its antiparticle

[12] In the V-A theory ψ_R does not couple to the gauge bosons of the $SU_L(2)$ group.

as: $L_{\overline{\nu}_i} = -L_{\overline{\nu}}$. When $\overline{\nu}_i \neq \nu_i$, we call the ν_i-$\overline{\nu}_i$ complex a "Dirac neutrino" and the constant m_D a "Dirac mass".

However, as ν_R (and $\overline{\nu}_L$) are not observed, Majorana proposed a more economical representation of neutrinos, where the field $\psi_\nu = \psi^C$, i.e. the neutrino is its own antiparticle. In this case a mass term can be introduced out of a single Weyl spinor, say ψ_L, and its C-conjugate $(\psi_L)^c = C\overline{(\psi_L)}^T = (\psi^c)_R$:

$$-\mathcal{L}_L^M = \frac{1}{2} m_L^M \left[\overline{(\psi_L)^c}\psi_L + \overline{\psi_L}(\psi_L)^c\right] \tag{1.40}$$

with eigenstate $\psi^M \equiv \psi_L + (\psi_L)^c$. It is important to note that, since $\overline{(\psi_L)^c}$ and ψ_L have the same lepton number, Majorana mass terms carry two units of lepton number and are therefore not L-conserving. A similar construction is done for $-\mathcal{L}_R^M$, but the result is in this case an $SU(2) \times U(1)$ invariant, unlike m^D and m_L^M who do break $SU(2) \times U(1)$.

If neutrinos are massive, in principle both Dirac and Majorana mass terms are possible and the most general form is:

$$-\mathcal{L}_{mass} = \frac{1}{2}\left(\overline{\nu_L}\ \overline{(\nu_R)^c}\right)\begin{pmatrix} m_L^M & m^D \\ m^D & m_R^M \end{pmatrix}\begin{pmatrix} (\nu_L)^c \\ \nu_R \end{pmatrix} + h.c.\ , \tag{1.41}$$

where the mass matrix turns out to be symmetric and can be easily diagonalized with a bi-unitary transformation $U_R^\dagger M U_L = M_{diag}$. The unitary matrix U_L, U_R is associated with a change of basis on the original neutrino fields:

$$\psi_L = U_L \eta_L \qquad \psi_R = U_R \eta_R \tag{1.42}$$

Eq. 1.41 holds also for N neutrino flavors simply interpreting m^D, m_L^M and m_R^M as $N \times N$ matrices and the neutrino fields as $N-$component vectors in the leptonic generation space. In this case ψ is used to describe a weak interaction eigenstate and η to describe a mass eigenstate.

1.5.2 Neutrino mass models

In the SM all charged fermion masses arise from spontaneous symmetry breaking of the electroweak $SU_L(2) \times U_Y(1)$, through Higgs mechanism. However for neutrinos, the absence of the ν_R field prevents the existence of Dirac's mass terms, while lepton number conservation (actually B-L accidental conservation) prevents Majorana mass terms.

Different mechanisms are available to introduce neutrino masses in the model, but they all must account for the fact that neutrino masses are much smaller ($\sim eV$ or lower) than any other fermion mass in SM. The least speculative models are:

1. The introduction of (Dirac) neutrino masses could be done directly, adding the ν_R field as a SU(5) inert singlet, but, as the Yukawa coupling to the minimal Higgs doublet is proportional to the mass, an unnaturally small coupling is required with no apparent explanation.

2. Majorana masses could be added, but as they carry weak isospin $T_L = 1$, they require enlargement of the Higgs sector beyond the minimal ϕ doublet:

(a) A Higgs triplet $\Delta = (\Delta^{++}, \Delta^{+}, \Delta^{0})$ could replace the doublet with a tiny Δ^0 VEV (*Vacuum Expectation Value*) to justify the smallness of neutrino masses.

(b) The singly and doubly charged Higgs singlets h^{+}, h^{++} could be added to the standard doublet and very small neutrino masses could be generated by radiative corrections.

But the most natural and elegant mechanism to introduce neutrino masses in the SM is the so-called *see-saw* mechanism.

The *see-saw* mechanism

The *see-saw* model relies on both Dirac and Majorana mass terms and for one leptonic family, it assumes:

$$m_R^M >> m_D >> m_L^M \tag{1.43}$$

where m_L^M is required to be zero or negligible and m_D is expected to be of the order of the charged lepton mass.

The mass matrix in eq. 1.41 has then two eigenvalues $m_1 = m_R^M$ and $m_2 = -m_D^2/m_R^M$: *see-saw* mechanism generates two neutrino masses and makes one of them very small by making the other one arbitrary large[13]. Different versions of the model postulate different m_R^M values ranging from $1TeV$ up to GUT scale ($\sim 10^{15}GeV$).

The matrix that diagonalizes the mass matrix is:

$$U = \begin{pmatrix} 1 & \frac{m_d}{m_L^M} \\ -\frac{m_D}{m_L^M} & 1 \end{pmatrix} \tag{1.44}$$

The interaction eigenstates relate to the mass eigenstate by:

$$\nu_L = \eta_{1L} + \frac{m_D}{m_R^M}\eta_{2L} \simeq \eta_{1L} \qquad \nu_R = \eta_{2R} - \frac{m_D}{m_R^M}\eta_{1R} \simeq \eta_{2R} \tag{1.45}$$

So for any practical purpose, the light mass eigenstate can be identified with the usual interacting left-handed neutrino and the *superheavy* eigenstate with the inert right-handed neutrino.

In the generalizations to 3 (or N) leptonic families the different versions of the mechanism may choose different masses for m_{Di} (leptons or quarks) and for m_{Ri}^M (identical or hierarchical), and result in "linear" or "quadratic" neutrino mass hierarchies.

1.5.3 Experimental limits on neutrino masses

Direct mass searches

The most obvious way to investigate a possible non-zero neutrino mass is to look into β-decays. In a β-decay spectrum a non-zero neutrino mass would introduce a distortion in the energy region close to the end-point. Obviously light nuclei with a low Q value allow a better sensitivity to the tiny expected neutrino masses and the ideal candidate

[13] A perfectly legal choice since m_R^M is SU(2)xU(1) invariant.

turns out to be tritium with $Q = 18.6keV$. A few independent measurements with different experimental setups have been performed. None of them observed the expected deformation, setting as best limits:

$$m_{\nu_e} \leq 2.5eV \qquad (95\%C.L.) \qquad \text{(Troitsk[62])}. \tag{1.46}$$
$$m_{\nu_e} \leq 2.2eV \qquad (95\%C.L.) \qquad \text{(Mainz[63])}. \tag{1.47}$$

Similarly m_{ν_μ} and m_{ν_τ} can be inferred analyzing respectively the muon spectrum produced in pion decay ($\pi^+ \rightarrow \mu^+ + \nu_\mu$) and the pions produced in τ decay ($\tau \rightarrow \nu_\tau + 5\pi$). The best limits date back to middle 90's:

$$m_{\nu_\mu} \leq 170keV \qquad (90\%C.L.) \qquad \text{(PSI proton beam, CH[64])}. \tag{1.48}$$
$$m_{\nu_\tau} \leq 18.2MeV \qquad (95\%C.L.) \qquad \text{(ALEPH at LEP[65])}. \tag{1.49}$$

It must be noted that the improper terms $m_{\nu_e}, m_{\nu_\mu}, m_{\nu_\tau}$ in this context, refer to the mass eigenstates giving the major contribution to the three interaction eigenstates.

Double Beta Decay (DBD) experiments

DBD experiments are the only way to reveal the possible Majorana nature of neutrinos[66]. DBD (${}^A_Z X \rightarrow {}^A_{Z+2} X + 2e^- + 2\overline{\nu}_e$) naturally occurs in a few nuclides for which the ordinary β-decay is kinematically forbidden. In addition to this L-conserving decay ($2\nu\beta\beta$), in case neutrinos are Majorana particles, a DBD can also occur without any (anti)neutrino emission ($0\nu\beta\beta$) and would be visible as a monochromatic line at the end-point of the $2\nu\beta\beta$ spectrum.

A number of experiments are ongoing, based on different candidate elements and different experimental techniques[137]. In absence of a $0\nu\beta\beta$ signature, a lower limit on its half-life can be set by experiments. The effective Majorana neutrino mass is defined as $\langle m_{ee} \rangle = \sum_i U_{ei}^2 m_{\nu_i}$, where U_{e1i} are the elements in the first row of the neutrino mixing matrix (sec. 1.5.4, eq. 1.67)[14]. The decay half life and the effective mass are related by:

$$\left[T^{0\nu}_{1/2}\right]^{-1} = G^{0\nu} \left|M^{0\nu}\right|^2 \frac{\left|\langle m_{ee} \rangle\right|^2}{m_e^2} \tag{1.50}$$

where $G^{0\nu}$ is the exactly calculable phase space factor ($\propto Q^5_{\beta\beta}$, the Q-value of the decay) and $\left|M^{0\nu}\right|^2$ is the nuclear matrix element of the isotope undergoing the decay. The calculation of the latter is affected by large uncertainties that introduce a range of possible values for the mass limits.

[14]Note that $\langle m_{ee} \rangle$ vanishes for Dirac massive neutrinos as the mass matrix and its diagonalization matrix becomes:

$$M = \begin{pmatrix} 0 & m_D \\ m_D & 0 \end{pmatrix} \qquad U = \begin{pmatrix} \frac{1}{\sqrt{2}} & \frac{1}{\sqrt{2}} \\ -\frac{1}{\sqrt{2}} & \frac{1}{\sqrt{2}} \end{pmatrix}$$

leading to:

$$\langle m_{ee} \rangle = \left(\frac{1}{\sqrt{2}}\right)^2 (-m_D) + \left(\frac{1}{\sqrt{2}}\right)^2 (m_D) = 0$$

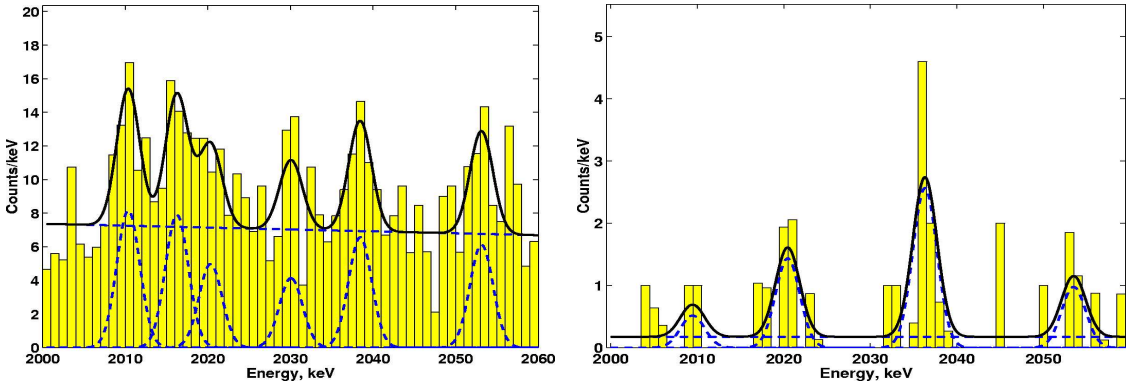

Fig. 1.10: *The Heidelberg-Moscow energy spectrum[71] for the 1995-2003 period (exposure* $56.7kg \cdot y$*) before (left) and after (right)* PSD *analysis is applied. The peak at* $2039keV$ *is the controversial claim of evidence for* $0\nu\beta\beta$ *decay.*

Up to 2000 the best $0\nu\beta\beta$ limit was available from the Heidelberg-Moscow (HDMS) experiment using ^{76}Ge [67]:

$$T^{0\nu}_{1/2} > 1.9 \times 10^{25} y \quad \Rightarrow \quad \langle m_{ee} \rangle \leq (0.33 \div 1.35) eV \qquad (90\% C.L.) \tag{1.51}$$

In 2001 a part of the HDMS collaboration claimed evidence for neutrinoless double-β decay [68]. Immediately the scientific community contested a few points of the analysis [69, 70] and concluded that the claim was not justified. In 2004 there were published results[71] with improved statistics and a new PSD analysis, that was able to suppress the γ-like background by searching single site events (fig. 1.10). The presence of a peak at $2039keV$ (the reaction Q value for ^{76}Ge) appears then more solid (4.2σ). The claim is:

$$T^{0\nu}_{1/2} = 1.19 \times 10^{25} y \quad \Rightarrow \quad \langle m_{ee} \rangle = (0.1 \div 0.9) eV \qquad (99.73\% C.L.) \tag{1.52}$$

where a $\pm 50\%$ uncertainty on the nuclear matrix element has been taken into account.

In GERDA (sec. 1.11.1), also using Ge detectors, the existence of this peak will be probed. Experiments based on different isotopes in the near future will test whether this result is due to new physics.

The running CUORICINO experiment, based on ^{130}Te, sports a sensitivity similar to HDMS and currently indicates[72]:

$$T^{2\beta 0\nu}_{\frac{1}{2}} > 1.8 \times 10^{24} y \quad \Rightarrow \quad \langle m_{ee} \rangle \leq (0.2 \div 1.1) eV \qquad (90\% C.L.) \tag{1.53}$$

Cosmological constraints

The standard *hot Big Bang* cosmological model is today able to place quite stringent limits on neutrino masses.

The Hubble constant, relating velocity of objects to their distance ($v = H_0 d$), has been measured to be:

$$H_0 = 100 \cdot h \frac{km}{s} \cdot Mpc \qquad \text{with} \qquad h = 0.72 \pm 0.05 \quad (68\% C.L.) \tag{1.54}$$

The Cosmic Microwave Background (CMB) radiation, by far the most abundant photons in the universe, has been measured to have blackbody radiation spectrum with $T_0 = 2.726 \pm 0.010K$ (95%C.L.)[73]. The photon density n_γ can be derived thereafter ($n_\gamma \propto T_0^3$).

The cosmological abundance of light elements (He^4, H^2, He^3, Li^7) fixes the relative density of baryons over photons $\eta \equiv n_B/n_\gamma$, which in terms of energy density ρ, places the bound: $0.02 \leq h^2\Omega_B \leq 0.025$, where $\Omega_B \equiv \rho_B/\rho_c$ expresses the baryonic energy density relative to the critical density[15].

During the cooling process, universe expansion proceeds as $H \sim T^2/M_P$ [16] and neutrino interactions proceeds as $\Gamma = n_\nu\langle\sigma v\rangle \sim G_F^2 T^5$. Decoupling of neutrinos occurs when Γ becomes smaller than H, i.e. at $T_D \simeq \left(\frac{1}{G_F^2 M_P}\right)^{1/3} \sim 1MeV$. Neutrinos with masses well below this energy, decouple while relativistic and their density can be found in analogy to the photon density ($n_\nu \propto T_\nu^3$, T_ν being bound to T_0). Using $\rho_\nu = n_\nu \sum_i m_{\nu_i}$ and $\rho_c = 1.1 \times 10^4 h^2 \frac{eV}{cm^3}$ one can write:

$$h^2\Omega_\nu^{\rm hot} = \frac{\sum_i m_{\nu_i}}{94eV} \tag{1.55}$$

where $\Omega_\nu^{\rm hot} \equiv \rho_\nu/\rho_c$ and the sum involves only neutrino species with $m_\nu \ll T_D$. Now $h^2\Omega_\nu^{\rm hot}$, previously only loosely bound by the age of the universe, has been recently more effectively constrained by the CMB observations of the WMAP experiment[74]:

$$h^2\Omega_\nu^{\rm hot} \leq 0.0076 \qquad \Rightarrow \qquad m_\nu \leq 0.23eV \qquad (95\%C.L.) \tag{1.56}$$

Other authors[75] prefer more conservative analysis of the WMAP data and indicate $m_\nu \leq\sim 0.7eV$. For heavy neutrinos with masses above T_D a more complicated relation between $h^2\Omega_\nu^{cold}$ and $\sum_i m_{\nu_i}$ has been worked out, resulting in $m_{\nu_i} \gtrsim 1GeV$.

1.5.4 Vacuum oscillations

If neutrinos do have mass, the weak interaction eigenstates $\nu_\alpha(\alpha = e, \mu, \tau)$ do not in general coincide with mass eigenstates $\nu_i(i = 1, 2, 3)$. The transition between the two orthogonal bases is given by:

$$\nu_\alpha = \sum_i U_{\alpha i}\nu_i \qquad \nu_i = \sum_\alpha U_{i\alpha}^\dagger \nu_\alpha \qquad U^\dagger U = I \tag{1.57}$$

where the so called *mixing matrix* U is a unitary 3×3 matrix (neglecting contribution from superheavy *see-saw* neutrinos), in good agreement with the CKM matrix of the hadronic sector.

Mass eigenstates propagate with different frequencies, therefore the mass eigenstate admixture of a propagating neutrino shows periodical variation. The neutrino acquires

[15] The critical energy density ρ_c is the one corresponding to a "flat" universe: for $\rho_{\rm tot} > \rho_c$ the universe will expand indefinitely, while for $\rho_{\rm tot} < \rho_c$ it will eventually re-collapse. From $H_0 \sim \sqrt{\rho}$ we know that ρ_{tot} is not far from ρ_c.

[16] $M_P \sim 10^{19}GeV$ is the Planck mass.

then the possibility to interact as a different flavor eigenstate with respect to the one it started with, violating the conservation of individual lepton numbers. This phenomenon, firstly postulated in 1957 by B.Pontecorvo[59], is known as *flavor oscillations* and currently represents the best explanation to all available experimental evidences in neutrino physics.

Propagation in space and time of the mass eigenstates is given by:

$$i\frac{\partial}{\partial t}|\nu_i\rangle = H|\nu_i\rangle \quad \Rightarrow \quad |\nu_i(t)\rangle = e^{-iHt}|\nu_i(0)\rangle \tag{1.58}$$

where H is the Hamiltonian operator.

In the mass eigenstates base and in the relativistic limit $p_i \gg m_i$, when $p_i = \sqrt{E^2 - m_i^2} \simeq E - \frac{m_i^2}{2E}$ (with $\hbar = c = 1$), we can write:

$$H = p \cdot I + \frac{1}{2E} \cdot M \tag{1.59}$$

where the two 3×3 matrices I and M are the identity and the diagonal mass matrix, respectively. The term $p \cdot I$ is of course not contributing to mixing so H is often identified with $M/2E$.

A neutrino originated in $x = 0$ as a pure interaction eigenstate $|\nu_\alpha(0)\rangle$ will be described at a distance $x \simeq ct$:

$$|\nu(x)\rangle = \sum_i U_{\alpha i} e^{-iHt}|\nu_i(0)\rangle = \sum_{i\beta} U_{\alpha i} U^*_{\beta i} e^{-iHt}|\nu_\beta(0)\rangle \tag{1.60}$$

where the last expression enforcing the unitarity of the mixing matrix is a superposition of interaction eigenstates.

The transition probability, i.e. the probability for $|\nu(x)\rangle$ to interact as eigenstate $\nu_\beta \neq \nu_\alpha$, is given by projection on the state itself:

$$\begin{aligned} P_{\nu_\alpha \to \nu_\beta}(x) &= |\langle\nu_\beta|\nu(x)\rangle|^2 = |\langle\nu_\beta|U|\nu_i(t)\rangle|^2 = |\langle\nu_\beta|Ue^{-iHt}|\nu_i\rangle = |\langle\nu_\beta|Ue^{-iHt}U^\dagger|\nu_\alpha\rangle|^2 \\ &\simeq \sum_{i,j} U_{\alpha i} U^\dagger_{i\beta} U^\dagger_{j\alpha} U_{\beta j} exp\left(-i\frac{\Delta m^2_{ij}}{2E}x\right) \end{aligned} \tag{1.61}$$

where $\Delta m^2_{ij} = |m_i^2 - m_j^2|$ and the last holds in the relativistic limit.

Most of the oscillation mechanics can be explained in terms of two-neutrino oscillations where the mixing matrix can be parametrized as:

$$U = \begin{pmatrix} \cos\theta & \sin\theta \\ -\sin\theta & \cos\theta \end{pmatrix} \tag{1.62}$$

where only one parameter is present, the rotation angle θ called the *mixing angle*.

The transition probability after traveling a distance L, becomes:

$$P_{\nu_e \to \nu_\mu}(L) = \sin^2 2\theta \sin^2 \frac{(p_1 - p_2)L}{2} = sin^2 2\theta \sin^2\left(\frac{\Delta m^2}{4E_\nu}L\right) \tag{1.63}$$

from where we can define the *Vacuum oscillation length*:

$$\lambda_{vac} = \frac{4\pi E_\nu}{\Delta m^2} \tag{1.64}$$

For a given $(\theta, \Delta m^2)$, at L equals to multiple integers of λ_{vac}, the flavor conversion is maximal.

The so called *survival probability*, i.e. the probability for ν to be still detected in its original flavor, is simply:

$$P_{\nu_e \to \nu_e}(L) = 1 - P_{\nu_e \to \nu_\mu}(L) = 1 - \sin^2 2\theta \sin^2 \left(\frac{L}{\lambda_{vac}} \pi \right) \tag{1.65}$$

With three neutrinos the oscillation can be described as subsequent rotations characterized by three mixing angles:

$$\begin{aligned} U &= U_{23} \cdot V \cdot U_{13} \cdot U_{12} = \\ &= \begin{pmatrix} 1 & 0 & 0 \\ 0 & c_{23} & s_{23} \\ 0 & -s_{23} & c_{23} \end{pmatrix} \begin{pmatrix} e^{i\delta} & 0 & 0 \\ 0 & e^{i\alpha} & 0 \\ 0 & 0 & e^{i\beta} \end{pmatrix} \begin{pmatrix} c_{13} & 0 & s_{13} \\ 0 & 1 & 0 \\ -s_{13} & 0 & c_{13} \end{pmatrix} \begin{pmatrix} c_{12} & s_{12} & 0 \\ -s_{12} & c_{12} & 0 \\ 0 & 0 & 1 \end{pmatrix} \end{aligned} \tag{1.66}$$

where $s_{ij} = \sin\theta_{ij}$, $c_{ij} = \cos\theta_{ij}$. The matrix V parametrized out of three phases δ, α and β, accounts for possible CP-violating processes. In case neutrinos are Dirac particles $\alpha = \beta = 0$.

1.5.5 MSW effect

When neutrino propagation occurs in matter, the interaction potentials with electrons must be added to the mechanism and this can lead to resonant effects under particular conditions that enhance the oscillation amplitudes greatly (L.Wolfenstein[60], S.P Mikheyev and A.Yu. Smirnov[61]). The resonant phenomenon was later named *MSW effect* for the initials of the three physicists.

The easiest way to model the matter effects on neutrino oscillations is the inclusion of a refraction index

$$n_l = 1 + \frac{2\pi\rho_{e^-}}{p^2} A_{\nu_l} \tag{1.67}$$

where ρ_{e^-} is the electron density (the diffusion centers) and A_{ν_l} is the forward scattering amplitude for l-flavored neutrinos. The effect of neutral current interactions is identical for all active neutrinos and plays no role in the oscillation[17]. The difference in the scattering amplitude of electron-flavor neutrinos compared to another active flavor ν_α is given only in terms of CC:

$$\Delta A_{e\alpha} = A_{\nu_e} - A_{\nu_\alpha} = A^{CC} = -\sqrt{2}\frac{G_F p}{2\pi} \tag{1.68}$$

[17] It is relevant instead for oscillation into sterile neutrinos, not covered here.

from which we write the *relative* refraction index for electron type neutrinos:

$$n_e^{rel} = 1 + \frac{2\pi\rho_{e^-}}{p^2}A^{CC} = 1 + \frac{\sqrt{2}G_F\rho_{e^-}}{p} \tag{1.69}$$

The Hamiltonian of neutrino propagation in matter expressed in the interaction eigenstate basis is:

$$H_{matter} = H_{vac} + H_{NC} + H_{CC} = H_{vac} + k^{NC}\cdot I + k_e^{CC}\cdot \begin{pmatrix} 1 & 0 & 0 \\ 0 & 0 & 0 \\ 0 & 0 & 0 \end{pmatrix} \tag{1.70}$$

where the term $H_{NC} \propto I$ doesn't contribute to mixing and H_{vac} is not diagonal in this basis ($H_{vac} = UHU^\dagger$, with U and H defined above.).

The CC interaction coefficient can be written as:

$$k_e^{CC} = \frac{G_F\rho_{e^-}}{\sqrt{2}} \tag{1.71}$$

In the two-neutrino case, H_{matter} can be diagonalized by a unitary matrix U^m parametrized in the same form as in eq. 1.62, which represents the mixing of *matter* mass eigenstates ν_1^m and ν_2^m:

$$\begin{pmatrix} |\nu_e\rangle \\ |\nu_\mu\rangle \end{pmatrix} = \begin{pmatrix} \cos\theta_m & \sin\theta_m \\ -\sin\theta_m & \cos\theta_m \end{pmatrix} \begin{pmatrix} |\nu_1^m\rangle \\ |\nu_2^m\rangle \end{pmatrix} \tag{1.72}$$

where θ_m is the *mixing angle in matter*:

$$sin2\theta_m = \frac{\frac{\Delta m^2}{4p}\sin 2\theta}{\sqrt{(\frac{\Delta m^2}{4p}cos2\theta - \frac{G_F\rho_{e^-}}{\sqrt{2}})^2 + (\frac{\Delta m^2}{4p}\sin 2\theta)^2}} \tag{1.73}$$

The resonant behavior can be then observed upon meeting the condition:

$$\rho_{e^-} = \rho_{e^-}^{res} \equiv \frac{\Delta m^2 cos2\theta}{2\sqrt{2}pG_F} \tag{1.74}$$

the angle θ_m becomes maximal irrespective of the value of θ.

However, since the diagonal Hamiltonian at resonance

$$H_{matter}^{diag}\Big|_{\rho_{e^-}=\rho_{e^-}^{res}} = -\frac{\Delta m^2}{4p}\sin 2\theta\sigma_3, \tag{1.75}$$

σ_3 being the third Pauli matrix, differs from $H_{vac}^{diag} \equiv H = -\frac{\Delta m^2}{4p}\sigma_3$ for a factor $\sin 2\theta$, this enters the transition probability as:

$$P_{\nu_e\to\nu_\mu}(E_\nu, L, \theta, \Delta m^2)\big|_{\rho_{e^-}=\rho_{e^-}^{res}} = \sin^2\left(\frac{\Delta m^2}{4p}\sin 2\theta L\right) \tag{1.76}$$

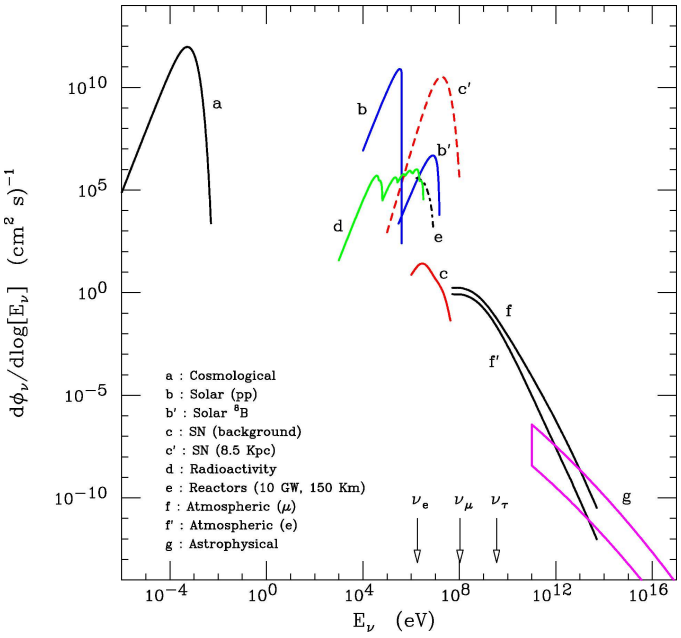

Fig. 1.11: *Neutrino spectra from different sources[120].*

For $\rho_{e^-} \ll \rho_{e^-}^{resonant}$ the matter effect is negligible, while for $\rho_{e^-} \gg \rho_{e^-}^{resonant}$ the oscillation is strongly suppressed by a constant factor

$$\frac{P_{matter}}{P_{vac}} \simeq \frac{\sin 2\theta_m}{\sin 2\theta} \tag{1.77}$$

In case of a neutrino traversing a density gradient as in the sun interior, we may assume it will eventually cross a layer where the density meets the resonance condition 1.74. If this is the case maximal conversion will take place in this layer provided that two conditions are met:

1. ρ_{e^-} must be large enough to assure the resonance condition, which through eq. 1.74 translates into an upper limit to E_ν.

2. Resonance layer must occur adiabatically, i.e. the density variation around the resonance point must be small compared to oscillation length. Since the oscillation length depends inversely on E_ν, the latter is given a lower limit by this condition.

For antineutrinos the sign of k_e is inverted and no resonance can occur.

The effect of the resonance condition on the solar neutrino spectrum is presented in sec. 1.11.1.

1.5.6 Detecting the oscillations

Oscillation experiments may involve different sources of neutrinos, either natural or artificial (fig. 1.11). Examples of natural sources are the interaction of cosmic rays in

source	Exp	P	log L (m)	log E (MeV)	log L/E (m/MeV)	logΔm^2 (eV^2)
sun(vac)	Cl,Ga,SK,SNO	$\nu_e \to \nu_e$	+11	[-1,+1]	[+10,+12]	[-12,-10]
sun(msw)						[-8, -4]
atmosph.	SuperK	$\nu_\mu \to \nu_\mu$	[+4,+7]	[+2,+4]	[0,+5]	[-5, 0]
react(S)	Bugey	$\overline{\nu}_e \to \overline{\nu}_e$	[+1,+2]	[0,+1]	[0,+2]	[-2,0]
react(I)	CHOOZ	$\overline{\nu}_e \to \overline{\nu}_e$	+3	[0,+1]	[+2,+3]	[-3,-2]
react(L)	KamLAND	$\overline{\nu}_e \to \overline{\nu}_e$	+5	[0,+1]	[+4,+5]	[-5,-4]
accel(S)	LSND	$\overline{\nu}_\mu \to \overline{\nu}_e$	[+1,+2]	[+1,+2]	+1	-1
accel(I)	NOMAD	$\nu_\mu \to \nu_\tau$	+2	+4	-2	+2
accel(L)	K2K	$\nu_\mu \to \nu_\mu$	+5	+3	+2	-2
	MINOS	$\nu_\mu \to \nu_\mu$	+5	[+3,+4]	[+1,+2]	[-1,-2]
	CNGS	$\nu_\mu \to \nu_\tau$	+5	+4	+1	-1

Tab. 1.4: *Sensitivity to Δm^2 for different experiment categories (the most relevant is indicated). P is a survival/transition probability for disappearance/appearance experiments. S,I,L=Short,Intermediate,Long Baseline.*

the atmosphere, supernova type-II explosions and the sun. Artificial neutrino sources are power reactors, used in the first Reines and Cowes neutrino detection experiment (sec. 1.1), and neutrino beams from particle accelerators.

Regardless of the neutrino source, experiments can measure a transition probability $P_{\nu_\alpha \to \nu_\beta}$ (*appearance* experiments) or a survival probability $P_{\nu_\alpha \to \nu_\alpha}$ (*disappearance* experiments), depending on whether the source flavor and the flavor to which the detector is sensitive are different or identical.

From eq. 1.63 we can write:

$$P_{\nu_\alpha \to \nu_\beta}(L/E) \simeq \sin^2\theta \sin^2\left(1.27 \frac{L[m]}{E[MeV]} \Delta m^2[eV^2]\right) \tag{1.78}$$

where it appears clear how the sensitivity to oscillation parameters, $\sin^2 2\theta$ and Δm^2 depends on the L/E ratio, the key parameter for an oscillation experiment.

Tab. 1.4 shows the Δm^2 sensitivity for different experiments

1.6 Atmospheric Neutrinos

Neutrinos are produced within the hadronic cascades initiated by cosmic rays in the higher atmospheric layers. The production mechanism involves the decay of charged mesons, namely pions and kaons and of the produced muons:

$$\pi^+, K^+ \longrightarrow \mu^+ + \nu_\mu \longrightarrow e^+ + \nu_e + \overline{\nu}_\mu + \nu_\mu \tag{1.79}$$

$$\pi^-, K^- \longrightarrow \mu^- + \overline{\nu}_\mu \longrightarrow e^- + \overline{\nu}_e + \nu_\mu + \overline{\nu}_\mu \tag{1.80}$$

Neutrinos (and antineutrinos) can therefore be detected in underground facilities in a ratio of muon flavor over electronic flavor of $R \sim 2$, for energies above $1GeV$. The exact

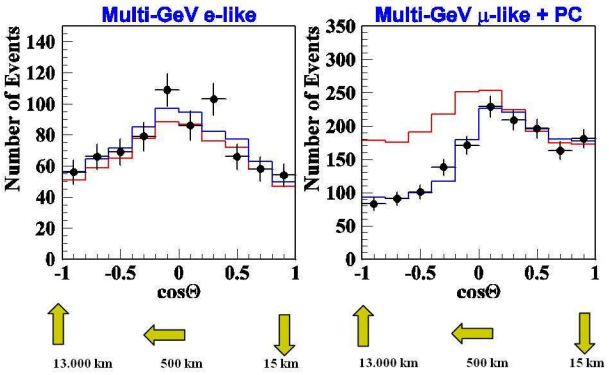

Fig. 1.12 (a): *Zenith angle distribution for e-like and μ-like atmospheric events in SK[80]. Red line: no oscillation. Blue line: best fit oscillation.*

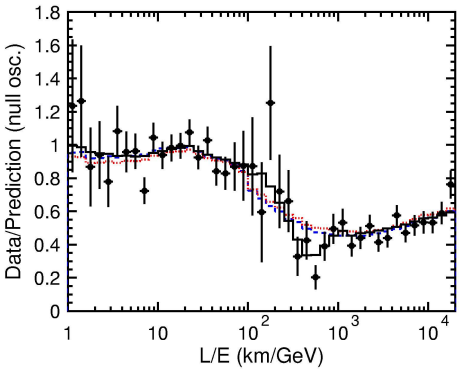

Fig. 1.12 (b): *L/E distribution of μ-like atmospheric events in SK[79].*

value of R is predictable with a 5% accuracy[18] and is decoupled from unknown aspects of the cosmic-ray spectrum and of the overall flux. This ratio can be observed by water Čerenkov detectors or iron calorimeters through charged current interactions on nuclei.

Already in the early 90s KamiokaNDE reported the so-called *atmospheric neutrino anomaly*[76], a deficit in the observed muon flavor neutrino flux and a consequent $\nu_\mu/\nu_e \sim 60\%$ with respect to predictions.

Atmospheric neutrino events have energies that range between $\sim 100MeV$ and $\sim 10TeV$ with an average of $\sim 1GeV$. The path length between production and detection is $\sim 15km$, for downward going events that cross the atmosphere only, and $\sim 13000km$, for upward going events that cross most of the earth. The observed deficit and its zenith angle dependency are an indication of possible oscillations for neutrinos passing through the earth.

In 1998, Super-KamiokaNDE (SK, sec. 1.7.1) with a much higher statistics found[77]:

$$\frac{R_{obs}}{R_{MC}} = 0.65 \pm 0.05(stat.) \pm 0.08(syst.) \tag{1.81}$$

Moreover SK produced zenith angle distributions of e-like and μ-like events (fig. 1.12(a)). The formers were symmetrically distributed while the latters showed clearly how the deficit was coming from below the horizon. Neutrino oscillations were able to explain this result with the $\nu_\mu \to \nu_\tau$ hypothesis fitting the data perfectly. The possibility $\nu_\mu \to \nu_e$ would instead require a negative zenith angle asymmetry (i.e. more up-going events) of the e-like events, due to the additional CC matter effect in the earth, but this is excluded at 3.4σ[80][19]. As opposite the oscillation into sterile neutrinos can be distinguished due to the absence of any matter effect in the earth and is also disfavored at 99% C.L.[78].

Recently[79], the SK collaboration published an interesting analysis on the L/E distribution of μ-like events. L and E of the neutrino are inferred from angle and energy of

[18] It depends on the probability of in-flight muon decay which is inversely energy dependent.

[19] The hypothesis was definitively ruled out by the results of Chooz (sec. 1.8.2).

the charged lepton for a sample selection with an L/E resolution better than 70%. The distribution, normalized to a Monte-Carlo calculation without oscillations, is reproduced in fig. 1.12(b). A clear dip is visible for $L/E \sim 500 km/GeV$ that can be interpreted as a minimum of the survival probability (eq. 1.78).

The SK latest best-fit corresponding to $1489d$ (1996-2001) and combining the two analyses yields[80]:

$$\Delta m^2_{atm} = 2.4^{+0.6}_{-0.5} \cdot 10^{-3} eV^2 \quad (1.82)$$

$$sin^2 2\theta_{atm} = 1^{+0}_{-0.08} \quad (1.83)$$

where the errors are given at 90% C.L.

The SK results, confirmed with a lower precision by other experiments like Soudan-2[81] and MACRO[82], are one of the cornerstones of the overall neutrino puzzle.

1.7 Second Generation Solar Neutrino Experiments

While first generation solar experiments were driven primarily by the astrophysical interest of probing the SSM, the latest generation experiments detecting neutrino fluxes from the sun were designed with the primary goal of testing the oscillation hypothesis.

As described in sec. 1.2 only electron-flavor neutrinos are generated in the sun. The baseline is the sun-earth distance $l \simeq 1.5 \times 10^{11} m$ and the neutrino energies span from $\sim 150 keV$ (the threshold of radiochemical experiments) to $\sim 15 MeV$ the end-point of ^8B spectrum. The sensitivity for vacuum oscillations is therefore given by:

$$\frac{L}{E} \simeq \frac{10^{11} m}{[10^{-1}, 10^{1}] MeV} = [10^{10}, 10^{12}] \frac{m}{MeV} \quad \Rightarrow \quad \Delta m^2 \simeq [10^{-12}, 10^{-10}] eV^2 \quad (1.84)$$

However if the MSW effect in the sun plays a dominant role, the sensitivity is given by the values of Δm^2 that allow meeting the resonance condition 1.74, in the range $10^{-8} \div 10^{-4} eV^2$.

In addition MSW effect in crossing the earth could lead to day-night modulations in the detected flux.

1.7.1 Super-KamiokaNDE

Super-KamiokaNDE (SK)[84] located in the Mozumi mine in Japan, is the evolution of the first water Čerenkov detector KamiokaNDE (sec. 1.4.2). The physical operating principles are therefore the same and the design is similar to its predecessor, but dimensions, performance and statistical possibilities are definitely higher. SK, as its predecessor is a multi-purpose detector and solar neutrinos are one of its research goals.

The external tank, $39.3m$ in diameter times a $41.4m$ height, houses $50kt$ of ultra-pure water. Out of the $32kt$ of the inner cylinder, a fiducial volume of $22.5kt$ is used as solar neutrino detector with an energy threshold of $\sim 5 MeV$.

The detector was equipped with 11146 20"-PMTs yielding an optical coverage of $\sim 40\%$. Phase-I of the experiment took place between May 1996 and July 2001[20].

The final result[85] of the measurement of ^8B neutrinos during phase-I (1496 days) was:

$$\Phi_{exp}(\nu_e^{^8B}) = (2.35 \pm 0.02[stat] \pm 0.08[syst]) \cdot 10^6 cm^{-2} s^{-1} \tag{1.85}$$

This is in agreement with the KamiokaNDE result (eq. 1.31), but with much lower uncertainties and shows a 41% reduction with respect to the SSM prediction (eq. 1.30).

Thanks to its high statistics of more than $10ev/d$, SK was able to provide a whole set of additional information on the ^8B emission:

Spectral shape For the first time a real spectroscopy was available. No spectral distortions could be inferred from data.

Day-Night asymmetry A -6% effect was seen, well compatible with zero. In the zenith angle distribution no distinction between *core-crossing* bins and *crust-crossing* bins was found.

Seasonal variations The expected orbit eccentricity modulation was observed and no other effects.

1.7.2 SNO

SNO (*Sudbury Neutrino Observatory*)[87] is a heavy water Čerenkov detector, located in the Creighton mine, near Sudbury (Ontario, Canada), in a cavity of irregular shape. The detector is made of an acrylic vessel, $12m$ in diameter, holding $1000t$ of heavy water (D_2O) and by a geodetic support structure mounting 9600 PMTs for a $\sim 55\%$ optical coverage. The cavity outside the vessel is filled with pure water for hydrostatic and shielding purposes, but no muon veto is required thanks to the rock coverage of $\sim 2000m$ ($\sim 6000m.w.e.$).

Three reactions are used for detecting solar neutrinos:

$\nu_e + D \longrightarrow e^- + 2p$ **(Charged Current, CC).** It is sensitive only to electron neutrinos and it yields a better neutrino-electron energy correlation with respect to $\nu - e$ scattering due to the relatively high mass of the protons that do not subtract a significant energy portion. Its energy threshold is $1.44MeV$ and the cross section is the highest of the three reactions: $30ev/d$ predicted (SSM).

$\nu_x + D \longrightarrow \nu_x + p + n$ **(Neutral Current, NC).** It is sensitive to all 3 neutrino flavors, therefore it offers the possibility for the first time to check the SSM prediction regardless of possible flavor conversion mechanism. The events are tagged with different methods for the neutron capture. The energy threshold is $2.2MeV$.

[20] After phase-I shut down, during the following maintainance operations, an accident caused the rupture of $\sim 55\%$ of the PMTs. A phase-II with the survived PMTs evenly rearranged and a lowered optical coverage of $\sim 19\%$ took place between December 2002 and the beginning of 2005, mostly as part of the K2K project (sec. 1.9.3). The detector is currently being refurbished with new PMTs and a Phase-III with the original configuration should start in 2006.

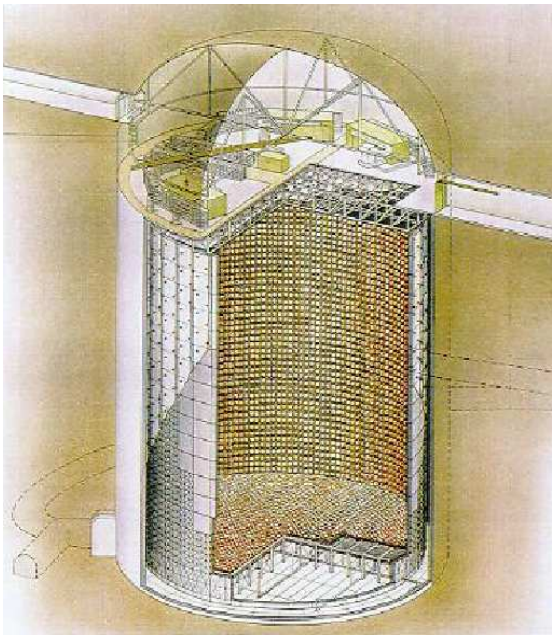

Fig. 1.13: *A sketch of the SK detector[83].*

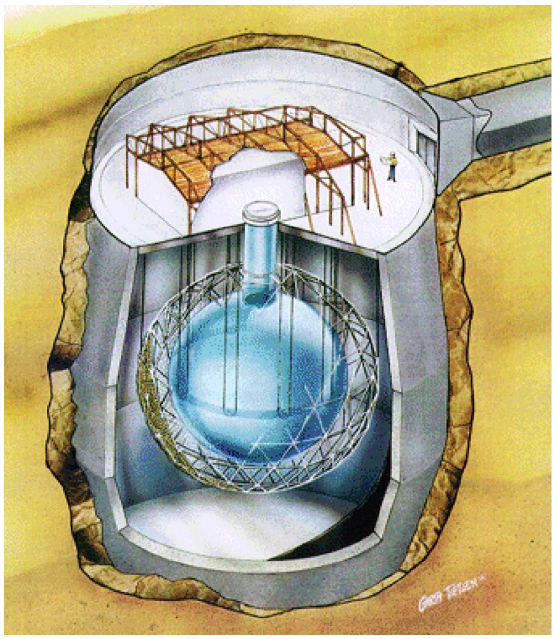

Fig. 1.14: *Sketch of the SNO detector[86].*

$\nu_x + e^- \longrightarrow \nu_x + e^-$ **(Elastic Scattering, ES).** In SNO $3ev/d$ of electron scattering are also expected (SSM). The measurement cannot compete in statistics with the much larger SK, but it provides a very important consistency check for the other two reactions. Moreover it is an interaction which preserves directional information of the original neutrino to confirm the flux's solar origin.

In all 3 cases the analysis threshold is set to $5.5MeV$ by background conditions, so as for SK the signal is made mostly of ^8B neutrinos with a tiny high energy component due to the *hep* emission. It is obvious that the three signals combined can probe possible flavor transitions in the solar ^8B ν's.

Data taking is performed in 3 phases:

1. Pure D_2O phase (Nov 1999 - May 2001). Though essentially devoted to CC measurement it has yielded also the first NC measurement by n-capture on deuterium ($6.3MeV$ de-excitation γ-ray).

2. Salt phase (July 2001 - August 2003). In 2001 $2tons$ of $NaCl$ have been added to the heavy water to increase the NC sensitivity. The neutron capture cross section on Chlorine is $44b$ and the de-excitation γ of $8.6MeV$ allows a clear separation from background events.

3. Neutral Current Detectors (NCDs) phase (January 2004 - December 2006). After the salt removal 800 meters of ^3He proportional counter tubes have been deployed in strings uniformly throughout the detector's volume. Data from this phase have not been released yet.

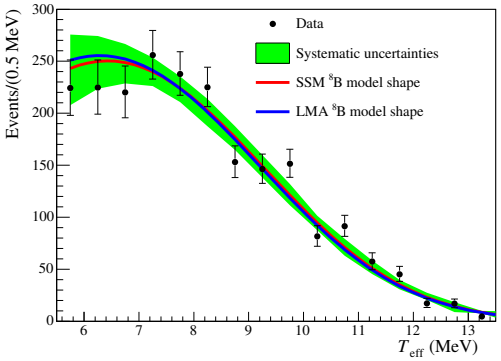

Fig. 1.15 (a): *SNO CC measured spectrum. No spectral distortion is evident nor it is foreseen by LMA solution (sec. 1.7.3)[91].*

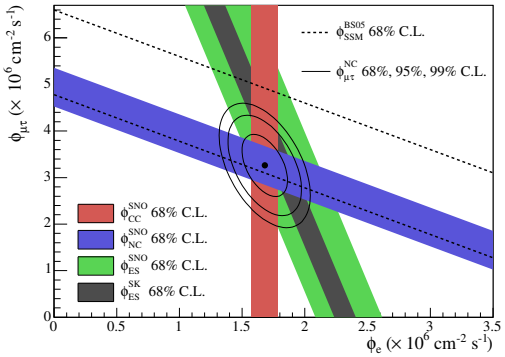

Fig. 1.15 (b): *SNO results[91]. Flux of ν_μ+ν_τ neutrinos vs. flux of ν_e neutrinos. CC, NC and ES fluxes are indicated by the filled bands ($\pm 1\sigma$). SSM predictions are shown as dashed lines. There is a strong evidence for a non-zero $\phi_{\mu\tau}$.*

The first ES/CC results appeared in June 2001[88]: while ES flux was fully compatible with SK, CC flux was significantly lower. Subtracting $\phi_{ES}^{SK} - \phi_{CC}^{SNO}$ (sec. 1.7.1) it was already possible to deduce a non electronic flavor at 3.3σ and to compute an all-flavor flux in good agreement with SSM.

Nevertheless the two following years saw the historical release of the NC results from phase-I first (April 2002)[89] and from the first part of salt phase later at the TAUP 2003 (September) conference[90]. Here the final salt phase data from the 2005 review[91] are reported:

$$\begin{cases} \phi^{\mathrm{CC}}(\nu_e) = 1.68 \pm 0.06(\mathrm{stat.}) \pm 0.09(\mathrm{syst.}) \times 10^6 \mathrm{cm}^{-2}\mathrm{s}^{-1} \\ \phi^{\mathrm{ES}}(\nu_x) = 2.35 \pm 0.22(\mathrm{stat.}) \pm 0.15(\mathrm{syst.}) \times 10^6 \mathrm{cm}^{-2}\mathrm{s}^{-1} \\ \phi^{\mathrm{NC}}(\nu_x) = 4.94 \pm 0.21(\mathrm{stat.}) \pm 0.36(\mathrm{syst.}) \times 10^6 \mathrm{cm}^{-2}\mathrm{s}^{-1} \end{cases} \quad (1.86)$$

While the electronic neutrino flux is given directly by the ϕ^{CC}, the non-electronic flavor is established by:

$$\phi(\nu_{\mu,\tau}) = \phi^{NC} - \phi^{CC} = 3.26 \pm 0.25(stat)^{+0.40}_{-0.35}(syst) \quad [7.6\sigma > 0] \quad (1.87)$$

This striking evidence (fig. 1.15(b)) is proof of flavor conversion (oscillation compatible) and a confirmation of the SSM prediction achieved on ^8B neutrinos.

Assuming neutrino oscillations, the solar global analysis including old and new results gives as best-fit point:

$$\tan^2\theta_{sun} = 0.45^{+0.09}_{-0.08} \quad (1.88)$$

$$\Delta m^2_{sun} = 6.5^{+4.4}_{-2.3} \times 10^{-5} eV^2 \quad (1.89)$$

However solar neutrino oscillations were not yet proven as neither spectral distortion

nor day night asymmetry[21] are foreseen by the model (nor observed) in the ^8B energy region (fig. 1.15(a)). Other flavor conversion mechanisms, like neutrino decay or RSFP ([146]), could also explain the results and it wasn't until KamLAND results (sec. 1.8.3) that oscillations were definitely established.

1.7.3 Global analyses

Oscillation results encompassing all available experimental evidences are presented in planes, where a pair of values $\Delta m^2, \sin^2 2\theta$ (or $\Delta m^2, \tan^2\theta$) correspond to every point.

Before 2000 the fluxes measured by radiochemical experiments (sec. 1.4) and by SK (sec. 1.7.1), were used, leaving $\Delta m^2, \tan^2\theta$ as the only free parameters in the fit.

Four solutions were possible: vacuum oscillations, MSW with Small Mixing Angle (SMA), MSW with Large Mixing Angle (LMA) and MSW at low Δm^2 (LOW), visible as local minima in the plot and contoured by iso-χ^2 curves which represent the allowed "islands" of parameter combinations (fig. 1.16).

The publications of new results every year progressively narrowed the space left for allowed solutions and at the same time the SSM constraints on the neutrino fluxes could be released (starting with ^8B). In 2004 the fit was already fully model independent (apart from the luminosity constraint).

In 2000 SK energy spectrum featuring no deformation was disfavoring the SMA solution. SNO CC results disfavored vacuum oscillations and oscillations into sterile neutrinos, while NC results started to indicate LMA as the final solution with only the LOW alternative still allowed. KamLAND results (sec. 1.8.3) finally pinned down the LMA solution.

The evolution of global analyses between 2000 and 2005 can be followed for example in [92, 93, 94, 95, 96, 147, 97] and is summarized in fig. 1.16.

1.8 Reactor Neutrino Experiments

A powerful source of neutrinos are commercial nuclear reactors. In the core of reactors, electron anti-neutrinos up to $\sim 8MeV$ are produced in fission reactions and can be detected in liquid scintillator by inverse β decay on target protons:

$$\overline{\nu}_e + p \longrightarrow n + e^+ \tag{1.90}$$

with a kinematic threshold of $1.8MeV$. The positron immediately annihilates in two $511keV-\gamma$'s determining a prompt energy of $E_{vis} = E_{\overline{\nu}_e} - E_n - 0.8MeV$ [22], where E_n is the usually small energy of the recoiling neutron. The neutron is thermalized with a mean time of the order of $\sim 200\mu s$, depending on material, and is later captured in a radiative process. The γ emitted is seen as a delayed event and constitutes a powerful tag to reject background. Capture on proton yields a $2.2MeV-\gamma$, but often the scintillator is loaded with nuclides, such as Gadolinium, to enhance the neutron capture cross section. This often leads also to a shorter capture times (i.e. less background accidental coincidences)

[21] Like in SK a small negative value is observed in SNO, compatible with zero at 1σ.

[22] 0.8MeV arises from the difference of the energy lost in the inverse β process and the extra energy from the annihilation.

Fig. 1.16: *Evolution of the global analysis (solar) over the period 2000-2005.*

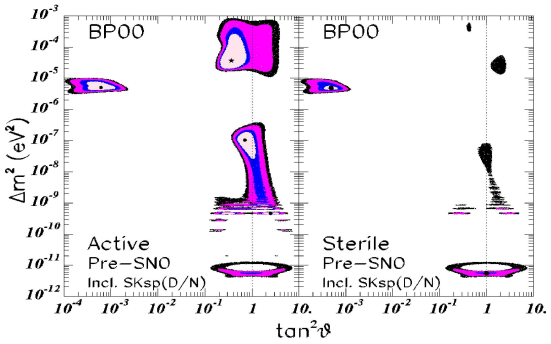

(a) 2000: before SNO results[93].

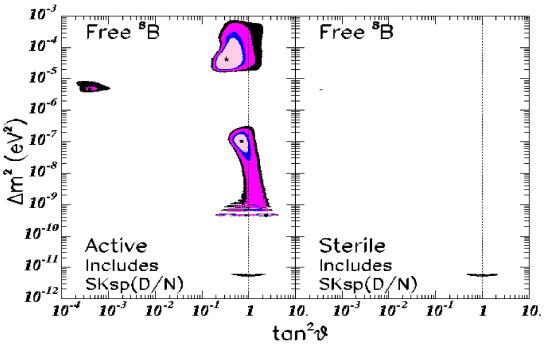

(b) 2001: ^8B flux becomes free. SNO CC disfavors sterile neutrinos[94].

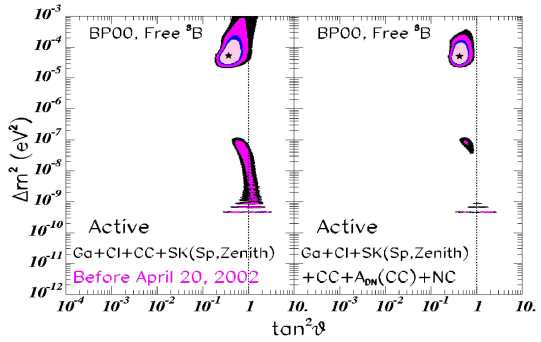

(c) 2002: SNO NC (D_2O) results favor LMA solution[95].

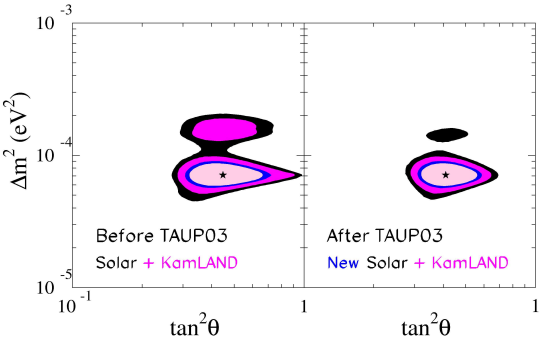

(d) 2003: KamLAND results indicate LMA as the only solution[96]. Final GNO and SNO NC (salt) results restrain it further[147].

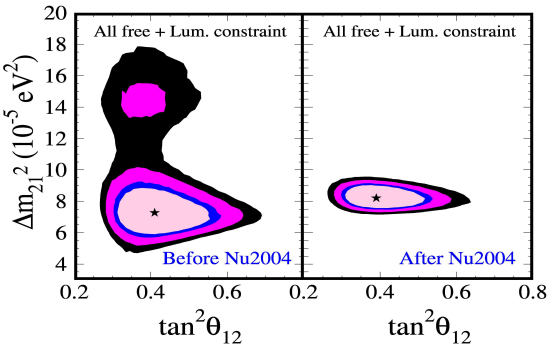

(e) 2004: All fluxes are let free (with $L_\odot$ constr.). New KamLAND data pin down Δm^2_{12}[97].

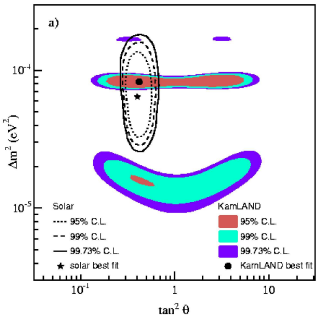

(f) 2005: Solar and reactor contributions to current (Δm^2_{12}, $\tan^2\theta_{12}$) best fit[104].

Site	Country	year	GW	L(m)	Type	tons	Seg	L.	mwe
ILL	France	1981	0.06	9	scint	0.4	30	-	10
Goesgen	CH	1986	2.8	38–46–65	scint	0.4	30	-	15
Bugey	France	1995	2.8	15+40+95	scint	0.6	98	Li	15
Rovno	URSS	1991	1.4	18	^3He	-	-	-	30
Krasnoyarsk	URSS	1994	3×1.8	57:57:231	^3He	-	-	-	600
Bugey(d)	France	1999	2.8	18	deut.	0.28	1	-	15
Palo Verde	USA	1999	11(3)	890:890:750	scint	12	66	Gd	32
Chooz	France	1999	8.5(2)	998:1115	scint	5	1	Gd	300
KamLAND	Japan	2002	130	180km	scint	1kt	1	-	1000

Tab. 1.5: *Short-Intermediate-Long baseline reactor experiments. Column 4 shows reactor power and number. Column 5 shows distance from reactor(s): $d_1 - d_2$ detector moved, $d_1 + d_2$ multiple detectors, $d_1 : d_2$ multiple reactors. Column 8 shows detector segmentation (1=unsegmented).*

and a higher energy of the radiative process. Expected signals depend on reactors operational times, but the companies provide these data allowing flux calculations accurate to a few %. Moreover the refueling periods ($\sim$ 1 month shutdown per year) allow the study of the background in absence of the signal.

Reactor experiments are (arbitrarily) divided in short (S), intermediate (I) and long (L) baseline experiments, reflecting the Δm^2 region explored. The characteristics of the mentioned experiments are summarized in tab. 1.5.

1.8.1 Short baseline experiments

Research in the reactor neutrino field started in the 1970s with a few experiments installed at distances in the $10m-100m$ range from one or more reactor cores. Many measurements were repeated at different distances from reactor core(s) either moving a single detector or using more identical detectors. In this way most of the systematics cancels out analyzing the subtracted spectra.

ILL-Grenoble and Goesgen. The European experiment was installed in 1977 at ILL research reactor (Grenoble). 30 liquid scintillator cells, sandwiched with ^3He proportional counters for neutron detection, were placed, along with the required shielding, $8.5m$ away from reactor core, sensing Δm^2 down to $0.15eV^2$. The detector was then moved to the more powerful reactor at Goesgen (Switzerland) and operated at three distances $38m$,$46m$ and $65m$ between 1981 and 1985 covering $\Delta m^2 > 1.5 \cdot 10^{-2} eV^2$. Observed signals were consistent with no oscillation previsions.

Bugey. At the beginning of the 90s, 3 identical detectors were placed at $15m$, $40m$ and $95m$ from the $2.8GW$ Bugey commercial reactor. Segmented detectors were made (each) of 98 cells holding $600l$ of organic scintillator loaded with ^6Li at 0.15%. The fast capture on ^6Li yields ^3He and ^4He whose signal can be easily extracted with PSD analysis. Bugey measurements sensed Δm^2 down to 10^{-2} excluding any oscillation effect.

Rovno and Krasnoyarsk. 2 Russian experiments were performed at Rovno reactor (18m baseline) and at the 3-reactor power station of Krasnoyarsk (baseline 57m with 2 reactors and 231m from the third one). Apart from specific technical setups, both detectors were made by ^3He proportional counters only, with no sensitivity to the positron signal. Consequently no energy spectrum could be measured.

Savannah River and Bugey-deuterium. Reactor antineutrino could interact with deuterons through:

$$\overline{\nu}_e + d \longrightarrow e^+ + 2n \qquad (CC) \tag{1.91}$$

$$\overline{\nu}_e + d \longrightarrow \overline{\nu}_e + p + n \qquad (NC) \tag{1.92}$$

and if double neutron signals can be efficiently separated by single neutron signals, a powerful oscillation test can be done. This scheme was exploited at the Savannah River reactor in 1980, indicating oscillations. The experiment was later repeated at the Bugey site with $276kg$ of deuterium and ^3He proportional counters to detect neutrons, placed $19m$ away from the reactor. The results allowed the rejection of the oscillation hypothesis proposed at Savannah River.

In conclusion none of the short baseline reactor experiments reported evidence of oscillations, but they successively (and impressively) improved the excluded region in the upper part of the parameter plane.

1.8.2 Intermediate baseline experiments

The *atmospheric neutrino anomaly*, pointed out by KamiokaNDE and SK (sec. 1.6), could be initially interpreted either as a $\nu_\mu \rightarrow \nu_e$ oscillation or as a $\nu_\mu \rightarrow \nu_\tau$. In the former case the Δm^2 region favored was spanning well below the $10^{-2}eV^2$ area sensed by Bugey. For this reason two experiments were constructed in the middle '90s with baseline $\sim 1km$, Chooz and Palo Verde:

Chooz. The detector was located at the Chooz power station in the Ardenne region in France ($8.5GW$, 2 reactors) at distances of $998m$ and $1115m$ from the two reactors in a deeper site ($300m.w.e.$). The detector was an unsegmented Gd-loaded (0.1%) liquid scintillator with a $5t$ target in a spherical acrylic vessel surrounded by $17t$ active buffer. Outside the containment sphere $91t$ of scintillator were used as active muon veto. The observed versus expected neutrino rate was published in 1999[100]: $1.01 \pm 0.028(stat.) \pm 0.027(syst.)$.

Palo Verde. The detector was located at the Palo Verde power station in Arizona, USA ($11GW$, 3 reactors) at a distance of $890m$ from 2 reactors and $750m$ from the third one in a shallow site ($32m.w.e.$), which required a large effort in terms of muon-induced background reduction (passive and active shielding). Moreover the detector had to be designed *segmented* into 66 cells with PMTs at each end, for an overall $11.6t$ of Gd-loaded (0.1%) liquid scintillator. The observed neutrino rate, divided by the non-oscillation expectation value, was also published in 1999[99]: $1.01 \pm 0.024(stat.) \pm 0.053(syst.)$.

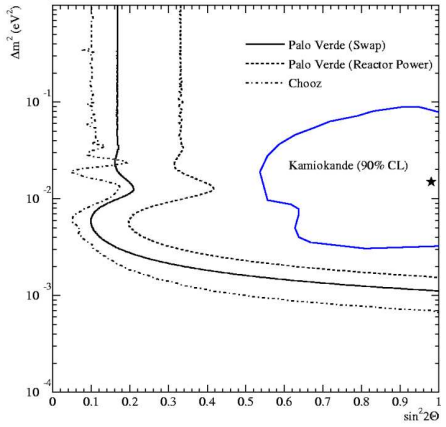

Fig. 1.17: *Exclusion plots for Palo Verde and Chooz results compared to SK atmospheric allowed region[99].*

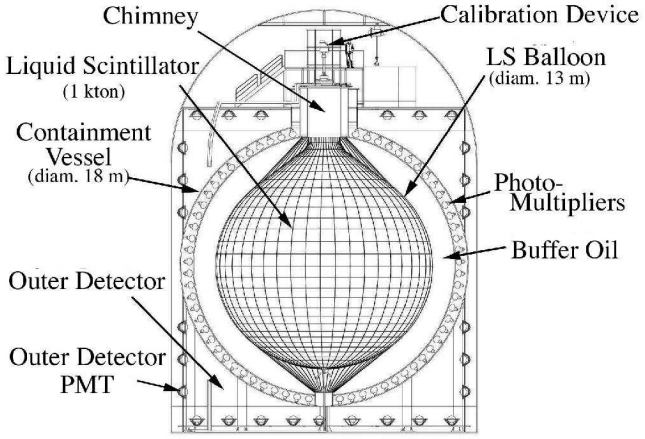

Fig. 1.18: *Schematics of the KamLAND detector[101].*

The Chooz experiment achieved a slightly higher sensitivity excluding the region of $\Delta m^2 > 7 \times 10^{-4}$ (fig. 1.17) and constraining the atmospheric oscillations to the $\nu_\mu \rightarrow \nu_\tau$ case[23].

In addition, the Chooz excluded area is up to now the best upper bound on the θ_{13} mixing angle: $\sin^2 2\theta_{13} < 0.2$ at $\Delta m^2 = 2 \cdot 10^{-3} eV^2$ and 90% C.L. To improve this measurement the experiment Double-Chooz is currently being designed (sec. 1.11).

1.8.3 KamLAND

The KamLAND (*Kamioka Liquid scintillator Anti-Neutrino Detector*) detector[102] is the only long baseline reactor experiment realized so far. It is situated in the former KamiokaNDE site (sec. 1.4.2) in Japan. The experiment is sensitive to neutrinos produced by reactors at a power-weighted average distance of $180km$, dominated (79%) by 26 reactors in the $138 - 214km$ range. Thanks to the relatively narrow band of reactor distances KamLAND is quite sensitive to spectral distortions in the LMA region, provided CPT invariance holds.

The detector was designed after BOREXino (chap. 2) and is therefore very similar in structure: the target, $1kton$ of organic liquid scintillator[24], is hosted in a nylon balloon of $13m$ diameter, which in turn is immersed in a buffer oil[25]. The organic fluids are contained in an $18m$ diameter stainless-steel sphere. The inner detector is made of ~ 1900 PMTs with an overall geometrical coverage of 34%. The space between the sphere and an external tank is filled with water and observed by additional 225 PMTs as active muon veto and background shielding from the rock.

[23] By the time this result was published there were already other independent indications in this sense as mentioned in sec. 1.6.

[24] 80% dodecane + 20% pseudocumene + $1.5g/l$ PPO, cmp. sec. 2.4.

[25] dodecane and iso-paraffin oils

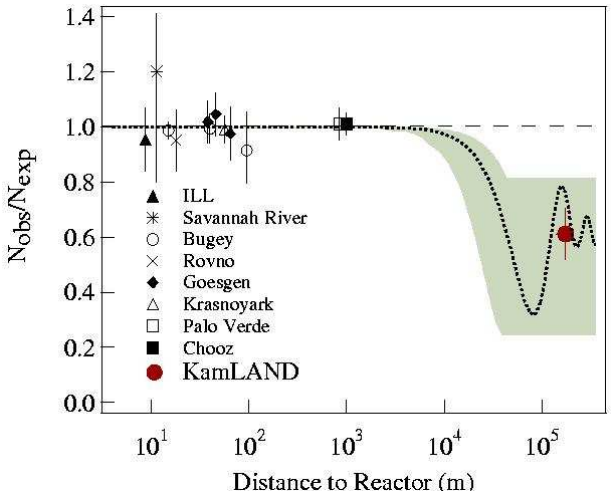

Fig. 1.19 (a): *Ratio of the $\overline{\nu}_e$ fluxes observed by reactor experiments over the expectations[103]. The dotted curve accounts for LMA best-fit parameters (in 2002). The shaded region is the 95% C.L. allowed area.*

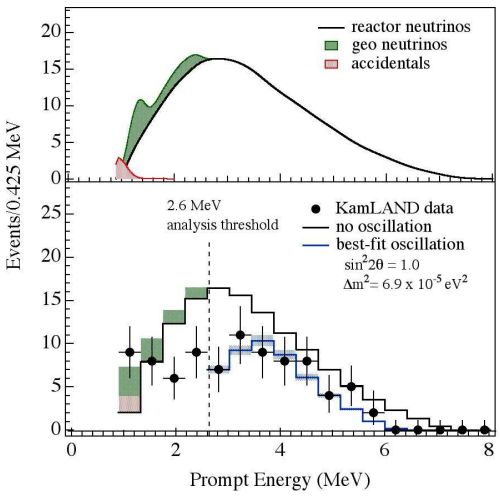

Fig. 1.19 (b): *KamLAND: expected reactor $\overline{\nu}_e$ energy spectrum with background contributions (up) and the prompt event spectrum observed (down)[103].*

The expected signal is of the order of $\sim 1ev/d$ and a careful background evaluation has been performed to extract it[102]. The analysis threshold had to be fixed to $2.6MeV$ due to the unknown background from geo-antineutrinos (sec. 1.11.4).

Data taking started in January 2002 and by the end of the year the first results were published[103]. The survival probability reviewed in 2004[104] is:

$$P_{ee} = \frac{N_{obs} - N_{BG}}{N_{expected}} = 0.658 \pm 0.044(stat) \pm 0.047(syst) \tag{1.93}$$

incompatible with the no disappearance hypothesis at 99.998% C.L.

The spectral distortion observed by KamLAND (fig. 1.19(b)) matches the oscillation hypothesis in the MSW-LMA solution with the latest solar best-fit parameters. This historical result was the final proof for neutrino oscillations as the solution of the SNP and establishing LMA as the relevant parameter space region. KamLAND together with all solar ν-results provides a measurement of Δm^2_{12} and θ_{12}[104]:

$$\Delta m^2_{12} = 7.9^{+0.6}_{-0.5} \times 10^{-5} eV^2 \tag{1.94}$$

$$\tan^2 \theta_{12} = 0.40^{+0.10}_{-0.07} \tag{1.95}$$

1.9 Accelerator neutrino experiments

Neutrino beams[105] are produced by the successive decays of π- and K-particles (e.g.: $\pi^+ \rightarrow \mu^+\nu_\mu, \mu^+ \rightarrow e^+\nu_e\overline{\nu}_\mu$) which are created in proton beam dumps. As for reactor

experiments it is convenient to classify accelerator neutrino experiments according to the baseline.

1.9.1 Short baseline experiments

The high Δm^2 region, above $0.1eV^2$, was explored in terms of $\overline{\nu}_\mu \rightarrow \overline{\nu}_e$ oscillations, with two appearance short baseline experiments: LSND and KARMEN. In both cases a proton beam of $800MeV$ was used to obtain an $\overline{\nu}_\mu$ flux ranging up to $\sim 53MeV$ and the two experiments looked for $\overline{\nu}_e$ appearance through the same detection technique presented in sec. 1.8 for reactor neutrino detectors.

LSND. After a moderate hint of a possible oscillatory effect from experiment E645 at LAMPF (Los Alamos National Laboratory, USA), the dedicated short baseline experiment LSND was realized at the same accelerator and took data between 1993 and 1998 in different phases and conditions. The detector was an unsegmented cylindrical detector ($5.7m$ in diameter and $9.3m$ long) with $167t$ of diluted liquid scintillator[26] and 1220 PMTs. It was placed $30m$ away from beam target and 12° off-axis.

KARMEN. The similar ISIS spallation source (Rutherford Appleton Laboratory, Oxford, GB), was simultaneously exploited by the KARMEN experiment from February 1997 until March 2001[27]. In this case the detector was a $56t$ Gd-loaded scintillator segmented in 512 modules. It was placed $17.6m$ away from beam target and 90° off-axis.

The two different beam intensities, cosmic shielding, experimental setups and background rejection techniques resulted in two rather different experiments with advantages and disadvantages on both sides.

The LSND experiment observed an excess of events above the predicted background that varied in different analyses according to data sets and spectral portions considered, but was anyhow always incompatible with the no oscillation hypothesis[106]. The impact of this result is rather large, because it would establish a third oscillation region (fig. 1.20) in the parameter space with $0.2 < \Delta m^2 < 4eV^2$, after the solar and the atmospheric regions. This implies the existence of at least one light sterile neutrino flavor.

The KARMEN experiment observed 15 events for an expected background of 15.8 ± 0.5[107]. At a first approach this is a partial contradiction to the LSND experiment. However the two sensitivity regions are not identical (fig. 1.20) and, according to some authors[105], there is enough space for compatibility.

To solve the controversy the MiniBooNE experiment[108] was constructed at Fermilab (Chicago, USA). The $800t$ liquid scintillator detector at $541m$ from a $700MeV$ neutrino beam, has a much larger sensitivity (fig. 1.20). Data taking started in 2004 and first results should be published in 2006.

[26] The concentration of scintillator was chosen low enough not to overwhelm Čerenkov radiation in order to reject background out of event direction.

[27] Dates refer to KARMEN-2 phase when an improved cosmic shielding was in place. Previous KARMEN data are not significant in this context.

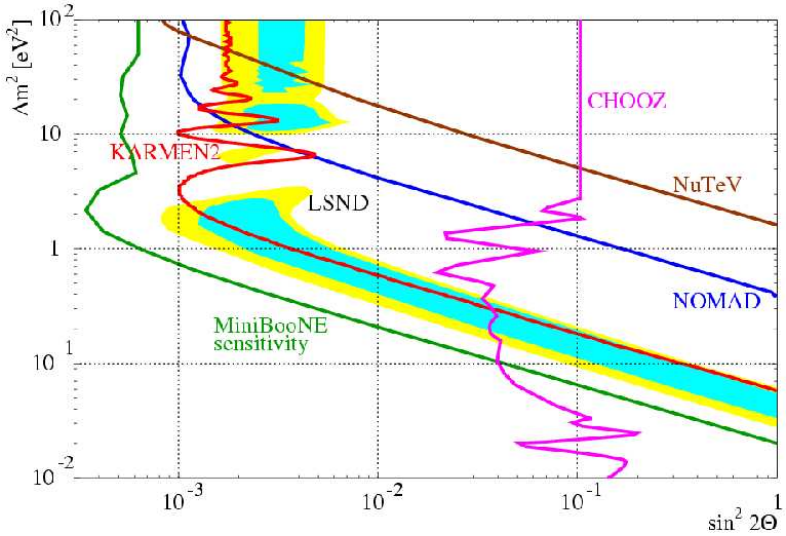

Fig. 1.20: *The LSND observed oscillation region and the KARMEN excluded area[107]. The MiniBooNE sensitivity well encompasses both regions.*

1.9.2 Intermediate baseline experiments

During the same time at CERN an attempt was made to detect $\nu_\mu \rightarrow \nu_\tau$ with appearance experiment. A wide band neutrino beam was obtained from the $450GeV$ SPS and two detectors, NOMAD (1994-97) and CHORUS (1995-98), were placed one after the other, $800m$ from beam target. The beam was composed for 93% of $\sim 24GeV$ ν_μ neutrinos, but contained traces of other flavors[105].

Both detectors had a composite structure in the high-energy style, with tracking and calorimetric sections. The two detectors were equally looking for decay products of the τ^- possibly formed after a CC-interaction of the ν_τ. However CHORUS was looking for tracks left in photographic emulsions, while NOMAD was using kinematic analysis in drift chambers immersed in a strong magnetic field. CHORUS and NOMAD observed no events above the expected background in any searched decay mode and placed an exclusion region in the parameter plane: $\Delta m^2 > 2 \times 10^{-1} eV^2$ for maximal mixing and $sin^2 2\theta < 2 \times 10^{-4}$ for $\Delta m^2 > 20 eV^2$.

In addition if NOMAD's result is reinterpreted in terms of $\nu_e \rightarrow \nu_\tau$ oscillations[109], assuming that the eventual ν_τ appearance was due to the 1% ν_e flux component, an exclusion region can be placed also in the LSND-KARMEN parameter plane (fig. 1.20).

1.9.3 Long baseline experiments

Three long baseline projects intend to confirm the present atmospheric oscillation results (sec. 1.6):

K2K (KEK-to-Kamioka). The Japanese experiment involves the KEK $12GeV$ proton synchrotron equipped with a $\sim 1GeV$ neutrino beam line and the far detector SK (sec. 1.7.1), which means a baseline of $250km$.

The neutrino beam is dominated by ν_μ (98%) and is monitored by two near ($300m$) detectors, a $1kton$ water Čerenkov chamber and the so-called *fine grained detector* a composite structure comprising scintillator fibers and strips, a lead glass calorimeter and a muon range detector[110].

So far K2K has observed a sharp ν_μ disappearance effect and no evidence of ν_e appearance. In the 1999-2004 period (8.9×10^{19} POT data) 107 ν_μ events were selected for an expected value of $151^{+12}_{-10}(syst)$ and an indication for significant spectral distortion is present, leading to the best fit points[110]:

$$\sin^2 2\theta_{23} = 1.0 \qquad \Delta m^2_{23} = 2.8^{+0.8}_{-0.9} \times 10^{-3} eV^2 \tag{1.96}$$

at 4.0σ from the no-oscillation hypothesis and in excellent agreement with the $\nu_\mu \rightarrow \nu_\tau$ oscillation scenario opened by the atmospheric neutrino anomaly.

MINOS. The American MINOS experiment[111] involves instead the new NuMI beam at Fermilab Main Injector made by tunable $2 - 20GeV$ ν_μ and a far detector in the Soudan mine (Minnesota) with a $732km$ baseline. It is a disappearance experiment like K2K, though aiming at a precise parameter determination. The $5.4kton$ detector, made of magnetized steel plates and plastic scintillator strips, started taking atmospheric neutrino data in 2003 and received a beam at the beginning of 2005. A very similar near detector is monitoring the beam at Fermilab. Publication of the first results is expected in 2006.

OPERA&ICARUS. The European project involves the CNGS (CERN-to-Gran-Sasso) $20GeV$ neutrino beam with a $730km$ baseline (very close to the MINOS one). The construction of the lead/emulsion OPERA[113] detector, aimed at ν_τ appearance detection, is ongoing and should be ready by beam delivery, foreseen for 2006. The first modules of the multi-purpose liquid argon TPC (*Time Projection Chamber*) ICARUS[112] have been recently installed in Gran Sasso[28] and hopefully will be operative in a short time.

1.10 Neutrino Telescopes

Neutrino Telescopes aim to observe very high energy neutrinos from point-like sources in space. They are large ($0.01 - 1km^3$) detectors exploiting the natural Čerenkov properties of sea water and of the Antarctic ice crust. In both cases arrays of downward looking optical modules (OMs), i.e. encapsulated PMTs or PMT pairs, are deployed at depths of a few km. Detectors are sensitive to neutrinos coming from the opposite side of the earth.

After crossing the earth, the neutrino interacts with hydrogen or oxygen nuclei yielding a muon whose energy and direction is reasonably correlated with the incoming neutrino. The separation of up- and down-going muons and the depth of the site are both essential to eliminate the background from atmospheric muons. Though the physical threshold is at the level of $10GeV$, the analysis for high energy neutrinos can start only above $1TeV$, because of the background represented by atmospheric neutrinos (fig. 1.11).

[28] Filling with argon is actually delayed due to the situation of the Gran Sasso laboratory (sec. 2.5).

1.10.1 High energy neutrino sources

Surveys that can be performed can be distinguished in terms of the possible neutrino source[114]:

- Surveys on galactic sources:
  1. SuperNova Remnants (SNRs). Neutrino emissions from SNRs could shed light into acceleration models of cosmic rays.
  2. Black Hole formation. Neutrino emission could allow the discovery of otherwise obscured galactic events.
  3. Neutrinos produced by cosmic rays in the galactic disk.
  4. Supernova explosion. Such an event could be detected by the increase of the single rates in each PMT in a time window of $\sim 10s$.
- Surveys on extra-galactic sources[29]:
  1. Active Galactic Nuclei (AGNs). The reference model involves a $10^6 M_\odot$ accreting black hole that accelerates protons and/or electrons up to $10^{20} eV$. These protons should interact with matter and produce pions and kaons. The subsequent decays of these particles are the source of high energy neutrinos.
  2. Gamma Ray Bursts (GRBs). Some models suggest that GRBs originate by a relativistic expanding fireball powered by the formation of a compact object. Again proton acceleration is involved in the expansion leading to neutrino emission. The eventual detection of neutrino emissions associated to GRBs would allow testing of the model.
- Particle physics:
  1. Cold Dark matter search. Annihilation of neutralinos or WIMPs above $500 GeV$ and $200 GeV$ respectively, in the galactic center or even in our sun, would be visible as neutrino emission, so an upper mass bound can be set in absence of such a signal.
  2. Additional searches for topological defects (in the frame of GUT theories), magnetic monopoles, and a charm component in the atmospheric muon flux.

Most of the sources are however speculative and the cross sections at such high energies are poorly known. Consequently it is difficult to foresee neutrino spectral shapes and signals, however the latters generally range in $1 - 100 ev/y$[114].

1.10.2 Detectors design

Concerning the detectors, ice scatters light more than water but absorbs it less, so under-ice detectors can tolerate a higher spacing of optical modules (i.e. larger covered area for the same cost) and are capable of a higher energy resolution. Water detectors should

[29] Also sources of *Ultra High Energy Cosmic Rays* (UHECR) $> 3 \times 10^{18} eV$.

have instead a sub-degree pointing resolution. The technical difficulties of deploying and maintaining optical modules in the two media are of course very different but equally challenging.

The under-sea hypothesis was first exploited by the relatively small Baikal Neutrino Telescope located in Lake Baikal in Siberia at a $1.1km$ depth. Operative since 1997 it has demonstrated the potentiality of the technique detecting atmospheric neutrinos with less than 200 modules. A partial upgrade of the detector to $10Mton$ volume is ongoing.

The most natural choice for larger scale water Čerenkov detector is the Mediterranean sea as it provides deep and relatively flat sea bed areas relatively close to shore. Dominating background sources include ^{40}K in the water and the so-called *bioluminescence*, i.e. light emitted by bacteria and other living organisms. A few sites have been evaluated in terms of optical properties of the water and background conditions and two concurrent projects are starting up:

- NESTOR[115], Southern Greece, 4.0km depth. The detector is a tower of 12 star-shaped floors with double OMs at each of the 6 arm extremities.
- ANTARES[116], Toulon, France, 2.4km depth. Here 12 strings of 25 *Storey*s (units of 3 OMs) will be anchored to the sea bed.

In 2003 both projects deployed and successfully operated test elements (1 floor or 1 string respectively) reporting atmospheric muon observations and showing that the technical difficulties are well under control. Deployment of both final detectors are expected to start in the near future.

In the longer term, the community is looking forward to instrument a km^3 water volume, ~ 6000 OMs being required for this goal[30]. The NEMO collaboration has located a $3.5km$ deep site, off-shore from Catania in Sicily. All collaborations signed a letter of intent to converge on the project that shows the best possibilities.

The under-ice hypothesis has been operative since 1997. The detector is named AMANDA and is the "small" (677 modules) version of the planned IceCube[119] detector ($1km^3$, 4800 modules), including a surface veto for down-going muons. Expansion toward the final configuration is ongoing and should be completed in 2010. Extensive analysis of the AMANDA data showed no evidence for diffuse or point-like sources setting the current upper limits[118].

Mediterranean and Antarctic observatories are complementary in the sky portion observed: northern sky for AMANDA/IceCube, southern sky for detectors in the Mediterranean sea.

1.11 Open questions

In spite of the establishment of the MSW-LMA solution to the SNP and of the long baseline confirmation of the atmospheric oscillations, neutrino physics is today perhaps more alive than ever, in the exciting attempt to answer the questions left open (or newly opened?) by recent experimental results[120, 121].

[30] To keep the cost (dominated by deployment) within reasonable limits, the design requires a new concept of foldable structures that unfold in site.

1.11.1 Particle physics

Three vs. four neutrino mixing. Solar and atmospheric data fit nicely into a three-neutrino scenario and are confirmed by reactor and accelerator long baseline experiments. As mentioned in sec. 1.9.1 the LSND result introduces a third Δm^2 which requires a fourth sterile neutrino to be explained. In the near future MiniBooNE will confirm or reject the LSND evidence. In the meantime the other open questions are discussed under a three-neutrino scheme.

Solar and Atmospheric parameters. Regarding oscillations, we presently know four of the six parameters involved:

- $\tan^2\theta_{12} = 0.45^{+0.09}_{-0.07}$
- $\Delta m^2_{12} = 7.9^{+0.6}_{-0.5} \times 10^{-5} eV^2$
- $\sin^2 2\theta_{23} = 1^{+0}_{-0.08}$
- $\Delta m^2_{23} = 2.4^{+0.6}_{-0.5} \times 10^{-3} eV^2$

with the first two being determined by solar+KamLAND data and the last two by atmospheric+K2K data.

The precision to which the solar parameters are known is already quite high. In the near future SNO phase III (sec. 1.7.2) could constrain a little further the mixing angle, which is large but already clearly non-maximal, and KamLAND (sec. 1.8.3) could further reduce the errors on Δm^2. The next step to determine the mixing angle could be a reactor experiment with a baseline of $\sim 50km$ chosen ad hoc from the current best fit Δm^2_{12} value in order to observe the first minimum in the survival probability (eq. 1.78).

Improvement on the atmospheric parameters should come instead from the NuMI-MINOS long baseline accelerator program (sec. 1.9.3). Three years of data taking should yield an accuracy of 10% in Δm^2_{23}.

Vacuum-matter transition. It is interesting to apply the MSW resonance conditions expressed at the end of sec. 1.5.5 to the solar neutrino spectrum (fig. 1.21).

For sub-MeV energies the resonant condition (eq. 1.74) is never met as it would require electron densities that are not present in the sun interior, therefore the oscillation occurs in a vacuum regime. Since $L \sim E/\Delta m^2 < 10^4 m$ is much smaller than the sun-earth distance, the effect is averaged: $P_{ee} \sim 1 - \frac{1}{2} sin^2 2\theta_{12} \sim 0.6$.

For energies above $10 MeV$ the oscillation is dominated by matter effects and $P_{ee} \sim sin^2\theta_{12} \sim 0.3$. In the intermediate transition region a spectral distortion could be observed. The low sensitivity of SNO and SK to the LMA solution arises from the fact that their energy threshold comprises only a minor part of the transition region and most of the spectrum lies in the "flat" matter-dominated area (fig. 1.15(a)).

The transition energy depends on neutrino emission: ^8B neutrinos are produced in the sun at small radii (high density), while *pp* are produced further out (lower

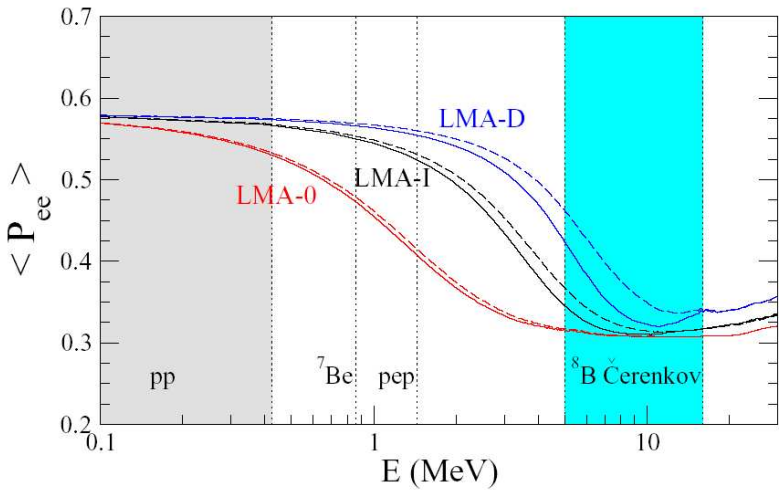

Fig. 1.21: *Neutrino survival probability in the* LMA *scenario (black curve). At energies of a few MeV there is visible the transition between vacuum and matter-enhanced oscillation regimes. LMA-0 and LMA-D are alternative models considered in [123].*

density) and ^7Be are intermediate[147]:

$$E_{trans} \sim 1.8MeV(^8B); \quad \sim 2.2MeV(^7Be); \quad \sim 3.3MeV(pp) \tag{1.97}$$

Up to now only ^8B neutrinos above $\sim 5MeV$ have been detected in spectrographic experiments, so everything which lies below awaits confirmation and could potentially reveal surprises. Therefore solar neutrino investigation of ^7Be and *pp* emissions is important. Due to the averaging effect, the detection of these emissions is insensitive to Δm^2_{12}, but is quite sensitive to $\sin^2 2\theta_{12}$.

In addition the *pep* detection or a ^8B spectral measurement below $5MeV$ are of great interest, as they would probe right the transition region where small deviations from the LMA are eventually expected to show up ([122, 123, 124]). Such measurements are very difficult in KamLAND due to the high cosmogenic background.

θ_{13} mixing angle. The Chooz experiment currently sets the upper limit: $\sin^2 2\theta_{13} < 0.2$ at $\Delta m^2 = 2 \cdot 10^{-3} eV^2$ and 90% C.L. (all limits given below are for these values of Δm^2 and C.L.). However we still don't know if $\theta_{13} = 0$ or not. A zero value would mean that the three neutrino scenario decouples into two two-neutrino oscillation patterns and that the CP-violating phase does not affect oscillations (and it cannot be measured) as it appears clear in eq. 1.67. A non-zero θ_{13} would instead imply a sub-dominant $\nu_\mu \rightarrow \nu_e$ oscillation in the atmospheric region and possibly a matter effect in the future long baseline experiments.

The present generation long baseline accelerator experiments (sec. 1.9.3) can achieve only a moderate improvement: in five years of operation they can reach about

$\sin^2 2\theta_{13} < 0.08$ depending on the actual beam intensity[127]. Therefore one or more experiments must be realized according to two possible strategies:

1. Reactor disappearance experiments with a baseline of $\sim 1.4km$[125], chosen ad hoc to observe the first minimum in the survival probability as inferred from Δm^2_{23}. A differential (near-far) measurement has to be performed with either two (or more) detectors required or involving a single movable detector. Three concurrent projects are being developed in Japan, USA-China and Europe. The most advanced is the latest, named *Double-Chooz*[126]. The French part of the Chooz collaboration with the involvement of other institutions is about to start the construction of a two-detector experiment at the Chooz site following a design similar to the Chooz detector. This approach is surely cheaper and faster to realize but the sensitivity achieved in three years of operation would be $\sin^2 2\theta_{13} < 0.03$ at $\Delta m^2 = 2 \cdot 10^{-3} eV^2$ and 90 % C.L.
2. Off-axis accelerator experiments measuring $\nu_\mu \rightarrow \nu_e$ appearance. Pion decay kinematics indicates that going off-axis allows a more tuned neutrino energy. Different projects are under discussion, NOνA[128] at NuMI beam and T2K (Tokai-to-Kamioka)[129] involving the new J-Parc accelerator complex in Japan and the SK detector (sec. 1.7.1). The latest is funded and beam delivery is foreseen for 2009. These longer term approaches have higher sensitivity. For example five years of T2K would yield $\sin^2 2\theta_{13} < 0.008$ at $\Delta m^2 = 2 \cdot 10^{-3} eV^2$ and 90 % C.L. if no ν_e appearance is observed.

CP-violating phase δ. This measurement is subordinate to a $\theta_{13} > 0$ result. The chance to observe it lies in the above mentioned off-axis accelerator experiments or, more precisely, in their long term ($\sim 15y$) evolution into the so-called *neutrino super-beams*[130]. These projects involve $4MW$ proton beams and future Mton-scale water Čerenkov detectors like Hyper-KamiokaNDE[131], UNO[132] or a detector in the Gulf of Taranto in the Mediterranean sea[130].

An asymmetric appearance observation $\frac{\nu_\mu \rightarrow \nu_e}{\overline{\nu}_\mu \rightarrow \overline{\nu}_e} \neq 1$ would be the signature of CP-violating leptonic processes and a first hint for *leptogenesis*, which can explain the baryon asymmetry in our universe[133].

Absolute mass scale. Active search in this sense is ongoing with the three strategies presented in sec. 1.5.3: tritium β-decay, 2β-decay and cosmological measurements. The next-generation KATRIN experiment[134], starting in 2007 using a very strong ^3H source, should reach a sensitivity of the order of $\sim 0.2eV$.

Mass hierarchy. The sign of Δm^2_{23} is still undetermined, unlike Δm^2_{12} fixed by MSW effect in the sun[31]. This allows two possible mass hierarchies, named *normal* and *inverted* (fig. 1.22). Determination of the sign of Δm^2_{23} and consequent mass hierarchy discrimination are not around the corner: this may come from accelerator appearance experiments if the baseline is long enough to allow the MSW effect in the earth, i.e. $L \gtrsim 1000km$.

[31] If Δm^2_{12} was negative eq. 1.73 could not allow any resonance behavior.

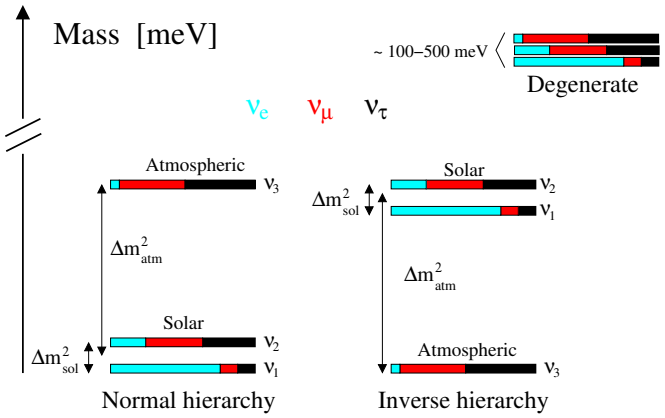

Fig. 1.22: *Possible mass hierarchies in three neutrino mixing[66]. Flavor eigenstate compositions are computed upon the best solar and atmospheric data.*

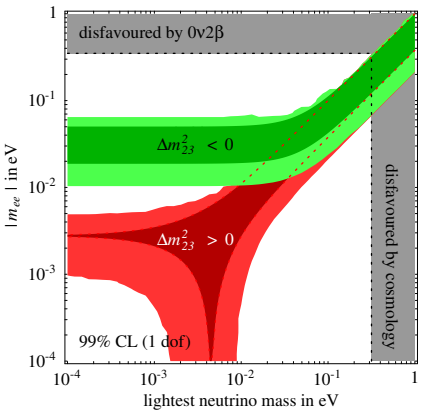

Fig. 1.23: *Relation between m_{ee} and the mass of the lightest neutrino[136]. The dark areas reflects the spread due to Majorana CP phases. The light ones the current errors on oscillation parameters.*

If the mass of the lightest neutrino is larger than $0.01eV$ then it becomes impossible to distinguish between the two options. In this case the neutrino masses are called *degenerate*.

Further information on the mass hierarchy as well as on θ_{13} could be obtained by observing supernova-ν's passing through the earth. In future large detectors with high energy resolution (e.g. LENA, sec. 1.12) the $\overline{\nu}_e$ spectrum would show wiggles which depend on these parameters.

Dirac vs. Majorana nature. The only kind of experiment that can solve this ambiguity is the search for neutrinoless double-beta decay (sec. 1.5.3). The recent controversy on the HDMS claim for a $0\nu\beta\beta$ evidence awaits confirmation. The upcoming GERDA experiment[138], still based on Germanium, will probe the existence of a peak at the reaction Q value, but will be bound to the same intrinsic Ge contamination. The observation of a signal in an experiment based on a different isotope is then mandatory. The most promising of the proposed projects[137] is perhaps CUORE[139], the upgrade of the running ^{130}Te CUORICINO experiment[72].

It should be noted that if the HDMS result is confirmed, in addition to evidence for Majorana nature of neutrinos and for non conservation of lepton number, there would be an indication of mass degeneracy. The claimed mass range of $0.1 - 1eV$ is still consistent with cosmological limits (sec. 1.5.3) and will be covered to a good extent by the upcoming KATRIN experiment. The astrophysical role of neutrinos in this case would be relevant in structure formation on large scales[135].

If on the other hand the HDMS result is not confirmed, a positive result from KATRIN would imply the neutrino is a Dirac particle[140], while a negative result would mean that the second generation DBD experiments (CUORE, GERDA phase-

II, ...) have to face the challenging goal of a $10meV$ sensitivity to probe the inverted hierarchy mass range. This can bee seen in fig. 1.23 where $\langle m_{ee} \rangle$ is related to the mass of the lightest neutrino in the three hierarchic cases (using eq. 1.67 and the mixing parameters).

Magnetic moment. Massive neutrinos are eligible to have a non-zero magnetic dipole moment.

The highest chances to observe μ_{ν_e} come from dedicated reactor experiments[141]. The MUNU experiment, installed at $18m$ from Bugey reactor's core in France, was a $1000l$ CF_4 TPC operated at $3atm$ ($11.4kg$) in an anti-Compton liquid scintillator detector. Background suppression via angular correlations allowed MUNU to reach a $700keV$ analysis threshold and the current best limit of $\mu_{\overline{\nu}_e} < 9.0 \times 10^{-11} \mu_B$ [143].

Neutrino magnetic moment would influence neutrino interactions in the Big Bang nucleosynthesis and Supernova cooling models. Cosmological constraints imply $\mu_\nu < 10^{-10} - 10^{-12} \mu_B$ but are inherently model dependent.

In presence of a non-zero magnetic moment the $\nu_e - e^-$ cross section gains an electromagnetic term (T being the electron recoil energy):

$$\frac{d\sigma}{dT} = \mu_\nu^2 \frac{\pi \alpha_{em}^2}{m_e^2} \left(\frac{1 - T/E_\nu}{T} \right) \tag{1.98}$$

that becomes dominant over the weak interaction term at low energies. Electron scattering experiments are therefore sensitive to neutrino magnetic moment, with SK (sec. 1.7.1) placing the most stringent limit $\mu_{\nu_e} < 1.5 \times 10^{-10} \mu_B$[142]. The BOREXino Counting Test Facility (chap. 9) was able to obtain a $\mu_{\nu_e} < 1.0 \times 10^{-9} \mu_B$ in the low energy region $(180 - 350keV)$[219].

A non-zero neutrino magnetic moment would make a $\nu - \overline{\nu}$ transition possible in the sun's magnetic field via spin flip. This hypothesis is being investigated by solar neutrino detectors by searching for a possible latent $\overline{\nu}_e$ component in the solar flux. The most stringent limit is currently placed by KamLAND: $3.7 \times 10^2 cm^{-2} s^{-1}$ [144] in the $E > 8.3MeV$ region (i.e. above reactor spectrum). SNO places a $3.4 \times 10^4 cm^{-2} s^{-1}$ [145] with $E > 4MeV$, while a limit down to the kinematical detection limit ($1.8MeV$) obtained with CTF data (chap. 9) is currently being published[223].

Additionally the so-called *Resonant Spin-Flavor Precession* (RSFP) [146], a mechanism by which flavor conversion results as a consequence of a spin interaction, was proposed to explain solar neutrino data flavor conversion up to and including SNO NC results. With the KamLAND results and the consequent establishing of the MSW-LMA scheme this phenomenon was relegated to a possible sub-dominant role.

As the strength of the solar magnetic field varies with time (11y periodicity), a non-zero neutrino magnetic moment could lead to a time dependent ν-rate.

1.11.2 Solar Astrophysics

The reference global analysis is performed with the available solar and reactor data, assuming MSW-LMA best fit parameters and leaving all fluxes freely varying within the luminosity constraint (sec. 1.7.3).

The following fluxes are obtained (normalized to SSM predictions)[147]:

$$\begin{array}{lcccc} pp & = & 1.02 & \pm 0.02 & (1\sigma) \\ {}^7Be & = & 0.93 & {}^{+0.25}_{-0.63} & (1\sigma) \\ {}^8B & = & 1.00 & \pm 0.04 & (1\sigma) \end{array} \tag{1.99}$$

where the good accuracy on the pp flux reflects the powerful bound of the luminosity constraint, while the ${}^8B$ flux is well determined by experiments.

${}^7Be$ flux. This emission is currently the most poorly determined. The 40% experimental uncertainty can be lowered to 10% (i.e. comparable to the SSM prediction uncertainty) by a ${}^7Be$ $\nu - e^-$ scattering experiment (or by a CC ${}^7Be$ experiment.) with a $\pm 10\%$ precision. A 3% accuracy would reduce ${}^7Be$ error to 5%[147]. This measurement is by far the most urgent requirement in solar astrophysics.

***pp* (or *pep*) flux.** The determination on this emission could be lowered $2\% \rightarrow 0.5\%$ by a $\pm 5\%$ ${}^7Be$ $\nu - e^-$ scattering measurement. However, since pp neutrinos contribute 91% of the total neutrino flux, a direct measurement via a $\nu - e^-$ scattering experiment is desirable. A precision of $\pm 3\%$ would also help in constraining $\tan^2\theta_{12}$[147].

Since the ratio $\phi(pp)/\phi(pep) = 425.9$[147] is only weakly model dependent and known to a good accuracy, a pep measurement would be just as good as a pp one.

Luminosity cross-check. Current global analysis is able to infer the solar luminosity from neutrinos only with a 20% error. Reducing this uncertainty would allow a direct comparison with the photon luminosity. This would test the fundamental SSM idea on thermonuclear energy production and the sun being in a quasi-steady state with a null energy balance. A $\pm 5\%$ ${}^7Be$ $\nu - e^-$ scattering measurement would reduce the neutrino luminosity indetermination to 13%, while a pp experiment with the same precision would further pin it down to 4%[147].

CNO rates. CNO neutrino fluxes are basically undetermined by the available data. In current global analysis they are set to zero in the best-fit case with 1σ upper limits of 2.4, 13 and 220 times the SSM predictions for ${}^{15}O$, ${}^{13}N$ and ${}^{17}F$ respectively[147]. A $\pm 5\%$ ${}^7Be$ $\nu - e^-$ scattering measurement would reduce these limits by a factor 2-5 but not much more, leaving a direct measurement as the only reliable way to know these fluxes and to establish the fraction of solar luminosity to be ascribed to the CNO cycle[148].

1.11.3 Supernova neutrinos

As mentioned in sec. 1.2 a star is in hydrostatic equilibrium throughout its evolution, with the gravitational pressure balanced by radiative pressure produced in thermonuclear

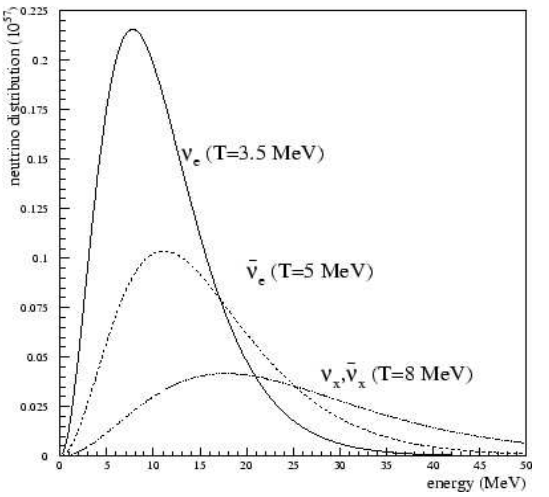

Fig. 1.24 (a): *Expected supernova neutrino spectrum for $\epsilon_B = 3 \times 10^{53}$[184].*

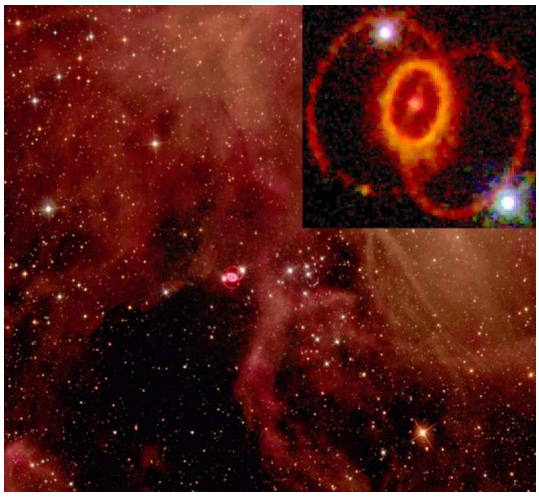

Fig. 1.24 (b): *Supernova SN1987A in the large Magellanic Cloud photographed by the NASA Hubble Space Telescope[149].*

reactions. However the star indeed undergoes important transformations during its life. Whenever a fuel reservoir is exhausted radiative pressure drops. As a result the star starts to collapse with the temperature of the core increasing until a new heavier (higher Z) fuel starts to burn. Finally a new (different) equilibrium condition is established.

The burning of silicon to iron, doesn't however have a follow-up reaction and represents the last stage of the star evolution, with iron accumulating inside as a solid core.

Supernova explosion

Stars that will end their life as type-II supernovae[150] are massive stars, namely red-giants with $M > 8M_\odot$.

In these stars the growing iron core does at one point exceed the Chandrasekhar mass limit ($1.4M_\odot$). At this point the core becomes unstable: due to the high gravitational pressure electrons start to undergo capture on protons (the so-called *neutronization*), neutrinos leave out and the core implodes under its own weight. In about $100ms$ its density increases by several orders of magnitude. Neutrinos are now radiatively produced in $\nu\overline{\nu}$ couples of any flavors, their scattering length is heavily reduced and above $10^{11} g/cm^3$ they start to be trapped. The collapse proceeds then adiabatically and the inner core reaches nuclear matter density $10^{14} g/cm^3$.

Next nucleon repulsion becomes relevant and the collapse is reversed in a bounce effect. A shock wave front is produced that expands while more matter is being attracted from the outer layers. Neutrinos are radiated out during this phase cooling the core. About $100ms$ after the bounce only the inner part of the core is left behind as a neutron star, while everything else has been blown into space with a spectacular explosion.

Theories of stellar evolution foresee a supernova explosion rate in our galaxy of about 3 per century and observations from nearby galaxies are consistent. In our galaxy, however, in the last 2000 years only 4 supernovae exploded, the latest in 1670, the explanation being debated.

Basically all the supernova observations available today date back to 1987 when SN1987A exploded in the nearby Large Magellanic Cloud. The neutrino burst[151] emitted in that explosion was observed by KamiokaNDE[152] and IMB[153] detectors.

Neutrino emission

Regardless of the core collapse dynamics, the full binding energy $\epsilon_B \sim 3 \times 10^{53} ergs$ has to be released and light emission accounts for no more than 1%. Neutrinos are then the most probable way the energy is carried out. A first burst of electron neutrinos is produced during the neutronization phase. More neutrinos are released during the core cooling phase as $\nu\overline{\nu}$ pairs of any flavor, though electron flavor should be enhanced due to the additional CC production channel.

Neutrinos are initially trapped in the so called *neutrino sphere* with density above $10^{11} g/cm^3$, high enough to reduce the scattering length to a few hundred meters. ν_μ and ν_τ, subject to NC interaction only, can escape higher densities than ν_e and this means that for them the neutrino sphere is smaller and hotter. Moreover, $\overline{\nu}_e$ suffer less neutron interaction than ν_e and decouple at an intermediate radius. The expected temperature hierarchy is believed to be: $T_{\nu_e} < T_{\overline{\nu}_e} < T_{\nu_x} \sim T_{\overline{\nu}_x} (x = \mu, \tau)$. If an equipartition principle is postulated (i.e. the same luminosity is emitted in any of the three flavors), the abundance hierarchy will be inverted with respect to the temperature one, with ν_e emitted in the highest amount (fig. 1.24(a)).

Physics from SN neutrinos

The neutrino luminosity has a time profile that rises steeply in $\sim 20ms$ and then decays exponentially with a $\tau_\nu \sim 3s$, the signal visible in earth detectors lasting about $10s$.

The various detectors offer multiple detection channels sensitive to some or all the neutrino or antineutrino flavors. Neutral current interactions are generally dominated by ν_μ and ν_τ, as the cross section is larger at the higher average energy of the "heavy" flavors, while the charged current interactions can isolate the ν_e ($\overline{\nu}_e$) burst.

If the detector offers a safe CC/NC separation, a few interesting possibilities are open:

Neutrino mass limits. A massive neutrino reaches the earth with a delay compared to an hypothetical massless neutrino given by:

$$\Delta t = \frac{L}{2c} \left(\frac{m_{\nu_x}}{E_\nu} \right)^2 \tag{1.100}$$

where L is the distance of the supernova. Assuming m_{ν_e} is negligible, Δt can be measured as the difference between the arrival times in the NC and CC channels and eq. 1.100 can then be used to probe m_{ν_μ, ν_τ} down to the $10 - 100 eV$ range, depending on detector performance.

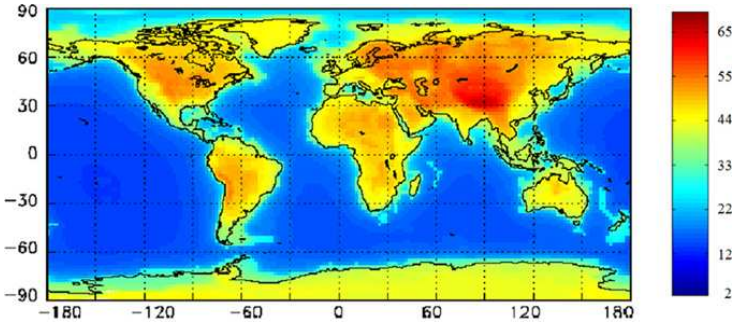

Fig. 1.25: *Map of predicted geo-neutrino events from Uranium and Thorium decay chains, normalized to* 10^{32} *proton yr and 100% efficiency[155].*

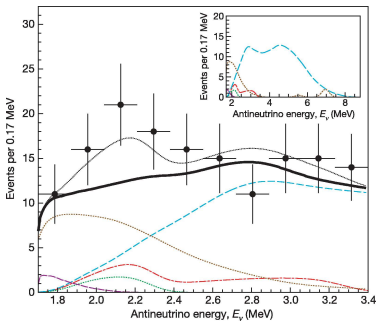

Fig. 1.26: *KamLAND* $\overline{\nu}_e$ *energy spectrum[157] compared to expectations with (dotted line) and without (solid line) geo-neutrinos* ($16TW$).

SN model tests. The SN model is by far not established, so neutrinos could be used also to question the model itself and its alternatives. In order to do this, the aim is an energy spectrum showing the features in fig. 1.24(a), which can be obtained if a NC channel yields enough statistics. Elastic scattering on electrons and interactions on nuclei are therefore of poor utility, leaving the (not yet fully established) possibility of exploiting the elastic scattering on protons. The scattered protons would be non-relativistic and would therefore require a scintillation detector as KamLAND or BOREXino to be detected.

Earth matter effects. The neutrino oscillations in Earth matter introduce modulations in the SN neutrino spectra[154]. These modulations are independent of the SN model and can be exploited to put a limit on the value of θ_{13} and to uncover whether the mass hierarchy is normal or inverted. A large scintillation detector with a signal of at least a thousand events and good energy resolution is ideal, though next generation *Mton* water Čerenkov detectors may also perform the measurement.

1.11.4 Geo-(anti)neutrinos

The heat flux emitted by the earth and measured at the surface averages to $80mW/m^2$ ($40TW$ integrated over the surface of the planet). The reference geophysical model of the earth composition is known as *Bulk Silicate Earth* (BSE) and accounts for planet formation based on observations of chondritic meteorites. In the BSE model 50% of the heat production is estimated to be radiogenic from natural long lived nuclides (^{40}K and elements of the ^{238}U and ^{232}Th chains), distributed in the mantle and the crust[155], with the iron core being non radioactive[32].

Neutrino detectors constitute an important possibility to test this model and its alternatives by recording antineutrinos from the β-decays in the ^{238}U and ^{232}Th chains

[32]Some authors believe instead in the presence of radioactive elements also in the core and the debate is currently open.

via reaction 1.90. The spectrum $E_\nu > 2.25MeV$ would be due to ^{238}U chain only, while subtracting this contribution from the lower spectral portion due to isotopes in both chains, the ^{232}Th chain contribution could be inferred.

This measurement requires however the detector to be located far away from nuclear power plants. In [155] it is estimated that a $5kt$ detector is required to measure the Geo-neutrino signal down to 5% in four years of operations. However ideally one would like to have more than one detector placed in different locations on the earth surface[156], in order to make individual estimates of the different oceanic and continental crust plates (fig. 1.25).

Among the models alternative to BSE, a rather speculative one[159] proposes a breeder reactor at the earth center, which could also be tested with neutrino detectors[160].

Recently the KamLAND collaboration published[157] the first evidence for geo-neutrinos (fig. 1.26). However the statistical uncertainties are large and no separation between models is possible[158]. Future large detectors (e.g. LENA, sec. 1.12) could reveal the correct model and additionally measure the U and Th content in the mantle and core.

1.12 Future solar neutrino experiments

As remarked in sec. 1.11, the low energy solar neutrino spectrum is now fundamental for the progress of neutrino research and the BOREXino experiment (chap. 2), to which the rest of this thesis is dedicated, will soon perform relevant measurements in this direction.

However numerous other projects have been proposed aiming at low energy spectroscopy of *pp*, *pep*, ^7Be and CNO neutrinos, either via Electron Scattering (ES) or via Charged Current (CC) interactions, and are briefly reviewed here.

Noble gases, if operated below their boiling temperature, can act as UV liquid scintillators with very interesting characteristics[33]. The first of these is the absence of ^{14}C, the threshold limiting factor in organic compounds, which makes them good candidate for ES *pp*-neutrino detection. On the other hand the UV light requires wavelength shifters to be coupled to ordinary PMTs and other characteristics like absorption length and light yield are in some cases not as good as for organic scintillators.

Proposals and ongoing studies for future solar neutrino detectors (with and without noble gases) include:

HERON (He). The proposal involving liquid Helium is the most challenging. The helium would be in a super-fluid state (i.e. absolutely pure of contaminants) that, in addition to scintillation, would allow detection through the emission of ballistic phonons/rotons. These, after migrating to the surface, would cause quantistic evaporation of helium atoms, whose detection should in turn be performed with a silicium calorimeter. However the low density makes helium very permeable to γ radiation requiring a complex shielding systems. The HERON project[161] aims at a $20-30t$ He target ($10t$ F.V.) at cryogenic temperature and is currently operating small prototypes.

[33] with the exception of Argon and Krypton which have high intrinsic radioactivity.

CLEAN (Ne). Liquid Neon has a higher density than Helium allowing for self-shielding, it doesn't require cryogenic temperatures ($< 27K$), is very cheap and relatively clean (or easily purified).

CLEAN is a proposal[162] for a steel tank detector holding $135t$ of liquid neon and $\sim$ 2000 PMTs immersed and anchored to a spherical structure. PMTs would be coated with organic fluor as wavelength shifter. Simulations indicate the possibility to set a $20keV$ threshold.

XMASS (Xe). Liquid Xenon has a high photon yield (~ 3 times the one of Helium and Neon) and a high density which makes the detector very compact and self-shielded. Moreover the high boiling point ($165K$) make it relatively easy to operate. The disadvantage of Xenon is the intrinsic radioactive background that requires complex purification systems similar to those of organic scintillator.

The XMASS project[163] located in the Kamioka mine (Japan), is most advanced, having realized and operated a $3kg$ (fiducial) prototype that showed the high self shielding potential. The intermediate step of $100kg$ (fiducial) would already be a valuable dark matter detector and the final $23t$ target ($10t$ F.V.) would only require a $1.22m$ cubic detector.

MOON (Mo). A planned double-beta decay experiment which also has potentiality in terms of *pp* CC spectroscopy. The proposed MOON detector[164] is $1t$ of ^{100}Mo in foils interlayed with fiber-plate scintillator planes. The collaboration has recently operated the lowest scale prototype.

Lithium. Lithium[165] is a Russian project, currently in R&D phase, for a radiochemical experiment based on $^7Li + \nu_e \rightarrow {}^7Be + e^-$ CC reaction and heading for a 10% precision measurement of CNO neutrinos. The chemistry for extracting beryllium atoms from the $10t$ (?) target of metallic Lithium needs to be further investigated, as well as the counting technique, still open between the use of cryogenic detectors (high efficiency) or high purity germanium detectors (easy use).

LENS (In). Spectroscopic observations of *pp* and ^7Be neutrinos via CC reactions may come from the Indium reaction: $\nu + {}^{115}In \rightarrow {}^{115}Sn^* + e^-$ proposed in 1976 by R.S.Raghavan[166]. It has an energy threshold of only $118keV$ and a fruitful coincidence in $4.7\mu s$ with the $613keV$ de-excitation γ-cascade of the Sn excited state. However ^{115}In is itself a long lived radioactive nuclide, β-decaying with a $495keV$ end-point. The suppression of this background requires a finely segmented and therefore expensive detector[167]. In-loaded scintillators have been developed[168] within the LENS project. Tests of the stability and of the optical properties are under way[169].

SNO+. The SNO-III phase (NCDs) is planned to end in 2006 (sec. 1.7.2). There is a proposal[170] from part of the SNO collaboration to successively replace the heavy water with liquid scintillator[34], with the goal of lowering the threshold and perform

[34]This would imply different vessel hydrostatic requirements and the construction of a new reversed support structure.

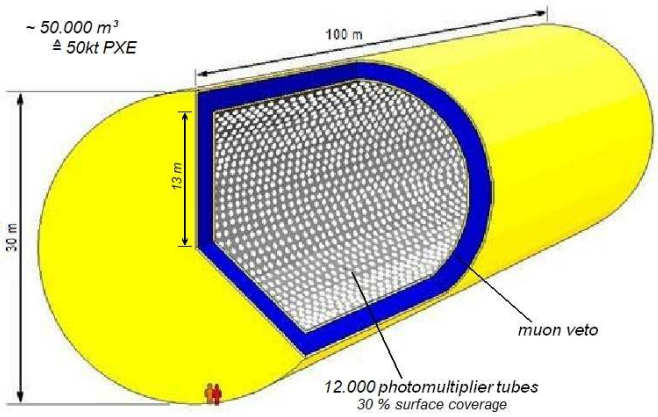

Fig. 1.27: *Sketch of the proposed LENA detector[171].*

spectrography of ^7Be, *pep* and CNO neutrinos.

LENA. The proposed[172] evolution of the current liquid scintillator neutrino detectors is LENA (*Low Energy Neutrino Astronomy*). The design features a cylindrical detector ($100m$ height, $30m$ diameter) with a $50kt$ target, whose PXE-based mixture is being developed at TUM. About 12000 20"-PMTs will achieve 30% geometrical coverage and a light yield of about $120pe/MeV$. The detector most probable location is the Pyhäsalmi mine in central Finland, offering $\sim 4000m.w.e.$ rock coverage and a surrounding region relatively free from nuclear power plants. LENA will be a multi-purpose detector encompassing the following topics:

1. *Solar neutrinos.* The solar signal composition will be similar to BOREXino (sec. 2.1.1) but with about 100 times higher statistics, reaching an accuracy of 0.5% on the indirect measurement of *pp-*ν's. The high precision ^7Be measurement will allow detection of the 1% day-night asymmetry postulated by LMA and of possible temporal fluctuations in the flux arising from solar g-modes invisible to helioseismology.
2. *Supernova Neutrinos.* A galactic $8M_\odot$ supernova explosion would yield a burst of about 20000 events in LENA, mostly due to $\overline{\nu}_e$ inelastic scattering on protons, allowing to probe the SN models proposed. In addition the $\overline{\nu}_e$ spectrum could show wiggles due to matter effect in the earth which depend on the mass hierarchy and on θ_{13}.
3. *Supernova Relic Neutrinos (*SRN*).* The diffuse background of neutrinos from past SN explosions can be probed down to $9MeV$, thanks to the neutron delayed coincidence available after $\overline{\nu}_e$ scattering on protons. ~ 6 events per year should be observed according to the most recent models.
4. *Atmospheric neutrinos.* $\overline{\nu}_e$ and $\overline{\nu}_\mu$ can be distinguished by the latter being followed by μ^+ decay $2.2\mu s$ later. The ratio $\overline{\nu}_e/\overline{\nu}_\mu$ can then be explored in the low energy region ($100Mev - 1GeV$) allowing to test the current oscillation scenario.

5. *Proton decay.* The $p \rightarrow K^+ + \overline{\nu}$ decay channel can be explored in LENA[173]. This channel is not visible directly in Čerenkov detectors like UNO or HyperKamiokaNDE. The expected sensitivity is $\tau_p \sim 4 \cdot 10^{34} y$.
6. *Geo-neutrinos.* Between $400 - 4000 ev/yr$ of $\overline{\nu}_e$ from natural radioactive elements in the earth (sec. 1.11.4) are expected in LENA. Thanks to the low background from nuclear power plants it will be possible to disentangle the crust and mantle contributions.
7. *Long Baseline Oscillations.* In case a neutrino beam from an accelerator facility is directed to LENA neutrino oscillations could be studied with respect to the MSW effect and in particular to the determination of the CP-violating phases. The discrimination of ν_e/ν_μ events requires the beam to be oriented along the detector axis.

Chapter 2

The Borexino Experiment

A direct measurement of the solar neutrino flux arising from the ^7Be decay (sec. 1.2) is still missing in order to complete the picture of the solar mechanisms as well as to probe neutrino oscillations in the unexplored low energy region (sec. 1.11).

The main goal of the BOREXino experiment[1] is to perform this measurement with at least 10% precision, via elastic scattering on electrons (sec. 1.3.2) in a $300t$ liquid scintillator detector[175].

The main challenge in the realization of this project is indeed the required high radio-purity of the scintillator and of the materials used in the detector construction or surrounding it. Only very low background levels will in fact allow detection of a signal of a few tens of events per day, in absence of an event-by-event tagging.

After the promising results of a prototype detector, the so called *Counting Test Facility* (CTF, chap. 9), the project has been developed since the early 90s, by a growing international collaboration which now counts more than 15 institutions belonging to seven European and North-American countries.

The detector construction in the INFN *Laboratori Nazionali del Gran Sasso* (Italy) was completed in 2004 and first data taking is expected at the beginning of 2006, after the completion of ongoing governmental works aiming to enhance the environmental safety conditions of the laboratory itself.

2.1 Physics Goals

The fundamental goal of the experiment is the measurement of the ^7Be solar neutrino flux, but the physics program is rather broad, encompassing the measurement of other solar neutrino emissions, as well as non-solar neutrino detection. In most of the cases the importance of the questions addressed is central in particle physics as well as in astrophysics (or even geo-physics).

[1] In 1987 R.S. Raghavan[176] proposed the BOREX project, a $1000t$ fiducial mass detector using trimethylborate as scintillator aiming to measure NC and CC ^8B neutrino interactions on ^{11}B. BOREXino was supposed to be just the prototype with a $100t$ fiducial mass. However the goal of the project changed (as well as the scintillator choice) toward the lower energy and more intense ^7Be neutrinos and BOREXino became the final detector, though retaining its name.

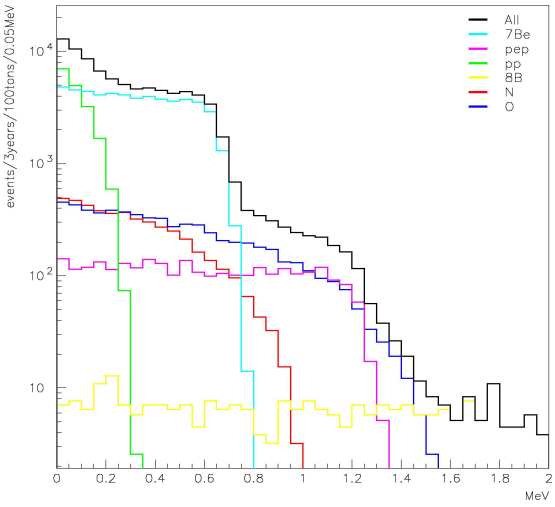

Fig. 2.1: *Simulated recoil electron energy spectra for BOREXino. BP04* SSM *3y statistics, 100t FV. The characteristic edge at* $\sim 0.67MeV$ *due to* ^7Be*-*ν*'s is the main signal. CNO fluxes include the last* S_{14} *measurements (sec. 1.8).*

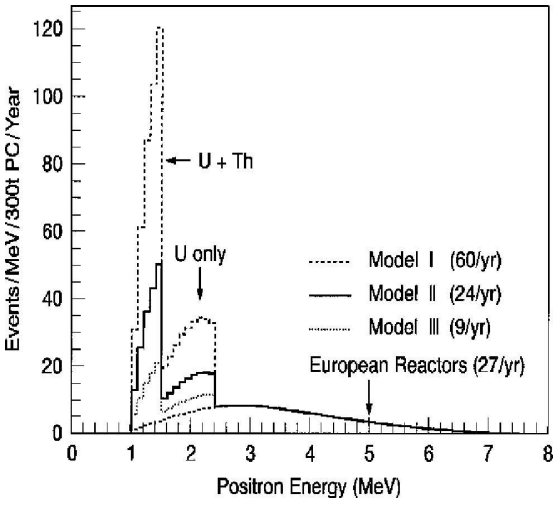

Fig. 2.2: *The expected spectra for* $\overline{\nu}_e$ *(positron energy) for three different geophysical models and from reactor power plants[156].*

2.1.1 Solar neutrino spectroscopy

Interaction of solar neutrinos in the detector occurs mostly through elastic scattering on electrons:

$$\nu_e + e^- \longrightarrow \nu_e + e^- \tag{2.1}$$

which doesn't have a kinematic threshold, as described in sec. 1.3.2.

Organic scintillators like the one used in BOREXino are produced out of crude oil, where the presence of the long-lived ^{14}C isotope creates a significant background in the $0 - 200keV$ region (sec. 2.3.1). Conservatively the energy threshold for the BOREXino experiment is fixed at $\sim 250keV$.

The isotropy of the scintillation process and the lack of any delayed coincidence tag leave only statistical means to extract the neutrino signal. However a seasonal modulation of $\sim 7\%$ is expected as a consequence of the earth orbit eccentricity and will be the signature of the solar origin of the neutrino flux.

A few solar neutrino emissions can be investigated in BOREXino (fig. 2.1), whose implications were also discussed in sec. 1.11:

^7Be **flux.** This measurement is of strategic importance in terms of solar astrophysics as its value is the most poorly determined by current experimental evidences. Moreover it could allow to reduce by a factor of ~ 4 the present indetermination in the fundamental *pp* flux, via the luminosity constraint. Finally it would be a first step to constrain also the luminosity measured in neutrinos. This value, if it matches the photon luminosity, would be the ultimate test of the SSM energy production scheme.

Not less interesting is the discovery potential of a sub-MeV neutrino spectroscopy in terms of intrinsic neutrino properties. The MSW-LMA solution predicts a survival probability shown in fig. 1.21. Tests of this model have occurred so far only for neutrino energies above $\sim 5MeV$, i.e. in the *matter-dominated* oscillation region. The ^7Be emission lies instead in the *vacuum-dominated* region and would provide a key proof of the model, allowing also to address possible sub-dominant effects that have been proposed.

BOREXino aims to a 10% precision measurement of the $862keV$ line (90% B.R.), in a few years of data taking, but the real precision obtained will critically depend on the background conditions achieved.

The elastic scattering cross-section (sec. 1.3.2) computed at ^7Be energy are $6 \times 10^{-45}cm^2$ and $1.2\times10^{-45}cm^2$ for ν_e and $\nu_{\mu,\tau}$ respectively. In the MSW-LMA scenario about $33ev/d$ are expected and will be visible as a Compton-like shoulder around $665keV$ in the recoil electron energy spectrum (fig. 2.1).

***pep* and CNO fluxes.** The ratio of the *pep* vs. *pp* reactions in the sun is known with very little model assumptions, therefore a measurement of the *pep* flux would be almost as important as a *pp* flux measurement. Moreover the *pep* energy of about $1.44MeV$ lies in the *vacuum-matter* transition region (fig. 1.21) of the LMA solution allowing an important test of the model at this intermediate energy.

CNO fluxes are experimentally almost undetermined. Their measurement would allow to establish the fraction of the solar power generation that occurs due to CNO cycle reactions and would make the neutrino luminosity cross-check more accurate.

BOREXino has the potentiality to measure the *pep* monochromatic emission as well as the three CNO fluxes in the energy range above $1MeV$, provided the cosmogenic background from ^{11}C can be suppressed. Signal and background considerations are deferred to chap. 10, entirely dedicated to the possibility of performing this measurement.

^8B spectrum. A measurement of the ^8B energy spectrum in the $[2.8, 5.5]MeV$ region[2] would probe the LMA solution in the *vacuum-matter* transition region. Unfortunately the signal and the cosmogenic background expected for electron scattering are $\sim 0.2ev/d$ and $0.65ev/d$ (tab. 10.2) respectively, not allowing a very significant measurement.

However a different interaction channel has been recently proposed[183] involving ^{13}C, a nuclide naturally present in organic scintillators with an isotopic abundance of $I = 1.07\%$. The reaction exploited is the neutrino capture:

$$\nu_e + ^{13}C \longrightarrow ^{13}N + e^- \tag{2.2}$$

where ^{13}N is in the ground state and the threshold is $Q = 2.22MeV$ (open essentially to ^8B neutrinos only). Neglecting the ^{13}N recoil, the electron kinetic

[2]The lower limit rejects most background from natural radioactivity, the upper one merely limits the focus of the measurement to energies unexplored by water Čerenkov detectors.

energy, $T_e \simeq E_\nu - Q$, faithfully reflects the incoming neutrino energy. The cross-section is known with great accuracy and, if folded on the ^8B spectrum, yields $\langle\sigma\rangle = 8.57 \times 10^{-43} cm^2$, about an order of magnitude above electron scattering. Moreover ^{13}N decays back with $\tau = 862.6s$:

$$^{13}N \longrightarrow {}^{13}C + \nu_e + e^+ \tag{2.3}$$

allowing a delayed coincidence with the positron event. Thanks to the extra annihilation energy, the delayed event will be visible in the $[1.02, 2.22] MeV$ region. If convection in the scintillator is negligible, also position coincidence can be applied. Applying a spherical cut with a radius a few times larger than detector's resolution ($\sigma \sim 10cm$) for a time as long as a few times the ^{13}N decay time, a sample of $\sim 5 - 17 ev/kton/yr$ (depending on prompt energy selection) can be extracted. Fake coincidences can be safely measured out of the coincidence and should amount to $\sim 1.5 ev/kton/yr$. Cuts can be optimized to reach a sensitivity of $\sim 20\%$ in extraction of the solar neutrino signal.

2.1.2 Anti-neutrino detection

The anti-neutrino detection via capture on protons in BOREXino follows the general mechanism explained in sec. 1.8 and allows a set of additional physics measurements:

Solar anti-neutrinos. As explained in sec. 1.11.1, it is particularly interesting to probe the presence of $\overline{\nu}_e$ in the solar flux, implied by non-standard physics mechanisms involving a non-vanishing neutrino magnetic moment. Thanks to the absence of nearby nuclear reactors, the BOREXino sensitivity is expected to be at the same level as the KamLAND detector, though this is about three times larger. For the same reason the energy region exploited can be lowered much below the KamLAND's $8.3 MeV$.

Geo-neutrinos. Following the arguments exposed in sec. 1.11.4, BOREXino is a very suitable detector for testing earth radiogenic thermal components via anti-neutrino detection, thanks to the absence of nearby nuclear reactors. The expected signal is of the order of a few tens of events per year and depends strongly on the geophysical model assumed, ultimately being a useful probe of the models themselves. Positron energy spectra reported in fig. 2.2, lie in the $[1, 2.6] MeV$ window with the components from ^{238}U and ^{232}Th radioactive chains clearly visible. Moreover since BOREXino lies on the Eurasian continental crust plate, while KamLAND is at the junction with the oceanic crust, the combination of results from the two experiments could allow to disentangle the continental and oceanic contributions to radiogenic heat.

Reactor long baseline. In Italy nuclear power plants are banned by law since after the Chernobyl accident. However, neighboring countries, especially Germany and France, do exploit this source of energy quite extensively. The overall European nuclear power plants account for about $500 GW$ and lie at an average distance of

reaction channel	$\langle E_\nu \rangle$ [MeV]	$\langle \sigma \rangle$ $[cm^2]$	N_{events}
$\nu_e - e$	11	1.02×10^{-43}	2.37
$\bar{\nu}_e - e$	16	6.03×10^{-44}	0.97
$\nu_x - e$	25	3.96×10^{-44}	0.81
$\bar{\nu}_x - e$	25	3.25×10^{-44}	0.67
total $\nu - e$			4.82
$\bar{\nu}_e + p \rightarrow e^- + n$	16	2.70×10^{-41}	78.9
$^{12}C(\nu_e, e^-)^{12}N$	11	1.85×10^{-43}	0.6
$^{12}C(\bar{\nu}_e, e^+)^{12}B$	16	1.87×10^{-42}	4.1
$\nu_e + ^{12}C$	11	1.33×10^{-43}	0.4
$\bar{\nu}_e + ^{12}C$	16	6.88×10^{-43}	1.5
$\nu_x + ^{12}$ C	25	3.73×10^{-42}	20.9
total $^{12}C(\nu, \nu')^{12}C^*$			22.9

Tab. 2.1: *Predicted neutrino events in BOREXino (300t), due to a supernova explosion at a distance of 10 kpc, with $\varepsilon_B = 3 \times 10^{53}$ ergs binding energy release[184].*

$\sim 800km$ from LNGS. This makes BOREXino a long baseline reactor experiment with a predicted signal of $\sim 30ev/y$ [3]. $\overline{\nu}_e$ disappearance would probe the LMA solution directly as first experiment after KamLAND. The expected spectrum in absence of oscillations is also shown in fig. 2.2.

2.1.3 Supernova neutrino detection

The explosion of a type-II supernova in our galaxy would be visible in BOREXino with a burst of events lasting about $10s$. It is convenient to consider as a *reference* event the explosion of a SN with binding energy $\epsilon_B = 3 \times 10^{53}$ in the center of the galaxy, i.e. at a distance of $\sim 10kpc$. Moreover the model exposed in sec. 1.11.3 and the spectra in fig. 1.24(a) are assumed.

The full $300t$ volume can be exploited with different interaction channels[184]:

1. Electron scattering (ES). $\nu_x + e^- \longrightarrow \nu_x + e^-$. A reaction accessible to all neutrino and anti-neutrino flavors. The individual cross sections are easily calculable from the standard electro-weak theory and, if folded on the expected spectra, yield an overall signal of $\sim 5ev$.

2. Inverse β-decay on proton (CC). $\overline{\nu}_e + p \longrightarrow n + e^+$. The reaction with the highest cross-section (well known) would yield $\sim 79ev$ from $\overline{\nu}_e$ only. The signature is clear thanks to the coincidence with the radiative capture of the neutron ($\tau \sim 200us$, $E_\gamma = 2.2MeV$).

3. Interactions on ^{12}C. Organic scintillator experiments also benefit from the following interactions:

[3] Computed with a 3% accuracy from the data published by the power companies.

(a) $\overline{\nu}_e$ capture (CC):

$$\begin{array}{lll} \bar{\nu}_e + {}^{12}C \longrightarrow & {}^{12}B + e^+ & Q = 13.37\ MeV \\ & {}^{12}B \longrightarrow {}^{12}C + e^- + \bar{\nu}_e & \tau_{1/2} = 20.20\ ms \end{array}$$

(b) ν_e capture (CC):

$$\begin{array}{lll} \nu_e + {}^{12}C \longrightarrow & {}^{12}N + e^- & Q = 17.34\ MeV \\ & {}^{12}N \longrightarrow {}^{12}C + e^+ + \nu_e & \tau_{1/2} = 11.00\ ms \end{array}$$

(c) *Inelastic Scattering* of ν_x (NC):

$$\begin{array}{lll} \nu_x + {}^{12}C \longrightarrow & {}^{12}C^* + \nu'_x & E_{thr} = 15.11\ MeV \\ & {}^{12}C^* \longrightarrow {}^{12}C + \gamma & E_\gamma = 15.11\ MeV \end{array}$$

The first two CC interactions enforce the delayed coincidence with the inverse reaction (the times are indicated), while the third one is only visible through the sharp γ-peak. The cross-sections, though complicated by the nuclear matrix elements, are now known with a reasonable precision and the overall expected signal reaches $\sim 23ev$. It should be noted that 91% of the inelastic scattering events are due to ν_μ and ν_τ (and antiparticles), due to their higher energy and consequently higher cross section, compared to ν_e (and $\overline{\nu}_e$).

4. Elastic scattering on protons (PS). $\nu_x + p \longrightarrow \nu_x + p$. Though substantial quenching effects (sec. 2.4.2) must be taken into account, the reaction is accessible to all neutrino flavors with cross sections that can be computed with little uncertainty. About 70-80 events would survive a $200keV$ threshold that rejects ^{14}C (sec. 2.3.1).

Signals from most interaction channels are reported in tab. 2.1.

The physics items introduced in sec. 1.11.3 can be addressed in BOREXino comparing the different interaction channels. 10^5 SN explosions ($10kpc$, $\epsilon_B = 3 \times 10^{53}\ erg$) were simulated in [184] to study the detector sensitivity:

SN model tests. In BOREXino the PS signal should allow a spectral reconstruction, where the temperature of the three distributions (fig. 1.24(a)) can be separated with a $\gtrsim 20\%$ accuracy.

Neutrino Mass Limits. The average $\overline{\nu}_e + p \rightarrow n + e^+$ arrival time distribution, $\langle t \rangle_{CC} \sim 3s$, is taken as the arrival time of the massless neutrino. Subtracting this value from the $\langle t \rangle_{NC}$, obtained from $\nu_x + {}^{12}C \rightarrow {}^{12}C^* + \nu'_x$, the delay of the "heavy" flavors is computed. For delays below $1s$ upper limits on the mass m_{ν_μ,ν_τ} can be obtained through eq. 1.100 in the range $30 - 100eV$, while delays above $1s$ would be already an indication of $m_{\nu_\mu,\nu_\tau} \neq 0$ (fig. 2.3).

Oscillation tests. BOREXino is not large enough to detect Earth matter effects in SN neutrino spectra. However the oscillation of ν_μ ($\overline{\nu}_\mu$) $\rightarrow$ ν_e ($\overline{\nu}_e$) would introduce ν_e ($\overline{\nu}_e$) with the energy of $T \sim 8MeV$. These would benefit, in the CC interaction

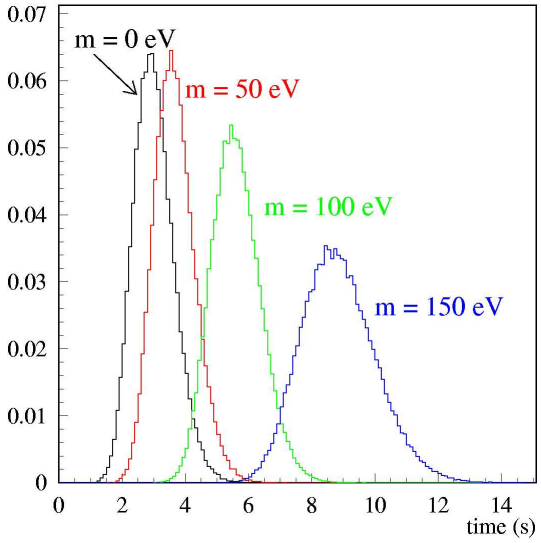

Fig. 2.3: *Simulated* $\langle t \rangle_{NC}$ *for different* $m_{\nu_\mu,\nu_\tau} \neq 0$ *[184].*

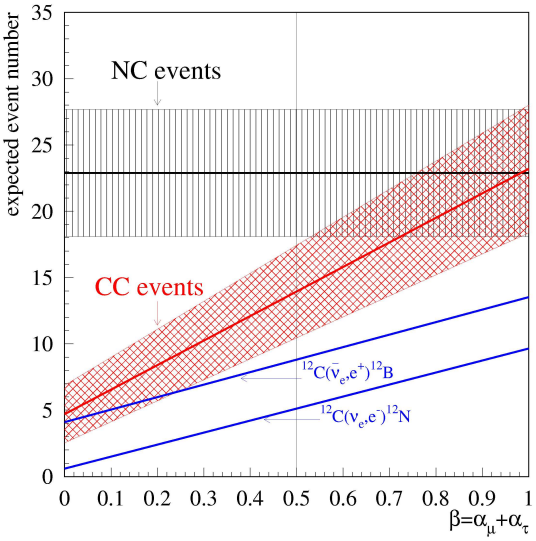

Fig. 2.4: *NC and CC expected signals for different conversion probability* β*[184].*

channel $^{12}C(\nu_e, e^-)^{12}N$ ($^{12}C(\bar{\nu}_e, e^+)^{12}B$), a cross-section enhanced by a factor 35 (5), compared to the one for $T \sim 3.5MeV$ ($T \sim 5MeV$). NC inelastic scattering is instead insensitive to neutrino flavor.

An increase in the CC/NC ratio compared to the predictions reported in tab. 2.1 would be an indication of oscillations (fig. 2.4).

It should be stressed however the intrinsic dependency on the SN model of any neutrino physics measurement.

2.2 Experimental Setup

2.2.1 The LNGS underground laboratory

The *Laboratori Nazionali del Gran Sasso* (LNGS, [174]) are situated some $150km$ North-East of Rome and are excavated aside the $10km$ highway tunnel passing under the Gran Sasso mountain. The altitude is $963m$ and the average dolomitic rock cover is $\sim 1400m$ (or $\sim 3800m.w.e.$). This rock, in addition of being a shelter against cosmic radiation, is entitled to good radiopurity conditions, compared to similar underground physics sites (tab. 2.2).

The LNGS are so far the only facility in the world especially designed and excavated for underground physics[4]: all the other sites mentioned in chap. 1 have been adapted from mines or other pre-existing structures.

The underground laboratory comprises three experimental halls (named A, B and C) with a variable length around $100m$ and height above $18m$ for an overall volume exceeding

[4] A few similar projects in North America are under discussion.

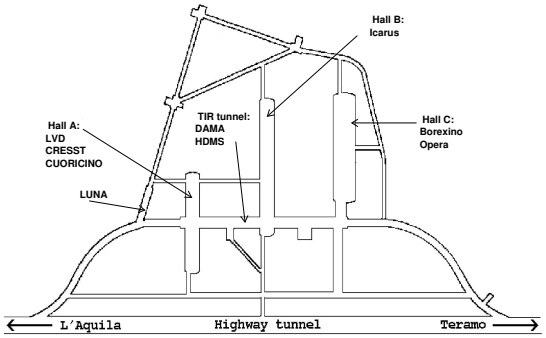

Fig. 2.5: *Laboratori Nazionali del Gran Sasso. Map of the underground experimental halls[174].*

Background source		Flux surface $(m^{-2}h^{-1})$	Flux LNGS $(m^{-2}h^{-1})$
μ	$> 1GeV$	3.1×10^6	1.16 ± 0.09
n	thermal	5×10^4	73 ± 2
	epi-therm.	2.5×10^5	46 ± 11
	$> 0.5MeV$	2×10^5	92 ± 10
	$> 2.5MeV$		3.2 ± 2.1
γ			$\sim 10^7$

Tab. 2.2: *Comparison between radioactive background conditions at ground level and in the LNGS.*

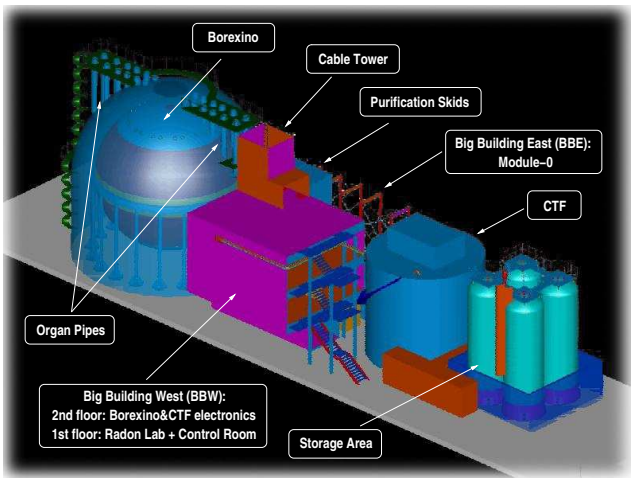

Fig. 2.6: *CAD view of North half of Hall C with the BOREXino experimental structures.*

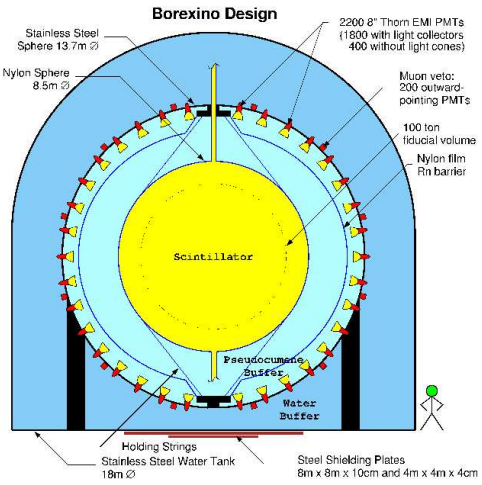

Fig. 2.7: *Schematics of the BOREXino detector[175].*

$180000m^3$. Experimental setups of a dozen differently sized projects are situated in the halls or in the net of service tunnels that complete the structure (fig. 2.5).

The BOREXino Experiment occupies the North half the Hall C aside to the Opera experiment. Its components are depicted in fig. 2.6.

2.2.2 The design

Designed after the idea of suppressing the external γ background emitted by the rock (tab. 2.2), the detector has a structure made of concentric layers with spherical symmetry. Requirements of radiopurity for construction material obviously become more stringent the closer the materials are to the detector's active volume.

Going outward from the center we find[179]:

General Characteristics	
Total Mass	~ 290 tons (8.5 m diameter IV)
FV Total Mass	100 tons (6 m diameter software cut)
Density	0.88 g/cm^3
Optical Characteristics	
Primary Light Yield	$\sim 10^4$ photons/MeV (@380 nm)
Peak Emission wavelength	365 nm
Attenuation length	$\geq 5m$ (@430 nm)
Decay lifetime without abs/reem	~ 3.5 $nsec$ (β particles)
Decay lifetime with abs/reem	~ 5 $nsec$ (β particles)
Physical Characteristics	
α-quenching (E)	$Q(E) = 20.3 - 1.3E[MeV]$
Radioactivity Characteristics	
^{238}U	$(3.5 \pm 1.3) \cdot 10^{-16} g/g$
^{232}Th	$(4.4 \pm 1.5) \cdot 10^{-16} g/g$
$^{14}C/^{12}C$	$(1.94 \pm 0.09) \cdot 10^{-18}$

Tab. 2.3: *Main characteristics of BOREXino liquid scintillator.*

The scintillator

Sensitive volume of the scintillator is $320m^3(280t)$. Nevertheless a fiducial volume cut is planned to be applied to the innermost $100t$ with the help of the position reconstruction algorithm.

After careful research on different organic scintillators both as small scale lab tests and as larger tests in the CTF detector, it was chosen as final solution a mixture of pseudocumene (PC, 1,2,4–trimethylbenzene, $C_6H_3(CH_3)_3$) as solvent and PPO (2,5–diphenyloxazole, $C_{15}H_{11}NO$) as fluor, with a $1.5g/l$ concentration (tab. 2.3). Many aspects of the scintillation process and light propagation in BOREXino are covered in sec. 2.4.

The collaboration has decided to perform also detailed studies on a backup mixture based on PXE, with a dedicated data taking campaign of the prototype detector (CTF-2, [222]).

The *Inner Vessel* (IV)

The scintillator is held in a transparent spherical nylon membrane, $8.5m$ diameter and $125\mu m$ thick, which must be absolutely tight as it separates fluids which should never mix. Pipes made out of steel and nylon connected to the upper and lower poles allow fluid loading and circulation from the numerous fluid handling facilities. Anchoring of *inner vessel* is guaranteed by a set of longitudinal nylon strings. Load cells at the end of each string allow monitoring of the *inner vessel* mechanical stability.

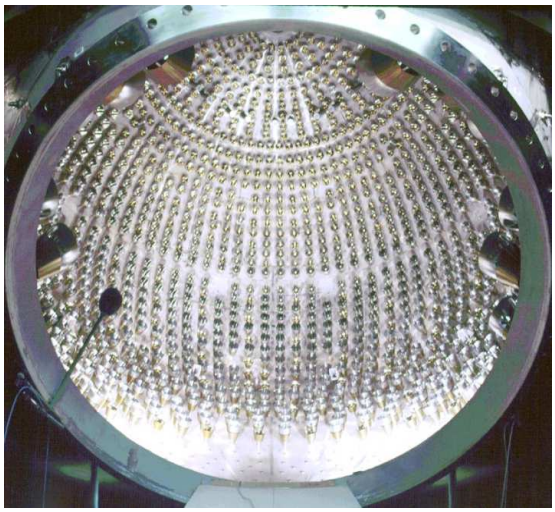

Fig. 2.8: *The Stainless Steel Sphere (SSS) with most of the PMTs mounted (2003). The lower portion was mounted later, after the nylon vessels installation.*

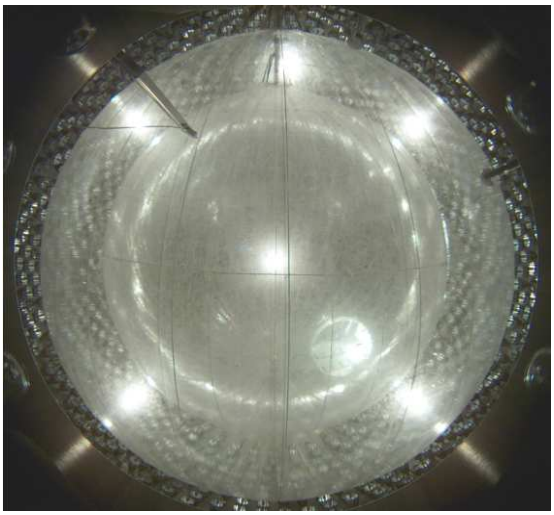

Fig. 2.9: *The two concentric nylon vessels installed and inflated with high purity nitrogen (2004).*

The *Buffer* liquid

A mass of $1040t$ shielding liquid is located outside the *inner vessel*. Density of the buffer liquid cannot be too different from the scintillator one, as the *inner vessel* nylon film would not sustain a big hydrostatic pressure without loosing its spherical shape or even risking mechanical ruptures. Pseudocumene density is $0.88g/cm^3$, too far from the water density. It is therefore necessary to use pure pseudocumene as buffer liquid with the addition of a *quencher*, dimethylphtalate (DMP) in $5g/l$ concentration, to further reduce residual fluorescence of pseudocumene in absence of fluor. DMP does not influence photon mean path, nor Čerenkov light emission.

The *Outer Vessel* (OV)

After CTF-1 experience revealed radon sources outside the *inner vessel*, a second nylon membrane in the buffer liquid was added in the design to stop radon gas diffusion toward the *inner vessel*. It has a diameter of $12.6m$ and a thickness of $125\mu m$.

The Stainless Steel Sphere (SSS)

All the components described so far are housed in a stainless steel sphere $8-10mm$ thick with a $13.7m$ diameter, which also supports the photomultipliers. 20 legs hold the sphere and are welded to the external water tank floor (see below).

The photomultiplier tubes (PMTs)

Photomultipliers used in BOREXino are 8" ETL-9351, developed out of a special low-radioactivity glass and with a complex sealing studied to resist pseudocumene corrosive action. They are sensitive to light with wavelength between $350nm$ and $500nm$ with a quantum efficiency peak of 26% at $420mn$.

They are installed in the sphere in dedicated feed-throughs and are connected from outside the SSS with a single submarine cable for signal and high voltage. Cables exit the water tank from dedicated openings in the upper dome named *organ pipes* and reach in $55m$ length the electronic room situated in the nearby *Big Building West(* BBW*)* (fig. 2.6).

2212 photomultipliers are installed in the sphere, 1838 of which are equipped with aluminum light concentrators to increase light collection capability. The overall geometrical coverage achieved in this way is $\sim 30\%$.

Muon Veto

The about 400 PMTs without light concentrators are the so-called *Inner Muon Veto*. Their higher acceptance angle allows them to collect a stronger signal in response to Čerenkov tracks produced by muons crossing the buffer liquid[5].

The *Outer Muon Veto* is instead composed of additional 208 PMTs installed in the water tank to detect Čerenkov light produced by muons in the shielding water. The development of the external muon veto accounts for a major part in the present PhD work, therefore it will be discussed in details in the next chapters.

External Tank and buffer water

The full experimental setup is housed in a dome shaped steel tank (fig. 2.7). The base cylinder diameter is $18m$ while the highest point of the dome is $17m$ above the floor. The tank will be filled with $2400t$ of ultra pure water as the outermost shielding of the detector. Inner water tank walls as well as outer SSS surface are covered with *Tyvek* sheets, a high reflectivity material that will enhance muon detection possibilities.

2.2.3 Fluid handling and purification plants

The BOREXino detector is connected with numerous plants that handle and purify fluids involved in the experiment. Most of them are in a fully working condition and served for the three data taking campaigns of CTF, while a few others are being commissioned in these months.

Water purification plant

$2000t$ of ultrapure water ($\sim \mu Bq/kg$ level) are required to fill the external water tank and $1000t$ have been used to fill the CTF tank (three times, so far). Many other cleaning and fluid handling operations require ultrapure water. In order to satisfy this demand the

[5]Muons crossing the scintillator will simply saturate the detector completely without being a relevant background

experiment built a water purification plant based on cascaded purification steps. These are reverse osmosis, de-ionization, micro-filtration, ionic exchange and nitrogen stripping. The plant is quite flexible by design and can work in *production* mode, with the help of a $5m^3$ storage tank, or in *recirculation* mode, looping the water directly through BOREXino (or CTF) tank. Reverse osmosis is preferred in production mode for its higher purification effectiveness, while the ionic exchanger is used in recirculation mode where the $\sim 25\%$ water discharge of the reverse osmosis would not be practical. This plant is able to suppress Uranium and Thorium concentrations from the typical site concentration of $10^{-10}g/g$, to the required $10^{-14}g/g$ at a maximal flow of $1.8m^3/h$. Radon content is instead reduced to $\sim 10mBq/m^3$.

Scintillator storage area

The scintillator ($300t$) is currently held in a complex of 4 storage tanks, $100t$ each hosted in a concrete containment pit under fire extinguishing systems. One of the tanks is kept empty (actually full of ultrapure nitrogen) to allow fluid movements. It is also able to perform a first nitrogen bubbling purification.

The buffer pseudocumene ($1000t$) will instead be procured *online* during the filling as no storage is available underground for this volume.

Scintillator Purification plant (Skids)

Scintillator purification is achieved in a complex system, generically named *skids*, able to perform distillation, *water extraction* as well as *nitrogen stripping* and micro-filtration. With a combination of the above operations, it is possible to reduce ionic impurities, particulate and gaseous contaminants. A much smaller version (CTF *skids* of the plant was first constructed and used in the first two phases of the CTF detector. The final plant has already been successfully operated during the CTF-3 campaign (except for distillation test which is still to come).

The Module-0

The so-called *Module-0*, located in the *Big Building East* (BBE, fig. 2.6) and designed for a high degree of flexibility, connects to several other components and can serve as complete liquid handling system for CTF[244].

In addition to fluid movements, the plant provides an additional (or alternative) purification method, the *silica-gel adsorption*. The silica-gel powder is hosted in two large "columns" through which the scintillator is pumped. Ionic impurities are trapped by the silica-gel molecules[225].

Finally the module-0 could eventually bubble water or nitrogen in one of its $7m^3$ tanks, being in this way an independent and complete purification plant by itself. Module-0 and the silica-gel columns have been tested in the CTF-2 and CTF-3 campaigns (chap. 9).

Nitrogen distribution system

A nitrogen distribution plant is situated in the main tunnel of the LNGS, next to Hall C entrance. Nitrogen is widely used in BOREXino (and in CTF) for a variety of uses such as fluid stripping, tubes and vessels flushing, or blanketing of liquid-filled tanks (including the main tanks of the two detectors). The air of the laboratory is in fact rich in radon gas and should never get in contact with the clean equipment of the experiment.

The plant includes 3 liquid nitrogen storage tanks, $6m^3$ each, 2 atmospheric evaporators and a heat exchanger that produces nitrogen gas up to $250m^3/h$. The plant has been fully operational for many years and has been upgraded with a charcoal purification column through which the liquid nitrogen can be purified. The maximum output of the plant in purification mode is $100m^3/h$.

2.2.4 Calibration systems

A few different concepts lie under the generic term *calibration*.

Individual channel calibration

A reliable event position reconstruction (sec. 7.4.4), primary tool in the external background rejection, can work only after an accurate time calibration of every channel. The α/β discrimination methods in turn rely on an accurate reconstructed position of the event. Therefore this and basically all other background rejection methods require a precise time and charge calibration of the individual channels, which turns out to be the most fundamental step in the calibration scenario.

The intrinsic PMT transit time jitter ($\sim 1ns$) sets the goal of the time calibration: to evaluate the response time differences among PMTs at a sub-ns level and to align the detector with a software correction. Charge calibration instead consists in finding conversion constant (and offset) from ADC bins and the number of detected photoelectrons.

Two independent optical calibration systems have been developed to calibrate the inner and outer detector PMTs as the goals of the two detectors are slightly different.

The inner detector timing calibration must aim basically to illuminate the PMTs in sub-Poisson range[6]. This is due to the fact that the average occupancy of channels in the energy region of interest is well below 1 pe/channel. This is achieved with a $400mW$ PicoQuant diode laser, usually referred to as the *timing* laser, placed on top of the water tank and a light distribution system based on optical fibers. This system, in 2 optical splitting steps, is able to reach all the 2212 PMTs with a final individual capillar fiber mounted at the edge of the light concentrator[7]. The laser emits short ($50ps$) light pulses with a $394nm$ wavelength where the PMT quantum efficiency is approximately $\sim 27\%$. Though it is provided with an internal trigger that can reach $40MHz$, its use is normally driven by an external pulser in the electronic room at $200Hz$ that drives also the acquisition during the so-called *laser runs* (sec. 4.4.5). The inequalities in the optical

[6]The number of detected photoelectrons follows the Poisson distribution with $n < 1$.

[7]PMTs without concentrators have been equipped with a thin fiber support that holds the fiber in the same geometry with respect to the photocathode surface.

fiber lengths have been measured to introduce negligible ($\sim 50ps$) contribution to the detector time misalignment.

The outer detector calibration system aims to a wider range in charge, as a muon detector is expected to see also much higher light pulses, without loosing the sensitivity for the single photo-electron detection. A system based on individual Light Emitting Diodes (LEDs) was developed and is described in details in chap. 8.

Scintillator monitor

This system, also based on lasers, aims to monitor the stability in time of different properties of the scintillator response. Actually two systems are in place: an internal system and an external one.

The first one is a mechanical insertion system that allows to place an optical fiber inside the *inner vessel* volume along the vertical axis and in off-axis positions. The idea is to study the absorption and reemission of light by the scintillator mixture, therefore 2 lasers with wavelength of $266nm$ (PC absorption region) and $355nm$ (overlap between absorption region and PPO emission region) may be used.

The external system is instead a set of fibers connected to a few feedthroughs in the water tank that point either radially to the center of the detector, to monitor its transparency, or obliquely through the buffer liquid to a PMT without concentrator, to monitor the buffer transparency. The *timing* laser described above is usually connected through a mechanical switch to one of these positions, but the $355nm$ could also be used.

Source calibration

Using radioactive sources important physical quantities of the detector can be determined accurately. There are three possibilities to place sources in BOREXino:

1. inside the *inner vessel*, through its neck with a segmented arm elongated down along the detector's z-axis. The final segment is mounted on a hinge and can be folded to reach off-axis positions. This system allows the use of any source type for the study of pulse shape analysis, position reconstruction, quenching effects.

2. in the buffer liquid, through dedicated feedthroughs. This allows to insert γ sources for the study of external background penetration effects and additional position reconstruction tests.

3. below the water tank, in an existing tunnel. This would be dedicated to a neutrino source. The best nuclide would be ^{51}Cr which decays β^- with energies very similar to ^{7}Be neutrinos: $0.75MeV$ with 90% B.R. and $0.43MeV$ with 10% B.R. Its life time of $27.7d$ is long enough to allow a good statistics: a $1.7MCu$ source like the one used in Gallex[48] would yield about 900 ev/month.

The calibration of the position reconstruction algorithm is crucial as it determines the systematics introduced with the fiducial volume cut on any measurement performed. The source insertion mechanics doesn't allow to know the position accurately enough, so

Isotope	Source	Typical conc.	Tolerable level	Strategy
^{14}C	radiogenic (in oil reservoir)	$1.2 \cdot 10^{-12} g/g$ in live organics	$3 \cdot 10^{-18} g/g$	selection of oil with low content
^{7}Be $\tau \simeq 53d$	cosmogenic (at surface)	$3 \cdot 10^{-2} Bq/t$	$2 \cdot 10^{-7} Bq/t$	distillation (?), undergr. storage
^{222}Rn	air, emanation from materials	$150 Bq/m^3$ in LNGS air	$0.1 \mu Bq/m^3$ (PC) $1 mBq/m^3 (H_2O)$	nitrogen stripping
^{210}Bi ^{210}Po	^{210}Pb	$5 \cdot 10^2 ev/d/t$	$0.5 ev/d/t$	avoid ^{222}Rn, Si-gel(?), distillation(?)
^{238}U ^{232}Th	suspended dust	$2 \cdot 10^{-5} g/g$ in dust	$< 10^{-16} g/g$ in PC	Si-gel, water extr., filters, distillation(?)
K_{nat}	dust or fluor contamination	$2 \cdot 10^{-6} g/g$ in dust	$< 10^{-14} g/g$ in scintillator	water extraction
^{39}Ar ^{85}Kr	air	$1 Bq/m^3$ in air	$0.1 \mu Bq/m^3$ in PC	nitrogen stripping

Tab. 2.4: *Radiopurity requirements for the BOREXino scintillator[185]. Effectiveness of purification methods marked with "(?)" is supported by lab measurements but not yet by CTF test.*

a *source locating system* is used[8][240]. Seven CCD cameras equipped with fish-eye lenses are mounted on the SSS in special housings. The source insertion system carries an LED close to the source itself which is photographed by all cameras simultaneously. After tracing a virtual ray from each camera to the LED, the point closer to all rays is taken as the source position in detector's coordinates. The achieved precision $\sim \pm 0.7 cm$. The picture of fig. 2.9 was taken with one of these cameras.

In addition to artificial sources, a few radio-nuclides present in the data samples allow a first energy scale estimate: ^{14}C, ^{214}Bi (when radon is present) and the $2.2 MeV$ γ-ray emitted in the capture of neutrons on protons. Anyhow only a neutrino source would allow an energy calibration free of systematics.

2.3 Background sources

The background sources in BOREXino can be subdivided in internal, external and surface background, where the emphasis is on the *inner vessel* membrane. The energy region mostly taken into account is $[250, 800] keV$, the so called *neutrino-window* (NW) where the ^{7}Be neutrino signal is expected.

2.3.1 Internal background

All background sources that generate energy depositions *inside* the *inner vessel* are generally ascribed to this category (tab. 2.4):

- ^{14}C (β^- decay, $Q = 156 keV$, $t_{\frac{1}{2}} = 5730 y$).

[8] Only with sources inside the detector of course.

At earth surface ^{14}C is cosmogenically produced via $^{14}N(n,p)^{14}C$, leading to a relative abundance on ^{12}C of $\sim 1.2 \cdot 10^{-12} g/g$ in living organic matter. In oil reservoirs, due to the old age, this contribution has decayed away. The concentration is therefore determined by a few site-dependent underground production mechanisms, initiated by the natural radioactivity of the rocks[177].

In scintillator procurement for the experiment, the choice of oil batches with lowest ^{14}C level was a major requirement, as ^{14}C, chemically identical to ^{12}C, cannot be removed by any purification process.

The detector's energy threshold for physics analyses is determined by the ^{14}C concentration. A leak of $1 ev/d$ in the NW is considered acceptable for BOREXino, which corresponds to a relative abundance of $3 \cdot 10^{-18}$.

Pseudocumene arriving from the production plant has been tested to fulfill, batch by batch, this requirement during the CTF-3 campaign (chap. 9).

- ^{238}U, ^{232}Th.

  Intrinsic scintillator radioactivity is mostly due to radio-isotopes belonging to the natural ^{238}U and ^{232}Th chains. Assuming secular equilibrium, BOREXino can tolerate concentrations of these elements not much greater then $10^{-16} g/g$.

  The CTF-1 and CTF-3 campaigns have demonstrated the ability of the available techniques to purify the scintillator to this order of magnitude. In chap. 9 detection methods in CTF and results will be explained.

- ^{40}K.

  Another intrinsic background component in organic material is ^{40}K, which decays with a half life of $1.3 \cdot 10^9 y$ in two different channels:

$$^{40}K \longrightarrow {}^{40}Ca \qquad (\beta^-, Q = 1.32 MeV, 89.3\% B.R.) \tag{2.4}$$

$$^{40}K \longrightarrow {}^{40}Ar + \gamma \qquad (EC, E_\gamma = 1.46 MeV, 10.7\% B.R.) \tag{2.5}$$

  ^{40}K has an isotopic abundance of $1.2 \cdot 10^{-4}$ with respect to K_{nat} which is present in the earth crust with a 2.4% concentration. BOREXino background requirements imply a scintillator cannot exceed a K_{nat} concentration of about $10^{-14} g/g$.

  Unfortunately the detection sensitivity at our disposal does not go below $10^{-11} g/g$ (CTF) or $10^{-12} g/g$ (NAA[9]). Water extraction purification of a concentrated PPO[10] solution showed an improvement of several orders of magnitude that should fulfill the requirement.

- ^{222}Rn and its daughters.

  Radon is a chemically inert gas that shows a high diffusion capability in air and in materials. Underground sites are rich in radon as the isotope is formed within

[9] Neutron Activation Analysis

[10] PPO is the fluor in the BOREXino scintillator mixture, as discussed below, and the main source of K.

the ^{238}U radioactive chain in secular equilibrium and diffuses away easily. In the Hall C of the LNGS facility, the activity evaluates to $\sim 30 Bq/m^3$, so any contact between scintillator and air must be avoided.

Radon decays with an half life of $3.8d$, but determines the build up of ^{210}Pb, a long-lived nuclide that can be absorbed on metal and plastic surfaces and give a hard time in terms of purification attempts. The two successive fast decays of ^{210}Pb are particularly dangerous: ^{210}Bi (β^-, $Q = 1.2MeV$) and ^{210}Po (α, $Q = 5.3MeV$, quenched to $\sim 350keV$).

Though various purification strategies showed different level of effectiveness, the purification from radon daughters is the only issue that still needs to be definitively addressed before the ^7Be measurement can be successful.

- ^{85}Kr (β^- decay, $Q = 690keV$, $t_{1/2} = 10.7y$)[11],
  ^{39}Ar (β^- decay, $Q = 570keV$, $t_{1/2} = 269y$).

  The air of the experimental hall also contains traces of ^{85}Kr (a man-made fission product) and ^{39}Ar (cosmogenic), with activities of $\sim 1.1 Bq/m^3$ and $\sim 13 mBq/m^3$ respectively. Avoiding air exposure of fluids is also important in order to limit these contaminations.

  Nitrogen stripping proved to be successful in purifying the scintillator from these gases, however since krypton and argon are present also in the incoming liquid nitrogen (used throughout the fluid handling system of the experiment), the collaboration has investigated the product offered by different companies in terms of these trace contaminants and a *Low Krypton and Argon Nitrogen* (LKAN) will be used in the final filling and purification phases.

- ^7Be ($EC + \gamma$, $E_\gamma = 478keV$, $t_{\frac{1}{2}} = 36.9d$, 10% B.R.).

  Cosmic rays can induce radioactive elements creation (*spallation*). In underground sites such as the the oil reservoirs or the LNGS laboratory, the hadronic component is removed by the rock shielding, so only high energy muons can penetrate these environments, resulting in a reduced spallation activity. Moreover in organic scintillator no elements heavier than carbon are present, therefore the possible cosmogenic radio-nuclides amount only to a limited number: ^{11}C, ^7Be, ^{11}Be, ^{10}C, ^8Li, ^6He, ^8B, ^9C, ^9Li, ^8He.

  As a matter of fact, the only nuclide that can contribute to background in the NW is ^7Be. Its *in-situ* production rate is sufficiently small to constitute no worry ($\sim 0.34 ev/d$, tab. 10.2). The pseudocumene production iter and its transportation to Gran Sasso is the only time spent by the scintillator material on surface, during which ^7Be may build up. Anyhow BOREXino scintillator was procured in 2001 and has been kept underground ever since. By the moment of detector filling (2006) the ^7Be content should have decayed to a well acceptable level.

[11] There is also 0.43% B.R. decay to an excited state useful for evaluating the contamination (sec. 9.3.3)

Component	^{238}U (g/g)	^{232}Th (g/g)	^{nat}K (g/g)	Total Mass (g)	Contribution (ev/day/100t)
2200 PMTs	$3 \cdot 10^{-8}$	$1 \cdot 10^{-8}$	$2 \cdot 10^{-5}$	$38 \cdot 10^{6}$	0.06
Buffer PC	$1 \cdot 10^{-15}$	$1 \cdot 10^{-15}$	$5 \cdot 10^{-12}$	$8.7 \cdot 10^{8}$	≤ 0.004
Outer Vessel	$2 \cdot 10^{-11}$	$2 \cdot 10^{-11}$	$1 \cdot 10^{-8}$	$5 \cdot 10^{4}$	≤ 0.04
Concentrators	$2 \cdot 10^{-10}$	$1 \cdot 10^{-9}$	$3 \cdot 10^{-7}$	$6 \cdot 10^{6}$	0.01
Sphere	$2 \cdot 10^{-10}$	$1 \cdot 10^{-9}$	$3 \cdot 10^{-7}$	$3.7 \cdot 10^{7}$	≤ 0.007
Cables	$2.1 \cdot 10^{-8}$	$2.4 \cdot 10^{-8}$	$7 \cdot 10^{-6}$	$2 \cdot 10^{5}$	≤ 0.003
Cameras					0.02
Rock					≤ 0.005
^{222}Rn[a]					0.03
Total					0.13 ± 0.05

[a] in the buffer PC with a $1 mBq/m^3$ activity.

Tab. 2.5: *External background in the NW ($250 - 800 keV$) from different components of the detector.*

2.3.2 External background

Any radiation source external to the *inner vessel*, but leading to an energy deposition in the scintillator, is regarded as *external* background. It is obviously only γ radiation. In order to suppress this background the detector was designed in concentric layers as it will be described in the next paragraph.

Moreover a careful selection of the materials used for *every* component of the detector has been carried out. The fiducial volume cut will allow to suppress residual contributions and will be adjusted around the foreseen value of $100t$, in accordance to the background conditions at data taking time. In tab. 2.5 are reported the estimated contributions based on lab scale measurements of the materials and detector simulations.

2.3.3 Surface background

We define *surface* background any contamination, intrinsic or acquired, of the nylon of the *inner vessel* membrane, the only material directly in contact with the scintillator. In ideal conditions there should not be contributions of this kind and aiming to this, the nylon extrusion, the *inner vessel* assembly and its transportation have been performed under the most stringent purity requirements. The main worry is that exposure to Radon could lead to a deposition of radon daughters and especially of ^{210}Pb, that the later fiducial volume cut will only partly be able to remove from the neutrino signal. Indeed the CTF *inner vessel*, constructed under slightly looser working conditions, shows such contamination.

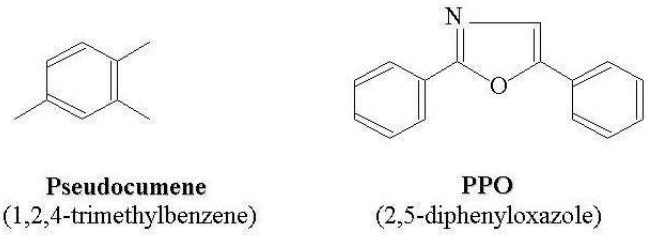

Fig. 2.10: *Molecular structure of the two components of the BOREXino scintillator mixture.*

2.4 Scintillation process in organic solutions

The physics of scintillation counting has been extensively studied in literature and exploited in particle detection throughout many decades[181]. In this section the mechanism is reviewed with particular emphasis on the mixture PC+PPO (1.5g/l) used in BOREXino, its light response, the *quenching* phenomenon and the photon interaction within a large volume of scintillator[178].

2.4.1 Light emission mechanism

Organic scintillator evaluated for BOREXino have a molecular structure made essentially of benzene rings (fig. 2.10). In these planar molecules, 2 or 3 valence electrons of the carbon atoms are localized among the atoms themselves in the molecular plane, while the remaining are de-localized in planes parallel to it. They account for the so called σ and π bounds respectively.

Transitions among the π energy levels (fig. 2.11) are responsible for the scintillation mechanism, while interactions involving excitation or ionization of σ electrons determine de-excitation or recombination processes where the energy is dissipated thermally, rather than through photon emission.

Singlet states excitation

Singlet states (spin 0) $S_0, S_1, S_2, \ldots$ are further subdivided in vibrational states. The energy separation between S_0 and S_1 is $\sim 3 - 4eV$, while separation between higher states is progressively smaller and vibrational sub-states separation is of the order of $\sim 0.15eV$. At thermal energies ($0.025eV$) most of the molecules are therefore in state S_{00}.

The energy deposition of a charged particle crossing the medium can determine excitation to any of the singlet states, but the molecule quickly ($\tau_c \simeq 1 \div 10ps$) moves to S_{10} through non-radiative processes. From S_{10} it de-excites to one of the S_0 states through the so called *fluorescence* that accounts for the quick component of the scintillator light response and whose intensity can be described simply as:

$$I = I_0 e^{-t/\tau_d} \tag{2.6}$$

where $\tau_d \simeq 1 - 10ns$ and the S_{10} population time was neglected ($\tau_r < 0.5ns$).

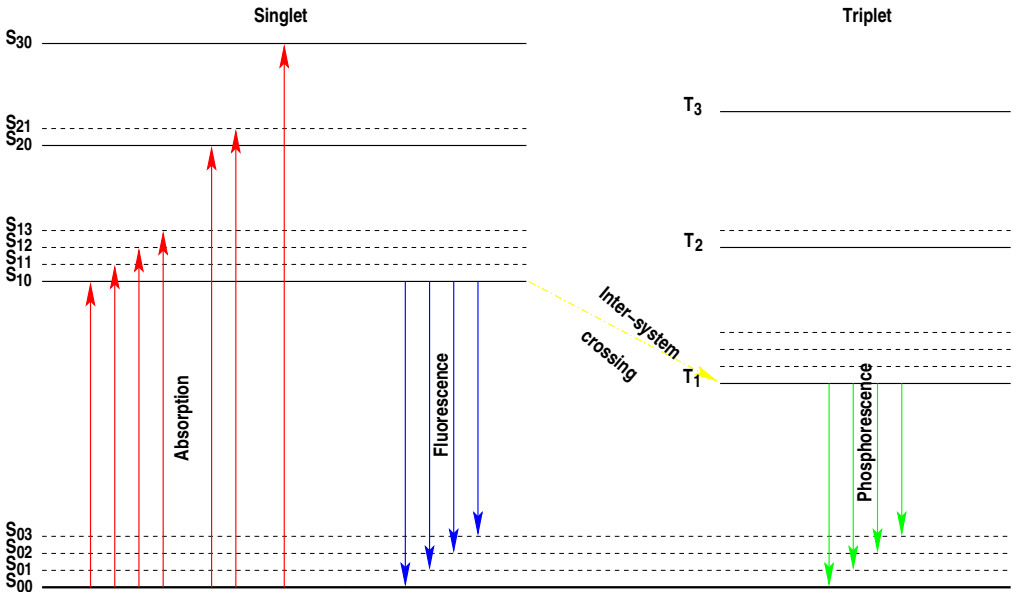

Fig. 2.11: *Energy levels of the π electrons in an organic scintillator molecule.*

Triplet states excitation

Population of triplet states (spin 1) can occur in two ways:

1. *inter-system crossing* from state S_1.
2. ionic recombination in higher energy triplet states and successive internal conversion to T_1.

The triplet state has a longer mean life compared to the singlet state ($\tau_d \sim 1 \div 10ms$) and the emission, called *phosphorescence*, occurs at higher wavelength compared to fluorescence as $E(T_1) < E(T_2)$. Consequently it doesn't play a role in the scintillation process.

However a pair of molecules in state T_1 can annihilate into a state S_1 and a state S_0. De-excitation occurs then with the fluorescence spectrum but in times typical of phosphorescence. This phenomenon is known as *delayed fluorescence*.

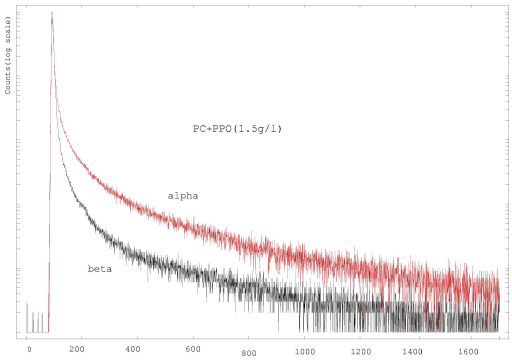

Fig. 2.12: *The time evolution of the scintillator emission for α and β particles from a laboratory test.*

For highly ionizing particles, like αs, characterized by a high specific energy loss dE/dx, ionic recombination and triplet state excitation occur more frequently. These particles can therefore be identified by the higher light emission at long times (fig. 2.12)[12].

[12] See also sec. 7.4.6 and sec. 9.1.5.

Excitation	$\tau_1(ns)$	$\tau_2(ns)$	$\tau_3(ns)$	$\tau_4(ns)$	q_1	q_2	q_3	q_4
β	3.57	17.61	59.50		89.5%	6.3%	4.2%	
α	2.19	12.02	56.13	433.6	63.6%	15.3%	10.4%	10.7%

Tab. 2.6: *Decay times of the PC+PPO (1.5 g/l) mixture for excitations due to β or α particles.*

Binary systems

Binary organic mixtures like those studied for BOREXino involve a solvent and a solute (fluor), whose molecular levels structure is similar to the solvent but where any level lies at a slightly lower energy. Incoming particles loose energy mostly to solvent molecules, where the primary excitation occurs as well as the energy degradation to states S_{10} and T_{10}. At this point the energy is rather transferred to solute molecules which have a higher scintillation efficiency. For example the addition of PPO in the concentration of $1.5g/l$ increases the light output of the pure PC by ~ 20 times, bringing it to the quoted $10000photons/MeV$. Moreover the solute is acting as *wavelength shifter* in the sense that it has spectral emission that matches more closely the sensitivity of the photomultiplier (fig. 2.13(a)).

The scintillating mixture PC+PPO ($1.5g/l$) has a light response which can be modeled as a sum of exponential functions:

$$S(t) = \sum_{i=1}^{N} \frac{q_i}{\tau_i} e^{-t/\tau_i} \tag{2.7}$$

where N=3 for β (or $\beta+\gamma$) excitations and N=4 for α excitations. Tab. 2.6 reports the values of τ_i and q_i measured in laboratory.

The first component accounts for the average PC $\rightarrow$ PPO excitation transfer time as well as the fluorescent de-excitation time of the PPO S_1 state ($\tau_d = 1.6ns$). In fact increasing the PPO concentration τ_1 decreases to τ_d.

Other exponential terms account instead for the more complex *delayed fluorescence* and result from a parameterization of the light profile studied in laboratory tests.

Indeed one of the valuable characteristics of liquid scintillators is the "fast" response, i.e. the high relative weight of the emission occurring at the ns scale, which for BOREXino is essential to perform a reliable position reconstruction of the events (sec. 7.4.4).

2.4.2 Scintillation efficiency and *quenching*

The *Scintillation Efficiency* (S) is defined as the fraction of the incident particle energy that is converted into visible light. Processes leading to non-radiative energy dissipation, such as σ electron excitation and especially ionization, account for scintillation inefficiencies and are generally indicated as *quenching* effects.

Generally S depends on the particle type (i.e. heavier, more ionizing particles are more quenched) as well as on the energy, though above a given threshold the energy dependency disappears.

For example the scintillator response to electrons above $125keV$ can be described simply as:

$$\frac{dL}{dx} = S\frac{dE}{dx} \tag{2.8}$$

where dL/dx is the specific light emission of the scintillator and dE/dx is the specific energy loss of the particle.

In general, however, it can be assumed that the density of ionized molecules along a particle track can be written as $B\frac{dE}{dx}$ and a fraction k of these leads to quenching effects. In this case the light response becomes:

$$\frac{dL}{dx} = \frac{S\frac{dE}{dx}}{1 + kB\frac{dE}{dx}} \tag{2.9}$$

known as the *Birk's formula*[182], where kB is treated as a single parameter characteristic of the specific scintillator in use. The experimental determination of kB is not a trivial task. Unpublished laboratory measurements indicated $kB = 0.015cm/MeV$, but a modeling of the CTF data seems to indicate $kB \simeq 0.010cm/Mev$ (sec. 9.2.2).

For fast electrons with a small dE/dx eq. 2.9 reduces to eq. 2.8, while for heavier particles such as α or protons with a large dE/dx, saturation occurs:

$$\left.\frac{dL}{dx}\right|_{\alpha} = \frac{S}{kB}\,, \tag{2.10}$$

A parameter often quoted in describing a scintillator is the *quenching factor* $Q = L(\beta)/L(\alpha)$, the ratio of luminosity emitted by β and α particles of the same energy. A small scale laboratory test indicates:

$$Q(E) = 20.3 - 1.3 \cdot E[MeV] \tag{2.11}$$

which pushes the $5 - 10MeV$ α's of the ^{238}U and ^{232}Th chains down[13] into the NW making α/β separation a fundamental background rejection tool.

2.4.3 Propagation of scintillation light

Ideally photons emitted in the scintillator should simply propagate in a straight line undisturbed until they reach photomultipliers and this indeed happens to a consistent fraction of them. However the propagation of light in a large volume of scintillator such as BOREXino has been studied[178] and can be described using the *attenuation length* $\Lambda(\lambda)$ and the relation:

$$I(x, \lambda) = I_0(\lambda)e^{-\frac{x}{\Lambda(\lambda)}} \tag{2.12}$$

where $I(x, \lambda)$ is the light intensity of a test beam after a path x and I_0 is the intensity at origin. The attenuation length of the BOREXino mixture at the peak of the emission spectrum is in the $5 \div 10m$ range.

Two possible interactions are determinant here:

[13] A side effect is that the visible separation of the different α peaks in the spectrum is increased.

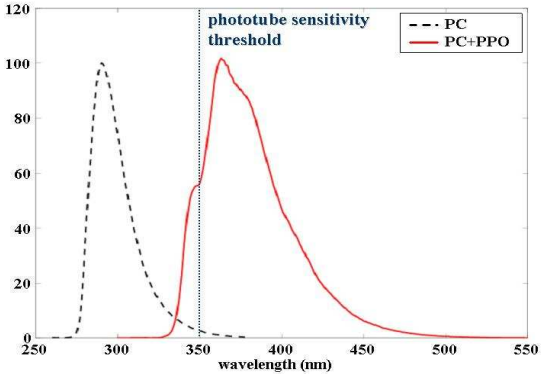

Fig. 2.13 (a): *PC+PPO(1.5g/l): emission spectrum.*

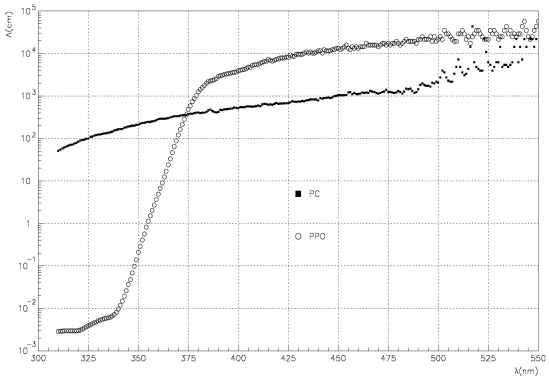

Fig. 2.13 (b): *Attenuation length of PC and PPO.*

1. Absorption and re-emission of the light on PPO molecules (*Inelastic Scattering*).
2. *Elastic (Rayleigh) Scattering* on PC molecules.

These effects do not essentially change the light yield of the mixture, but they can make the response somewhat slower.

Absorption and re-emission

Comparing the laboratory measurements of the PPO emission spectrum (fig. 2.13(a)) and the attenuation length of PC and PPO (fig. 2.13(b)), it can be seen how the PPO is able to absorb most of its own emission at small wavelengths ($\lambda < 360nm$) within a few cm from the emission point. The PPO quantum efficiency in re-emitting the absorbed photon is $\sim 80\%$ and re-emission occurs according to the same emission spectrum. The process can be iterated a few times, until it is re-emitted with a wavelength above the absorption region. Consequently the spectrum is slightly shifted toward red light.

Re-emission is isotropic with no correlation with the direction of the absorbed photon, but this does not affect the position reconstruction capability of the detector as the spatial resolution is anyhow larger than the distance between emission and re-emission points. The relevant effect for BOREXino is instead the increase of the fast decay constant of the scintillator to about $5ns$.

So a higher fluor concentration improves the transfer efficiency and therefore the light yield, but at the same time absorption effects can make the time response slower. The PPO concentration for BOREXino was an optimized compromise between these two aspects.

Elastic Scattering

The lowest transition energy of PC molecules is at about $320nm$, out of the PPO emission spectrum, so absorption on PC molecules is negligible. However above the PPO absorption

region ($\lambda > 380nm$) Rayleigh scattering starts to dominate on absorption and re-emission.

The attenuation length for this process is above 1m so the number of scatters a photon can undergo is limited (in CTF it should rarely be more than 1) and the scattered photons have a $1 + cos^2(\theta)$ angular dependency, i.e. the usual deflection of the process is not too large.

This phenomenon makes trajectories somewhat longer and less linear, limiting to some extent the spatial resolution of the detector.

2.5 Status of the project

In 2002 the CTF-3 campaign (chap. 9) was ongoing involving the test of the different scintillator purification strategies in view of the final detector's filling. On August 16^{th} of that year, $\sim 50l$ of pseudocumene were accidentally spilled in the laboratory drain system and reached the Mavone creek in the Teramo province.

Though the environmental impact was negligible, the small accident triggered a survey of the responsible authorities. Within this context a few design flaws were evidenced in the laboratory piping, potentially harmful for the Gran Sasso water basin in the case of a major accident. Consequently all activities involving the manipulation of fluids in the laboratory have been suspended while civil works are being carried out, commissioned by the Italian government under a special urgency procedure. They involve covering the floor of the three experimental areas with impermeable resin and the lay down of new drain pipes independent of the drinking water system.

In the past three years, the collaboration works could only be limited to hardware "dry" operations. Nevertheless the activity has been very large and in 2004 the detector was completed with the installation of the nylon vessels, of the last PMTs and of the outer detector (chap. 3). Moreover the electronics (chap. 4) and the data acquisition system (chap. 5) have been commissioned and tested in multiple *air runs* (chap. 6), some of which involved the use of a source[14], and a major effort has been done in the development of the offline software (chap. 7).

The CTF detector was operated throughout this period in static regime and the large amount of data collected ($\sim 800d$ live time), has given the possibility of performing a few interesting measurements (chap. 9 and 10).

In April 2005 the collaboration was given again the permission to operate fluids and the CTF campaign restarted together with the operations on all fluid handling plants. With the completion of the final part of the works, expected by middle 2006, also the permission to discharge water and to procure the buffer pseudocumene will be granted and filling of BOREXino should proceed.

[14] A small vial with scintillator loaded with radon or ^{210}Po

Chapter 3

The Outer Muon Veto

Though the rock shielding greatly reduces their flux, high energy muons originating within cosmic ray interactions in the atmosphere are still able to penetrate into the depth of the Gran Sasso laboratory, where the BOREXino experiment is located. In this context they constitute a relevant source of background for the experiment and must be tagged with high efficiency for the success of the ^7Be neutrino flux measurement as well as of the rest of the physics program.

Among the tagging methods, a key role is played by the *Outer Detector* (OD) of the experiment, a separate Čerenkov detector realized with 208 additional PMTs in the volume of the external *Water Tank* (WT) where a water buffer is present for shielding purposes.

The installation of the equipment was completed in summer 2004 and the detector was then tested and fully commissioned in the course of serveral air runs. In this chapter, after the issue of cosmogenic muons in underground facilities is introduced, there are presented the goals, the detection principles, the design and the installation of the outer detector[1].

3.1 Cosmogenic muons in underground facilities

Apart from neutrinos, muons are generally the only products of cosmic ray interaction in the atmosphere able to penetrate the rock cover of underground physics sites.

Though for BOREXino they constitute mostly a source of background, other experiments in Gran Sasso and in other sites have been studying them as important indirect clues to the primary cosmic rays that generated them.

3.1.1 Primary Cosmic Ray spectrum

Cosmic rays[186] are one of today intriguing topics in astro-particle physics, with their origin and propagation being questioned in many theoretical works and their interaction in the atmosphere being investigated by different experiments.

[1] Electronics, data acquisition software, the detector tests and its calibration system are instead covered in chapters 4, 5, 6 and 8 respectively.

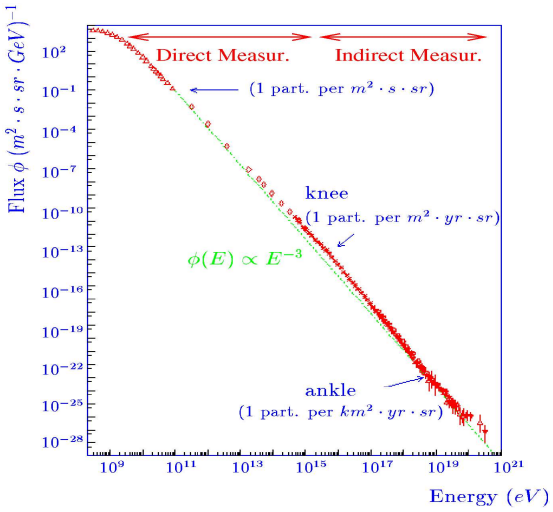

Fig. 3.1 (a): *Cosmic ray spectrum.*

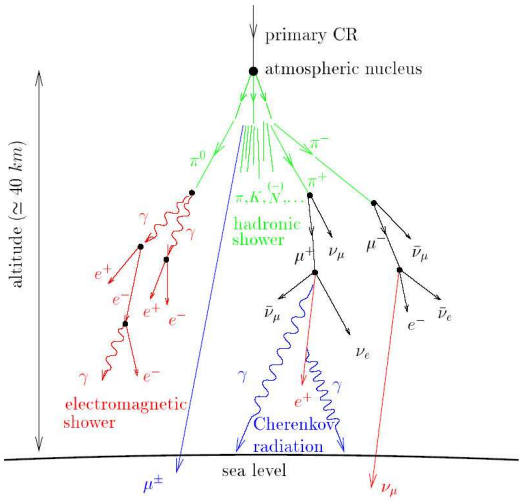

Fig. 3.1 (b): *Simple sketch of the shower produced by cosmic ray interaction in the atmosphere.*

Their observed flux is $\sim 10^3 m^{-2} s^{-1}$ and is composed for 90% by protons, for 9% by α particles and for the rest by heavier ionized nuclei. The spectrum (fig. 3.1(a)) spans over many orders of magnitude up to $10^{20} eV (\sim 20J)$.

It is believed that the lower energy component up to $200 MeV$ has origin from the sun and that the *Ultra-High Energy Cosmic Rays* (UHECR) above $10^{18} eV$ may come from extra-galactic sources. The region in between, i.e. the bulk of the spectrum, is generated within our galaxy but outside the solar system. Its shape may be empirically described by the inverse power law:

$$\frac{dN}{dE} \propto E^{-(\gamma+1)} \tag{3.1}$$

and is characterized by a "discontinuity" at about $10^6 GeV$ denoted by the transition $\gamma \sim 1.7 \rightarrow \gamma \sim 2.0$.

This is usually referred to as the *knee* and incidentally marks also the approximate boundary between direct experimental measurements available from telescopes (flown on balloon, aircrafts or in outer space) and indirect measurements from large earth detectors (air-shower arrays and fluorescence sensors) observing the cascade of secondary particles produced by cosmic rays in the atmosphere.

The opposite change in slope marking the transition to UHECR region is instead known as the *ankle*.

3.1.2 Cosmogenic Muons

Today, muons are quite well known particles. They are charged leptons with a mass of $\sim 105 MeV$ and decay with a mean lifetime of $\sim 2.2 \mu s$ into $\mu^{\pm} \rightarrow e^{\pm} + \nu_e(\overline{\nu}_e) + \overline{\nu}_\mu(\nu_\mu)$.

In the interaction of primary cosmic rays into the atmosphere, muons are produced from the decay of pions and kaons originated within the hadronic shower (fig. 3.1(b)):

$$\pi^{\pm}, K^{\pm} \longrightarrow \mu^{\pm} + \nu_{\mu}(\overline{\nu}_{\mu})$$

Surface Energy Spectrum

The muon spectrum at sea level can be derived from integrating the production spectrum over the path from primary interaction point ($\sim 15km$ altitude)[186]:

$$\frac{dN_0}{dE_0}(E_0, \cos\theta) \sim 0.14 \cdot E_0^{-(\gamma+1)} \cdot \left(\frac{1}{1 + \frac{1.1 E_0 \cos\theta}{115 GeV}} + \frac{0.054}{1 + \frac{1.1 E_0 \cos\theta}{850 GeV}} \right) \tag{3.2}$$

which holds for $\theta < 60^{\circ}$ (earth curvature neglected) and $E_0 > 10GeV$ (muon decay and interaction neglected). The two terms in parenthesis account for production from π and K meson respectively. It should be noted how in first approximation the term $E_0^{-(\gamma+1)}$ reflects the shape of the primary cosmic ray spectrum.

Underground Intensity

In order to reach an underground site the muon traverses a so-called *slant depth*, defined as $X(x, \rho(x)) = \int_0^x \rho(x')dx'$, $\rho(x)$ being the density function in the medium. X is measured in g/cm^2 or $m.w.e.(\equiv 100 g/cm^2)$.

The intensity in an underground site can be written as:

$$I(X, \cos\theta) = \int_0^{\infty} P(E_0, X) \frac{dN_0}{dE_0}(E_0, \cos\theta) dE_0 \tag{3.3}$$

where $P(E_0, X)$ is the probability that a muon of surface energy E_0 survives traversing a slant depth of rock X and is usually computed with MC simulations for a given site of known profile and composition, taking into account the muon interactions described below.

Interactions in the rock

Two kinds of interactions are relevant for relativistic muons in matter (fig. 3.2):

1. Continuous ionization of the traversed medium along the track. The relative specific energy loss (above $10GeV$) has only a moderate energy dependence:

$$\frac{dE}{dx} \sim - \left[1.9 + 0.08 \ln \left(\frac{E_{\mu}}{m_{\mu}} \right) \right] \sim - \alpha \tag{3.4}$$

   where α is generally taken $\sim 2MeV/(g \cdot cm^{-2})$.

2. Discrete radiative processes, namely bremsstrahlung, pair production and muon hadro-production. The energy loss of all these processes depend linearly on E:

$$\frac{dE}{dx} = -\frac{E}{\xi} \qquad \text{with} \qquad \xi^{-1} = \xi_{BS}^{-1} + \xi_{PP}^{-1} + \xi_{HP}^{-1} \tag{3.5}$$

   and $\xi \sim 2.5 \times 10^5 g/cm^2$

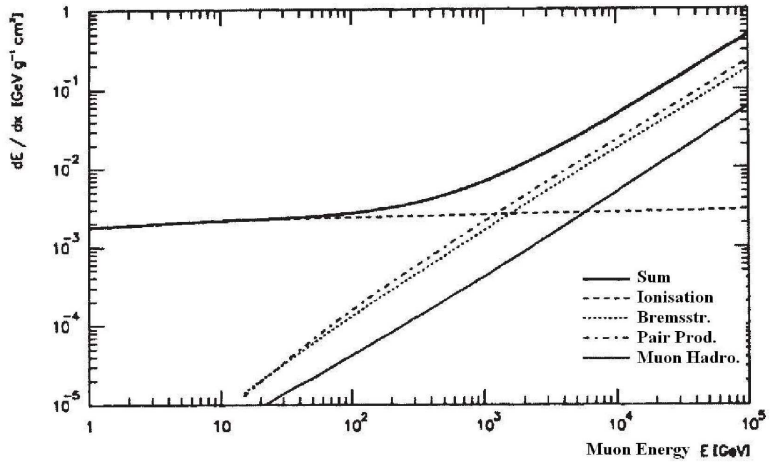

Fig. 3.2: *Energy loss of muons traversing the rock. Contributions from ionization and discrete radiative processes are visible.*

The so-called critical energy $\epsilon = \alpha\xi \sim 500GeV$ defines the boundary above which discrete processes start to dominate on ionization.

Depth-intensity relation

The mean energy at slant depth X of a muon starting with a surface energy E_0 is given by:

$$\langle E(X)\rangle = (E_0 + \epsilon)e^{-X/\xi} - \epsilon \qquad \Rightarrow \qquad E_0 > E_0^{\min} \equiv \epsilon(e^{X/\xi} - 1) \tag{3.6}$$

In other words the *vertical* muon intensity in an underground site is given by the portion of muon spectrum at surface that lies above the minimal energy to traverse the slant depth X:

$$I_v(X) = \int_{E_0^{\min}(X)}^{\infty} \frac{dN_0}{dE_0}(E_0, \cos\theta = 1)dE_0 \tag{3.7}$$

At LNGS (sec. 2.2.1), where the *minimal* rock coverage is of $3100m.w.e.$, E_0^{min} is about $\sim 1.3TeV$.

Muon detectors with a sub-degree angular resolution, such as MACRO and LVD, can convert (θ, ϕ) of the muon events to an average slant depth and produce plots like those in fig. 3.3, known as *depth-intensity relation*.

Underground Energy Spectrum

The underground spectrum can be obtained exploiting eq. 3.6:

$$\frac{dN(X)}{dE} = \frac{dN}{dE_0}\frac{dE_0}{dE} = \frac{dN}{dE_0}\exp(X/\xi)\Big|_{E_0 = e^{X/\xi}(E+\epsilon)-\epsilon} \tag{3.8}$$

where the surface spectrum dN/dE_0 is given in eq. 3.2.

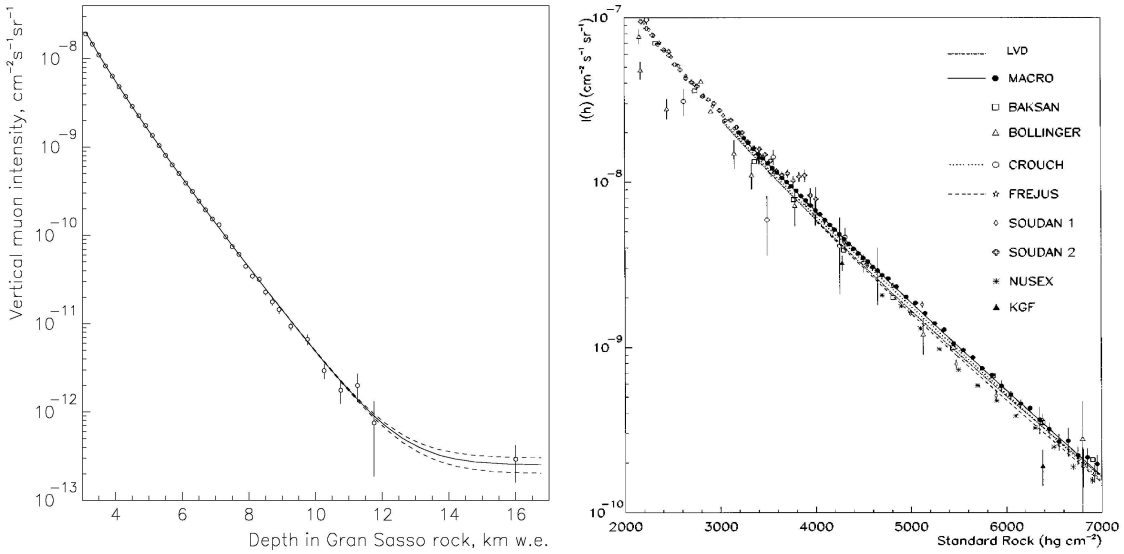

Fig. 3.3: *Depth-intensity relation measured in Gran Sasso by the LVD[189] (left) and MACRO[187] (right) experiments. Data measured at other sites are also reported.*

However, parameterizing the integral muon flux at surface as $N_0 \sim KE_0^{-\gamma_\mu}$, with $\gamma \leq \gamma_\mu \leq \gamma + 1$, the following approximation holds:

$$\frac{dN(X)}{dE} \sim K \cdot \left(E + \epsilon(1 - e^{-X/\xi})\right)^{-(\gamma_\mu+1)} \tag{3.9}$$

The shape at shallow sites is characterized by a flat low energy component ($E(X) \ll \alpha X$) and by an inverted power law behavior at higher energies which reflects the surface spectrum. For sites deeper than $\xi \sim 2500 m.w.e.$ the behavior is similar but the transition energy becomes $\epsilon \sim 500 GeV$ independent of depth.

The average energy is given by:

$$\langle E \rangle = \frac{\epsilon(1 - e^{-X/\xi})}{\gamma_\mu} \quad \underset{X \to \infty}{\longrightarrow} \quad \frac{\epsilon}{\gamma_\mu} \tag{3.10}$$

The muon spectrum at LNGS was measured by the MACRO (fig. 3.4) and LVD experiments [187, 189]. The average energy amounts to:

$$\langle E_{\rm LNGS} \rangle = (320 \pm 12) GeV$$

and the flux is $1.16 \mu/m^2/h$, i.e. about 10^6 times lower than at surface.

Stopping vs. through-going muons

The ratio of stopping to through-going muons in a detector of thickness ΔX at depth $X \gg \Delta X$ is given by:

$$R(X) = \frac{\Delta N}{N} = \gamma_\mu \frac{\Delta E_0}{E_0} \sim \gamma_\mu \frac{\Delta E e^{X/\xi}}{(e^{X/\xi} - 1)\epsilon} \tag{3.11}$$

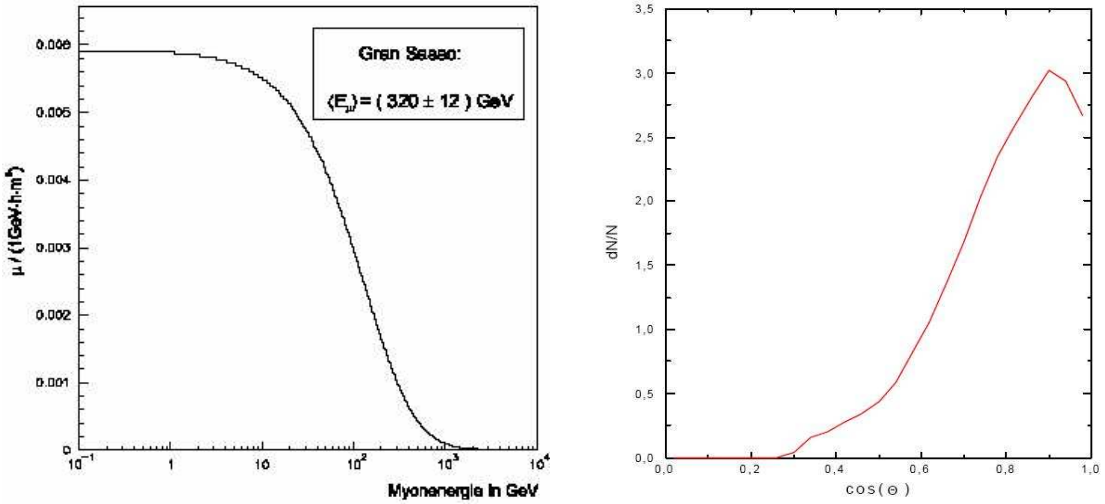

Fig. 3.4: *Energy spectrum (left) and angular distribution (right) of muons in the Gran Sasso laboratory as measured by the MACRO experiment[188].*

where $\Delta E \sim \alpha X$ is the minimum energy required to traverse the detector. This leads to a $1/X$ dependency for shallow depth ($X \ll \xi$) and a constant $\gamma_\mu \Delta E/\epsilon$ value for deep sites ($X \gg \xi$).

In the latest case, considering a detector of the BOREXino size $\sim 20m$ and a density $\rho \sim 1 g/cm^3$ (i.e. $2MeV/cm$ energy loss), the muons that stop in the detector are $\sim 1{-}2\%$.

3.2 Muons in BOREXino

As in BOREXino most of the muons are through-going, the signal left in the detector depends on the crossing geometry only.

Muons crossing the *inner vessel* saturate the inner detector without constituting a relevant background. However muons crossing only the *buffer* liquid, where no significant scintillation takes place, would be detected only by Čerenkov radiation that is about 50 times weaker than scintillation light. In this case events inside the energy region relevant for physics analysis could be generated.

The number of muon interactions expected in different BOREXino (and CTF) detector segments are reported in tab. 3.1.

Detector Region	Flux (μ/d)
– BOREXino –	
IV	2025
Buffer	3125
SSS	5150
Water Tank	9900
– CTF –	
IV	130
Water Tank	2900

Tab. 3.1: *Muon events expected in BOREXino[230] and measured in CTF (chap. 10).*

3.2.1 Three muon tagging strategies

BOREXino requires a muon tagging efficiency of $\sim 99.99\%$. Three independent muon veto systems are present, each one with the goal of $\sim 95\%$ efficiency:

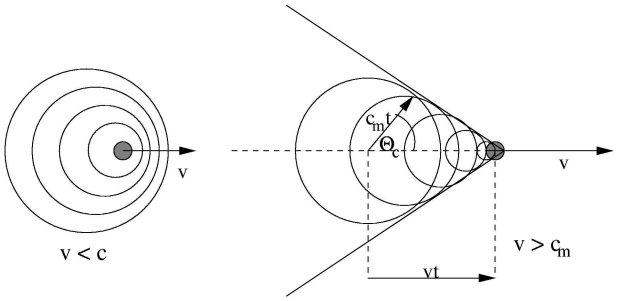

Fig. 3.5 (a): *Čerenkov light emission scheme.*

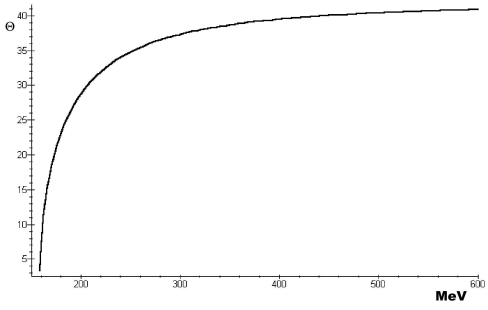

Fig. 3.5 (b): *Čerenkov emission angle in water as a function of muon energy.*

- *Inner Muon Veto.* As mentioned in sec. 2.2.2, 374 of the inner detector PMTs are not mounting a light concentrator. Therefore their acceptance angle is wider than the others and light from muons crossing the buffer will more likely be detected by these PMTs. As a net effect the ratio of the number of hit PMTs without and with concentrators will be higher for muon events rather than for scintillation events.

- *Geometrical Pattern Analysis.* Muon events can be distinguished from scintillation events by two parameters:

  - Photon arrival time spread. Point-like or quasi-point-like scintillation events are characterized by a narrower photon time spread compared to Čerenkov photons emitted along a muon track.
  - Up-down charge asymmetry. As muons events are mostly down-going they are characterized by a relatively higher deposited charge in the lower hemisphere compared to isotropic scintillation events.

- *Outer Muon Veto.* As the volume between the SSS and the dome-shaped tank must be filled with water to ensure the proper shielding against the γ radiation from the surrounding rocks, the volume can be exploited also as a Čerenkov detector with an independent set of photomultiplier tubes in order to detect the through-going muons. The rest of the chapter deals with this system.

3.2.2 The Čerenkov effect

The Čerenkov effect was firstly observed in 1934 by Pavel Čerenkov during his studies with radioactive sources (in particular Radium) in different fluids. The correct mathematical formulation came in 1937 by Frank and Tamm.

The effect occurs when a charged relativistic particle propagates in a medium with refractive index $n > 1$, or, more precisely, when the motion is faster than the light speed in the medium: $v > c_m \equiv c/n$. In this case a shock wave is produced, in analogy with the known sound barrier break-up process. This is generated in the electromagnetic field of

the particle from the fact that the field source is faster than the propagation speed. The shock wave is visible as light rays emitted in a cone with axis in the particle direction (fig. 3.5(a)). The opening angle of the cone depends on the particle speed and on the refraction index:

$$\cos\theta_C = \frac{c_m t}{vt} = \frac{1}{n\beta} \tag{3.12}$$

where $\beta = v/c$.

The minimum required energy for the Čerenkov light emission can be inferred from the total energy conservation for a relativistic particle:

$$E^{(tot)} = \gamma_0 c^2 = \frac{m_0 c^2}{\sqrt{1-\beta^2}} \qquad \Rightarrow \qquad E^{(tot)}_{min} = \frac{m_0 c^2}{\sqrt{1-\frac{v^2_{min}}{c^2}}} \tag{3.13}$$

with $v_{min} = c/n = c_m$

A more precise derivation of the Čerenkov effect can be obtained from the Lorentz transformation of a charge moving in the electromagnetic field[190]. However this longer calculation brings the same result as the above graphical considerations.

In the case of water ($n = 1.344$) the minimum speed is $v_{min} = 2.232 \cdot 10^8 m/s$. So for example:

$$\begin{array}{lcll} (\mu^{\pm}) & m_0c^2 = 106MeV & \Rightarrow & E^{(tot)}_{min} \sim 160MeV \\ (e^{\pm}) & m_0c^2 = 511keV & \Rightarrow & E^{(tot)}_{min} \sim 765keV \end{array}$$

Muons penetrating the Gran Sasso underground laboratory have an average energy of $320GeV$, i.e. they can be regarded as ultra-relativistic. In this limit ($\beta \sim 1$) the Čerenkov angle becomes independent from particle energy:

$$\theta_C = \arccos\frac{1}{n} \sim 42^\circ$$

Only in the low energy region the angle shows an energy dependency (fig. 3.5(b) for μ):

$$\cos\theta_C(E) = \frac{c_m}{v(E)} = \frac{1}{n\sqrt{1-\frac{m_0^2c^4}{E^2}}}$$

where $\beta = \sqrt{1 - m_0^2c^4/E^2}$ for a relativistic particle was used.

The specific energy loss of a particle by Čerenkov radiation is given by:

$$\left(\frac{dE}{dx}\right)_{rad} = \frac{(ze)^2}{c^2} \cdot \int_{\epsilon(\omega)<(1/\beta^2)} \omega\left(1 - \frac{1}{\beta^2\epsilon(\omega)}\right) d\omega \tag{3.14}$$

where ze is the charge of the particle and $\epsilon(\omega)$ is the dispersion relation. As the integrand is positive only for $\beta^2\epsilon(\omega) > 1$, the Čerenkov radiation is emitted only in a frequency band where the dispersion is large (larger than $1/\beta^2$). For water this happens to be in the blue light and UV region.

The number of photons per unit path and wavelength is given by[191]:

$$\frac{d^2N}{d\lambda dx} = \frac{2\pi\alpha z^2}{\lambda^2}\left(1 - \frac{1}{\beta^2 n^2(\lambda)}\right) = \frac{2\pi\alpha}{\lambda^2}\sin^2\theta_C(\lambda) \tag{3.15}$$

where α is the fine structure constant, eq. 3.12 was used and the charge number z was set to 1 for muons. It is worth noting that the photon yield depends inversely on λ^2, i.e. the radiation is concentrated in the high frequency portion of the emission band.

The next step is to compute the number of *detectable* photoelectrons per unit path in BOREXino OD:

$$\frac{dN_{pe}}{dx} = \int_{\lambda_1}^{\lambda_2} \epsilon_{PMT}(\lambda)\cdot p \cdot \frac{d^2N}{dxd\lambda} \sim 45pe/cm \tag{3.16}$$

where $\epsilon_{PMT}(\lambda)$ is the PMT quantum efficiency at wavelength λ (fig. 3.7) and $p = 0.6$ is the so-called *practical factor* that accounts for the probability of a photo-electron to actually generate a detectable pulse at the anode[192].

Considering that a muon crossing the SSS has a minimum path in water of $2.15m$ it generates almost $10000pe$ detectable in OD.

The OD PMT coverage is only $\sim 0.3-0.4\%$ allowing to detect directly just a few tens of pe, however simulations show that including reflections on Tyvek surface (sec. 3.3.2), at least $200pe/ev$ are to be expected.

3.3 Outer Detector Design

The outer detector of BOREXino consists of 208 PMTs of the same model used for the inner detector, i.e. 8" ETL-9351, whose nominal characteristics are listed in tab. 3.2. Fig. 3.7 shows the quantum efficiency as a function of wavelength and in comparison with the Čerenkov emission spectrum.

3.3.1 PMT encapsulation

Unlike the ones mounted inside the sphere, OD PMTs are equipped with a full encapsulation (fig. 3.6). This is a steel cone-shaped case, housing the PMT, the voltage divider, the μ-metal and a female HV connector. The μ-metal is a thin metal foil required to shield the PMT against the earth magnetic field. The HV connectors match $55m$ submarine cables identical to the ones used for ID PMTs. These cables carry both High Voltage and the signal connecting the PMT to the electronics chain located in the nearby BBW (fig. 2.6). The sensitive photocathode is covered only by a transparent (90-92% in the sensitivity range) PET foil, so the PMT retains an acceptance angle close to 180°. The space between the case (including the PET foil on the front) and the PMT is filled with transparent mineral oil. This minimizes refraction index discontinuities in the light path to the photocathode. A detailed description of the encapsulation design and its under-pressure tests can be found in [241].

Voltage for gain 10^7	1650 V	typ.
Maximum voltage	2200 V	max
Maximum voltage between cathode and first anode	900 V	max
Rise time	4 / 6 ns	typ.
Fwhm	7 / 10 ns	typ.
Fall time	8 / 12 ns	typ.
Linearity peak current at gain 10^6	8 mA	typ.
Linearity peak current at gain 10^7	10 mA	typ.
Linearity integrated charge at gain 10^6	80 / 120 pC	typ.
Linearity integrated charge at gain 10^7	100 / 150 pC	typ.
SPE Peak-to-Valley ratio	2.5	typ.
Photo-cathode sensitivity at $420nm$	26.5 %	typ.
Transit time spread fwhm	2.8 ns	typ.
Pre-pulsing $(2\sigma - 20\sigma)$	3 / 6 %	max
After-pulsing $(0.05 \div 12.4\ \mu s)$	2.5	typ.
Dark current at gain 10^7	25 nA	typ.
Dark counts at gain 10^7	3000	typ.

Tab. 3.2: *Manufacturer specification for 8" ETL-9351 Photomultiplier Tubes[193].*

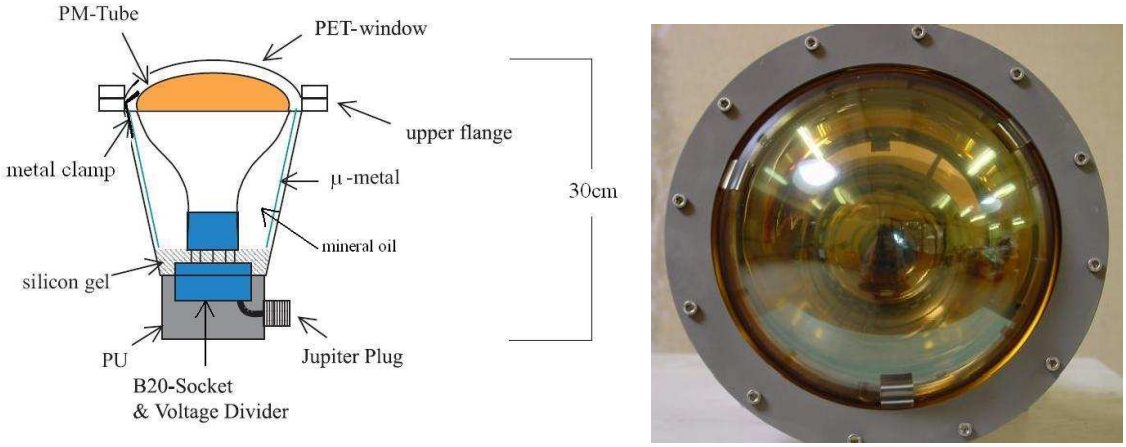

Fig. 3.6: *Sketch of the encapsulation of the outer detector PMTs (left) and a front picture of an encapsulated PMT (right).*

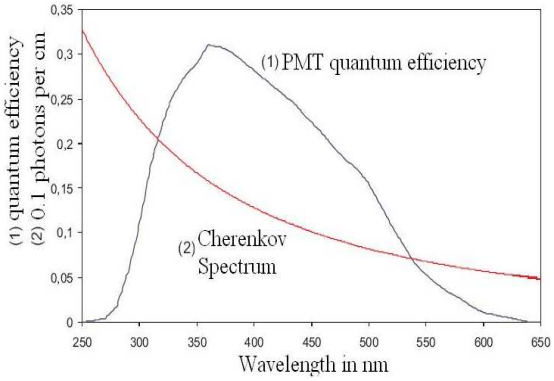

Fig. 3.7: *PMT quantum efficiency vs. Čerenkov light emission spectrum.*

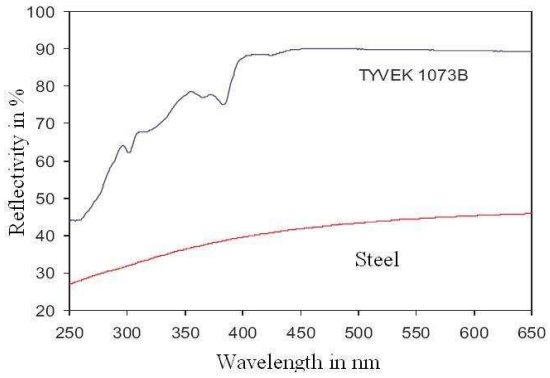

Fig. 3.8: *Tyvek reflectivity as a function of wavelength compared to steel surface.*

Fig. 3.9: *Pictures of the water tank: upper (left) and lower (right) outer detector segments are covered with Tyvek sheets. The walking grid will also be covered before WT closure.*

3.3.2 The Tyvek Reflector

In order to increase the amount of actually detected light, the steel surfaces of the SSS and of the Water Tank are covered with Tyvek sheets[2].

Tyvek is a white paper-like material, about $\sim 200\mu m$ thick, made of pressed polyethylene fibers that shows a highly enhanced reflectivity compared to steel. Integrating the two curves in fig. 3.8 over the PMT quantum efficiency, the effective reflectivity for steel and Tyvek can be obtained:

$$R_{eff}^{\mathrm{STEEL}} \sim 38\% \qquad \Longrightarrow \qquad R_{eff}^{\mathrm{TYVEK}} = 79.5\%$$

[2]To be precise only about 95% of the surface could be covered, due to the presence of cables and pipes.

Ring	Position	# PMTs
+6	SSS-NE	4
+5	SSS-NE	12
+4	SSS-NE	17
+3	SSS-NE	21
+2	SSS-NE	24
+1	SSS-NE	26
-1	SSS-SE	26
-2	SSS-SE	24
-3	45°-slope	20
-4	WT-floor	14
-5	WT-floor	10
-6	WT-floor	6
-7	WT-floor	4

Tab. 3.3: *Outer Detector PMT layout.*

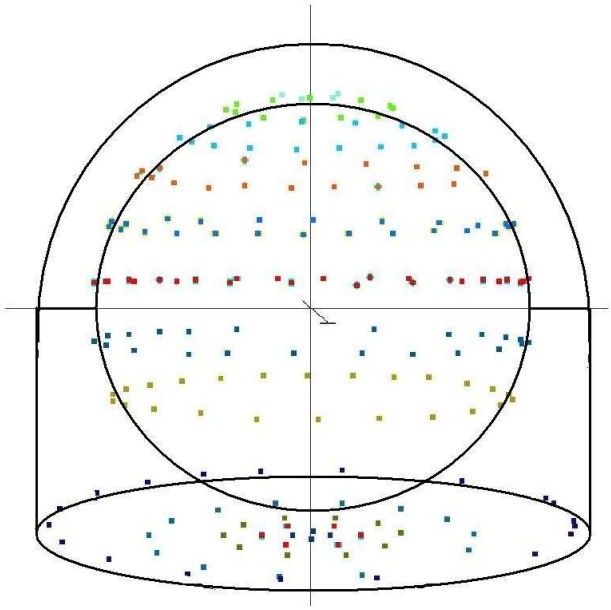

Fig. 3.10: *The layout of the Outer detector PMTs as represented in the official GEANT4 simulation package[241].*

3.3.3 The layout

The original detector's layout was featuring all the 208 PMTs disposed in 12 horizontal rings on the outer SSS surface, every PMT looking radially outward. In this way the $590m^2$ surface of the SSS was populated by one PMT every $2.8m^2$ ($1.7m$ linear average distance) and, according to simulations, the detection efficiency was met.

Though not required for the ^7Be primary physics goal of BOREXino, the possibility to reconstruct the track of the through-going muon would be of fundamental help in the reduction of ^{11}C background for *pep* and CNO measurements, as discussed in chap. 10.

This ambitious goal requires the detection of direct light as far as possible, reflected light being of hinder in this respect. In the original design, only northern hemisphere PMTs were seeing direct light, while the downward looking PMTs on the lower hemisphere were sensitive to reflected light only.

In 2002 a modification to the outer detector design was proposed to the collaboration and received the general approval. The lowest half of the lower hemisphere PMTs was re-positioned on the water tank floor looking upward in four concentric rings plus one ring situated on the "slope". This is a structural feature of the water tank: along the base circle, the volume up to a height of $\sim 1m$ and degrading inward for about the same length is massive steel for engineering reasons. This offers a surface with a $\sim 45°$ inclination, where installed PMTs look roughly toward the SSS.

For the new design, the number of PMTs installed in the now 13 rings is listed in tab. 3.3.

The simulation was run again with the new configuration and showed no appreciable

difference in the muon detection efficiency[241]. Moreover the simulation showed that in average the rearranged PMTs see about twice as much light and mostly unreflected photons. So this re-allocation allows the development of a tracking algorithm without worsening the tagging performance.

3.4 Measuring the PMTs positions.

Shortly after the installation was completed, a topographical survey was performed during which the position of the installed PMTs was determined.

3.4.1 The requirements

The Outer Detector PMTs are fixed to the surface by pairs of studs gun-welded into steel in positions that to a first approximation are evenly spread. However, large areas on the SSS surface are covered with bunches of PMT cables[3] and other equipment (optical fibers, pipes, the calibration sources insertion system, ...), therefore the actual positions depend on the space availability to weld the studs and can be distant from nominal positions up to a few tens of centimeters.

Though this indetermination wouldn't have affected the veto tagging capabilities of the detector, the goal of performing also a reliable muon track reconstruction required PMT positions to be known better. A measurement was therefore required.

The aimed precision was to be negligible in comparison to irreducible indeterminations of the hit space-time location capability of the detector:

- The time resolution of the electronics processing the PMT signal (sec. 4.3) is about $1ns$, enough for the light to travel $\sim 22cm$ in water.
- The photocathode diameter is $\sim 20cm$.

Consequently the goal was set to $\pm 2cm$.

3.4.2 The Topographical Survey

The survey was performed with the collaboration of two professional topographers[194]. The instrument used was a Leica TCR 705 total laser station (fig. 3.11) able to measure angles with a resolution of $5''$ and distances down to $2mm + 2ppm$.

The measurement required all PMTs to be visible from one or more "stations", i.e. positions of the instrument linked in a reference net. Length and angle of every connecting segment was measured twice with the instrument at the one end and a reflecting prism at the other one and in the opposite configuration.

A three level reference net was built (fig. 3.12):

- 9 base stations in a circle on the floor of the water tank.

[3]The Suhner submarine cable used is about $1.5cm$ in diameter and rather inflexible, therefore a bunch of cables with both ends connected constitutes a pretty fixed obstacle. About 2400 cables for inner and outer detector are laid on the sphere under the tyvek sheets.

Fig. 3.11: *Leica TCR 705.*

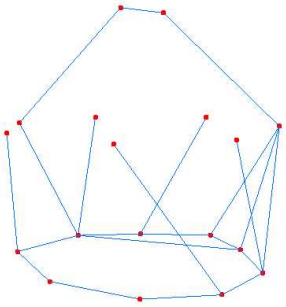

Fig. 3.12: *The reference net: 9+7+2 stations.*

Fig. 3.13: *Topographic survey: one of the stations on top of the SSS.*

- 7 out-stretches on the equatorial grid (1^{st} level)
- 2 out-stretches on top of the SSS (2^{nd} level), on opposite sides of the large north-pole flange (fig. 3.13).

For every PMT it was attempted to measure three of the nuts of the top flange of the encapsulation (fig. 3.6) and later obtain the center of the circle by software interpolation. This worked well in most of the cases but not in all, due to visibility problems given by the legs of the SSS or other material:

- 196 PMTs were measured by three nuts yielding $\pm 1cm$ precision .
- 2 PMTs were visible only by the tip of the fiber holder: $\pm 8cm$ precision .
- 2 PMTs were visible by just one of the nuts on the flange: $\pm 12cm$ precision.
- 8 PMTs could not be seen at all. Their positions were later interpolated on the circles fitting the other PMTs in the same ring. About $10 - 50cm$ indetermination is left depending on the ring.

3.4.3 SSS Reference Frame

The BOREXino reference frame has origin in the center of the sphere and x-axis heading north, opposite to the SSS door, along one of the main welding lines. In order to translate the measured positions into this system, about 350 points on the SSS surface were measured, some of which along the x-axis welding (fig. 3.14). The points on the upper and lower hemisphere were fit with two independent hemispherical functions whose results are reported in tab. 3.4.

	Stat	x	y	z	r	dev
North	98pts	12.333m	-3.180m	7.804m	6.856m	1.79cm
South	247pts	12.345m	-3193m	7.879m	8.866m	1.23cm
Δ		1.2cm	1.3cm	7.5cm	1.0cm	

Tab. 3.4: *Results of the two hemispherical fits on the SSS. The x and y are referred to the arbitrary frame of the laser station, z is instead referred to the water tank floor.*

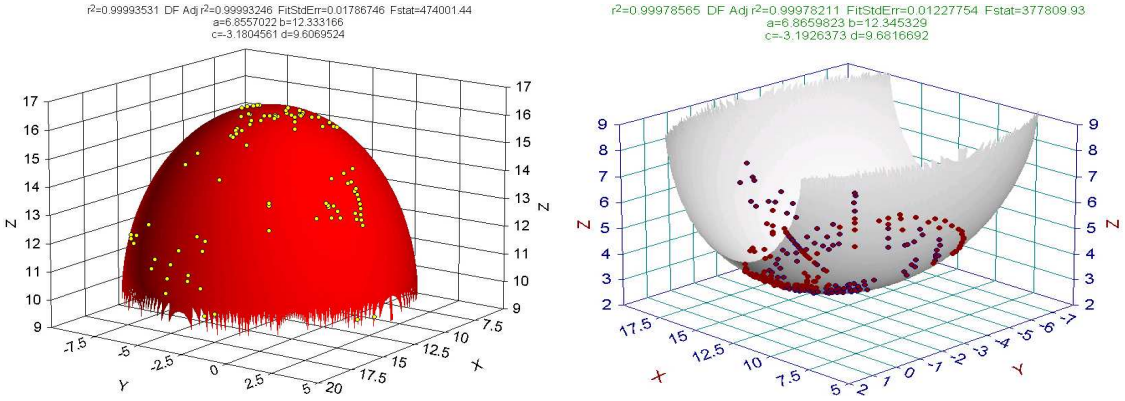

Fig. 3.14: *Fit of the dots taken on the SSS: north hemisphere (left) and south hemisphere (right).*

As it can be seen the average deviation of the points from the interpolating surface (last column) in both cases is very small. The agreement of the x and y coordinate of the center is very good and so is the radius to be compared with a nominal value of $6.860m$. This is the first time the sphericity of the SSS is measured and is indicating an excellent construction and assembly work.

The agreement of the z coordinate of the center is instead rather poor indicating that a problem may have occurred in one of the two measurements. Instead of averaging the two values, the Southern fit was chosen for two reasons:

1. The points could be taken only in areas where the surface of the sphere was not covered by tyvek or cables. In the souther hemisphere these areas were more spread out than in the northern hemisphere where the points had to be taken relatively close to each other.

2. The nominal position of the center is $7.862m$.

The measured positions have been inserted in the database collection (sec. 5.6)[4].

[4]Database `bx_geometry`, table `MuonHolesMapping`

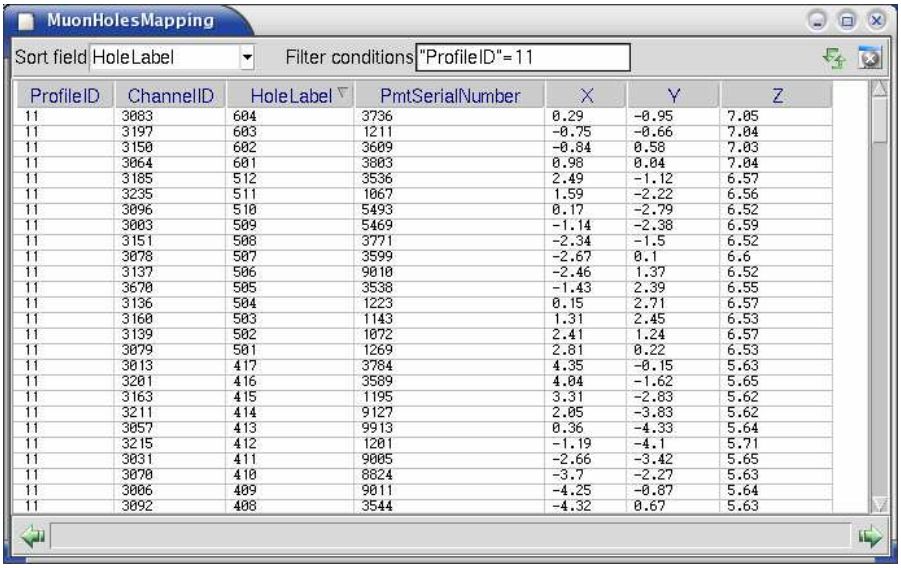

MuonHolesMapping

Sort field HoleLabel Filter conditions "ProfileID"=11

ProfileID	ChannelID	HoleLabel	PmtSerialNumber	X	Y	Z
11	3083	604	3736	0.29	-0.95	7.05
11	3197	603	1211	-0.75	-0.66	7.04
11	3150	602	3609	-0.84	0.58	7.03
11	3064	601	3803	0.98	0.04	7.04
11	3185	512	3536	2.49	-1.12	6.57
11	3235	511	1067	1.59	-2.22	6.56
11	3096	510	5493	0.17	-2.79	6.52
11	3003	509	5469	-1.14	-2.38	6.59
11	3151	508	3771	-2.34	-1.5	6.52
11	3078	507	3599	-2.67	0.1	6.6
11	3137	506	9010	-2.46	1.37	6.52
11	3670	505	3538	-1.43	2.39	6.55
11	3136	504	1223	0.15	2.71	6.57
11	3160	503	1143	1.31	2.45	6.53
11	3139	502	1072	2.41	1.24	6.57
11	3079	501	1269	2.81	0.22	6.53
11	3013	417	3784	4.35	-0.15	5.63
11	3201	416	3589	4.04	-1.62	5.65
11	3163	415	1195	3.31	-2.83	5.62
11	3211	414	9127	2.05	-3.83	5.62
11	3057	413	9913	0.36	-4.33	5.64
11	3215	412	1201	-1.19	-4.1	5.71
11	3031	411	9005	-2.66	-3.42	5.65
11	3070	410	8824	-3.7	-2.27	5.63
11	3006	409	9011	-4.25	-0.87	5.64
11	3092	408	3544	-4.32	0.67	5.63

Fig. 3.15: *The topographical survey results in the* `bx_geometry` *database.*

Chapter 4

Electronics

The electronics of the BOREXino detector is housed in a dedicated room at the second floor of the building named *Big Building West* (fig. 2.6). Here in fact arrive[1] the submarine cables connected to inner and outer detector PMTs along which high voltage and signal travel.

The ID and OD electronics are two independent systems with two different designs, that reflect the signal processing needs of the two detectors. A complex trigger system takes care of the integration.

The ID PMTs also provide signal to the additional waveform digitizers (*Flash ADC*), which under some respect also constitutes an independent subsystem.

A general scheme of the electronic setup is shown in fig. 4.1.

In this chapter a complete description of the BOREXino electronics is given. However the OD front end and digital electronics as well as the OD trigger system are covered in more details.

4.1 High Voltage Power Supply

All BOREXino PMTs are operated at the nominal gain of 10^7. Operative voltages for this gain have been measured in dark room tests before the installation of the PMTs in the detector. They span from $\sim 1150V$ up to $\sim 1750V$ and the current drawn is in average $\sim 100\mu A/channel$.

To supply this power we use 15 CAEN SY527 mainframes, 14 for ID and 1 for OD. Control over these units can proceed in three ways:

1. Manually through the key-pad and the LCD display located on the front panel.
2. Locally through an alphanumeric terminal (e.g. a VT100) connected to a proper RS232c connector.
3. Remotely through a proprietary serial bus, named CAENet, mastered by a PC card and therefore fully software programmable.

[1] The extra length of the cables is rolled up in the so-called *cable tower* on the roof of the building. The cables enter then the electronic room from special openings in the ceiling.

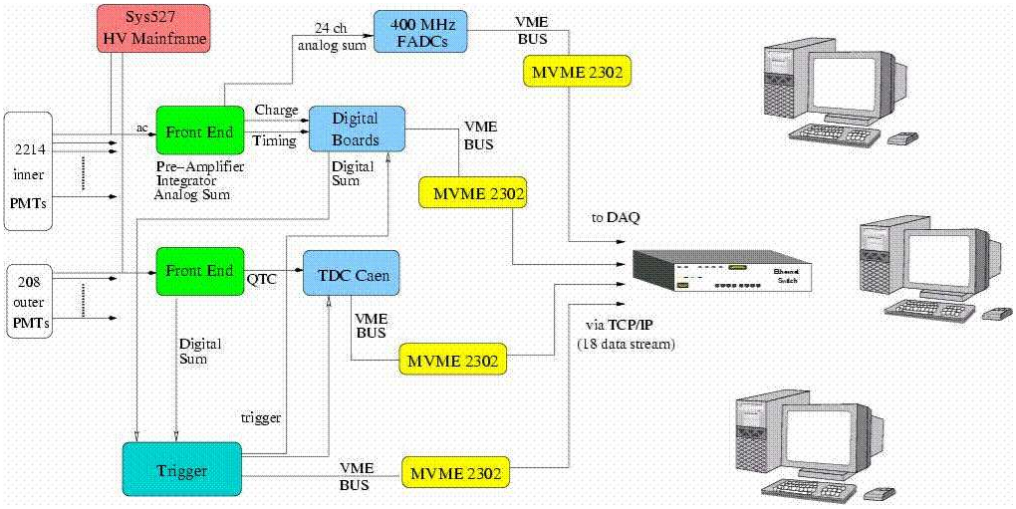

Fig. 4.1: *Simplified schematics of the BOREXino Electronics.*

Fig. 4.2: *CAEN SY527 Mainframe. Front View (left) and rear view (right), where seven A932AP boards are visible.*

While the second possibility has been often useful during tests and air runs (chap. 6), for the data taking phase the third option is the default access mode, over which the *slow control* system is implemented (sec. 5.7).

The HV boards, housed in the mainframes, are CAEN A932AP units, with 24 channels each and a maximum output of $2500V$. ID mainframes are equipped with 7 boards each, the OD one with 9.

The limitation of this unit is that the individual channels are derived from a master channel and are kept within $900V$ from its value. It is a hardware feature and holds regardless of the voltage setting and even for turned off channels. This doesn't allow too much flexibility in use, especially during tests.

Moreover the current threshold and the consequent trip condition (automatic turn off) belong to master channels only. This implies that a PMT showing a pathological behavior and drawing excessive current turns off the full board it belongs too. At this

point a manual intervention is required to check the 24 channels individually, find the responsible, disconnect it and finally restart the board.

Two multi-wire cables per board bring HV to the decoupling stage of the front-end electronics (sec. 4.2.2 for ID and sec. 4.3.2 for OD). These cables include safety pins that disable HV output when not connected.

4.2 Inner Detector electronics

The ID electronics is housed in 14 identical racks (fig. 4.3). Every rack has 168 channels and accepts 160 PMT signals, 8 channels being spare.

The PMT cable is connected to a front-end channel that decouples it from HV and extracts a fast linear signal for timing purposes and an integrated signal for charge evaluation. The two signals reach then the digital part of the chain where they are acquired. Here the coincidence condition is also evaluated and sent to trigger for eventual trigger formation. Whenever a trigger is received back the digital memory is read and sent to DAQ system.

Within a rack the following components can be identified (from top to bottom):

- the *Patch Panel* (PP) on the top accepting the dry end of PMT cables.
- the calibration signal fan-out (sec. 4.4.5).
- the *Low Voltage* (LV) power supply for the front-end crate.
- the adder board (sec. 4.6) with the scaler module mounted on its front (sec. 4.7).
- the front-end crate (sec. 4.2.2).
- the VME crate with the digital electronics (*Laben* boards) and the *PowerPC* (PPC).
- the HV mainframe (sec. 4.1).

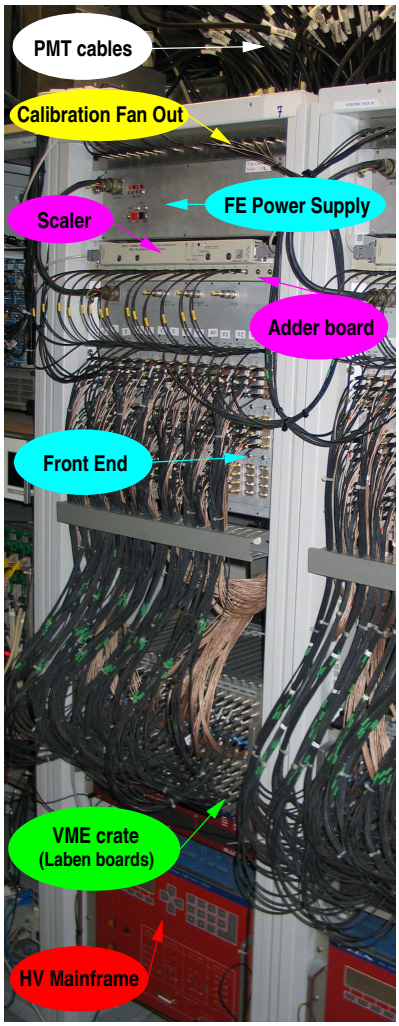

Fig. 4.3: *One of the 14 ID racks.*

4.2.1 Acquired signal

The BOREXino PMTs are AC coupled, i.e. the signal and the HV travel along the same cable. After the necessary decoupling stage, the negative signal has therefore a bipolar shape with a positive overshoot and a null area. The overshoot is however very small

Single Photo-Electron Signal	
Amplitude	$-12mV$
FWHM	$5ns$
Rise time	$4ns$
Fall time	$10ns$
Charge	$1.6pC$

Tab. 4.1: *Single Photo-Electron characteristics for PMT ETL-9351.*

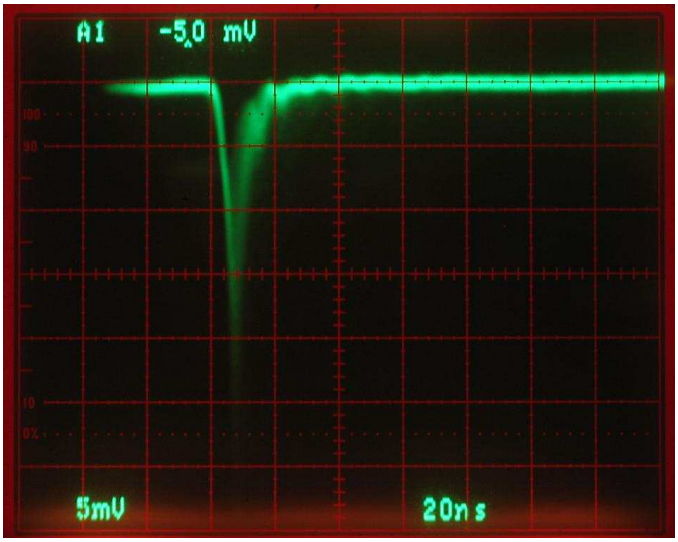

Fig. 4.4: *PMT signal as seen on the analog oscilloscope.*

and long ($\sim ms$) and its interference in the signal processing can be easily kept to a minimum.

The PMT operating voltage is regulated in order to obtain a gain of $\sim 10^7$. In this condition the Single Photo-Electron signal has the characteristics listed in tab. 4.1 and the shape visible in fig. 4.4.

In case of a $1MeV$ event at the center of the detector, the probability of multiple photo-electrons originating within the same PMT is below 10%. This number scales with the energy of the event and increases with the radial distance as the solid angle seen by PMTs closer to the event will increase in that case. In other words, within the ^7Be energy window ($250keV - 800keV$) and applying a radial cut, the number of hit channels can give, within a first approximation, the energy of the event. A precise energy evaluation should instead take into account the charge seen by the single channel and the design of the electronics, of course, ensures this possibility.

4.2.2 Front-end electronics

The 14 front-end crates house 14 boards each. A front-end board features 12 electronic channels.

The front-end electronics should:

1. connect the HV provided by the mainframe to the the coaxial cables reaching the PMTs.

2. decouple the signal from HV traveling along the same cable, providing optimal impedance matching (50Ω) and noise filtering along a wide frequency range.

3. provide a fast amplified signal for every channel for timing purposes.

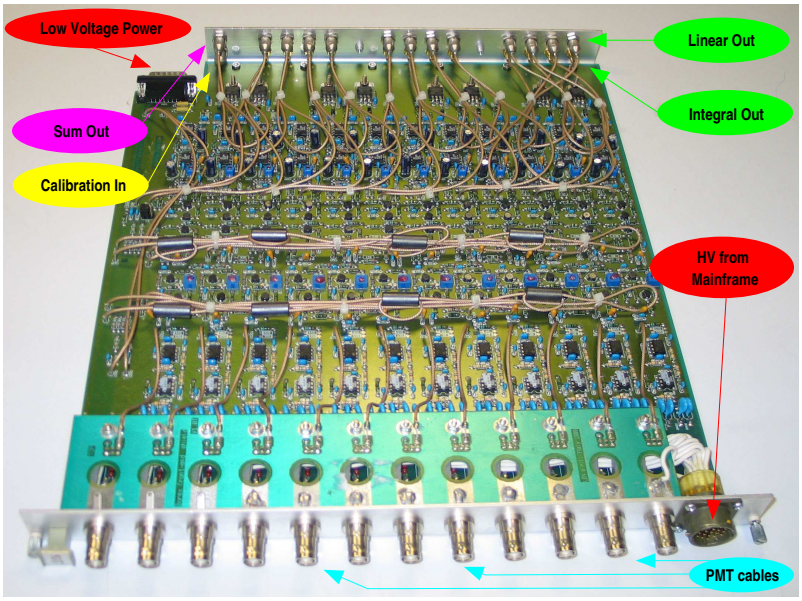

Fig. 4.5: *One of the ID front-end board. The front of the module is on top.*

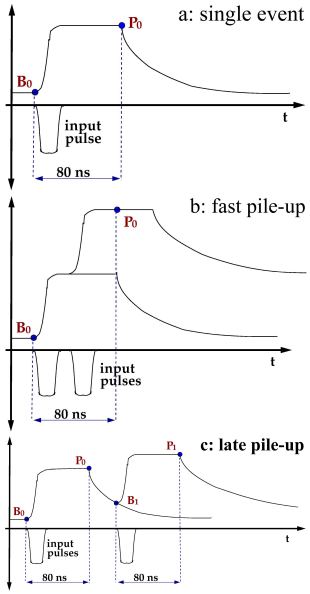

Fig. 4.6: *Gate-less charge integrator.*

4. provide an integrated signal for every channel for charge evaluation.

5. distribute in parallel to all channels an incoming calibration signal.

6. build the analog sum signal of all channels.

The coaxial cables screwed on the patch panel are prolonged inside the rack with junction cables (SHV, $2m$) reaching the back of the front-end boards (fig. 4.5). The HV power from the mainframe also reaches the back of the front-end board on a 12-wire cable[2]. Single channel linear and integrated outputs are instead on the front panel as well as the calibration input and the analog sum output.

The timing signal is simply an inverted and ~ 20 times amplified copy of the PMT signal. The integrated signal is instead built with the principle of the gate-less integrator depicted in fig. 4.6.

A zero dead time device is implemented, which keeps the full charge plateau for $T = 80ns$ and then starts an exponential decay with $\tau = 500ns$ constant. The digital electronics (sec. 4.2.3) samples this signal twice (points B_0 and P_0 in fig. 4.6(a)), with the charge corresponding to the samples difference. This filters any offset along with all possible baseline drifts and low frequency noise.

In case of piled-up events with time distance $\Delta t < 80ns$, the double sampling methods keeps working fine as it can be noted in fig. 4.6(b), while for piled-up events with $\Delta t > 80ns$, a software correction must be applied to the second hit charge which becomes:

$$Q_1 = (P_1 - B_1) - Q_0 \cdot e^{-\frac{\Delta t}{\tau}} \left[1 - e^{\frac{T}{\tau}}\right] \tag{4.1}$$

[2]One HV distributor serves two front-end boards.

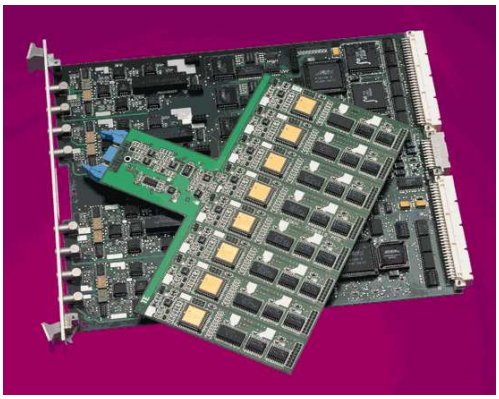

Fig. 4.7 (a): *ID Laben digital boards.*

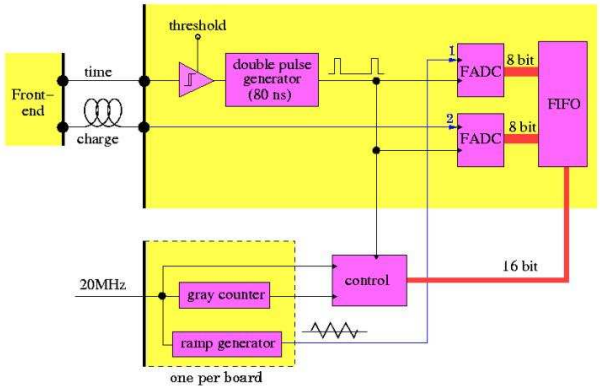

Fig. 4.7 (b): *Laben channel acquisition block.*

The bipolar shape of the PMT signal actually disturbs slightly the charge evaluation (i.e. the flat top is not entirely flat), but as the undershoot time constant is much longer than T, the effect is small.

4.2.3 Digital electronics

The goal of the digital electronics is to digitize time and charge information for every PMT signal and to provide information to the trigger system (sec. 4.4.1) on the number of channels firing in coincidence.

In every VME crate are housed 20 boards, each one processing 8 channels (fig. 4.7(a)). These boards were developed in collaboration with the *Laben S.p.A.* company.

Each channel functional block (fig. 4.7(b)) receives the linear amplified pulse and the integrated pulse from a front-end channel. The acquisition occurs continuously and asynchronously from any possible trigger formation.

The linear signal is fed to a programmable *dual threshold* discriminator, whose *high* and *low* thresholds are set to $50mV$ and $20mV$ respectively. These values correspond to 0.25 and 0.1 of the average (amplified) *Single Photo-Electron* (SPE) signal. In the SPE) spectrum (fig. 6.13(a)), *high* threshold corresponds to the valley between the exponential and the Gaussian components. The discriminator fires if the signal crosses the *high* threshold, but the *time pick-off* is done in relation to the *low* threshold. In this way the dark noise component under the exponential is filtered out and at the same time the *amplitude walk* is kept small.

When the discriminator fires it latches the content of a 16-bit counter (named *Gray counter*), driven by a $20MHz$ external clock (sec. 4.4.2). This provides the coarse time information ($50ns$ resolution).

The discriminator also determines the issuing of two logic pulses $30ns$ wide and $80ns$ apart that are used to gate twice two identical 8-bit ADCs:

1. The first ADC samples a $10MHz$ *Triangular WaveForm* (TWF) generated syn-

chronously with the $20MHz$ clock. This provides the fine time to be added to the coarse one mentioned above. The second sample is useful to resolve ambiguities arising when the first one is close to a spike of the waveform. The time reconstruction mechanism (sec. 6.3.1) has a nominal resolution of $50ns/255 \sim 200ps$.

2. The second ADC samples *base* and *peak* of the integrated input digitizing in this way the charge information.

To allow time for the acquisition, the discriminator is disabled for the $140ns$ following the high threshold crossing.

A pulse arriving later than $140ns$ after a previous one is instead acquired as a different hit, whose charge will be software re-corrected according to eq. 4.1 (sec. 7.4.2).

The dead time of the system is limited to the interval between $80ns$ and $140ns$, which for a typical physics event of BOREXino translates only to a few percent overall dead time.

Finally the discriminator output fires the board coincidence unit (not shown) which provides the number of channels fired in the board in an adjustable time window of $50ns$ for triggering purposes (sec. 4.4.1).

Data from the two ADCs and from the the gray counter are stored locally on a memory queue (FIFO). Since the memory is handled circularly with a $6\mu s$ depth, data older than this time are overwritten in absence of triggers. Whenever a trigger is received, the board DSP (*Digital Signal Processor*) receives an interrupt on a dedicated VME line and a 16-bit pattern that identifies the event. The latter is copied by the DSP, together with all data present in the channel FIFOs, to a $2KB$ dual-port RAM[3]. This process requires as much as $80\mu s$, so in order not to be blind to faster event coincidences during this time, the DSP is able to accept and queue a second interrupt to be processed thereafter. However in this case a BUSY flag is risen and no further trigger can be accepted by the board until data processing is complete.

After processing of an event is complete, the condition is signaled by the DSP to the PPC, which proceeds to read out the data through the VME bus (sec. 5.2) from the dual-port RAM, while the board is immediately ready to accept the following trigger.

4.3 Outer Detector electronics

The OD electronics is housed in two racks, the *blue* one and the *orange* one, named after their outer colors (fig. 4.8).

The 208 PMT cables from WT arrive on the blue rack, where the signals are decoupled from HV before being moved on to the orange rack. Here front-end QTC boards produce a logic signal whose length is proportional to the charge and send it to TDCs for digitization. A *Muon Trigger Board* (MTB) evaluates the signal coincidence producing eventual muon triggers.

The blue crate houses, from top to bottom:

[3] A memory register that can be read and written at the same time, though obviously not the same chunk.

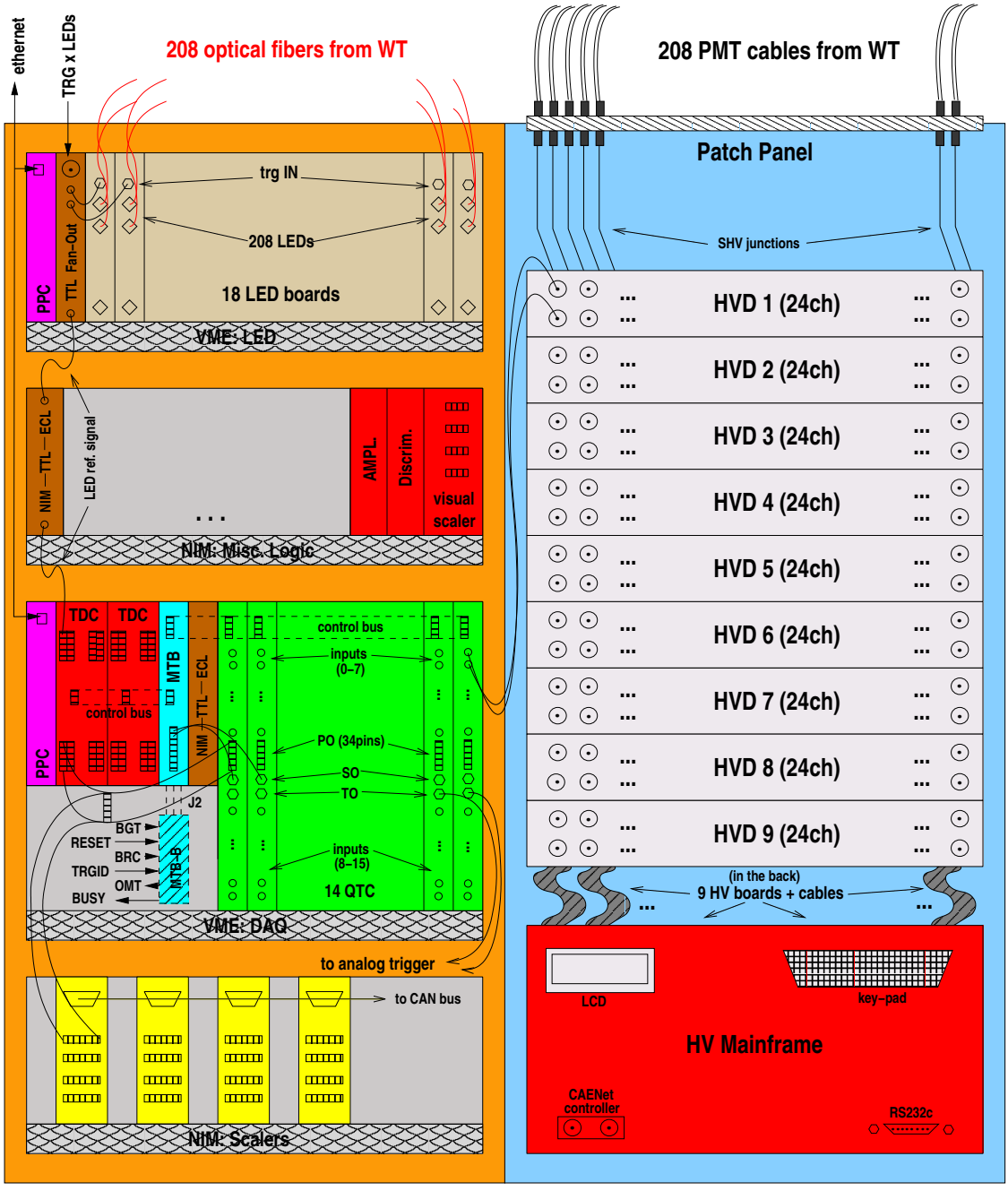

Fig. 4.8: *The two OD electronic racks.*

- the *Patch Panel* (on the top).
- 9 *High Voltage Decouplers* (HVD).
- the High Voltage mainframe.

Junction cables (SHV, $2m$) inside the rack connect the Patch Panel and the HVD.

The orange crate houses, from top to bottom:

- the calibration LEDs crate (VME).
- a multi-purpose NIM crate.
- the main DAQ crate (VME) with (right to left):
  - 14 QTC (*Charge-to-Time Converter*) boards.
  - a NIM-TTL-ECL logic translator.
  - the *Muon Trigger Board* (MTB).
  - 2 TDC (*Time-to-Digital Converter*) boards.
  - the PowerPC (PPC).
- the scalers NIM crate (sec. 4.7).

4.3.1 Acquired signal

The OD PMTs are operated in the same way as the ID devices, so the SPE signal looks pretty much the same to the one illustrated in sec. 4.2.1.

The difference arises in the hit multiplicity, that a Čerenkov muon detector can easily reach $100pe$ for PMTs seeing the direct light cone. ID electronics saturates at $\sim 6.5pe$ and would therefore not suit the OD needs. A different system was designed to ensure a much wider dynamic range, without sacrificing too much the resolution on the SPE signal.

4.3.2 Front-end electronics (QTCs)

The high voltage decoupling is performed externally. Custom decoupling boxes (HVDs) have been developed to accomplish this task. These are passive units with 24 channels each.

The front-end electronics of the OD is made of 14 *Charge-to-Time Converters* (QTCs). These are custom boards whose design was initiated at the Princeton University within our collaboration and later transferred here at TUM, where essential improvements have been made during the last prototyping phase before the serial production was carried out.

The board (fig. 4.9) is a 9U single VME unit which takes only power from the VME backplane with no connection to the data-way bus. One QTC board is made of 16 channels, though the first one (#0) is actually not used to process a PMT signal as it will be explained below.

The board has three outputs:

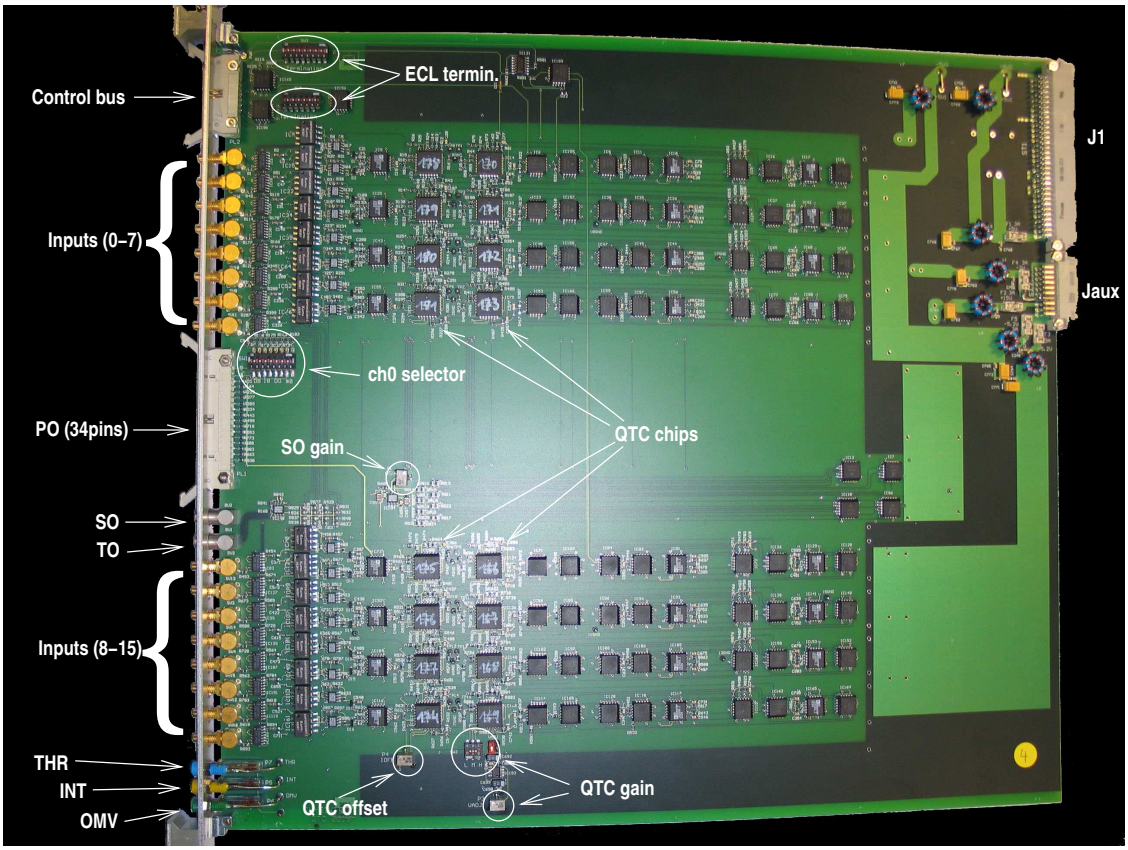

Fig. 4.9: *One of the 14 OD QTC boards.*

Primary Output (PO). This is a logic (differential ECL) signal which is basically the output of the QTC chip. Since the first edge gives also the time of the input pulse, the digitization of the two edges of this signal allows to infer both time and charge of the PMT pulse. PO of the 16 channels are grouped in the 34-pin[4] connector visible at the center of front panel.

Secondary Output (SO). This is a one-per-board logic step function pulse whose height, in steps, represents the number of channels firing in coincidence. Both height and width of the steps can be adjusted. The width defines the coincidence window. These outputs are sent to the MTB for the Outer Muon Trigger (OMT) formation (sec. 4.4.6).

Tertiary Output (TO). This is a one-per-board analog pulse given by the sum of the input signals with a built-in fixed amplification factor of about 2. These outputs are sent to the additional analog trigger formation system (sec. 4.4.6).

[4]A differential ECL signal travels on two wires: in absence of signal the "positive" (+) wire is kept at HIGH level ($-0.8V$) and the "negative" (−) wire is kept at LOW level ($-1.6V$). A signal is defined as a switch of the two levels. In the PO connector: 2 wires x 16 channels + 2 grounds = 34-pin.

In the QTC front panel the following connectors are found (from top to bottom):

1. Control bus input. 14-pin flat cable connector.
2. Channel input: 0-7. 8 SMB golden plated connectors.
3. PO. 34-pin flat cable connector.
4. SO. LEMO connector.
5. TO. LEMO connector.
6. Channel input: 8-15. 8 SMB golden plated connectors.
7. Three potentiometers with relative sampling points:
   (a) THR. Channels threshold.
   (b) INT. Channels integration gate.
   (c) OMV. SO steps width, i.e. OMV coincidence window.

Channel layout

Two concepts are used in this section:

1. a *bussed line* is an analog level set by trimmer (on front panel or internal) and distributed to all channel blocks.
2. a *control line* is a logic state set through the control bus (through software) and distributed to all channel blocks.

The channel block drawing is shown in fig. 4.10.

The input signal is received by buffer amplifier which merely performs impedance matching. Thereafter the signal is split in three paths with individual feedback operational amplifiers that reach:

1. the TO board summing block (amplif.: $\times 6$)
2. the QTC chip input (amplif.: $\times 5$)
3. the threshold comparator (amplif.: $\times 11$)

The tertiary output is totally analogic and is therefore always active. With this exception, the channel fires whenever the comparator fires, i.e. when the signal crosses the bussed line THRESHOLD (THR front panel trimmer). An optimized threshold value was found during air runs: $-20mV$ corresponding to $0.2pe$ against the $\times 11$ amplified copy of the input signal. Lower values make most channels trigger on noise at a non negligible rate, while higher values start to distort the SPE charge spectrum. The output of the comparator is ANDed with the control line RUN whose absence inhibits therefore the board functionality (at least the ones that depend on input).

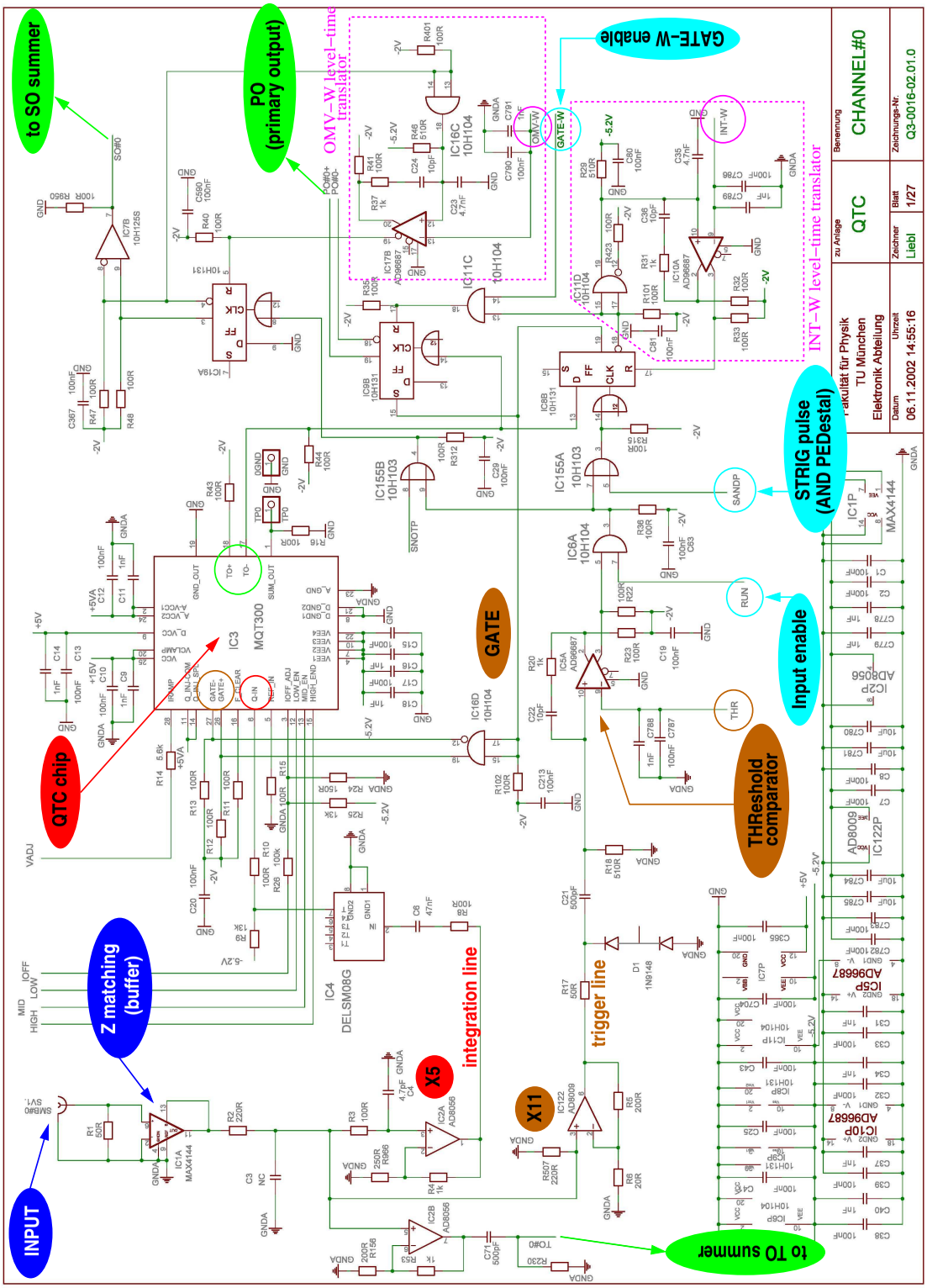

Fig. 4.10: *Layout of the QTC channel acquisition block.*

The logic pulse is split in two copies named *Primary Logic Pulse* (PLP) and *Secondary Logic Pulse* (SLP). They are ORed respectively with the SANDP and SNOTP control lines that allow to emulate either pulse for debugging and calibration purposes.

The heart of the channel block is the QTC chip LeCroy MQT300. The PLP clocks a flip-flop, whose output gates the QTC chip. The integration gate Δt is provided by the bussed line INT-WIDTH (INT front panel trimmer) and can be adjusted in the $60-150ns$ range. The voltage level is converted in time through a classical scheme composed with a comparator and a capacitor. The capacitor, charged in absence of signal, keeps the positive input of the comparator below the negative one, which is connected to the bussed line, yielding no output. The signal opening the gate for the QTC chip also determines the start of the capacitor discharge process. After a time Δt the positive comparator input will finally exceed its counterpart, inverting the output and resetting the flip-flop producing the gate. In a linear approximation of the exponential capacitor discharge law, the time Δt is proportional to the bussed line level.

The chip integrates the input pulse together with V_0, its offset (or *pedestal*), issuing a logic pulse whose length is given by:

$$\mathrm{PO} \propto V_0 \cdot \Delta t + \int_{\Delta t} S(t)dt \qquad \Rightarrow \qquad \mathrm{PO} = P + G \cdot Q \tag{4.2}$$

where P is the pedestal length[5] in ns and G is the channel gain in ns/pC. G can be adjusted in $[10, 60]ns/pC$ through the bussed line VADJ (internal potentiometer). We currently use the lowest possible gain that ensures a dynamic range up to $200pe$, though it is planned to increase this value to better exploit the resolution at SPE. Similarly the bussed line IOFF, allows to tune the pedestals.

The output of the chip disables the flip-flop generating the gate (as the chip is busy) and clocks another flip-flop whose output is directly connected to the PO board connector.

This flip flop can be reset also by the end of gate condition if the control line GATE-WIDTH is enabled (it is ANDed to the flip flop reset input). This operation mode is used to measure the integration gates.

It is possible to gate all QTC chips in absence of input signal. In this way the pedestal only is issued and can be measured. This is done through the control bus SANDP mentioned above which emulates the PLP. The operation is performed at the beginning of every run and constitutes the main precalibration task of the OD veto electronics (sec. 7.4.1). The measured pedestals are then subtracted at reconstruction level from the raw charge information (sec. 7.4.2).

The SLP also clocks a flip-flop which generates an output for the SO board summing block. The reset to this flip-flop, determining the end of the output, is provided by the OMV-WIDTH bussed line (front panel trimmer) after a level-to-time conversion identical to the one described above for INT-WIDTH. In this way the width of the steps in the SO step function can be adjusted. A typical value is $\sim 150ns$.

Common blocks

The QTC board common blocks drawing is shown in fig. 4.11.

[5] Corresponds to the chip output when gated without a pulse on the input.

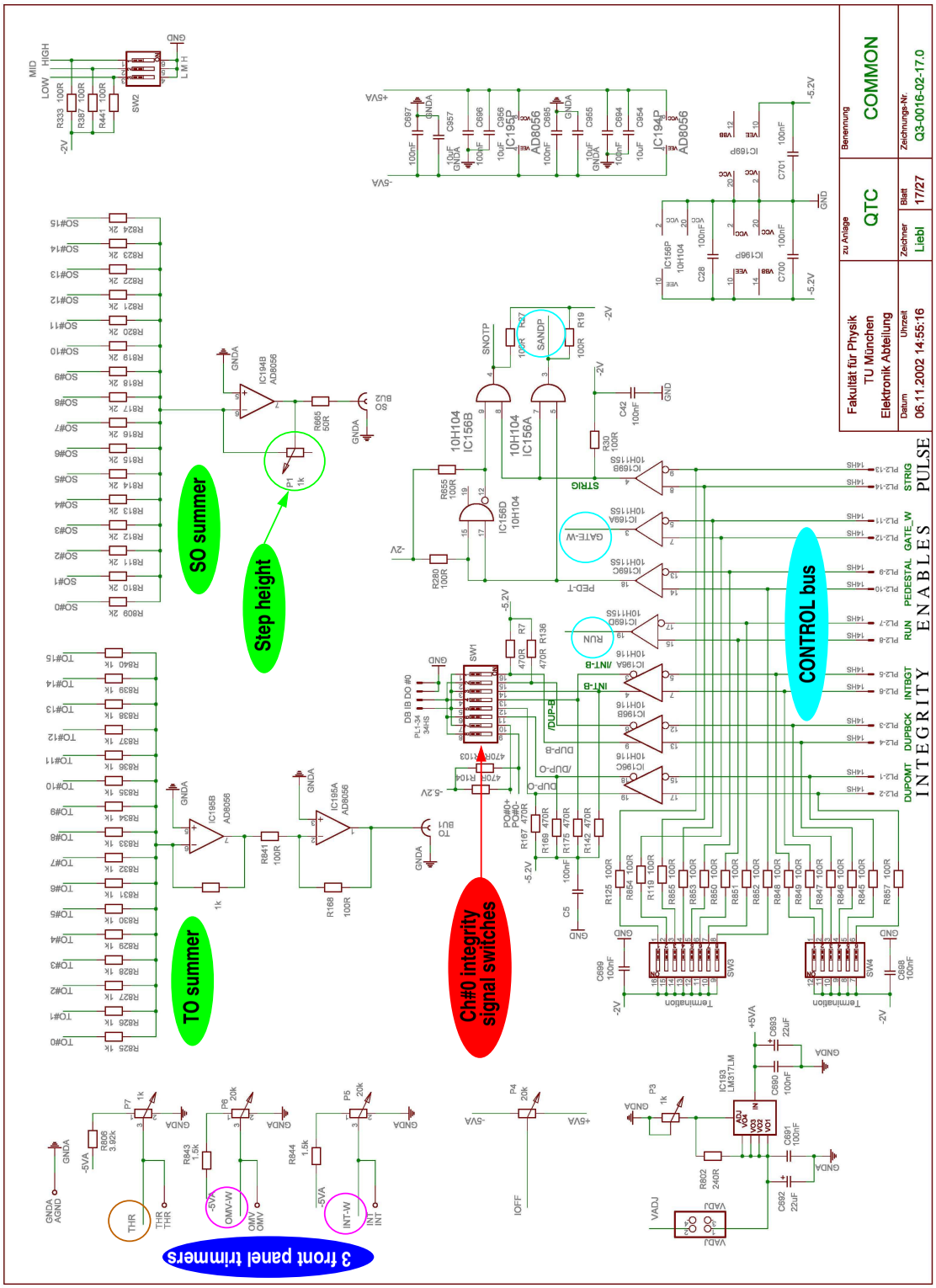

Fig. 4.11: *Layout of the QTC common block.*

The main board common block is the control bus. The QTC boards are daisy chained with a single 14-pins flat cable which plugs in all the connectors at the top of the QTC front panels. The MTB is the bus master and issues control commands along these 7 differential-ECL lines. The last QTC board in the chain provides the required 110Ω termination (jumper enabled). The behavior of the MTB in this respect is fully programmable through the PPC.

The 7 control bus lines are:

1. RUN (level). Enable for the channel input receiving sub-block which includes the threshold comparator.

2. PEDESTAL (level). It determines the SANDP control line to be pulsed in coincidence with a pulse on the STRIG line (see below). In absence of this level the SNOTP is pulsed in this case.

3. GATE-WIDTH (level). Enable that forces the primary output to close at gate closure ignoring the QTC chip output.

4. STRIG (pulse). A pulsed line that is used to emulate the PLP or the SLP signals described above on all channels. Which of the two occurs is determined by the state of the PEDESTAL line.

5. DUPOMT (pulse). Copy of the OMT (*Outer Muon Trigger*) generated by the MTB.

6. DUPBRC (pulse). Copy of the BRC (*Borexino Reference Clock*) forwarded by the MTB.

7. INTBGT (pulse). Copy of the BGT (*Borexino General Trigger*) forwarded by the MTB.

.

The first four lines determine the behavior of the board. Four possibilities are available:

1. Normal run. In normal run condition only the line RUN is set.

2. Pedestal issuing. PEDESTAL is set and STRIG is pulsed externally. This is the precalibration state.

3. Gate width issuing. GATE-WIDTH and PEDESTAL are set and STRIG is pulsed externally. This is a precalibration option which has not been exploited so far. Eventually it will be introduced in the standard run procedure.

4. Secondary output issuing. Only STRIG is pulsed externally. This is a debugging possibility which proved to be very useful in studying the board behavior but does not play any role at run time.

Though it is possible to force the MTB to pulse the STRIG through software, writing in a given register, it has been preferred to dispose this line to accept (unshaped) precalibration pulses (sec. 4.4.5).

The last three signals are possible integrity signals that can be routed to channel #0 through jumpers. They are required by TDC internals (sec. 4.3.3): they require at least 1 hit per event in order not to loose synchronism. Currently INTBGT is used on all boards, therefore only 15 channels are left on every board for signal processing.

Two more board common blocks are the summing stages for the secondary and tertiary outputs. The last one is a non amplified analog sum (the amplification factor is given at channel level as explained above). The first one instead includes a potentiometer that allows to regulate the height of the steps. Currently they are set to about $\sim 100mV$ per channel.

Finally the distribution of the power line, the bussed lines and the control lines complete the board level circuitry.

4.3.3 Digital electronics (TDCs)

The digital electronics of the BOREXino OD is made of 2 commercial TDC units (fig. 4.12). They are CAEN model v673, a double 6U VME unit developed in collaboration with the KLOE experiment in Frascati.

The block diagram of the unit is reproduced in figure fig. 4.13. The unit houses 4 identical and (almost) independent TDC chips, each one with 32 channels, yielding an overall 128 channel. The internal gray counter driving the chip operation runs at $960MHz$ resulting in a time resolution of LSB$\simeq 1.04ns$ (*Least Significant Bit*).

The TDCs are multi-hit devices accepting differential ECL signals. They have the ability to record in one event up to 16 signal edges (both rising or falling) in a time depth programmable up to $64\mu s$. In our case the signal to be parsed spans between $\sim 700ns$, a typical QTC pedestal, and $\sim 2\mu s$ a $\sim 200pe$ signal at typical QTC gain. In most cases only 2 edges will be recorded by fired channels, nevertheless it was decided not to limit the maximum number of edges acquired and postpone the eventual rejection of spurious edges to reconstruction level. In this way the channel dead time is kept to zero[6].

The time window depth is adjusted to $\sim 8.5\mu s$ to closely match the trigger gate to the Laben boards (sec. 4.4.3). The minimum time distance between 2 successive edges is $8ns$, a requirement well met by our typical signals.

The unit works in common stop mode, with the trigger signal (BGT, sec. 4.4) being the stop (fig. 4.14). The unit keeps digitizing incoming pulses but data are periodically overwritten unless a trigger occurs. In this case the edges of the last $\sim 8.5\mu s$ will be copied in the next available event memory buffer. The trigger stop signal is properly delayed to let the physical event fall in the mentioned time window.

Each chip has 4 event memory buffers that allow deadtime-less operation but that could be easily filled in case of a fast sequence of triggers. Stop signals arriving when the

[6]Should the programmed maximum number of hits be exceeded, the board would execute some internal copies to discard the old hits and this would introduce dead time.

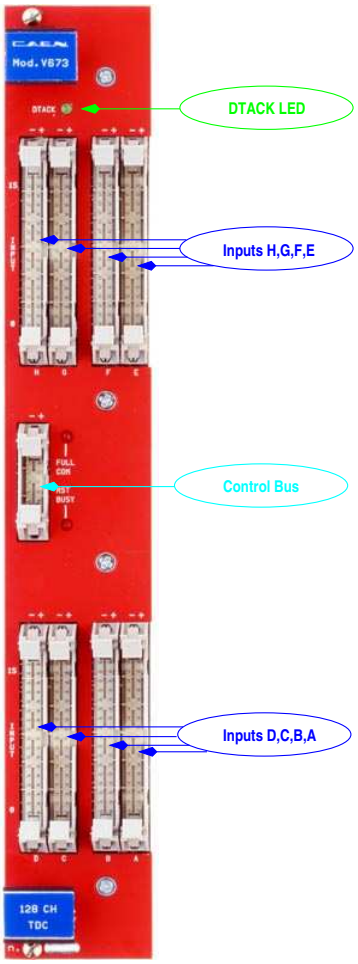

Fig. 4.12: *TDC front panel.*

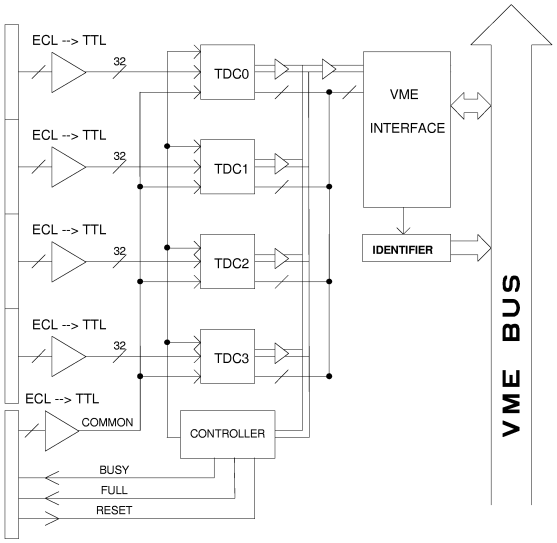

Fig. 4.13: *TDC block diagram.*

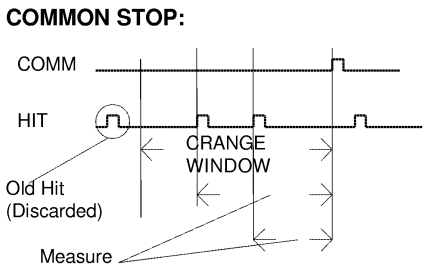

Fig. 4.14: *The common stop logic.*

4 buffers are full are being ignored by the board. For this reasons the ability of the DAQ to empty the buffers in the shortest possible time is particularly critical (sec. 5.2.3).

The front panel of the unit (fig. 4.12) is crowded with 8 34-pin (16 channels + 1 ground) flat cable input connectors. In the middle a 10-pin flat cable connector brings the control bus, daisy-chained among the boards and mastered by the MTB (sec. 4.4.6). These are the 4 lines carried by the bus:

1. COMMON. The common start/stop signal.
2. RESET. A global reset command.
3. FULL. A flag signaling that a board has at least 3 of the 4 event buffer full.
4. BUSY. A flag signaling that a board has all 4 event buffer full.

The first 2 of the above are commands issued by the MTB to the TDC units, while the last 2 are flags risen by the TDCs and checked by the MTB. The last board in the bus

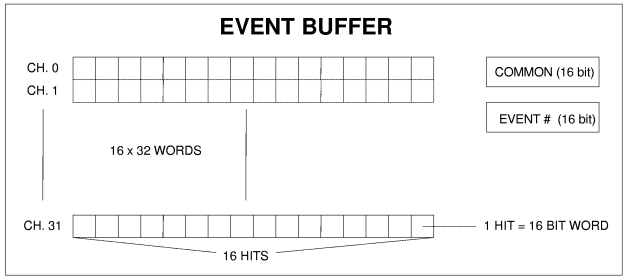

Fig. 4.15: *The event buffer of a TDC chip.*

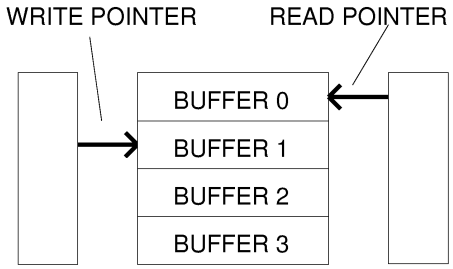

Fig. 4.16: *The read and write operations on the 4 event buffers.*

internally terminates the bus with the required 110Ω (jumper enabled).

Three LEDs are also present on the front panel showing DTACK (*DaTa ACKnowledgement*, i.e. the board is being read through VME), FULL and BUSY conditions.

When the BUSY condition is on (OR of the two boards), the MTB issues a VETO to the BTB to avoid DAQ jamming.

Synchronism among the 8 chips is in principle not guaranteed by the units themselves: a FULL or a BUSY condition may regard only one or a few chips, while the others having enough free buffers may keep recording data. Moreover a read-out operation may in principle result in data chunks belonging to different event number according to the presence or absence of data in a chip for a given event. In order to avoid all these potential problems, in our design the synchronism is insured externally by the presence of integrity channels (see also sec. 4.3.2). These are 1 channel per chip where a special integrity signal is always fed, resulting in a minimum guaranteed of one hit per event in every chip. In this way event buffer occupancy of the 8 chips can be described by a single variable.

Data transfer capabilities

From the VME point of view, the boards are used in A32/D32[7], though there are also other possibilities available. The addresses of the boards are settable on 4 rotary switches accessible from the side of the board.

The board interfaces with J1 and J2 VME connectors as well as the auxiliary Jaux connector introduced in the CERN V430 bus extension. The board houses a VME RORA (*Reset On Register Access*) interrupter that generates an interrupt whenever there are data to be read in the event memory buffers. The PPC DAQ software is designed to listen to the analogous interrupt raised by the MTB, therefore TDC interrupts are actually ignored (sec. 5.2.3).

The event buffer structure is shown in fig. 4.15. It is organized in 16-bit words, one for every hit recorded plus 2 special ones. Hit words are the gray counter values upon edge arrival, COMMON is the gray counter value upon common start/stop arrival and EVENT # is counter for number of commons arrived since last reset (normally issued

[7] 32 bit used for addressing and 32 bit for data transfer.

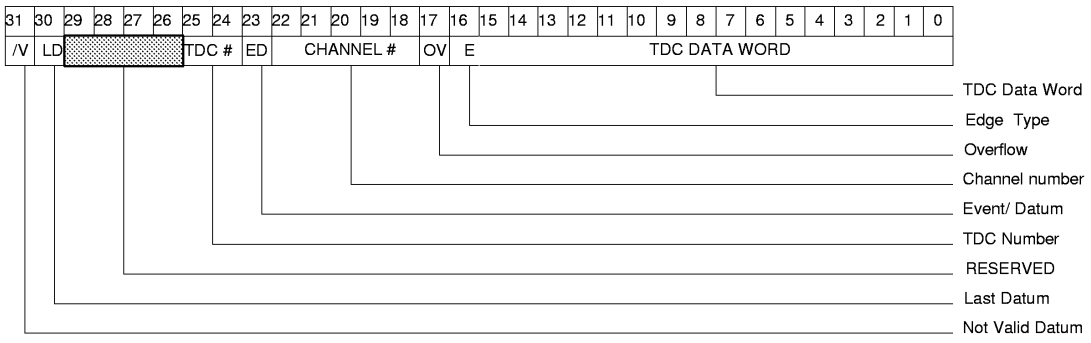

Fig. 4.17: *The 32-bit data word of the TDC units.*

at the beginning of run only). Up to 16 hit words can be present depending upon hit depth selected by the user (VME register). As mentioned before the full depth is used in BOREXino.

A VME register (CRANGE) contains the programmed time depth (in our case 13-bit = $\sim 8.5\mu s$). A continuous check on this register word discards hits older then the selected time span.

Read and write operation are independent, a buffer can be read while another one is being written as shown in fig. 4.16. Upon COMMON arrival, the write pointer is incremented, freezing the previous buffer content. Read pointer is incremented automatically upon buffer read-out accomplishment[8]

Read operations yield sequences of 32-bit words, where the 16 LSB are typically an event buffer word, while the 16 MSB hold service informations (fig. 4.17). The first word is the EVENT# counter value, followed by the hit words. These contain the subtraction of the hit gray counter value from the COMMON one yielding a (negative) time relative to the trigger signal in clock ticks. The last hit has an end-of-block flag set, used by the DAQ to complete read-out (sec. 5.2.3).

The read-out can occur in sequential mode where events are simply read one after the other or in event request mode (ASKEV), where an event number is specified by writing it in a dedicated register and that event is returned by the board discarding all events with a smaller ID. We prefer the last possibility, though we have no need to discard events, thanks to the very robust protocol.

The board supports different data transfer protocols including sequential read-out, where words are transferred one at a time, and *BLock Transfer* (BLT), a programmed operation that transfers a larger amount of data. More details on data transfer modes are given in sec. 5.2.3 where the DAQ is introduced.

4.4 Trigger System

The BOREXino trigger system (fig. 4.18) performs the following operations:

[8]Clearly the last allowed position for the read pointer is one before the write pointer.

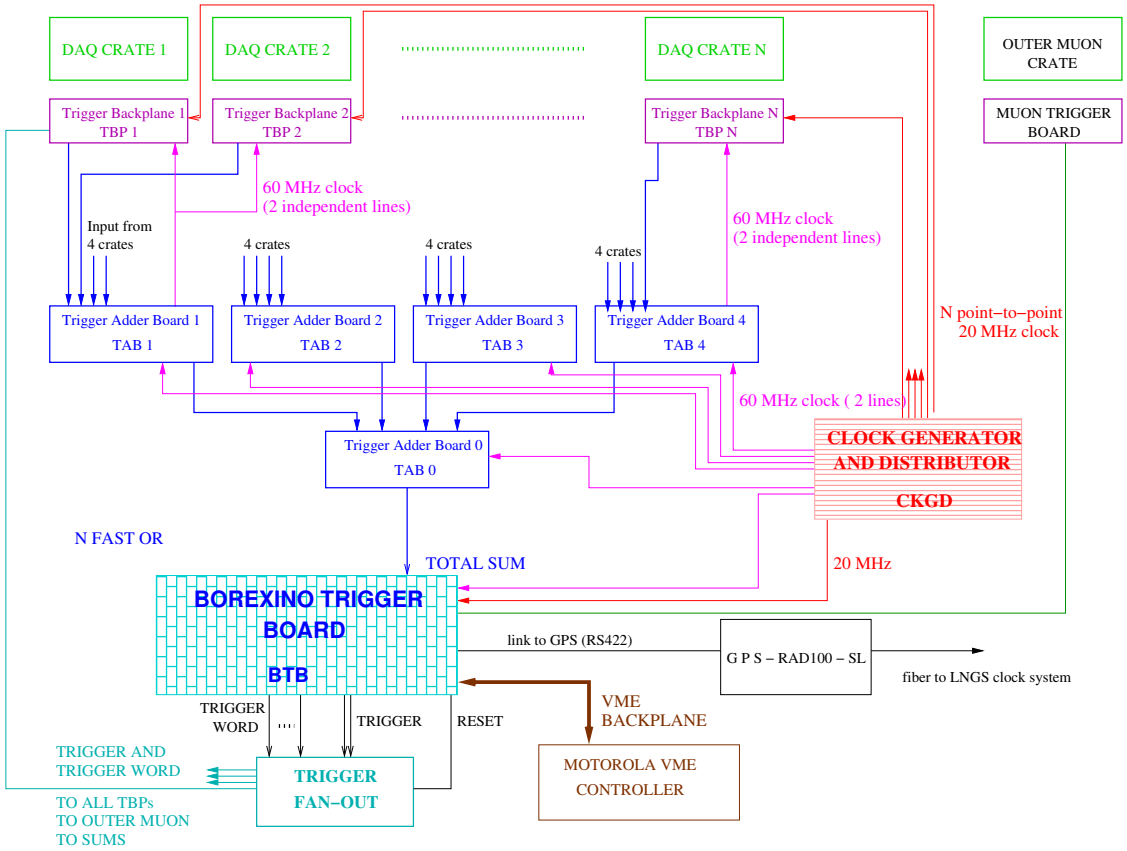

Fig. 4.18: *BOREXino trigger layout logic.*

- Evaluates the channel coincidence condition from the ID. This is optimistically named "neutrino" trigger.
- Evaluates the OD trigger conditions based on two criteria:
  1. Number of fired channels.
  2. Analog sum discrimination.
- Provides test and calibration service triggers.
- Provides laser systems triggers, firing the lasers or handling their internal triggers.
- Couples to the GPS receiver for absolute time reference.
- Distributes trigger signals and event identifiers to all subsystems.

The *Borexino General Trigger* (BGT) condition is a general condition for the whole system, which means that all detector subsystems are acquired simultaneously, no matter which subsystem or service procedure determined the trigger condition. No partial detector acquisition is foreseen.

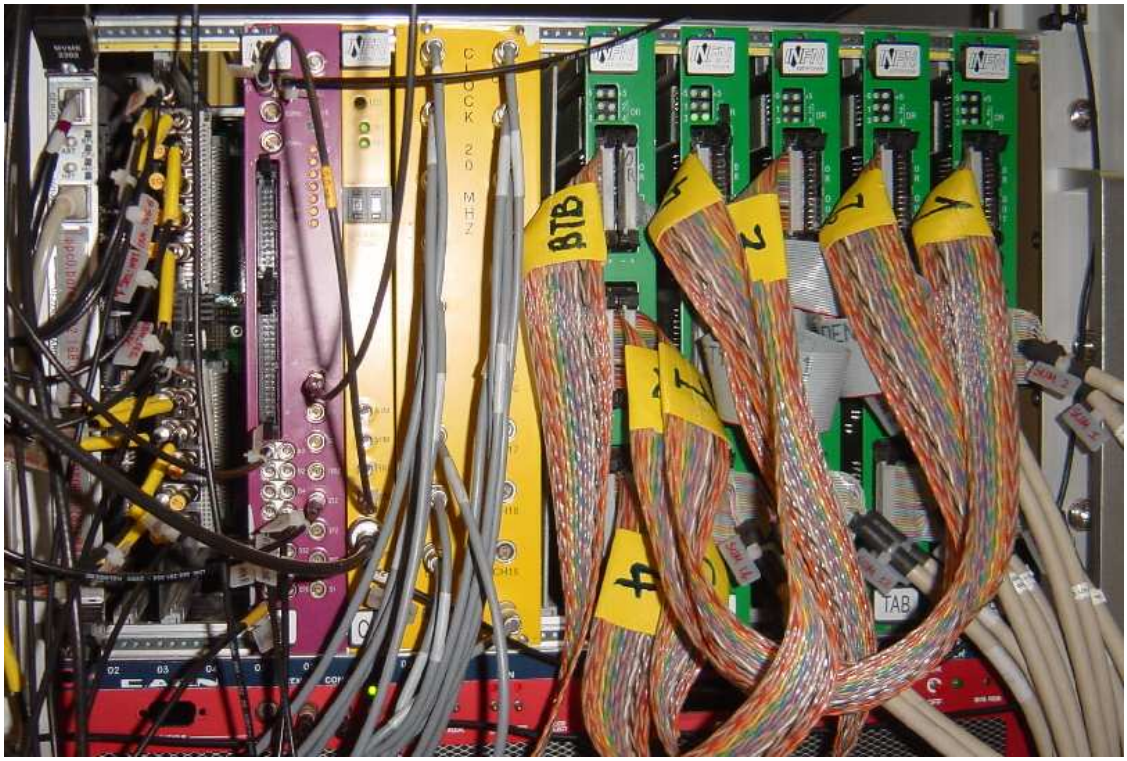

Fig. 4.19: *The trigger VME crate. From left to right: the PowerPC (gray), the BTB (red), the CKG and its additional front panel (yellow), the 5 TABs (green).*

Most of the trigger electronics is housed in a dedicated rack at the center of the electronic room. A VME crate (fig. 4.19) with the digital electronics takes part in the DAQ process, while two NIM crates host the numerous modules involved in the different service signal handling described in this section. The heart of the system is the *Borexino Trigger Board* (BTB) located in the VME crate (magenta front panel).

The trigger rack houses also the GPS receiver unit (sec. 4.4.4) and the slow control server computer (sec. 5.7).

4.4.1 Inner Detector trigger

The generation of the ID trigger is made of four steps:

1. Laben boards compute the sum of the fired channels. A monostable is brought up upon channel threshold crossing and kept up for three cycles of an external clock. The sum is sampled at every cycle of another external clock. Clocks are described below (sec. 4.4.2).

2. Laben crates are equipped in the back with *Trigger BackPlane* (TBP) units that perform the crate level sum upon the same clock signals. This is sent encoded in an 8-bit word to the trigger crate on a special multi-wire cable. Actually TBPs

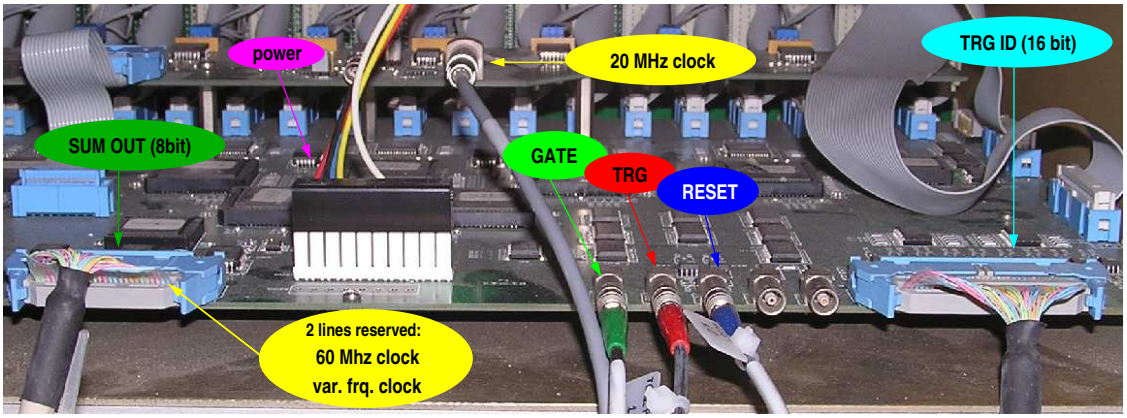

Fig. 4.20: *The Trigger BackPlane (TBP) unit in the rear of every Laben crate.*

perform I/O of many signals from/to the trigger crate and distribute them among the boards (fig. 4.20).

3. In the VME crate, 5 TABs (*Trigger Adder Board*) perform the overall ID sum in two cascaded steps and pass it to the BTB, on a 26-pin flat cable.

4. The BTB compares it with a programmable threshold that can be set from the Trigger Setup Page (sec. 5.3.1).

The overall trigger formation time is of the order of $\sim 3 - 4\mu s$.

The BTB is a custom double 6U VME device designed around a fully programmable DSP (*Digital Signal Processor*).

In addition to discriminating the detector's channel sum, the board handles a number of service triggers (sec. 4.4.5).

As a reference it follows a list of the connections available on the BTB front panel (fig. 4.21):

- Left side, from top to bottom:
  - CK. The $20MHz$ clock input.
  - STOP. A signal that latches the GPS receiver (sec. 4.4.4) upon BGT generation.
  - The $20MHz$ and $60MHz$ clock output (useful in stand-alone tests).
  - COMPARATOR. The 26-pin comparator input.
  - OR. The 34-pin input for the channel-OR signal (foreseen for additional partial trigger conditions).
  - I0 to I7. 8 LEMO conn. Service trigger inputs (sec. 4.4.5).
  - O0 to O7. 8 LEMO conn. Service trigger outputs (sec. 4.4.5).
- Right side, from top to bottom:
  - A manual RESET button.

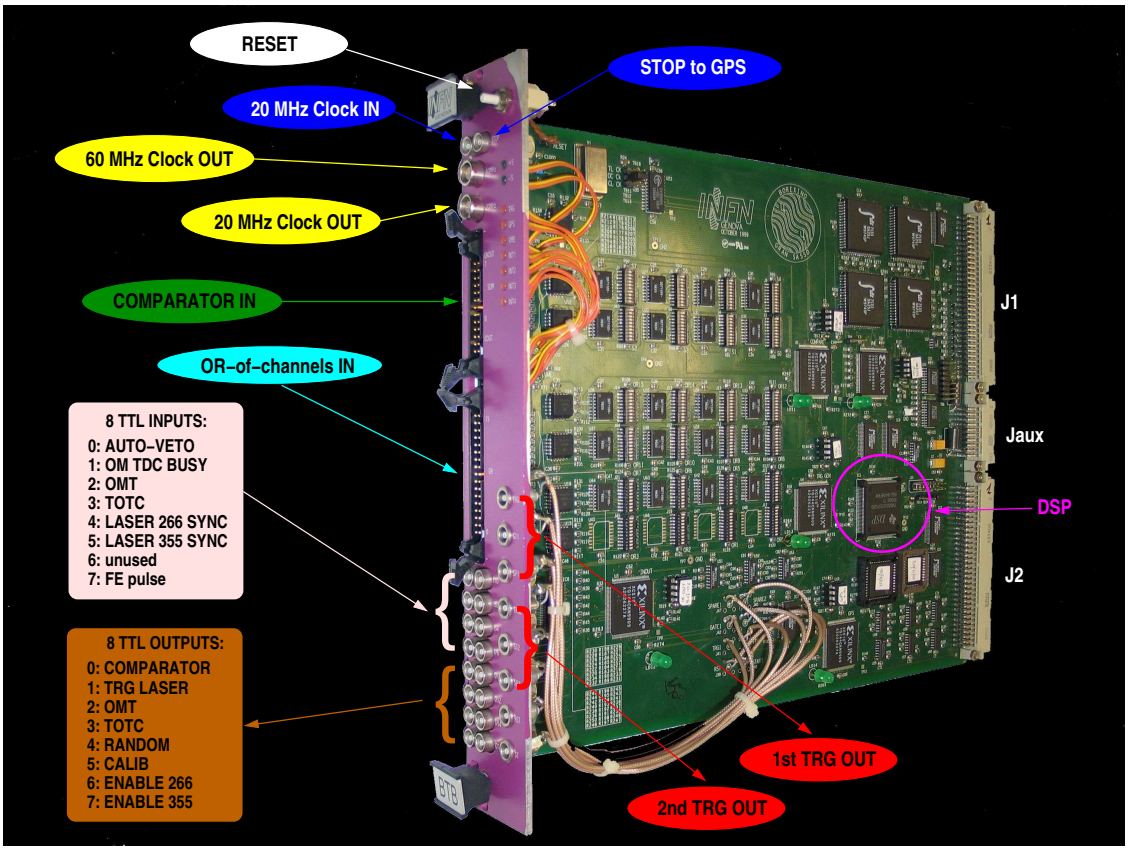

Fig. 4.21: *The BTB and its connections.*

- +5V/-5V. 2 green LEDs for power lines.
- TRG, GPS, VME, INT1, ...INT4. 7 yellow LEDs. Show respectively trigger generation, GPS connection, VME bus traffic and IRQ on 4 lines.
- TRG1, GT1, TRG2, GT2, RESET, ... Front copies of some signals available on the backplane fan-out (trigger, gate, reset, ...).

On the backplane fan-out units make available (through user-reserved lines of the VME J2 section) the TRIGGER, GATE, RESET signals and the trigger ID pattern in many copies. In this way it is possible to distribute signals synchronously to all acquisition units.

4.4.2 Clock signals

Four different clock signals are in use within the BOREXino electronics and are distributed to all Laben boards:

- A $20MHz$ signal drives the time and charge acquisition at channel level (sec. 4.2.3).
- A programmable frequency ($30 - 70MHz$) signal (PRG) is used to define the duration of the monostables of the summers at trigger level 1, 2 and 3. Monostables

are kept up for three clock cycles. The typical frequency is $60MHz$ which defines a trigger window of $48ns$.

- A $60MHz$ signal is used to sample the sums at trigger levels 1, 2 and 3.
- A $50MHz$ signal is used to drive the FADC modules (sec. 4.6).

The four clock signals are all produced by the same board: the *ClocK Generator* (CKG), the single yellow unit in fig. 4.19. It houses a quartz oscillator with a native frequency of $20MHz$ and a $1ppm$ precision. The $20MHz$ signals (20) are derived directly from the oscillator and brought to an additional front panel, the double yellow "unit" in fig. 4.19. From here individual cables (gray) take signals to TBPs (fig. 4.20).

The $60MHz$ and the PRG signals are instead generated through an on-board microprocessor, internally fanned $\times 16$ (each) and sent to the J2 VME connector where user-reserved lines distribute them to the TABs[9]. The TABs, apart from using the clocks themselves, forward them to the TBPs using two lines on each of the 26-pin flat cables through which they receive the crate sum words.

The main unit front panel houses a switch to select the variable frequency signal and report a few copies of the generated signals on LEMO connectors. One of the $20MHz$ is fed to the BTB CK input, one is scaled down to $\sim 600KHz$ with an external custom NIM unit and fed to an OD TDC spare channel and one is sent to a FADC channel.

The $50MHz$ signal is also generated by the processor but is brought only to two front panel outputs from where it is sent to FADC racks to be fanned into every module (sec. 4.6).

4.4.3 Trigger handling and distribution

Whenever a trigger condition of any kind occurs, the BTB issues three signals:

1. TRIGGER. A $\sim 2\mu s$ TTL pulses on a LEMO cable. It signals the trigger condition.
2. GATE. A $\sim 6.5\mu s$ TTL pulse on a LEMO cable. It gates the Laben boards. The TRIGGER signal is properly delayed to let the physical event lie $\sim 400ns$ after gate opening.
3. TRGID. A 16-bit pattern on a multi-wire cable. The value of a BTB event counter that flags the event uniquely [10].

These signals are issued from the backplane fan-out to the 14 TBPs but also to the MTB (sec. 4.4.6) and to the FADC system (sec. 4.6). In addition the RESET signal (TTL pulse on a LEMO cable) is issued at run start for synchronization purposes.

Whenever the comparator fires or a service trigger is received, an interrupt (high or low priority respectively) for the DSP is generated. The interrupt handling procedure, among other things, issues the three signals mentioned above. Then the DSP builds the trigger register on a local dual-port FIFO. This is made of 14 short words with useful information, the main ones being:

[9] The VME specifications[197] in fact do reserve most of the J2 lines for custom uses.
[10] Counter crossing conditions are handled at event building level (sec. 5.4).

Trigger	Trigger Type (dec)	Trigger Word (hex)	BTB In	BTB Out	MSB	Priority
Neutrino	1	0x0001	Comp	1	0	1
MuonMTB	2	0x0402	3	4	32	2
MuonTotC	128	0x0880	4	3	8	3
Laser355	4	0x1004	5	7	16	4
Laser266	16	0x2010	6	8	32	5
Laser394	8	0x4008	7	2	64	7
Calibration	32	0x4020	7	5	64	6
Random	64	0x4040	7	6	64	8

Tab. 4.2: *Trigger Types and Trigger Word values available in BOREXino.*

- Comparator Threshold.
- Trigger Time. From a $20MHz$ gray counter similar to the Laben ones.
- Trigger Number. The TRGID counter value.
- TAB sum value.
- *Trigger Word* including:
  - LSB: *Trigger Type*.
  - MSB: Fired inputs (bit-field).
- GPS registers (5 words).

The possible values of the "trigger word" are shown in tab. 4.2. The MSB is a bit-field where it is kept track of which BTB inputs were active at trigger generation. The *Trigger Type* (LSB) is a code assigned considering the priority shown in the last column.

The time required for generating and writing the trigger record is $\sim 10\mu s$, during which further triggers will be ignored. This is a real dead time of the system and is considered acceptable as no one of the searched delayed coincidences lies in the $6 - 10\mu s$ range. In addition to this, the dead time arising from the Laben data read-out process must be taken into account. Since $80\mu s$ are required in that case and the boards have the possibility to queue one incoming trigger during read-out before becoming BUSY, an auto VETO prevents a third trigger in less than $100\mu s$. This is generated upon the BTB output TRG2, manipulated with some external logic and sent back to BTB input I1. This dead time also has no impact on physics performance.

4.4.4 GPS absolute time

GPS time is important for coupling events to absolute time, for example in case of a supernova explosion, and for analysis on delayed coincidence, when the coincidence time is longer than the $3.2ms$ gray counter range (sec. 4.2.3). The GPS offers μs precision, more than enough for both of these tasks.

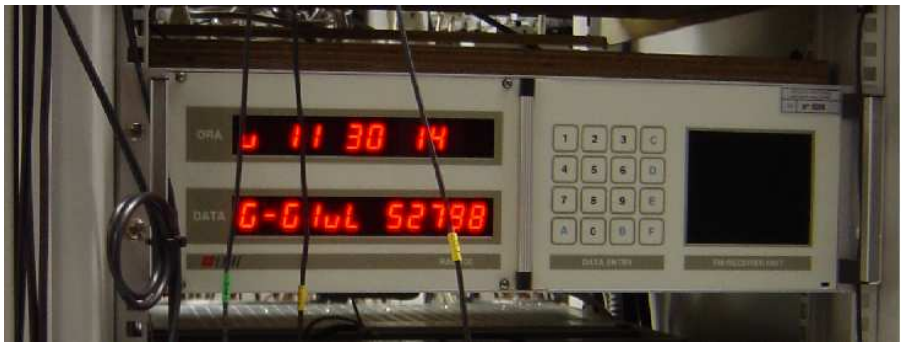

Fig. 4.22: *The GPS receiving unit installed in the trigger rack.*

The LNGS is equipped with a GPS receiving facility. The signal is brought underground with dedicated optical links. The one reserved for BOREXino arrives in the trigger rack where a decoding unit is present (GPS-RADIO100-SL).

This unit is connected to the BTB via flat cable and a custom "plug" to the VME bus. A few user-reserved lines in the J2 areas are used for this purpose. Upon trigger generation the BTB issues a latch signal through the STOP front-panel output (fig. 4.21). This "freezes" the GPS time on the receiver unit. The BTB reads it then during the composition of the trigger record (sec. 4.4.3).

4.4.5 Service triggers

As already mentioned a number of additional service trigger signals are required in BOREXino. Most of these are generated by the BTB upon an external periodic pulse.

For this purpose a NIM dual timer unit is used. The two submodules are connected in a standard *flip-flop* configuration, where the ENDMARKER of each unit is sent to the START of the other one. In this way, after an initial pulse the system oscillates indefinitely. The timer of the submodule from which the signal is taken allows to tune its length, while the other one does the same for the period, in our case $200Hz$.

Pulses from this unit are sent to BTB input I7 and can be served as three different trigger types:

calibration triggers. The idea is to use the calibration inputs of the front-end boards to distribute a calibration pulse to all ID channels.

Upon incoming pulses from the timing unit, the BTB responds with a pulse on its output O7. From this logic pulse a signal similar to a PMT signal is obtained with external units. This is in turn sent to a fan-out and distributed to all front-end crates. Here a local fan-out is present (fig. 4.3) to distribute it to every board.

random triggers. For *random* trigger we intend a trigger that is simply artificially generated, without any light or electronic pulse being sent to any part of the detector or of the electronics. This can be useful to study PMT dark noise.

Output O5 is fired in coincidence and is available, though currently not used.

laser394 (timing) triggers. These are the events where all ID PMTs are illuminated with the timing laser system (sec. 2.2.4) and the OD PMTs are illuminated with analogous LED calibration system (chap. 8).

In this case the BTB output O2 is fired in coincidence and is used to trigger the laser box on top of the water tank as well as all the LED boards. The laser SYNC-OUT is used to generate reference signals (sec. 4.5).

The first CALIB_MAX events (default: 1000) from the timing unit at the beginning of the run are served as calibration events. This is the so called *precalibration phase* of the run (sec. 6.3.1), where parameters of both ID and OD electronics are measured.

In standard runs, after precalibration, the BTB pre-scales the incoming pulses by a programmable factor (CALIB_PRESCALE, usually set to 100), and serves the remaining ones issuing one event for each of the three types above throughout the run for miscellaneous checks.

The BTB behavior can be customized before starting the run through the Web Trigger Setup page (sec. 5.3.1).

Other laser triggers

The two other lasers ($266nm$ and $355nm$) run exclusively on an internal $11KHz$ oscillator, so the timing unit cannot be used in this case. They can be enabled from the trigger setup page exclusively as run modes.

This turns constantly on a specific BTB output (O6 and O7 respectively) which is ANDed with the laser SYNC-OUT signal. After an external pre-scaling to match the DAQ acquisition capabilities of a few hundred Hz, the signal is sent back to a BTB input (I4 and I5 respectively) for trigger generation (fig. 4.23). Events are flagged with the specific trigger type.

Triggers from Outer Detector

The generation of the two possible Outer Muon Trigger conditions is discussed below. Here we only want to mention that the BTB inputs I2 and I3 are reserved for them[11] and that, if enabled from trigger setup page, pulses on either on these inputs determine BGT formation and handling. A $\sim 3-4\mu s$ delay is introduced to emulate ID trigger formation time. Two event trigger type are also reserved for these cases (tab. 4.2).

4.4.6 Outer Muon Trigger system

The outer muon detector has its own trigger subsystem, fully integrated in the main one.

Its main functions are:

- Receiving the BGT and handling it correctly.
- Generating the Outer Muon Trigger signal (OMT).

[11] As well as the unused outputs O2 and O3.

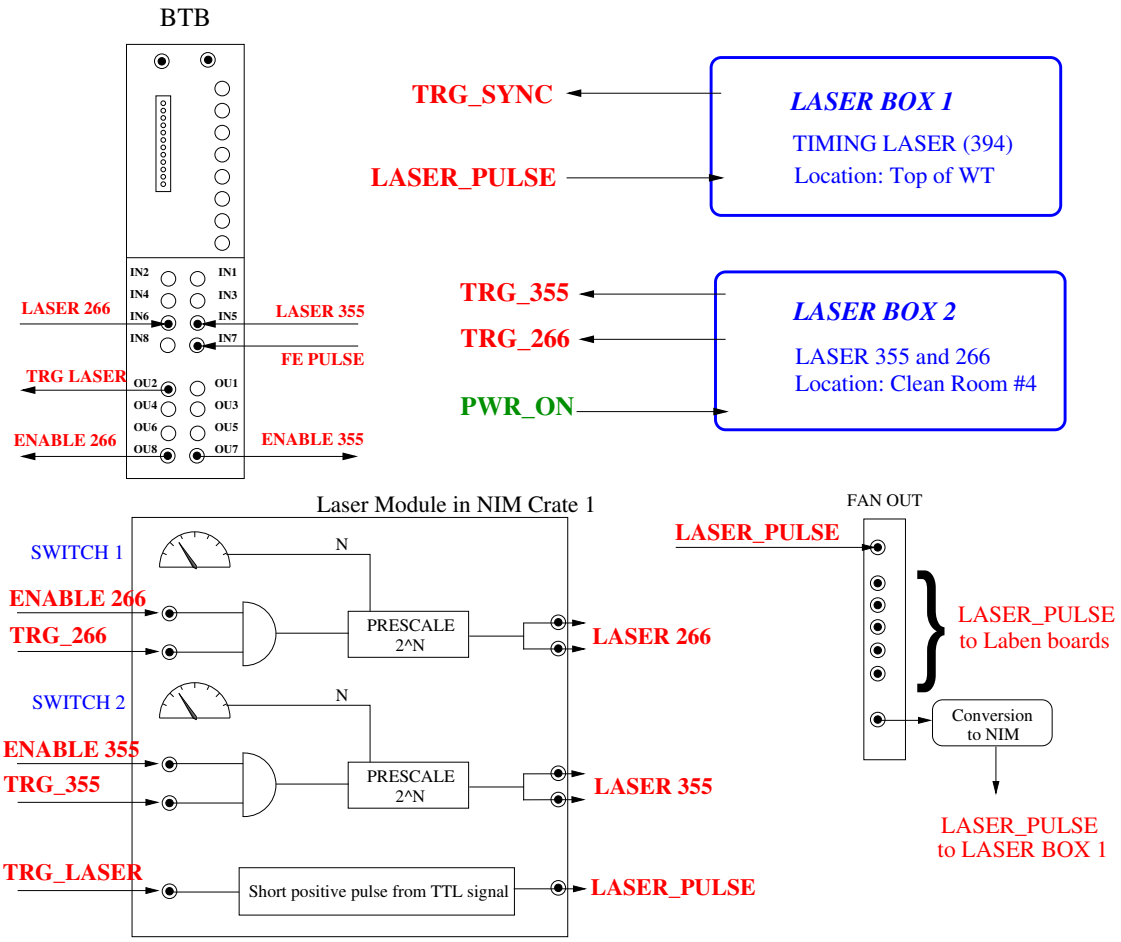

Fig. 4.23: *The overall trigger logic for the three laser systems.*

- Generating the analog outer muon trigger signal (TOTC).

The first 2 tasks are carried out by the MTB which also handles the control buses for TDCs and QTCs. The last task is performed by external NIM logic.

Muon Trigger Board

The *Muon Trigger Board* (MTB) is a custom 6U VME unit developed for BOREXino at MIT[12]. The unit is made of a mother board which interfaces with the VME backplane and a daughter board, the MTB-D, to which the task of OMT formation is delegated for better noise isolation.

The board interfaces with QTCs and TDCs through front panel multi-pin connectors (from top to bottom):

- J4 (14-pin). QTC control bus master. 7 lines listed in sec. 4.3.2. Accessing specific VME registers of MTB, the levels of the bus lines are controlled through PPC

[12]Massachusset Institute of Technology

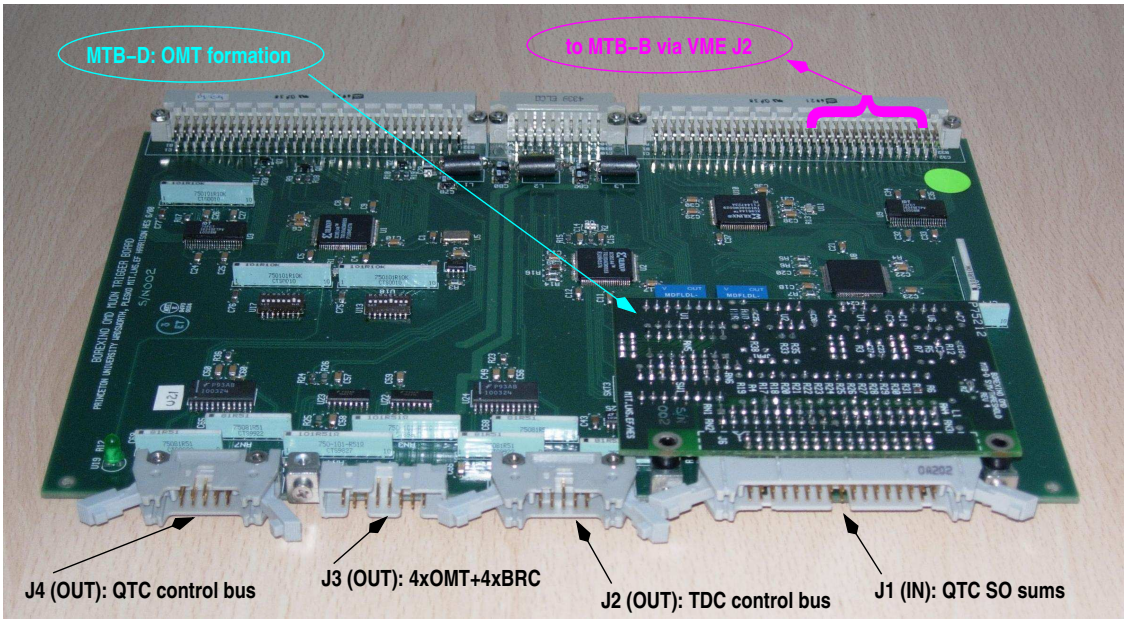

Fig. 4.24: *The Muon Trigger Board (MTB), before front panel application.*

software.

- J3 (16-pin). Synchronization signals for TDCs. 4 copies of OMT and 4 of BRC. 2 of each are sent to spare channels on both TDC boards.
- J2 (10-pin). TDC control bus master. 4 lines (+1 ground) listed in sec. 4.3.3.
- J1 (34-pin) to MTB-D. Inputs from QTC SOs for OMT formation.

where (apart from J1) all handled signals are differential ECL logic pulses.

Additionally the board interfaces with the BTB through a second external daughter board MTB-B, plugged in the VME backplane, sharing the following lines:

- BGT (input). The main trigger signal.
- TRGID (input). The 16-bit trigger ID on a multi-wire cable.
- RESET (input). Reset for initialization. Also forwarded to TDCs through a control bus line.
- BRC (input). Borexino Reference Clock. A copy of the $20MHz$ clock, scaled to $\sim 600KHz$, forwarded to TDCs through the J3 connector lines.
- OMT (output). The Outer Muon Trigger signal.
- BUSY (output). The OR of the TDC BUSY condition forwarded from the TDC control bus as a VETO for the BTB (sec. 4.3.3).

where apart from TRGID all other signals are TTL logic pulse traveling on LEMO cables.

Upon BGT arrival, the MTB performs three important operations:

1. Issues a $\sim 25ns$ BGTINT integrity signal to the QTCs along the QTC control bus.

2. Issues a $\sim 150ns$ COMMON STOP signal to the TDCs along the TDC control bus. This is delayed $\sim 70ns$ with respect to BGTINT.

3. Acquires the TID pattern on an internal register.

4. Raises a VME interrupt on its dedicated line (IRQ4), within $200ns$ from the COMMON STOP pulse.

where the second operation determines the TDC buffers read-out, while the last one drives the DAQ process informing the driver that an event is ready to be read (sec. 5.2.3).

Outer Muon Trigger (OMT) formation

As described in section sec. 4.3.2, the QTC boards issue as SO a step function encoding the number of channels fired in the board. The width of the steps defining the trigger time window is usually set to $150ns$, while the height is set to $100mV/channel$.

These signals are brought to the MTB on coaxial LEMO cables where one end is equipped with a 2-pin DUPONT connector in order to plug in a line of the multi-pin J1 connector. The MTB-D daughter board simply adds the 16 inputs[13] and discriminates the sum against a programmable threshold (8-bit DAC). The inputs have a dynamic range that spans up to +2V before saturation occurs, allowing the threshold to be set up to almost 20 channels, in the standard QTC setup. Whenever the threshold is crossed, the OMT signal is generated and sent to BTB input I2 for BGT generation. In addition the OMT is forwarded to TDCs through J3 lines for synchronization purposes.

Analog Outer Muon Trigger formation

In general, it will be difficult to lower the number of channels in coincidence for OMT below 6 without introducing many accidental triggers. However there are a few muon events that for geometrical reasons might deposit charge only in a few PMTs. In order to be sensitive also to these events an additional OD trigger condition was introduced based on the discrimination of the analog sum of the detector.

The TO of the QTC boards was added to the design for this purpose (sec. 4.3.2). These signals are the analog sum of the channel inputs with a fixed built-in amplification factor of 2. The 14 signals are handled by external NIM modules. They are first summed together in 2 stages using cascaded *Fan-in Fan-out* units (4+1). The output is then discriminated in a Leading Edge Discriminator. The eventual trigger condition, named TOTC from "Total Charge", is then sent to BTB I3 input for BGT generation.

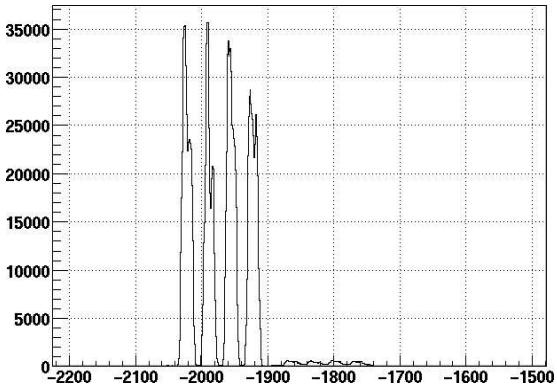

Fig. 4.25 (a): *Trigger reference time (in ns). The four broad peaks are due to the DSP jitter.*

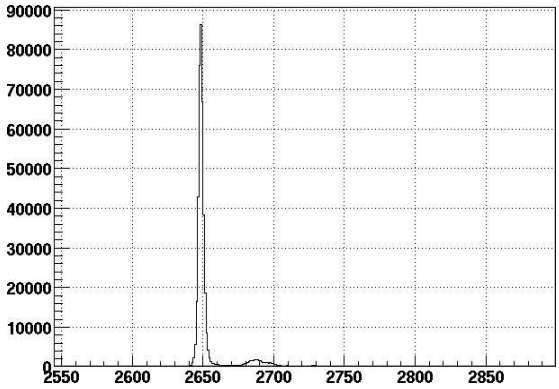

Fig. 4.25 (b): *Time difference (in ns) between hit times and laser reference time.*

4.5 Reference signals

The BTB generates the trigger signal upon the execution of a custom firmware on its DSP. This operation doesn't always require the same time. The result is that the delay between the occurrence of the trigger condition and the issuing of the trigger system is not fixed but can vary in a $\sim 100ns$ window (fig. 4.25(a)). The Laben hit distribution for one event must therefore be coupled to the trigger time (to which the GPS time belongs) in some way.

This is achieved by using one spare channel per rack. A copy of the trigger signal from the fan-out in the back of the trigger crate is inverted and shaped to obtain a pseudo analog pulse. 16 copies of this pulse are then distributed to the 14 ID racks, to one FADC channel and (unshaped) to one muon TDC channel[14].

Similarly during timing laser events it is important to have a laser reference time in order to filter out spurious hits falling inside the gate but not coupled to the light pulse (fig. 4.25(b)). One more spare channel per crate is used for this purpose and fed with the laser SYNC-OUT TTL signal, converted in the same way as the trigger signal above. For the same reason, one of the spare OD TDC channels accepts a signal from the TTL fan-out that fires the LEDs (sec. 8.3).

The reference trigger and laser times for ID are averaged over the 14 Laben channels. Moreover they are used to measure and correct inter-crate hardware delays (sec. 7.4.5).

The scheme of the trigger and laser reference signal distribution is shown in fig. 4.26.

[13] Only 14 are used.

[14] Actually the OD doesn't need this as the TDCs are operated in common stop mode with the trigger signal being the stop: OD hits are therefore naturally synchronized with the trigger signal. The signal is acquired as a redundancy check.

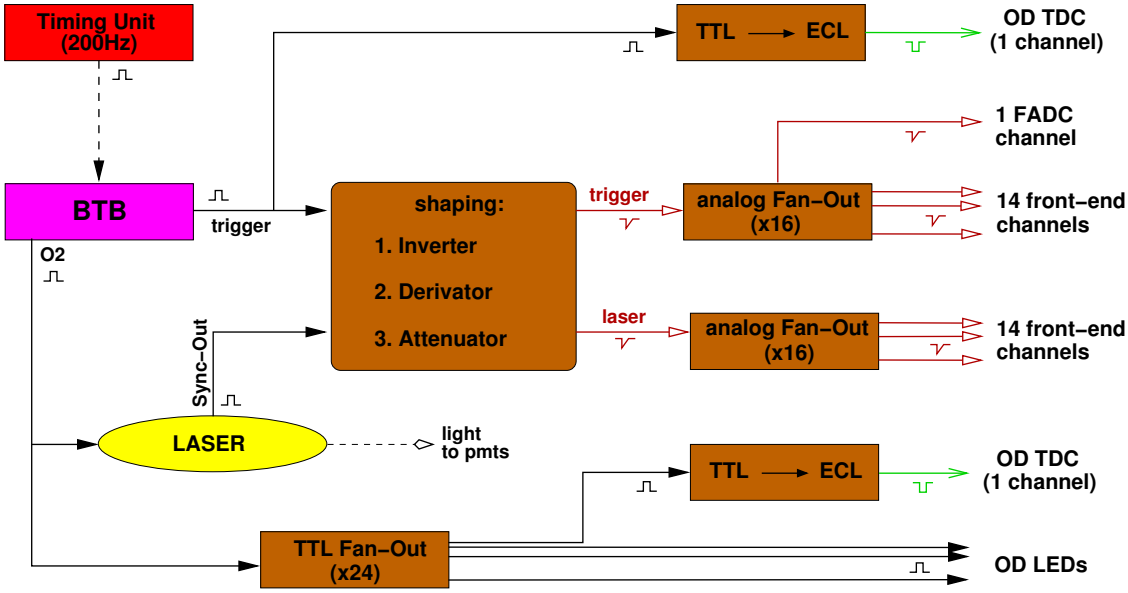

Fig. 4.26: *Scheme of the hardware setup to acquire trigger and laser reference signals.*

4.6 Fast Waveform Digitizers

Over the years, an additional high energy electronics has been added to the original design of BOREXino. The goal is to extend the energy region up to $15 - 20 MeV$ to encompass the full ^8B spectrum and to be sensitive to supernova neutrinos (sec. 2.1).

During the latest air runs the Laben electronics showed a performance outstanding previsions in terms of energy range: at $15 MeV$ saturation effects are still relatively small. Nevertheless the high energy electronics based on an entirely different design, can give an independent redundant measurement of the most important event parameters.

The idea is to multiplex PMT signals in groups of 24 and to acquire the sum signal shape with 98 Fast Waveform Digitizers, which we commonly name *Flash ADC* (FADC). This will allow especially PSD analysis in an energy region where the pulse shape reconstructed with Laben electronics is not accurate[15].

In order to have FADC channels corresponding to physical regions of the sphere, it was desirable to cable the ID racks grouping neighboring PMTs on the same boards. For practical reasons this could be done only partially.

The summing devices can be observed in fig. 4.3. These active units receive the 12-channel sum outputs of the front-end boards (sec. 4.2.2) and sum them 2 by 2, producing 24-channel sums with adjustable gains[16]. Sums of 8 inputs are also provided and further summed by an external passive system to yield the total detector sum.

[15]This arises from the fact that the only time provided by the Laben channel is the time of the first hit, so in case of high hit multiplicity relevant information is lost. In lower energy regions, for which the Laben system was designed, the hit multiplicity is small and the effect is negligible.

[16]In the last sum channel of each crate only 16 PMTs are present, as the last front-end board accommodates 8 spare channels.

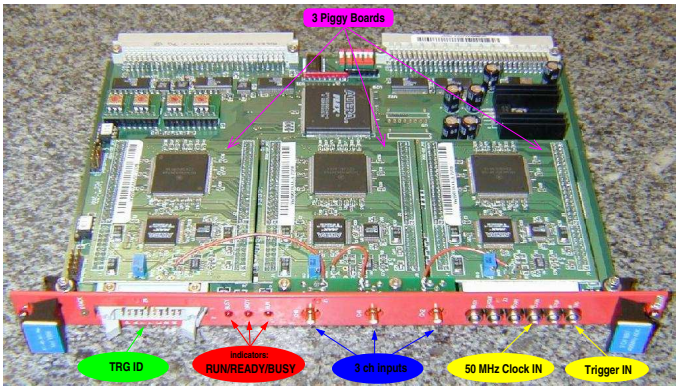

Fig. 4.27: *One of the CAEN v896 waveform digitizers.*

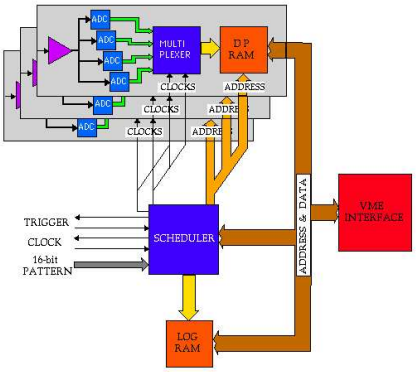

Fig. 4.28: *CAEN v896 block diagram.*

The FADC Boards have been designed in College De France within the BOREXino collaboration and realized in collaboration with CAEN, as model v896. They are 6U VME boards with 3 analog channels realized as piggy boards (fig. 4.27).

On the front panel the unit receives the following signals:

- 3 channel analog inputs (golden-plated SMB connectors) from summer modules.
- $50MHz$ clock pulse (TTL) from CKG.
- TRIGGER pulse (TTL), the BGT.
- TRGID. Trigger ID on a 16-pin connector.

The digitization process proceeds at $400MHz$ with an 8-bit resolution. Every channel houses 4 identical flash ADCs that work at $100MHz$, using both edges of the external $50MHz$ pulse. Every ADC component sees the clock with an additional $\pi/2$ phase compared to the previous one. Samples from the 4 ADCs are multiplexed (fig. 4.28) resulting in an effective $400MHz$ signal sampling (i.e. $2.5ns$ sample separation).

The memory is organized in 64 circular buffers of $\sim 10\mu s$ each, named *pages*. Digitization is continuously ongoing and the memory page is being periodically overwritten unless a trigger signal arrives. An incoming BGT determines the write pointer to move to the next page freezing in this way the previous one for reading. As memory is dual-port the previous page can be read through VME bus, while the next one is being written, yielding a zero dead time system.

In addition to the 98 ordinary channels, the following 3 special signals are also acquired:

1. Attenuated analog sum of the whole BOREXino detector. This channel plays a fundamental role for the online software (sec. 5.2.4).
2. A $100ns$ triangular waveform in phase with the $20MHz$ clock.
3. A $100ns$ ramp in time with BGT (trigger reference time, sec. 4.5).

the last two signals allowing synchronization with the Laben electronics.

The 34 boards required to handle the 101 input signals are arranged in 4 VME crates[17] housed in 2 dedicated racks. The 4 crates are connected with VME bus extension cards and are read by a single PPC. The clock, trigger and TRGID arrive as single lines from the trigger crate and are fanned locally with NIM and/or custom logic.

4.7 Scalers

In an experiment with as many PMTs as BOREXino, it is particularly useful a hardware method to check the health state and the dark noise rates. A system based on digital scalers was developed in Moscow by the Marathon group within the BOREXino collaboration and is now operative.

The ID scalers are slim horizontal modules that plug on the front panel of the summer modules (sec. 4.6) and are visible in fig. 4.3. They are all connected in a CAN bus line mastered by a PCI controller. The sensed signals are the copies of the 12 channel analog sum signals provided by the front-end boards. Therefore only the cumulative rate of the 12 PMTs in the board can be monitored.

The OD modules are instead 4 double NIM units (fig. 4.29) hosted in a dedicated crate in the orange rack (fig. 4.8). They pick up the logic ECL signals halfway through the QTC and the TDC boards, through a middle connector in the cable. The input impedance of the units by design is high enough not to alter the signal. Every module picks 4 QTC cables with 16 channels each yielding 64 channels per module. Unlike the ID case, single channel rates can be monitored. Modules are read through a parallel CAN bus line with another PCI controller.

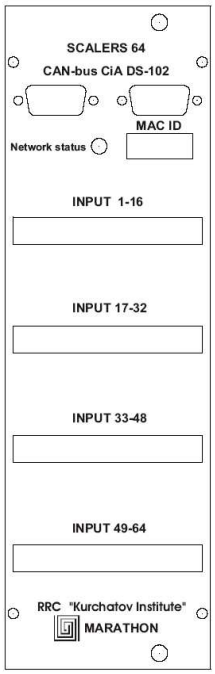

Fig. 4.29: *OD scaler front panel.*

Apart from channel multiplicity, another relevant difference between the two systems is that, while the ID modules acquire an analog pulse and discriminate it with their own threshold, OD scalers acquire directly the logic pulse from the QTCs and are therefore bound to their thresholds. Moreover OD scalers can be used only at run time when QTCs are in RUN mode.

The CAN bus scalers are mastered by 2 PCI CAN bus controller cards, mounted on `bxscalers` (sec. 5.1), one for ID and one for OD sub-systems. Drivers for these cards where developed by the Marathon group that built the hardware of both systems.

A single server program acquires data from the two lines and a web interface is under development (fig. B.4). For each of the two systems, it presents a clickable map of the available scaler channels, where the rates are reproduced by gray shades. Upon clicking on a channel square, the single channel is shown, with a plot of the rate history in a programmable time window.

[17] Two Crates would in principle be enough, but the distribution among four crates was chosen in order to enhance the heat dissipation.

Chapter 5

Online software

The BOREXino Online Software is a complex system that runs on 27 CPUs of different architectures, involves over 100 processes, scripts and other software instances programmed in different languages[1] and entirely custom made.

The tasks fulfilled at run time are the following:

1. *Data read-out.* Read-out of the event information from digital electronics.

2. *Event Building.* Assembling the event from the sub-systems data chunks.

3. *Run Control.* Control over the data taking run.

4. *Slow Control.* Control over the hardware.

5. *Online Monitor.* Run-time detector performance check-up.

6. *Dark noise monitor.* Acquisition of the scalers.

To put it in one sentence, the general idea is that every VME crate, where digital electronics is to be read, houses a PowerPC that accesses the boards through the VME bus. A local software reads the data, formats and sends them through network to a remote process. Here the event is being built and written to disk by other processes. All the components implement a state machine and a run controller process issues commands to all other processes ensuring the synchronization and the overall behavior as a single state machine. Web technology is used to provide the user with comfortable interfaces to all relevant processes.

In this chapter a full description of the online software architecture is given. However the Outer Detector DAQ and the Slow Control system are described in more details.

Throughout the chapter a basic knowledge of advanced network programming[199], kernel modules development[200] and Object-Oriented design patterns[209, 210] is assumed.

[1] Currently: C, C++, Perl, bash, HTML, Javascript.

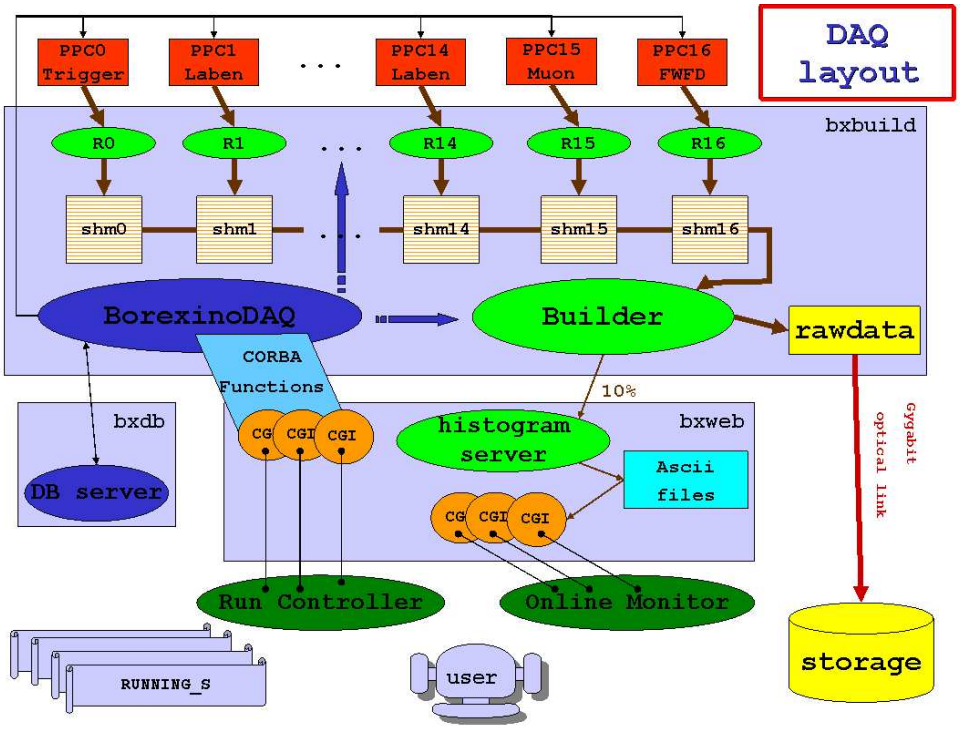

Fig. 5.1: *Block diagram of the overall BOREXino* DAQ *system. Event Building and Run Control are visible.*

5.1 Computing infrastructure

18 Motorola PowerPCs are housed in the VME crates in the electronics room and 7 x86 PCs (tab. 5.1) are located in the nearby counting room. All the machines are organized in a local cluster (fig. 5.2) and run the operating system Linux Debian. The *Potato* version (kernel 2.2) is used on PPCs while the PCs have been upgraded to the *Woody* version (kernel 2.4). The network facility is a private LAN (*Local Area Network*) powered by a 1GBit/s switch and all communications among remote processes occur over the TCP/IP protocol. Physical connection to the external world is provided by the optical cables of the LNGS: a fast data line and a users line reserved for BOREXino reach the external offline computing farm. In addition WAN (*Wide Area Network* connection through the laboratory network is provided.

The offline farm, its master node (`bxmaster`) and the users terminals (both underground and in the external laboratory) are also handled within the same LAN. Since users are in most cases developers of online and offline code, this creates a very comfortable environment to work. On the cluster in fact the same home areas are mounted through NFS (*Network File System*) on all the machines, a cross-compiling environment for PPCs is installed, "official" versions of compilers, analysis and simulation packages are maintained, a CVS repository holds any code released or in development and of course standard LAN services (DHCP, WiFi, printing, ...) are provided.

Name	CPUs	Hardware	Tasks	sec.
`bxmon`	1	2 ethern. adapt.	LAN router, firewall, NAT[a]	
			BOOT server for PPCs	5.2
			Error logger[b]	
`bxbuild`	2	SCSI disks RAID-2[c]	Event Building	5.4
		tape unit	Run Control	5.3
`bxdb`	1	SCSI disks RAID-2[c]	Database server	
`bxweb`	2		Web server	
			Online Monitor	5.5
`bxslow`	1	CAENet/PCI adapt.	slow control server	5.7
`bxhome`	1		NFS disk server	
			NIS authentication server	
			User home areas backup	
`bxscalers`	1	2 CAN bus PCI adapt.	Scalers acquisition	4.7

[a] *Network Address Translation*, a system to map (and eventually share) public IP addresses to machines inside a LAN.

[b] The Unix *syslogd* system is used.

[c] *Redundant Array of Independent Disks*, a technology to mirror a logical disk unit on parallel physical supports in order to minimize the data lost in case of a disk failure.

Tab. 5.1: *The 7 PCs of the online cluster with hardware features, tasks and sections where these are mentioned. Only* `bxweb` *and* `bxdb` *are available for users login, all other machines accept only superuser or eventually the virtual user* `daqman`*, an ordinary account used for data taking. the external SCSI disks and the tape unit mounted* `bxbuild` *acted as a temporary data storage and backup facility during Air Runs (chap. 6).*

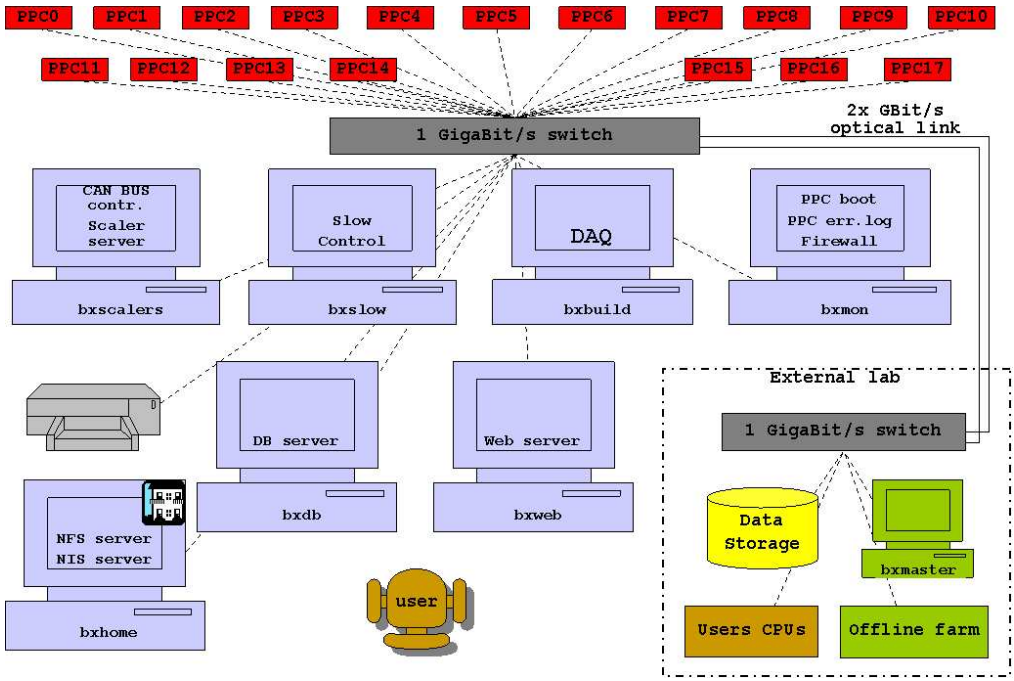

Fig. 5.2: *The online computing cluster. Connection to the offline farm is also shown.*

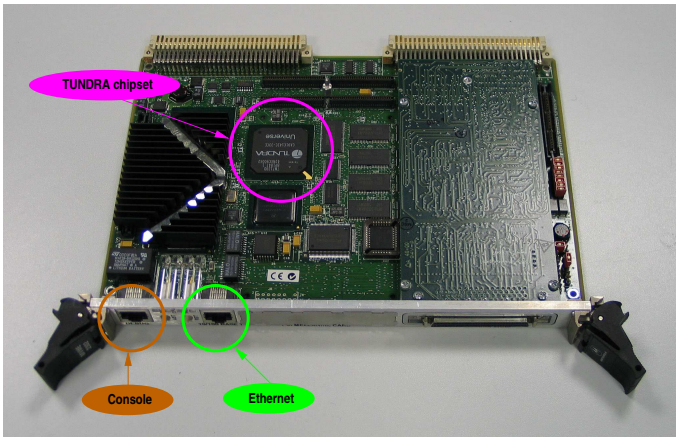

Fig. 5.3: *The Motorola PowerPC board.*

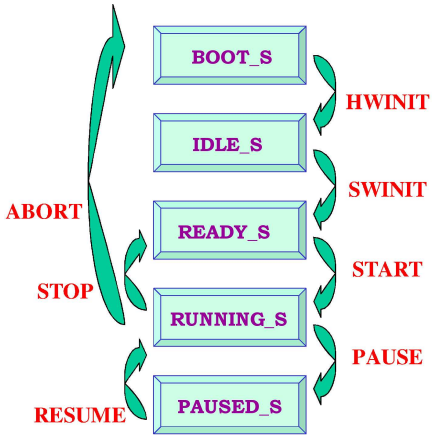

Fig. 5.4: *The common state machine implemented by all PowerPCs.*

5.2 On crate read-out

The first and most critical stage of data read-out happens at crate level, where the digital electronics is read by the VME bus master. In BOREXino PowerPCs are used for this task and custom software has been developed for the various subsystems.

5.2.1 The Motorola PowerPC

The PowerPC is a computer architecture especially designed for data read-out on the VME bus. Motorola PowerPCs are standard 6U VME boards with no disk and no local console.

They can be reached through a RS232 connection to a remote console or through fast ethernet connection ($100 MBit/s$). The two RJ48 connectors are visible in fig. 5.3. The first possibility is always available, as the firmware of the board handles plain telnet connections. For this task we use a terminal server connected to all PPCs and visible on the LAN. The possibility of ethernet connection to the PPC is instead only possible after an operating system has been loaded.

The Motorola produces different models with slightly different characteristics. The most used in BOREXino is the MVME 2302 with a $200 MHz$ processor and 32MB of RAM.

The natural operating system for this architecture is a proprietary Unix-like system named *Lynx* OS, but upon budget and flexibility considerations the collaboration decided to develop a custom version of Linux (Debian), the popular open-source operating system.

The board firmware boots the operating system via a network BOOTP request, handled by `bxmon`. During the boot operation a dedicated remote disk area, exported by `bxhome`, is mounted through NFS. Here are located kernel modules to be loaded (like board drivers) and DAQ executables to be launched upon boot completion.

The *Universe* chip and VME read-out modes

Regardless of specific model, the PPC mounts the *Universe* chip-set manufactured by TUNDRA and visible in fig. 5.3. This chip bridges the VME-bus into the PCI-bus, which means it performs all the low level operations that allow the user to see the VME bus almost as a standard PCI bus. A driver kernel module has been developed by Gabriel Paubert[198] and allows two possible VME interaction strategies.

The simpler one is the *Memory MAPping* (MMAP) of the VME virtual memory area, corresponding to boards registers, into standard user-space memory. In this way no specific hardware driver is required and a user-space application can operate on the board simply accessing the MMAPed area. However this has two limitations:

1. No interrupt handling is possible, so boards must be *polled*[2] to know when there are data to be read.

2. Only sequential read-out is possible, i.e. data are read word-by-word.

Both these features lead to increased CPU overhead and slower performance.

To overcome them the other more complex possibility must be explored, which implies developing a kernel module device driver. This is layered upon the Universe driver and is therefore naturally able to register interrupts or other VME related resources. Moreover from within this module, it is possible to schedule the very efficient DMA (*Direct Memory Access*) read-out operation. This operation is performed by the Universe chip and transfers data in blocks directly from the VME boards registers to the PPC RAM without involving the CPU. DMA is possible only if the hardware to be read supports BLT *BLock Transfer* mode[3] and pays a fixed time overhead given by the scheduling operation that is independent of data size. For this reason it becomes of dramatic importance if a large amount of data has to be transferred, whereas for small data sets a sequential read-out might be more efficient.

In BOREXino either access philosophy has been used according to specific needs.

5.2.2 PPC flavors and interface

All parts of the software running on PPCs, including kernel modules specific to our electronics, have been programmed (in C) within the collaboration.

From the software point of view the 18 PPCs can be distinguished in 5 different "flavors":

1. *Trigger.* 1 PPC

2. *Laben.* 14 PPCs.

3. *Muon.* 1 PPC.

4. *Sums.* 1 PPC.

[2]The bus master periodically checks a register on the board. The board changes its status to signal a condition.

[3]Actually we could say that DMA is just BLT, seen from the bus master point of view.

5. *Leds.* 1 PPC (not daq related).

the last of which is used to control the OD calibration LEDs (chap. 8).

Every software flavor has been developed to read the specific hardware present in its crate but respecting a common command interface. Every flavor features a process named `Main` which acts, among the other things, as a command interpreter implementing the state machine of fig. 5.4: the process is always in a well defined state and commands can be issued to change this state. `Main` starts in BOOT_S state and opens a server TCP/IP socket (on port 5000) where it listens for incoming commands.

The list of flavor-independent commands implemented by all PPCs is reported in tab. 5.2. Every command has one or more states in which it can be accepted. Issuing a command in a state where it cannot be accepted generates an error. For example, a run can be started only if the PPC is in READY_S state. ABORT is always accepted.

In addition, every PPC implements his own set of flavor-specific commands through which for example hardware parameters can be set.

5.2.3 Muon flavor

The *Muon* PPC tasks are the most complex because they involve interaction with a miscellaneous set of boards, TDCs (sec. 4.3.3) and MTB (sec. 4.4.6), for both data readout and trigger operations.

In addition the CAEN v673 TDC boards have only 4 event buffers, therefore the efficiency in emptying them is a chief requirement to prevent data loss.

Upon these considerations a kernel module has been developed.

The kernel driver module

It was chosen to design a single driver for the whole system, rather than independent TDC and MTB modules. Combined operations are better handled in this way.

The driver is loaded at PPC boot, before the `Main` program is started. The presence of MTB and at least one TDC board is checked by accessing the VME addresses where the boards could be located. If the check fails (a bus error is caught) the loading operation aborts.

The other major operation performed at load time is the registration of resources, which proceeds very similarly to what would happen for a standard PCI block device, thanks to the functions exported by the Universe driver. These are the resources registered:

1. the memory region where TDC and MTB registers are located.
2. an IRQ (*Interrupt ReQuest*) handler function for the MTB interrupt line (IRQ4).
3. a DMA EOT (*End-Of-Transfer*) handler function.
4. the device itself with its implemented system calls:

   OPEN, IOCTL, MMAP, RELEASE;

   the other system calls are not implemented by design (including READ and WRITE).

Command	Parameter	Description	Initial state(s)	Final state
HWINIT		Performs all hardware initialization operations.	BOOT_S	IDLE_S
SWINIT		Loads parameters to boards according to selected profile.	IDLE_S	READY_S
START		Starts run, spawns data handling processes.	READY_S	RUNNING_S
STOP		Flushes buffers, stops run and data handling processes.	RUNNING_S, PAUSED_S	READY_S
PAUSE		Pauses run.	RUNNING_S	PAUSED_S
RESUME		Resumes run.	PAUSED_S	RUNNING_S
ABORT		Aborts run without flushing buffers.	any	BOOT_S
GET	HWID	Returns MAC address of PPC ethernet adapter.	BOOT_S, IDLE_S, READY_S	unchanged
GET	STATUS	Returns machine status as numerical code.	any	unchanged
GET	MACHINE	Returns machine status as string.	any	unchanged
SET/GET	CID	Sets/gets logical crate ID (0 to 16).	BOOT_S	unchanged
SET/GET	TADD	Sets/gets IP address to which data must be sent.	BOOT_S, IDLE_S, READY_S	unchanged
SET/GET	TPORT	Sets/gets IP port to which data must be sent.	BOOT_S, IDLE_S, READY_S	unchanged
SET/GET	TSEND	Sets/gets size (in events) of data packet to be sent.	BOOT_S, IDLE_S, READY_S	unchanged
REBOOT		Reboots the PPC.	any	BOOT_S
TEST		Tests the boards.	BOOT_S	unchanged

Tab. 5.2: *Flavor-independent commands implemented by* PPCs.

With the first of the above, the on-board registers are made visible in kernel-space and can be accessed from within the module. No user access is given, though. All operations on MTB and TDC different than data read-out, like parameter setting, status polling and command issuing, proceed by simple access to registered area.

The `open()` implementation, among various initializations, takes care of allocating a 1024-slot circular buffer for TDC events and of preparing the DMA vectors (i.e. lengths and flags are set). The memory allocation must be page aligned and is therefore done by direct kernel page request (i.e. `get_free_pages()`). Slots are 2 pages large (8KB) for a total 2MB area which will be deallocated at `release()`.

The read-out sequence

The data read-out sequence is shown in fig. 5.6. A user space process, at run START, performs a specific IOCTL operation, named `wait_event()`. The implementation of this sys-call enters an interruptible sleep on the registered IRQ. This function therefore doesn't return until the arrival of a BGT signal to the MTB, which generates the waited interrupt on line IRQ4. At this point the registered interrupt handler is called. This performs the read-out operation through a *Universe* lower level function. Actually the real job is delegated asynchronously to the so-called *Bottom-Half* (BH). In this way the handler itself, which merely schedules and queues the incoming triggers to be served, remains always free to be called upon a new interrupt generation, without any dead time.

The BH first reads the MTB word (i.e. the Trigger ID, sec. 4.4.6), then proceeds to read TDC buffers. As mentioned in sec. 4.3.3 there are three data transfer modes supported by the v673 modules. All the three have been implemented in the module to study the best possibility as a function of event occupancy[4].

Sequential access. Data are transferred one word at a time, no DMA occurs, no EOT handler function is required. The BH simply reads words accessing repeatedly 8 registers (1 per chip) and fills the allocated slots. The transfer is terminated by the presence of a word flagged with the last datum bit.

Block Transfer (BLT). In this case the BH schedules the DMA operations to transfer the full TDC buffers from specific board level registers. The v673 board has a BLT capability limited to 16 words per operation. For this reason, a vector of many transfers must be scheduled for the full length of the 8 chip event buffers (2052 words per board). The boards provide the valid data available plus invalid data up the full scheduled BLT size. The EOT handler function is called only at the end after data from both boards have been read.

Block Transfer with Bus Error. If enabled, the TDC module can issue a VME Bus Error (BERR) at the end of valid data. This interrupts the DMA operation and calls the EOT handler immediately, avoiding the transfer of invalid data. Two DMA scheduling and handling occur in this case (i.e. one per board).

[4]Commands to switch data transfer mode have been provided to the user as IOCTL calls, for greatest flexibility.

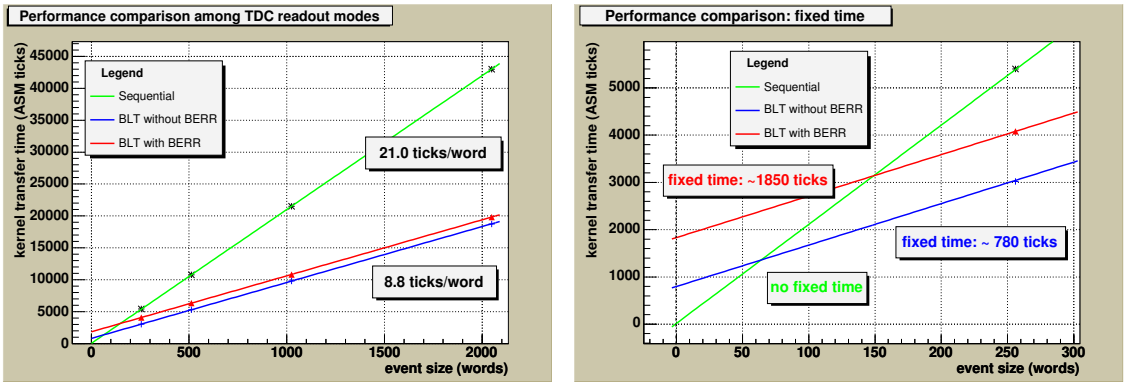

Fig. 5.5: *Performance comparison of the three different* TDC *read-out modes implemented. On the right a blow out of the zero crossing region.*

If a BLT occurred, the EOT handler goes through the data just read to check consistency of event number words with the MTB word. Moreover it determines the size of valid data and stores this information in a slot variable for the user. Eventual invalid data are discarded in this way. In case of sequential read-out the checks and the size evaluation are done directly while reading the words.

Sequential read-out vs. Block Transfer: a performance comparison

In order to understand which read-out mode is the most convenient in our case, the module performance was bench-marked in the three cases (fig. 5.5). This was possible using the hardware counter of the PPC, accessible through ASM directives[5]. One tick of this counter corresponds to $\sim 60ns$.

- Sequential access: $21.0 ticks/word$. No fixed time involved.
- BLT: $8.8 ticks/word$ plus fixed time:
  - without BERR. Single DMA scheduling: $780 ticks$.
  - with BERR. DMA scheduling and BERR handling for 2 boards: $(780 + 130) \times 2 \simeq 1800 ticks$.

So the time required to transfer a word (4 bytes) in a DMA operation is definitely smaller than the time required in sequential read-out. The fixed time to pay for this is quite limited, if a fixed amount of words to be transferred can be accepted (padded with invalid data if event is smaller, truncated if event is bigger). The more sophisticated BLT with BERR option, which always transfers in DMA the right event size, pays a relatively large fixed time overburden. The choice is therefore ultimately related to the typical event size, which in turn depends on the trigger type:

1. muon triggers. Relatively low occupancy, ~ 200 words, according to simulations.

[5]Inline Assembly instructions

2. timing laser with LEDs at high intensity ($> 95\%$ efficiency). ~ 500 words (2 edges $\times$ 208 channels + 8 integrity channels + 8 event ID words).

3. timing laser with LEDs in single-pe mode (5% efficiency). ~ 50 words.

4. calibration, random, laser266, laser355, neutrino (ID trigger). Very low occupancy, ~ 24 words.

In a standard run the trigger rate will be by far dominated by ^{14}C events, visible as *neutrino* triggers, letting the sequential access mode be the preferred one. Muon events are rare enough ($\sim 0.1Hz$) to be handled properly in this read-out mode. In laser runs aiming to timing calibration (i.e. LEDs at low intensity) sequential access is also the most convenient option. Currently sequential access is the default option. In case of laser runs aiming to charge calibration (i.e. LEDs at high intensity), it may be worth switching to BLT, either limited to 512 words or featuring BERR.

User access to the memory slots is provided through implementation of MMAP, where the area is mapped to user space. However, since MMAP did not prove to be fully reliable under all run conditions, it was temporarily disabled and a simple copy to user space slots is performed. A specific function is in charge of this task and is called by the IRQ handler Bottom Half (sequential access) or by the EOT handler (BLT). The overhead of this additional copy was measured to be $\sim 1.1 tick/word$, i.e. well tolerable. Recovery of the full MMAP functionality will be done in the future as a lower priority job.

The user-space processes

The `Main` program is started at BOOT, after loading the kernel module. Its first operations involve opening the device and attaching the listening socket for incoming commands.

At HWINIT a set of hardware specific parameters are sent to the TDC boards:

1. Working mode: COMMON STOP.

2. Data read-out mode: event request.

3. Buffer time depth: 13 bit ($\sim 8.5\mu s$).

4. Edge type: both.

5. Maximum number of edges: 16.

6. Channels enabled: all.

These commands are served through independent IOCTL system calls. The driver implementation of the sys-calls actually writes to the proper board registers.

At SWINIT two shared memory areas are created:

- `Com` SHM. A service configuration area for sharing parameters among the different processes.

- `Data` SHM. A data storage segmented in event slots and handled as a circular buffer.

At START `Main` receives a set of parameters regulating the run (TADD, TPORT and TSEND described in tab. 5.2) and stores them into `Com` SHM. Immediately after, two processes are spawned: the `Reader` and the `Sender` which both attach the two SHMs.

The `Reader` reserves a semaphore and issues the IOCTL sys-call described above going to sleep until this one returns. When this happens, an event has just been read by the driver into a memory area MMAPed into user space. The `Reader` then copies the event to the first available slot in the `Data` SHM, thereby incrementing an internal event counter.

The `Sender` opens a socket connection to a remote process according to the TADD and TPORT parameters, then checks the status of the semaphore. This operation does not return until the `Reader` unlocks the semaphore. When the `Reader` reaches TSEND events (default 30) in its internal counter it unlocks the semaphore. The `Sender` then wakes up, reads the events packet from the `Data` SHM and sends it over network.

At STOP the `Main` issues a SIGTERM signal to its children. This is caught and handled in both cases by a proper signal handler. The `Reader` flushes the eventual current event, unlock the semaphore regardless of event count, releases resources and exits. The `Sender` sends the last packet (probably below TSEND events), releases resources and exits. This clean exit brings the system into READY_S for a new START.

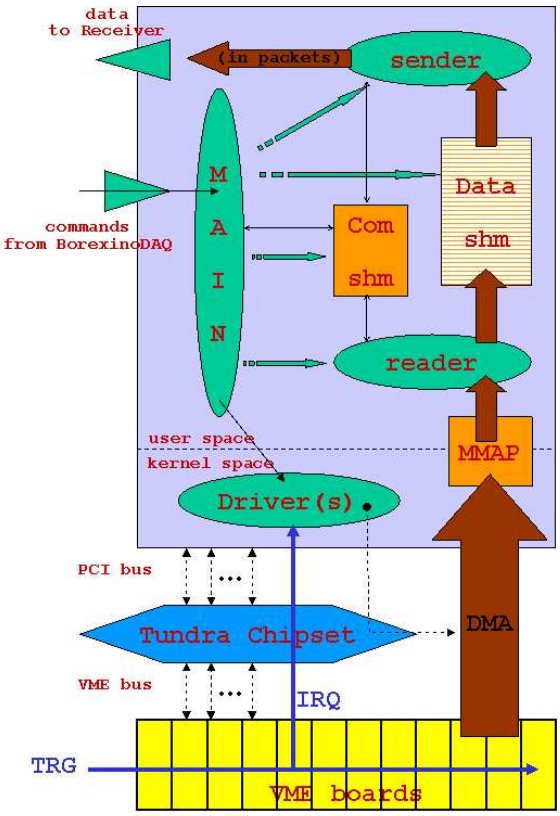

Fig. 5.6: *Block diagram of OD PowerPC software.*

Shared memories, signals and semaphores are standard IPCs (*Inter-Process Communication*) tools[199].

The communication with the driver described above happens in reality through a large library. This was developed to wrap the sys-calls into higher level functions and handle internally the complexity of dealing with the device.

User-space precesses run asynchronously from hardware triggers and are queued by the Linux scheduler in the normal CPU duty cycle. Nevertheless their performances have been also bench-marked with half full events[6]:

- The `Reader` takes $\sim 550 ticks/event$ unless it is the last in the packet, in which case $\sim 70000 ticks$ are required for IPCs.

[6] 2 edges per channel in about 100 channels

Parameter	Description
PULSEGATE	Relative time of the gate pulse with respect to trigger.
GATEWIDTH	Width of the gate pulse. $\sim 6.5\mu s$.
CALIBMAX	Number of precalibration events. Default 1000.
CALIBPRE	Pre-scale factor to be applied to input I7 (timing unit). Default 100.
LASER394	Enable to timing laser run.
LASER355	Enable to calibration laser run.
LASER266	Enable to calibration laser run.
MTB	Enable to OMT triggers in standard run.
TOTC	Enable to TOTC muon triggers in standard run.
RANDOM	Enable to dark noise run.
THRESH1	Hardware threshold for comparator.
THRESH2	Additional software threshold.

Tab. 5.3: *Trigger specific parameters for* [SG]ET *commands.* SET *is not available in* RUNNING_S. *For physical meaning refer to sec. 4.4.*

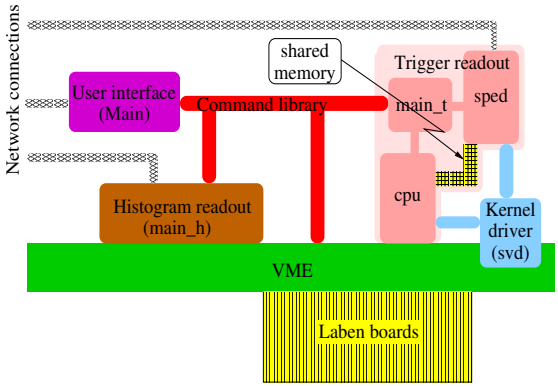

Fig. 5.7: *Schematics of the Laben* PPC *read-out software[246].*

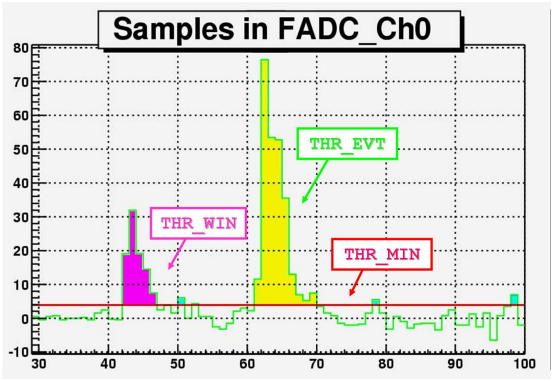

Fig. 5.8: *The three thresholds of the* FADC *online data reduction algorithm[243].*

- The `Sender` takes $\sim 31000 ticks$ to send a packet of 30 events. This value is the optimized one for the buffer of the PPC ethernet adapter. Changing it in either direction increases the time required per event significantly.

In these conditions the system was tested to sustain $500Hz$ of periodic trigger for $\sim 10^7$ events.

5.2.4 Other flavors

A multi-process architecture is used also for the Trigger, Laben and Fadc PPCs. This includes a `Main` and at least two more processes with reader and sender functions, but the different developers have implemented them according to specific hardware needs and personal design choices.

Trigger. Surely the simplest of the PPC flavors, it issues trigger parameters to the BTB

(tab. 5.3) and reads the trigger record (sec. 4.4.1). No driver required.

Laben. 20 Laben boards per crate must be read. A kernel driver is used with an acquisition philosophy similar to the muon one, though no trigger board is present here and the interrupts listened to come from the Laben boards themselves (fig. 5.7). A forth process reads the histograms created on the Laben boards with the out-of-gate hits and sends them to the histogram server (sec. 5.5). Among the parameter settings available, the most important are the channel thresholds (sec. 4.2.3).

Fadc. FADCs produce an enormous amount of data ($\sim 400KB/ev$[7]), most of which are just baseline and noise samples. An online zero-suppression procedure is therefore present that isolates windows around physical events using the analog sum channel (sec. 4.6). It works in three steps:

1. Whenever the sum level crosses parameter THR_WIN the integral of the region above is computed.
2. If the integral crosses parameter THR_MIN there is a candidate window.
3. The candidate can be validated if one of the two is verified:
   (a) The integral crosses parameter THR_EVT.
   (b) There is another candidate within ± TIMEOUT_READ.

   and in this case samples within the window are acquired for *all* channels.

The real energy threshold of the event is THR_EVT, however delayed coincidence can be looked for also at lower energies (fig. 5.8).

This double threshold system reduces data flow but is clearly CPU consuming, which results in a reduced sustained rate. Evaluation of optimal parameters values accounting for both physics and DAQ considerations is a complex ongoing task[243].

5.3 Run Control and Web interface

The DAQ supervisor program is named BorexinoDAQ and runs on `bxbuild` (sec. 5.1). It is a C++ server running at any time[8].

BorexinoDAQ wraps the state machines of all PPCs in a single consistent state machine (fig. 5.4). In other words when the user issues a command that changes the state of BorexinoDAQ, this one will in turn forward the command to all PPCs and keep them aligned. Communication to the PPCs `Main` processes occurs through socket connections to their command port 5000 (sec. 5.2.3). Connections are opened (closed) before (after) every command to minimize possible interferences.

Communication with the user occurs through web technology, a widespread design choice in BOREXino. The server implements a CORBA[9] interface, a protocol to share code execution over network. In other words a remote process (with the right key) can execute

[7] 4096 8-bit samples × 101 channels

[8] A daemon is in charge of restarting it upon eventual failures.

[9] *Common Object Request Broker Architecture*, a wide-spread protocol of distributed computing[201].

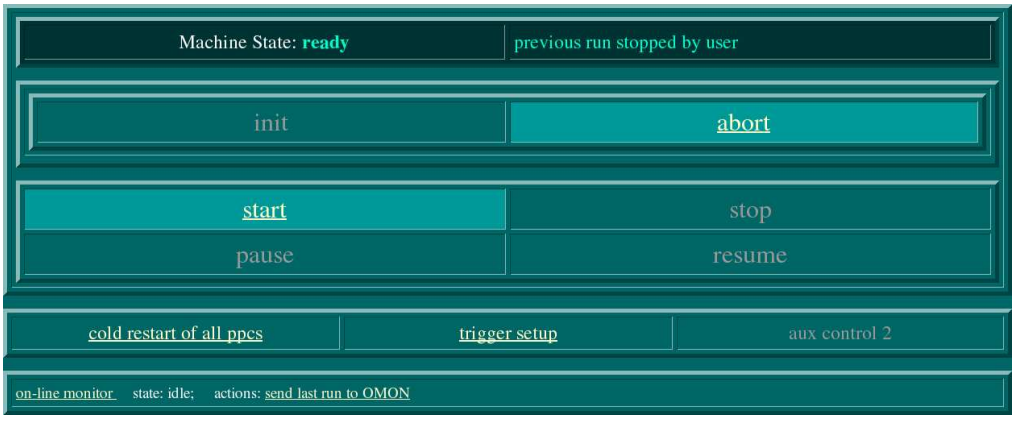

Fig. 5.9: *Snapshot of the main run controller page (detail).*

functions of BorexinoDAQ. In our case the remote processes are a set of CGI (*Common Gateway Interface*) scripts written in Perl and executing the web server `bxweb`.

The user logs into the DAQ web page, where a few sections are present.

1. Run Controller (described here)
2. Config Manager (sec. 5.6).
3. Online Monitor (sec. 5.5).
4. System Monitor (sec. 5.5).

The *Run Controller* is a set of pages where the user can issue commands to the overall state machine driving the data taking (fig. 5.9). For example, clicking the START button executes a CGI script that calls a CORBA function of BorexinoDAQ, which in turn serves the command starting all PPCs (among other tasks).

All the parameters to be sent to PPCs at initialization are in the database. The CGI scripts that serve HWINIT and SWINIT commands retrieve them and send them to PPCs.

Apart from the web interface, a child process of BorexinoDAQ gathers all its messages and composes the text console that can be seen in fig. 5.10. The `bxbuild` display constantly shows this information screen allowing an additional lower level monitor of the ongoing run which is fast and web independent.

5.3.1 Trigger Setup Page

When the system is in READY_S the Run Controller allows access to the Trigger Setup Page (fig. 5.11).

Here the user can configure trigger parameters (sec. 4.4). For example the BTB and MTB comparator thresholds may be changed, as well as the parameters CALIB_MAX and CALIB_PRESCALE.

Most important is the selection of the run mode:

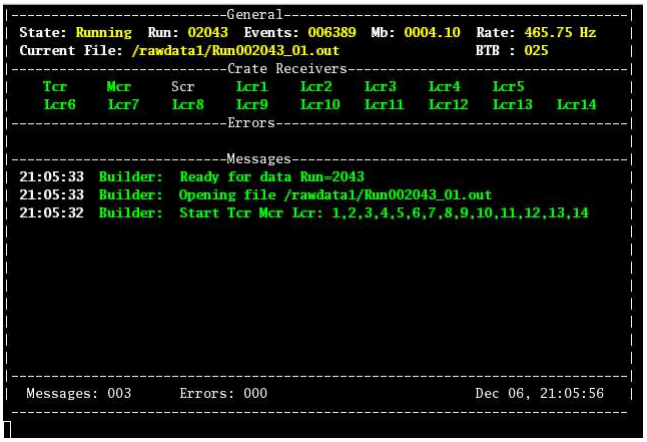

Fig. 5.10: *Snapshot of the BorexinoDAQ text console.*

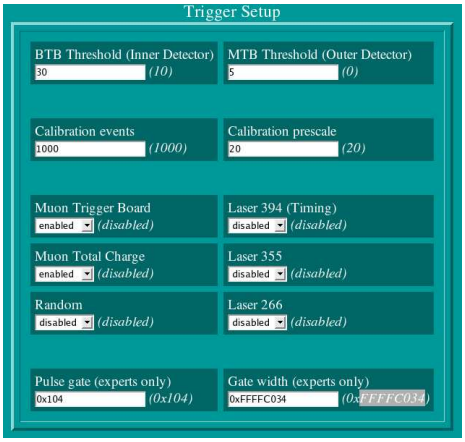

Fig. 5.11: *Snapshot of the Trigger Setup Page (detail)[213].*

1. Standard runs. The BTB triggers from the comparator. Calibration, random and laser394 triggers are served pre-scaled ($2Hz$ each). OMT and TOTC triggers can be enabled.

2. Laser394 runs. Pre-scaling is ignored and laser394 triggers are served at $200Hz$. This is what is usually referred as *timing laser run* or simply *laser run*.

3. Dark noise runs. Pre-scaling is ignored and random triggers are served at $200Hz$.

4. Calibration runs. Pre-scaling is ignored and calibration triggers are served at $200Hz$.

5. Laser266(Laser355) runs. The $266nm(355nm)$ laser is on and triggers are received at $200Hz$. The laser can be in either radial or oblique position (sec. 2.2.4).

5.4 Event building

The event building procedure is shown in fig. 5.1.

At START BorexinoDAQ creates a set of 17 shared memories, one for every PPC. These are organized in event slots and handled as circular buffers.

Immediately after, BorexinoDAQ spawns 17 receiver processes belonging to 4 flavors, as the PPC softwares. Each receiver program attaches its own shared memory, opens a server socket on a dedicated port (10000+n, where n is the receiver number from 0 to 16) and waits. BorexinoDAQ also spawns the `Builder` process which attaches all the shared memories.

The last action is the issuing of the START command to PPCs, the trigger one coming last.

Whenever an event packet arrives to a receiver, this writes it to its shared memory in the next free slot. The `Builder` periodically checks the status of the shared memories.

Whenever it finds an event complete (i.e. present in all SHMs) it reads all its chunks and marks the slots as free. The data read are organized into rawdata format, completed with a few words of general information (run and event number, daq status, cpu time, ...) and written to file. In the new configuration this occurs over the optical link directly to the data storage in the external lab.

5.5 Online Monitor

During data taking it is often desirable to monitor the detector's performance and to be immediately aware of any possible problem. To achieve this task a complex online monitor system has been developed.

The main process is the histogram server running on `bxweb`. This is actually the offline reconstruction code[10], run in a special mode that features two major differences:

1. Rawdata are accepted through a socket connection, rather than read from file. The builder sends a programmable fraction of events ($\sim 10\%$) to the open socket.

2. ASCII histogram files are produced instead of the ROOT file. A set of web pages and CGI scripts is in charge of displaying the histograms produced.

Due to this double use of the same program a large amount of algorithms (like data decoding) had to be implemented only once. Moreover any desirable reconstruction feature can be activated and histogrammed, even position and energy reconstruction, provided that enough CPU power is available for the programmed fraction of events.

Among the large amount of information available, these are the most basic parameters:

1. PMT dark rates (from random triggers). Dead channels are immediately visible.

2. Time and Charge for each channel. Misalignments and drifts in the gain can be detected in this way.

3. Trigger types. Of basic importance to monitor the trigger flavors.

4. Event coincidence times. Reflections, re-triggers and other artifacts can be easily spotted in this way.

The dark rate information can be displayed in many different geometries. For ID the standard one is the sphere projected on cylindrical surface and opened along a meridian (fig. 5.12). Here every PMT is represented by a small square, whose gray shade represents its dark rate. Alternative sphere projections methods are available that allow to inspect different possible geometrical patterns. Moreover the channels could be ordered for front-end boards, digital boards and other logical groupings to identify possible electronic failures or misbehaviors (e.g. cross-talk effects). For the outer detector a similar projection is done for PMTs mounted on the SSS, while PMTs on the floor are simply reproduced below (fig. B.1). All the maps for ID and OD are interactive: clicking on one of the PMT squares produces the page with histograms relative to that channel (fig. B.2). In addition a few global histograms are made available (fig. B.3).

[10] Currently the old `bx_rec`, in the near future the new `echidna` (chap. 7).

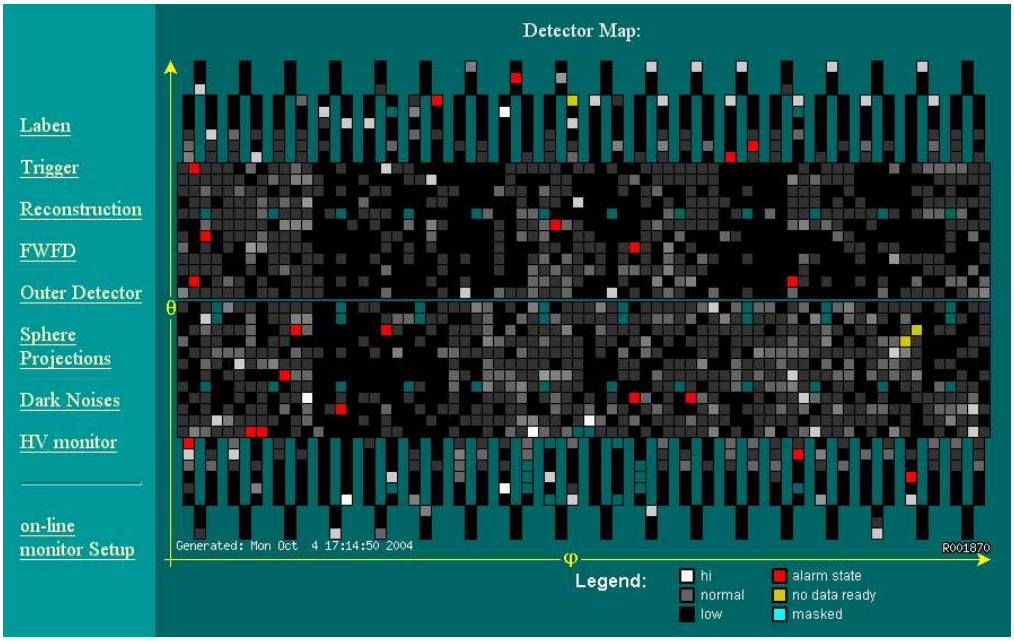

Fig. 5.12: *Snapshot of the Online Monitor main ID map[213] taken during Air Run 9 (chap. 6) with the full detector on.*

5.6 DataBase and Profile Manager

Due to a precise design choice that turned out to be extremely successful, in BOREXino all software components of different areas (online, offline, simulation, fluid handling, ...) share information using a network DataBase (DB) system. A single server application is used running on `bxdb` (sec. 5.1).

The choice fell on PostgreSQL a freely distributed package which enforces the SQL (*Standard Query Language*) syntax. APIs (*Application Program Interface*) for this communication protocol are available for most programming and scripting languages including C/C++ and Perl, widely used in BOREXino. In this way instead of having hundreds of configuration, output and log files around with different application having to check each other's files, every application develops its own DB access routine and reads/writes over TCP/IP whatever information needs to be shared or stored.

Though we often simply talk about "the database", the server actually hosts a collection of them, each one grouping tables holding logically related information. The hierarchical organization of the database collection is pretty straightforward and is shown in fig. 5.13 together with the lists of the 8 BOREXino databases and the application families that most often access each one of them. While reading access is never limited, writing permissions are instead granted to specific applications and users, which are usually unique to every single table in order to avoid interferences and enforce data security.

The key database for online software is `daq_config`, whose tables are:

1. `CrateMapping`. Network addresses and ports used by PPCs.

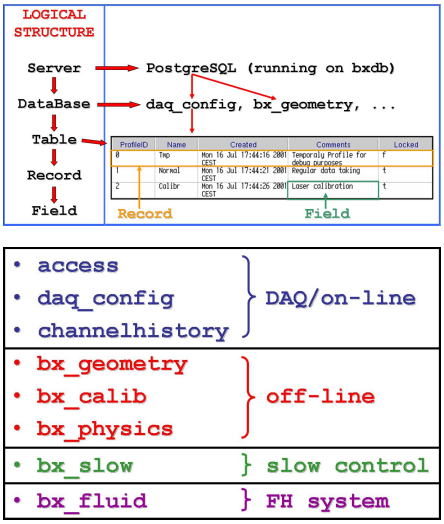

Fig. 5.13: *DataBase structure (up). BOREXino DB collection (down).*

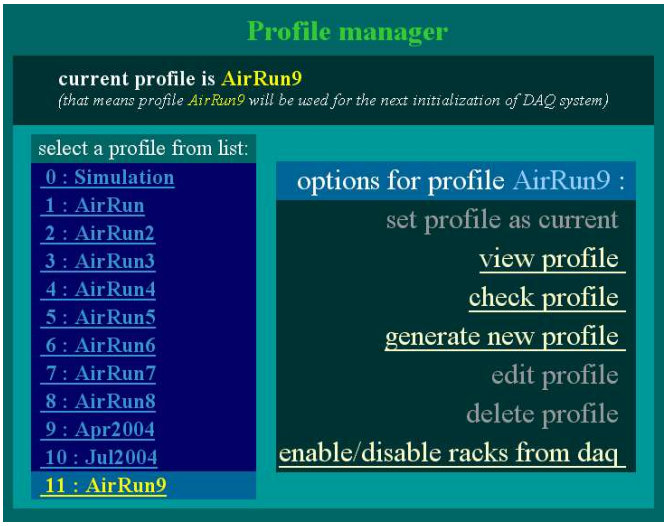

Fig. 5.14: *The Profile Manager page in the BOREXino Web interface.*

2. `LabenBoardSetting`, `LabenChannelMapping`, `LabenChannelSetting`. ID channel cabling information through the electronic chain and parameters to be sent to PPC at [HS]INIT.

3. `MuonChannelMapping`, `MuonGeneralSetting`. Cabling and parameters for OD.

4. `SumsBoardSetting`, `SumsChannelSetting`. Cabling and parameters for FADCs.

5. `Run`. Basic run information: date, events, duration, type, shifter's comment, files produced, ...

6. `Profile`. Basic profile information: date, comment, trigger type codes, ...

7. `DataStorage`. File location and backup information for every run.

For example BorexinoDAQ is in charge of writing table `Run` during data taking.

A very important concept in the DAQ of BOREXino is the *profile*. A given PMTs & electronics overall status is assigned a profile ID number and all runs taken in these conditions are associated to this number. Whenever some changes are introduced (new PMTs installation, board replacements, cabling rearrangements, different electronic settings, ...) a new profile is introduced and all DB tables that are indexed with profile ID are updated with a new set of records for the new profile.

The *Profile Manager* (fig. 5.14) is the DB web interface that can be accessed from the online web page (after authentication). It allows to check available profiles and decide which to use for DAQ, as well as the guided creation of a new profile and its validation.

The reconstruction code (or any other data consumer), using the profile ID key, can load from DB the exact detector configuration at the time the run was taken.

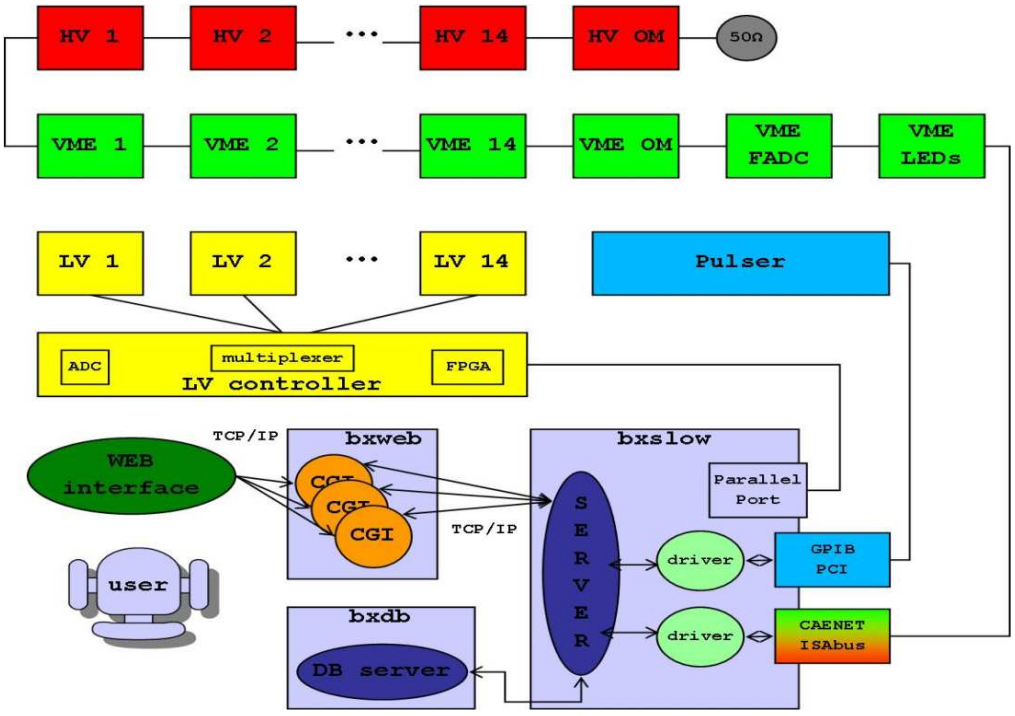

Fig. 5.15: *Schematics of the Slow Control System.*

5.7 Slow Control

The *Slow Control System* is a DAQ-independent remote monitor and control system for the following hardware devices:

1. 15 HV mainframes (14 ID + 1 OD).
2. 21 VME crates (1 trigger + 14 ID + 1 OD + 4 FADC + 1 LEDs).
3. 14 ID front-end power supplies, named *Low Voltages* (LV).

Its main functions can be listed as follows:

- Monitor
  - Read and display the status and the alarms of any device.
  - Read and display V/I of the VME and LV power lines.
  - Read and display the HV for every channel and the board current consumption.
  - Read and display temperatures and fan speeds of the VME crates.
- Control
  - Turn devices ON/OFF and issue RESET.
  - Set VME fan speeds.

  - Set VME current thresholds for different power lines.
  - Set HV values.
  - Set HV board current thresholds.
  - Set additional HV parameters (ramp up/down, Vmax, ...).

- DB interface
  - Periodical and alarm-triggered dump to `bx_slow` of all values.
  - Load dark room HV values from `bx_geometry` to mainframes.
  - Restore HV values from `bx_slow` to mainframes (key: time or run).

5.7.1 Hardware setup

The layout of the Slow Control System is shown in fig. 5.15.

The VME crates and the HV mainframes are all equipped with CAENet device controllers. CAENet is a bus protocol[11] that allows to control up to 99 devices of different nature. Devices are connected with standard LEMO coaxial cables in a single serial line and are given a numeric address that identifies them uniquely. The line is 50Ω-terminated and is mastered (in our case) by an ISA-bus card mounted on `bxslow` (sec. 5.1), for which a custom driver was developed[202].

LV units are custom made and do not support CAENet protocol. Instead they can be remotely controlled through RS232 serial connection running on a multi-pin flat cable. To control the units in this way a hardware controller has been assembled. It features a fast ADC, a multiplexer, a programmable logic (FPGA) running a custom firmware and interfaces to all 14 flat cables. Voltage and Current of the $\pm 14V$ power lines are monitored. The controller can be accessed through a PC parallel port and therefore it requires no specific kernel module.

In addition to the currently handled devices, in the near future it is foreseen an upgrade to include a programmable pulser through a GPIB controller.

5.7.2 Software structure

A server application runs continuously[12] on `bxslow` and accepts commands through multiple TCP/IP socket connection. In this way different client processes or instances can issue commands during a run without interference. A web interface has been developed as the main client, but others are also possible. The server output is attached to one of the text consoles of `bxslow` and visible to the shifter. Here messages are printed and emergency commands may be issued, in the very rare case of a network failure.

A detailed log file is also available to reconstruct the history of a potential hardware problem, while a few configuration files determine which hardware elements are enabled.

[11] Proprietary, developed by CAEN.

[12] A daemon checks its presence and restarts it upon failures.

5.7.3 Server syntax and available commands

Commands (case insensitive) to the server are to be composed by three compulsory tokens and variable numbers of optional tokens, as follows:

TARGET COMMAND MODIFIER [KEY=W]
[CRATE=X BOARD=Y CHANNEL=Z] [LCHANNEL=L]
[VALUE=V]
[RUNMIN=R_1 RUNMAX=R_2] [TIMEMIN=T_1 TIMEMAX=T_2]

where:

- TARGET = HV, VME, LV, SYS. Compulsory.
- COMMAND = DO, SET, GET or QUERY. Compulsory.
- MODIFIER = INIT, ON, OFF, RESET, MONITOR, ... (for DO);
  V0SET, VMON, I0SET, ... (for [SG]ET and QUERY). Compulsory.
- KEY = a numeric security key received at logon (if enabled).
- CRATE=X BOARD=Y (HV only) CHANNEL=Z (HV only) specify, if required, the subsystem to which the command is referred. 0=ALL.
- LCHANNEL=L (HV only) where L is a logical channel: 1 to 2214 for ID, 3001 to 3216 for OD. An alternative way to specify command sub-target. It is internally converted to the three values above by querying `bx_geometry` database.
- VALUE=V (SET only). The value to be set for the parameters specified as MODIFIER. Accepted ranges depend on specific parameter.
- RUNMIN=R_1 RUNMAX=R_2 or TIMEMIN=T_1 TIMEMAX=T_2 (QUERY only). Run numbers or timestamps to be used when reading `bx_slow` database.

Parsing includes checking that all values supplied are within meaningful ranges. In case parsing fails, an error code is returned indicating which token was not accepted.

A complete reference list of the about 120 commands implemented is given in app. C.

5.7.4 Server implementation

The server is programmed in C++ following an Object-Oriented design. The main (static) classes are shown in fig. 5.16.

Initialization

The main program creates a few singletons[13]:

[13] A design pattern for static objects[210].

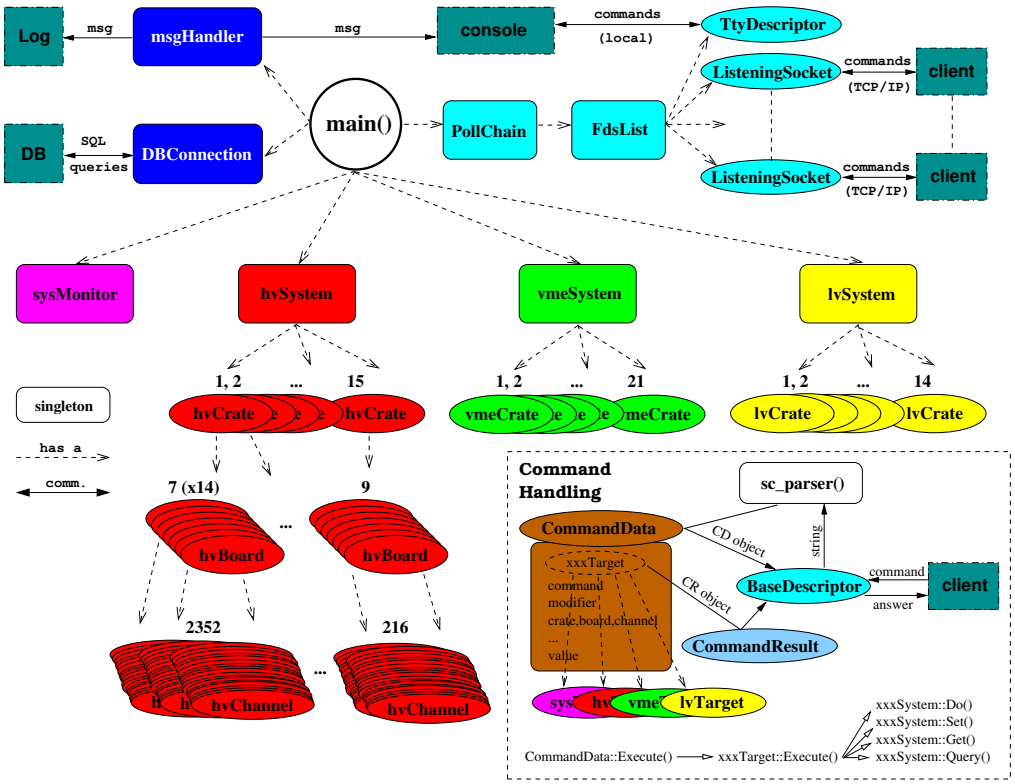

Fig. 5.16: *Schematics of the Slow Control Server structure. In the dashed corner the command handling procedure (`BaseDescriptor` is a base class for tty or socket descriptors).*

1. `msgHandler` takes care of dumping to console and to log file messages that exceed a programmed level[14] (usually `info` level).

2. `DBConnection` is in charge of establishing a socket connection to database, whenever a command execution requires it, and to perform all the proper hand-shaking procedure.

3. `sysMonitor` is in charge of performing programmed hardware checks and to write parameters to DB (`bx_slow`).

4. `hvSystem` represents the whole HV system holding an array of `hvCrate` objects, corresponding to the physical mainframes. These in turn hold arrays of `hvBoard` objects which then similarly hold arrays of `hvChannel` objects.

5. `vmeSystem` represents similarly the whole VME system holding an array of `vmeCrate` objects that correspond to the physical crates.

6. `lvSystem` is the same for the LV system, with `lvCrate` representing the front-end power supply units.

[14]Standard message levels are used: `debug, info, warn, fatal, panic`.

7. `PollChain` polls over a list of opened file descriptors, contained in the class `FdsList`. `TtyDescriptor` is the file descriptor corresponding to the local text console of `bxslow`, while all network clients are served by a `ListeningSocket` object.

The constructors of the HV, VME and LV system objects read the respective configuration files and create sub-objects for hardware devices that are enabled. Units are asked to identify themselves providing their serial numbers, if an enabled unit doesn't answer an error condition is risen. At the end of this initialization the main program simply asks the `PollChain` object to start polling. Nothing more happens until a command is received.

Command handling

Upon receiving a command, the socket (or the tty) object invokes a parser[15], passing it the command string. If parsing is successful (i.e. the user respected the syntax) a `CommandData` object is returned by the parser.

The class `CommandData` holds a "target" object that can be of type:

`hvTarget, vmeTarget, lvTarget` or `sysTarget`

depending on the TARGET addressed by the user. This object in turn has a method named `Execute()` that will start the real work. According to the value of COMMAND, a specific method of the relative `xxxSystem` singleton is selected. According to the value of MODIFIER, this may or may not require to descend into analogous methods of one or more `xxxCrate` object (for HV also `hvBoard` or `hvChannel` methods may be called).

For the hardware related operations (most of them), when the cascade ends, the final method calls a CAENet library function that reads or writes the right words to the CAENet device. The CAENet library is a C library developed aside the server to wrap the CAENet bus syntax and its hand-shaking protocol. All this remains in this way hidden in the library and decoupled from the server logic. LV commands benefit instead from an analogous library for the communication with the multiplexer unit (sec. 5.7.1).

The `xxxTarget::Execute()` method returns a `CommandResult` object holding an error code (0 if everything went fine) and any requested parameter value (if command was GET or QUERY). The tty/socket descriptor class will extract this information and stream it to the client.

5.7.5 Web interface

The Slow Control Web Interface is a set of pages and CGI scripts coded in Perl that allow the user (shifter) to visualize the status and parameters of the three physical subsystems and to issue commands to them. As BOREXino has to run for years, a large number of collaborators will play a role as shifters, in most cases knowing nothing of the slow control implementation. The Web Interface was developed to be as friendly as possible to this class of users and to allow them full control just through simple mouse clicks.

[15] The stand-alone function `sc_parser()`.

The design principle is the following. Most of the pages displayed depend upon the status of the hardware, for example the graphics reflects the number of crates detected and their status or numeric information are to be displayed. For this reason, most of the pages cannot be just static HTML documents. In fact clicking a link, in all but the simplest cases, fires a Javascript applet that checks if the entered parameters are correct (form elements are often present in the page) and then calls a CGI script. The script composes one or more commands with the right syntax and sends them to server through socket connection. Using the information returned, the script generates *on-the-fly* the HTML code and displays the new page to the user.

The information displayed is refreshed automatically after any operation is performed or after a user request (clicking the browser refresh button). In this way the display status is kept always synchronized with the hardware.

The client-server socket connection is established upon login in the main page and held until logoff. If security keys are enabled the connection is exclusive, i.e. a new user connecting will logoff the others to avoid interference.

The main page shows a summary of the detected hardware and the general status of the three subsystem, through virtual LEDs that can be RED (OFF), GREEN (ON) or YELLOW (ALARMED). In the top frame of the page three hyperlinks lead to the pages related to the subsystems.

VME control page

The top section of the frame (fig. 5.17) is occupied by the crate array[16] showing the most important pieces of information:

1. Crate name and logical ID number.
2. Status LED. Can be RED (OFF) or GREEN (ON).
   It may be clicked to toggle the status.
3. Alarm LED. Can by GRAY (no alarm) or YELLOW (ALARMED).
   It may be clicked to issue a CLEAR(ALARM)
4. The temperatures of the Crate (sensed at fan tray top) and of the Power Supply.
5. Arrow link to *details* frame.

The left menu frame provides buttons to issue ON/OFF/RESET/CLEAR(ALARM) commands to the full system. The button PLOT opens a widget where the user can ask a plot of a power line Voltage (or Current) for all the crates. The button QUERY starts a similar tool but for a given time interval in the past using DB information. This goes anyhow through server as a QUERY command: no direct DB connection is performed by the interface.

[16]The server returns information only for crates enabled in its configuration file. Disabled crates are not shown at all.

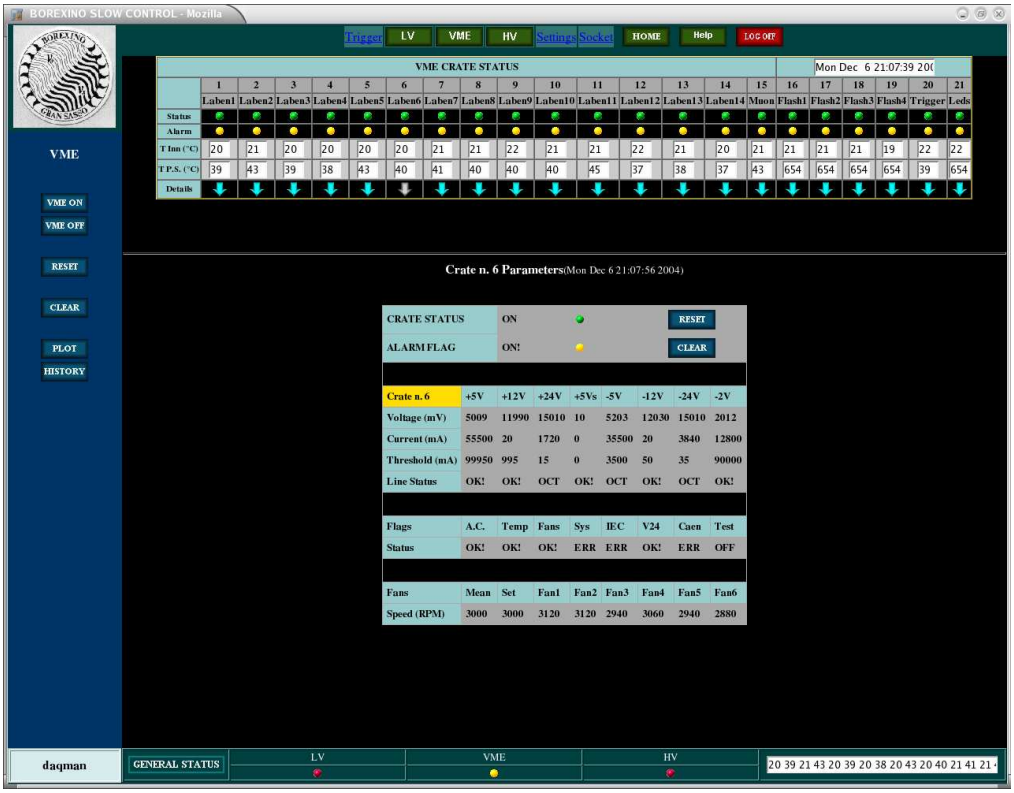

Fig. 5.17: *Snapshot of Slow Control Web Interface for the* VME *subsystem.*

More detailed information on a specific crate is accessible through the *details* arrow link. This generates a lower frame where RESET and CLEAR(ALARM) buttons for the single crate are provided. It follows a summary of Voltage, Current and the set Threshold for the 8 power lines as well as the line status code returned by the crate (ok, under-voltage, over-current, ...). Below a few more technical flags and the speed of the six fans are displayed.

HV control page

The HV control page is divided horizontally in 4 frames. The top one contains the array of the mainframes available (i.e. enabled in server config file) with the following information:

1. Crate name and logical ID number.
2. Power LED. Can be RED (OFF) or GREEN (ON).
   Can be changed acting with a physical key on the mainframe.
3. Enable LED. Can be RED (disabled) or GREEN (enabled).
   Status of the physical HV enable switch on the mainframe.
4. HV status LED. Can be RED (no HV) or GREEN (HV in at least 1 channel).
   Can be clicked to toggle the whole crate HV status.

Fig. 5.18: *Snapshot of Slow Control Web Interface for the* HV *subsystem.*

5. Alarm LED. Can be GRAY (no alarm) or YELLOW (ALARMED).

6. Arrow link to *details* frame.

To the left of the array ON/OFF buttons allow to toggle the status of the system as a whole.

The arrow links populate the lower three frames in cascade with crate, board and channel *details* frames. Each element shown is given a clickable status LED an arrow link to the lower level and a list of detected parameters (V0SET, I0SET, VMON, TRIP, ...). Some of the values shown may be changed and sent to hardware pressing SET button.

On the left menu frame PLOT and QUERY button are present as in the case of VME.

LV control page

Similar but simpler than the two pages described above, the LV page reports the array of the Power Supply units, with clickable status LEDs, optional *details* frames with V/I information of a specific unit, global ON/OFF buttons, PLOT and QUERY facility.

Unfortunately no ALARM condition is produced by the hardware, so it will be implemented as a set of software thresholds on the V/I values of the two unit lines.

Chapter 6

Test of the System: *Air Runs*

The BOREXino detector was turned on for the first time in February 2002 for the first of a long series of *Air Runs*. These are data taking periods with a wide program of tests, performed with the detector filled just with (clean) air.

The detector was gradually brought into its final configuration and during the last air runs the nitrogen occupying the SSS volume was the only remaining difference with the forthcoming regular data taking.

In this chapter the main achievements of these campaigns regarding both Inner and Outer Detectors are reported.

6.1 Programs and chronology

Up to now 9 Air Runs have been performed (tab. 6.1) with about 10^8 events (100GB) written to disk in various run conditions. The goals and achievements are listed here in random order:

1. Accurate test of the PMT status for ID and OD, in the last case on a channel by channel basis. Test of the PMT powering system and fine tuning of the HV values where needed.

2. Test of the full electronic chains of the three subsystems (laben, muon, fadc) and debugging of the hardware. Addressing of problems, development and test of the precalibration procedure to solve them.

3. Definition, implementation and test of the trigger logic (sec. 4.4) and of the interplay among subsystems.

4. Debugging and test of the online software including DAQ, OMON, Slow Control, DB collection, scalers acquisition, ...

5. Test of the optical calibration systems for ID: timing, radial and oblique lasers. Definition and test of the time and charge calibration procedures for ID[1].

[1] Calibration of OD with LED system (chap. 8) will take place at the next air run, as the long work on the LEDs was finished only recently.

Nr.	Date	Measurement Types	Main Results
AR1	Feb 2002	Pulser/Dark Noise	First PMT debugging
AR2	Apr 2002	Pulser/^{222}Rn source	PMT debugging and electronics checks
AR3	Jun 2002	Pulser/Laser	Identified a time measurement problem
AR4	Aug 2002	Pulser/Laser	Solved the time measurement problem
AR5	Dec 2002	Laser/^{210}Po source	Identified a charge measurement problem
AR6	Apr 2003	Outer detector only	First debugging of the outer detector
AR7	Aug 2003	Dark Noise/Laser	Solved the charge measurement problem
AR8	Dec 2003	Laser/^{222}Rn source	Good energy and position performances
AR9	Aug 2004	Dark Noise/Laser	Complete detector run

Tab. 6.1: *List of the BOREXino Air Runs.*

6. Acquisition of a real data pool for offline software development (chap. 7). Radioactive sources were used within this context.

7. Definition of standard procedures for detector operation at data taking time. Development and test of a training iter for shifters.

Hundreds of runs were taken under all normal run modes (sec. 5.3). Moreover a few special run modes were used including firing the timing laser with normal trigger setup to test the trigger threshold sensitivity (sec. 6.4.5)) or laser runs with double light pulses for testing the clustering algorithm (sec. 7.4.3).

6.2 Status of the detector

At the time of the first Air Run only 1993 ID PMTs were installed. The remaining 219 PMTs belong to the south pole of the SSS and to the door area. They could be installed only after the *inner vessel* around May 2004. The OD installation (chap. 3) was just starting, so in the first runs it was not involved.

The first air run was extensively prepared:

1. All the cabling information was debugged and loaded into database. Integrity control protocols and the concept of profile (sec. 5.6) were defined during this phase.

2. The dark room data of the PMT tests were retrieved and loaded to database. HV values were loaded to mainframes with the help of the Slow Control (sec. 5.7).

3. The SSS was not sealed yet. It was in communication with two clean room environments (CR2 through the main door and CR4 through the north pole flange), which were not designed to be light tight. A large effort in darkening these environments was done and repeated before every run until SSS sealing (i.e. up to AR8).

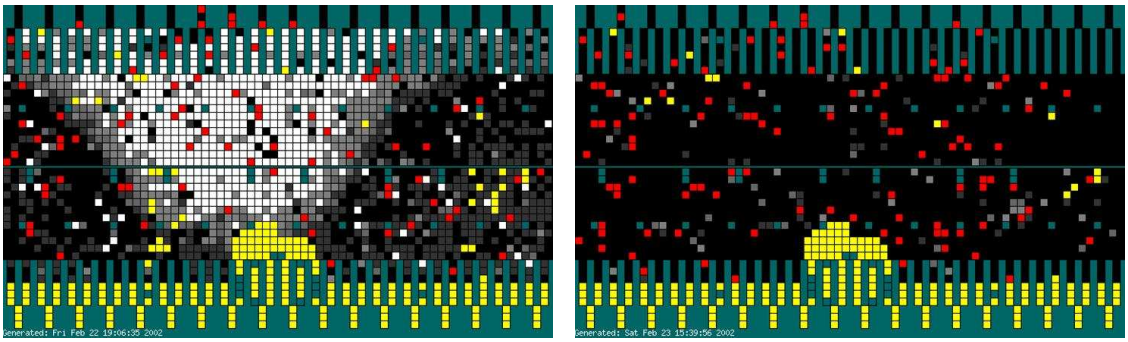

Fig. 6.1: *OMON main PMT map before (left) and after (right) the brightest flasher was identified and disconnected (Feb. 2002). Cmp. fig. 5.12. PMT not yet installed in the south pole and in the door area are visible in yellow.*

6.2.1 First runs: the flashing PMTs

The first days of AR1 were dedicated to manually turning on most of the PMTs. This was the first time they were operated after their installation underground and in connection with the front-end boards[2]. Comprehensibly it was therefore a delicate and slow operation.

During this phase an unexpected phenomenon was observed. A few faulty PMTs were emitting light and this was detected by a large number of PMTs on the opposite side of the SSS. This was happening in bursts of different duration and without regular periodicity, so we named these PMTs *flashers*[3]. Flashes were visible as temporary increase in "dark" rates up to hundreds of KHz[4].

The OMON map of the PMT rates showed very clearly the patterns and helped to understand the phenomenon. The first and brightest of the flashers ($\sim 600KHz$) is visible in fig. 6.1.

Every flasher PMT was identified in the following way. A few reference channels were kept under observation with a visual scaler. The 14 mainframes were turned down one by one until a sharp rate decrease was observed. Once the crate was identified the procedure was repeated first at board level and finally at channel level. In a few days all flashers were identified and disconnected[5].

The evaluation of the detector status proceeded and other PMTs were disconnected, because noisy or unstable, up to about 80. After AR1 ~ 150 channels showed problems including bad PMTs, bad cables, bad electronic channel (front-end or digital component), software and DB problems. At the beginning of 2002, though the system was in principle fully developed, basically *everything* needed tests and debugging and the identification

[2]The decoupling stage in principle affects the PMT behavior.

[3]The same phenomenon was observed also by SNO collaboration, who is also using ETL PMTs[87].

[4]This was initially mistaken for a light leak in the tank and triggered an extensive leak-hunt with torch lights which gave no results.

[5]Turning a flashing PMT off is not enough, because the HV board keeps all channels within $900V$ from the common channel (sec. 4.1). Due to the PMT voltage divider design, the first $600V$ go on the Zener diode that keeps the first dynode up and this was in many case enough to generate the flashes.

of the problems origin was far from trivial.

6.2.2 Last runs: the present situation

In the two following years and through the various air runs, PMTs have been replaced or recovered (e.g. tuning HV), electronic boards have been replaced and repaired, all the online software has been finalized, debugged and extensively tested and the understanding of the detector has grown significantly.

In AR9, after the installation was finished, the residual problems in the (now complete) ID are the following:

1. 30 PMTs result faulty[6]:
   (a) 10 give no life sign.
   (b) 20 have been disconnected because flashing or too noisy.
2. 55 Electronic channels have problems (front-end or laben):
   (a) 20 give no signs of life.
   (b) 20 show time measurement problems.
   (c) 15 show charge measurement problems.
3. 30 Optical fibers deliver no light.

The second problem is being addressed and should be fully solved before detector's filling by replacing boards with units that are currently under repair.

6.3 Debugging the electronics

During AR3, timing laser runs pointed out a few problems of the laben boards that had to be understood and addressed.

6.3.1 Time measurement problems

The first surprise was the presence of hits outside the $\sim 7\mu s$ trigger gate (fig. 6.2). However they can be easily filtered out in the reconstruction program by reapplying the gate as a software cut, so they do not actually represent a problem.

The hit time distribution with respect to laser reference channels (sec. 4.5) is shown in fig. 6.3. The continuum is given by the PMT dark noise and the highest visible peak is the direct laser light. Unexpected additional peaks shifted by $50ns$ or $100ns$ are clearly visible (plus a smoothed reflection after $41ns$). This structure is due to non ideal board behavior as later confirmed by pulser runs.

Ideally the reconstruction of the hit time information on laben electronics (sec. 4.2.3) works as follows (fig. 6.4). The value of the gray counter, multiplied by its period ($50ns$)

[6] They could not be replaced because no longer reachable in the SSS.

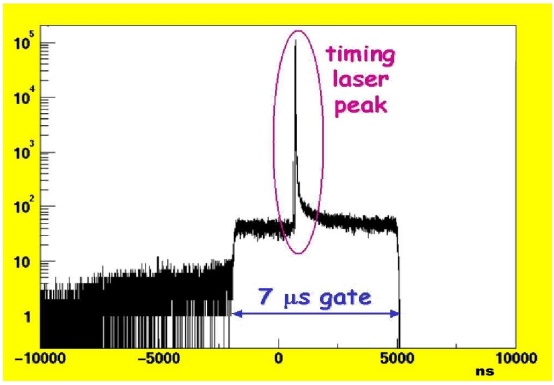

Fig. 6.2: *Hits occurring outside the trigger gate.*

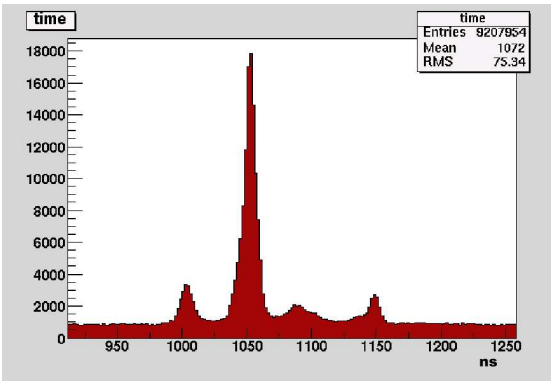

Fig. 6.3: *Laben hit time distribution during a timing laser run (AR3). The anomalous multi-peak structure is visible.*

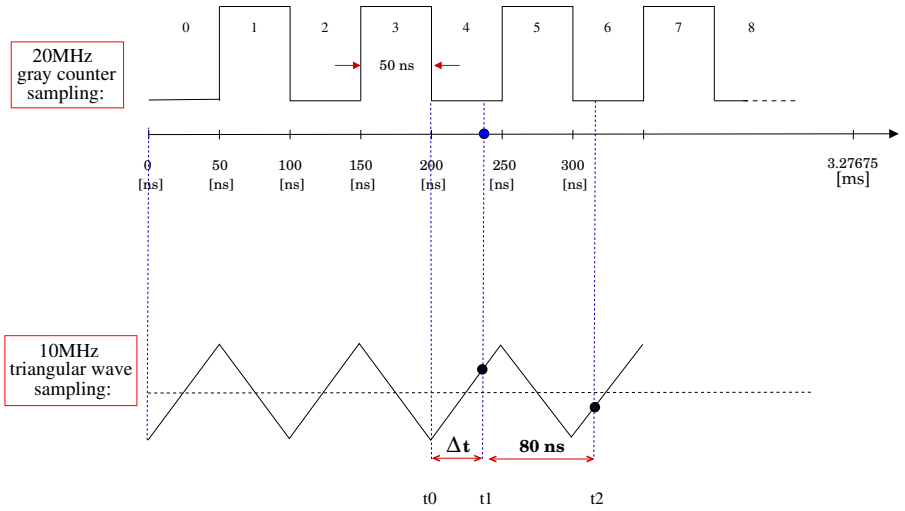

Fig. 6.4: *Hit time reconstruction in laben electronics.*

provides the coarse time. The fine time is inferred from the first of the two TWF sampling $t_{1,2}$:

$$\underbrace{t_{\text{fine}} = (t_1 - b_l)\frac{b_h - b_l}{50ns}}_{\text{rising slope}} \quad \text{OR} \quad \underbrace{t_{\text{fine}} = (b_h - t_1)\frac{b_h - b_l}{50ns}}_{\text{falling slope}}. \tag{6.1}$$

where b_l and b_h are the ADC bins corresponding to low and high spikes respectively (to be determined). The choice between the two possibilities above relies on the nominal *parity* between the TWF and the gray counter, i.e. *rising-on-even* (fig. 6.4).

Three effects can introduce deviations from the ideal behavior:

gray counter misalignment. At run start the BTB issues a RESET signal for all laben boards. This ideally aligns all gray counters to zero "at the same time". However (fig. 6.5) some boards may receive it slightly before or later resulting in an offset of

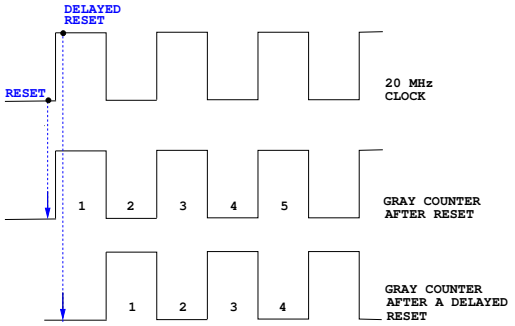

Fig. 6.5: *Effect of gray counter misalignment.*

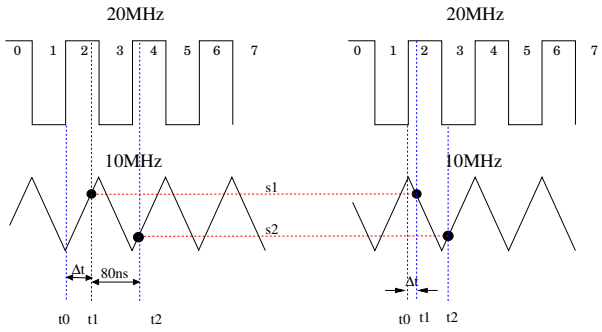

Fig. 6.6: *Effect of indetermination in parity between gray counter and TWF.*

± 1 count, i.e. $\pm 50ns$. The effect is run dependent.

varying parity. The relative parity of TWF and gray counter is not always *rising-on-even* as it should. Some channels show opposite parity with consequent misreconstruction of the time. The effect is run dependent.

smoothed slope edges. Unlike the others, this effect was expected. The triangular waveform in practice cannot be perfectly triangular but its edges are somewhat smoothed, resulting in a poor time determination if t_1 falls in their proximity. However, if this is the case for t_1, it cannot be true also for t_2 (the $80ns$ delayed sample) in the same hit, so the latter should be used in these cases[7]. What perhaps was not expected is the fact that the delay is not exactly $80ns$ and is board dependent.

After AR3, the so-called *precalibration* procedure was established with the goal of determining the ADC active range (i.e. b_h and b_l of eq. 6.1) and to correct the three mentioned effects.

At the beginning of every run a programmable number of calibration events, usually 1000, are distributed to all channels (sec. 4.4.5). As the timing unit driving the trigger is set to $200Hz$ the precalibration lasts about $5s$.

When the run is processed by Echidna a few modules take care of computing the relevant parameters which are then used to successfully decode the hit time (sec. 7.4.1).

The precalibration procedure was successfully tested and finalized during AR4.

In addition to the mentioned run dependent effects, the 14 crates receive the trigger with fixed intrinsic delays. An echidna calibration module computes the delays using pulser data (sec. 7.4.5). The effect of the realignment is visible in fig. 6.7.

After all corrections are applied, the overall electronics resolution is about $1.2ns$.

[7]The expressions relating t_{fine} to t_2 are similar to eq. 6.1, though 4 cases must be distinguished and the arithmetics is slightly more complex.

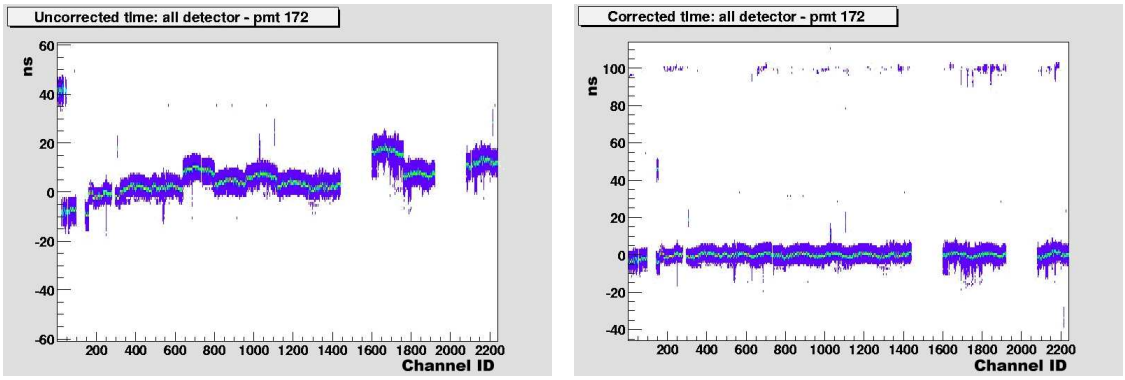

Fig. 6.7: *Difference (in ns) of the hit time measurements of all laben channels with respect to a reference channel before (left) and after (right) the correction of the crate systematic delays. In both cases gray counter realignment is performed.*

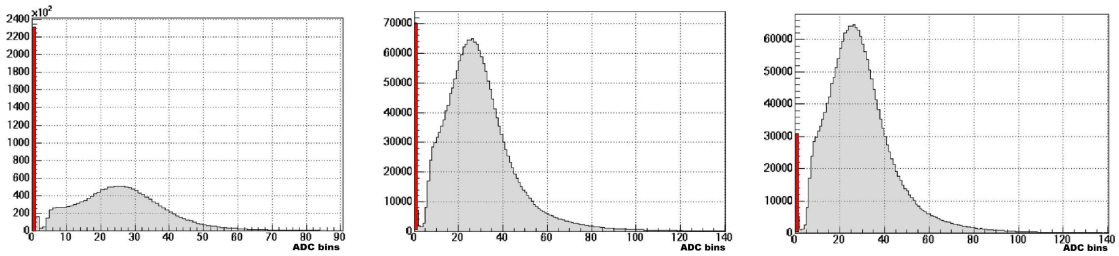

Fig. 6.8: *The "zero-charge" problem. Hit charge distribution for timing laser runs before (left) and after (center) LV cable replacement. Excluding 40 bad channels further reduces the problem (right).*

6.3.2 Charge measurement problems

Concerning the charge measurement, in the first laser runs about 30% of the channels were recording zero charge for most of the hits. The problem was especially puzzling because it was independent of PMT gain, the channels affected were spread out in the whole detector and they differed in every run. Finally the origin of the problem was identified in the cables connecting the front-end crates and their Low Voltage power supplies (fig. 4.3). They provided poor connection, inducing low frequency noise on the channels. Consequently the baseline of the integral output was occasionally drifted outside the range of laben ADC.

The faulty components were replaced in June 2003 with better quality connectors and shielded cables. This cut the effect down to 4% of the hits and mostly localized on a few channels (about 40). The exclusion of these channels further reduced the effect to below 2%. These faulty channels were later replaced and/or repaired.

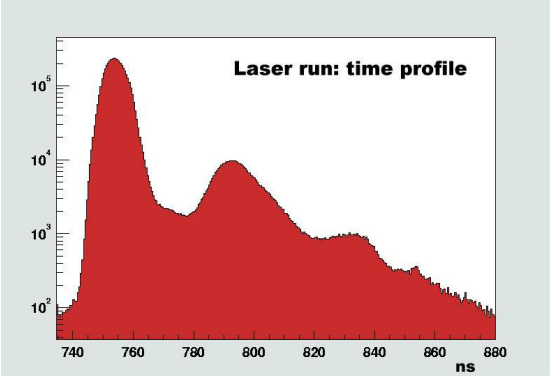

Fig. 6.9: *AR4 timing laser run (I=5). Time profile in ns. Direct light peak as well as two successive reflection peaks are visible.*

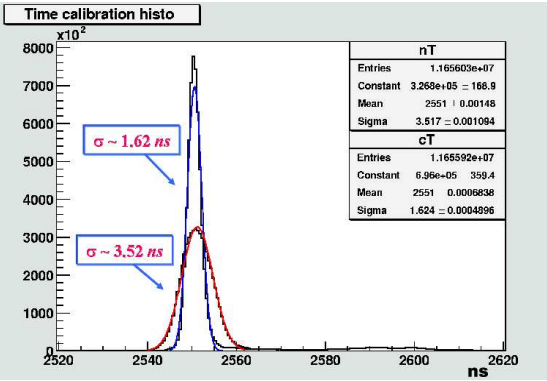

Fig. 6.10: *AR9 timing laser run (I=4.5). Effect of time calibration of the overall detector's resolution.*

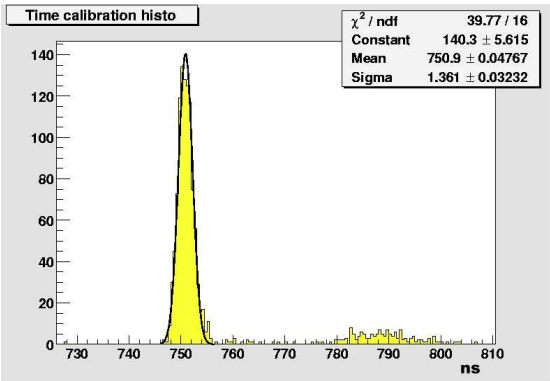

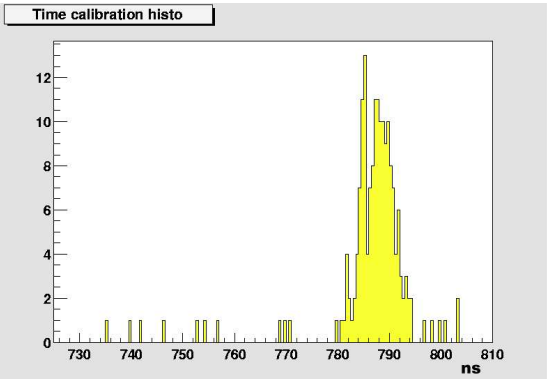

Fig. 6.11: *AR4 timing laser run. Hit time distribution for single PMT illuminated by a working fiber (left) and by a weak one (right).*

6.4 Laser runs

Starting with AR4 when the hit time measurement was considered reliable, a number of tests of the laser calibration systems (sec. 2.2.4) could be performed. The general time profile observed is shown in fig. 6.9. The first and highest peak is the direct light, while successive peaks account for reflected light. The time-of-flight for photons crossing the full SSS in air is $\sim 41ns$ and this is indeed the separation between successive peaks.

6.4.1 Time calibration

The raw spread of the direct light peak in timing laser runs is $3.6ns$ (fig. 6.10). This accounts not only for the transit time jitter of PMT and electronic channel but also for small offsets among the channels. This second component can be significantly reduced by a software inter-channel equalization. The following procedure was setup for this goal.

The reconstruction program includes a dedicated module (sec. 7.4.5) that runs on laser data to compute the time offset of every channel with respect to the laser reference time.

The values are then uploaded to database[8]. Every time a standard run is processed the latest offsets available are read back from DB and subtracted at decoding stage (sec. 7.4.2).

The module computes the offset producing a hit-time histogram per channel (fig. 6.11 (left)) and fitting each one with a Gaussian in the region where the laser direct light is expected ($\pm 20ns$). However during AR4 about 70 PMTs showed illumination problems receiving little direct light or none at all (fig. 6.11 (right)) and were excluded from calibration.

The laser intensity to be used must be tuned to meet two requirements:

1. the incidence of multiple hit events must kept to a few percent. From Poisson statistics this is about $\mu/2$ where μ is the mean hit occupancy. The usual goal is $\mu < 6\%$.

2. the incidence of dark noise hits in the fit window must be kept to a few percent. This sets instead a lower limit on μ. For example a conservative mean dark noise of $10kHz$ corresponds to a hit occupancy of $\mu_{dark} = 0.04\%$. A μ of a few percent is therefore required to keep this contribution negligible[9].

The laser intensity can be varied acting on a potentiometer on the laser controller, however the units shown are arbitrary $I = 1, 2, \ldots, 9$ and in non-linear relation with the light output. In AR9 a scan of laser intensities was performed to fine tune the calibration procedure and the intensity $I = 4.5$ with $\mu = 5.8\%$ was selected as optimal for most channels. In addition about 40 channels with weak but not null fiber efficiency could be recovered performing an additional run at higher intensity.

The result of timing calibration can be seen processing a laser run and applying the corrections computed from a previous one (fig. 6.10). The overall detector resolution decreases from $3.52ns$ to $1.62ns$, in good agreement with the expected value:

$$\sqrt{(1.1ns)^2 + (1.2ns)^2} \sim 1.63ns$$

where $1.1ns$ is the average PMT jitter and $1.2ns$ is the electronic resolution (sec. 6.3.1).

6.4.2 Charge calibration

The channels map of uncalibrated charge is shown in fig. 6.12(a). The channels are already pretty well aligned, thanks to the careful work of PMT gain equalization performed during the first air runs. It is under discussion the possibility of implementing an automated gain equalization procedure that, through the Slow Control (sec. 5.7), acts to correct the HV values whenever needed in order to compensate drifts.

No matter whether this will be realized or not, a charge calibration is needed in order to convert the ADC-bins scale into *pe*. With this goal a procedure was established during AR7, after the charge measurement problem was solved (sec. 6.3.2).

[8] Write access to DB is protected, so only during official calibration the user has the privileges to update tables.

[9] $\mu < 1 - 2\%$ would also make a laser calibration impractically long at the standard service trigger rate of $200Hz$.

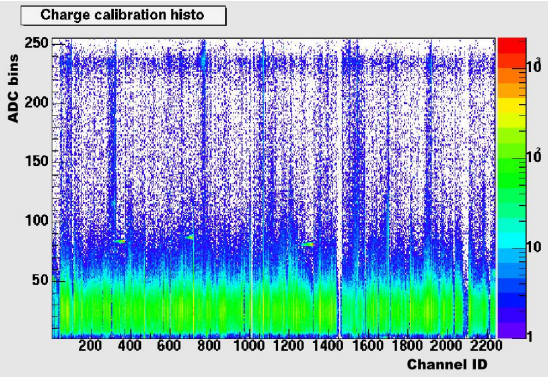

Fig. 6.12 (a): *AR7. Charge spectrum for all ID channels before calibration.*

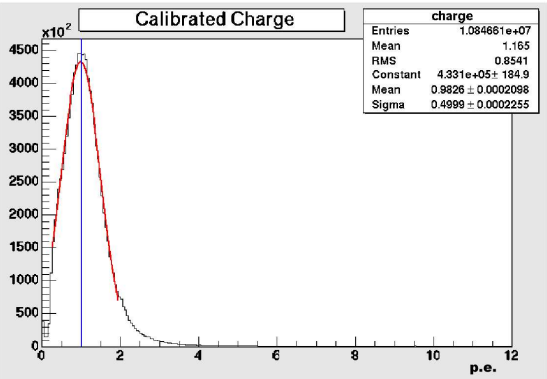

Fig. 6.12 (b): *AR9. Overall detector charge spectrum after calibration.*

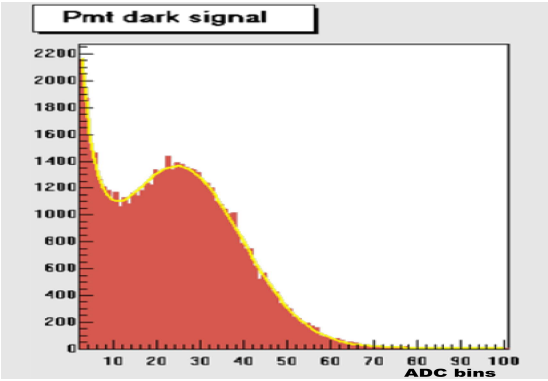

Fig. 6.13 (a): *PMT SPE charge spectrum as measured in dark room (low threshold).*

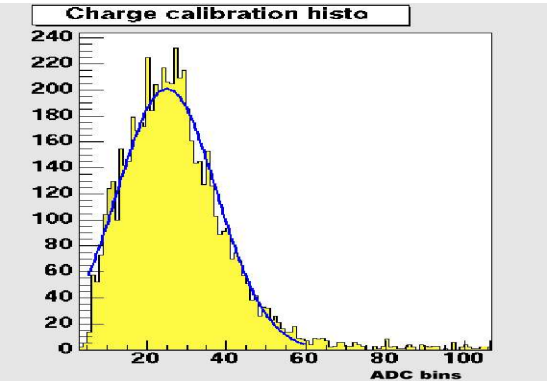

Fig. 6.13 (b): *PMT SPE charge spectrum produced by the charge calibration module.*

The idea is to exploit the same timing laser runs used for time equalization with a parallel offline module (sec. 7.4.5). This produces hit-charge histograms for every channel and finds the SPE peak position.

The SPE spectrum in principle includes contributions from a decaying exponential and a Gaussian. The latter accounts for thermo-ionic or photo-electric effect on the regular photocathode, while the first one has a complex origin including emission from dynodes and from photocathode material deposited elsewhere in the PMT [192] during the evaporation process.

Indeed the PMT SPE spectrum showed such a shape in dark room tests (fig. 6.13(a)), but the laben board threshold (sec. 4.2.3) cuts the visible part of the exponential completely (fig. 6.13(b)). For this reason fitting the spectrum with the sum of the two contributions usually gives poor results. A simpler Gaussian fit of the region around

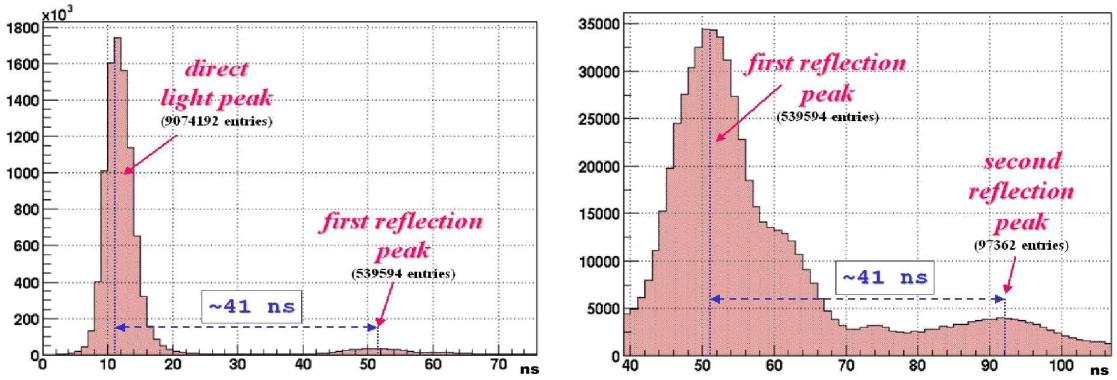

Fig. 6.14: *AR4 timing laser run. Comparison between direct light peak and first reflection peak (left) and between first and second reflection peaks (right).*

the peak proved to be reliable enough and is indeed more robust within an automated procedure.

The Gaussian centroid is the conversion factor between ADC bins and *pe* scales and is handled through the DB in analogy to the timing offset mentioned above.

The overall detector resolution after calibration and conversion to *pe* scale is shown in fig. 6.12(b).

6.4.3 SSS reflectivity

The presence of reflection peaks in the hit time distribution (fig. 6.9) of timing laser runs allows a few considerations upon reflectivity of materials inside the detector. These can be only qualitative as the relative weight of the peaks is done simply integrating the areas around them with a good degree of arbitrariety in choosing the integration limits.

The optical fibers are mounted to point directly to the photo-cathodes, so the first reflection peak is due only to the reflectivity of this surface. This parameter is known from laboratory tests to be around 10%. The ratio of areas under first reflection and direct light peaks yields about 6%.

The second reflection occurs instead on a surface composed of steel and glass whose two contributions cannot be disentangled. The ratio between second and first reflection peaks indicate a composite reflectivity at the level of 20%. Though too primitive to be considered a real measurement, it allows to exclude with a reasonable confidence a reflectivity higher than 30-40%.

It is worth noting that all these considerations are done with the detector filled just with air. The reflection on glass in PC will be lower because the PC/glass boundary features a smaller refraction index discontinuity compared to the air/glass one (glass accounts for 30% of surface). Moreover the impact of reflected light will be diminished due to PC self absorption (attenuation length $8m$).

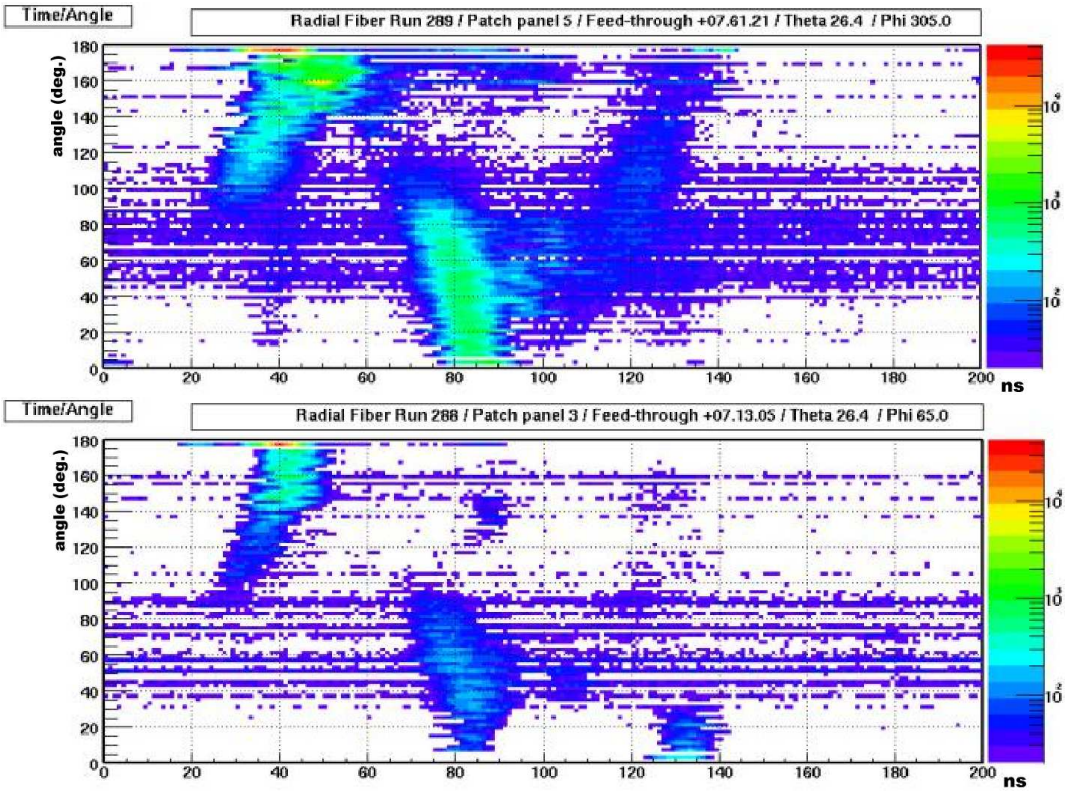

Fig. 6.15: *AR3 radial (above) and oblique (below) laser tests. Scatter plot of hit angular distribution vs. arrival time.*

6.4.4 Radial and oblique lasers

During AR3 also the fibers pointing radially through the sphere and in different oblique directions were tested with the $394nm$ laser. Fig. 6.15 shows the scatter plots of the hits angular distribution versus the time profile. The angle is defined with respect to the light beam, 180° being the forward direction. Direct light is visible as the red spot at about $40ns$ and almost 180°. First and second reflection peaks are also visible.

All 12 radial and 19 oblique positions have been tested. Beams are rather well focused, in particular oblique fibers point to a single PMT (without concentrator). This allowed an important test of the cabling information in the DB `bx_geometry` (sec. 5.6).

Here a complex system of channel maps links the PMTs to their position in the SSS, to the dark room parameters, to cable and Patch Panel numbers and finally to the electronic channels. Errors in this sequence could affect for example the position reconstruction capabilities, making a careful debugging extremely valuable.

Part of this sequence could be tested before the first air run using pulser data, however another part required PMTs on and could be tested only using radial and oblique laser data. The channels hit in direct and reflected light patterns always matched the expected ones and no cabling problem was discovered.

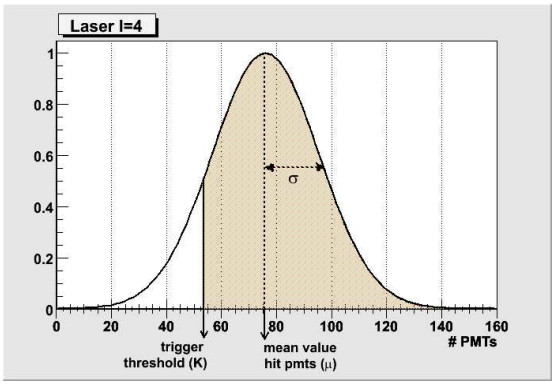

Fig. 6.16 (a): *Gaussian function of the number of PMTs hit for laser run.*

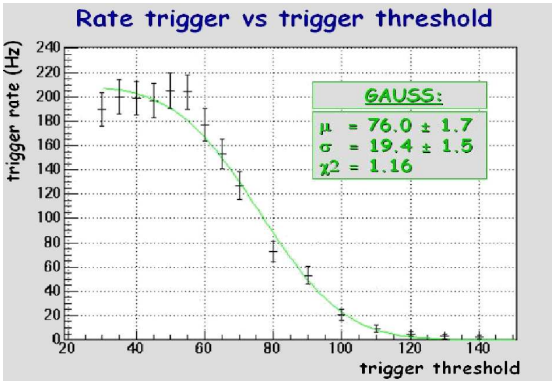

Fig. 6.16 (b): *Study of the trigger efficiency for different comparator thresholds.*

6.4.5 Trigger studies

During AR7 the trigger efficiency was studied running with the normal trigger (BTB comparator) and pulsing the laser independently ($I = 4$, $R = 200Hz$). A series of runs was taken with different comparator thresholds, measuring the trigger rate. For each value a run with laser off was also taken. In this way the trigger rate due to dark noise was measured independently and subtracted away. The net laser trigger rate measured as a function of the threshold K is shown in fig. 6.16(b).

The number of hit PMTs per event follows a Poisson distribution with mean value μ, but for large μ this can be safely approximated with a Gaussian distribution (fig. 6.16(a)). The expected rate is then the integral of the Gaussian portion above K:

$$R_{\mu,\sigma}(K) \propto \int_K^\infty g(x)dx = \int_K^\infty \frac{1}{\sqrt{2\pi}\sigma} e^{-\frac{(x-\mu)^2}{2\sigma^2}} dx = \frac{1}{2} Erfc\left(\frac{K-\mu}{\sqrt{2}\sigma}\right) \qquad (6.2)$$

where $Erfc(x)$ denotes the complementary error function.

Eq. 6.2 is used as fitting function for the plot in fig. 6.16(b) with μ and σ as free parameters. The fit yields $\mu = 76$ and $\sigma \sim 20$.

The value can be checked on a standard laser run taken during AR5 with the same intensity. Here the average number of channels hit was $\mu = 147$ and $\mu = 74$ respectively for laser394 and random triggers. The difference between the two yields once more the net laser hit occupancy, i.e. $\mu \sim 73$ in good agreement with the threshold scan study.

6.5 Dark noise runs

Random trigger runs (sec. 5.3.1) provide a good handle to test the status of the detector and will be used periodically throughout BOREXino operation along with timing laser runs. In this trigger mode the detector is not pulsed in any way, therefore only dark counts may fall inside the trigger gate.

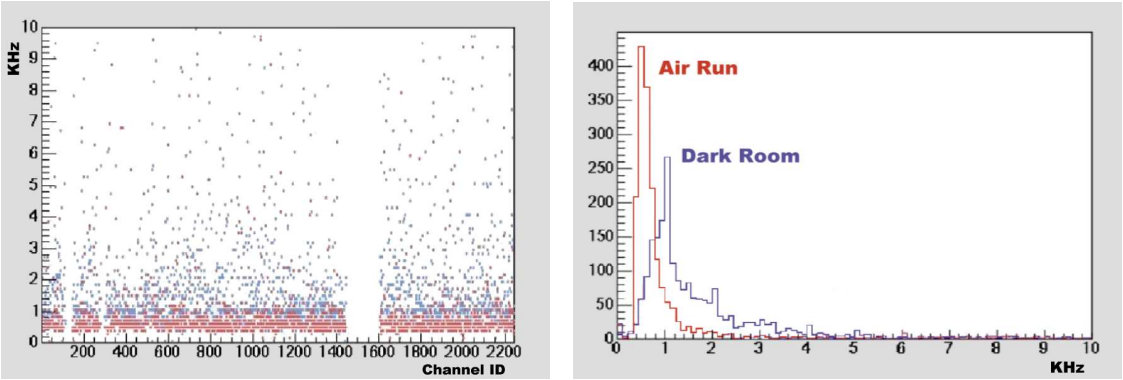

Fig. 6.17: *Comparison between PMT rates measured in dark room (blue) and during AR5 dark noise run (red). Channel map (left) and its y-projection (right).*

The offline software includes a calibration module (sec. 7.4.5) to process this kind of runs. It computes single channel and average dark rates, marking dead and hot PMTs. These pieces of information are then useful for clustering and position reconstruction as explained in chap. 7.

Every air run included one or two days of dark noise data taking which proved to be very useful in debugging and development of hardware and software. For example fig. 6.17 shows the dark noise map for all channels in comparison with the dark room values. The latters were higher, probably due to the higher temperature of and the external laboratory where the dark room is located, compared to Hall C.

6.6 Radioactive source tests

To test the detector performance in realistic conditions some of the air runs included the use of radioactive sources.

They were made of a small quartz vial, filled with some cm^3 of scintillator. The scintillator had been previously loaded with ^{222}Rn by exposure to a ^{226}Ra source.

The sources were suspended on a rope and inserted through the north pole flange. A rough displacement along the z-axis was obtained varying the length of the rope.

Three sources were used:

1. AR2. ^{222}Rn source. Spherical vial.

2. AR5. ^{210}Po source. Spherical vial.

   It was obtained with a preliminary storage to allow ^{222}Rn decay and ^{210}Po build-up. Residual ^{222}Rn was removed by N_2 stripping.

3. AR8. ^{222}Rn source. Cylindrical vial.

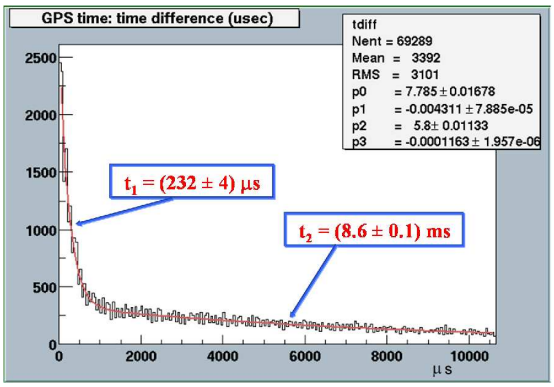

Fig. 6.18 (a): *AR2 source run. GPS time difference.*

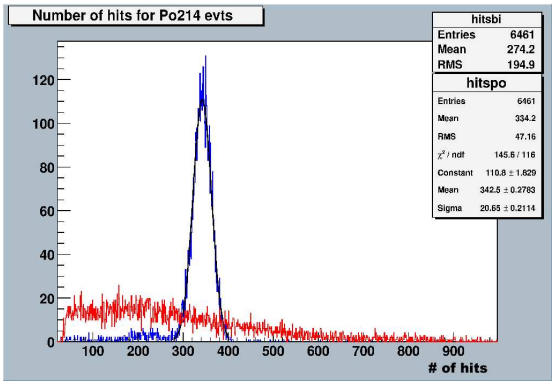

Fig. 6.18 (b): *AR8 source run. Energy of the ^{214}Bi (red) and ^{214}Po (blue) events.*

6.6.1 Delayed coincidences

In AR2 the status of the detector was still messy to allow accurate measurements. Nevertheless the GPS absolute time of the event (sec. 4.4.4) has a resolution of $\sim 1\mu s$, enough to observe the delayed coincidence $^{214}Bi - ^{214}Po$ ($\tau_{Po} = 236.6\mu s$).

The time difference between successive events is plotted in fig. 6.18(a) and can be fitted with the sum of two exponentials yielding $\tau_1 = 232 \pm 4\mu s$ and $\tau_2 = 8.6 \pm 0.1\mu s$. The fast component agrees very well with the nominal $^{214}Bi - ^{214}Po$ coincidence time, while the slow one simply accounts for the probability distribution of uncorrelated events, given the $\sim 120Hz$ trigger rate.

This apparently trivial result was instead very important as it assessed for the first time the stability of the DAQ in "natural" run conditions[10], i.e. with a non-periodic trigger. Moreover it assessed the reliability of the trigger efficiency and the correct GPS time acquisition and reconstruction.

During AR8 the measurement was repeated with the detector in much better conditions. The coincidence time was consistent, $\tau_1 = 238 \pm 4\mu s$, and the first-order energy spectra of the two isotopes could be extracted. In fig. 6.18(b) the $\beta+\gamma$ shape of ^{214}Bi and the α peak of ^{214}Po are visible. If the latter is fitted with a Gaussian the centroid lies at $343 \pm 21pe$. Assuming a "standard" α quenching factor (sec. 9.2.2), this indicates a light yield of about $460pe/MeV$. The ^{214}Bi spectrum, which has an end-point of $3.3MeV$, is instead heavily distorted toward low energies because of the poor γ containment in the source vial.

6.6.2 α/β separation

The $^{214}Bi - ^{214}Po$ coincidence allows also to test the α/β separation on relatively pure samples. The most straightforward technique is the so-called *tail-to-total ratio*. It is the

[10] Actually much more stringent than normal run conditions, when the average trigger rate will not exceed $10Hz$.

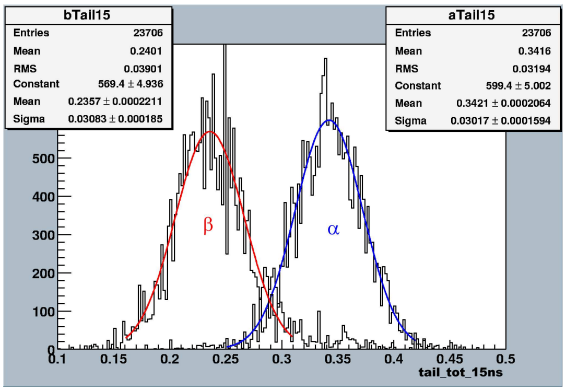

Fig. 6.19: *AR8 source run. α/β separation with the tail-to-total method.*

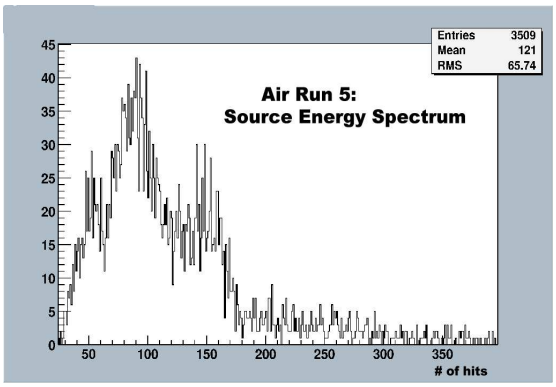

Fig. 6.20 (a): *AR5, ^{210}Po source energy spectrum. The α peak should be at 150pe.*

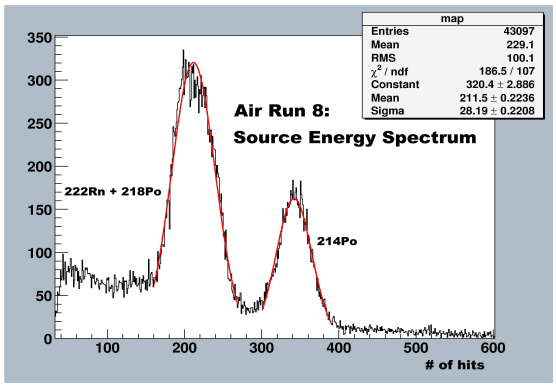

Fig. 6.20 (b): *AR8, ^{222}Rn source energy spectrum. The two α peaks are visible.*

ratio of the pulse integrals in the [15,100]ns and [0,100]ns windows[11]. The distribution of the computed parameter for $^{214}Bi - ^{214}Po$ events in AR8 is shown in fig. 6.19 with the two particle types gathering around pretty distinct values. The two peaks are anyhow overlapped (they always are), so α rejection implies a small sacrifice of β events. For example in this case a β acceptance of 93% allows to reject 98% of the α component. These results are of the same order of the CTF ones (sec. 9.1.5) and represent only a first check of the good detector's health state. A detailed study including more sophisticated PSD methods and achieving better results can be found in [242] and is summarized in sec. 7.4.6.

6.6.3 Energy spectrum

Looking at the source energy spectra, the ^{210}Po source used in AR5 should have featured only an α peak around 150*pe*. The measured spectrum (fig. 6.20(a)) showed instead a

[11]The word *integral* actually refers to software sums of hits over their time distribution.

^{210}Po source position	x	σ_x	y	σ_y	z	σ_z
$x = 0;\ y = 0;\ z = 0$	-1.7	25	2.6	16	8.4	25
$x = 0;\ y = 0;\ z = 100$	4.6	20	5.0	13	93	29
$x = 0;\ y = 0;\ z = 200$	-0.4	22	5.0	18	192	25
^{222}Rn source position	x	σ_x	y	σ_y	z	σ_z
$x = 10;\ y = 0;\ z = 60$	12	13	0.7	12	71	18
$x = 10;\ y = 0;\ z = z_1$	10	13	1.3	12	-21	15
$x = 10;\ y = 0;\ z = z_1 + 53$	11	13	-1.6	12	24	16
$x = 10;\ y = 0;\ z = z_1 + 153$	12	13	2.3	13	112	20
$x = 10;\ y = 0;\ z = z_1 + 253$	13	14	1.0	14	219	22
$x = 10;\ y = 0;\ z = z_1 + 403$	14	16	-0.8	16	373	28

Tab. 6.2: *Nominal and reconstructed positions, for the ^{210}Po and ^{222}Rn sources, as measured respectively in AR5 and in AR8. All numbers are quoted in cm. $z1$ is an unknown offset.*

large structure at lower energies. This can be explained by total reflection effects at the quartz-air border. A fraction of scintillation photons may be trapped and eventually absorbed in the medium before they manage to escape. The effect was known from CTF, where photons also cross media with different refraction indexes, but here the surface-to-volume ratio of the vial is much higher and the effect is consequently enhanced. The interpretation was later confirmed by simulations involving the correct source geometry.

To reduce this problem, in AR8 the source was prepared using a cylindrical source and indeed the energy spectrum has the expected shape (fig. 6.20(b)): two α peaks and an underlying continuous spectrum. The lower energy α peak is given by the unresolved contributions of ^{222}Rn and ^{218}Po, while the higher energy one is ^{214}Po. The continuous shape is given by β+γ events from ^{214}Pb and ^{214}Bi, with a large fraction of γ's escaping the vial.

6.6.4 Position reconstruction

Finally the source runs allowed preliminary tests on the position reconstruction algorithm (named "milan" in sec. 7.4.4).

Before any position reconstruction can be attempted the event must be correctly *clustered* (sec. 7.4.3), so the source data taken during AR5 allowed to improve and finalize the clustering algorithm[242].

The nominal and reconstructed source positions for AR5 and AR8 are shown in tab. 6.2, however the nominal positions are to be considered as indications, due to the very primitive "source insertion system" used (i.e. a rope). We can say the nominal coordinates are known with an accuracy of about $10cm$.

Looking at the data a few considerations may be done:

- The matching of nominal and reconstructed coordinates is very good within the uncertainty on the first ones.
- The differences in x and y among runs taken at different z are due to physical

displacement of the source occurred during the lifting operation.

- The higher energy of the ^{222}Rn source allows a better performance compared to the ^{210}Po source data.
- The x and y resolutions for positions close to the center are $\sim 12-13cm$ which can be regarded as very satisfactory, considering that:
  - No energy cut was applied, so also low energy events present in the source spectrum were included.
  - The algorithm is optimized for PC. Running in air the refraction index was simply replaced.
- The z reconstruction was affected by the 220 PMTs that were still missing on the bottom of the SSS. Its resolution was therefore worse than the one obtained for x and y and further worsens when approaching the north pole. A hypothetical[12] test performed now with the complete detector should yield results comparable to the x and y resolutions.

6.7 Outer Detector status

All the PMTs installed in the inner and outer detector of BOREXino were tested in a dark room in the external LNGS buildings. Only PMTs that *after* delivery to Gran Sasso were showing a reliable behavior have been installed.

However transportation underground and installation are subject to mechanical stress that can induce a few failures. Moreover the installation of the outer detector started in 2001 but was then delayed and subdivided into different operating periods over a few years[13]. This unfortunate situation let the PMTs age under different conditions and may have produced surprising results.

It is then clear how tests of the PMTs after the installation in the WT are of particular importance for OD.

6.7.1 Online tests

Through the different installation periods, access to the detector's areas occurred sequentially as the complex geometry of the environment made the movement of the scaffolding very costly and the re-access to a completed area an almost forbidden hypothesis. For this reason PMTs and cables were tested day by day in order to allow an immediate replacement of the faulty units.

Moreover a large amount of logistic information was produced during the installation and required careful handling. In fact PMT serial number, cable serial number, logical position (ring+column), electronic channel, dark room information and online tests results

[12] This kind of source runs can no longer be performed due to the presence of the vessels.

[13] This was partly due to the external conditions exposed in sec. 2.5 and partly because the delayed *inner vessel* installation did not allow the removal of a clean room located in the water tank volume until summer 2004.

had to be matched together for 208 channels. Comprehensibly several conflicts arose in this phase and they have all been resolved. The data have been then loaded to DB[14] (sec. 5.6) where the reconstruction program and other consumers regularly access them.

The main problem arising in the tests of the PMTs was the poor light tightness of the water tank. Generally PMTs could be turned on after a major darkening effort but could not be brought to full gain: $\sim 200V$ under-gain the typical counting rate was already exceeding $100kHz$, indicating a dangerous amount of light was still present. So just the bare existence of a signal could be attested in this phase.

For AR6, dedicated to OD, 12 PMTs not yet surrounded by Tyvek were bagged with black material, only letting the optical fibers through. The first important test of the DAQ, trigger and calibration system was performed in this condition. The bagging proved to be excellent with all PMTs having rates below $2kHz$ and most often showing just $200 - 400Hz$. Unfortunately the bags had to be removed at the end of the run to allow Tyvek installation.

In the last period, after the removal of the clean room, a $5m \times 5m$ patch was created in clean environment with four layers of alternated black cloth and aluminum foils, and applied to the water tank entrance. This marked a major step ahead for what concerns the lower portion of the PMTs, but the upper portion still suffered light incoming from the ventilation tubes.

In a few occasions, relatively meaningful tests could be done turning off the main lights in the experimental Hall[15], a possibility restricted to night hours and weekends and rarely available due to the complex safety implications.

6.7.2 Final test results

The results reported here refer to the final complete test of the OD, performed in the night between August 7th and 8th 2004 in the best darkness conditions ever achieved[16]

The PMTs were turned on gradually and observed one by one with the analog oscilloscope. They were powered with the HV mainframe (sec. 4.1) and the signals were taken from HVDs (sec. 4.3). The Dark Room HV values were considered only as references, the gain had to be adjusted by eye in about 20% of the cases. Dark rates were measured using three NIM modules: amplifier (x10), discriminator, visual scaler. The threshold of the discriminator was set to $30mV$ corresponding to about $0.25pe$ on the amplified signal.

The lower hemisphere was relatively dark with PMT rates in the $2 - 10kHz$ range, well acceptable for PMTs which had been exposed to light up to a few hours before. The upper hemisphere was not completely light tight but rates were in the $10 - 50kHz$ range which still allowed a meaningful inspection.

Out of 208 tested channels:

- 190 channels showed "perfect" behavior.

[14] tables `MuonHolesMapping`, `MuonCableMapping` and `PmtParameters` in DB `bx_geometry`.
[15] Emergency lights could not be turned off in any case.
[16] Previous results are available on log-books.

Ring	Col.	Rate	Problem	Strategy
5	3	-	only noise, poor connection	re-connect
5	8	-	ghost (conn. ok)	replace PMT
4	7	30-60	ok, past instability	observation
3	6	1000	noisy, previously ok.	observation
2	8	31	ok, past instability	observation
2	16	15	ghost (conn. ok)	replace PMT
1	16	8.5	ok, past instability	observation
-1	11	5.5	ok, past instability	observation
-1	12	10	ok, past instability	observation
-1	18	-	no signal, no connection	replace cable
-1	26	-	no signal, no connection	replace cable
-2	2	-	only noise (conn. ok)	replace PMT
-2	12	> 50	noisy	observation
-2	16	6	ok, past instability	observation
-2	17	8	ok, past instability	observation
-3	1	3.2	ghost (conn. ok)	replace PMT
-3	11	15	ok, poor connection	re-connect
-4	7	-	no signal, connection ok	replace PMT

Tab. 6.3: *Outer Detectors PMTs showing problems of different severity. Rates are in kHz.*

- 9 channels were either noisy or showed instabilities in previous tests. These are probably good enough but require observation under a continuous operation period of a few days.
- 4 channels showed a problem either in the cable or in its connection to the PMT[17]. This was discovered sending a signal along the cable and checking if the impedance was matched on the other end. The presence of partial reflections probably indicates a poorly connected cable (2 cases), while a complete reflection (2 other cases) might indicate the cable is faulty or was damaged during the installation.
- 2 channels had no signal but a good connection and must be replaced.
- 3 channels had PMTs with a very surprising behavior (*ghost*). They show a perfect (low noise) signal that periodically fades away, only to later show up again. The periodicity is of the order of tens of minutes and the transition occurs in about $5 - 10s$. Replacement of these units is suggested. Unfortunately it cannot be excluded that other PMTs have the same feature that would show up only in a longer observation time.

The PMTs batch that was purchased, encapsulated and tested in the Gran Sasso dark room counted about 20 spare units. However most of them have been already used during the installation and 5 are left, i.e. exactly the amount required in case no further failure is observed before WT door closure.

[17]The submarine HV connector requires a special connection care.

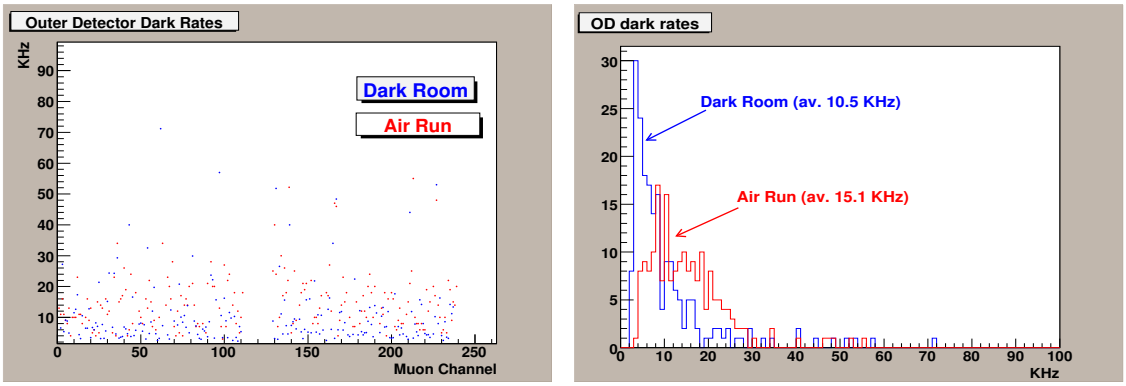

Fig. 6.21: *Comparison between OD PMT rates measured in dark room (blue) and during a dark noise run (red). Channel map (left) and its y-projection (right).*

During this last test a dark noise run was also taken for a few hours with the full OD on. It was the first time the complete system was operated and represented an important integral test of full chain correct behavior in real data taking conditions. The offline program includes a calibration module parallel to the one mentioned for ID to process these data computing rates and marking PMTs status. The measured dark rates are shown in fig. 6.21 in comparison with Dark Room values.

6.7.3 QTC commissioning and characterization

During 2003 the electronic department at TUM produced the 14 QTC boards (sec. 4.3.2), following the indications resulting from our analysis of the second prototype. Upon delivery to Gran Sasso, as usual for custom electronics, a long commissioning phase was necessary before they could be considered reliable.

The major problem at the beginning was the frequent burning of the fuses in the power lines[18]. This induced a re-analysis of the power lines consumption and stability performed in the prototyping phase and of the VME crate power supply, but no misbehavior could be identified. In the end the origin of the problem proved to be trivial: after mounting the front panels, the boards could not fully penetrate in the slots of the VME crate, leaving a $\sim 1mm$ gap. The resulting connection was "just enough" to let the board work, but otherwise poor and was probably causing current spikes at startup that were responsible for the fuses burn-out. A minor mechanical modification in the front panels solved the problem.

Apart from this, a number of misbehaviors were pointed out, mostly due to faulty components that were subsequently replaced. In this phase the 2 second-generation prototypes were made identical to the specimen of the serial production by implementing the last modifications and became the spare units.

[18]In the mess of the initial phase of understanding the board behavior it was also not easy to detect this problem upon occurrence. A LED showing the AND of the fuses status was added on the front panel for this reason.

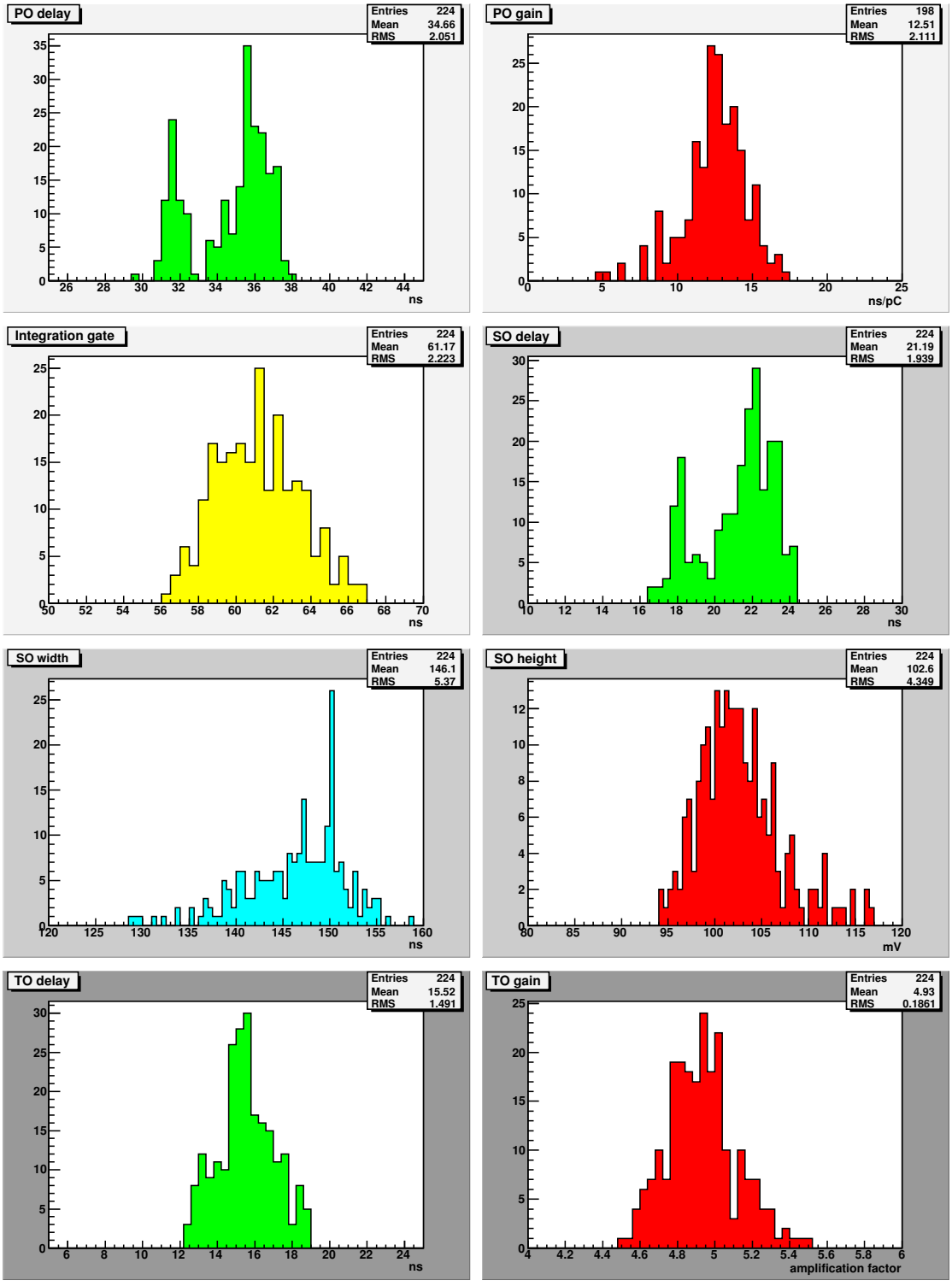

Fig. 6.22: *QTC parameters from the mass measurement in Gran Sasso (Feb. 2003).*

The boards settings had been equalized in Munich after production according to our specifications. In Gran Sasso a mass test was performed to measure all parameters characterizing the boards behavior.

Unfortunately a major design flaw of the board is the lack of a calibration input such as the one present in the ID front-end (sec. 4.2.2). The channels can therefore be pulsed only from their individual inputs with two big disadvantages:

1. The calibration is a lengthy manual and serial operation and cannot be implemented within the DAQ as it happens for ID.

2. The measurement cannot be performed while the channel is connected to a working PMT, so it cannot account for its effects.

These considerations do not apply however to the measurement of pedestals and of gate widths as these parameters are input-independent[19] .

The 224 channels were pulsed one after the other with a fast PMT-like signal of $26.5mV$ ($\sim 2pe$) and the parameters of the three outputs have been measured with a digital oscilloscope.

The results are shown in fig. 6.22, where plots feature one entry per channel. The spread in the parameter values can be due to misalignment among the boards with channels within the board being pretty much aligned or to channels misalignment with boards mean values being correctly aligned (or a combination of the two effects). In both cases the difference can arise from an uneven setting or from intrinsic differences among IC components.

Considerations follow in the order of the figure. The physical meaning of the parameters was introduced in sec. 4.3.2:

PO delay Not settable.

The spread is mostly inter-board, channels in the same board are aligned within $0.5ns$.

The spread must be corrected, i.e. the channels must be software aligned. The channel calibration algorithm (sec. 7.4.5) computes a single corrective offset that accounts for both electronic misalignment (this effect) and PMT transit time differences.

PO gain Setting requested: $10ns/pC$ (i.e. the minimum).

The spread is mostly inter-channel.

The channel calibration algorithm (sec. 7.4.5) computes the conversion constants that account for both PMT and QTC gains, so neither the absolute value nor the spread are critical.

Gate width Setting requested: $60ns$ (i.e. the minimum).

The spread is acceptable and mostly inter-channel.

[19] They require only a logic pulse on the STRIG control line (sec. 4.3.2).

SO delay Not settable.

The spread is mostly inter-board, channels in the same board are aligned within $1ns$.

The spread should be (and is) small compared to SO width, not to compromise the contemporaneity of signals in OMT generation.

SO width Setting requested: $150ns$.

The boards show an unexpected variation depending on which channel is pulsed. The setting was done looking at ch0 and in fact this channel well meets the request on all boards, while the value gradually decreases with increasing channel number. When ch15 is pulsed, the SO width is $\sim 140 \pm 5ns$ long. The worst case reads $128ns$.

SO step height Setting requested: $100mV$.

All channel values are within 5-10% of request. This allows a safe discrimination of the channel number from the step function height.

TO delay Not settable.

The spread is mostly inter-board, channels in the same board are aligned within $1ns$.

The spread must be small not to endanger the contemporaneity of signals in TOTC generation. It may be necessary to align boards applying short junction cables.

TO gain Nominal amplification: $\times 5$.

All channels lie within 5-10% of nominal gain. An easy signal discrimination should be possible.

The absolute values of the three delays are not relevant and actually include arbitrary constants due to the length of the cables used for the measurement.

6.7.4 QTC pedestals and precalibration

The reconstruction of the hit charge in OD (sec. 7.4.2) requires QTC pedestal values (sec. 4.3.2). Therefore their knowledge is of particular importance in the characterization of the QTC boards.

The input baseline is actually quite sensitive to drifts and noise from the PMTs.

Drift effects cannot be addressed precisely yet, because the opportunities to turn on a significant number of PMTs were too few until now. However qualitatively there are indications of changes of a few ns on the day time-scale.

Noise from the PMTs is instead clearly visible in fig. 6.23, where the plots on the right refer to the data of sec. 6.7 and fig. 6.21. With the PMTs off, the pedestals can be determined with a $\sim 1ns$ RMS, while turning on the PMTs worsens this result significantly.

It was decided to perform the measurement on a run-by-run basis, taking advantage of the precalibration procedure (sec. 6.3.1). At the beginning of the run the PPC software

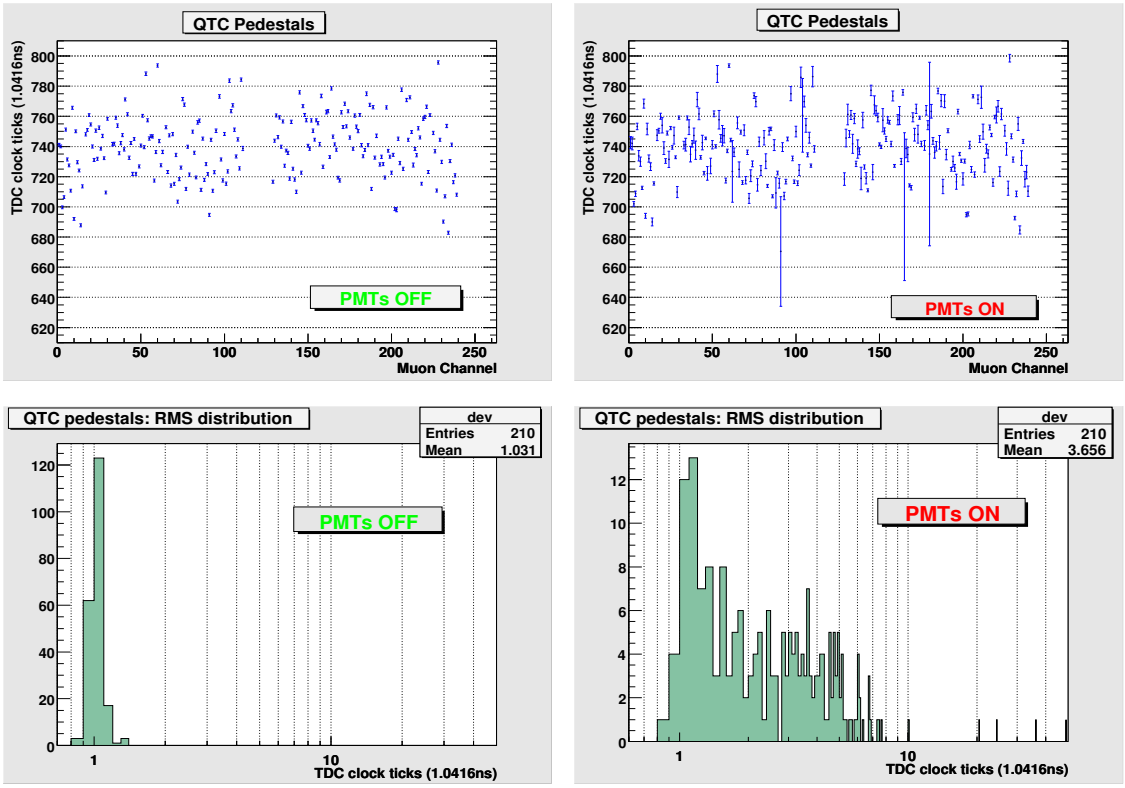

Fig. 6.23: *Above: QTC pedestal distribution with PMTs off (left) and on (right). Below: the RMS measured over the 1000 samples in the two cases.*

(sec. 5.2.3) sets the QTCs in *pedestal* mode. The 1000 precalibration triggers are used to externally pulse the STRIG line of the control bus. After the precalibration phase, the PPC sets the board to *run* mode for the rest of the run.

This procedure was developed on pulser data and tested with success on PMT data during AR6.

The 5 channels with large instabilities in fig. 6.23 (right) correspond to problematic PMTs with very high rates ($> 200kHz$). In this case the QTC is often busy processing noise pulses and for most of the 1000 events it misses the calibration pulse. Though not relevant for healthy channels, the effect has been corrected disabling the QTC comparator (i.e. keeping low the RUN line of the control bus) during the precalibration phase. This prevents the channel from firing, but doesn't disconnect the input from the QTC chip, in this way the precalibration still happens in real *noisy* condition as wanted. It will be tested on next opportunity to turn on PMTs in the WT.

6.7.5 Cross-talk effect

During the trigger studies described in sec. 6.7.6, a minor cross-talk effect was discovered on the QTC boards. When a channel is receiving a pulse above $10pe$, one or more neighboring channels may experience induced pulses. Though these pulses are tiny, of

THR	Q($p.e.$)	CH1	CH2	CH3	CH4	CH5	CH6	CH7
15	1.67	X	-	-	-	-	-	-
15	4.6	X	-	-	-	-	-	-
15	43	X	0.46	0.01	0.04	-	-	0.21
15	83	X	74	0.8	29	6.9	5.4	62
20	4.5	X	-	-	-	-	-	-
20	43	X	-	-	-	-	-	-
20	83	X	14.5	-	-	-	-	-
20	110	X	82.5	-	-	-	-	-
20	4.3	-	X	-	-	-	-	-
20	43	-	X	-	-	-	-	-
20	82	-	X	0.49	-	-	-	-
20	108	-	X	9.3	-	-	-	-

Tab. 6.4: *Qualitative study of cross-talk effect in QTC boards. Channel marked "X" is the pulsed one. Values are in %. Minimum* 10^4 *events were taken in each run segment, therefore a "-" indicates an effect smaller than 0.01%. Channel 0 was used as integrity channel (sec. 4.3.3).*

the order of $0.1 - 0.2pe$, they may accidentally cross the threshold if this is low. The effect is present only for pulses as fast as PMT signals and could not be reproduced with the pulser.

A preliminary and qualitative study of the cross-talk effect in relation with threshold and signal amplitude is shown in tab. 6.4. A few remarks can be drawn:

1. Pulses of $5pe$ or lower do not induce any cross-talk in any condition.
2. Pulses of $40pe$ or lower (and probably up to $50pe$ or $60pe$) induce an effect not larger than 1%.
3. A significant effect is therefore limited to very high pulses, for which no triggering issues are expected.
4. Raising the threshold to $20mV$ already improves the situation significantly.
5. The effect generally depends on the specific channel pulsed[20].
6. The effect is down-ward only in the board: pulsing CH2 doesn't affect CH1 even at high pulses and low threshold.
7. The dependence on the number of channels separating the pulsed and the observed channels is not trivial. For example pulsing CH1 affects CH4 much more than CH3. CH7 seems to be particularly sensitive.
8. The upper (0-7) and lower (8-15) channel groups never talk to each other. This is obvious since in the board layout they are much further away than the typical channel separation (fig. 4.9).

[20]The cross-talk arise from the physical layout of the channel blocks and of the grounding planes, therefore it is not expected to be symmetric with respect to pulsed input.

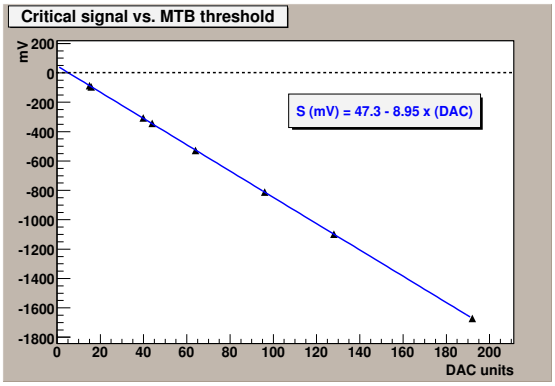

Fig. 6.24 (a): *Scan of the MTB threshold. For each setting the critical signal height producing OMT is determined.*

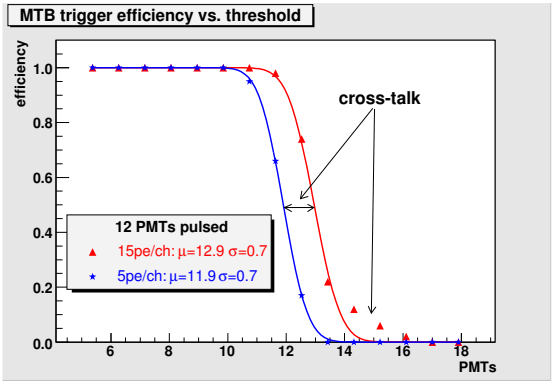

Fig. 6.24 (b): *Test of MTB trigger efficiency with 12 PMTs pulsed by LEDs.*

The cross-talk effect could be easily eliminated by raising the QTC thresholds: at $30mV$ the effect is already negligible. However since the induced pulses are so tiny, they could be easily filtered out at reconstruction level. On the other hand loosing a portion of the SPE charge peak, though tolerable, would complicate the charge calibration (sec. 7.4.5) of the channel in SPE regime (a simple Gaussian fit would probably be no longer sufficient for a visibly cut spectrum).

Now that the calibration system is in good shape and is itself calibrated (chap. 8) a better strategy is to perform a thorough study of the effect on all boards, scanning on both LED intensity and input channel and add it to the simulation of the electronics.

6.7.6 Trigger studies

During the preparation of AR6, a scan of the MTB threshold (sec. 4.4.6) was performed pulsing one of the J1 inputs with a pulser. A few values in the dynamic range of the 8-bit DAC were used and the *critical* signal height was determined in each case, i.e. the minimum signal height (in absolute value) required to generate the OMT. The result is shown in fig. 6.24(a) and can be summarized as follows:

$$S = (47.3 - 8.95 \times DAC)mV \tag{6.3}$$

Considering the average QTC SO step height of $-101.5mV/ch$ (sec. 6.7.3), an increase in the number of PMTs in trigger by one corresponds to 11.3 DAC units.

During the AR6 the MTB efficiency was tested in a much similar way to what exposed for the BTB in sec. 6.4.5. The 12 bagged PMTs were pulsed with the LEDs at about $15pe$ and the fraction of events for which the OMT was generated was measured as a function of threshold. Unlike the BTB case, here the trigger rate doesn't experience any accidental contribution from dark noise. The result is the red graph in fig. 6.24(b) where the x-axis was converted from DAC units to PMTs using the pulser test mentioned above. The fit

function is again eq. 6.2[21], but the fit yields 12.9 ± 0.7 PMTs not exactly the 12 expected. More important the efficiency doesn't drop to zero as sharp as it should, but shows a long tail that is poorly reproduced by the fit.

In the attempt to understand this behavior the cross-talk effect (sec. 6.7.5) was discovered on the QTC boards, the QTC thresholds being at $15mV$. Another trigger efficiency scan was then performed with LEDs at $\sim 5pe$, where no cross-talk is present. The blue line in fig. 6.24(b) shows this set of measurements. Here the "tail" is no longer present and the fit with eq. 6.2 yields 11.9 ± 0.7 in better agreement with the nominal value.

The introduction of the cross-talk effect in the simulation of the electronics will help to compute the "effective" MTB threshold for OMT generation.

[21] As mentioned in sec. 6.4.5, eq. 6.2 is valid only for a high average value, when the Poisson distribution can be approximated with a Gaussian. Here 12 is regarded high enough for this.

Chapter 7

Data Reconstruction: Echidna

In this chapter the new reconstruction code of BOREXino entitled to offline data processing is introduced.

The data acquisition system (chap. 5) produces the so-called *rawdata* files, containing, for every event, the information in the "raw" form as recorded by the digital electronics of the various detector's subsystems.

However before the physics analyses can take place, rawdata files must be processed *offline*, computing the relevant physics parameters of the event. These include for example the position of the interaction vertex, the energy of the particle, the timing between successive events, *Particle IDentification* (PID) tags and many more parameters.

Comprehensibly it is a very articulate and delicate part of the software. To accomplish this task, starting from 2004, a new program has been developed named *echidna*[1].

Through the chapter some familiarity with C++ programming[209], Object Oriented design[210] and the ROOT analysis platform[211] is assumed.

7.1 Project generalities

7.1.1 Physics tasks

The main physics tasks performed by the reconstruction program are:

1. Pre-decoding (Pre-calibration). Computation of electronics parameters (sec. 6.3.1).
2. Decoding of the raw information.
   (a) Decoding GPS time for absolute time reference.
   (b) Decoding of Laben hit time and charge from ADC raw information using pre-calibration and calibration parameters.
   (c) Analogous decoding of OD hit time and charge.
   (d) FADCs pedestal subtraction and construction of a digital sum of channels.

[1] The Echidna is a small ant-eater that lives in Australia, but Echidna is also the name of a mythological figure of ancient Greece, half woman and half snake, who gave birth to a vast variety of monsters.

3. Clustering of hits into physical events and precise evaluation of event start time. Selection and synchronization of the correspondent FADCs windows.
4. Vertex position reconstruction of the event.
5. Splitting of overlapped events within a cluster.
6. Reconstruction of the event energy.
7. Computation of PID tags:
   (a) α/β discrimination.
   (b) Muon tagging.
   (c) Sphericity of the event and other geometrical parameters.
8. Muon track reconstruction.
9. Calibration tasks:
   (a) Single channel calibration: time and charge for ID and OD.
   (b) Dark rate of PMTs.
   (c) Scintillator and water quality evaluation.
   (d) Electronics status evaluation.
   (e) Calibration system auto-monitor.

Of course the list is not exhaustive, nor can it account for new ideas being delivered every month as the work proceeds.

7.1.2 History and motivation

The development of a first offline program, named `bx_rec`, started in the early 90s based on simulated data and proceeded through the years thanks to the effort of many collaborators, each one adding contributions according to his/her own skills and sensibility. With years the project grew out of control and started to show a few structural problems. For example, the use of three different languages (Fortran, C, C++), brought to an interface that was extremely fragile and prone to the introduction of tricky bugs. The high interdependence of the different routines (lack of modularity) had made it very difficult to maintain and upgrade the code. Finally it was impossible to enforce data protection as the Fortran *common blocks* areas were always writable by any routine.

A fundamental reorganization was badly needed and this resulted in a new project named *echidna*, where most of the well established physics algorithms of `bx_rec` could be re-implemented in a completely new program, together with many additional features.

The project started in March 2004 and in about six months a working infrastructure was built. Currently, about 30 modules are ready or in development, covering most of the tasks listed above.

7.1.3 Design principles

The guiding principles of the new design are:

Modularly. The physics algorithms are organized into independent modules run by a framework engine. The framework and a large set of ancillary routines constitute the *infrastructure* of the program.

Data protection. Every module is assigned a data area within the event system of classes, of which it is responsible. Writing outside this area is not allowed (i.e. compilation fails). In this way it is immediately possible to track a bug or a miscomputed parameter to its very source.

Use of ROOT. The collaboration agreed that the official analysis platform in use in BOREXino is ROOT. Echidna therefore produces its output as a standard ROOT file.

Use of Database. The program is able to access all sort of required information (mapping, geometry, calibration, fluid handling) from the BOREXino database (sec. 5.6). The databases `bx_calib` and `bx_precalib` are mostly written by `echidna`.

Single language. A robust offline program has to be coded using one programming language only and the most natural choice was C++, as it is the language used by ROOT and by its interpreter. Moreover the Postgres database to which the program interfaces provides API for C++ and not for Fortran.

***Object-Oriented* (OO) programming.** This design philosophy comes pretty natural in C++ and constitutes an advantage in enforcing modularity and data protection. However there are different degrees to which it can be pushed, requiring increasing programming skills. It was decided that the accessibility of the code to a large group of developers was a higher requirement than extreme orthodox OO style.

Network oriented. Database and rawdata files are normally accessed over TCP/IP *at run time* from the DB server and the disk storage respectively, both of them located in the Gran Sasso computing cluster (sec. 5.1)[2]. Local copies of DB and rawdata are needed only if running on an isolated machine.

7.1.4 Organization

Currently about twenty collaborators have joined the project, equally distributed among *developers* and *testers*.

Every module is assigned a maintainer (usually the main developer) and a tester.

Testers have a fundamental role. After understanding the module's algorithm (from documentation, without reading the code), they define a list of test histograms that monitor its correct behavior. Test hostigrams are then produced by running the module on a set of simulated or real data, respectively generated or selected by the testers in

[2] In the future it is foreseen to build a mirror in the Lion (France) in2p3 computing facility.

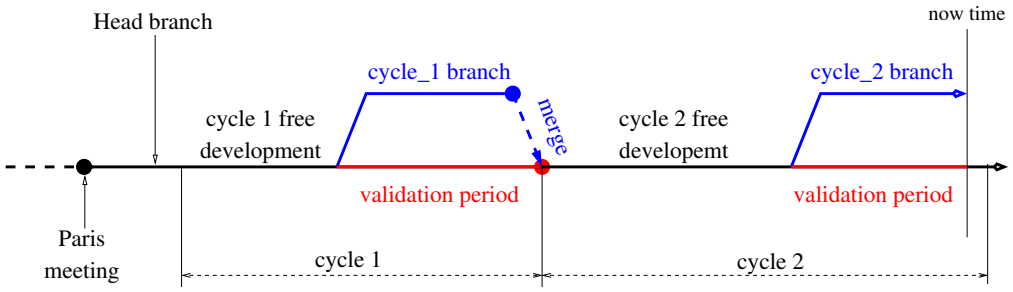

Fig. 7.1: *The time evolution of Echidna working cycles.*

order to evidence the module's performance. A written report is then filled and archived at every new release of the code.

The interaction among developers working in parallel is handled with CVS[3] and the code is stored in the official BOREXino CVS repository in Gran Sasso.

Under the guide of a project manager, the work is organized in production cycles lasting about 2 months. Each cycle includes in order:

Meeting. A meeting where the *Request-For-Changes* (RFCs) proposed by co-workers are discussed, approved and scheduled.

Development. About 6 weeks are devoted to the implementation of the scheduled tasks. Documentation of the code produced must also be supplied and/or updated.

Branch spawning. Upon schedule fulfillment, the project manager decides to "freeze" the code in a parallel CVS branch.

Tests. Testing and debugging proceeds on the test branch (about 2 weeks), while the main branch remains available for further development.

Merging. At the following cycle meeting, if all testers report positively, the branches are merged back into one.

7.2 Infrastructure

The infrastructure takes care of everything that is not directly related to event processing. All *technical* tasks are so separate from physics modules, though themselves organized into modular programming units.

Moreover any collaborator that proposes a physics algorithm is encouraged to develop a module, no matter what his/her programming skills are. For this reason, the infrastructure was designed to make their life as easy as possible, letting them concentrate on physics issues only.

The infrastructure does:

1. Run the modules.

[3] *Concurrent Version System*, a standard tool for this goal[207].

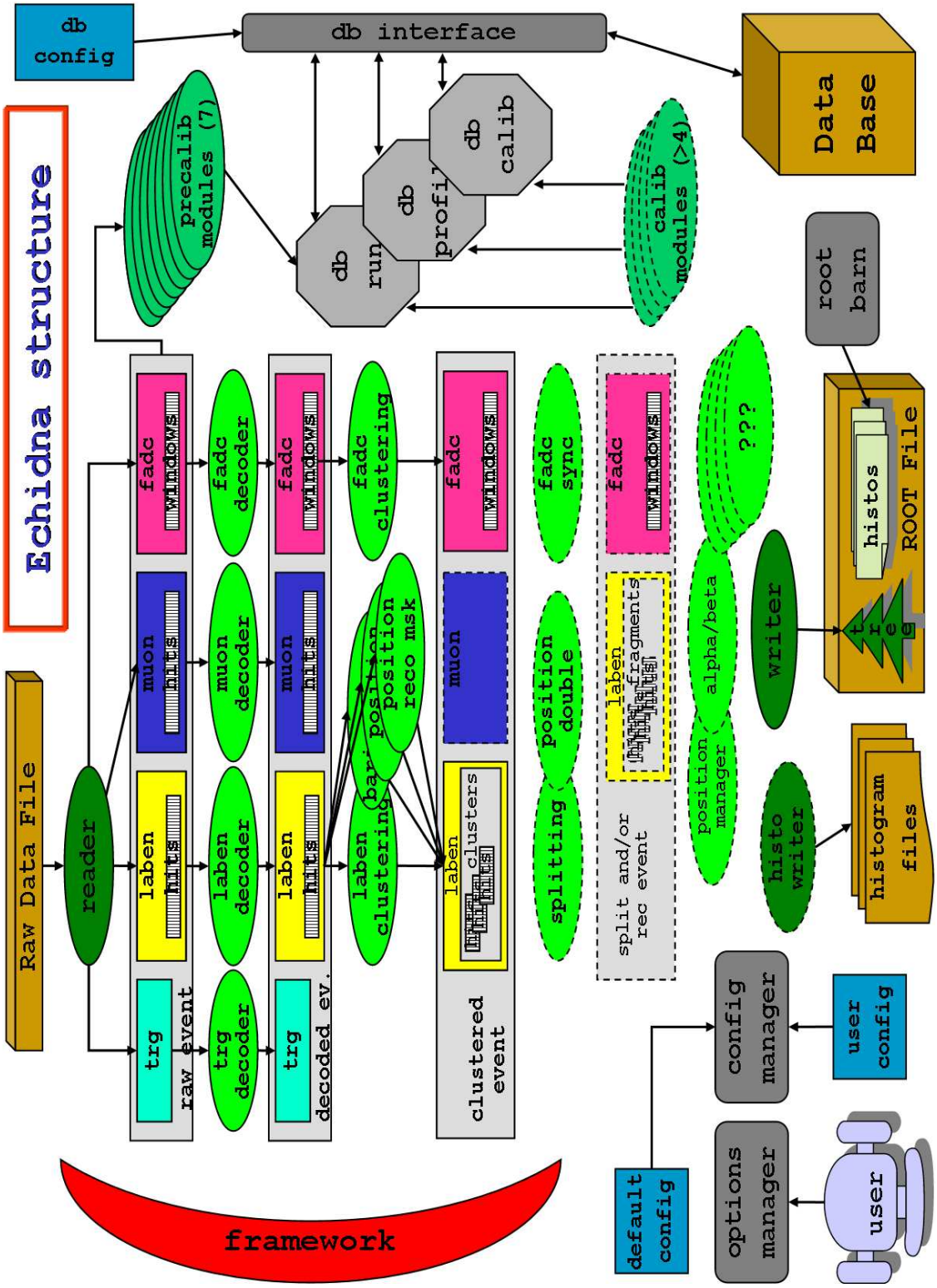

Fig. 7.2: *Echidna general scheme (see text).*

2. Handle the internal event area.
3. Read the rawdata file and build the raw event.
4. Write the ROOT file:
   (a) Write a ROOT tree with events.
   (b) Handle module's test histograms.
5. Interface with database (READ and WRITE).
6. Interface with the user:
   (a) Handle messages and log file.
   (b) Handle parameters and configurations.

The scheme of the program is shown in fig. 7.2. The physics modules are shown with green ovals: brilliant green for main loop modules, sea-water green for pre-calibration and calibration modules, dark green for special infrastructure modules.

The engine of the program is the framework, a single instance object which holds the list of modules, initializes and runs them. Running starts with pre-calibration loops, where only pre-calibration events and pre-calibration modules are used (up-right). Then the main loop takes place, where ordinary work occurs.

7.2.1 Internal event

Data relative to the events are organized according to two concepts:

detector segment. This refers to the components of the detector introduced in chap. 5: trigger, laben, muon, fadc. Two non physical segments are also present: one with high level Particle ID information (PID) and one with Monte Carlo truth (mctruth).

reconstruction stage and *reconstruction step*. These refer to the iter the event is undergoing in the program. At every stage the event becomes richer of information. A module is normally in charge of performing a reconstruction step that brings the event into its next stage. For example the `bx_laben_decoder` module brings the laben segment of the event from `raw` to `decoded` stage.

Different detector segments may have different reconstruction steps/stages.

Event Classes

The event structure is depicted in fig. 7.3. The most general class in this context is the `bx_echidna_event`, which holds the event header information (event number, run number, daq config, ...)[4] and 6 objects, one for each detector segment:

- `bx_trigger_event`

[4]The event header is written by the `builder` (sec. 5.4).

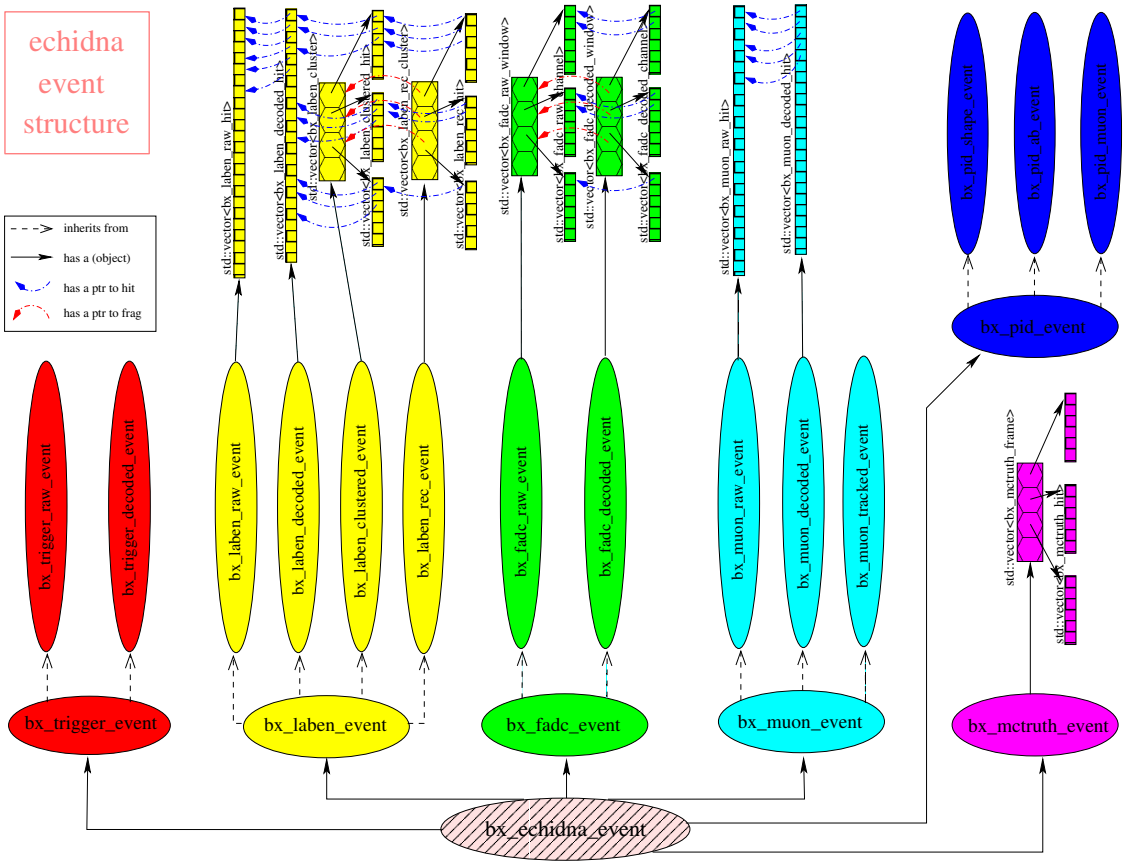

Fig. 7.3: *Echidna internal event structure.*

- `bx_laben_event`
- `bx_muon_event`
- `bx_fadc_event`
- `bx_pid_event`
- `bx_mctruth_event`

Every one of the above inherits from a number of classes, relative to different reconstruction stages. For example `bx_laben_event` inherits from:

- `bx_laben_raw_event`
- `bx_laben_decoded_event`
- `bx_laben_clustered_event`
- `bx_laben_rec_event`

Each class is writable by a specific module through a `friend` declaration enforcing in this way data protection.

Hit Classes

If appropriate, a hit class is defined for each reconstruction stage. In this case the event class holds an STL vector of these hits. For example class `bx_laben_decoded_event` holds a `std::vector<bx_laben_decoded_hits>`.

Since the module performing a given reconstruction step may decide to discard hits according to its own criterion, vectors of hits in successive reconstruction stages may be misaligned. Every hit class is then given a pointer to its correlated hit in the previous stage.

In addition decoded hit classes have a pointer to a `db_channel` object containing database (`bx_geometry`) information on the relative channel. These pointers can be indirectly accessed at any subsequent stage[5].

Clusters, Fragments, Windows

Starting with clustered stage, laben hits are organized in *clusters* (up to 3 per event) according to the result of clustering module (sec. 7.4.3). Hits not belonging to any cluster are discarded in this step. Clusters refer to physical events within the BOREXino trigger gate that are not piled up, i.e. whose time separation is longer than $150ns$. Depending on the performance of the splitting module (sec. 7.4.7), clusters may be converted in *fragments* at a later stage, where also piled-up events are separated.

Fadc data are "naturally" (i.e. by the DAQ) organized in *windows* (sec. 5.2). In early reconstruction stages, windows contain *channel* objects. Clustering for this detector segment selects the three most significant windows and performs the alignment with laben clusters.

7.2.2 Raw Event construction

A special module `bx_reader`, whose internals are not covered here[204], is in charge of reading the rawdata file. This module then invokes the raw event constructors in cascade, passing them only a pointer to a memory slab where the rawdata have been read.

Building the raw event in principle implies just a formatted copy from this area. However there are a few cases where some intelligent unpacking of the data is required. Among these, the most significant case is the muon raw event constructor.

Muon raw event constructor

Muon rawdata are sequences of TDC edges (sec. 4.3.3). This constructor performs the job of coupling edges into physical PMT hits, a relatively complicated task that proceeds as follows.

A loop is done over edges with a step of 2. Edges reporting *event number*[6] or flagged as *invalid* are silently discarded.

A local TDC chip counter is incremented whenever an edge flagged as *last-datum* is found. The TDC data do not contain information on the board number, so this must

[5] Not available during pre-calibration.

[6] These edges are present only for DAQ reasons (sec. 5.2.3).

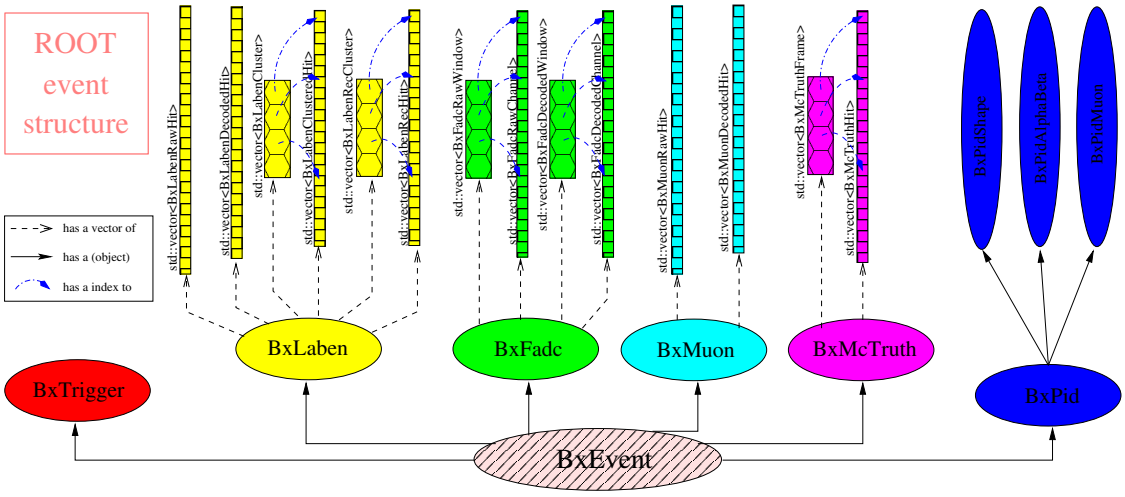

Fig. 7.4: *Echidna* ROOT *event structure.*

be evaluated through this chip counter. Moreover the total number of chips is checked against 8, due to the presence of the integrity channels (sec. 4.3.2).

A method named `m_check_validity()` is in charge of checking if the two edges do belong to the same QTC pulse:

1. The slopes of the two edges must be opposite and edges must belong to the same TDC channel. If this is not the case then probably an edge was lost. The first edge is then spurious and is being discarded with a debug level message. The second edge instead could be a valid first edge for the following hit and must be reprocessed. Control is returned to the loop with appropriate index correction.

2. The time ordering of the two edges must be correct, i.e. the first edge time must be higher than the second one [7]. If this is not the case, both edges are discarded with a debug level message and control is returned to the loop. This pathological behavior appears usually when a LED is firing at high intensity, resulting in a high after pulse rate.

If both checks are passed, a raw hit is constructed and pushed into the vector.

7.2.3 ROOT interface

Echidna produces a ROOT file which is the base of all the official physics analyses of the experiment. This file contains a ROOT *tree* object and some test histograms.

Event tree

ROOT uses a more flexible concept of n-tuple named *tree*, where not only plain variables can be stored but any kind of object like containers, histograms, functions, etc. Objects

[7] In common stop mode the TDC yields times that go backward from trigger instant.

can be organized in one or more *branches*. Single branch designs are easier to handle (for users) while multi-branch designs are more effective in terms of file I/O. ROOT enforces also the powerful concept of *splitting* that conjugates the two advantages. Split objects are written to file internally handling the sub-objects as separate branches. This also has advantages in terms of graphical tools functionality (e.g. the `TBrowser`).

In echidna it was decided to design an event class stored in a single branch and that benefits from splitting.

This class, named `BxEvent`, has a structure of sub-objects (fig. 7.4) similar, though different, to the internal `bx_echidna_event` class. The major difference is that, as `BxEvent` is written in a single step, the inheritance from base classes for the various reconstruction stages is not needed: the sub-objects of the different detector segments hold variables or containers directly.

All classes designed inherit from the base ROOT class `TObject` which allows the streaming to file and the generation of a dictionary through the `rootcint` utility.

The choice of being complaint to ROOT splitting, though very advantageous, sets some design restrictions:

1. Polymorphic objects cannot be used. This would have been useful to handle the need of a double light/heavy version of the event, where the light version contains only high level information and is meant for standard analysis, while the heavy version is to be produced only for more particular tasks.

2. Creating and destroying the `BxEvent` object at every event is not possible, as ROOT needs to cache some pointers to be able to split the object. Consequently a single instance of `BxEvent` is created and is filled with an assignment operator (from the internal event).

3. Nesting containers[8] is not possible (they are not split). Therefore the sub-objects of the different detector segments hold in parallel all the containers (STL vectors) of hits and clusters (or windows). Indexes are provided to link a hit to the cluster it belongs to (and for similar relationships).

The design was the result of a long study of the ROOT capabilities in handling such a complex class system. This was performed in correspondence with R.Brun and P.Canal of the ROOT development team, who also introduced a few upgrades to ROOT in order to meet our needs.

A special infrastructure module, `bx_writer`, takes care of opening the ROOT file, of initializing the tree and the event objects and of filling them for every event. It is executed after all physics modules have run. A set of user parameters (sec. 7.2.5) allows to customize which lists of hits and clusters are actually written to file, achieving in this way the flexibility exposed in pt. 1 above.

Test histograms

Modules often need to use ROOT histograms to perform computation (e.g. fits) and/or to produce a direct test of their performance independently of the ROOT tree.

[8] For example a vector of cluster objects, which in turn contain a vector of hit objects.

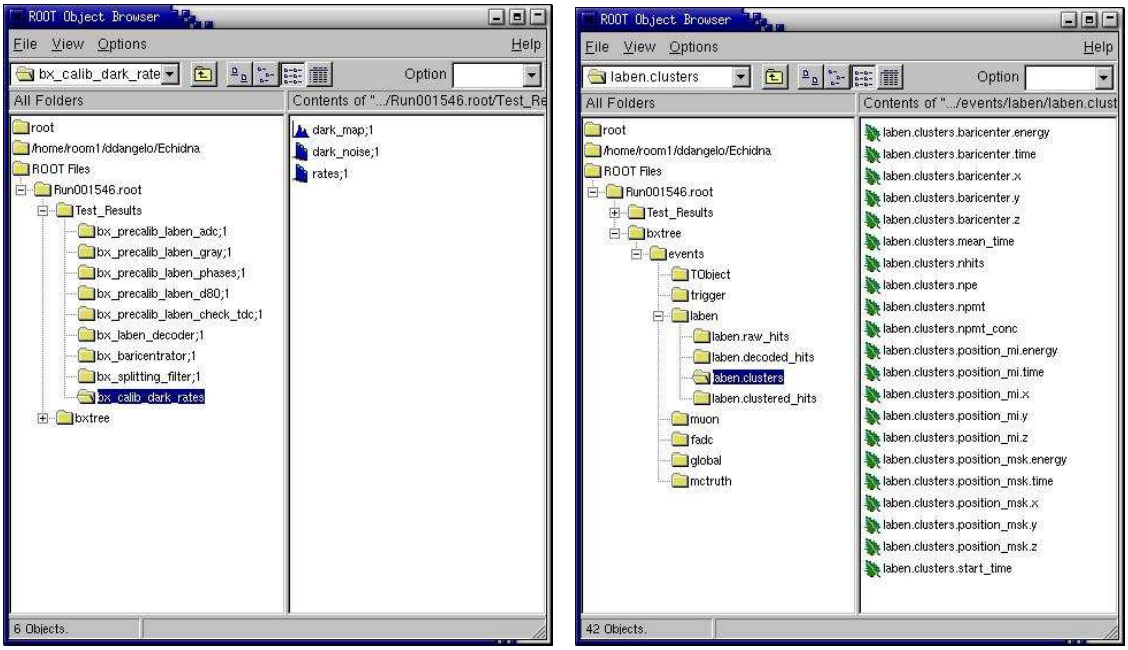

Fig. 7.5: *The BOREXino* ROOT *file as seen by the* `TBrowser` GUI. *The histogram (left) and the tree (right) folders are expanded in the two panels.*

A singleton object named `root_barn` handles these objects and writes them to the ROOT file (if the module requested this). Moreover it performs name look-up and garbage collection services for the modules.

Histograms are organized in a folder (separate from tree) divided in sub-folders, one for any module that made this request.

In this way module developers and testers share a set of histograms to monitor the module's performance on different data sets and across the program development.

7.2.4 DataBase interface

DataBase Interface (DBI) involves both read and write operations. A singleton class named `bx_dbi` takes care of the connectivity, of the handshaking protocol and of the query formation in SQL syntax.

The database information is mapped into a structure that reflects the keys used to store it rather than the physical DB organization. So three visitors[210] are initialized and filled by `bx_dbi`:

1. `db_run`:
   (a) DAQ run data.
   (b) Pre-Calibration data.
   (c) Channel calibration data.
2. `db_profile`.

   (a) Electronics config data.
   (b) Detector geometry and fluid handling parameters.
   (c) Logical channel mapping.

3. `db_calib`.

   (a) Scintillator calibration parameters.

Module's access (I/O) to these visitors is described in sec. 7.3.

If DB is really to be written (i.e. it is an official echidna run), the user, through parameters, can make `bx_dbi` export the visitors to DB (the part written within echidna).

7.2.5 User interface

User module communication involves two concepts: customization and messages.

Customization

The behavior of modules and of some infrastructure classes is customizable by the user through parameters. Every module has a parameter named `enable` and one named `priority` that allow to control which modules have to be executed and in which order. Examples of module specific parameters include physical values like thresholds or normalization factors and mode control parameters that choose a specific sub-algorithm. Examples of infrastructure parameters are instead the number of events to be processed (`bx_framework`), the input file name (`bx_reader`), which detector segments to enable (`bx_detector`), the database URL (`bx_dbi`) and many more[204].

Every parameter is given a default value in the main configuration file (`echidna.cfg`). However a higher priority user configuration file (empty by default) is available to overwrite defaults (`user.cfg`). With even higher priority, parameters can be overwritten also through command line options.

A singleton object named `parameter_broker` reads configuration files[9] and holds all parameters organized in namespaces, one for every "named"[10] object.

Messages

A message handler is present as a singleton object available throughout the program. Modules are allowed to produce messages only through its methods. Messages follow a fairly standard severity hierarchy: `debug`, `log`, `info`, `warn`, `error`, `critic`.

The message handler takes care of printing to log file and to standard output messages with minimum severity of "log" and "warn" respectively. These levels are customizable through command line options that control the program verbosity.

The message handler also terminates the execution cleanly upon receiving a `critic` severity message.

[9] It receives also command line options from another singleton called `bx_options` which makes the parsing.

[10] implemented with inheritance from a pure virtual base, `bx_named`, which grants access to the parameter broker as a static pointer member.

7.3 Modules implementation

In this section there are covered the main aspects of how a module is implemented. A more complete document with many examples is [205].

A module is a persistent object of a specific class, initialized and handled by the framework (sec. 7.2). Only one instance of any module class can exist in the running program.

Construction

Module inherits from a (pure virtual) base class named `bx_base_module`. This provides indirect inheritance from `bx_named` base class (i.e. modules are "named" objects, sec. 7.2.5) and many of the methods used to interface with the infrastructure.

The module's constructor (and destructor) is trivial, involving only name and role registration through provided methods. The role specifies whether it is a pre-calibration module, a main loop one or a special infrastructure module (reader, writer, ...).

In the module's constructor two kinds of requirements can also be made (by calling the provided methods):

1. *event stage*. It can be required that a given event segment is in the correct event stage or, in other words, that logically preceding modules have been run on the event segment of interest. For example a clustering module will require that the event has been previously decoded.

2. *trigger type*. The module can be required to execute only on events with a specific trigger type. For example a laser calibration module will require trgtype "laser394".

The framework skips the execution of the `doit()` method (see below) on events that fail to meet a requirement.

Interface

The module's interface is inherited from `bx_base_module` and is therefore fixed. The developer must implement three (public) methods:

`begin ();` executed once, before the loop on events starts. Initialization of resources occurs here.

`doit (<ptr_to_event>);` executed for every event in the loop. Event-level computation occurs here.

`end ();` executed once, after the loop on events has terminated. Run-level computation occurs here. Resources allocated in `begin()` are released here.

The "private" section of the module is left instead entirely to the developer: e.g. local data can be stored, helper methods or classes can be defined, ...

There are two logical categories of modules:

1. *Ordinary* modules perform event-level computation and write to an event area. They mark the achieved event stage, just before (successfully) returning from the `doit()`. This is done by calling a provided method which increments an `enum` in the event detector's segment. In this way logically following modules can set a requirement for this stage as explained above.

2. *Pre-calibration* and *calibration* modules perform their main task at run-level (`end()` method). Such modules do not write to the event, but to the DB visitors (sec. 7.2.4). They also require local storage of data or objects (e.g. ROOT histograms filled in the `doit()` and processed in the `end()`).

Accessing the event

Access to the event occurs through the pointer `bx_echidna_event* e`, received in the `doit()` method. Hence `const` references to any event area can be obtained through provided getter methods[11].

Ordinary modules will also need a non-`const` reference to write to. This requires a dynamic up-cast to the area the module is allowed to write (i.e. to which it is `friend`, sec. 7.2.1). The program fails to compile upon accidental attempts to write to other areas, enforcing in this way data protection.

Accessing Database

The DB information can be obtained from the three visitor classes described in sec. 7.2.4 via getters of `bx_dbi` like:

```
const db_run& run_info = bx_dbi::get ()->get_profile ();
```

and similarly for `db_run` and `db_calib`. Hence getters are available for any variable.

Pre-calibration and calibration modules use non-const references and write through setters methods like:

```
run_info.set_my_variable(channel, value, this);
```

where `this` is passed as a sort of ID card. An ACL class checks if the module is allowed to call the setter.

Accessing User Parameters

Access to user parameters inside a module occurs via methods inherited from `bx_named`, like:

```
const vdt& get_parameter (const std::string& par_name) const;
```

This returns the parameter value as a `vdt` object (*variable-data-type.*). This is a custom `union`-like object with smart getters that provide the value as any basic type.

[11] There is no need to refer to a specific reconstruction stage for reading, since overloading of getter names is not allowed in the event classes and all getters are available from the derived class.

Sending messages

Message interface is inherited from `bx_base_module`. To print a message it is enough to call:

```
get_message(bx_message::warn) << "Unusual jitter in channel " << ch
<< dispatch;
```

where `bx_message::warn` is the msg level and `dispatch` is a function object[209] that determines buffer flushing.

Multi-line messages are treated in a slightly different way.

Registering histograms

The module registers the ROOT object it uses to the `root_barn` (sec. 7.2.3) with:

```
bx_root_barn::get ()->store (bx_root_barn::test, my_histo, this);
```

where `my_histo` is pointer to a valid ROOT object (any class inheriting from `TObject`: `TH1F`, `TH2F`, ...) and the `enum` value `bx_root_barn::test` requests the streaming to file. Alternatively, `junk` can be used for temporary objects.

7.4 Physics modules

In this sections echidna physics modules are reviewed following approximately the task list reported in sec. 7.1.1.

7.4.1 Pre-calibration

From the data-taking point of view, the *pre-calibration* procedure was introduced in sec. 4.4.5 and 6.3.1.

In echidna, when a run is processed for the first time, the *pre-calibration* parameters must be computed. Before the main event loop, the framework performs 4 pre-calibration event loops, selecting only events with *calibration* trigger type, in particular the first 1000 events of the run. Modules registered with `role=precalibX (X=1,2,3,4)` are executed in one of these loops.

The computed parameters are stored in `db_run` visitor and from here `bx_dbi` will save them in DB `bx_precalib`. If the run is processed again pre-calibration is skipped and parameters are read from DB[12].

Laben pre-calibration

The laben rawdata for every hit include the two ADC samples $t_{1,2}$ of the $10MHz$ TWF, $80ns$ apart (sec. 4.2.3) and the gray counter value. Four pre-calibration modules compute the parameters necessary for the hit time reconstruction (sec. 6.3.1):

[12] Unless pre-calibration is forced by the user with a user parameter.

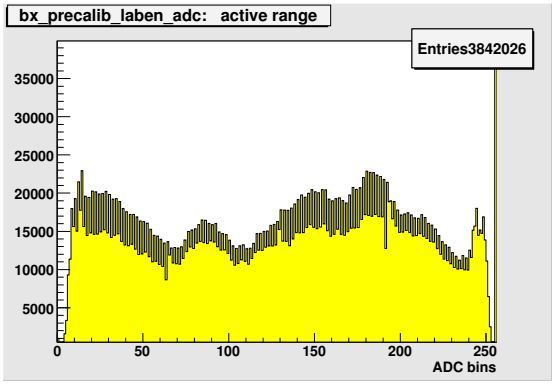

Fig. 7.6 (a): *Laben pre-calibration: the ADC active range.*

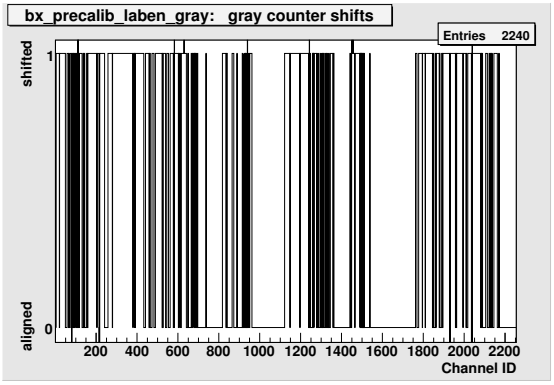

Fig. 7.6 (b): *Laben pre-calibration: map of the gray counter shifts.*

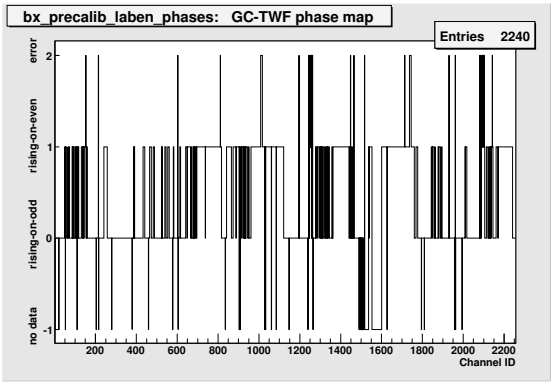

Fig. 7.6 (c): *Laben pre-calibration: map of the phases between gray counter and TWF.*

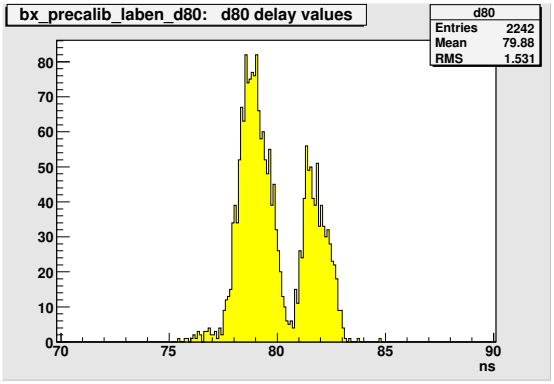

Fig. 7.6 (d): *Laben pre-calibration: measured "80ns" delay between ADC samples.*

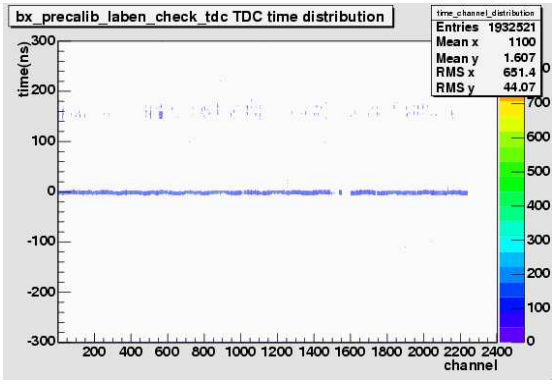

Fig. 7.6 (e): *Laben pre-calibration: check of TDC performance.*

`bx_precalib_laben_adc.` It finds the ADC bins corresponding to the TWF spikes. The calibration hits have a random phase, so they can be put in an histogram (fig. 7.6(a)) from which the edges are determined.

`bx_precalib_laben_gray.` Pre-calibration hits are perfectly time aligned, so gray counter shifts can be computed relative to a reference channel (fig. 7.6(b)).

`bx_precalib_laben_phases.` It computes the parity between gray counter and TWF using a heuristic method. Given the sample t_1, the ideal position of the sample t_2 is calculated for the two parity cases, *rising-on-even* and *rising-on-odd*, and compared with the measured one. If the sample is clearly closer to one of the two than to the other, the hit is counted for the relative parity, otherwise it is discarded. The parity with higher statistical occurrence is assumed for the run (fig. 7.6(c)).

`bx_precalib_laben_d80.` It measures the real delay between t_1 and t_2 (fig. 7.6(d)), to be subtracted when the fine time is computed out of t_2.

While gray counter shifts and phases are run dependent, ADC ranges and "80ns" delays are in principle hardware parameters of the channels/boards and should be keyed to the profile ID. However as they require little CPU power the latest policy is to run all four on a run basis. In this way even unexpected drifts may be accounted for (e.g. the A/C system breaks down).

A fifth module (`bx_precalib_laben_check_tdc`) checks the resulting overall TDC performance (fig. 7.6(e)).

Muon pre-calibration

Within the pre-calibration loops also two modules are executed that work on OD data:

`bx_precalib_muon_findpulse.` This module finds the time of the pre-calibration pulse used by the following module. Avoiding to hard wire this number in the code, makes hardware changes (like cable replacement) harmless for the procedure.

`bx_precalib_muon_pedestals.` This module computes the pedestals of every channel, averaging the 1000 events (sec. 6.7.4). Spurious hits are filtered out by selecting a $20ns$ window around the time found by the previous module. The RMS of the pedestals are also computed. A value larger than a few ns marks the channel as unstable and a warning is issued. Examples of plots produced are shown in fig. 6.23.

7.4.2 Decoding

After pre-calibration is complete, the main event loop starts and the raw events undergo the first reconstruction step, i.e. decoding. The parameters computed by pre-calibration and (channel) calibration modules are used here. They are retrieved from `db_run` and `db_profile` visitors respectively.

Every detector's segment has its own decoder module.

Trigger Decoder

1. It decodes the trigger type by comparing it with DB codes for the profile in use.
2. It decodes the GPS time (in s and ns since midnight 01.01.2001) out the 5 low level words recorded by the receiver unit (sec. 4.4.4).

Laben Decoder

1. It computes the decoded hit time as:

$$t_{\text{dec}}(ns) = (50ns) \cdot (C - S)_{\text{gray}} + t_{\text{fine}} - t_{\text{crate}} - t_{\text{off}} \tag{7.1}$$

   where C is the gray counter value, S is its shift (precalib #2) and t_{fine} is given by eq. 6.1 using the measured $b_{l,h}$ (precalib #1). In the computation of t_{fine} the slope of the TWF is chosen according to the observed parity with the gray counter (precalib #3). If t_1 is within 10 bins from either b_l or b_h, t_{fine} is computed out of t_2 and then corrected with a $-d80$ (precalib #4).

   t_{crate} is a correction for misalignment in the trigger arrival time to different crates (fig. 6.7) and t_{off} is the channel time offset, both computed in calibration modules (sec. 7.4.5).

2. It computes the decoded hit charge as:

$$Q_{\text{dec}}(p.e.) = (P - B) \cdot \frac{1}{s}, \tag{7.2}$$

   where P and B are the *peak* and *base* sampling of the PMT pulse (sec. 4.2.2) and s is the SPE peak position from the calibration module (sec. 7.4.5).

   However if the time difference with the previous hit is smaller than $\sim 5\tau$ ($\tau = 500ns$ being the front-end integrator decay constant), pile-up effect is taken into account using eq. 4.1.

3. It processes laser and trigger special channels to provide reference times (sec. 4.5).
4. It sorts the hits for time to make clustering work easier (sec. 7.4.3).
5. It provides a 2D test histogram to check the time resolution of every channel.

Muon Decoder

1. It computes the decoded hit time as:

$$t_{\text{dec}}(ns) = (\Delta W - t_{\text{lead}} - t_{\text{off}}) \cdot \frac{1}{f} \tag{7.3}$$

   where ΔW is the TDC window depth (usually 8192 c.t.), t_{lead} is the raw time of the leading edge recorded by the TDC in c.t. *before* the common stop (trigger) signal. f is the TDC clock frequency ($960MHz$) and t_{off} is the time offset of the channel, calculated by the calibration module.

2. It computes the decoded hit charge as:

$$Q_{\mathrm{dec}}(p.e.) = (t_{\mathrm{trail}} - t_{\mathrm{lead}} - t_{\mathrm{ped}}) \cdot \frac{1}{s} \tag{7.4}$$

where t_{lead} and t_{trail} are the raw times of the leading and trailing edges respectively, t_{ped} is the pedestal (in c.t.) as computed by the pre-calibration module. s is the SPE peak position (in c.t.) calculated by the calibration module.

The decoded hit is constructed and pushed into the relative vector in the muon decoded event. A map of the number of hits per channel is also kept in the muon decoded event.

Laser394 events are handled somewhat differently. The decoded time is referred to the time of the reference channel (sec. 4.5), filtering out the $\sim 100ns$ jitter of the BGT generation time. As the calibration module runs *after* the decoding, no offset correction is applied in this case. For the same reason the charge is left in c.t., without multiplying for $1/s$ as this is not available yet. Optionally a user parameter can be used as s, useful for example in the LED calibration procedure (sec. 8.5.4).

Fadc Decoder

1. It computes and subtracts pedestals.
2. It decodes the trigger ramp in the special channel (sec. 4.6).
3. It computes the software sum of all channels (sample per sample).
4. It computes *amplitude*, *peak* and *charge* for every channel. Only these parameters are saved from this stage onward.

7.4.3 Clustering

The BOREXino trigger gate for Laben electronics is $\sim 6.5\mu s$ wide (sec. 4.4). Looking at the hit distribution in this window (fig. 7.7), the physical event pulses can be seen superimposed on the PMT random counts. The extraction of the pulse start time requires a fine algorithm.

Moreover, pairs of fast correlated (physical) events do appear in the same (DAQ) event and must be somehow separated.

In echidna the *clustering* module groups the hits belonging to the same physical event, building one or more *clusters* (up to three).

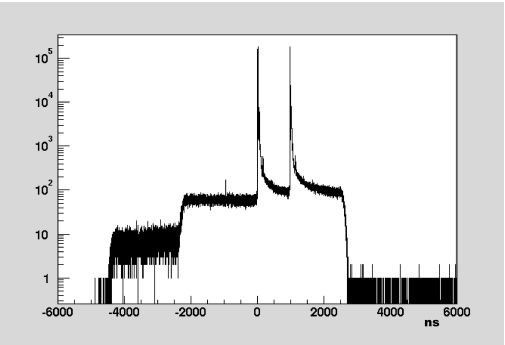

Fig. 7.7: *Double laser pulses: two clusters in the trigger gate.*

The decoded hit distribution, sorted in time by the decoder, is first binned by $16ns$. Then the condition for the beginning of a cluster is looked for:

1. a bin exceeds 3σ over average dark noise.

2. at least 20 hits ($\sim 50keV$) are found in the first $48ns$.
3. [1^{st} cluster only] integral of hits exceeds 80% of trigger threshold (in PMTs).
4. [1^{st} cluster only] cluster start time lies $2\mu s \pm jitter$ after trigger reference time.

where the last two conditions apply only to the first cluster, i.e. the one that determined trigger condition.

The end of the cluster is set when the hit distribution falls back below dark noise fluctuations. If between two successive physical pulses this condition does not occur, they are considered *piled-up* and a single cluster is generated for them. Handling of piled-up events is the job of the *splitting* module (sec. 7.4.7).

The cluster object is then constructed, containing the vector of its own hits, and is pushed into the cluster vector (*bx_laben_clustered_event* in fig. 7.3).

A second function determines the precise cluster start time. The candidate hit can be:

1. the first of 5 hits closer in time than one tenth of the average dark hit separation. As an example if all tubes were featuring a $1kHz$ dark noise, the detector would be "firing" at $2MHz$. In this case the average separation would be $500ns$.
2. the first of 3 hits closer in time than $2ns$.

where if there are two different hits fulfilling the two requirements, the second one is preferred. The necessity of the second condition applies if the detector is very quiet, when the first condition may be met too early.

A few other physics variable of the cluster are then filled, like number of hit PMTs, number of detected photoelectrons, mean time, ...

7.4.4 Position reconstruction(s)

The ability to reconstruct the position of the event within the *inner vessel* is crucial for the application of the radial cut that rejects the external background and for an effective α/β discrimination. For this reason, concurrent algorithms have been proposed and developed within the various institutions of the collaboration. Echidna was designed to handle multiple vertex reconstruction algorithms:

baricentrator. Not a real position reconstruction[13], it was born to compute the geometrical center of the positions of the hit PMTs, used as starting point by other algorithms. This as a simple vector sum:

$$\overline{x} = \frac{b}{N_{hits}} \sum_{i=1}^{N_{hits}} \overline{P_i} \cdot [Q_i] \cdot \left[\frac{1}{t_i + a}\right] \tag{7.5}$$

where b is a normalization constant. The two terms in square brackets are optional weights (user enabled) that take into account charge (Q_i) and time (t_i) recorded by PMT at location P_i (a is a user parameter of the order of the event mean time).

[13]The funny name comes from the Italian "baricentro", i.e. center of mass.

In addition, if enabled, the module finds the event time t_0 minimizing:

$$R(t_0) = \sqrt{\frac{\sum_{i=1}^{N_{hits}} \left[D_i - c(t_i + t_0)\right]^2}{N_{hits}}} \tag{7.6}$$

where D_i is the distance of the i^{th} PMT to the center computed before and c is the speed of light in the medium.

Milan. The historical and most well tested algorithm based on the (log) likelihood minimization of:

$$f(t_0, x, y, z) = -\sum_{i=1}^{N_{hits}} \log\left(pdf\left(\frac{D_i}{c} - (t_i + t_0)\right)\right) \tag{7.7}$$

where the symbols are defined as above and the *pdf* (*Probability Density Function*) is the simulated PPO emission curve (first $80ns$). The same algorithm is applied in CTF (sec. 9.1.4).

Moscow. Also quite well tested, it is based on a different *pdf*, namely a Landau function with five free parameters: t_0, x, y, z, E. It is therefore also an energy reconstruction algorithm.

Dubna. Similar to the "Milan" code, but based on an analytical *pdf*, this algorithm is still in the development phase.

The results of all enabled modules are stored in the `bx_laben_clustered_event`. This is mostly useful in this development phase where results have to be compared.

A further technical module is in charge of selecting only one algorithm and produce the `bx_laben_rec_event` with its result. In this way, logically following modules that rely on the reconstructed position (splitting, α/β filters) are decoupled from the specific algorithm in use. At run time only the most performant algorithm will be used.

7.4.5 Calibrations

Calibration modules are main loop modules to be executed on dedicated runs, taken with a specific trigger setup (sec. 5.3.1).

Only the low level calibrations are in place for the moment:

`bx_calib_dark_rates`. Module for *random* runs to compute PMT dark noise and to flag dead and noisy PMTs. Plots similar to those in fig. 6.17 and fig. 6.21 are produced.

`bx_calib_fiber_bundle`. Module for *laser394* runs to flag ID dead fibers and to compute the relative luminosity of the different bundles.

`bx_calib_gate`. Module for *random* runs to compute the exact laben gate extremes.

`bx_calib_laben_time_align`, `bx_calib_laben_charge_peak`. Modules for single channel time and charge calibration out of *laser394* runs (sec. 6.4). Perform Gaussian fit on time and charge SPE histograms. Produce t_{off} and s mentioned in sec. 7.4.2.

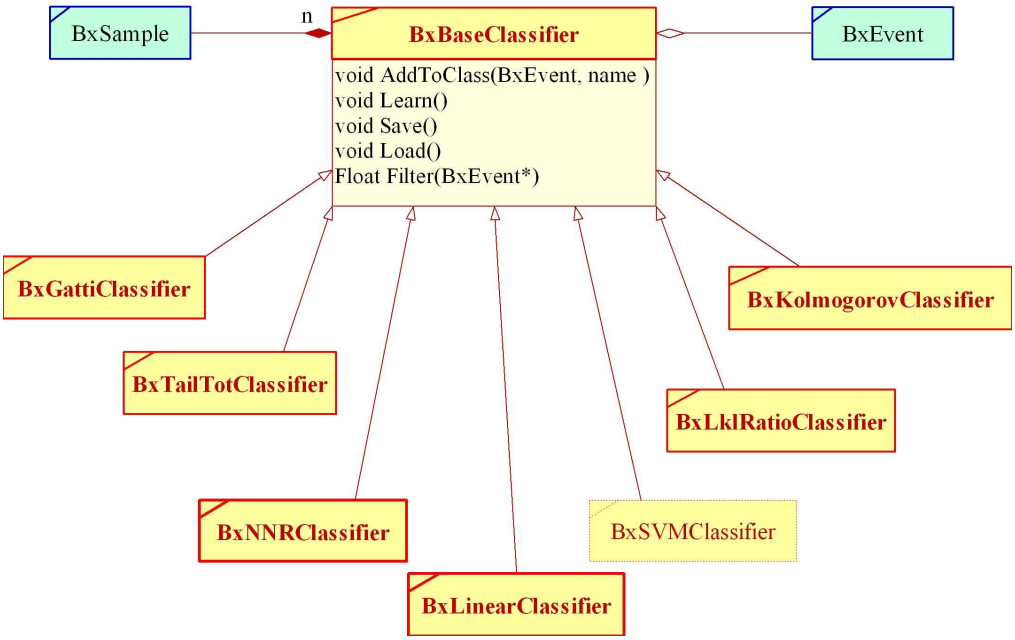

Fig. 7.8: *Particle ID package being transferred into echidna.*

`bx_calib_muon_time_align`, `bx_calib_muon_charge_peak`. Two modules for OD analogous to the ones above.

`bx_calib_laben_crate_delay`. Module for *pulser* runs to compute the relative delay in the BGT delivery time to ID crates (t_{crate} of eq. 7.1).

`bx_calib_laben_electronics`. Module for *pulser* runs to monitor the electronic status. It flags different pathological conditions of the laben electronics.

These modules run after the decoding stage and usually with most of the following physics modules disabled.

Future higher level calibration modules will probably run also on physics runs (e.g. energy calibration).

7.4.6 α/β discrimination

α/β discrimination in BOREXino is a pulse shape analysis that takes into account the differences in the light emission curves for α and β particles (sec. 2.4).

A package to accomplish this task was developed in 2003 before echidna was born[242]. This was a stand-alone set of ROOT macros and is today being finalized and integrated as an echidna module (fig. 7.8).

The module works on the cluster (assuming no piled-up events), using the time distribution of the hits, binned with a variable optimized bin size ($\mathbf{x} = x_i$). Clearly the ability of the clustering module of finding the true cluster start time (to which the distribution is reported) is crucial for α/β performance.

It was developed using source runs (sec. 6.6) both as reference known samples of α and β events and as test benches[14] (not the same runs, of course).

Six algorithms are in use:

Tail-to-Total. The simplest method consists in integrating the *normalized* distribution starting from a bin corresponding to about $20 - 30ns$ after the cluster start. β and α particles gather around values ~ 0.1 and ~ 0.25 respectively as shown in fig. 6.19.

Gatti filter. This is the optimum filter technique proposed in [226]. A set of known α and β events are averaged (sample by sample) to obtain reference curves α_i and β_i. The linear discriminant variable is then:

$$g = \sum_{i=1}^{\Omega} \frac{\alpha_i - \beta_i}{\alpha_i + \beta_i} \cdot x_i$$

Maximum Likelihood. This method simply assumes Poisson population of the different bins (neglecting correlation) with expectation values given by the (averaged) reference curves. Minimization of the global log-likelihood function built out of the likelihood of the individual bins, yields two independent parameters: $\mathcal{L}_\alpha(\mathbf{x})$ and $\mathcal{L}_\beta(\mathbf{x})$.

Kolmogorov distance. This test works computing the maximum distance of the *cumulative* distribution to the two (averaged) cumulative reference curves.

Primary SVM. A *Support Vector Machines* (SVM) is a learning algorithm that transforms a non linearly separable parameter space into a higher order space where a linear hyper-plane separating the samples does exist. The transformation among these parameter spaces, the *kernel function* of the SVM, can have different forms (generally non-linear) and include parameters that are tuned through the learning process. Here polynomial kernels have been used, trained on known source samples of α and β events.

Global SVM. A second SVM uses as input parameters the discriminating variables produced by all the previous methods, including primary SVM. The training set of the global SVM is different than the one used for its input classifiers.

With the source in the center, the Gatti and likelihood methods provide very good and similar results, while the tail-to-total and Kolmogorov, as expected, are always worse. The SVMs are however the best methods, with no significant difference between the two.

A worsening of the performance for events not located in the center is expected, as a hit time distribution more "dispersed" can mask the α/β shape differences. Runs taken with the source up to $+150cm$ above detector's center still show excellent results. Runs taken at $+250cm$ start to show a significant worsening of all methods and runs at $+400cm$ show very poor discrimination capabilities[15]. Attempts to use hit times re-corrected for

[14] The radon source in AR8 allowed the isolation of $^{214}Bi - ^{214}Po$ delayed coincidence, where a β event is followed by an α event.

[15] However the nominal $100t$ FV corresponds to a radial cut at $310cm$.

the photon TOF from the reconstructed position have not shown encouraging results so far. The studies on the use of position dependent reference/training sets seem more promising and more activity is scheduled on these tasks for the near future.

7.4.7 Splitting

A module that handles the piled-up events within the same cluster is currently under development.

The original goal of the *splitting* module was to produce two separate lists of hits and to run reconstruction and PID modules on each. Unless the pile-up is marginal, this doesn't seem feasible at the moment as there is no clear way to assign single hits to the one event or to the other in the overlap region. Currently the module finds peak positions within each cluster and computes the charge belonging to them.

The module applies an optimum filter technique with a filter function reproducing the scintillator emission profile: an up-going ramp ($10ns$) followed by a decaying exponential ($40ns$). The convolution, obtained via FFT, yields an unbinned time profile, on which derivative inversion regions define candidate peaks. Conditions on peak-to-valley ratio and on persistence of the slope around the peak allow to filter out ripples and statistical spikes.

7.4.8 Future modules

In addition to the modules mentioned so far that are either ready, under test or in development, many others have been proposed and their realization is scheduled for the next cycles:

- A special reconstruction module dedicated to piled-up events. If more than one peak are found by the splitting module, this module should perform a global fit to assess the positions of the two events at the same time.
- A module to compute geometrical patterns, like the sphericity of the event.
- One or more muon identification modules that compute and combine the information from the three muon tagging techniques (sec. 3.2.1).
- A module to reconstruct the track of through-going muons using both ID and OD information.
- Energy calibration modules based on different radioactive contaminants of the scintillator (^{14}C, ^{214}Bi, α peaks, ...) or for the analysis of source runs.
- Modules to monitor scintillator properties out of radial and oblique laser runs.
- An alternative writer module to produce ASCII histogram files. Echidna will soon work also as the histogram server of the Online Monitor (sec. 5.5). This mode will be handled as a configuration, with the reader accepting data over network and the new module in place of the standard writer of the ROOT file.

Chapter 8

The Outer Detector Calibration System

In this chapter there are introduced the calibration system of the BOREXino Outer Detector (chap. 3), its calibration procedure and the results obtained in two measurement campaigns.

8.1 Calibration tasks

Timing. When a muon crosses the Water Tank, it is highly desirable to determine with nanosecond precision the arrival times of the photons on photo-cathodes[1] of OD PMTs. This is important in order to perform a reliable muon track reconstruction, but also for the development of accurate muon identification methods.

In order to correct the differences in transit time among PMTs and electronic channels, it is mandatory to develop a calibration system able to pulse all PMTs at the same time, just as the *timing* laser system does for ID (sec. 2.2.4).

Charge. OD PMTs are used in a much wider dynamic range as compared to the ID ones. Simulations show that PMTs can easily detect burst of $50pe$ or even $100pe$, if directly hit by the Čerenkov cone. On the other hand PMTs seeing only light diffused by the Tyvek surfaces will detect only one or very few photo-electrons.

It was therefore decided to develop an independent channel calibration system for OD that was able to align the PMTs in time and perform a charge calibration in SPE mode as well as in charge regimes up to $40pe$ and possibly beyond.

It was also decided that the calibration of ID and OD should go in parallel during the same *laser runs*, so the two systems had to be integrated at DAQ level.

[1] The electronics actually allows to record only the time of the first photon in every channel (sec. 4.3).

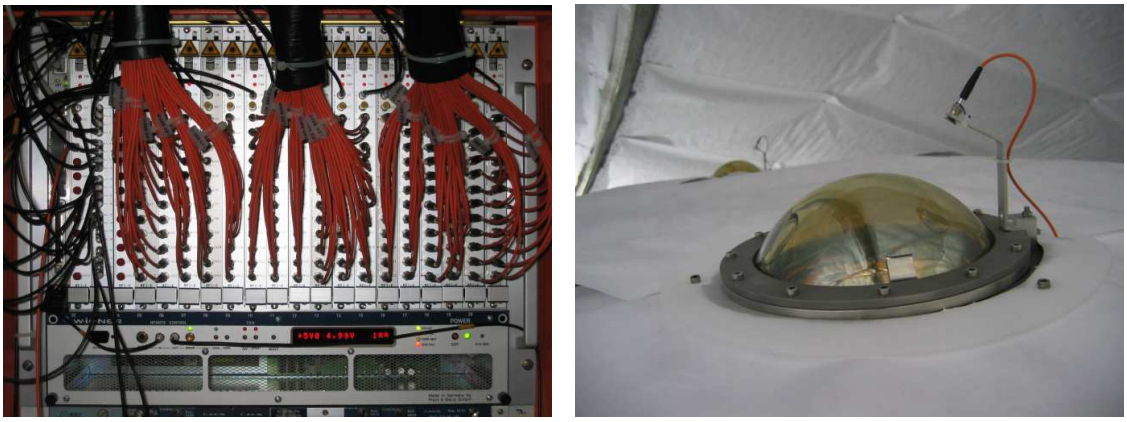

Fig. 8.1: *The Outer Detector calibration system. LEDs housed in electronic boards (left) deliver light pulses to PMTs in the water tank (right) through optical fibers (orange). The black tubes enclosing the fibers are also visible.*

8.2 System layout

The system, developed in collaboration with the Max-Planck Institut für Kernphysik (MPIK) in Heidelberg (Germany), is composed of 208 *Light Emitting Diodes* (LEDs), housed in custom boards and located in the electronics room (BBW), each one delivering the light pulse to one PMT in the Water Tank through an optical fiber (fig. 8.1).

The LEDs

The Roithner Lasertechnik NSHU550 LED was selected. It is a UV LED with a $370nm$ peak emission, that well matches the photo-tube sensitivity (fig. 3.7). The signal in sub-Poisson mode is about $8ns$ wide and the jitter is below $0.8ns$, which is acceptable if considered that PMT+electronics are expected to contribute almost twice as much. The LED starts emitting light when a forward bias of at least $3.5V$ is applied.

The optical fibers

The optical fibers are commercial[2] Huber-Suhner cables, $55m$ long and $200\mu m$ in diameter, equipped with SMA connectors on both ends. One end is mounted on the PMT with a steel support that holds it about $8cm$ and 30° off-axis. Considering the opening angle of the fiber (15° semi-aperture) the support was designed for 100% geometrical efficiency and minimal shadowing of the photocathode.

The crate

The dedicated VME crate of fig. 8.1 (21 slots) is organized as follows:

Slot 1 A Motorola PowerPC (sec. 5.2) that masters the crate bus.

[2]Normally used for telecommunication applications.

Slot 2 A TTL 1x24 Fan-Out board used as distributor of the trigger signal.

Slots 3-20 18 LED boards for a total of 216 channels (8 spares) are required to pulse the whole OD.

Slot 21 Spare. An additional LED board could be used here with 2 possible uses:

1. The *inner vessel* has 20 tiny optical fibers along its meridians ending at the equator which could be pulsed to calibrate the position reconstruction code.
2. A few spare fibers have been laid into the WT. They are headed to a distant PMT and will be used to test optical quality of the water and its long term stability.

The boards (sec. 8.3) need an external TTL trigger. They can also return it for daisy-chaining purposes, however this would introduce a progressive delay among them and require correction. To avoid this small complication the Fan-Out unit was built. The trigger to the LED system comes from the trigger rack and is forked out of the trigger signal fed to the ID timing laser (sec. 4.4.5).

8.3 The LED board

The LEDs are housed in custom 6U VME boards (fig. 8.2), each featuring 12 channels arranged in 3 parallel groups.

8.3.1 Interface

On the front panel are visible (top to bottom):

- 2 hexadecimal rotary switches to set the VME address.
- 2 control red LEDs that indicate power status and VME bus traffic.
- 2 LEMO connectors for trigger IN and OUT.
- The 12 calibration UV LEDs housed in steel cases (grounded) with front FSMA connectors.

The behavior of each channel is customizable through:

- 2 VME accessible registers (write-only):
  1. An 8 bit PDU (*Programmable Delay Unit*) with $500ps$ LSB, which means a $128ns$ dynamic range.
  2. A 12 bit DAC that sets the amplitude of the light pulse (see below).
- 2 analog trimmer controls (side access):
  1. A $0 - 3ns$ fine tuning delay line.

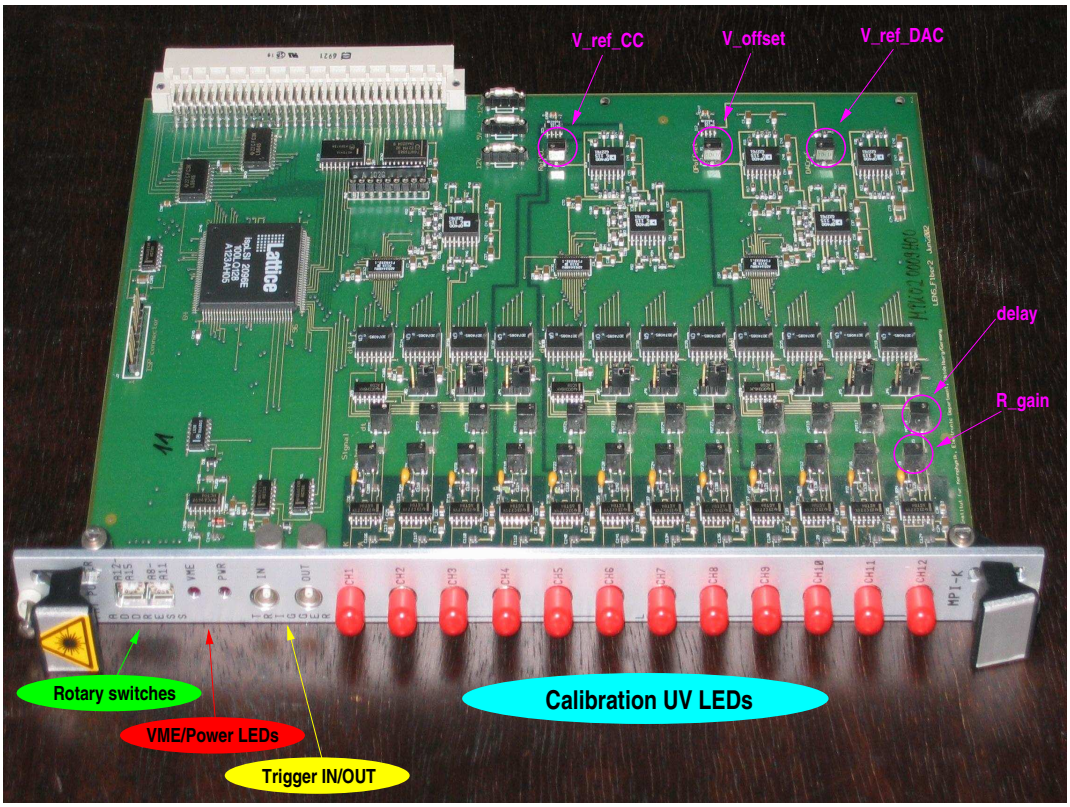

Fig. 8.2: *LED calibration board. The LEDs are protected from dust with red caps.*

2. R_{gain} to tune the channel "gain" (see below).

In addition a few controls are accessible at board level:

- 2 VME registers (write-only):
  1. An internal trigger register, whose access causes all channels to fire simultaneously[3].
  2. An enable register for the TRG OUT signal.
- 3 Analog trimmer controls (side access):
  1. V_{offset} (typical value: 3.3V).
  2. $V_{\text{ref}}^{\text{DAC}}$ (typical value: 5V).
  3. $V_{\text{ref}}^{\text{CC}}$ (typical value: 4.8V).

[3]Unless a complex driver enforcing *real-scheduling* is developed, internal trigger is limited to $\sim 50Hz$ by the Linux Scheduler, not much for sub-Poisson calibration. Therefore internal trigger is generally used only in tests.

8.3.2 Implementation

In absence of trigger, the voltages on the LED pins are:

$$V_{\text{anode}} = V_{\text{offset}} + V_{\text{ref}}^{\text{DAC}} \cdot \frac{[\text{DAC}]}{4095} \qquad V_{\text{cathode}} = V_{\text{ref}}^{\text{CC}} - \Delta V(R_{\text{gain}}) \tag{8.1}$$

whose difference is normally smaller than the $3.5V$ required for conduction.

The incoming trigger pulse, after going through the two delay units, brings down V_{cathode} to 0, setting the condition for conduction (fig. 8.3). However V_{cathode} quickly regains its static level, charging a $100nF$ capacitor and ensures a fast light output. Both falling and rising slope of signal at V_{cathode} have been made as short as possible by tuning passive elements values on the board.

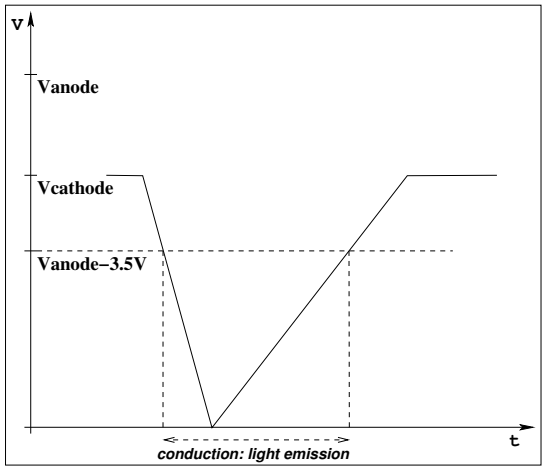

Fig. 8.3: *Schematics of the LED operation.*

The light output depends on how long the conduction regime persists. Hence a higher light intensity corresponds intrinsically to a longer pulse. The charge (integral of PMT pulse) therefore results being *not* proportional to signal height.

While $V_{\text{ref}}^{\text{DAC}}$ and $V_{\text{ref}}^{\text{CC}}$ are *reference* voltages and should not be manipulated in normal operating conditions, setting a higher DAC value increases V_{anode} achieving a longer/higher pulse as the V_{cathode} will set conduction earlier and terminate later. A similar effect can be obtained increasing R_{gain}, which in turn decreases the static V_{cathode}. The latter possibility applies regardless of DAC values and is used to equalize channels.

The expected behavior for a correctly tuned channel is the following. When DAC=0 (or very low values) $V_{\text{anode}} = V_{\text{offset}} \sim 3.3V$ and conduction never occurs. The LED starts to output light between DAC=200 and DAC=600 and keeps in (almost) SPE regime for another ~ 500 DAC values, before starting to increase toward its maximum.

However if the V_{offset} is too high, most of the channels happen to fire in absence of trigger (at high DAC values) as ΔV between the pins approaches or crosses the operating voltage. This makes the output extremely unstable and the board unusable. On the other hand if V_{offset} is too low, the channels start to fire only at high DAC values (> 2000) and then rise very steeply to their maximum leaving no space for an accurate tuning. In a few pathological cases there is no "good region" left between these two extremes to correctly tune V_{offset} (sec. 8.5.5).

The layout of the LED borad is shown in fig. 8.4.

8.4 The control software

The LED control software is a client-server application, developed following the design philosophy of the BOREXino DAQ system (chap. 5) and fully integrated in it.

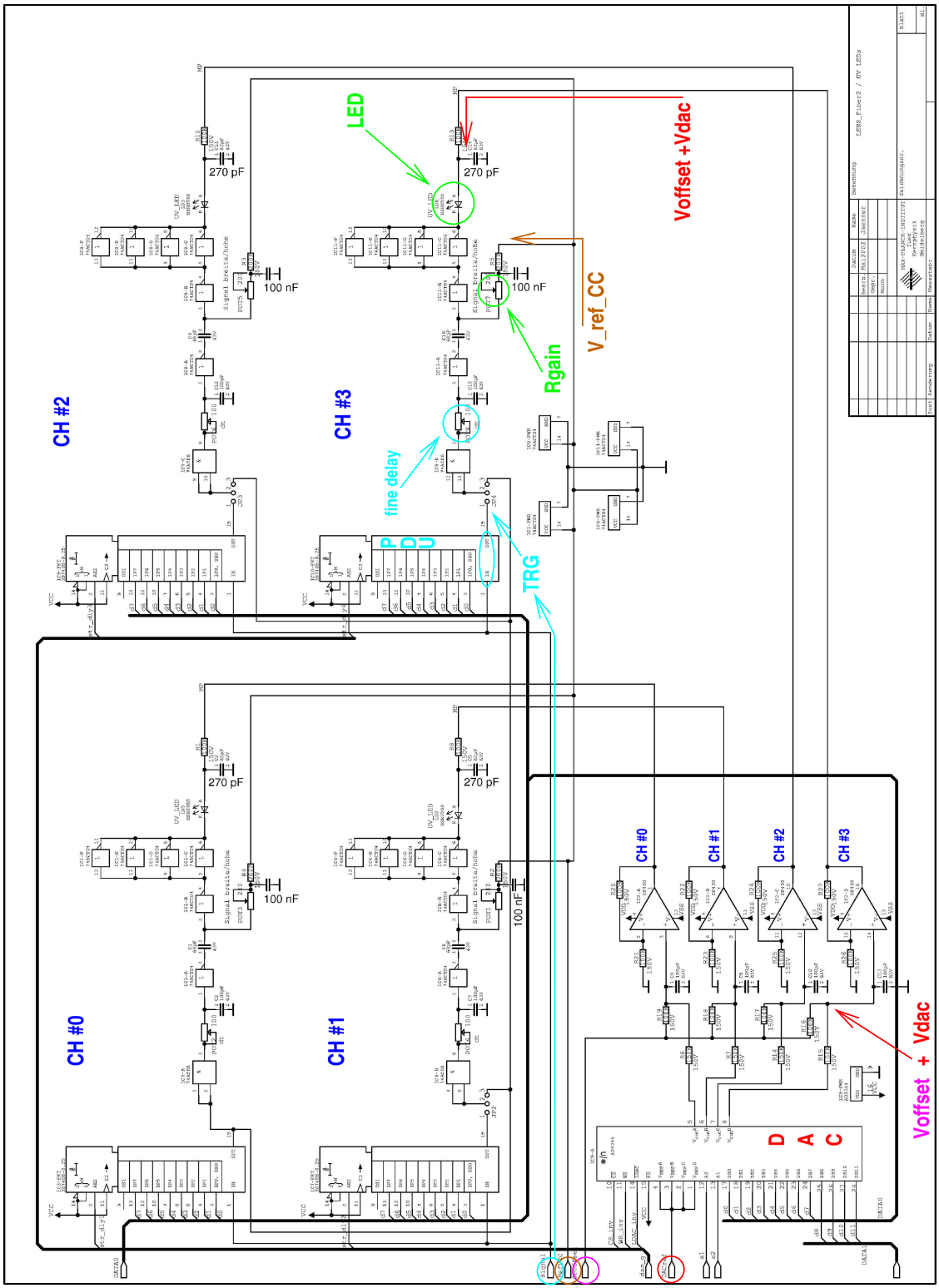

Fig. 8.4: *Layout of the LED board (1 group).*

CMD	MOD	BRD	CH	VAL	NOTE
S/GET	VOL	1-18	1-12	0-4095	S/Gets channel DAC value.
S/GET	DEL	1-18	1-12	0-256	S/Gets channel delay (500ps units).
SET	ALL	1-18	-	0-256	Sets delay of all channels (500ps units).
S/GET	OUT	1-18	-	0-1	Toggles TRG OUT enable.
S/GET	TRG	1-18	-	0-10^6	S/Gets internal trigger rate (Hz, 0=OFF).
RESET	-	-	-	-	Sets all system voltages and delays to 0. Disables all int. trg and TRG OUT.
EXIT	-	-	-	-	Cleans up and exits.

Tab. 8.1: *Commands implemented by the LED control server application.*

The server application is written in C and runs on the PPC of the LED crate. No data taking or dynamic control is involved here but merely the issuing of user-driven slow commands. Most of the tasks can therefore be performed within a single user-space process, started automatically upon PPC boot:

1. The VME registers of all boards are MMAPped to user-space(sec. 5.2). A local copy is also created.
2. A full reset is performed writing '0' to all boards registers.
3. A server TCP/IP socket connection is opened for incoming commands.
4. Received commands are parsed according to the following format:

   COMMAND MODIFIER [#BOARD #CHANNEL] [#VALUE]

   Accepted commands are listed and explained in tab. 8.1. Wrong format of the command or out-of-range values for any parameter return error codes.
5. Resolution of DO/SET type commands is implemented writing in parallel to the relative MMAPped area and to the local copy.
6. Resolution of GET type commands returns the locally stored parameters.
7. Resolution of SET TRG command causes the spawning of a child process. This keeps accessing the internal trigger register in a loop leaving the father free to serve other commands. Up to 18 processes can be spawned (1 per board). Turning off the internal trigger on one board (setting the rate to '0') simply kills the relative child process. IPC[4] is handled through Unix signals.

All board registers are write-only. The lack of read access determines the necessity, at process start-up, to reset an eventually running system whose status would be unknown. The same board limitation leads to the necessity of handling GET operations by keeping a local copy of the MMAPped area, whose consistency with hardware is fully under the server responsibility.

[4]Inter-Process Communication.

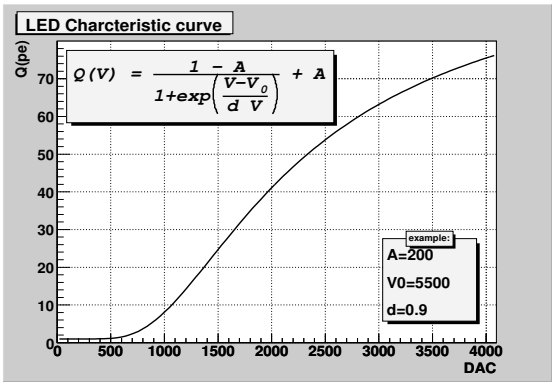

Fig. 8.5: *Empirical function found to fit the experimental LED characteristic curve.*

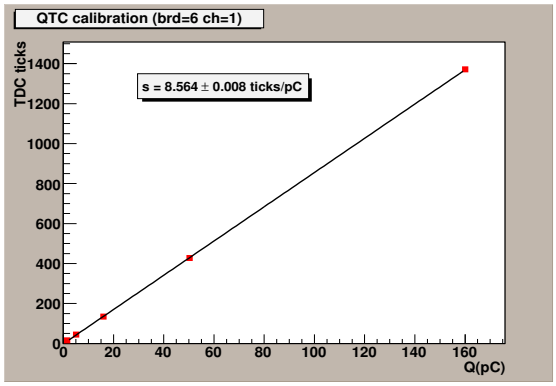

Fig. 8.6: *Calibration of the QTC channel used for LED calibration.*

Direct communication with the server is restricted to expert users and applications like the one described in sec. 8.5.3.

For shifter's use, a GUI[5] (fig. B.5) was developed by other collaborators[213] with the usual WEB technology. The GUI is also able to connect to DB and load to the hardware a full configuration using a special key named `LedProfile`. The role of DB will be clarified in sec. 8.5.4.

8.5 Calibration of the LEDs

The LEDs need themselves a calibration before they can be used to calibrate the detector.

8.5.1 Motivation

There are two levels at which the system can operate that pose different calibration issues:

1. *Single Photo-Electron* (SPE) mode. The goal is to have all LEDs firing in sub-Poisson regime with an efficiency of 5%. The issues leading to this choice have been already exposed in sec. 6.4.1 for ID. In this mode timing calibration of the PMTs and SPE charge calibration are performed.

   To operate the system in this mode two pieces of information must be known for every channel:

   (a) The DAC at which the LED is in the correct mode.

   (b) The intrinsic delay of the channel, to be corrected through the delay lines.

2. Full range calibration. The goal is to be able to perform additional PMT charge calibrations, setting the LEDs intensity to a few values in the $1 - 40pe$ range. The pieces of information to be determined are the conversion curves for translating

[5] Graphical User Interface

DAC values to the mean number of photoelectrons emitted. These curves are highly non-linear. For a typical LED correctly tuned, an empirical Boltzmann-like function (fig. 8.5) is found[245] to fit the data relatively well:

$$Q(V) = \frac{1-A}{1+e^{\frac{V-V_0}{d\cdot V}}} + A \tag{8.2}$$

where A, V_0 and d are the free parameters to be determined in the calibration.

While the former goal is fundamental and the detector could not be operated without it, the latter goal, though it is the distinctive feature of this calibration system, should be considered as a fine tuning of the calibration achieved in SPE mode.

The LED boards were delivered to Gran Sasso without any calibration information. Therefore it was decided to develop an in-situ calibration strategy. It was also decided that this calibration should not be considered a preliminary operation to be executed only once, but rather a repeatable (almost) standard operation for a detector that has to run for several years and may undergo different hardware modifications.

8.5.2 Strategy

The in-situ calibration procedure benefits of the following setup:

- One of the spare OD PMTs is used to calibrate all PMTs. This is placed in a black box in the electronic room, complete with fiber holder and a spare optical fiber. Powering of the PMT is done with an independent HV power supply and a simple passive decoupler. The light-tightness achieved is very good: a typical rate of $\sim 1600Hz$ was recorded with all lights on in the room, and $\sim 800Hz$ with nearby lights off.

- One reference channel of the standard OD electronic chain is used to acquire the PMT in the black box. The QTC gain was pre-calibrated using a precision pulser (Camac LeCroy 1976). This was set to $160pC$ and successively attenuated by $0, 3, 6, 9, 12dB$. The QTC PO length was measured in response to these signals. The result (fig. 8.6) indicates a gain of $s = 13.71 \pm 0.01 ticks/pe$ (assuming $1pe = 1.6pC$).

- The ordinary data acquisition, trigger and data processing systems are used to take special `led` runs, where only the OD is operated together with the trigger. From the trigger point of view, they are "laser runs", where the LEDs and the acquisition are driven at $200Hz$ by the same timing unit (sec. 4.4.5).

The idea is to sample the characteristic curve over a programmed number of *dots*, defined as a DAC value together with the number of events to be acquired at that intensity. This is achieved varying LED intensity during the run through PAUSE/RESUME operations.

The runs are then processed with `echidna`, forcing the muon decoder to use s (above) as calibration of the reference QTC channel (sec. 7.4.2). The ROOT files are finally analyzed to find the correct SPE regime, its timing calibration and the full reconstruction of the conversion curve.

The data taking time is the dominant component[6] and must be optimized:

1. Dots are taken denser in the regions where the curve changes slope and sparser where it is roughly linear. Unfortunately the very uneven distribution of performance among the channels (sec. 8.5.5) makes these concepts rather loose and introduces additional complexity in the procedure to account for "all" possible curves.

2. A few hundred hits are enough for a good determination of the dot charge peak. The first dots, where the LED is strongly in sub-Poisson regime with an efficiency of a few %, are sampled at 10000 events. This value is then progressively reduced in subsequent dots as the hit occupancy increases, settling to 500 events above DAC=2000, where most of the LEDs already sport about 95% hit occupancy.

The optimized pattern is reported here:

DAC	#ev.	DAC	#ev.	DAC	#ev.	DAC	#ev.	DAC	#ev.
200	10000	750	5000	1050	2000	1500	1000	2500	500
350	10000	800	5000	1100	2000	1600	1000	3000	500
500	10000	850	5000	1150	2000	1700	1000	3400	500
600	10000	900	2000	1200	2000	1800	1000	3700	500
650	10000	950	2000	1300	1000	2000	500	3900	500
700	5000	1000	2000	1400	1000	2250	500	400	500

Tab. 8.2: *Programmed sampling dots of the LED characteristic curve.*

Obviously the user can provide a different pattern or even perform calibration with a fixed dot density and/or dot statistics.

Two rather complex tools have been designed to handle data taking and data analysis of `led` calibration runs[7].

8.5.3 The data taking tool

A Perl script named `LedCalib` was developed to drive the DAQ for the data taking of `led` calibration runs. Each execution allows to calibrate one board, and lasts about 2h (after many optimization steps).

The script executes on `bxweb` (sec. 5.1) after the PPCs involved (`trigger`, `muon` and `leds`) have completed boot operations (sec. 5.2) and after BorexinoDAQ process is running (sec. 5.3).

Upon starting it performs a few initializations: opening of CORBA communication object, INIT of DAQ system, trigger setup for laser run, reset of LEDs, retrieving from DB of run info and writing of the log file header (the log file is fundamental for the offline tool described below).

Then the loop on channels starts. For every channel:

1. Beeps the user asking to connect the LED to the fiber to the black box.

[6]Data processing is faster and may go in parallel to data taking as the CPUs involved are different.
[7]These programs are now part of the official BOREXino online and offline code.

2. Makes an entry in the log file stating channel number and number of dots.

3. Starts to loop on dots. For every dot:

   (a) Sets the DAC to next predefined value.

   (b) Asks BorexinoDAQ the system status:

   - if READY_S ⇒ issues START (first dot of first channel);
   - if PAUSED_S ⇒ issues RESUME (all other dots).

   (c) Keeps asking the BTB for number of issued triggers at about $1Hz$[8].

   (d) When the required statistics for this dot is met the run is paused, unless the board is complete in which case the run is stopped.

   (e) A log entry is made with DAC value and events collected for this dot.

4. Resets DAC to '0' (protects operator's eyes while switching the fiber).

After startup, the only operation that requires operator's intervention is the switching of the fiber to the next channel (approximately every $10min$).

The script communicates with BorexinoDAQ either directly through CORBA function calls (trigger setup, get state) or indirectly through the run control CGI scripts (INIT, START, STOP, PAUSE, RESUME). These scripts are meant to be called by Javascript applets within HTML pages, so they expect arguments and return values according to that standard. `LedCalib` emulates this environment.

The script communicates also with `trigger` PPC (get event number), `leds` PPC (set voltage) and DB (get last run) through TCP/IP socket connections[9].

In spite of its complexity `LedCalib` was designed for being easily run by users of average experience, though maybe not by the common shifters. Its behavior is customizable through command line options and is furnished with in-code POD[10]. However the development of a web interface consistent with other similar tools is foreseen in the near future.

8.5.4 The data analysis tool

To process the ROOT files relative to LED calibration an interactive analysis tool was designed. This is a ROOT-based C++ compiled program. The program, though complex in its implementation, is very easy to use: it accepts command line options and argument with standard syntax and is provided with a detailed help function.

For every channel, the dots are reconstructed sectioning the run according to the log file of `LedCalib`. Only hits whose time is within a $\pm 20ns$ window from the LED signal

[8] In a previous version the number of events was asked to BorexinoDAQ, but *built* events differ from the *issued* events due to BTB and builder event buffers. The BTB command interpreter was then upgraded to handle this request directly.

[9] Opened and closed after every command to avoid occupying resources of the back-end application.

[10] *Plain Old Documentation*, a simple yet efficient side language of Perl to provide manual and help pages.

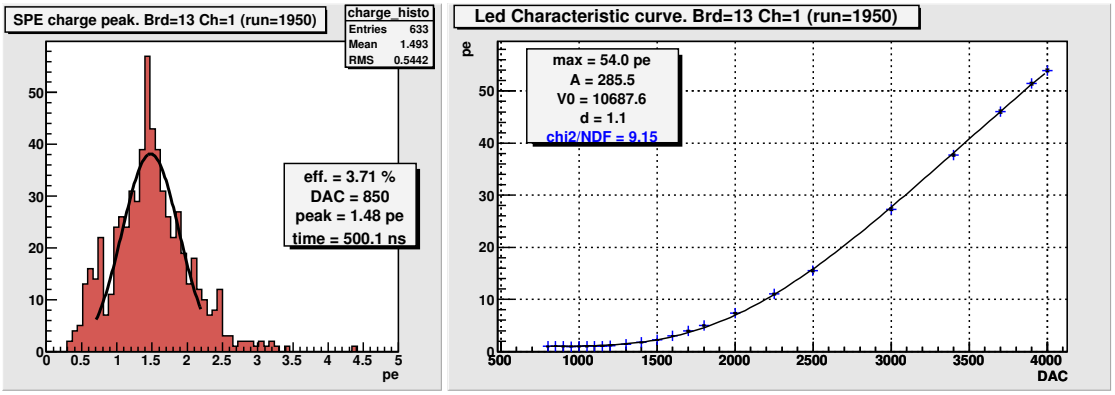

Fig. 8.7: *Example of a ROOT canvas produced by the LED calibration tool.*

time[11] are considered, rejecting spurious hits (e.g. dark noise). The histogram is fited with a Gaussian and fit parameters of all dots are used to build a graph[12], which in turn is fitted with the function of eq. 8.2.

While processing dots of a channel, the efficiency is monitored (#hits/#events). Whenever this crosses a threshold (typically 5%) for the first time, all preceding events are used to perform SPE calibration. A charge and a time histogram are built, filled and fit with Gaussian functions. The SPE charge is also used to renormalize the characteristic curve (i.e. all dots) before the fit, removing the dependency on the actual PMT gain. The last DAC value before threshold crossing is saved as the SPE-DAC.

The program tries to handle most of the pathological LED behaviors encountered so far, dynamically rebinning histograms where needed, replacing poor Gaussian fit results with histogram mean and RMS values, discarding the dots with poor statistics or the ones showing instabilities. However only a human can confirm that *everything* went well enough to declare the calibration successful and the channel usable. For this reason the program provides an interactive ROOT canvas fig. 8.7 upon which the user can perform additional analysis and take the decision.

In case the user accepts the results, the database is written. A dedicated table named `LedParameters` was created in database `bx_calib` (fig. 8.8). The results of LED calibrations are stored there under a special key, named `LedProfile`. If a new `LedProfile` number is used (command line option), the new calibration is simply added to DB, without overwriting the previous one. The LED web interface (sec. 8.4) can choose and load a set of calibration parameters using this key.

The most significant parameters determined by a successful calibration are:

1. The three parameters A, V_0 and d that nail down the characteristic curve.

2. SPE-DAC. The DAC at which the LED is in the correct SPE regime. This is the DAC of the last dot before threshold crossing.

[11] This is dynamically determined scanning the run at startup. In this way hardware changes that modify this value (like replacement of cables) can be handled transparently.

[12] A ROOT `TGraphErrors` object.

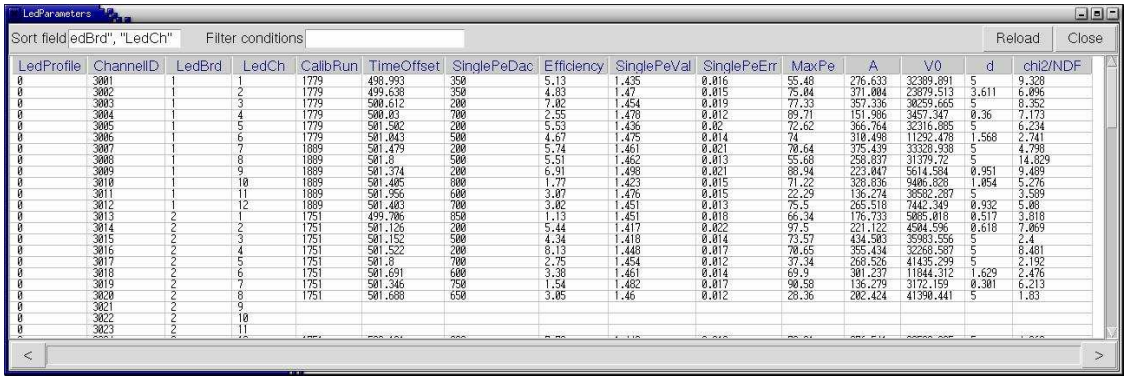
LedParameters

Sort field edBrd", "LedCh" Filter conditions Reload Close

LedProfile	ChannelID	LedBrd	LedCh	CalibRun	TimeOffset	SinglePeDac	Efficiency	SinglePeVal	SinglePeErr	MaxPe	A	V0	d	chi2/NDF
0	3001	1	1	1779	498.993	350	5.13	1.435	0.016	55.48	276.633	32389.891	5	9.328
0	3002	1	2	1779	499.638	350	4.83	1.47	0.015	75.04	371.004	23879.513	3.611	6.096
0	3003	1	3	1779	500.612	200	7.02	1.454	0.019	77.33	357.336	30259.665	5	8.352
0	3004	1	4	1779	500.83	700	2.55	1.478	0.012	89.71	151.986	3457.347	0.36	7.173
0	3005	1	5	1779	501.582	200	5.53	1.436	0.02	72.62	366.764	32316.885	5	6.234
0	3006	1	6	1779	501.043	500	4.67	1.475	0.014	74	310.498	11292.478	1.568	2.741
0	3007	1	7	1889	501.479	200	5.74	1.461	0.021	70.64	375.439	33328.938	5	4.798
0	3008	1	8	1889	501.8	500	5.51	1.462	0.013	55.68	258.837	31379.72	5	14.829
0	3009	1	9	1889	501.374	200	6.91	1.498	0.021	88.94	223.047	5614.584	0.951	9.489
0	3010	1	10	1889	501.405	800	1.77	1.423	0.015	71.22	328.836	9406.828	1.054	5.276
0	3011	1	11	1889	501.956	600	3.07	1.476	0.015	22.29	136.274	38582.287	5	3.589
0	3012	1	12	1889	501.403	700	3.02	1.451	0.013	75.5	265.518	7442.349	0.932	5.08
0	3013	2	1	1751	499.706	850	1.13	1.451	0.018	66.34	176.733	5085.018	0.517	3.818
0	3014	2	2	1751	501.126	200	5.44	1.417	0.022	97.5	221.122	4504.596	0.618	7.069
0	3015	2	3	1751	501.152	500	4.34	1.418	0.014	73.57	434.503	35983.556	5	2.4
0	3016	2	4	1751	501.522	200	8.13	1.448	0.017	70.65	355.434	32268.587	5	8.481
0	3017	2	5	1751	501.8	700	2.75	1.454	0.012	37.34	268.526	41435.299	5	2.192
0	3018	2	6	1751	501.691	600	3.38	1.461	0.014	69.9	301.237	11844.312	1.629	2.476
0	3019	2	7	1751	501.346	750	1.54	1.482	0.017	90.58	136.279	3172.159	0.301	6.213
0	3020	2	8	1751	501.688	650	3.05	1.46	0.012	28.36	202.424	41390.441	5	1.83
0	3021	2	9											
0	3022	2	10											
0	3023	2	11											

Fig. 8.8: *The table* `LedParameters` *(database* `bx_calib`*) where LED calibration parameters are stored.*

3. The time offset of the LED signal (at SPE).

They are used by the web interface to set the system in the correct state for PMT calibration. In addition a few other parameters are produced that allow cross-checks and additional studies:

1. The efficiency at SPE.

2. The SPE charge peak position and its error.

3. The maximum light output in photoelectrons.

4. The G.o.F. of the characteristic curve fit.

8.5.5 Results of the calibration

First calibration

A first mass calibration of all LED boards was performed in August 2004. The operation uncovered a few hardware problems of different severity:

- 3 boards had a dead group (4 contiguous channels), probably due to a burned component. They were sent back to MPIK for repair and replaced with spares.

- 2 boards showed large instabilities on all channels, regardless of settings. The problem was not understood, the boards were sent back to MPIK for investigation and replaced with spares.

- 2 boards do not permit a valid V_{offset} setting, resulting in either of the wrong behaviors described in sec. 8.3.2. Having used the available spares in the cases described above, these two boards have been made somewhat usable with a compromise setup. They will be sent back to MPIK as soon as the units in repair are returned.

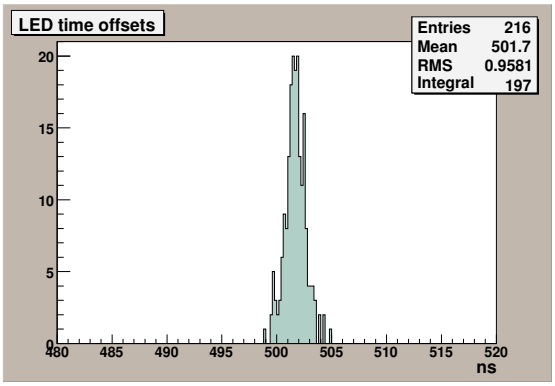

Fig. 8.9: *LED time offsets registered during the mass calibration of August 2004.*

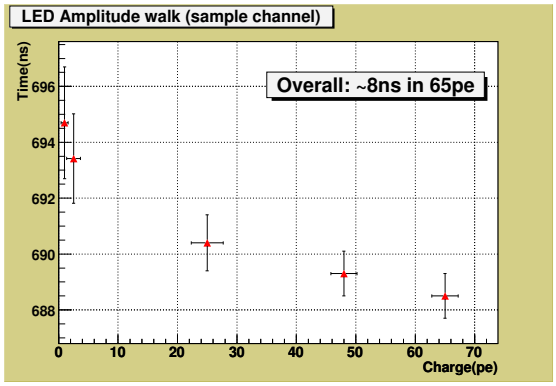

Fig. 8.10: *LED amplitude walk as measured on a sample channel.*

However the channels without major problems showed a fairly good time alignment (fig. 8.9), well within the correction possibilities of the delay lines. The amplitude walk across the LED range was measured on a few channels to be about $\sim 8ns$ (fig. 8.10). This confirmed the importance of performing timing calibration in SPE regime.

Tune-up

The analysis of the data taken in August 2004 also evidenced that the boards required further tuning as many channels evidently were not operating correctly. A tune-up was performed in November 2004 using the following setup (fig. 8.11).

The LED board under observation is mounted in the VME crate with the help of an extender board that grants access to the side controls while the board is operating. Trigger is provided with a *flip-flopped* timing unit (sec. 4.4.5) at about $1kHz$. The LEDs are connected one after the other to the optical fiber leading to the PMT in the black box (sec. 8.5.2). The PMT pulses are decoupled from HV with a passive box, amplified $\times 10$ and discriminated against a $30mV$ threshold.

To measure the efficiency of the LED in SPE regime filtering away the overwhelming dark noise, a sharp ($\sim 50ns$) gate is generated upon the timing unit pulse and delayed to be coincident with the LED-related PMT pulse. A visual scaler is counting on one channel the timing unit pulses and on another the AND between the gate and the PMT pulse (obtained in a logic unit). The efficiency is given by the ratio between the number of counts in the second and first channels. A third scaler channel is used to monitor the PMT overall rate.

The measurement of the intensity is instead performed with the digital scope integrating the pulses and averaging over a minimum of 10^4 signals[13].

Ideally one would like to set the channel for a SPE condition, defined by an efficiency of 5% and occurring for DAC$\leq$ 1000. Efficiencies between 2% and 6% can be anyhow

[13]The measurement is relevant at high intensities. In this case the dark noise can be filtered away setting a relatively high trigger threshold for the scope.

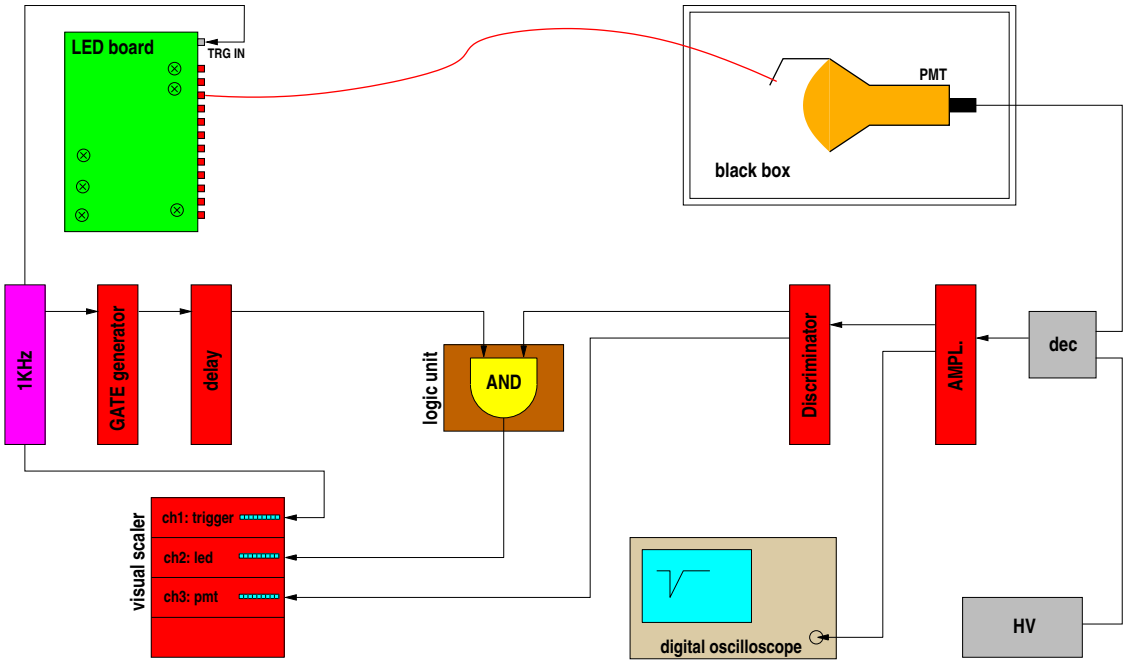

Fig. 8.11: *Logical scheme of the setup used to tune the LED boards in November 2004.*

considered acceptable.

As explained in sec. 8.3.2 one can play with V_{offset} and the 12 R_{gain}'s to achieve this goal.

The primary goal of the tuning campaign was to recover those channels which already had $> 5\%$ at DAC=200 (first dot) and the ones that were crossing 5% at high DAC values (~ 2000).

Second calibration

The week after the tuning, the mass calibration was repeated. The results of the two calibration campaigns are shown in fig. 8.12. A few considerations can be done:

Number of channels. In August, the calibration was attempted on 216 channels (18 boards), however only on 197 it was somehow successful, the other 19 channels being dead, almost dead or so unstable that the algorithm failed to do anything at all. In November 216 channels were successfully calibrated. The different histogram entries (left-right) in fig. 8.12 arise from this.

SPE-DAC value. The distribution of August was much dispersed, 45/197 channels lying above DAC=1000. The re-tuning worked well and in November only 7/216 could not be brought below 1000. The empty bins in the histograms reflect the discrete nature of the characteristic curve sampling (tab. 8.2).

SPE efficiency. In August 119/197 channels were below 3%, mostly with tiny values and 36/197 were above 5%, 6 of which even above 10%. In November 13/216 $< 3\%$

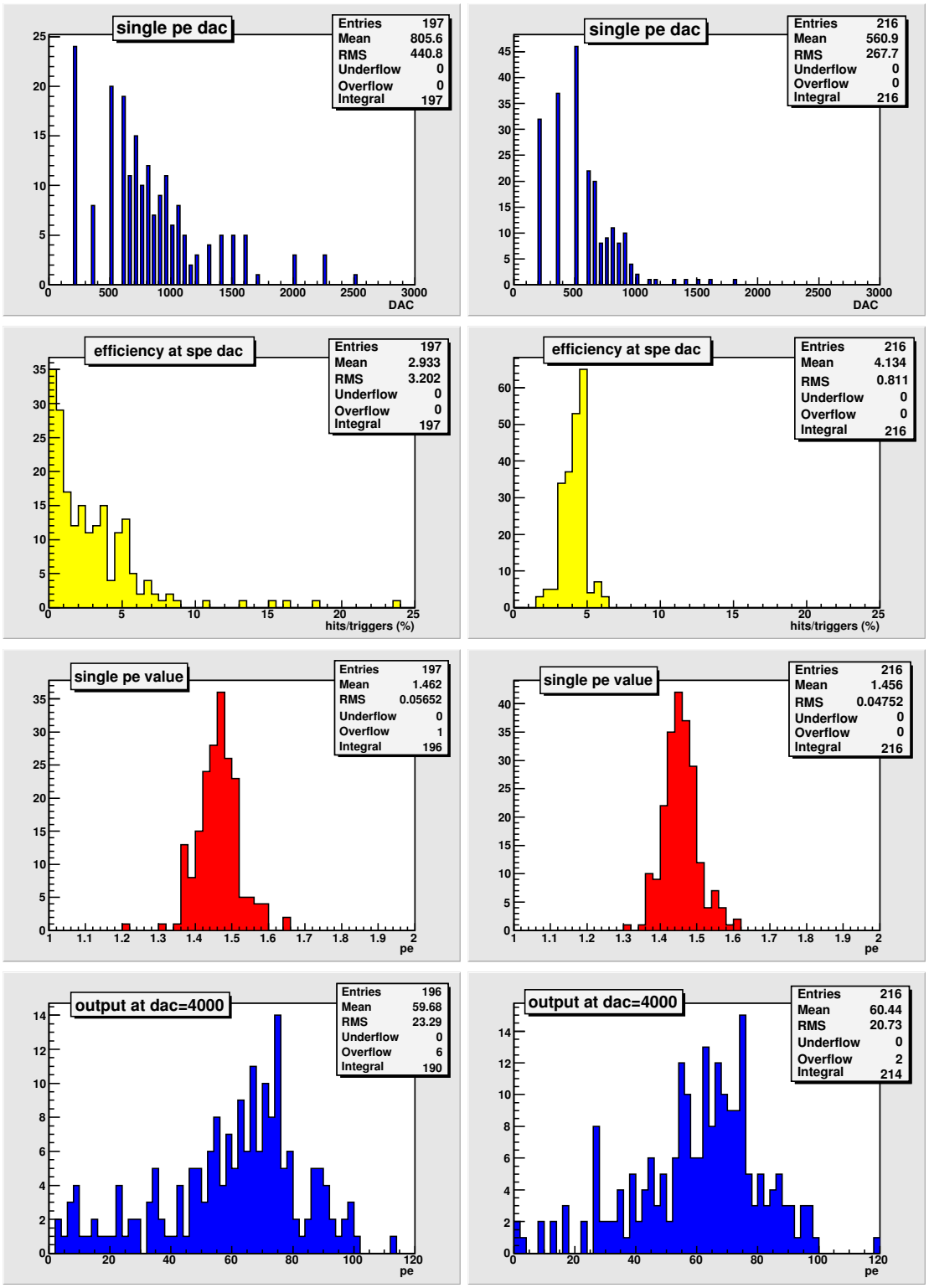

Fig. 8.12: *Results of the LED calibrations of August 2004 (left) and November 2004 (right).*

(but $> 1.5\%$) and $14/216 > 5\%$ (but $< 6.5\%$). This result, above the others, remarks the success of the tuning campaign and makes the calibration of the PMTs in SPE mode finally possible.

SPE peak value. This is a measure of the gain of the PMT used for the calibration so its absolute value is not relevant. However it should be the same value for all LEDs in SPE regime, so it can be used as a check of the correct tuning. LEDs that register values out of average are probably not being calibrated correctly. August RMS=$0.57pe$ (196 ch.) $\longrightarrow$ November RMS=$0.48pe$ (216 ch.).

Maximum output. This is very irregularly distributed and in general higher than the requested $40pe$[14], with a consequent minor loss of resolution. During the re-tuning an adjustment was attempted with partial success on channels with very low ($< 10pe$) or very high output ($> 100pe$). The policy was however to give priority to the setup that allows the best SPE regime. In fact the uneven performance of the LEDs can be handled defining a charge calibration policy where the LED settings are channel dependent and each PMT is calibrated in the range allowed by its LED.

Most of the channels which still show non-ideal behavior in SPE regime, belong to the 2 boards with the setup problems mentioned above.

8.6 Mapping of the optical fibers

The optical fibers in use do not have a serial number to distinguish them (like the PMT cables) and have not been labeled before installation. Consequently the *mapping* of the LEDs, that is the correspondence between LED board+channel and PMT (or electronic channel), was unknown after the installation.

Fortunately the wide dynamic range ($\Delta t_{\mathrm{MAX}} = 128ns$) of the delay lines in the LED boards can be exploited to determine this information with the following idea.

Three *laser* runs are taken with all the outer detector on and the LEDs firing at high intensity (e.g. DAC=3000):

1. A reference run with all delays set to '0'.

2. A run with each board set to a different delay (the same on all channels):

$$\Delta t_i = (i-1)\frac{\Delta t_{\mathrm{MAX}}}{N-1} \qquad i = 1 \rightarrow N \equiv 18$$

3. A run with each channel set to a different delay (the same on all boards):

$$\Delta t_j = (j-1)\frac{\Delta t_{\mathrm{MAX}}}{M-1} \qquad i = 1 \rightarrow M \equiv 12$$

[14] In Heidelberg the output was erroneously measured assuming Q/V proportionality (sec. 8.3.2). This generated the conviction that the output was not enough and lead to last minute modification on the boards that increased it.

A simple Perl script has been written to put LEDs in the three required configurations. It computes the appropriate delays and issues the relative commands to the LED control software (server).

A ROOT-based application processes the three ROOT files produced after standard reconstruction with `echidna`. For every (muon) Channel ID it performs a Gaussian fit of the hit time distribution present in the three files. The Gaussian peak value yields the arrival time t_{ref}, t_1, t_2 in the three runs The board+channel will then be simply:

$$i = int\left((t_1 - t_{ref})\frac{N-1}{\Delta t_{\mathrm{MAX}}}\right) \qquad j = int\left((t_2 - t_{ref})\frac{M-1}{\Delta t_{\mathrm{MAX}}}\right)$$

where the rounding to the nearest integer is safe because the smallest distance between peaks ($7.5ns$) is much larger than the typical peak width (1-2ns). The correspondence is then saved to DB in the `LedParameters` table (fig. 8.8, columns 2-4).

The procedure was tested with success, however the final mapping will take place right before the closure of the WT door as the connection of the fibers to the PMTs on the floor is still to be done. The whole procedure takes less than $1h$ and can be repeated upon necessity[15].

[15]The two tools are part of the official online and offline BOREXino software.

Chapter 9

The Prototype CTF

In the early '90s the collaboration started the construction of a reduced scale prototype of the BOREXino detector, named *Counting Test Facility* (CTF)[215], with the goal of testing if the high radiopurity levels required for the experiment could be effectively achieved.

In its first data taking campaign, from February 1995 to July 1997, CTF studied the fundamental characteristics of the BOREXino scintillator mixture, both in terms of optical properties and regarding the radioactive contaminants. Upon the positive CTF results (tab. 9.1, [216]) the construction of the BOREXino detector was started.

Element	conc. (g/g)
^{238}U	$(3.5 \pm 1.3) \cdot 10^{-16}$
^{232}Th	$(4.4 \pm 1.5) \cdot 10^{-16}$
$^{14}C/^{12}C$	$(1.94 \pm 0.09) \cdot 10^{-18}$
^{nat}K	$\leq 2.4 \cdot 10^{-11}$

Tab. 9.1: *Radiopurity levels reached in CTF-1.*

During summer 2000 a second short campaign, named CTF-2[222], was performed with an alternative scintillator mixture based on PXE, and including the test of the three volumes filling procedure for BOREXino and of the newly installed muon veto system. In addition the CTF-2 data were exploited for a number of physics studies alternative to the main objectives of the collaboration, namely the evaluation of limits to the electron decay time[217], to the nucleon decay into invisible channels[218], to the neutrino magnetic moment[219], to the decay of heavy sterile neutrinos[220] and to the possible violations of the Pauli exclusion principle[221].

The third campaign CTF-3 started at the end of 2001 with the aim to monitor the properties of the final incoming scintillator for BOREXino as well as the performance of the four purification methods available (sec. 2.2.3). The definition of the filling and purification strategy of BOREXino highly depends on the measurements performed with the prototype.

The tests of these purification methods were suspended in August 2002 due to the safety issues that arose in Gran Sasso (sec. 2.5). The detector continued to take data in a static condition (no scintillator movements were allowed) until February 2005 in a long *quiet* data taking, which allowed a deep understanding of the detector and of the scintillator properties as well as specific measurements like the search for $\overline{\nu}$'s in the ^{8}B solar flux[223] and the evaluation of the ^{11}C background in the energy window of *pep* and CNO neutrino spectroscopy ([224] and chap. 10).

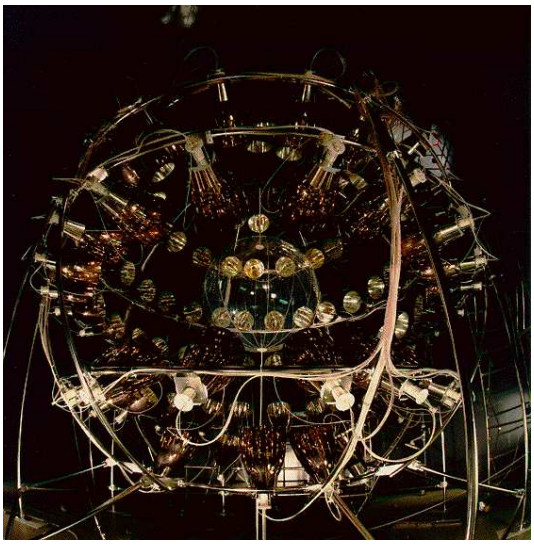

Fig. 9.1: *A picture of the CTF detector.*

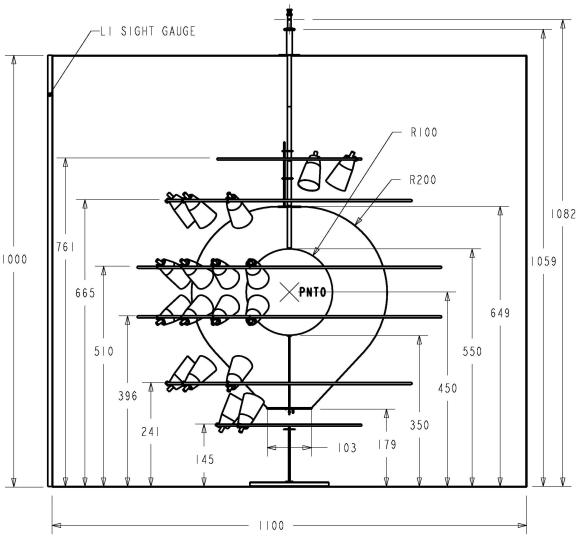

Fig. 9.2: *Schematic view of the CTF detector. All sizes in cm. Muon Veto PMTs on the floor are not represented.*

Recently, with the legal matters coming to a successful conclusion, the detector is being operated again in its original idea of Counting Test Facility.

In this chapter, the detector is presented along with the main data analysis techniques and the results achieved during the CTF-3 phase.

9.1 The detector

The CTF detector is situated in the Hall C of the Gran Sasso National Laboratory (sec. 2.2.1), next to the BOREXino structures (fig. 2.6).

9.1.1 The structure

The structure of the prototype CTF is quite similar to BOREXino (sec. 2.2.2), but with a few relevant differences:

1. Dimensions. The *inner vessel* has a radius of $1m$ and hosts $\sim 4.2m^3$ of scintillator watched by 100 PMTs. The PMTs are identical to the ones used in BOREXino, but are equipped with different light concentrators, as different is the solid angle with which they *watch* the vessel. The geometrical coverage achieved is $\sim 21\%$.

2. The PMTs holding structure. PMTs are mounted on a spherical structure of stainless steel tubes with a radius of $\sim 3.3m$ (fig. 9.1). The structure is *open*: it doesn't separate fluid volumes.

3. Buffer liquid and *inner vessel*. The only buffer liquid present outside the *inner vessel* is ultrapure water ($1000t$) in which the PMTs are fully immersed. CTF

reduced dimensions yield a higher surface-to-volume ratio for the *inner vessel*, with respect to BOREXino so that it can retain its spherical shape even when filled with pseudocumene ($0.88 g/l$). However to ensure this possibility the thickness of the nylon membrane was increased to $0.5 mm$.

4. The water tank. The outer water tank has a cylindrical shape ($11m$ diameter, $10m$ height). Below its floor a steel slab, $10cm$ thick, ensures additional shielding against γ's from the rocks.

5. The *outer vessel*. Starting with CTF-2 an additional *outer vessel* (*shroud*) was introduced with the goal of testing the filling strategy on a three volume system. The thickness of this second membrane is identical to the BOREXino one, while the nominal radius is $2m$. However it is not tight by design and its sphericity heavily depends on the overpressure applied.

6. The muon veto. Starting with CTF-2 a muon veto has been added to the detector. It is made of 16 PMTs mounted in 2 concentric rings ($R_1 = 240cm$ and $R_2 = 490cm$) on the floor of the tank and looking upward to detect the Čerenkov light produced by muons in water.

9.1.2 The readout electronics

In this section a short review of the CTF acquisition electronics (fig. 9.3) is given. A complete description can be found in [237].

The acquisition chain developed performs the following functions:

1. High voltage supply to PMTs.

2. PMT analog signal decoupling, amplification and distribution to a set of ADCs.

3. *time pick-off* of the analog signal and logical signal distribution to a set of TDCs.

4. Trigger signal formation and distribution.

5. Detector analog sum formation, sampling and digitization.

6. Acquisition of event information: hit charge and time, analog sum pulse shape, coincidence time between successive events, ...

7. PMT dark rate monitor.

8. System dead time monitor.

In order to be sensitive to pairs of correlated events with coincidence times of μs or ns (U and Th chain respectively), a duplicated system was implemented, where the first set of ADCs and TDCs is named *group-1* and the second set is named *group-2*.

The necessity arises because the *group-1* is blind after every event for about $\sim 75ms$ due to the data transfer time of the Camac system. During this time, the group-2 is armed and catches the next event within the following $8.3ms$. If one such coincidence

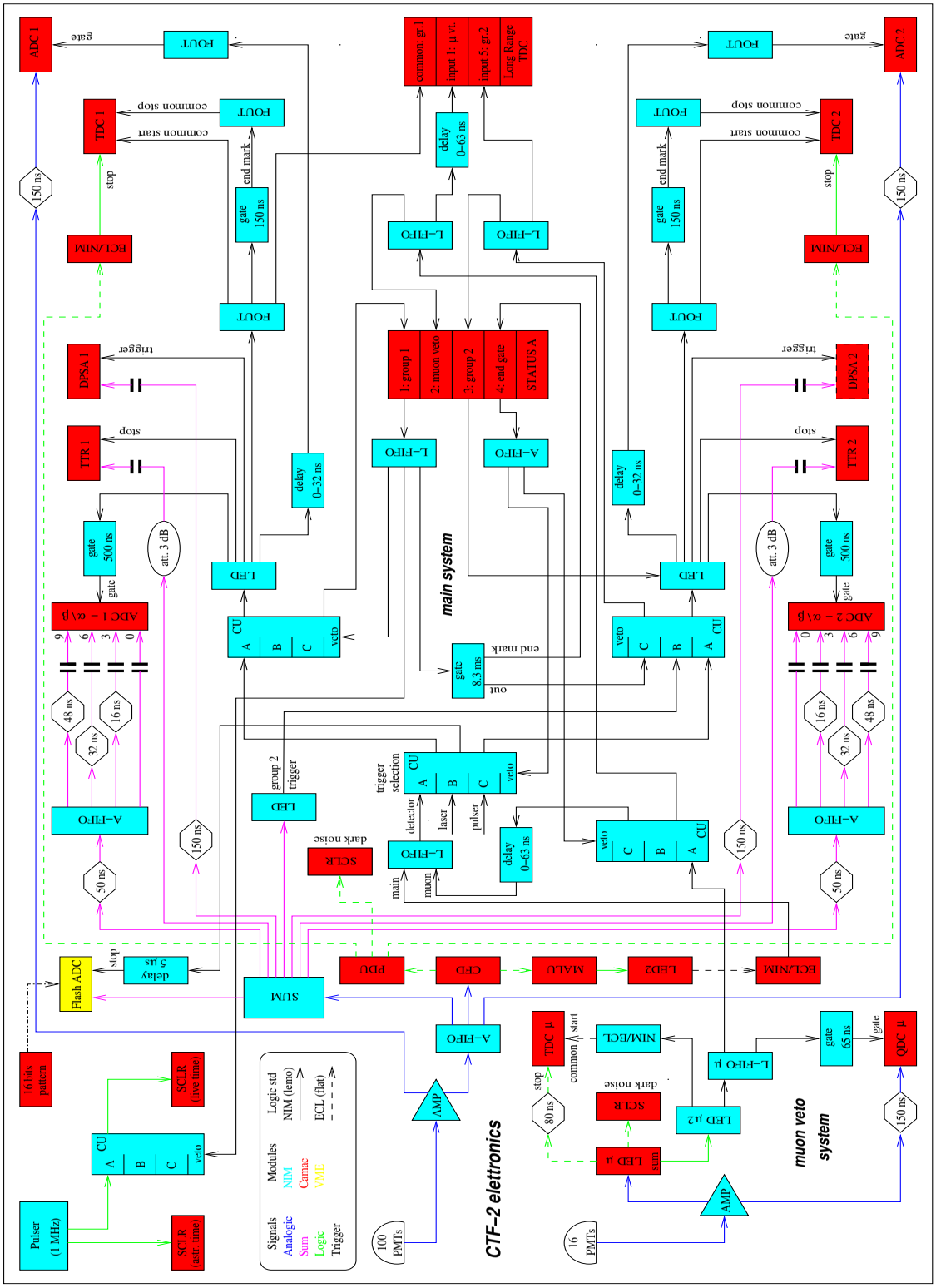

Fig. 9.3: *Schematics of the CTF readout electronics.*

arises the group-2 modules are also read. In this way the dead time of the system is limited to about $50ns$. The coincidence times between the two groups and relative to the eventual muon veto trigger (see below) are measured by means of a *Long Range* TDC .

The electronics only has 64 channels, leading to 36 channels accepting 2 contiguous PMT signals. Nevertheless for CTF-2 and CTF-3 the group-1 ADCs have been increased to 100.

PMTs are connected with BOREXino-like submarine cables that leave the water tank from light-tight flanges in the upper surface. The electronics is housed next to the BOREXino one in the BBW (fig. 2.6). The PMT gain and signal characteristics are identical to the ones specified for BOREXino in sec. 4.2.1.

After a passive decoupling stage and a $\times 30$ amplification, signals are sent to group-1 ADCs and to multiplexers (analog FIFO units). The multiplexed signals feed group-2 ADCs, the analog sum formation system, and a set of CFDs (Constant Fraction Discriminator).

The analog sum is built with cascaded FIFO units and a proper attenuation to ensure operation within the linearity of the modules. It's pulse shape information is acquired in different ways (see below).

The CFDs perform time pick-off with reduced amplitude walk[1]. The logical signal extracted by CFDs goes to the trigger formation system and, upon a programmed delay, to TDCs of both groups and to scalers for dark rates monitor.

Trigger

The trigger is determined by the concurrent signal in n electronic channels in a $\Delta t = 30ns$ time window. The minimum number of PMTs that can be put in trigger depends on the dark rates as the possibility of random coincidences must be negligible. The rate at which such a coincidence is expected is given by

$$P = \left(\begin{array}{c} 100 \\ n \end{array} \right) r^n \Delta t^{n-1} \tag{9.1}$$

and an average PMT dark rate of $500Hz$ leads to $n \geq 6$ in order to have $P < 1y^{-1}$.

The CFDs outputs are fed to a set of cascaded MALUs (*MAjority Logic Unit*) that build a step function with encoded the number of instantly firing channels. The trigger time window is therefore given by the (tunable) CFD output width. This trigger signal is obtained discriminating the step function against a programmable threshold and is then ORed with the trigger from the muon veto.

Triggers for group-2 follow the same iter and can occur between $50ns$ and $8.3ms$ after a group-1 trigger, where the lower boundary is given by the minimum output width of the trigger discriminator and the upper one by the buffer extension of the long range TDC measuring the coincidence time.

There are a few conditions that could trigger both groups (so called *re-trigger* conditions):

[1] see [237] for a more detailed discussion of the advantages of CFDs against Linear Edge Discriminators (LEDs).

1. Intrinsic re-trigger of the scintillator light whose de-excitation time is of the order of $100ns$. The $50ns$ boundary limits this possibility

2. Muon Čerenkov events due to multiple reflections could generate re-trigger events. To avoid this occurrence, group-2 is vetoed up to $20\mu s$ after muon-flagged event.

3. In case of high energy events, PMT *after pulsing* can induce re-triggers with delays above $1\mu s$ [2]. The group-2 features also an additional threshold at about $150keV$ to limit this possibility. This is implemented discriminating the analog sum signal.

4. Reflections at the end of the cables. After CTF-1 a better design of PMTs, cables and HV (de)coupling have solved this problem.

The logic implementing the distribution of the trigger signal and the interplay between the two groups and the muon veto will not be described here (fig. 9.3 and [237]).

The live time of the system is measured feeding a $1MHz$ pulse to a couple of scalers, one of which is vetoed during data readout.

Muon Veto System

The third sub-system is the muon veto.

PMT powering and signal decoupling are analogous to the one described above.

After a $\times 10$ amplification stage, PMT pulses are sent to QDC (*Charge-to-Digital converter*) units that integrate it and digitize it. A copy of the amplified pulse reaches a LED (Leading Edge Discriminator) whose threshold is set to be sensitive to single photoelectron signals. After the time pick-off, the logical signal goes to scalers for dark rates monitor and to TDC for time acquisition. The logic sum output of the discriminator is sent to a second LED for trigger generation. The threshold of this second LED is normally set to a level corresponding to a coincidence of 4 PMTs. The trigger signal provides the common start to TDCs and the gate the ADCs. Moreover it is sent to the main system to be ORed with the other trigger conditions and to a latch unit (status A) that records the flag in the data. Finally a copy of the muon veto trigger reaches the long range TDC and its time relative to possible other trigger conditions is registered.

Data Acquisition

All acquisition modules producing data to be read are Camac units hosted in four racks. The system is read trough ethernet connections with crate controllers being given an IP address within a private LAN. A three-process data acquisition system runs on a VAX-Station and produces locally the raw data files. The official reconstruction code, named `ctf_rec` is run offline to produce the *standard n-tuple*. This holds a selection of the relevant raw information, the reconstructed position of the event as well as other computed physical quantities, like the α/β discrimination parameters.

[2] In this case after-pulsing is given by ions created by the primary pulse in the residual gas, which later find their way back to photocathode.

Information acquired

1. Charge of every channel. The resolution of ADCs is 10-bit with $100ns$ integration gate[3]. Gain is adjusted to yield $-0.25pC/bin$. Saturation arises around 23 photoelectrons.

2. Time of every channel. TDCs with 12-bit resolution are used in *common start* mode. Roughly $50ps/bin$ are achieved. If the channel is seeing more than one photon, only the time of the first can be recorded.

3. Pulse shape information of the analog sum signal.

   (a) α/β ADCs. The analog sum is sent to 4 ADCs with a $500ns$ gate and 4 different delays 0, 16, 32, $48ns$. The last one lets the signal fall entirely inside the gate, while the other three are instead truncating different portions of signals head. The tail-to-total ratios used by the α/β discrimination method (sec. 9.1.5) are computed out of this information.

   (b) TTR (Transient Time Recorder) waveform. The TTR is a $200MHz$, 8-bit waveform digitizer which allows linear acquisition of signals up to $340pe$ ($\sim 1MeV$). Its circular buffer memory has a depth of $1\mu s$ and is used in stop mode (i.e. the $1\mu s$ before the trigger is read.).

   (c) DPSA (Digital Pulse Shape Analyzer) waveform. The DPSA is a custom made integrator and waveform digitizer with a $120MHz$ clock, 10-bit resolution and $600ns$ memory depth. It is used in α/β discrimination (sec. 9.1.5).

   (d) FADC waveform. One of the BOREXino FADC board (sec. 4.6) is installed since CTF-2 as a test and to provide redundancy with the main electronics. It is a quasi stand-alone system and is read independently with a PPC-based DAQ similar to the BOREXino one (sec. 5.2).

4. STATUS-A flags. This is a latch record that flags trigger conditions in different sub-groups (including muon veto).

5. Long Range TDC. This records relative times occurring between different trigger conditions (group-1 and group-2, group-1 and muon veto, ...).

Fig. 9.4 shows a scintillation event as seen by the CTF event display, where most of the information described above is reported.

9.1.3 Calibration system

The main calibration instrument is a $410nm$ laser situated on top of the water tank and coupled to a 1×100 optical splitter. 100 individual optical fibers reach PMTs of the main detector. The sub-Poisson regime (sec. 6.4.1) is ensured with optical filters on the laser output. A pulser in the electronic room is normally used to drive both the laser and the acquisition system at $\sim 100kHz$.

[3] gate opens $20 - 30ns$ before signal arrival

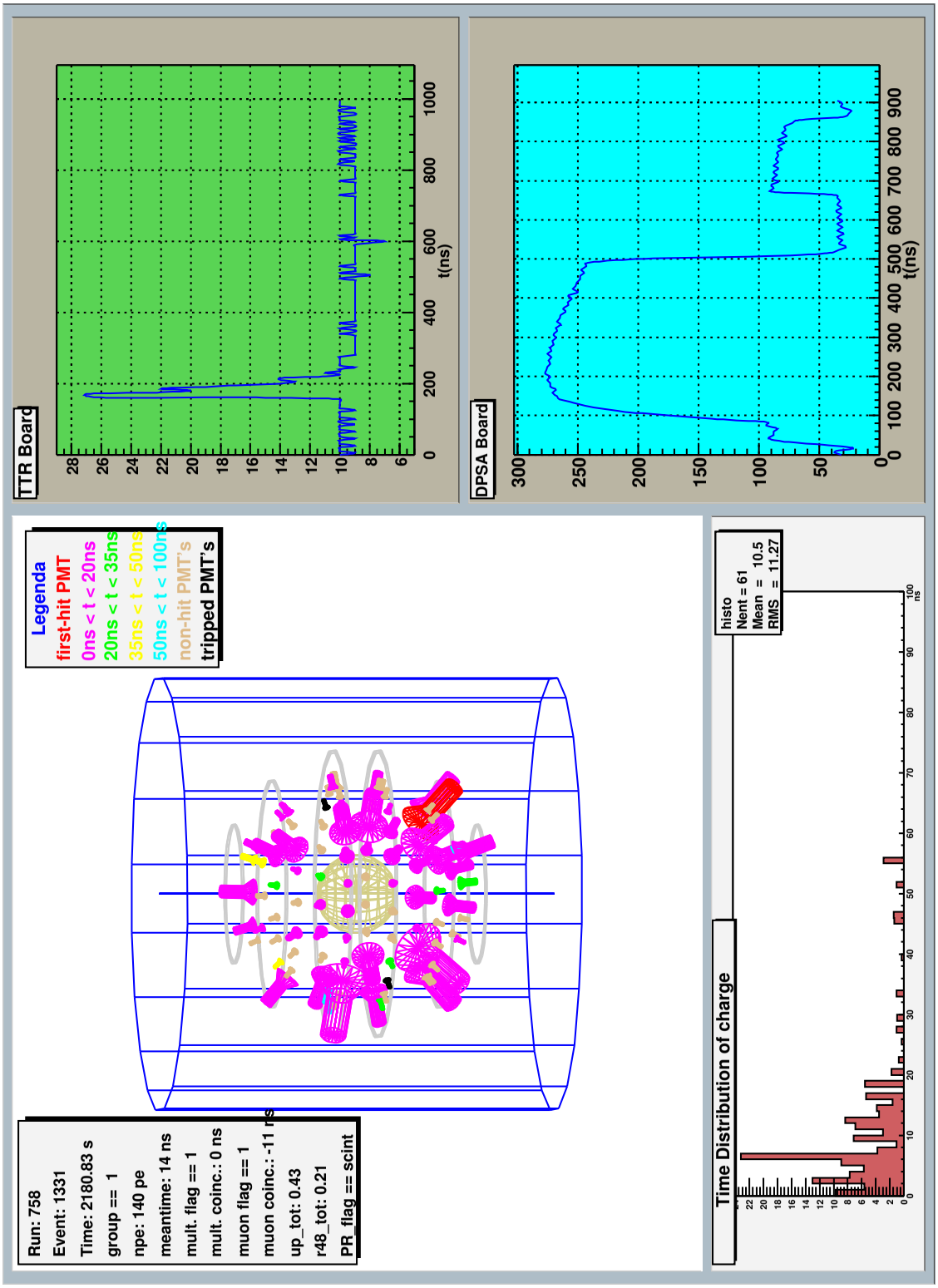

Fig. 9.4: *A scintillation event as seen by the CTF event display.*

Periodically short laser runs are taken to calibrate the system. These yield ADC tables with the position of the pedestal (P_0) and of the single photo-electron peak (P_1) in terms of ADC bins. Similarly TDC tables are produced with the time offsets T_0 of each channel. The reconstruction code reads the latest available laser tables and computes the hit charge and time:

$$Q(npe) = \frac{Q_{ADC} - P_0}{P_1 - P_0} \qquad T(ns) = (T_{TDC} - T_0) \times s \tag{9.2}$$

where the slope s (in ns/bin) was determined with a pulser introducing 4 different delays and producing a calibration line for every channel.

For the Muon Veto a different calibration system is foreseen. It is composed by 4 LEDs ($450nm$) equipped with Teflon diffusers and mounted downward-looking in the tank to illuminate 4 PMTs each. This system has not been used yet and the muon veto is temporarily used as a veto only.

9.1.4 Position reconstruction

In order to study the intrinsic (*bulk*) contamination of the scintillator, the rejection of surface and external background is essential. Consequently it is very important to reconstruct the position of the energy deposit within the scintillator.

The algorithm was introduced also in sec. 7.4.4 for BOREXino as "milan" module. It works on the information of the arrival time of the (first) photon on the photocathode in every channel:

$$t = t_e + t_d + t_f + t_j \tag{9.3}$$

where:

1. t_e is the absolute time at which the energy deposit occurred.

2. t_d is the scintillator decay time (sec. 2.4.1) distributed as:

$$f(t, \mathbf{q}, \lambda) = \sum_i q_i \lambda_i e^{-\lambda_i t} \tag{9.4}$$

   where $\lambda_i = 1/\tau_i$ are the different decay constants of tab. 2.6 and q_i are the relative weights of the components ($\sum_i q_i = 1$).

3. t_f is the Time-of-Flight (TOF) of the photon from the event real position $\mathbf{r}_e$. Assuming linear propagation, it can be expressed as:

$$t_f = \sum_i \frac{n_i l_i}{c} \tag{9.5}$$

   where n_i and l_i are respectively the refraction indices and the distances covered in the different media crossed.

However the total reflection at the surface separating the two media[4] and the phenomena described in sec. 2.4.3 (elastic scattering, absorption and re-emission) deviate the photon from a straight line propagation. These effects are difficult to model and are accounted for using an *effective* refraction index n_{eff} in place of the real scintillator one ($n_{PC} = 1.51$). Its value $n_{eff} = 1.75$ is determined from MC studies and especially from source tests, for which the nominal position of events can be compared with the reconstructed one. These tests, included in every CTF campaign, involve radon sources similar to those described in sec. 6.6, inserted with a precise mechanical arm inside the *inner vessel*.

4. t_j is the PMT transit time *jitter*, represented by a Gaussian with $\sigma \simeq 1ns$.

The probability that a photon reaches a given PMT in the time interval $[t_1, t_2]$ is:

$$P_N(t_1 \leq t \leq t_2) = \int_{t_1}^{t_2} f(t, \mathbf{a}_N, \mathbf{r}_e, t_e)dt \tag{9.6}$$

where $\mathbf{a}_N$ is the parameter vector that includes t_d, t_j and the PMT coordinates. The *p.d.f.(probability density function)* $f(t)$ is given by the convolution of the scintillator decay function $f_d(t)$ with the PMT time *jitter* function $f_j(t)$:

$$f(t^*) = \int_{-\infty}^{t^*} f_d(t')f_j(t^* - t')dt' \tag{9.7}$$

where $t^* = t - t_e - t_f = t_d + t_j$.

Every photon is detected independently, therefore one can define a Maximum Likelihood function:

$$L(\mathbf{r}_e, t_e) = \prod_{i=1}^{n} f(t_i^*, \mathbf{r}_e, t_e) \tag{9.8}$$

where n is the number of hit PMTs.

The algorithm uses the MINUIT package[229] and looks in the parameters space for the values of (x_e, y_e, z_e, t_e) for which eq. 9.8 has an absolute maximum[5], taking the center of the detected charge as initial value.

To overcome the optical problems mentioned above, leading to a spread of the arrival times distribution, hits occurred outside 3σ from the average time are discarded. The average time is then recalculated and the selection is repeated within 2.5σ.

The space resolution obtained for a $1MeV$ event at the center of the detector is $\sim 10cm$.

9.1.5 α/β discrimination

The differences in α and β signal shapes are pointed out in sec. 2.4.1 and the PSD methods developed for BOREXino are introduced in sec. 7.4.6. In CTF, the *tail-to-total* and the optimum filter (Gatti) technique are implemented.

[4] Clearly a problem unique to CTF that BOREXino will not experience.

[5] Actually the function maximized is $L(\mathbf{r}_e, t_e) = \sum_{i=1}^{n} ln(f(t_i^*, \mathbf{r}_e, t_e))$.

Tail-to-total method

The information comes from the 4 ADCs operating on the analog sum signal (sec. 9.1.2). One of them records the total charge of the event in the $500ns$ gate, while the others record the charge seen after the first $16ns$, $32ns$ or $48ns$, i.e. different portions of the signals tail. The ratios of the charge seen by the last three divided by the first are computed by the offline code and included in the n-tuple. α and β events gather in two gaussians around different values of these parameters (fig. 9.6, left).

The $48ns$ delay yields the best result with PC+PPO scintillator mixture and is the one commonly in use in CTF-3.

Optimum filter method

The information in use is the one coming from the DPSA board (sec. 9.1.2). Fig. 9.5 shows the curves acquired for known β and α events.

Sample curves are selected averaging known events and, after normalization, two parameters are evaluated:

$$G_\alpha = \sum_i P_i \alpha_i \qquad G_\beta = \sum_i P_i \beta_i \tag{9.9}$$

where $\{P_i\}$ is a vector of weights to be chosen in order to emphasize the parameters separation. The best possible choice comes out to be[226]:

$$P_i = \frac{\alpha_i - \beta_i}{\alpha_i + \beta_i} \tag{9.10}$$

Then an analogous parameter is associated to any unknown pulse S:

$$G_S = \sum_i \frac{\alpha_i - \beta_i}{\alpha_i + \beta_i} S_i \tag{9.11}$$

In the distribution of G_S, α and β events gather in gaussians around G_α and G_β (fig. 9.6, right).

A performance comparison

The energy of the events affects the spread of the gaussian distributions of both methods, making the separation intrinsically less efficient at lower energies. Besides, both discrimination methods work better for events close to the *inner vessel* center as optical border effects at the nylon surface may mask the pulse shape differences and the latter are more relevant for photons emitted close to it.

As it can be seen in fig. 9.6, in both cases the gaussian distributions of α's and β's do have some overlap. Therefore choosing a separation value implies sacrificing a few percent β events and accepting a few percent α contamination.

As a sample comparison the performances can be quoted in the $500 - 800keV$ region, with a $75cm$ radial cut and retaing 98% of the β's. The tail-to-total method rejects 95% of the α's while the Gatti filter reaches 98%.

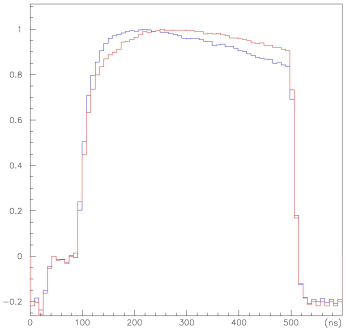

Fig. 9.5: *Sample curves from the DPSA board for α (red) and β (blue) events.*

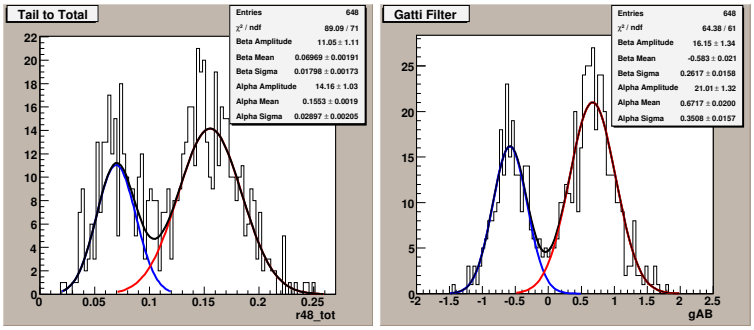

Fig. 9.6: *Tail-to-Total and optimum filter parameters for α/β discrimination in the 500-800keV energy region and with 75cm radial cut.*

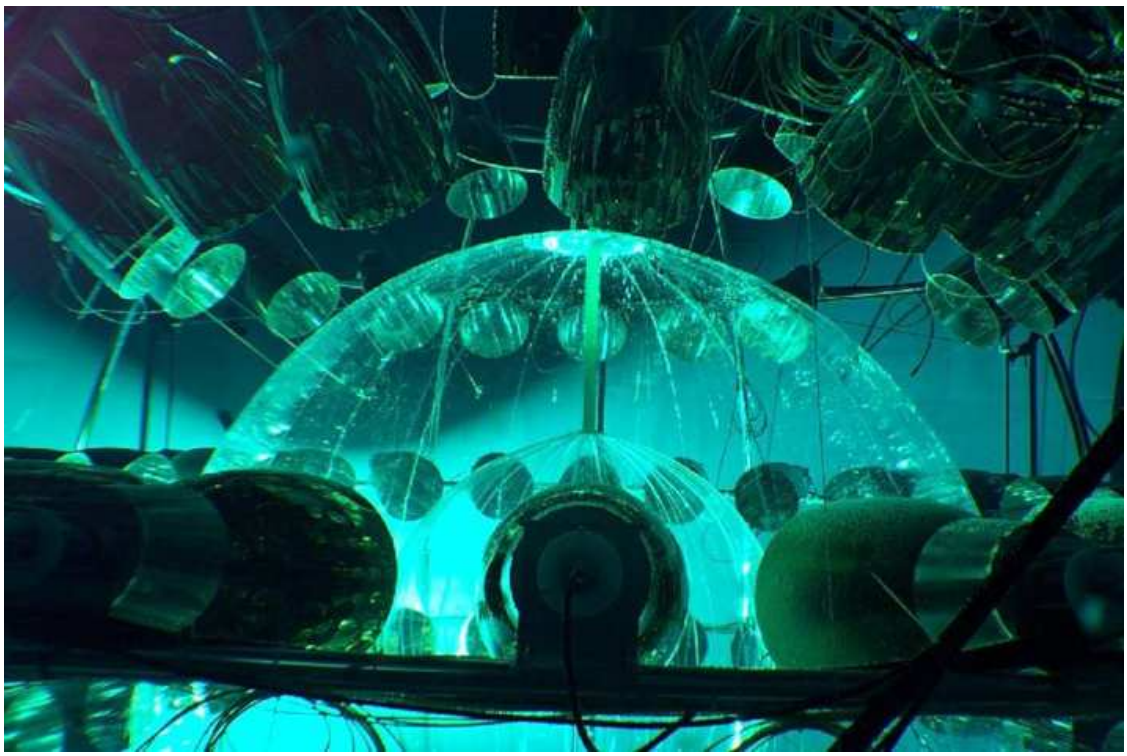

Fig. 9.7: *View of the CTF detector during the water run in June 2001.*

9.2 The CTF-3 Campaign

The CTF was filled with water for the third time in May 2001. Thereafter the electronics and the calibration system were re-commissioned.

In November 2001 the *inner vessel* was filled with pseudocumene ($4268 \pm 10l$ or $3756 \pm 9kg$) from the first batch arrived in Gran Sasso for BOREXino. For the following 7 months the detector was very useful to evaluate the intrinsic scintillator radiopurity levels

Date	Runs	Operation	comments
2001 Feb		nylon vessel installed	
2001 May		water filling	
2001 Jul 21	2000	data taking started	water runs
2001 Nov 22-28	2042-2047	scintillator loading	
2002 Jan 10-11	2074-2075	^{14}C test	
2002 Feb 6-11	2094-2103	silica gel column test	continuous loop mode
2002 Mar 20-28	2123-2130	water extraction (1)	continuous loop mode
2002 Apr 2	2150-2152	blank loop	
2002 Apr 26	2153	^{14}C test	
2002 May 9-23	2162-2173	water extraction (2)	stop-and-go, nitric acid
2002 Jun 3	2180	^{14}C test	
2002 Jun 9-20	2184-2187	silica gel column	batch mode
2002 Jun - 2005 Feb	2188-2520	*quiet* data taking	611d L.T.
2005 Feb 14		Gate Valve installed	
2005 Mar 17-18	2532-2540	Radon Source test	for position rec. calib.
2005 Mar 19-date	2541-2582	data taking	

Tab. 9.2: *The CTF-3 campaign.*

as well as to perform tests of the different purification strategies available for BOREXino.

^{14}C contamination. The ^{14}C intrinsic content of the scintillator was evaluated with the fit described in sec. 9.2.2. The scintillator procurement campaign for BOREXino ($300t$) proceeded in four successive production batches, whose ^{14}C contents were all tested in CTF replacing each time about $500kg$ of scintillator from the *inner vessel* with the newly arrived. The $^{14}C/^{12}C$ ratio ranged in $[1.6, 5.1] \times 10^{-18} g/g$ and was considered acceptable for BOREXino.

Silica Gel Purification. The silica gel column, present in the Module-0 (sec. 2.2.3), was operated twice. In the *Column Loop Test* (CLT) the scintillator was circulated from the *inner vessel* through the column and back into the *inner vessel* in a closed continuous loop. However the purification factor that can be achieved in this mode is limited to a few units by the establishing of an equilibrium (breakthrough) condition between silica-gel and scintillator in terms of ionic impurities contained[244]. In the *Column Batch Test* (CBT) the *inner vessel* volume was instead first replaced with water. The scintillator was then circulated through the column using two different storage tanks to avoid the mixing between "clean" and "dirty" masses and was finally reloaded to CTF.

Water Extraction Purification. Also the test of the water extraction plant was done twice. In both cases the scintillator was circulated in a closed loop that included also stripping with nitrogen to remove gaseous impurities like radon, krypton and argon. In the first test (WET-1) the operation was continuous, while in the second one (WET-2) a *stop-and-go* strategy was attempted to prevent the establishing of possible flow patterns along the vertical axis that could leave part of the scintillator

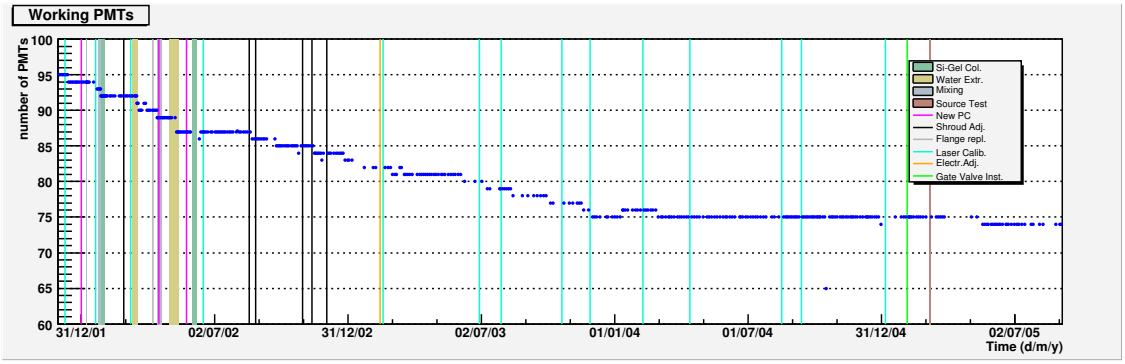

Fig. 9.8: *Number of working PMTs during CTF-3 campaign.*

untreated. Moreover the last few cycles were done adding nitric acid to the water, as previous lab tests showed how a lower pH should enhance the purification efficiency.

The preparation of the distillation test was ongoing, when the accident mentioned in sec. 2.5 blocked any activity involving fluids in the Gran Sasso laboratory. The following *quiet* data taking period lasted almost three years and allowed an improved understanding of the detector and of the analysis techniques.

In February 2005 operations resumed with the installation of a Gate Valve on the neck of the *inner vessel* that allows radon-free source insertion. In March 2005 a radon Source test was performed to calibrate the position reconstruction algorithm (sec. 9.1.4).

The duration of a data taking run is variable in a 1-3 days range, though during the purification tests also shorter runs were often performed. In many of the following analyses the low statistics conditions impose to collect together runs belonging to the same *phase*, defined as a stable detector's configuration and usually referring to a period between two successive purification tests or similar operations. Tab. D.1 lists the runs that have been excluded from all the analyses for different motivations.

9.2.1 Live PMTs

The sealing of the PMTs studied for BOREXino (sec. 2.2.2) proved to work well also in water in CTF as in 4.5 years only 22% of the PMTs went lost. 99 PMTs were mounted of the planned 100, 4 died immediately during water filling, probably due to water infiltration through the connector, while the others were turned off after showing high noise or instabilities (typically an excess of drawn current) during one or more runs[6]. The amount of working PMTs during the CTF-3 campaign is shown in fig. 9.8.

The sealing of the Muon Veto PMTs, also identical to the final BOREXino one, proved to be even more reliable: out of 16 PMTs installed only 2 died and they died immediately after the water filling.

The failure of a PMT does not constitute a discontinuity in the data taking phase as the light yield is computed run per run. However in one case the adjustment of the high

[6] A few recovery attempts are usually done before definitively marking a PMT as malfunctioning.

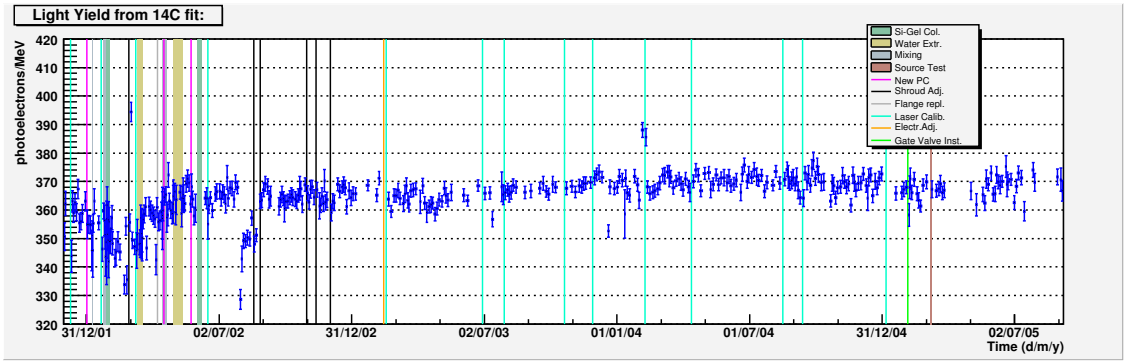

Fig. 9.9: *Light Yield from ^{14}C spectral fit. Values are renormalized to 100 PMTs.*

voltage in a few channels was necessary and indeed introduced a potential discontinuity, named EADJ (Electronic Adjustment) in the rest of the chapter.

The electronics showed long term instabilities and a laser calibration is now performed at least once per month to minimize their impact. Data taken before such a policy was established may however be affected by a small unknown systematic error.

9.2.2 Light Yield

The low part of the CTF energy spectrum is dominated by β events due to ^{14}C decays up the end-point energy of $156keV$ (sec. 2.3.1). The ^{14}C spectrum can be fitted run per run with the theoretical shape convoluted with the detector's resolution. The fit is performed in the $[30, 60]pe$ range with a $60cm$ radial cut and features two free parameters[7]:

1. the normalization constant, from which the ^{14}C content is evaluated (sec. 9.2).
2. the conversion from the charge scale in *npe* (number of photoelectrons) of the experimental spectrum to the energy scale to which the theoretical shape is referred. This is the *light yield* or *photo-electron yield*.

The detector's resolution function includes the *quenching* effect for electrons after Birk's model (sec. 2.4.2) with $kB = 0.010cm/MeV$[8]. However if this value is varied in the $[0, 0.015]cm/MeV$ range (values found in literature for PC-like scintillators) an uncertainty of 7.5% can be quoted on the light yield.

The positions of the α peaks (tab. 9.6) in the spectrum calibrated on electrons is not stable throughout the campaign, indicating that the quenching effects (sec. 2.4.2) in the scintillator are variable. The reference peak for α's is ^{214}Po visible on the group 2 especially in the periods with high radon contamination (sec. 9.3.1). The peak is reconstructed at $802 \pm 3keV$ at the beginning of campaign and progressively degrades down to $716 \pm 4keV$ in the last periods, none of which is too far from the $751keV$ observed in CTF-1 (tab. 9.6). The energy resolution on the ^{214}Po peak is $\sim 9\%$.

[7] A third one is present in the shape factor of the theoretical spectrum, but is not useful in this context.

[8] The parameter kB cannot be left free in the fit due to the presence of secondary minima of the parameter space.

9.3 Delayed coincidence analyses

A powerful tool to evaluate the background condition in the CTF detector (and later in BOREXino) are the so called *delayed coincidence analyses*, i.e. the tagging of pairs of correlated events naturally occurring in the ^{238}U and ^{232}Th chain and in the ^{85}Kr decay scheme.

9.3.1 Radon and Uranium contamination

The Uranium radioactive chain (fig. A.2) features the fast delayed coincidence $^{214}Bi - ^{214}Po$ that can be exploited to evaluate the ^{238}U content of the scintillator, provided that secular equilibrium can be assumed.

^{214}Bi decays β (or β+γ) to ^{214}Po with a $3.23MeV$ end-point energy. ^{214}Po has a mean life of $236\mu s$ and decays to ^{210}Pb emitting an α particle of $7.69MeV$, that is visible in CTF around $750keV$ (sec. 9.2.2). The β-α coincidence time is short enough for the second event to be caught on the group 2 of the electronic chain (sec. 9.1.2).

However the $^{214}Bi - ^{214}Po$ coincidence is situated below the ^{222}Rn in the decay chain and actually ^{214}Bi goes fast ($33min$) in equilibrium with ^{222}Rn, so whenever this element is present in large quantities the estimation of ^{238}U content of the scintillator is very difficult. In CTF this typically happens after a fluid handling operation that implies even a minor contact between air and scintillator, while a long quiet data taking leaves time to ^{222}Rn to decay away and makes the measurement possible. Even in these cases however the results should be considered as upper limits as it cannot be excluded that radon gas is permeating through the nylon from the buffer water into the scintillator.

Analysis details

To select the $^{214}Bi - ^{214}Po$ coincidences the following cuts are applied:

1. $2\mu s < t_{\text{coinc}} < 710\mu s (\sim 3\tau)$, where the lower cut rejects the faster $^{212}Bi - ^{212}Po$ events (sec. 9.3.2). Acceptance 94.4%.

2. $E_{gr1} < 3.5MeV$ where 2σ above the ^{214}Bi energy are allowed. Acceptance 99% (from simulations) due to the hardware threshold.

3. $E_{Po} - 3\sigma < E_{gr2} < E_{Po} + 3\sigma$ where in different campaign periods the E_{Po} peak energy is determined applying the preceding two cuts (plus a $60cm$ radial cut). Acceptance 99.6%

The overall acceptance is 93.1%.

Fig. 9.10 shows the two energy spectra and the coincidence time for the selected event pairs in the initial period of CTF-3. The observed coincidence time, $217 \pm 10\mu s$ is reasonably close to the nominal ^{214}Po mean life.

The $^{214}Bi - ^{214}Po$ activity is computed run by run and shown in fig. 9.11. The time evolution between two plant operations can be fitted with:

$$f(t) = A \cdot exp(-t/\tau) + B \tag{9.12}$$

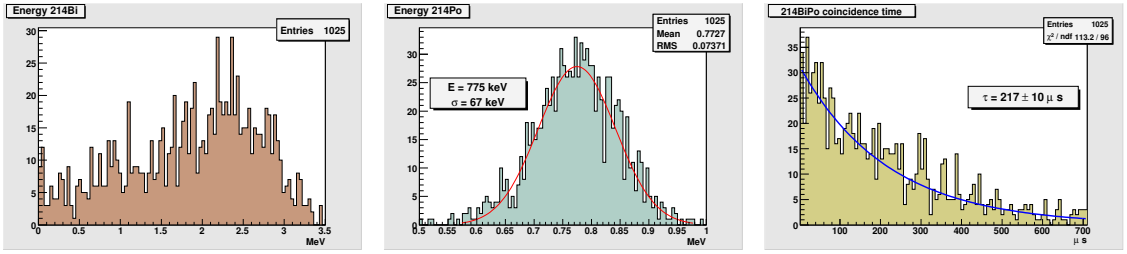

Fig. 9.10: $^{214}Bi - ^{214}Po$ *delayed coincidence analysis.* ^{214}Bi *energy spectrum (left),* ^{214}Po *energy spectrum (center) and coincidence time (right). Data refer to period A of tab. 9.3.*

	Period[a]	Runs	L. T. (days)	τ (d)	A (e/d)	B (e/d)	^{238}U ($10^{-16}g/g$)
A	1^{st} PC batch	2056 → 2073	22.2	6.1±0.7	271	6.3 ± 1.1	15.8 ± 2.6
B	CLT → WET-1	2103 → 2115	14.8	5.0±0.4	249	2.9 ± 1.6	7.2 ± 3.9
C	After WET-1	2130 → 2146	17.0	7.3±0.9	43	1.5 ± 0.7	3.7 ± 1.9
D	After Mixing	2155 → 2161	7.0	4.3±0.8	239	< 4.2	< 10.5
E	After WET-2	2173 → 2179	9.8	6.0±0.6	45	< 10	< 25
F	After CBT	2188 → 2219	47.9	6.2±0.7	30	2.3 ± 0.3	5.8 ± 0.7
G	EADJ → GVI	2285 → 2520	458	n.a.	n.a.	2.7 ± 0.1	6.8 ± 0.2
H	After SRC	2541 → 2546	11.2	6.3±0.5	29	< 6.2	< 16
I	Last period	2549 → 2582	59.9	n.a.	n.a.	2.7 ± 0.2	6.8 ± 0.6

[a]CLT = Column Loop Test; WET = Water Extraction Test; CBT = Column Batch Test; EADJ = Electronic Adjustment; GVI = Gate Valve Installation; SRC = Source Test;

Tab. 9.3: $^{214}Bi - ^{214}Po$ *in CTF-3 and* ^{238}U *equivalent content of the scintillator. Figures in the last three columns are obtained fixing* τ *to the radon mean life* $5.52d$.

so that A corresponds to the radon activity at the beginning of the period under examination and B accounts for the contribution from ^{238}U in secular equilibrium. The results of the fit in the different phases are reported in tab. 9.3. The uranium concentration in the scintillator is computed knowing that $10^{-16}g/g$ correspond to $0.4ev/d$ of $^{214}Bi - ^{214}Po$.

Discussion of results

Leaving the decay time as free parameter of the fit, the latter finds values consistent with the nominal ^{214}Po mean life (column 5 in tab. 9.3). However in the attempt to estimate the ^{238}U contamination of the scintillator the decay time was fixed in the fit. The constant contribution obtained in the different periods is visible in column 7. Periods D, E and H are too short and the fit prefers a purely exponential model. Only a loose upper limit could be derived (95% C.L.) in these cases.

The shroud was sometimes refilled with water during the first year of the campaign to maintain its shape (sec. 9.1.1). However it was noticed that this operation was inducing a temporary permeation of radon through the *inner vessel*, clearly visible in fig. 9.11. This practice was later abandoned to avoid introducing this and other instabilities and

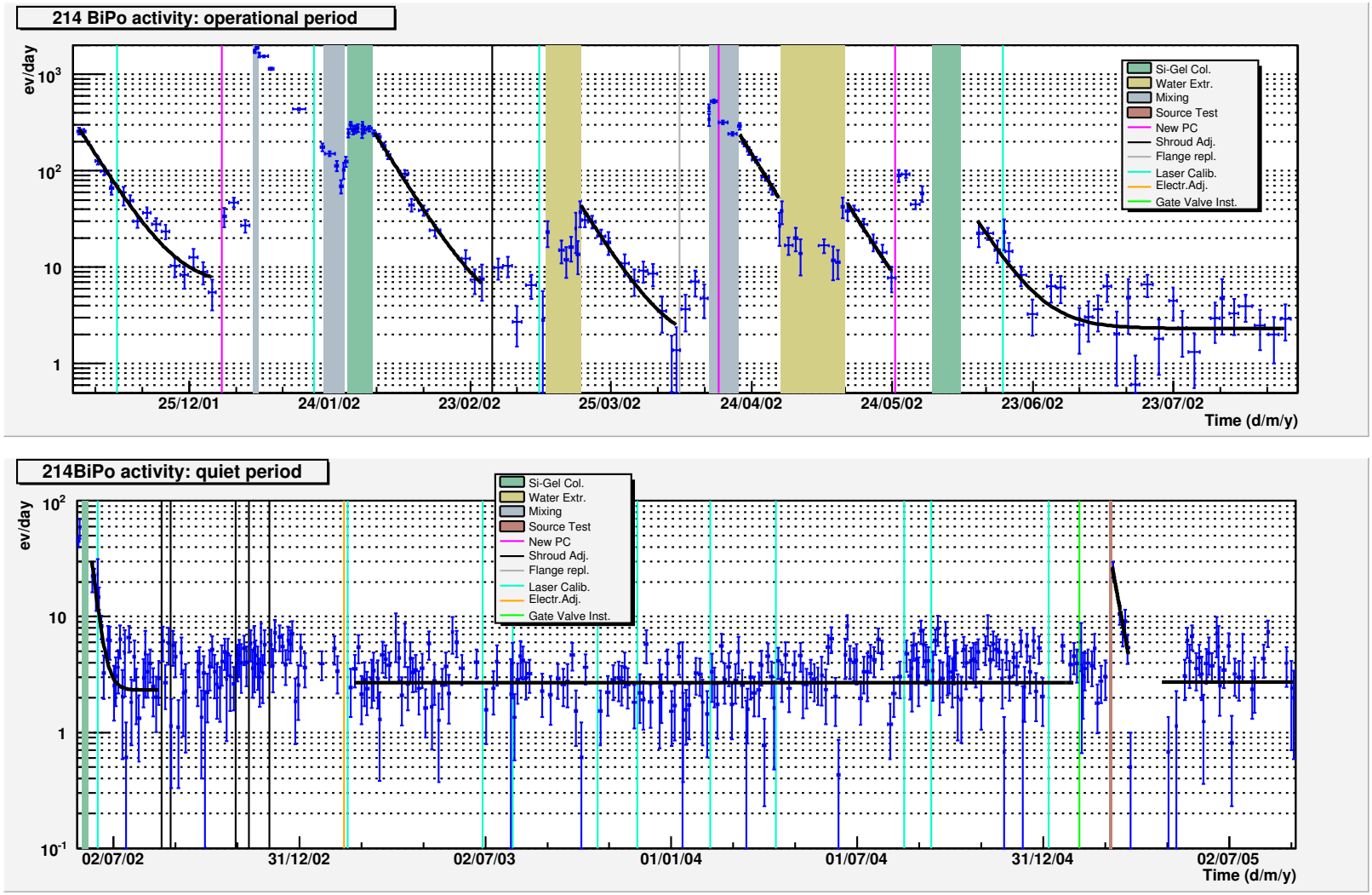

Fig. 9.11: $^{214}Bi - ^{214}Po$ *events in CTF-3 runs: operational (above) and quiet (below) periods. Fit functions are described in the text.*

the shroud was left collapsing on the *inner vessel*. In the definition of the periods in tab. 9.3, the shroud refills do play a role as well as ^{14}C tests and plant operations.

The only clear statement arises comparing the initial period (A) with the long quiet one (G). It is clear that the purifications applied reduced the uranium content by a factor 2-3. The fit of period 2 would attest the relative weight of CLT and WET-1, if it wasn't for the minor shroud refill operation which limits its extension and determines the large error. Intermediate numbers are consistent within 1σ, so any consideration about a specific purification method would be speculative.

9.3.2 Thorium contamination

The Thorium radioactive chain (fig. A.1) also includes a fast delayed coincidence: $^{212}Bi-^{212}Po$. ^{212}Bi decays β(or $\beta+\gamma$) to ^{212}Po with a 64% branching ratio and a $2.25MeV$ end-point energy. ^{212}Po in turn decays α with a mean life of $433ns$ and a nominal energy of $8.79MeV$ (quenched to about $900-1000keV$).

Also in this case a radon isotope, ^{220}Rn, is present in the chain above the coincidence. As it can play somehow the role of ^{222}Rn described above, it is generally named *thoron*. However in this case the decay time is only $10h$, so its presence in CTF can be noted almost only *during* the fluid handling operations and the estimation of the ^{232}Th contamination of the scintillator is not significantly endangered by its presence.

Analysis details

The $^{212}Bi-^{212}Po$ coincidence is selected with the following cuts:

1. $80ns < t_{coinc} < 2\mu s(\sim 4.6\tau)$. The lower bound is a sharpening of the $\sim 50ns$ dead time mentioned in sec. 9.1.2. Acceptance: $\simeq 88\%$.

2. $0.3MeV < E_{gr1} < 2.5MeV$ where 2σ above the ^{212}Bi energy are allowed. The lower cut is useful to reject low energy spurious events. Acceptance: $\simeq 87\%$ (from simulations).

3. $E_{Po} - 3\sigma < E_{gr2} < E_{Po} + 3\sigma$. In general the ^{212}Po peak position cannot be determined well due to the low statistics. However in the three periods when thoron was present the peak was well visible. Its ratio to the ^{214}Po position was 1.24 ± 0.01 in all three cases[9] and this number was assumed to hold for the whole campaign. The cuts are applied on this assumption and moved according to the ^{214}Po position. Acceptance: $> 99\%$.

The overall acceptance is 73%.

Fig. 9.12 shows the two energy spectra and the coincidence time for the selected event pairs in the period of CLT when thoron was present. The mean coincidence time is $506 \pm 91ns$ in good agreement with the ^{212}Po mean life. The average energy of the second event is $962keV$ and degrades down to $\sim 900keV$ (low statistics) in the last runs, to be compared with $1.01MeV$ observed in CTF-1.

[9]Measured applying a 60cm radial cut.

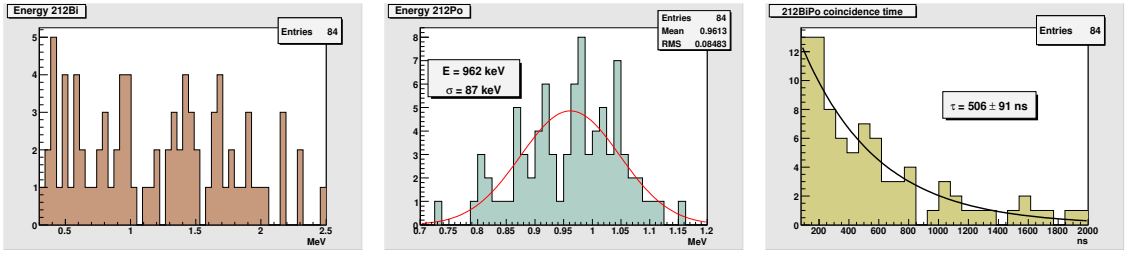

Fig. 9.12: $^{212}Bi-^{212}Po$ *delayed coincidence analysis.* ^{212}Bi *energy spectrum (left),* ^{212}Po *energy spectrum (center) and coincidence time (right). Data refer to period 3 of tab. 9.4. A* $70cm$ *radial cut is applied.*

Accidental background may come mostly from $^{214}Bi-^{214}Po$ coincidence events. This is estimated and subtracted run per run applying the same energy cuts to the $3-20\mu s$ time region[10].

As a $10^{-16}g/g$ contamination of ^{232}Th in equilibrium yields only $0.083ev/d$ of $^{212}Bi-^{212}Po$, the statistics is generally very limited and several runs must be grouped together whenever stability allows it.

Results of the thorium delayed coincidence analysis are reported in tab. 9.4.

The surface contamination

Initially the $^{212}Bi-^{212}Po$ analysis was performed without any radial cut, thanks to its strong tagging.

After CLT, the ^{212}Po α peak is shifted to a lower energy by about 25%, going to lie only partially inside the selection cuts. Though less evident, also the ^{212}Bi β spectrum shows an energy shift. Periods 3, 5 and 8 during plant operations with a large amount of thoron are instead not affected. Though the coincidence time keeps reflecting the ^{212}Po mean life, the radial profile appears moved somewhat outward. In this context, the radial analysis (sec. 9.4) applied to the first period assigns most of the events to bulk contaminants, while after CLT about 50% are indicated as surface contribution (fig. 9.14).

The hypothesis that a contamination of some element of the ^{232}Th chain is either attached or embedded in the nylon could also justify the energy shift: part of the energy may be lost in the nylon (especially of the α) or due to optical border effects.

Though it cannot be excluded that the contamination was introduced by the CLT, more probably it was pre-existent and CLT made it visible by reducing the thorium content of the scintillator which was previously high enough to mask it.

After this consideration the analysis has been performed also with a radial cut at $62cm$ (2.5σ away from surface), that selects only the innermost ton of scintillator.

The results of the analysis with and without the radial cut agree in the initial period and in the thoron reference periods (3, 5 and 8), while in other periods they show different degrees of disagreement confirming the hypothesis of a surface contamination.

To summarize, in spite of the strong coincidence tagging, the application of a radial cut cannot be avoided in the attempt to evaluate the scintillator ^{232}Th contamination

[10] In first approximation ^{214}Po can be considered flat in this range as $20\mu s \ll \tau = 236\mu s$.

	Period[a]	Runs	L. T. (days)	ev. (#)	$^{212}BiPo$ (ev/d)	^{232}Th equiv. ($10^{-16}g/g$)	ev. (#)	$^{212}BiPo$ (ev/d)	^{232}Th equiv. ($10^{-16}g/g$)
				No radial cut			$r < 62cm$		
1	1^{st} PC batch	2063 → 2073	17.3	47	3.81 ± 0.56	46.1 ± 6.8	13	4.34 ± 1.25	52.5 ± 15.1
2	Before CLT	2092 → 2093	0.86	2	3.10 ± 2.39	37.5 ± 28.9	1	6.9 ± 6.9	83.5 ± 83.5
3	During CLT	2095 → 2102	4.24	176	58.3 ± 4.4	n.a.	49	67.9 ± 9.8	n.a.
4	CLT → WET-1	2109 → 2122	17.8	24	1.86 ± 0.39	22.5 ± 4.8	5	1.59 ± 0.76	19.2 ± 9.2
5	During WET-1	2123 → 2130	4.11	77	26.4 ± 3.0	n.a.	28	40.2 ± 7.7	n.a.
6	After WET-1	2133 → 2149	18.6	15	1.14 ± 0.30	13.7 ± 3.6	2	0.60±0.47	7.3 ± 5.6
7	Before WET-2	2156 → 2161	6.39	10	1.99 ± 0.73	24.1 ± 8.9	2	1.44 ± 1.45	17.4 ± 17.6
8	During WET-2	2162 → 2174	8.00	51	8.9 ± 1.3	n.a.	10	7.3 ± 2.4	n.a.
9	After WET-2	2176 → 2179	6.71	10	2.1 ± 0.7	25.2 ± 8.1	1	0.88 ± 0.88	10.7 ± 10.7
10	(1^{st}) After CBT	2188 → 2239	79.1	94	1.7 ± 0.2	20 ± 2	8	0.58 ± 0.22	7.1 ± 2.6
11	(2^{nd}) After CBT	2240 → 2281	74.2	69	1.3 ± 0.2	16 ± 2	10	0.78 ± 0.26	9.5 ± 3.1
12	(1^{st}) After EADJ	2285 → 2319	78.0	81	1.5 ± 0.2	18 ± 2	9	0.68 ± 0.23	8.3 ± 2.8
13	(2^{nd}) After EADJ	2320 → 2345	53.7	44	1.1 ± 0.2	14 ± 2	1	0.10 ± 0.12	1.2 ± 1.4
14	(3^{rd}) After EADJ	2346 → 2382	68.6	50	1.03 ± 0.15	12.4 ± 1.8	0	< 0.18	< 2
15	(4^{th}) After EADJ	2386 → 2422	91.9	84	1.29 ± 0.14	15.6 ± 1.7	0	< 0.12	< 1.6
16	(5^{th}) After EADJ	2423 → 2470	84.9	72	1.2 ± 0.14	14.5 ± 1.7	1	0.07 ± 0.07	0.8 ± 0.8
17	(6^{th}) After EADJ	2471 → 2520	81.2	52	0.89 ± 0.13	10.8 ± 1.5	2	0.13 ± 0.11	1.6 ± 1.3
18	GVI → SRC	2522 → 2531	21.0	12	0.78 ± 0.24	9.4 ± 2.9	1	0.25 ± 0.30	3.0 ± 3.6
19	After SRC	2541 → 2582	72.4	53	1.03 ± 0.14	12.4 ± 1.7	2	0.15 ± 0.12	1.9 ± 1.4
	Periods [10-12]	2188 → 2319	231	244	1.48 ± 0.10	18.0 ± 1.2	27	0.68 ± 0.13	8.2 ± 1.6
	Periods [13-17]	2320 → 2520	380	302	1.12 ± 0.06	13.5 ± 0.8	4	0.06 ± 0.03	0.7 ± 0.4

[a]CLT = Column Loop Test; WET = Water Extraction Test; CBT = Column Batch Test; EADJ = Electronic Adjustment; GVI = Gate Valve Installation; SRC = Source Test;

Tab. 9.4: *Thorium contamination from $^{212}Bi - ^{212}Po$ coincidence analysis in CTF-3 campaign. Periods 3, 5 and 8 include thoron contamination and no equilibrium can be assumed. Errors are given at 1σ, upper limits at 95% C.L. Each of periods 10-17 correspond to approximately 4 months astronomical time. $^{212}Bi - ^{212}Po$ activity and ^{232}Th equivalent are renormalized to full volume, the number of events is not.*

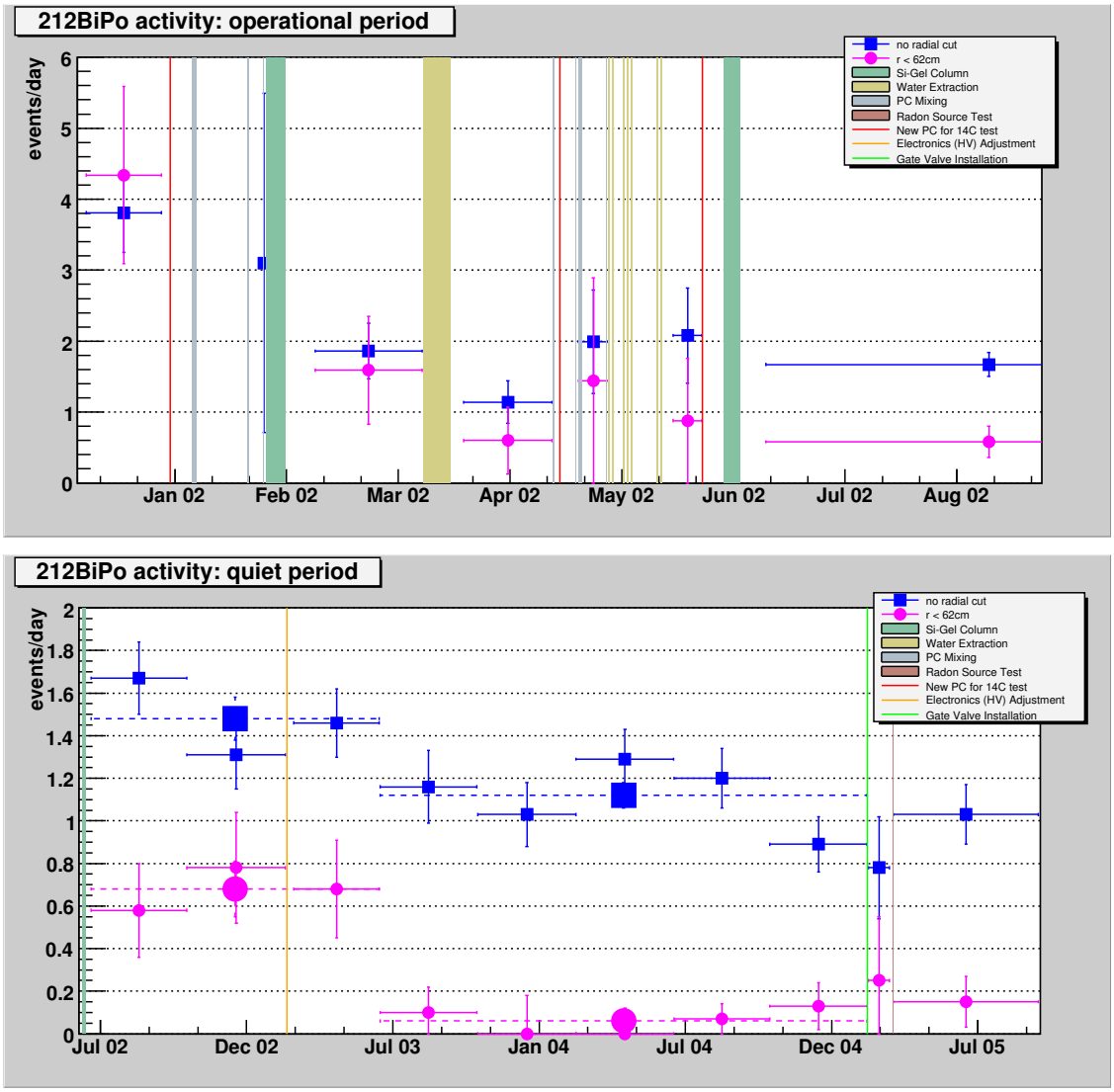

Fig. 9.13: $^{212}Bi - ^{212}Po$ *events in CTF-3 campaign: operational (above) and quiet (below) periods.*

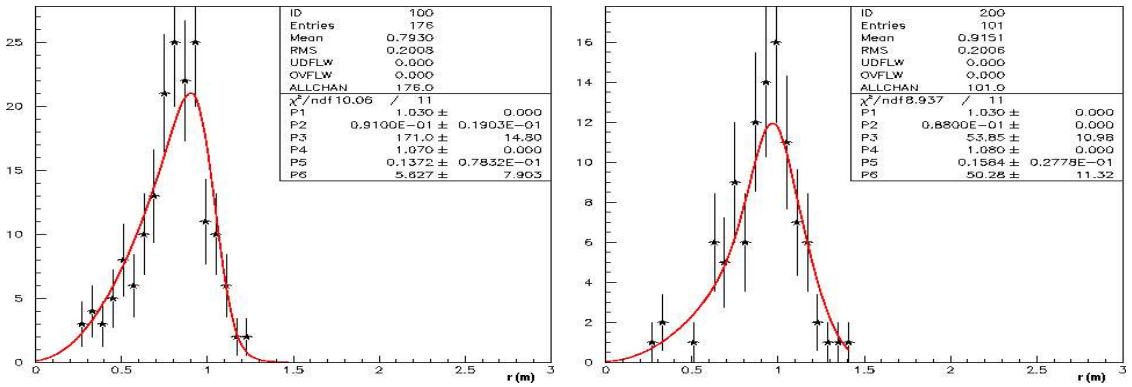

Fig. 9.14: *Fit of the radial profile for $^{212}Bi - {}^{212}Po$ events: during CLT with thoron (left) and after CLT (right). Fit parameters p3 and p6 are the internal and surface contamination.*

It is under discussion whether the radial distribution of a surface contamination can be regarded as gaussian or if it features an inward tail. In the latter case also the results of the analysis performed applying the radial cut should be regarded as upper limits.

Discussion of results

The following considerations rely mostly on the analysis performed with radial cut due to the arguments reported above.

The 1^{st} PC batch contained about $5 \cdot 10^{-15} g/g$ of Thorium. CLT purified the scintillator by a factor ~ 2.5 (cmp. periods 1 and 4) while a factor 4.5 was expected by the loop purification model after breakthrough[244]. WET-1 further purified the scintillator by an additional factor of 2 (cmp. periods 4 and 6), while the effect of WET-2 and of CBT seems negligible (cmp. periods 6 and 10-12). Periods 7 and 9 across WET-2 tests are very short and their statistical significance is limited.

Another striking feature is the clear drop between periods 12 and 13. The statistical importance is very large, at least one order of magnitude (cmp. last two rows in tab. 9.4), and the current thorium level thereafter is below our sensitivity limit, i.e. $\leq 10^{-16} g/g$. The analysis without radial cut shows also a 30% decrease, suggesting that the bulk contamination is affected while the surface is not. The drop is localized around middle June 2003 with a couple of weeks precision, about when the authorities sealed Hall C (sec. 2.5). However at that time the detector was untouched since many months and there is no clear way to explain the sudden decrease. One hypothesis could be related to the stop of the water purification loop previously operating on the CTF water tank. Possibly the loop was keeping a temperature gradient on the vessel that was favoring convective motions in the scintillator. Such flow was rubbing away some particulate from the nylon surface bringing it into the core of the vessel. If this was the case then one of the purification methods applied actually reduced the bulk thorium contamination to the present level.

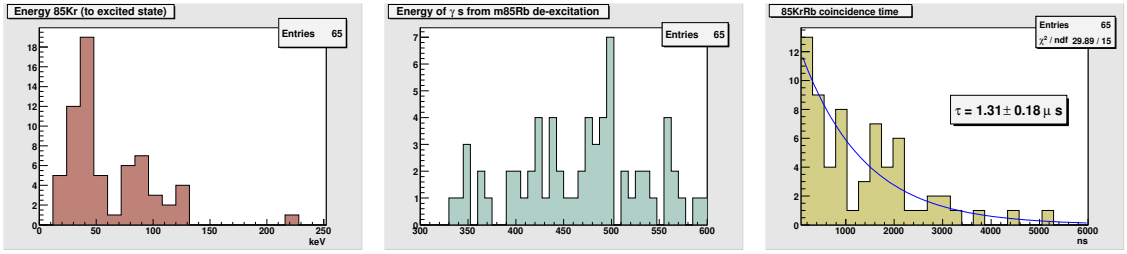

Fig. 9.15: $^{85}Kr - ^{85m}Rb$ *delayed coincidence analysis.* ^{85}Kr *energy spectrum (left),* ^{85m}Rb *de-excitation gamma (center) and coincidence time (right). Data refer to periods 1-3 of tab. 9.5.*

9.3.3 Krypton contamination

^{85}Kr decays β into ^{85}Rb ground state with a $687keV$ end-point energy (99.57% BR). However it also decays into the meta-stable ^{85m}Rb ($173keV$ end-point energy, 0.43% BR). The ^{85m}Rb in turn de-excites to ground state with a mean life of $1.46\mu s$ emitting a $514keV$ γ-ray. The coincidence with the de-excitation gamma can be exploited to evaluate the ^{85}Kr content of the scintillator though the statistics is limited by the small BR.

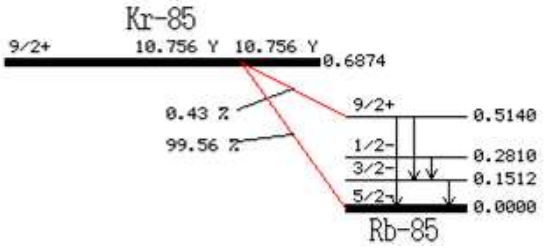

Analysis details

These are the cuts applied to select the $^{85}Kr - ^{85m}Rb$ coincidence:

1. $80ns < t_{coinc} < 6\mu s (\sim 4\tau)$. The lower bound is a sharpening of the $\sim 50ns$ dead time mentioned in sec. 9.1.2. Acceptance: $\simeq 95\%$.

2. $E_{gr1} < 274keV$ where 3σ above the ^{85}Kr energy are allowed. Acceptance is however limited to $\simeq 61\%$ due to threshold effects (estimated by simulation).

3. $300keV < E_{gr2} < 600keV$. As some of the γ-rays, especially those generated close to the IV membrane, manage to escape the scintillator before loosing all their energy, a continuous spectrum is present ranging from threshold energy to the photo-peak. Simulations of this spectrum allow to state the acceptance of the cut: $\simeq 83\%$.

The overall acceptance is 48%.

Fig. 9.15 shows the two energy spectra and the coincidence time for the selected event pairs in the initial period (i.e. before N_2 stripping was operated). The observed coincidence time, $1.3 \pm 0.18\mu s$ is consistent with the mean life of ^{85m}Rb.

Background from accidental coincidences has been checked varying the time window as for the $^{212}Bi - ^{212}Po$ analysis, but the contribution is in this case negligible.

The results are shown in tab. 9.5.

	Period[a]	Runs	L. T. (days)	ev. (#)	^{85m}Rb (ev/d)	^{85}Kr (ev/d)	ev. (#)	^{85m}Rb (ev/d)	^{85}Kr (ev/d)
				No radial cut			$r < 62cm$		
1	1^{st} PC batch	2056 → 2073	22.2	18	1.7 ± 0.4	390 ± 90	3	1.2 ± 0.7	270 ± 160
2	Before CLT	2074 → 2093	15.8	14	1.8 ± 0.5	420 ± 110	3	1.7 ± 1.0	380 ± 220
3	During and after CLT	2094 → 2122	27.7	33	2.5 ± 0.4	570 ± 100	11	3.5 ± 1.0	800 ± 240
4	During and after WET-1	2125 → 2149	25.2	4	0.33 ± 0.16	76 ± 38	0	< 0.7	< 160
5	Before WET-2	2150 → 2161	12.5	1	0.17 ± 0.17	38 ± 38	0	< 1.4	< 320
6	During and after WET-2	2162 → 2179	16.7	2	0.25 ± 0.18	58 ± 41	0	< 1.0	< 240
7	After CBT	2188 → 2281	153	36	0.49 ± 0.08	110 ± 20	1	0.06 ± 0.06	13 ± 13
8	(1^{st}) After EADJ	2285 → 2345	132	25	0.39 ± 0.08	91 ± 18	4	0.27 ± 0.13	61 ± 31
9	(2^{nd})After EADJ	2346 → 2422	160	34	0.44 ± 0.08	102 ± 18	2	0.11 ± 0.08	25 ± 18
10	(3^{rd})After EADJ	2423 → 2520	166	38	0.48 ± 0.08	110 ± 20	1	0.05 ± 0.05	12 ± 12
11	Between GVI and SRC	2522 → 2531	21.0	6	0.59 ± 0.24	140 ± 60	1	0.42 ± 0.42	96 ± 96
12	After SRC	2541 → 2582	72.4	15	0.43 ± 0.11	99 ± 26	1	0.12 ± 0.12	28 ± 28
	$1^{st}N_2$ stripping → GVI	2125 → 2520	766	161	0.44 ± 0.03	101 ± 8	10	0.12 ± 0.04	27 ± 9

[a]CLT = Column Loop Test; WET = Water Extraction Test; CBT = Column Batch Test; EADJ = Electronic Adjustment; GVI = Gate Valve Installation; SRC = Source Calibration;

Tab. 9.5: *Krypton contamination from $^{85}Kr - ^{85m}Rb$ coincidence analysis in CTF-3 campaign. Errors are given at 1σ, upper limits at 95% C.L. Each of periods 7-10 correspond to approximately 8 months astronomical time. ^{85m}Rb and ^{85}Kr activity are renormalized to full volume, the number of events is not.*

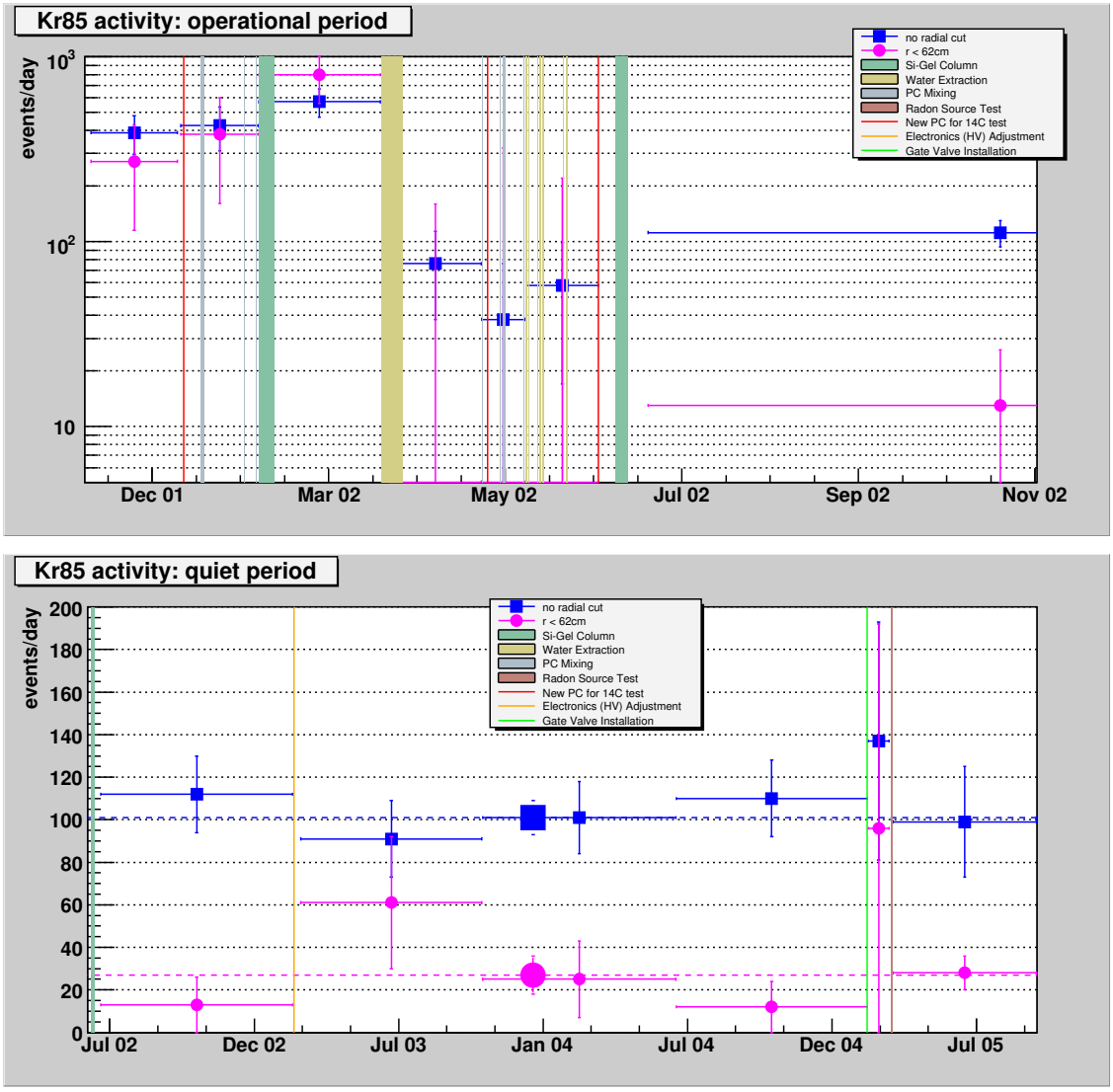

Fig. 9.16: ^{85}Kr *events in CTF-3 campaign: operational (above) and quiet (below) periods.*

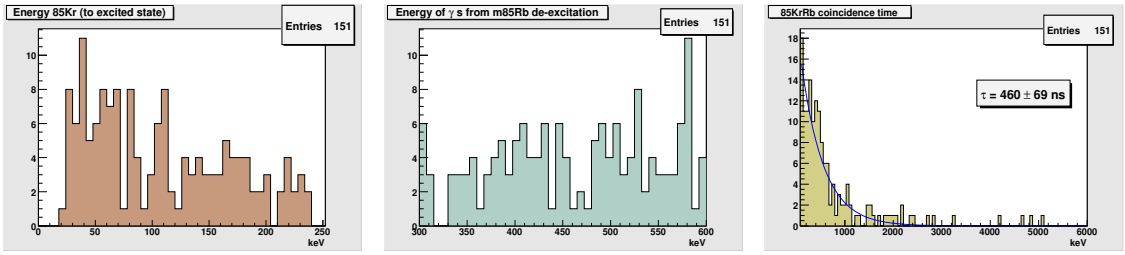

Fig. 9.17: *Events selected with the $^{85}Kr - ^{85m}Rb$ delayed coincidence analysis after N_2 stripping (periods 4-12). Comparing with fig. 9.15 it is clear how the spectra are dominated by events of other nature.*

The surface contamination

There are evidences that the thorium surface contamination (sec. 9.3.2) is heavily contributing to counts inside the krypton selection cuts. These may be noticed only after the first N_2 stripping of the scintillator which occurred at the beginning of the WET-1.

1. Both energy spectra deviate significantly from the typical shape of β and γ spectra shown before.

2. Coincidence time reduced to significantly lower values, approaching the ^{212}Po decay time.

The effects are visible comparing fig. 9.17 with fig. 9.15.

As a consequence the analysis is performed also with the application of a radial cut at $62cm$ ($1ton$ of scintillator selected, 2.5σ's from surface).

The agreement between the analysis with and without radial cut is very good before the stripping and very poor after, as expected after the surface contamination hypothesis.

Theoretically even the results obtained with the radial cut should be regarded as upper limits, since the possibility that some or all of the inner events are also due to the surface contamination cannot be neglected. However the 10 event pairs that survive the radial cut appear distributed in energy (both events) and in coincidence time according to the expectations for real $^{85}Kr - ^{85m}Rb$ couples.

Discussion of results

Due to the above considerations only the analysis with radial cut is useful to evaluate the ^{85}Kr contamination of the scintillator.

During CLT some krypton was introduced probably due to air contact, however the N_2 stripping, that operated along with WET-1, successfully removed it to below the sensitivity limit: $\leq 30ev/d$. Following operations apparently did not affect the ^{85}Kr level.

About 49% of the ^{85}Kr spectrum lies inside the NW, so the present level would correspond to $350 - 400ev/d$ in BOREXino if truly internal. However, the residual level of krypton is probably dictated by the traces of krypton in the nitrogen gas used for the stripping. The Low Argon and Krypton Nitrogen ($LAKN_2$) that will be used in

BOREXino[11] has 10^{-3} less krypton so there is a general confidence that Krypton should not be an issue in BOREXino.

9.4 Other analyses and the present situation

Beside the delayed coincidence analyses, other different techniques are used within the working group to understand the background conditions of the detector[228]:

1. Total count rate analysis. A sharp radial cut is applied at $60cm$.
2. Radial fit analysis. The radial distribution of events in the run (or in a group of runs if statistics is low) is fitted with a function including a bulk (volumetric) and a surface (gaussian) contribution, both convoluted with the detector's resolution.
3. α/β analyses. Both α/β methods (sec. 9.1.5) are applied to disentangle β from α counts.
4. Energy fit analysis. The energy spectrum is fitted with contributions from the spectral shapes of different nuclides including ^{210}Bi, ^{210}Po, ^{85}Kr, ^{39}Ar, ...

This section reports a summary of the main results regarding the CTF-3 campaign up to summer 2005. Results on the bulk scintillator contaminations are always referred to the activity in the NW $(250 - 800keV)$ and in the full *inner vessel* volume (i.e. they are rescaled in case a radial cut/fit is applied).

The surface contamination

Fig. 9.19 shows the results of the radial fit analysis. The surface and/or external contamination at the end of 2001 was at the level of $1000ev/d$ and slowly decreased to the current $700ev/d$ basically unaffected by any operation performed on the detector.

In the analyses of the internal scintillator contamination, a $\sim 60cm$ radial cut is generally enough to reduce the surface contribution to below a few tens of events. However in the periods when the bulk contamination is small ($< 100ev/d$), this residual activity may no longer be neglected (see below).

9.4.1 Polonium contamination

The first PC batch loaded at the end of 2001 included a contamination at the level of a few thousand events per day, with an energy spectrum dominated by a pronounced peak around $400keV$ (fig. 9.18). α/β tools clearly indicated the peak was due to α decays on top of a continuous component of β and $\beta+\gamma$ events.

As radon was introduced in the loading operation, part of the α peak could be ascribed to the unresolved contributions of ^{222}Rn and ^{218}Po (tab. 9.6). However these contributions were not dominant: they could be assumed in equilibrium with $^{214}Bi - ^{214}Po$,

[11] The plant will be commissioned in spring 2006.

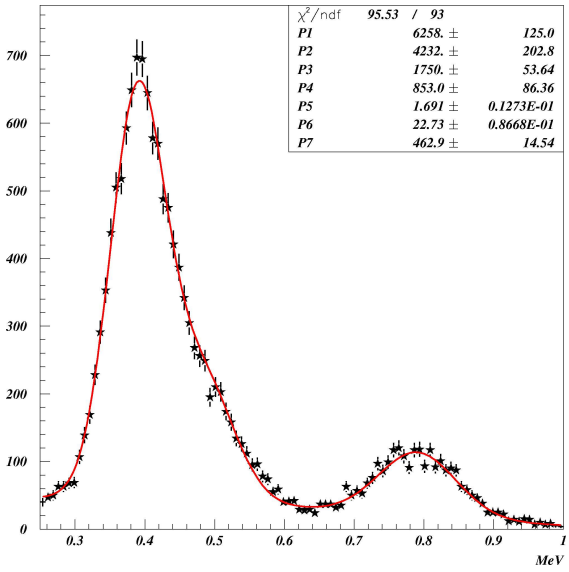

Fig. 9.18: *Energy spectrum in the initial CTF-3 period. The fit includes contributions of* ^{210}Po, ^{210}Bi, ^{85}Kr, *and* ^{222}Rn *sub-chain[238].*

Element	Energy	Quenched energy
^{222}Rn	5.49	410
^{218}Po	6.02	483
^{210}Po	5.30	395
^{214}Po	7.69	751
^{212}Po	8.79	1010
^{220}Rn	6.29	524
^{216}Po	6.54	558

Tab. 9.6: *Natural* α *sources present in the scintillator used for BOREXino and CTF. The first 4 nuclides belong to the Uranium chain and their quenched energies have been measured in CTF-1[216]. The last 3 nuclides belong to the Thorium chain and their quenched energies are calculated indirectly with Birk's formulas[182] starting from the first 4.*

evaluated from the delayed coincidence analysis and subtracted away and still the residual α activity amounted to $\sim 2000 ev/d$.

If the activity in the α peak is fitted with two exponential decay components the one of the decay times converges to a value close to the nominal ^{222}Rn mean life, while the other is much longer ($> 130d$). This is true for the initial period but also in most of the following periods in which the campaign is segmented (sec. 9.2).

A good candidate radio-nuclide is ^{210}Po, assumed out of secular equilibrium with the ^{222}Rn segment. ^{210}Po decays α to the stable ^{206}Pb with a mean life of $200.2d$ and a nominal energy of $5.30 MeV$. The α energy was measured to be quenched to $395 keV$ both in lab scale tests and in CTF-1.

The most natural origin of ^{210}Po counts would be a build up of the long-lived radon daughter ^{210}Pb, after ^{222}Rn decay. ^{210}Pb decays β to ^{210}Bi with an energy that lies below CTF threshold. ^{210}Bi, also a β emitter, features instead an end-point energy of $1.16 MeV$ and should be well visible. However, the α/β and spectral analyses point out how ^{210}Bi in general does not match the ^{210}Po amounts. In other words the secular equilibrium in the Uranium chain is generally broken in more than one point.

The insertions of PC (pure, without PPO) for the ^{14}C tests have often lead to an increased ^{210}Po activity indicating that the contamination is possibly intrinsic of the scintillator solvent.

The purification operations

The initial ^{210}Po contamination ($2000 ev/d$) was reduced first by a factor 2 by CLT and then by an additional factor 5 by WET-1. After these two operations the internal con-

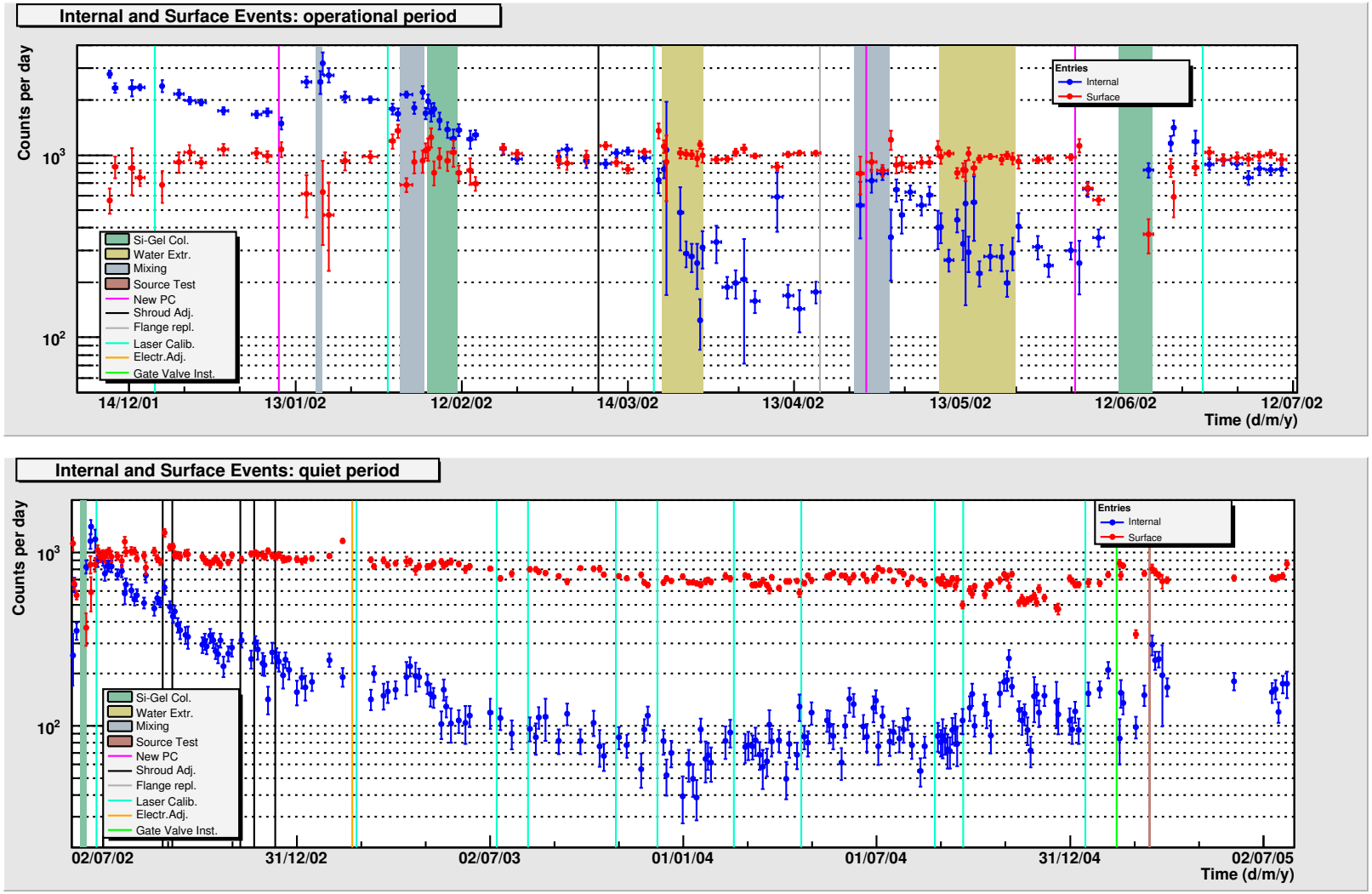

Fig. 9.19: *Results of radial analysis in CTF-3 campaign: operational (above) and quiet (below) periods.*

tamination amounted to $\sim 200ev/d$, of which $\sim 150ev/d$ were indicated as ^{210}Po by α/β discrimination.

The role of some blank loops, performed to stir the scintillator and the subsequent WET-2 is unclear. Apparently the first dissolved some ^{210}Pb from nylon or from the pipes into the scintillator, as the increased contamination of $600ev/d$ was due to ^{210}Bi and ^{210}Po decays in equal quantities. The WET-2 purified again the scintillator by a factor 2 ($300ev/d$). The use of nitric acid did not introduce any improvement compared to WET-1.

CBT suffered an unknown inconvenience[12] as the number of internal counts spiked up to above $1000ev/d$ right after the test. This was very surprising as lab tests show a very high purification potential for CBT.

However this activity, though having energy and shape typical of ^{210}Po, decayed with a profile that was including a fast component ($\sim 30-70d$) in addition to the ^{210}Po one. This may suggest that some artifact was present, e.g. particulate or silica gel grains could have entered the scintillator and could be slowly sinking to the lower end-cap[13].

All numbers given above include the subtraction of the ^{222}Rn-^{214}Po segment from the delayed coincidence analysis.

9.4.2 Where do we stand?

The long quiet data taking gave time to ^{210}Po to decay away and by the beginning of 2004 the internal contamination was reduced to about $80ev/d$, after subtraction of radon segment ($8ev/d$). α/β analysis indicates that very few ($< 10ev/d$) are α (residual ^{210}Po, now probably in equilibrium with ^{210}Pb and ^{210}Bi).

The composition of this background was examined with spectral analyses (with $60cm$ radial cut), combined with inputs from all other instruments. The systematics are very large and difficult to estimate and arise from the uncertainty in the absolute energy scale (no source calibration has been performed yet), from the unknown shape of the external background and the similarity of some spectral shapes that cannot be disentangled in the fit. Therefore the following results can be taken only as qualitative, yet useful indications:

1. About $\sim 40ev/d$ are assigned to ^{85}Kr and ^{39}Ar whose spectral shape are too similar to be disentangled in the fit. Being ^{85}Kr bound to $\sim 15ev/d$ by the delayed coincidence analysis (sec. 9.3.3), ^{39}Ar should account for $\sim 25ev/d$[14].

2. ^{210}Bi accounts for $\sim 5ev/d$ and the equilibrium with ^{210}Po could hold in this period.

3. ^{212}Bi and the thorium chain do not contribute significantly ($\sim 1ev/d$).

[12] One hypothesis is the use of a contaminated vessel in the operations.

[13] The rigid nylon tube present at the bottom of the IV. Due to its design, little or no light collection is possible for events generated there.

[14] This high value cannot be explained just considering the argon content in the nitrogen used for the stripping. The origin probably dates back to June 2001 when, before water filling, upon an accidental nitrogen shortage in the laboratory, an unknown volume of argon was used to complete the *inner vessel* inflation.

4. The fit includes external background penetrating the $60cm$ radius, modeled with a 1 degree polynomial, but it cannot disentangle it from ^{40}K. About $30ev/d$ are due to these two contributions.

   An upper limit of $7c/d$ on ^{40}K may be put independently, exploiting its secondary decay channel (sec. 2.3.1) in a radial analysis at the energy region around the $1.5MeV$ γ[15]. So the external contribution seems relevant and higher than $20ev/d$.

These results seem to indicate that the current sensitivity level of CTF has been reached.

In view of BOREXino the forthcoming high purity nitrogen ($LAKN_2$) with reduced argon and krypton contents should solve the issue about noble gas traces. Also the external contribution will not be a problem in BOREXino as the $100t$ FV definition is obtained with a radial cut at $1.4m$ from the nylon surface.

Scaling the ^{210}Bi activity from CTF about $100\beta/d$ can be expected in BOREXino. Posing the goal for the ^{7}Be measurement in BOREXino ($33ev/d$ signal in the LMA scenario) to a *Signal-to-Background* ratio of ~ 1, the above scenario requires an additional purification factor of ~ 3 in ^{210}Pb (from which ^{210}Bi arises) compared to the present situation. According to lab scale tests this seems well feasible with the distillation of the pseudocumene.

A test of the distillation plant for BOREXino is foreseen in CTF in January 2006. The focus will be on testing that the plant and the procedure do not introduce contaminants in the scintillator. After the above considerations the bulk activity is expected to remain at the same level and in this case the filling of BOREXino will start immediately after.

The last period

In the last $1.5y$ the internal contamination slowly increased by a factor 2 with no apparent explanation, with the extra events being exclusively ^{210}Po α's. There is a moderate indication for a column-like distribution of these events along the z-axis of the *inner vessel*. This favors the hypothesis that vibrations due to civil works in Hall C determined precipitation of particulate from the north pipe and filter in the scintillator. One possible candidate would be Si-Gel grains left from CBT, but no clear indication is available. However the works were recently concluded and this evolution is of little concern, the reference period remaining the one described above.

[15] In this case an exponential external contribution is used rather than the surface gaussian mentioned before.

Chapter 10

Cosmogenic ^{11}C background detection in BOREXino and CTF

As mentioned in sec. 2.1.1, BOREXino has the potentiality to probe solar neutrinos belonging to the *pep* fusion reaction as well as the three emissions of the CNO cycle, both being among the next awaited steps in solar neutrino physics (sec. 1.11.2).

However the measurement is endangered by cosmogenic nuclides produced *in situ*, namely ^{11}C, accounting for a background ~ 5 times higher than the expected signal[230].

In this chapter, after the signal and background issues are introduced, an event by event tagging method is presented and the correspondent *Signal-to-Background* levels achievable in BOREXino are estimated. The method is then applied to the CTF-3 data to evaluate the ^{11}C production rate in Gran Sasso and compare it with independent theoretical and experimental expectations.

10.1 Signal and background

The *pep* and CNO neutrino spectroscopy in BOREXino represents an experimental challenge due to the relatively small signal, whose visibility is affected by the radiopurity levels of the scintillator and of the construction materials and especially by the cosmogenic background induced by the residual muon flux in the LNGS site.

10.1.1 *pep* and CNO signal in BOREXino

The *pep* neutrino emission is a spectral monochromatic line at $1.44MeV$, visible in BOREXino as a Compton-like shoulder around $1.2MeV$ in the electron recoil spectrum.

The three CNO reactions which emit neutrinos are β^+ decays characterized by the following maximum neutrino energies (tab. 1.2 and fig. 1.4):

1. ^{13}N: 1198 keV
2. ^{15}O: 1732 keV
3. ^{17}F: 1739 keV

	full range (ev/d)	NW-2 0.8-1.4 MeV (ev/d)
pep	2.1	0.9
CNO(<LUNA)	6.6	1.1
CNO(>LUNA)	3.5	0.6
pep+CNO	5.6	1.5

Tab. 10.1: *Expected* pep *and CNO neutrino rates in BOREXino in 100t FV.*

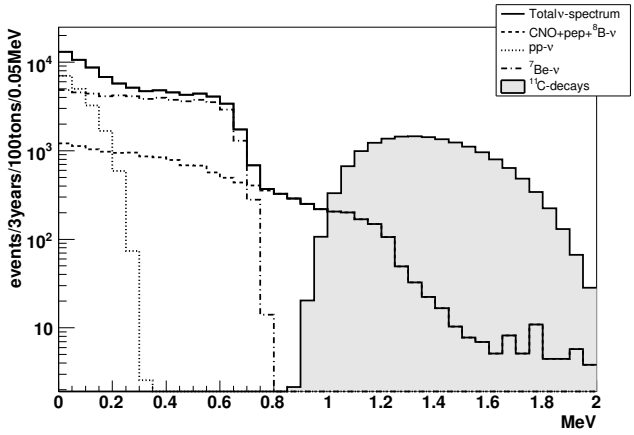

Fig. 10.1: *Simulation of BOREXino energy spectrum from different solar neutrino sources[233]. Simulation accounts for SSM BP04, MSW-LMA best-fit, LUNA 2004 results, 100t fiducial volume and 3y statistics. The gray area is the expected ^{11}C background.*

The target energy region in BOREXino is the window $0.8 - 1.4MeV$ of the recoil electron spectrum, named NW-2 (*Neutrino Window 2*). Here the signal is disentangled from ^{7}Be flux and the background can be handled properly as discussed in this chapter.

The expected neutrino interaction rates in BOREXino for the nominal $100t$ fiducial volume are shown in tab. 10.1. The rates reported in the first two rows are calculated starting from the latest SSM (sec. 1.2.2) and assuming the current best-fit parameters for the MSW-LMA solution of the solar neutrino problem (sec. 1.11.1). However, in 2004, the LUNA collaboration published data on the $^{14}N(p,\gamma)^{15}O$ reaction, which depress the whole CNO cycle activity by a factor ~ 2 (sec. 1.2.3). The third row in tab. 10.1 presents the corrected predictions for BOREXino.

The expected combined signal is $\sim 1.5ev/d$ in $100t$ and in NW-2. Fig. 10.1 reports a simulation of the expected signal spectrum in BOREXino considering neutrinos from different solar reactions under the assumptions outlined above.

10.1.2 Non Cosmogenic background

The visibility of *pep* and CNO neutrinos in NW-2 is affected by the radioactive contaminants present in the scintillator (sec. 2.3.1).

A radiopurity at the level of $10^{-17}g/g$ in ^{238}U and ^{232}Th, combined with a ^{nat}K concentration of $10^{-15}g/g$, yields a background of $0.6ev/d$ in NW-2 and in $100t$ FV.

In addition in CTF-3 campaign we had evidence of broken secular equilibrium in the ^{238}U chain at the level of the Radon daughters, namely direct contamination of ^{210}Pb and ^{210}Po occurred under different circumstances (sec. 9.4). A ^{210}Pb contamination would be a risk also for NW-2 as the daughter ^{210}Bi decays β with a $1.17MeV$ end-point energy. For this reason a careful filling and purification strategy is essential in this context.

External γ contaminations are also a concern as a larger background is expected in

Isotope	full range	$250 - 800KeV$ $^7Be - \nu$	$0.8 - 1.4MeV$ $pep + CNO - \nu$	$2.8 - 5.5MeV$ $^8B - \nu$
^{11}C	14.55 ± 1.49	0	7.36 ± 0.75	0
^7Be	0.34 ± 0.04	0.34 ± 0.04	0	0
^{11}Be	< 0.034	$< 4.3 \cdot 10^{-4}$	$< 1.0 \cdot 10^{-4}$	< 0.01
^{10}C	1.95 ± 0.21	0	0	0.56 ± 0.06
^8Li	0.07 ± 0.017	$(2.5 \pm 0.6) \cdot 10^{-4}$	$(8.0 \pm 2.0) \cdot 10^{-4}$	0.020 ± 0.005
^6He	0.26 ± 0.03	0.040 ± 0.004	0.07 ± 0.01	0.011 ± 0.001
^8B	0.11 ± 0.02	0	$(3.3 \pm 0.06) \cdot 10^{-5}$	0.020 ± 0.004
^9C	0.077 ± 0.025	0	0	0.016 ± 0.005
$^9Li + ^8He$	0.034 ± 0.007	$< 6.8 \cdot 10^{-4}$	$< 1.0 \cdot 10^{-3}$	< 0.014

Tab. 10.2: *Muon induced background rates from different nuclides[230]. All rates in ev/d in 100t.*

the *pep* and CNO energy window compared to the ^7Be one. As discussed in sec. 2.3.2, in BOREXino a great care was posed to choose the construction materials with the lowest possible radioactivity. The background expected is difficult to estimate but from the values reported in tab. 2.5 it should be below $\sim 1ev/d$ in $100t$ in NW-2. This background may be effectively suppressed with a stronger fiducial volume cut: γ contribution in $70t$ drops by an order of magnitude, while retaining 70% of the signal, compared to the standard $100t$.

10.1.3 Cosmogenic background

The by-products of the muon induced electromagnetic and hadronic cascades and the background contribution they introduce in BOREXino was studied at the end of the 90s within the collaboration[230]. The experiment at the NA54 CERN facility consisted in a muon beam impinging on a $240cm$ concrete target, followed by $200cm$ of water. Particles produced in the shower were detected using scintillation detector sets. Cross sections were measured for all processes leading to production of radio-nuclides, whose decay could potentially represent a background for BOREXino (and for other scintillation detectors). Using two different muon energies ($100GeV$ and $190GeV$) it was then possible to scale the results to the $320GeV$ average muon energy of the LNGS site. The results are reported in tab. 10.2, where the neutrino windows for ^7Be, *pep* and CNO, ^8B, are taken separately into consideration.

Focusing on NW-2 for the *pep* and CNO analysis, the expected background is as high as $7.4ev/d$ in $100t$, i.e. ~ 5 times the neutrino signal and almost entirely due to a single radio-nuclide: ^{11}C.

^{11}C is a β^+ emitter with an end-point energy of $0.96MeV$, but due to the positron annihilation energy, the detected energy of this decay in BOREXino lies between 1 and $2MeV$, partially covering NW-2.

In order to accomplish the *pep* and CNO neutrino measurement, the ^{11}C background must be tagged on an event-by-event basis.

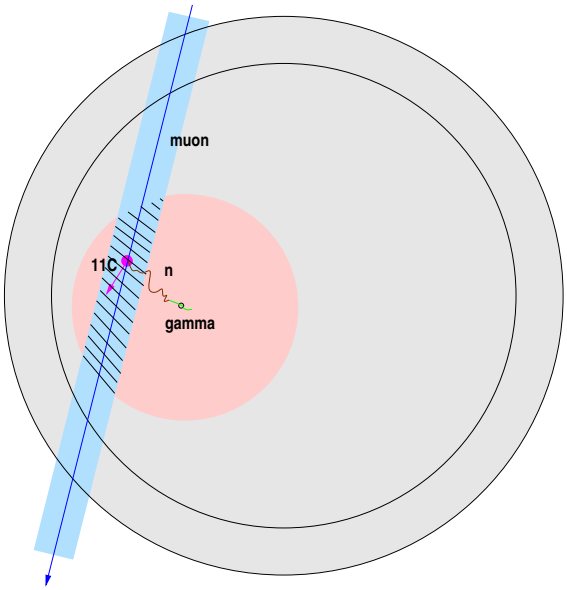

Fig. 10.2: *Schematics (not in scale) of the Three-Fold Coincidence (TFC) tagging strategy for ^{11}C background suppression.*

	reaction	weight
with n	$^{12}C(\gamma, n)^{11}C$	59.4%
	$^{12}C(n, 2n)^{11}C$	13.4%
	$^{12}C(p, p+n)^{11}C$	9.2%
	$^{12}C(\pi^-, \pi^- + n)^{11}C$	6.8%
	$^{12}C(\pi^+, \pi^+ + n)^{11}C$	1.8%
	$^{12}C(e, e+n)^{11}C$	0.7%
	$^{12}C(\mu, \mu+n)^{11}C$	4.0%
invisible	$^{12}C(p, d)^{11}C$	1.0%
	$^{12}C(\pi^+, \pi^0 + p)^{11}C$	3.5%

Tab. 10.3: *^{11}C production reactions and relative weights as computed in simulations in [231].*

10.2 ^{11}C tagging: the Three-Fold Coincidence (TFC) technique

The idea behind the event-by-event tagging of the cosmogenic ^{11}C background is roughly 10 years old and was firstly proposed by Martin Deutsch in [236]. It is based on the assumption that, no matter how the muon induced shower develops, obtaining a ^{11}C out of a ^{12}C atom requires to knock off a neutron through the net reaction[1]:

$$\mu(+\ secondaries) +^{12} C \longrightarrow \mu(+\ secondaries) +^{11} C + n \tag{10.1}$$

The neutron is then thermalized and captured on a free proton in a few hundred μs with the emission of a $2.2 MeV \gamma - ray$:

$$n + p \longrightarrow d + \gamma_{2.2MeV} \tag{10.2}$$

a clear distinctive signature in a scintillation detector like BOREXino.

Neutrons can also be captured on carbon isotopes emitting a $4.4 MeV$-γ, but the cross section is two orders of magnitude lower than for hydrogen.

Finally the ^{11}C will decay:

$$^{11}C \longrightarrow {}^{11}B + e^+ + \nu_e \tag{10.3}$$

with a mean life $\tau = 29.4 min$

^{11}C background suppression then consists on the tagging of a *Three-Fold Coincidence* (TFC): $\mu - \gamma - e^+$.

[1] As explained in sec. 10.2.1, this actually happens only in 95.5% of the cases.

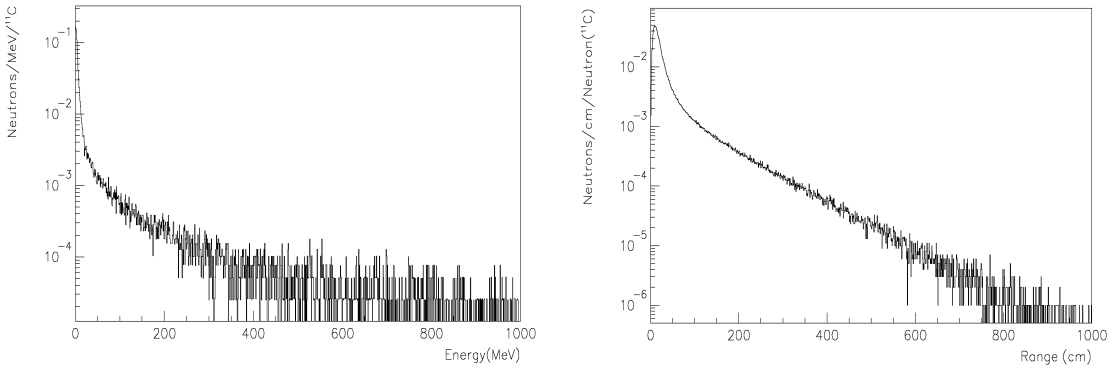

Fig. 10.3: *Neutrons emitted in association with ^{11}C. Energy spectrum (left) and covered distance (right). Simulations performed in [238].*

10.2.1 ^{11}C production mechanisms

The ^{11}C production has been investigated within the BOREXino collaboration[231]. Starting from published cross-sections, a simulation established the relative contribution of the different production mechanisms in organic liquid scintillator.

The study identified nine different processes (tab. 10.3) for the ^{11}C production in muon showers and provided a quantitative estimate for the rate in all the production channels. The result seems robust in view of the fact that the calculated overall production rate matches the one measured in the mentioned accelerator experiment (sec. 10.1.3).

The production of a neutron is involved in 95.5% of the produced ^{11}C nuclei ($\varepsilon_{vis} = 0.955$). The remaining 4.5%, due to the two channels that do not involve the production of a neutron, is an intrinsic inefficiency of the method ("invisible channels"). Nevertheless the TFC can be a reliable tagging strategy.

Fig. 10.3 shows the energy spectrum and the range covered in the thermalization process by neutrons emitted in the scintillator within the ^{11}C production reactions.

10.2.2 Background suppression vs. dead mass-time.

The $2.2MeV$ de-excitation γ emitted after the neutron capture on hydrogen can travel about $20 - 30cm$ in the detector and is reconstructed by the position reconstruction algorithm (sec. 9.1.4) approximately in the middle of the track.

^{11}C background suppression can be archived at first level by blinding out, after the identification of a $\mu - \gamma$ coincidence, a spherical volume of radius r centered in the γ reconstructed position (fig. 10.2). The veto should be applied for a time t equal to a few ^{11}C mean lives, while r is to be chosen considering the typical distance traveled by neutrons before capture.

The idea hinges on the assumption that, on the time scale of the ^{11}C mean life, no convective currents intervene to move the nuclide away from its production spot. Recently the KamLAND collaboration published data that imply the absence of convective currents in the time scale of a few days, achieved by controlling the overall temperature gradient

of the scintillator within $4°C$[103]. BOREXino implements a similar temperature control system, therefore the assumption seems justified.

The efficiency of the space-time cut can be defined as:

$$\varepsilon(r,t) = \varepsilon_S(r) \cdot \varepsilon_T(t) \tag{10.4}$$

where ε_T and ε_S are given by:

$$\varepsilon_T(t) = 1 - e^{(-t/\tau)} \qquad , \qquad \varepsilon_S(r) = \frac{\int_0^r c(r')dr'}{\int_0^\infty c(r')dr'} \tag{10.5}$$

and $c(r)$ is the distribution of distance covered by neutrons in the scintillator (fig. 10.3 (right))[2].

The *Signal-to-Background* (S/B) ratio achieved with this suppression is:

$$\frac{S}{B}(r,t) = \frac{S}{B_{\text{trace}} + f_{\text{inv}} \cdot B_{11C} + (1 - f_{\text{inv}}) \cdot (1 - \varepsilon(r,t)) \cdot B_{11C}} \tag{10.6}$$

where $S = 1.5ev/d$ is the combined *pep* and CNO signal, $B_{11C} = 7.36ev/d$ and $B_{trace} = 0.6ev/d$ are the backgrounds expected from ^{11}C and from non-cosmogenic[3] sources respectively and $f_{inv} = 0.045$ is the fraction of ^{11}C produced without neutron emission ("invisible channels").

Choosing a target S/B ratio, determines a required value for $\varepsilon(r,t)$. A couple of values (r,t) satisfying the requirement, in turn determines the mass-time fraction of the detector to be blinded out:

$$D(r,t) = 1 - e^{-\frac{4}{3}\pi\rho r^3 \cdot t \cdot N} \tag{10.7}$$

where $\rho = 0.88g/cm^3$ is the scintillator density and N is the number of neutrons tagged per unit mass and time, estimated from CTF-3 data in $0.58 \pm 0.03n/d/t$ (sec. 10.3.2).

Expressing t as a function of r (or vice versa) through eqs. 10.4-10.5, $D(r,t)$ can be minimized.

For example $S/B = 1$ requires $\varepsilon(r,t) = 0.92$ and this in turn requires a minimum dead mass-time fraction $D \sim 8.8\%$, obtained for $t = 3.9\tau$ and $r = 0.82m$. Tab. 10.4 reports other examples. It should be noticed that $S/B = 1.6$ is the highest ratio achievable due to the non taggable background components ($B_{trace} + f_{inv} \times B_{11C} = 0.93ev/d$).

S/B	$\varepsilon(r,t)$	D	r	t
		%	m	$\#\tau$
0.5	0.706	1.5	0.52	2.44
0.6	0.777	2.4	0.58	2.84
0.7	0.828	3.5	0.64	3.13
0.8	0.866	4.9	0.70	3.38
0.9	0.895	6.6	0.76	3.61
1.0	0.919	8.8	0.82	3.87
1.1	0.938	12	0.88	4.21
1.2	0.955	15	0.95	4.52
1.3	0.968	21	1.03	4.93
1.4	0.980	29	1.14	5.35
1.5	0.990	44	1.30	6.12
1.6	0.999	90	1.85	8.51
>1.6	not achievable			

Tab. 10.4: *Relation between target S/B values, combined tagging efficiency, minimum dead mass-time fraction and pairs (r,t) at which the minima occur.*

Though the measurement of *pep* and CNO neutrinos is in principle feasible even with this first level tag, a powerful improvement can be introduced by the ability to track muons in BOREXino, mentioned throughout this work. In this case the volume to be blinded out

[2]Also fig. 10.12 (dashed line) can give an good idea of $\varepsilon_S(r)$, though the detector simulated in this case is CTF (sec. 10.3.4).

[3]Sec. 10.1.2. No external γ's and ^{210}Pb contamination are taken into account here.

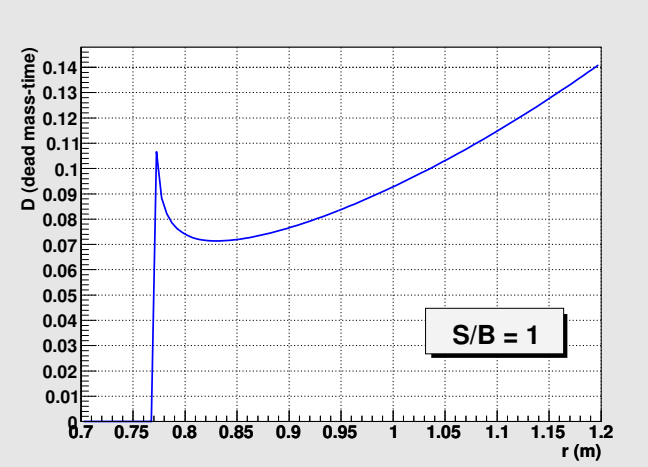

Fig. 10.4: *Sample dependency of D vs. r. In any point t is bound to match S/B=1. The minimum is found at r=0.82m and t=3.9τ. For r ≲ 0.77m S/B=1 cannot be met.*

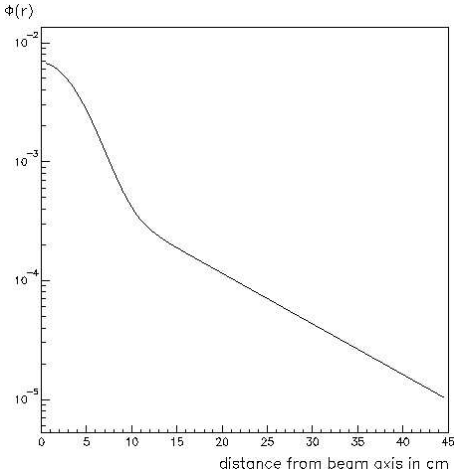

Fig. 10.5: *Lateral distribution of the produced ^{11}C in the muon beam experiment at CERN[230]. Arbitrary units on the y axis.*

is just the intersection of the sphere mentioned so far, with a cylinder whose axis is taken along the muon track (fig. 10.2).

The experiments with beam on target mentioned in sec. 10.1.3, measured also the ^{11}C produced off-axis with a set of scintillation detectors placed aside of the beam (fig. 10.5). About 95% of the ^{11}C events are produced within $30cm$ from the muon beam and this is a good theoretical target radius for the cylindrical cut. However the real radius will depend of the resolution achieved with the forthcoming muon track reconstruction algorithm. Therefore the aim of the algorithm is to achieve a resolution not larger than this value.

10.3 ^{11}C in CTF-3 campaign

During the CTF-3 campaign (sec. 9.2), the stop in the operations in the Gran Sasso laboratory imposed a *quiet* data taking lasting for $2.7y$. This offered an ideal situation for testing the TFC strategy on real data, with the goal of measuring the muon induced ^{11}C rate.

The analysis presented in this section refers to data taken in the *quiet* period for a comprehensive live time $T = 611d$, starting from the last purification test around middle June 2002 until middle February 2005 when the operations resumed in Hall C.

From this data set, a few runs had to be removed under different motivations (electronic and daq problems, laser runs, ...). Details can be found in app. D.

10.3.1 Muon selection

The muon flux at LNGS is measured in $\Phi_\mu = 1.16\mu/h/m^2$ (sec. 3.1). The CTF muon veto system (sec. 9.1.1) registers about $\sim 2900\mu/d$ crossing the whole water tank.

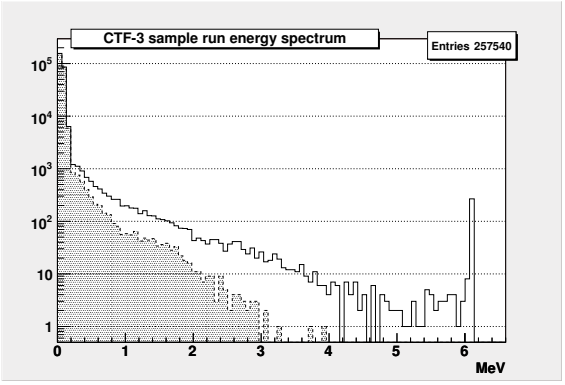

Fig. 10.6: *CTF-3 energy spectrum from a sample run. Solid line: all events. Dashed line: events not triggering the muon veto. The run time was about 2.7d.*

However for TFC the interest is only on muons crossing directly the *inner vessel*. Taking into account that a muon going through the scintillator generates about $2MeV/cm$, the events aimed at belong entirely to the visible saturation peak at $\sim 6MeV$ (fig. 10.6).

Muon events for TFC are selected with the following two requirements:

1. the energy must be greater than $4.5MeV$.

   A possible inefficiency could arise from muons passing in water but close enough to the *inner vessel* that part of the hadronic shower invests the scintillator leading to ^{11}C production. However the cross sections for ^{11}C production[231] start to be significant only above $15MeV$ ($(\pi^{\pm}, n)$ channel, the lowest one) or $20MeV$ ((γ, n) channel, the most contributing one). This energy is mostly transferred to the n and successively lost in scattering on protons in a few tens of ns. Hence it contributes to the prompt event, which is then well above $4.5MeV$.

   After this consideration the inefficiency is considered negligible[4].

2. the event must trigger the muon veto system.

   The fraction of events above $4.5MeV$ not seen by muon veto is 0.29%. From the simulation exposed in sec. 10.3.4, these are mainly γs (91.8%) and $e^+ - e^-$ pairs (8.1%) originating from muons not crossing the water tank at all.

   Their non visible contribution to the ^{11}C rate has been estimated in less than $5 \times 10^{-4} c/d$ (99.99% C.L.)[5] by convoluting their rates with the ^{11}C production cross sections[231].

Consequently the selection of muon events leading to ^{11}C production is believed to have efficiency ~ 1.

The selection yields $N_\mu \sim 81000$ muons in the data set, corresponding to $\sim 130 ev/d$.

[4]This was also confirmed varying the cut within a $\pm 1MeV$ range and observing no change in the analysis results.

[5]Confirmed releasing the requirement on the muon veto flag and observing no visible change in the analysis result.

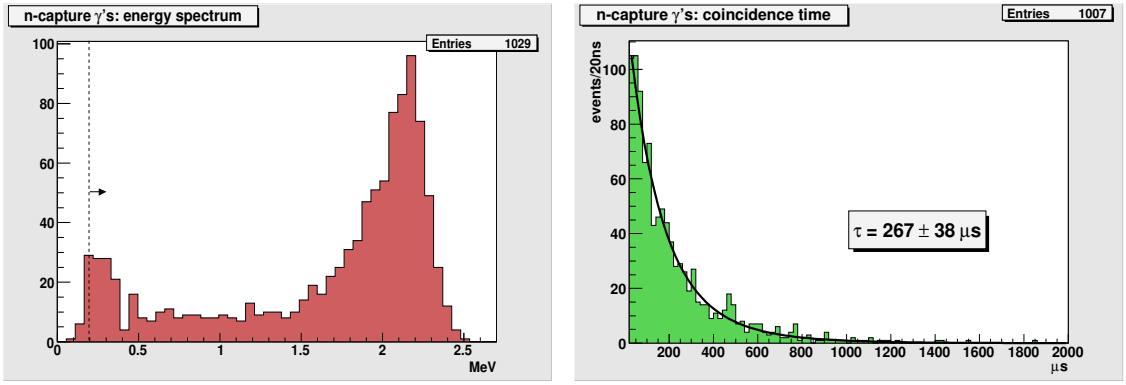

Fig. 10.7: *Observed energy spectrum (left) and capture time profile (right) of the 2.2MeV-γ from neutron capture.*

10.3.2 Neutron selection

As neutral particles, thermal neutrons can be detected only through the $2.2MeV$ γ (eq. 10.2) that is emitted after their capture on protons.

Typical capture time for neutrons with these energies is $\tau \sim 250\mu s$. Hence they can be tagged in CTF via a delayed coincidence analysis (sec. 9.3).

The requirements for candidate neutron events are the following:

1. it must be a group 2 event directly following a muon event (selected as in previous paragraph).

2. the coincidence time with the parent muon must lie in the $[20, 2000]\mu s$ window.

   The low cut simply sharpens the hardware anti-retrigger veto (sec. 9.1.2) to a precise and stable value. The high cut is ~ 8 times the mean capture time expected from simulations (sec. 10.3.4).

3. the energy must be in the $[0.2, 2.7]MeV$ range.

   The necessity of a sharp energy cut at $200keV$ is to filter out the hardware threshold, that cannot be easily modeled due to the subsidiary nature of the group 2 in the electronics (sec. 9.1.2). The efficiency is evaluated by MonteCarlo simulations (sec. 10.3.4).

   The high energy cut simply filters out a few spurious events without introducing appreciable inefficiency as it lies above the nominal γ energy by more than 3 times the detector energy resolution.

The selection yields $N_n = 1007$ events in the data set (1029 without the low energy cut) whose energy spectrum and capture time profile are shown in fig. 10.7.

The coincidence time profile may be fitted with:

$$f(t) = \frac{A}{\tau} \cdot e^{\left(-\frac{t}{\tau}\right)} + \frac{B}{\tau/2} \cdot e^{\left(-\frac{t}{\tau/2}\right)} \tag{10.8}$$

where A, B and τ are free parameters of the fit.

The second exponential accounts for events with double neutron emission[6], while events with triple or higher neutron multiplicity have been neglected. The fit finds $\tau = 267 \pm 38 \mu s$ and the fitted function may be used to evaluate analytically the efficiency of the cuts applied on the coincidence time: $\varepsilon_t = 0.925\%$. Moreover the contribution of double neutron events is $B \sim 0.3$, after unitary normalization.

It must be underlined that the γs selected are not all produced in the scintillator. Especially the part of the spectrum at lower energies includes γs emitted in water by the capture of neutrons either produced in the water immediately around the *inner vessel* or in the scintillator and that have successively escaped.

The neutron production rate per meter of muon track can be calculated as:

$$R_n = \frac{N_n}{T \cdot \Phi_\mu \cdot V_{iv} \cdot \varepsilon_t \cdot \varepsilon_\gamma} = (1.82 \pm 0.06[stat] \pm 0.05[syst]) \cdot 10^{-2}\ n/\mu/m \tag{10.9}$$

where V_{iv} is the volume of the *inner vessel*, and $\varepsilon_\gamma = 0.836$ is the fraction of neutrons that pass the $200keV$ selection cut. ε_γ is obtained from the simulation exposed in sec. 10.3.4 with the addition of the neutrons produced in the water buffer[7].

R_n compares with published data:

CTF-1 [239] $R_n = (1.5 \pm 0.1) \cdot 10^{-2} n/\mu/m$

LVD [234] $R_n = (1.5 \pm 0.4) \cdot 10^{-2} n/\mu/m$.

The neutron rate per unit mass used in eq. 10.7 is obatined as:

$$N = \frac{R_n \cdot \Phi_\mu}{\rho_{PC}} = (0.58 \pm 0.03) n/d/t. \tag{10.10}$$

Accidental coincidences

The possibility to have accidental coincidences in the neutron selection process was evaluated as it could lead to a distorted capture time profile. The CTF average trigger rate is $R \sim 1.13Hz$ but it is mostly due to ^{14}C (sec. 2.3.1): in fact the event rate above the $200keV$ energy threshold required in the neutron selection process is only $R_{E>200keV} \sim 0.04Hz$. The probability to have an accidental coincidence in a $\Delta T = 2ms$ time window is then:

$$P_{acc} = R_{E>200keV} \times \Delta T = 8 \cdot 10^{-5} \tag{10.11}$$

The accidental background in the selected sample of 1007 events is:

$$B_{acc} = N_\mu \times P_{acc} = 6.5ev \tag{10.12}$$

well below 1%. Therefore it is not necessary to add a constant background component in eq. 10.8. In eq. 10.9, N_n is instead corrected accordingly.

[6] For which only the first one is recorded by the electronics (sec. 9.1.2).

[7] These neutrons were instead not included in the ^{11}C analysis and in particular for the evaluation of ε_c mentioned in sec. 10.3.4.

The group 2 of the electronics registers only the first event occurring during the group-1 acquisition dead time (sec. 9.1.2). In principle an accidental coincidence occurring in between a $\mu - \gamma$ coincidence could introduce an inefficiency to the neutron selection process and a dangerous bias to the following ^{11}C selection that would be related in space to the wrong event.

This effect is however negligible as the average number of neutrons per muon event is:

$$P_n = \frac{N_n}{N_\mu} = 1.2 \cdot 10^{-2} \tag{10.13}$$

and a probability to have both a neutron and an accidental coincidence after the same muon:

$$P_{comb} = P_n \times P_{acc} \sim 10^{-6} \tag{10.14}$$

Moreover a simple simulation of competing signal and background shows that due to the fast exponential shape of the neutron signal, the background is able to prevent signal acquisition in only 5% of the coincidence cases.

10.3.3 ^{11}C selection

After each muon-neutron coincidence, ^{11}C candidate events are selected according to the following requirements:

1. the absolute event time must be within a $300min$ ($\sim 10\tau_C$) window after a $\mu - \gamma$ coincidence.

   The long time window allows a strong background identification.

2. the energy must be in the $[1.15, 2.25]MeV$ region.

   The window is chosen to select a high signal fraction (fig. 10.1) and to limit at the same time the systematic error arising from the uncertainty in the energy scale.

3. the reconstructed position must be within $80cm$ from the *inner vessel* center.

   In case one of the $511keV - \gamma$ s from the positron annihilation escapes the vessel, the detected energy of the ^{11}C decay event falls below the observation range. Defining a $0.8m$ radius fiducial volume, non-contained events are reduced by a factor 20. Further, the radial cut avoids distorting optical effects on the border like the total reflection due to the different refractive indexes of the scintillator and the buffer.

4. the distance between the reconstructed position and the one of the related neutron must be shorter than $35cm$.

   This selects a spherical volume around to the neutron capture point where the number of ^{11}C atoms per unit volume is maximal. Background is reduced by a factor ~ 20, while signal is reduced only by a factor ~ 2.

5. it must not be a precursor of a delayed coincidence, i.e. the following event must not be a group 2 event.

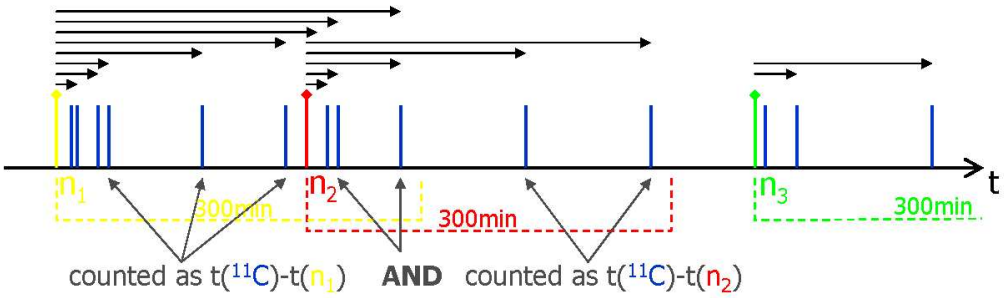

Fig. 10.8: *Schematics of the selection process of ^{11}C candidate events illustrating the overlapping windows effect.*

This requirement removes a few events (below 1%) clearly identifiable as ^{212}Bi or ^{214}Bi decays from the subsequent group 2 event having the energy and coincidence time characteristics of a ^{212}Po or ^{214}Po alpha decay (sec. 9.3.1 and sec. 9.3.2).

Random coincidences collected in this window are mainly ^{210}Bi (Q_β=1.16 MeV) and ^{40}K (Q_β=1.32 MeV BR=0.893 and Q_{EC}=1.51 MeV BR=0.107) contamination and especially external radiation. The time profile of the background is expected to be flat on the scale of $300min$ since random coincidences are not correlated with cosmic muons.

The choice of the cuts must take into account in primis the necessity to maximize the *Signal-to-Background* (S/B) ratio, but must also allow a precise estimation of the efficiencies and minimize the systematics introduced. In order to find the best compromise among these requirements the analysis was repeated automatically for a large number of combinations of possible energy ranges, radial cut and distance cut. This allowed also to check the stability of the results against these variations. The values reported above have been indicated through this study.

The ^{11}C rate is estimated out of the event time relative to the parent $\mu-\gamma$ coincidence, which allows to separate it from the background (sec. 10.3.5). Consequently, care must be posed in avoiding analysis artifacts in the time profile histogram (fig. 10.13), in particular for what concerns the windows pile-up effect and the occurrence of the run terminations.

Pile-up effects

With a detected neutron rate of $\sim 1.6ev/d$, the $5h$ windows opened after each $\mu-\gamma$ coincidence are affected by an intrinsic pile-up effect. Given a $\mu-\gamma$ coincidence, the probability that a second coincidence occurs within the ^{11}C selection window, is of the order of 35%. If the selection of ^{11}C candidates was interrupted at the occurrence of a new $\mu-\gamma$ coincidence, a fake and undefined "decay" effect would be introduced to the tail of the time profile histogram compromising the background estimation and the analysis results.

Consequently the search for ^{11}C candidates is performed independently for each $\mu-\gamma$ coincidence (fig. 10.8).

The run analysis starts looking for a couple of events satisfying the requirements for a $\mu-\gamma$ coincidence. Whenever these are found, the search for $\mu-\gamma$ coincidences is

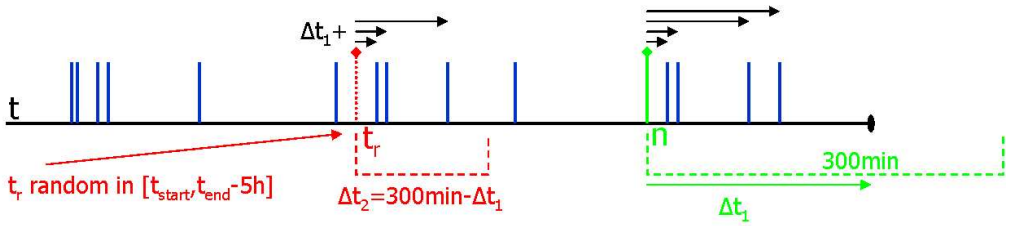

Fig. 10.9: *Schematics of the selection process of ^{11}C candidate events illustrating the handling of run termination within a window.*

suspended and the following $300min$ of the run are searched for candidate ^{11}C events. After the ^{11}C search is complete, the upper level search for $\mu-\gamma$ coincidences is resumed from where it was interrupted, i.e. with the event following the last coincidence. Upon the identification of the next $\mu-\gamma$ coincidence, a new independent search for ^{11}C candidates starts. As a result if there are overlapping windows, candidate ^{11}C events in the overlap region are counted twice and their time differences to both parent muons are filled in the time profile histogram.

In principle with independent windowing, the real ^{11}C events belonging to the second coincidence go to enrich the background in the tail of the first window, but as the two coincidences are time-uncorrelated, also this (small) component can be regarded as flat (in time) and is naturally accounted for in the background estimation.

End-of-run handling

Considering the average run duration of $2.2d$, the probability that a $300min$ window is interrupted by the run termination is 9.4%, i.e. not negligible. Ignoring this effect would introduce a distortion in the tail of the time profile histogram.

Ideally, one would like to prolong searches interrupted by run termination into the following run, but this is in general not possible as runs are often not immediately contiguous[8].

On the other end sacrificing the last $5h$ of every run (unless for selection windows to be completed), would imply loosing $\sim 10\%$ of the detector live time.

The solution adopted is illustrated in fig. 10.9. Supposing run termination interrupts a selection window after a time $\Delta t_1 < 300min$ from the $\mu-\gamma$ coincidence. In this case a random time instant t_r is chosen in the same run (excluding the last $5h$, to avoid iteration) and the search for ^{11}C candidates is continued thereafter opening a second window up to the completion of the $300min$. Candidates found in this second window at absolute time t_c contribute to the overall time profile histogram with $t_c - t_r + \Delta t_1$.

Since in the second window no ^{11}C events can be present, a small inefficiency is introduced and calculated as:

$$\varepsilon_{eor} = 1 - \frac{\sum_i \int_{t_i}^{\infty} e^{-\frac{t}{\tau}} dt}{N_n} = 0.9904 \tag{10.15}$$

[8]Different hardware inspections can occur between runs lasting from a minimum of $1h$ (electronic or PMT checkups) up to 1 or 2days (*inner vessel* visual inspection, shroud refilling).

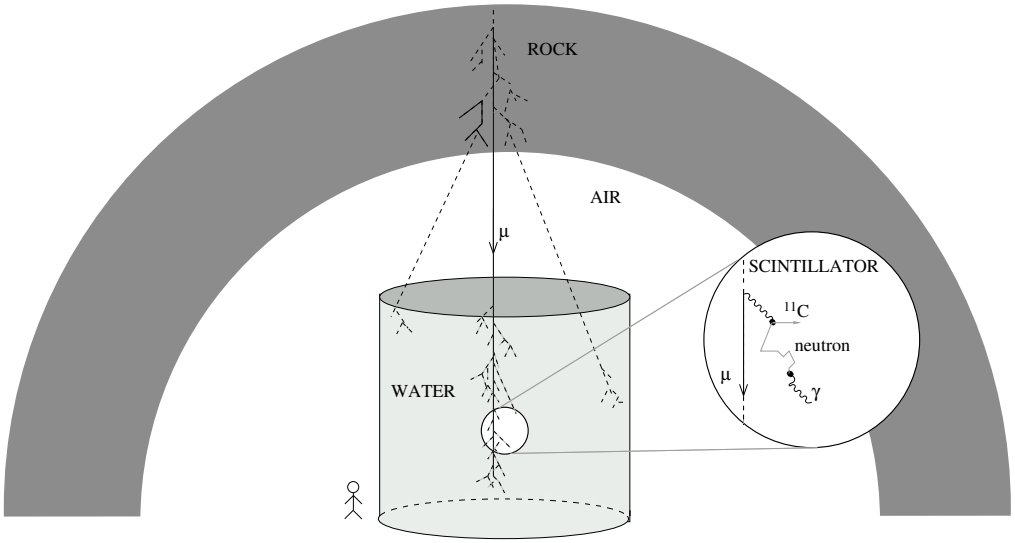

Fig. 10.10: *The geometry and the physical processes included in the simulation[233].*

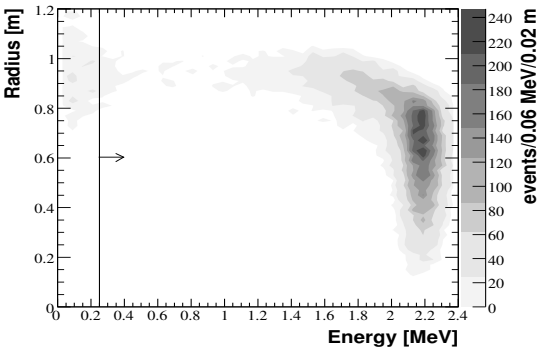

Fig. 10.11 (a): *Scatter plot of the simulated 2.2MeV-γ from neutron capture: radial position vs energy[233]. The solid line represent the cut applied in the analysis.*

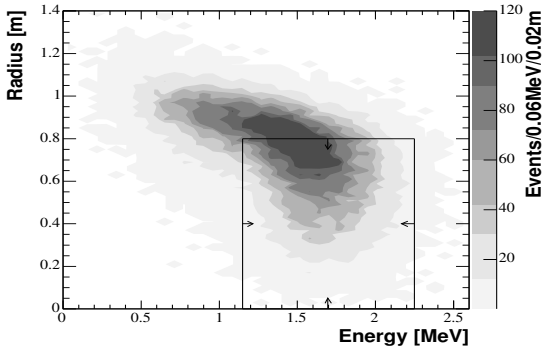

Fig. 10.11 (b): *Scatter plot of the simulated ^{11}C-decay: radial position vs energy[233]. The solid lines represent the cuts applied in the analysis. Events with an energy lower than 1.022 MeV are due to the escaping positron annihilation γ's.*

where i is varying over the windows truncated by the end-of-run at time t_i after the neutron event and N_n is the overall number of windows opened (i.e. the number of detected neutrons).

10.3.4 Simulation and selection efficiencies

The accurate quantification of the cut efficiencies requires a full simulation of the ^{11}C production process from the muon-induced showers originated in the rock to the neutron

capture and to the ^{11}C decay.

First a downward oriented $320GeV$ muon-beam is simulated and propagated, uniformly distributed over the CTF water tank. The geometry is simplified to four volumes: 4 m of rocks ($CaCO_3$ and $MgCO_3$), the air, the water of the CTF tank and finally the scintillator (fig. 10.10). In this step, the package FLUKA[235] is used for the generation of neutrons in scintillator and their propagation in the whole detector.

Next, the neutron production and capture points are passed over to the official CTF simulation package and are used to generate and track the ^{11}C decay and $2.2MeV - \gamma$ respectively. The CTF code simulates in detail the detector geometry including the nylon vessel and the photo-tubes. Each energy deposit is converted into optical photons which are propagated inside the detector until they are absorbed in the detector material or detected on the PMT's. The optical processes of sec. 2.4 and diffusion on the nylon vessel are included.

After all, the same reconstruction code used on the real data is used to introduce the energy and spatial resolution effects on the simulated set.

Fig. 10.11 shows scatter plots of neutron and ^{11}C events obtained with the simulation. The radial position is put in relation to the energy of the events.

The simulated neutron capture mean time, $254 \pm 1\mu s$, is in good agreement with the measured one, $267 \pm 38\mu s$ (sec. 10.3.2).

The main inefficiency in the measurement is due to neutrons escaping the vessel. If the neutron is captured in water and the subsequent γ does not deposit energy in scintillator the signal is lost. Neutrons escaping the $1m$ CTF vessel account for 26.8% ($\varepsilon_n = 0.732$) of the total.

For $\sim 50\%$ of the fully contained neutrons, the associated ^{11}C event falls in a $35cm$ radius sphere centered on the reconstructed $2.2MeV\gamma$, as shown in fig. 10.12.

The simulation is used to compute the efficiency for the low energy cut on the $2.2MeV\gamma$, of the energy window in the ^{11}C candidate selection and of the γ-C distance cut. However these efficiencies are correlated, i.e. the order with which the cuts are applied on the simulated set does influence the three values as it can be observed also in fig. 10.11(b). Therefore only a combined efficiency is quoted in this context as $\varepsilon_c = 0.563$.

10.3.5 ^{11}C rate

The time profile of the data sample selected by the TFC technique shows a distinct ^{11}C signature (fig. 10.13) and may be fitted with:

$$P(t) = \frac{A}{\tau} e^{-\frac{t}{\tau}} + b, \tag{10.16}$$

where the free variables in the fit, A and τ, are the number of ^{11}C nuclides and the ^{11}C mean life, respectively. The background rate b is constrained to:

$$b = \frac{N - A}{\Delta T_w} \tag{10.17}$$

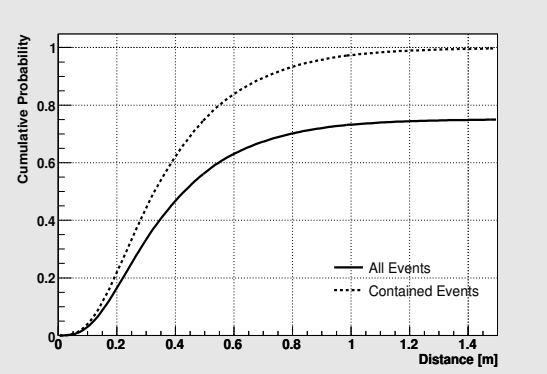

Fig. 10.12: *Cumulative probability to contain a ^{11}C event in a sphere of radius r centered on the reconstructed position of the 2.2MeV-γ event[233].*

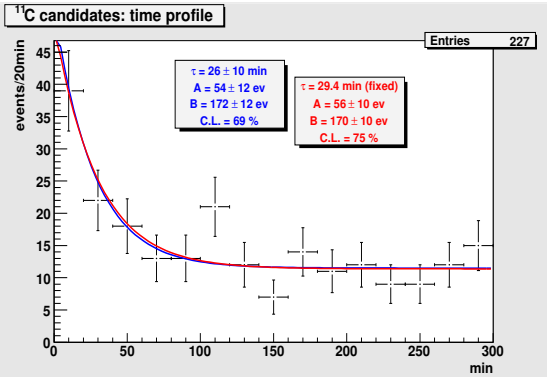

Fig. 10.13: *Time profile of candidate ^{11}C events with respect to parent muon time. The fit function is described in the text. The red and blue line are the fit results with fixed and free τ respectively. The agreement is very good.*

where N is the total number of events in the sample and $\Delta T_w = 300min$ is the window length.

The fit finds $\tau = 27 \pm 10 min$ ($A = 54 \pm 12$, $N = 227$, $\chi^2/d.o.f = 10.0/13$) in agreement with the nominal value ($29.4 min$). The achieved S/B ratio is 0.32.

If the $300 min$ window is started independently from the $\mu - \gamma_{2.2MeV}$ coincidence, the fit is unable to identify any feature compatible with a decay function.

Performing the fit with τ fixed to the nominal value, it yields $A = 56 \pm 10$ ($\chi^2/d.o.f = 10.0/14$). The ^{11}C rate can then be computed as:

$$\begin{aligned} R(^{11}C) &= \frac{A}{\frac{4}{3}\pi r^3 \cdot \rho \cdot T} \cdot \frac{1}{\varepsilon_{vis} \cdot \varepsilon_{eor} \cdot \varepsilon_t \cdot \varepsilon_n \cdot \varepsilon_c} \\ &= 0.135 \pm 0.024(stat) \pm 0.014(syst)/(day \times ton) \end{aligned} \tag{10.18}$$

where r is the selected volume radius ($0.8m$), $\rho = 0.88 g/cm^3$ is the scintillator density and $T = 611d$ is the detector live time. All the efficiencies in eq. 10.18 have been introduced above and are reported in tab. 10.5.

The rate measured in CTF is in agreement within 1 sigma with the expected one from the CERN experiment (sec. 10.1.3): 0.146 ± 0.015 counts/day/ton.

Systematic errors

There are four potential sources of systematic errors:

Live Time. The live time of the detector is known with a μs precision (sec. 9.1.2), therefore no systematic is actually considered from this source. In addition the live time is corrected run-by-run for events missing in the data, presumably due to a damaged disk unit in the acquisition computer. The extension of this correction is run dependent, but when averaged on the whole data set it amounts to 0.95%.

Neutron capture mean time. The error on the neutron capture mean life from the fit in eq. 10.8 accounts for an ε_t variation of $^{+1.1\%}_{-0.8\%}$.

Light Yield. The light yield is estimated with the method presented in sec. 9.2.2 and is known with a precision of $\pm 7.5\%$. Propagating this uncertainty to the efficiency evaluation of the energy cuts, the following systematic errors are obtained:

1. $E_\gamma < 200keV$. ε_c varies by $^{+0.3\%}_{-0.4\%}$
2. E_C in $[1.15 - 2.25]MeV$. ε_c varies by $^{+2.8\%}_{-0.0\%}$. The range was especially chosen trying to minimize these systematic errors (sec. 10.3.3).

Reconstructed position. The uncertainty of the reconstruction position is estimated in the following way.

The amount of scintillator contained in the *inner vessel* is known to be $\sim 3800 \pm 80kg$[9]. Assuming a spherical vessel[10] this value corresponds to a radius of $1.015m$. Performing the fit of the events radial profile as in sec. 9.4, the radius obtained is instead 1.030. The difference between these two values is taken as the uncertainty in the reconstruction position at $1m$. Scaling and propagating this uncertainty to the efficiency evaluation of the spatial cuts, the following systematic errors are obtained:

1. $P_\gamma - P_C < 35cm$. ε_c varies by $^{+4.5\%}_{-1.8\%}$.
2. $P_C < 80cm$. The fiducial volume definition varies by $^{+4.4\%}_{-4.6\%}$.

The contribution of the position uncertainty is dominant with respect to the one of the absolute energy scale.

Combining the above sources one obtains $^{+7.0\%}_{-5.0\%}$, however the systematic error in eq. 10.18 has been conservatively set to $\lesssim 10\%$ to account also for the stability of the result with respect to small variations of the arbitrary parameters in the analysis.

10.4 Conclusion

In this chapter the feasibility of *pep* and CNO neutrino spectroscopy in BOREXino has been investigated. The combined rate for *pep* and CNO neutrinos in the energy range of observation $[0.8, 1.4]MeV$, beyond the ^7Be-ν electron recoil spectrum, is $0.015/d/ton$.

[9] Two independent measurements agree on this value:

1. The flux meters of the module-0 measured $\sim 3800 \pm 170kg$ during the filling after CBT (sec. 9.2). The 4.5% error is due to pump induced irregularities in the flux to which the instruments did not react properly.
2. The *inner vessel* buoyancy is balanced through a net of strings holding it down and that include load cells calibrated to below 2% accuracy. The *inner vessel* volume can be obtained as $V_{iv} = F/(\rho_{water} - \rho_{PC}) = 4320 \pm 90l$, where $F = 520 \pm 10kg$ is the force registered by the load cells during the *quiet* CTF-3 period. The correspondent mass is $3800 \pm 80kg$.

[10] Actually pictures show some deviations from sphericity due to buoyancy. This effect has not been taken into account yet.

Eff.	Reason	Value	syst(%)		source
ε_{vis}	visible channels	0.955			
ε_{eor}	end of run	0.990			
ε_t	μ-2.2$MeV\gamma$ coincidence	0.925	-0.8	+1.1	n capt. time
ε_n	contained neutron events	0.732			
	^{11}C energy E $\in$ [1.15, 2.25] MeV		-0.0	+2.8	light yield
ε_c	2.2$MeV\gamma$ energy E $>$ 0.2 MeV	0.563	-0.4	+0.3	light yield
	^{11}C-2.2$MeV\gamma$ distance d $<$ 0.35 m		-1.8	+4.5	position rec.
	fiducial volume		-4.6	+4.4	position rec.
Total		0.360	-5.0	+7.0	

Tab. 10.5: *Summary table of all efficiencies and systematics involved in the ^{11}C analysis.*

The expected contamination from cosmogenic ^{11}C is about 5 times higher. A tagging strategy for this background was introduced, based on the *Three-Fold Coincidence* (TFC) technique. Its application hinges on the prediction that 95.5% of the ^{11}C production involves a free neutron in the final state[231].

A second background contribution arises from the trace contaminants in the scintillator mixture. Assuming for the ^{238}U and ^{232}Th a concentration level of $10^{-17}g/g$ and $10^{-15}g/g$ for the ^{nat}K, non-cosmogenic contaminants contribute to the *pep*+CNO window with $0.006/d/ton$.

Nevertheless, even considering the ^{11}C produced without free neutrons and including the trace contamination, the TFC technique can reach a Signal-to-Background (S/B) ratio equal to 1 loosing only 9% of the data. A possibility to significantly improve the TFC technique lies in the reconstruction of the muon track. This would lead in fact to the definition of a cylindrical volume around the track itself. Via its intersection with the spherical volume centered on the $2.2MeV - \gamma$ from the neutron capture, BOREXino can maximize the S/B ratio achieved, while reducing the fraction of lost mass-time.

The TFC technique was successfully applied to the data from the CTF-3 campaign (2002-2005): for the first time, deep underground ^{11}C production has been detected *in situ* event by event[11].

The ^{11}C production rate has been measured to $0.135\pm0.024(stat)\pm0.014(syst)/d/ton$. The agreement between the production rate observed in CTF and the value extrapolated from the measurement performed at the NA54 CERN facility in a muon on target experiment[230] and with the theoretical calculation in [231], demonstrates the robustness of TFC technique.

In prospective, such result opens a new window in *pep* and CNO neutrino spectroscopy in BOREXino.

[11] Currently under publication as[224].

Conclusion

In the last years, results from solar neutrino and reactor antineutrino experiments have provided compelling evidence for neutrino oscillations as the explanation of the long-standing solar neutrino problem. The next goal in solar neutrino physics is probing in real time the low energy ($< 2MeV$) component of the solar neutrino spectrum, which accounts for more than 99% of the total flux.

In the frame of current solar neutrino research the BOREXino detector is among the most awaited experiments to come, as it will perform spectroscopy of neutrinos from the ^7Be, and *pep* nuclear fusion reactions and from the CNO-cycle, with important consequences both in particle physics and in solar astrophysics.

The liquid scintillator detector is constructed in the Gran Sasso National Laboratory and it has been fully operational since the beginning of 2005. Filling with scintillator is expected in the next few months.

A large effort was put in the realization of the electronics for the readout of the photomultiplier signals. The system has been assembled, commissioned and tested as well as the trigger setup. The data acquisition software has been developed and tested and so have the run control and slow control tools.

Multiple data taking campaigns with the detector filled just with air (*Air Runs*) were performed to debug the detector and bring it to its final configuration. The analysis of these data sets allowed a deep understanding of the system as a whole and led to the definition of a pre-calibration procedure for the acquisition of the relevant parameters of the electronics. The tests included dark noise runs, laser runs with the use of the three optical pulsing systems, trigger studies and also the use of radon sources for the study of the position reconstruction, α/β discrimination and delayed coincidence analyses.

A new offline data processing program was proposed, named *echidna*. The infrastructure has been designed and coded and it is now operational. The physics algorithms developed so far using the *air runs* data include the precalibration of the electronics, the low level data decoding, the clustering of hits into physical events, multiple position reconstruction algorithms, pulse shape discrimination methods, the splitting of piled-up events and a variety of calibration tasks. A strong group of developers and testers has been introduced to the code and is now working to complete the physics tasks required.

The outer water Čerenkov detector of the experiment plays an essential role in the reduction of residual cosmic muon flux. Beside its high efficiency as a muon veto, it has been designed and constructed to allow the possibility to reconstruct the track of the through-going muons. The outer detector has been fully constructed and installed. For

its data acquisition a custom front-end electronics (QTCs) has been developed, commissioned and tested. The digital electronics (TDCs) has been brought into operation and a dedicated on-crate acquisition software has been developed to manage the relative data transfer duty. It is now operative and integrated in the DAQ of the experiment. The two outer detector trigger sub-systems have been also commissioned and integrated with the main trigger. The outer detector has been equipped with a dedicated calibration system based on UV LEDs and individual optical fibers reaching the PMTs in the water tank. The system has been calibrated and commissioned. The full outer detector chain has been tuned and repeatedly tested within the *air runs*. The precalibration tasks, the low level data decoding and the LED calibration algorithms have been implemented within the *echidna* program.

The CTF-3 ($3.8t$) data taking campaign, ongoing since 2001, has provided insightful data on the scintillator radiopurity levels and on the purification degree that can be achieved with the methods developed for BOREXino. The delayed coincidences analyses attested that the Silica-gel adsorption and the water extraction of the scintillator succeeded in bringing down the ^{238}U level from $16 \pm 3 \cdot 10^{-16} g/g$ to $6.8 \pm 0.2 \cdot 10^{-16} g/g$[12]. The ^{232}Th level decreased from $53 \pm 15 \cdot 10^{-16} g/g$ to below the detector sensitivity of $10^{-16} g/g$, while the high initial krypton amount of several hundred counts per day was efficiently stripped to the level of $27 \pm 9 ev/d$, compatible with the intrinsic krypton contamination of the nitrogen used in the operation.

The initial scintillator contamination of about $2000 ev/d$, mostly due to ^{210}Po-αs, was reduced by an order of magnitude through successive purification operations and it later decayed to a few counts per day. The spectral analysis of the post-purifications period indicates a residual bulk contamination of $\sim 50 ev/d$, of which $\sim 40 ev/d$ are ascribed to krypton and argon and $\sim 10 ev/d$ to the radon daughters ^{210}Bi and ^{210}Po in equilibrium. However in view of BOREXino the noble gases issue will be solved with the use of high purity Nitrogen and taking into account the good α/β performance seen in the air runs, the CTF result translates into $\sim 100 ev/d$ in the BOREXino $100t$ FV in the ^{7}Be energy range. An additional purification factor of ~ 3 (achievable with distillation of the scintillator) would match the expected signal of $33 ev/d$ (MSW-LMA).

The measurement of *pep* and CNO neutrinos in the $0.8 - 1.4 MeV$ region hinges on the possibility to suppress the 5 times higher cosmogenic background from ^{11}C. This possibility is in turn assured by the neutrons emitted in the ^{11}C production reactions. The signal and background issues and the so called *Three-Fold Coincidence* (TFC) technique have been investigated. TFC links the parent muon, the $2.2 MeV$ gamma emitted in the neutron capture on protons and the ^{11}C decay. Sacrificing a fraction of the detector mass-time the *Signal to Background* (S/B) level can be significantly increased: a $S/B = 1$ can be reached with a loss of 9%, while $S/B = 1.5$ would require a loss of 44%. The possibility to track the muon will highly reduce the lost detector mass-time fraction by limiting the veto to a cylindrical volume along the muon track.

The TFC technique has been successfully applied to the CTF-3 data and the ^{11}C rate was measured as $R(^{11}C) = 0.135 \pm 0.024(stat) \pm 0.014(syst)/(day \times ton)$ in good agreement with previous experimental results and with the theoretical expectations.

[12] or below if radon permeation through the nylon vessel is considered.

Appendix A

Radioactive chains

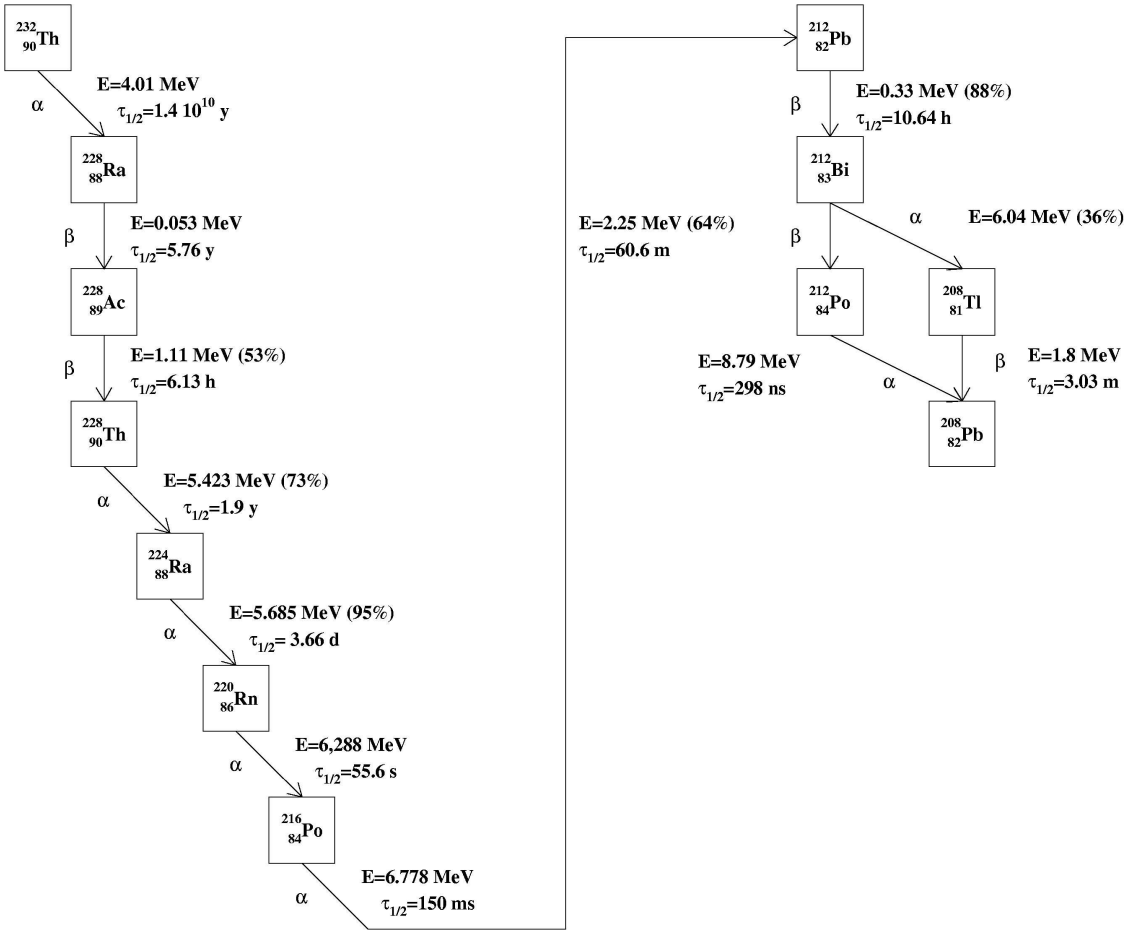

Fig. A.1: *The Thorium chain.*

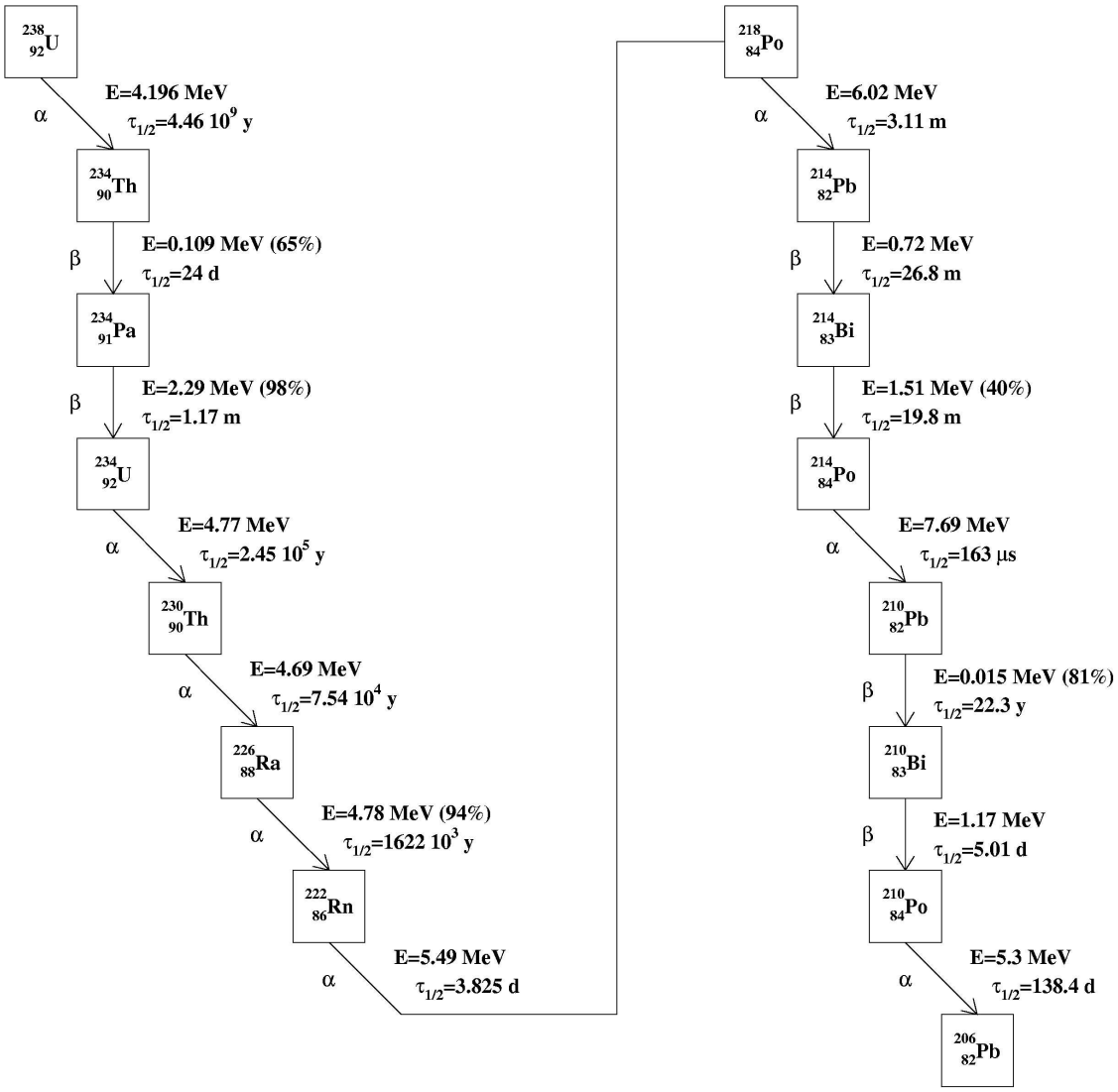

Fig. A.2: *The Uranium chain.*

Appendix B

Snapshots of Web Interface DAQ Tools

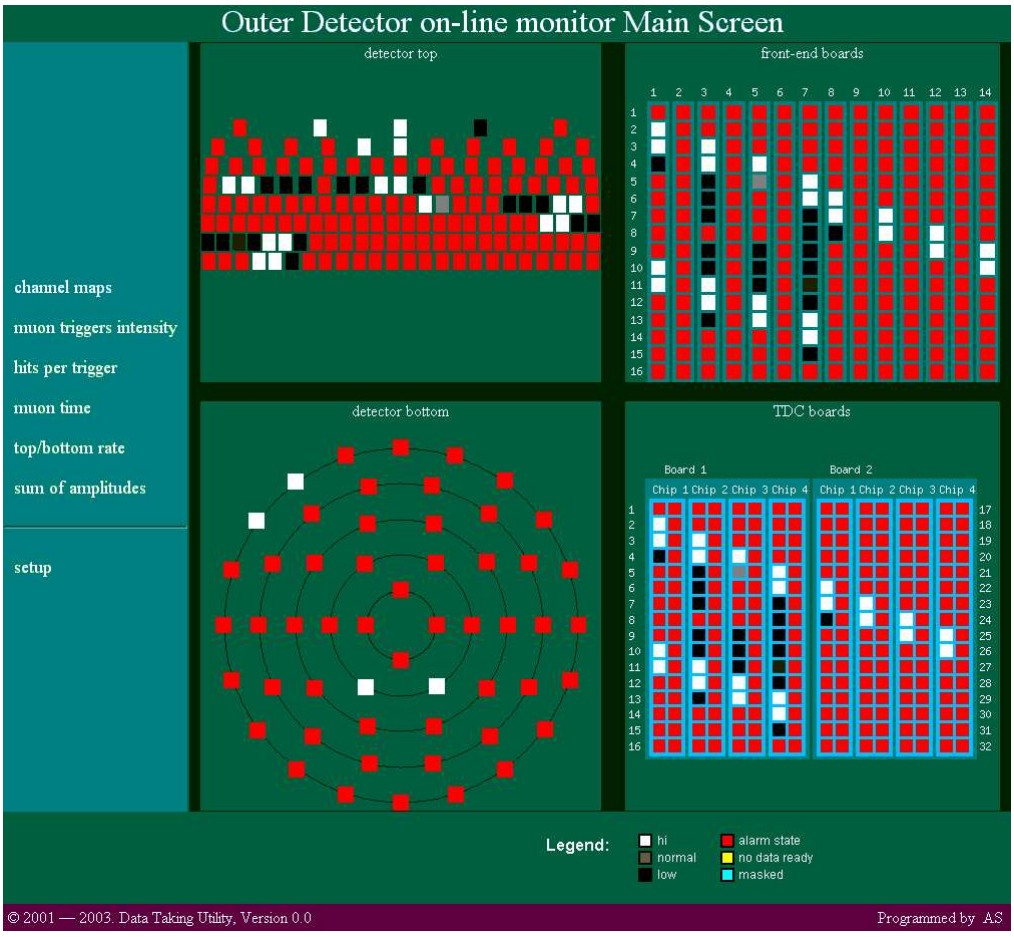

Fig. B.1: *Online Monitor main OD map (sec. 5.5)[213].*

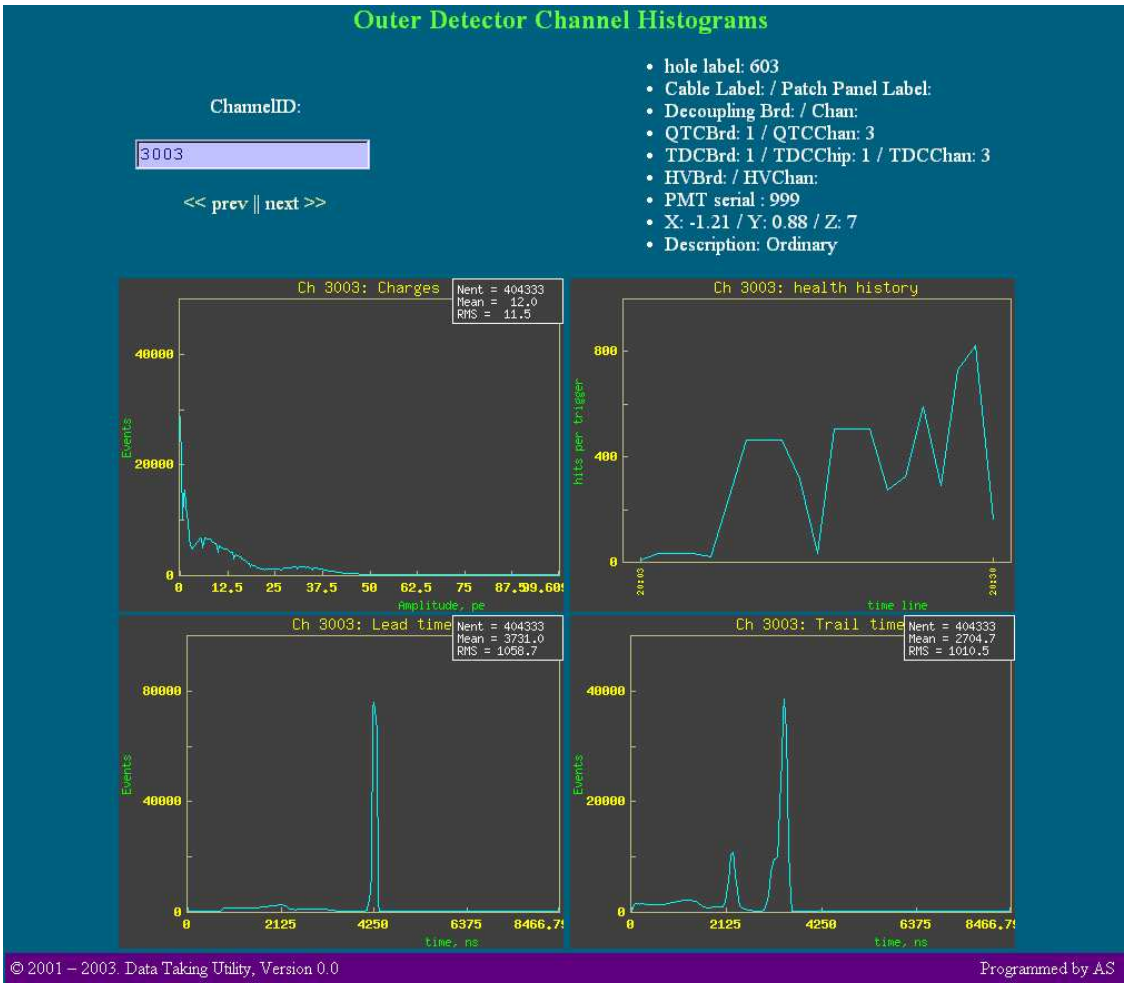

Fig. B.2: *Online Monitor single channel histograms for OD (sec. 5.5))[213].*

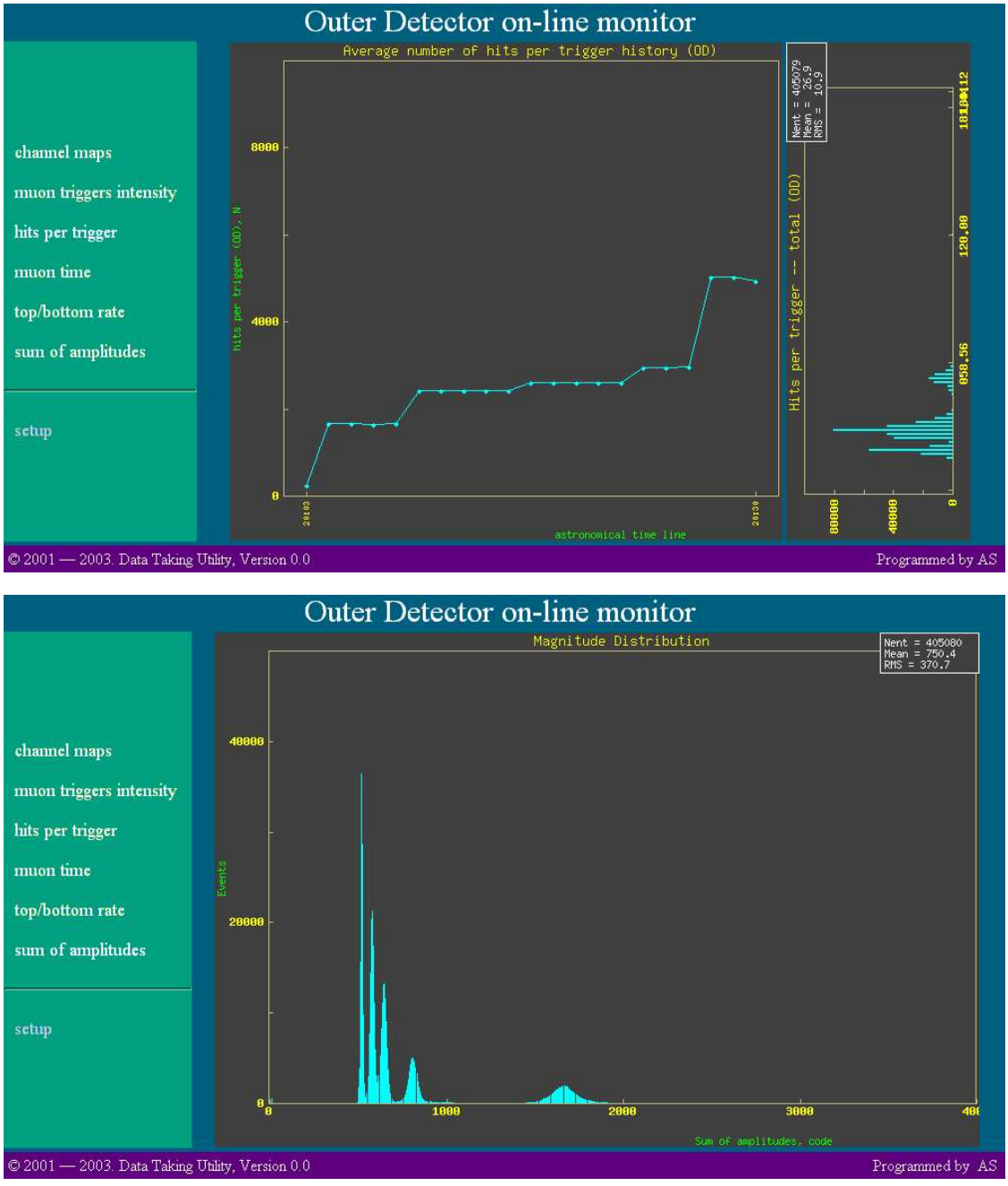

Fig. B.3: *Examples of global OMON)[213] histograms for OD (sec. 5.5): trigger history (left) and sum amplitude (right). Images refer to a run with an* LED *intensity scan.*

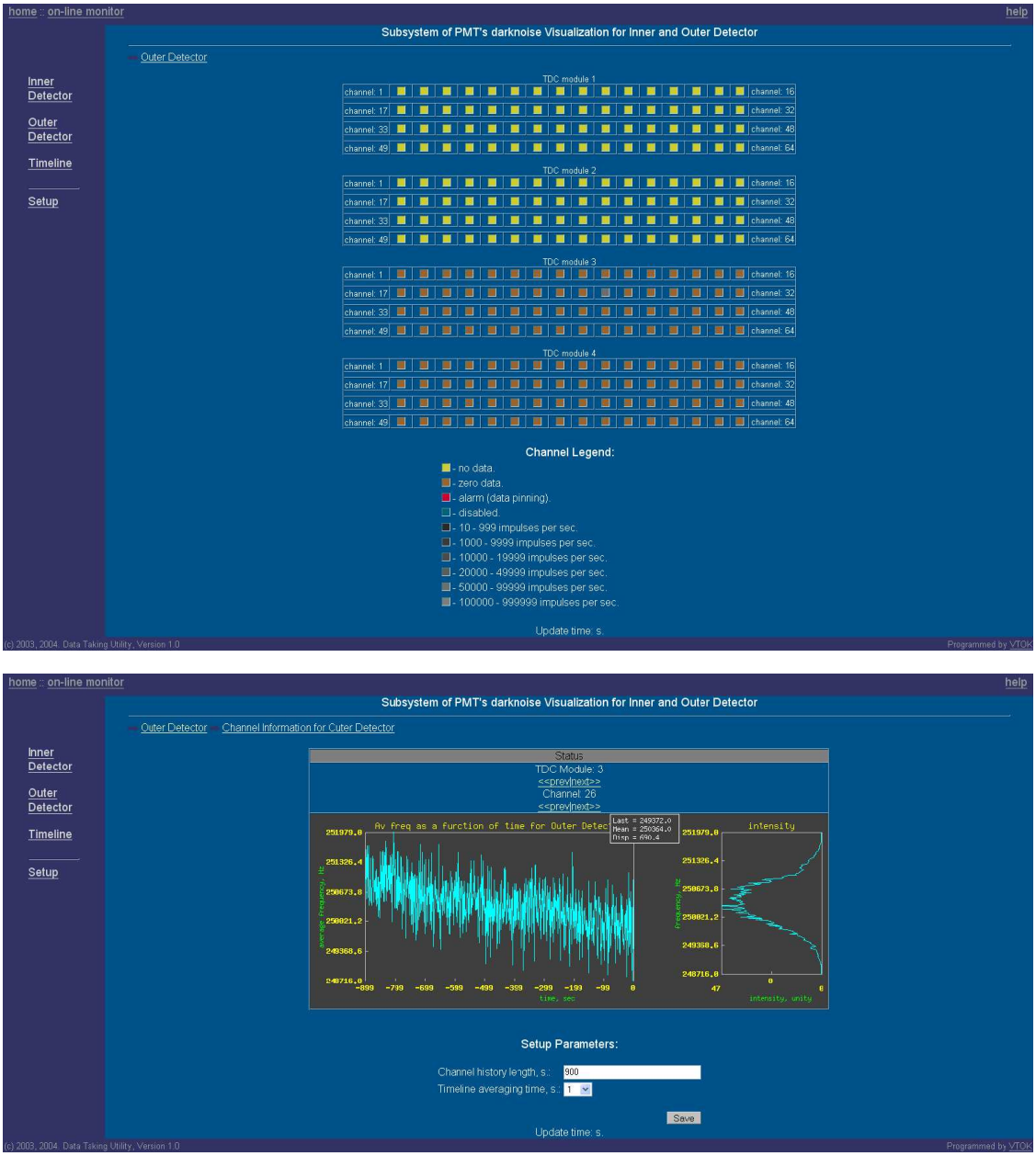

Fig. B.4: *Scalers Web Interface for OD (sec. 4.7))[213]. Clickable channels map (above) and single channel page (below).*

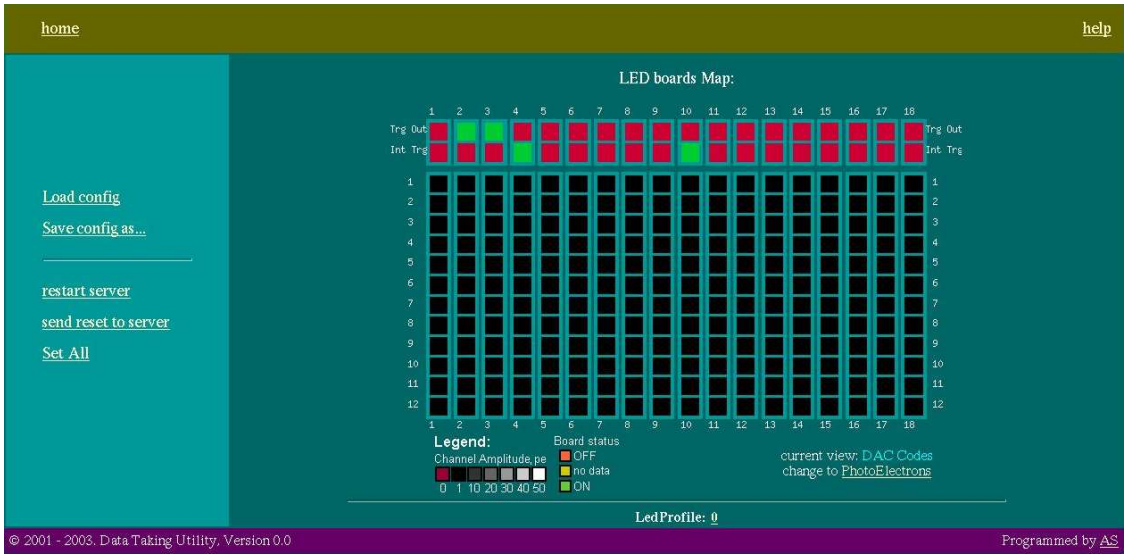

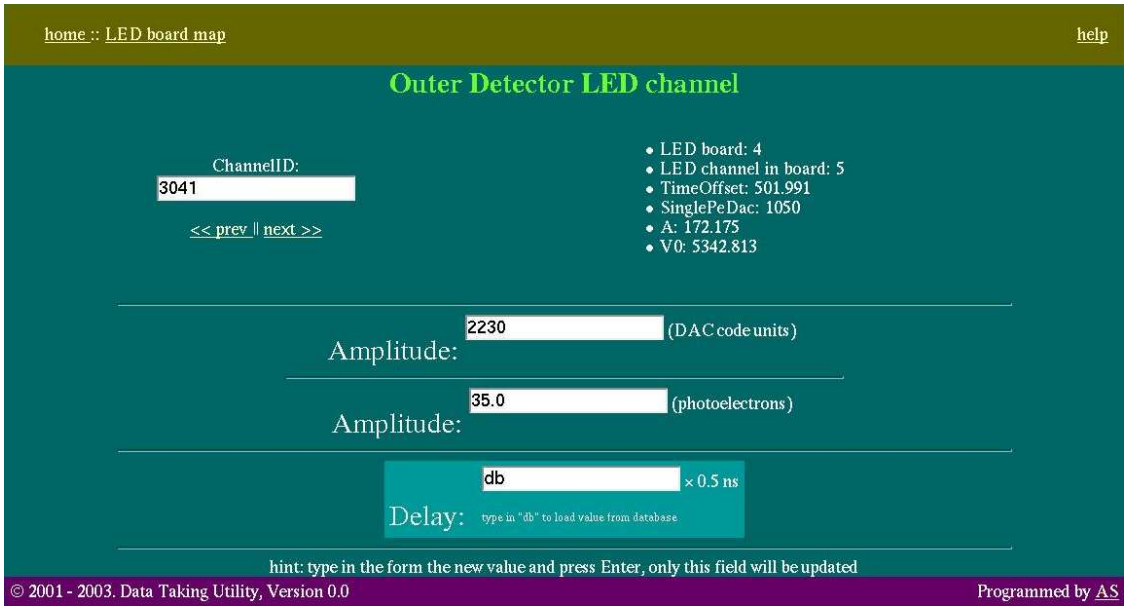

Fig. B.5: *LEDs control GUI (sec. 8.4))[213]. The main channel map (above) shows amplitudes as shades of gray. Clicking on a square leads to the specific channel setup page (below).*

Appendix C

Slow Control Server Commands

The Slow control system of Borexino is fully described in section sec. 5.7. Here is reported a reference table with the complete list of the $\sim$ 120 commands implemented by the Slow Control server with a brief descriptive note. The goal is to address as precisely as possible the syntax, the range of required parameters and the nature of returned values. It is meant for programmers willing to develop a client application or experienced user with the emergency need to interact directly with the server through socket or console connection. Normal shifters are supposed to rely on the web interface alone.

The forth column SUB indicates the finest sub-target element that can be specified. Reference to larger superset of these elements can be achieved using the special value 0 (all) as CHANNEL, BOARD, CRATE specifier.

Note on syntax of QUERY command

QUERY commands retrieve information from the slow control database on the history of a given parameter in an interval that can be specified either in time or in run numbers. Therefore QUERY commands must include one of the 2 following couple of tokens (but not both):

- TIMEMIN=timestamp1 and TIMEMAX=timestamp2. Timestamps are in SQL standard style: yyyy.mm.dd_hh:mm:ss (Note the "_" replacing the space).

- RUNMIN=run1 and RUNMAX=run2. Run1 and run2 must be valid integers not greater then current run number.

QUERY commands return a list of space-separated items organized two-by-two as key-value couples, with key being the timestamp and value being the physical quantity requested. It is therefore care of the user to interpret odd elements as timestamps and even elements as values and to group them correctly in couples. Since a QUERY command returns a list of values with a built-in degree of freedom (time), it cannot support 0=ALL in CHANNEL, BOARD, CRATE specifier as there would be no way to refer results to different sub-target elements.

Note on Monitor function. TIME_STEP and TIME_GAP parameters

The server performs a monitor operation with a period set by TIME_STEP (system) parameter. The monitor operation occurs independently for the three subsystem (HV, VME, LV).

Within each subsystem, the time elapsed since the previous operation is checked against the TIME_GAP (subsystem) parameter. If it is found larger, all monitored parameters in the subsystem, will be written to database. If not, parameters variations since the previous operation are checked against fixed thresholds[1]. A parameter variation exceeding thethreshold determines the DB writing of the relevant sub-target element. In this way both periodic and alarmed (fast variations) DB writing are handled.

The TIME_STEP and the three TIME_GAP parameters can be modified with SET commands with VAL (integer) interpreted as follows: 1-100 $\rightarrow$ seconds; 101-200 $\rightarrow$ minutes; 201-300 $\rightarrow$ hours; 301-400 $\rightarrow$ days, -1=disabled. GET commands of the same parameters simply return the value in seconds.

[1] Set through config files

TRG	CMD	MODIFIER	SUB	VALUE	NOTE
HV	DO	INIT	SYS		Reread config file and poll HW again.
		ON	CH		Turn on crate.
		OFF	CH		Turn off crate.
		CLEAR	CR		Clear crate alarm.
		MONITOR	BR		Perform asynchronous board monitor.
		WRITE	BR		Perform asynchronous board db writing.
	SET	TIME_GAP	SYS	[1-400]	Gap between monitor operations. See note above for values.
		BV0SET	BR	[0-2500] (V)	Board Common Channel HV.
		BI0SET	BR	[0-10000] (μA)	Board current threshold.
		BVMAXSW	BR	[0-2500] (V)	Board Common channel software max HV.
		BRUP	BR	[0-1000] (V/s)	Board Common channel ramp up speed.
		BRDOWN	BR	[0-1000] (V/s)	Board Common channel ramp down speed.
		BTRIP	BR	[0-1000] ($10^{-1}s$)	Period of I threshold comparison.
		V0SET	CH	[0-2500] (V)	Channel HV.
		V0SET_DEF	CH	–	Channel dark room HV from db (bx_geometry).
		V0SET_TIME	CH	–	Channel HV from db (bx_slow) not later than TIMEMAX.
		V0SET_RUN	CH	–	Channel HV from db (bx_slow) not later than RUNMAX.
		VMAXSW	CH	[0-2500] (V)	Channel software max HV.
		RUP	CH	[0-1000] (V/s)	Channel ramp up speed.
		RDOWN	CH	[0-1000] (V/s)	Channel ramp down speed.
	GET	TIME_GAP	SYS	[1-8640000] (s)	Gap between monitor operations.
		NCRATES	SYS	[0-15]	Number of enabled AND detected crates.
		NBOARDS	CR	[0-150]	Integral number of boards.
		NCHANNELS	BR	[0-3600]	Integral number of channels.
		NAME	CR	string	Logical crate name.
		MODEL	CR	string	Mainframe model and firmware version.
		OCCUPATION	CR	10 bool	Crate 10 slots occupation state (0=free, 1=board present).
		HDSTATUS	CR	[0,1]	Mainframe ON/OFF status.
		CRSTATUS	CR	[0,1]	At least 1 channel has HV ON.
		CRERROR	CR	[0-4]	Crate OR. 0=Ok, 1=OverVolt, 2=UnderVolt, 4=OverCurr.
HV	GET	CRRAMP	CR	[0-2]	Crate OR. 0=Stable, 1=Going Down, 2=Going Up.
		CRAGGRSTATUS	CR	3 int	Return the 3 above in sequence.
		ENABLE	CR	[0,1]	Status of hardware *enable* switch.

		FANSTATUS	CR	[0,1]	0=Ok, 1=Alarm.
		BSTATUS	BR	[0,1]	At least 1 channel has HV ON.
		BERROR	BR	[0-4]	BR OR. 0=Ok, 1=OverVolt, 2=UnderVolt, 4=OverCurr.
		BRAMP	BR	[0-2]	BR OR. 0=Stable, 1=Going Down, 2=Going Up.
		BAGGRSTATUS	BR	3 int	Return the 3 above in sequence.
		BVMON	BR	[0-2500] (V)	Measured board Common channel HV.
		BIMON	BR	[0-10000] (μA)	Measured board current.
		BV0SET	BR	[0-2500] (V)	Board Common channel HV (set).
		BI0SET	BR	[0-10000] (μA)	Board current threshold.
		BVMAXSW	BR	[0-2500] (V)	Board Common channel sofware max HV.
		BRUP	BR	[0-1000] (V/s)	Board Common channel ramp up speed.
		BRDOWN	BR	[0-1000] (V/s)	Board Common channel ramp down speed.
		BTRIP	BR	[0-1000] ($10^{-1}s$)	Period of I threshold comparison.
		BPARAMS	BR	12 int	A set of 12 low priority board parameters.[2]
		STATUS	CH	[0,1]	Channel HV ON/OFF status.
		ERROR	CH	[0-4]	0=Ok, 1=OverVoltage, 2=UnderVoltage, 4=OverCurrent.
		RAMP	CH	[0-2]	0=Stable, 1=Going Down, 2=Going Up.
		AGGRSTATUS	CH	3 int	Returns the 3 above in sequence.
		VMON	CH	[0-2500] (V)	Measured channel HV.
		VMAXSW	CH	[0-2500] (V)	Channel sofware max HV.
		RUP	CH	[0-1000] (V/s)	Channel ramp up speed.
		RDOWN	CHR	[0-1000] (V/s)	Channel ramp down speed.
	QUERY	VMON	CH	(T,[0-2500] (V))	History of Channel measured HV.
		V0SET	CH	(T,[0-2500] (V))	History of Channel HV (set).
		BVMON	BR	(T,[0-2500] (V))	History of Board Common Channel measured HV.
		BV0SET	BR	(T,[0-2500] (V))	History of Board Common Channel HV (set).
		BIMON	BR	(T,[0-10000] (μA))	History of Board Common Channel measured I.
VME	DO	INIT	SYS		Reread config file and poll HW again.
		ON	CR		Turn on crate.
		OFF	CR		Turn off crate.
		RESET	CR		Issue reset to a crate (restarts PPC).
		CLEAR	CR		Clear crate alarm.
		MONITOR	CR		Perform asynchronous crate monitor.

[2] In order: units, sern, vern, nchann, vmax, imax, rampmin, rampmax, vres, ires, vdec, idec. See manual for meaning, values and units.

		WRITE	CR		Perform asynchronous crate db writing.
	SET	TIME_GAP	SYS	[1-400]	Gap between monitor operations. See note above for values.
		FANSPEED	CR	[1200-3120] (rpm)	Will be rounded to nearest integer multiple of 120.
		I5P	CR	[0-1000000]	Current threshold for power line +5V.
		I12P	CR	[0-1000000]	Current threshold for power line +12V.
		I24P	CR	[0-1000000]	Current threshold for power line +24V.
		I5S	CR	[0-1000000]	Current threshold for power line +5Vs.
		I5N	CR	[0-1000000]	Current threshold for power line -5V
		I12N	CR	[0-1000000]	Current threshold for power line -12V
		I24N	CR	[0-1000000]	Current threshold for power line -24V
		I2N	CR	[0-1000000]	Current threshold for power line -2V
	GET	TIME_GAP	SYS	[1-8640000] (s)	Gap between monitor operations.
		NCRATES	SYS	[0-25]	Number of enabled AND detected crates.
		CRARRAY	SYS	bool[25]	Bools array showing crates that are present and enabled.
		NAME	CR	string	Logical Crate name.
		MODEL	CR	string	Crate model and firmware version.
		STATUS	CR	[0,1]	Simple ON/OFF crate status.
		ALARM	CR	[0,1]	Crate alarm flag. Corresponds to LED&NIM on fan tray.
		LINESTATUS	CR	8 x [0-8]	8x: 0=Ok, 1=UnderV, 2=OverV, 4=OverCurr, 8=OverThr.
		OTHERSTATUS	CR	8 bools	8 flags: AC, Temp, Fans, Sys, IEC, V24, Caen, Test.
		TRIPCOND	CR	4 bools	PS trip reason. 4 flags: AC fail, OverHeat, Fan fail, Line fail
		TEMPS	CR	2 int (C)	Inner crate temperature and power supply temperature.
		PARAMS	CR	8 x 4 x int	8 lines x 4 val: V (mv), I (mA), Thr (mA), LINESTATUS.
		FANSPEEDS	CR	8x[1200-3120] (rpm)	Fan speeds: mean, set, fan1, ... fan6.
VME	QUERY	I5P	CR	(T,[0-???] (mA))	History of +5V line current.
		I12P	CR	(T,[0-???] (mA))	History of +12V line current.
		I24P	CR	(T,[0-???] (mA))	History of +24V line current.
		I5S	CR	(T,[0-???] (mA))	History of +5Vs line current.
		I5N	CR	(T,[0-???] (mA))	History of -5V line current.
		I12N	CR	(T,[0-???] (mA))	History of -12V line current.
		I24N	CR	(T,[0-???] (mA))	History of -24V line current.
		I2N	CR	(T,[0-???] (mA))	History of -2V line current.
		V5P	CR	(T,$\sim 5000mV$)	History of +5V line current.
		V12P	CR	(T,$\sim 12000mV$)	History of +12V line current.
		V24P	CR	(T,$\sim 24000mV$)	History of +24V line current.

		V5S	CR	(T,$\sim 5000mV$)	History of +5Vs line current.
		V5N	CR	(T,$\sim 5000mV$)	History of -5V line current.
		V12N	CR	(T,$\sim 12000mV$)	History of -12V line current.
		V24N	CR	(T,$\sim 24000mV$)	History of -24V line current.
		V2N	CR	(T,$\sim 2000mV$)	History of -2V line current.
LV	DO	INIT	SYS		Reread config file and poll HW again.
		ON	CR		Turn on crate.
		OFF	CR		Turn off crate.
		MONITOR	CR		Perform asynchronous crate monitor.
		WRITE	CR		Perform asynchronous crate db writing.
	SET	TIME_GAP	SYS	[1-400]	Gap between monitor operations. See note above for values.
	GET	TIME_GAP	SYS	[1-8640000] (s)	Gap between monitor operations.
		NCRATES	SYS	[0-14]	Number of enabled AND detected crates.
		STATUS	CR	[0,1]	Simple ON/OFF crate status.
		V14P	CR	sim14000(mV)	Voltage of the +14V line.
		V14N	CRR	sim14000(mV)	Voltage of the -14V line.
		I14P	CRR	[0-30000] (mA)	Current of the +14V line.
		I14N	CRR	[0-30000] (mA)	Current of the -14V line.
		PARAMS	CR	4 int	Returns the 4 parameters above in sequence.
LV	QUERY	V14P	CR	(T,sim14000 (mV))	History of the of the +14V line voltage.
		V14N	CR	(T,sim14000 (mV))	History of the of the -14V line voltage.
		I14P	CR	(T,[0-30000] (mA))	History of the of the +14V line current.
		I14N	CR	(T,[0-30000] (mA))	History of the of the -14V line current.
SYS	DIE				Terminates the server.
	SET	TIME_STEP		[1-400]	Step between monitor operations. See note above for values.
	GET	TIME_STEP		[1-8640000] (s)	Step between monitor operations.
		RUN		int	Returns latest run number in *Run* db table.
		PROFILE		int	Returns profile associated with latest run in *Run* db table.
	LOCK			key	Returns a numeric key and locks the connections.
	UNLOCK				Releases the lock.

Appendix D

CTF discarded runs

Tab. D.1 reports the list of runs not included in any of the analyses presented in chap. 9 and 10. The reasons are the most diverse:

1. Electronic failures in crates or modules: 4 runs.
2. Air conditioning failure with visible drifts in offsets and gains: 2 runs.
3. Daq unrecoverable[1] crashes: 5 runs
4. Calibration laser runs: 28 runs.
5. Missing run numbers: 14 runs.
6. Column Batch Test (CBT) with the *inner vessel* only partially filled: 3 runs.
7. Radon Source insertion: 8 runs.
8. Very short test runs: 14 runs.
9. Black out: 1 run.
10. Occasional electronic noise from a lamp: 1 run.
11. ^{14}C spectral fit does not converge: 1 run

Tab. D.2 reports additional runs discarded in the ^{11}C analysis only (chap. 10):

1. Runs where some events had corrupted absolute time: 9 runs.
2. Runs shorter then $10h$ astronomical time[2]: 1 run.

[1] When the DAQ hangs, the run portion already taken is valid and the live time reported is correct as the DAQ stops synchronously its measurement. The run is therefore generally usable apart from the few cases listed when the run resulted corrupted or the live time was not available.

[2] Difficult to apply the *end-of-run* correction explained in sec. 10.3.3.

run	problem
2058	electr. failure
2062	laser
2083	missing
2085	laser
2090	test
2112	daq crash
2116	laser
2121	laser
2124	test
2136-39	missing
2166	A/C failure
2184	CBT: partial fill
2185	CBT: partial fill
2186	CBT: partial fill
2187	lamp electr. noise
2191	laser
2212	electr. failure
2230-31	daq crash
2282-84	laser
2291	black-out
2322	laser
2326	electr. failure
2329	laser
2347-49	laser
2358	laser
2363	daq crash
2374	missing
2378-81	laser
2383-85	laser
2406	laser
2419	test
2423	test
2441-42	laser
2448-49	missing
2455-56	test
2457	no light yield
2458	laser
2460	test
2465	test
2479-80	missing
2488-89	missing
2492-93	missing
2494-96	test
2503	test
2512-14	laser
2517	electr. failure
2521	test
2532-39	source
2540	test
2548	A/C failure
2552	daq crash

Tab. D.1: *CTF runs not included in the analyses of chap. 9 and 10.*

run	problem
2196	corrupted abs time
2199	corrupted abs time
2263	corrupted abs time
2267	corrupted abs time
2279	corrupted abs time
2336	corrupted abs time
2338	corrupted abs time
2370	shorter than $10h$
2515	corrupted abs time

Tab. D.2: *Additional CTF runs not included in the* ^{11}C *analysis of chap. 10.*

List of Acronyms

General Physics terms

AGN	Active Galactic Nucleus
BR	Branching Ratio
BSE	Bulk Silicate Earth
CC	Charged Current
C.L.	Confidence Level
CKM	Cabibbo-Kobayashi-Maskawa
CMB	Cosmic Microwave Background
CNGS	CerN to Gran Sasso
CNO	Carbon-Nitrogen-Oxygen
DBD	Double Beta Decay
EC	Electron Capture
ES	Electron Scattering
FV	Fiducial Volume
FWHM	Full Width at Half Maximum
G.o.F.	Goodness of Fit
GRB	Gamma Ray Burst
h.c.	hermitian conjugate
LMA	Large Mixing Angle
(k)m.w.e.	(kilo)meters of water equivalent
MC	MonteCarlo
NAA	Neutron Activation Analysis
NC	Neutral Current
NCD	Neutral Current Detector
MSW	Mikheyev-Smirnov-Wolfenstein
OM	Optical Module
PDF	Probability Density Function
PMT	Photo-Multiplier Tube
ppb	*part-per-billion* (10^{-9})
ppm	*part-per-million* (10^{-6})
PSD	Pulse Shape Discrimination
R&D	Research & Development
RSFP	Resonant Spin Flip Precession
S/B	Signal-to-Background
SK	Super-Kamiokande
SM	Standard Model (of Electro-Weak Interactions)

SN	SuperNova
SNP	Solar Neutrino Problem
SNR	SuperNova Remnant
SNU	Solar Neutrino Unit
SPS	Super Proton Synchrotron
SRN	Supernova Relic Neutrinos
SSM	Standard Solar Model
TAUP	Topics in Astroparticle and Underground Physics
TFC	Three-Fold Coincidence
TOF	Time-Of-Flight
TPC	Time Projection Chamber
UHECR	Ultra-High Energy Cosmic Rays
UV	Ultra-Violet
VEV	Vacuum Expectation Value
WIMP	Weakly Interacting Massive Particle

Borexino specific terms

BBE	Big Building East
BBW	Big Building West
CBT	Column Batch Test
CLT	Column Loop Test
CTF	Counting Test Facility
DMP	Dimethylphtalate
EADJ	Electronic ADJustment
ETL	Electron Tubes Limited
ID	Inner Detector
INFN	Istituto Nazionale di Fisica Nucleare (I)
IV	Inner Vessel
GS	Gran Sasso
GVI	Gate Valve Installation
$LAKN_2$	Low Argon and Krypton Nitrogen
LNGS	Laboratori Nazionali del Gran Sasso (I)
NW	Neutrino Window $(250 - 800keV)$
OD	Outer Detector
OV	Outer Vessel
PC	Pseudocumene, 1,2,4-Trimethylbenzene
PPO	2,5-Diphenyloxazole
PXE	Phenyl-ortho-xylylethane
SRC	SouRCe Test
SSS	Stainless Steel Sphere
TFC	Three-Fold Coincidence
TUM	Technische Universität München (D)
WET	Water Extraction Test
WT	Water Tank

Electronics terms

AC	Alternate Current
ADC	Analog to Digital Converter
BLT	BLock Transfer

BNC	Bayonet Neill-Concelman
CAMAC	Computer Aided Measurement And Control
CAEN	Costruzioni Apparecchiature Elettroniche Nucleari (I)
CAN	Controller Area Network
CCD	Charge Coupled Device
CFD	Constant Fraction Discriminator
CPU	Central Processing Unit
DAC	Digital to Analog Converter
DC	Direct Current
DMA	Direct Memory Access
DPSA	Digital Pulse Shape Analyzer
DSP	Digital Signal Processor
DTACK	DaTa ACKnowledgement
ECL	Emitter Coupled Logic
FADC	Flash (or Fast) ADC
FE	Front-End
FIFO	First-In First-Out
	Fan-In Fan-Out
FPGA	Field Programmable Gate Array
FWFD	Fast WaveForm Digitizer
GPIB	General Purpose Interface Bus
GPS	Global Positioning System
HV	High Voltage
IC	Integrated Circuit
IRQ	Interrupt ReQuest
LAM	Look-At-Me
LED	Light Emitting Diode
	Leading Edge Discriminator
LCD	Liquid Crystal Display
MALU	MAjority Logic Unit
NIM	Nuclear Instrument Modules
PCI	Peripheral Component Interconnect
PDU	Programmable Delay Unit
pe	photo-electron
PET	PolyEthylene Terephthalate
PPC	Power PC
QDC	Charge (Q) to Digital Converter
QTC	Charge (Q) to Time Converter
RAID	Redundant Array of Independent Disks
RAM	Random Access Memory
RORA	Reset On Register Access
SCSI	Small Computer System Interface
SMA	Sub-Miniature version A
SMB	Sub-Miniature version B
SPE	Single Photo-Electron
TDC	Time to Digital Converter
TTL	Transistor-Transistor Logic
TTR	Transient Time Recorder
VME	VERSAmodule Eurocard

Borexino Electronics terms

BGT	Borexino General Trigger
BRC	Borexino Reference Clock
BTB	Borexino Trigger Board
CKG	ClocK Generator
HVD	High Voltage Decoupler
MTB	Muon Trigger Board
OMT	Outer Muon Trigger
PLP	Primary Logic Pulse
SLP	Secondary Logic Pulse
TAB	Trigger Adder Board
TBP	Trigger BackPlane
TRGID	TRiGger ID
TWF	Triangular WaveForm

Software terms

ACL	Access ControL
API	Application-Program Interface
ASCII	American Standard Code for Information Interchange
CGI	Common Gateway Interface
CORBA	Common Object Request Broker Architecture
CVS	Concurrent Version System
DAQ	Data AcQuisition
DB	DataBase
DHCP	Dynamic Host Configuration Protocol
EOT	End-Of-Transfer
FFT	Fast Fourier Transform
HTML	Hyper-Text Markup Language
IOCTL	Input Output ConTroL
IP	Internet Protocol
IPC	Inter Process Communication
LAN	Local Area Network
LSB	Least Significant Bit (or Byte)
MAC	Media Access Control
MSB	Most Significant Bit (or Byte)
NAT	Network Address Translation
NIS	Network Information Service
NFS	Network File System
OMON	Online MONitor
PID	Particle IDentification
RFC	Request For Change
SHM	SHared Memory
SQL	Standard Query Language
STL	Standard Template Library (C++)
TCP	Transfer Control Protocol
WAN	Wide Area Network

Bibliography

Chapter 1

[1] Pauli W., transl. in L.M.Brown, Phys. Today Sept. (**1978**).

[2] Bohr N., J. Chem. Soc. (Lond.), vol. 135, p. 349, (**1932**).

[3] Chadwick J., Nature, vol. 129, p. 312, (**1932**).

[4] Fermi E., Z. Phys. 88, vol. 88, p. 161, (**1934**).

[5] Bethe H.A., Peierls R.E., Nature, vol. 133, p. 532, (**1934**).

[6] Gamow G., Phys. Today, vol. 6, July (**1948**).

[7] Allen J., Phys. Rev., vol. 61, p. 692, (**1942**).

[8] Reines F., Rev. Mod. Phys., vol. 68, p. 317, (**1996**).

[9] Lee T.D., Yang C.N., Phys. Rev., vol. 105, p. 1671, (**1957**).

[10] Goldhaber M., Grodzins L., Sunyar A.W., Phys. Rev., vol. 106, p. 826, (**1957**).

[11] Danby G. et al., Phys. Rev. Lett., vol. 9, p. 36, (**1962**).

[12] Kobayashi M., Maskawa T., Prog. Theor. Phys., vol. 49, p. 652, (**1973**).

[13] DONUT Collaboration, "Observation of tau neutrino interactions", Phys. Lett. B, vol. 504, p. 218-224, (**2001**), [arXiv:hep-ex/0012035].

[14] Particle Data Group, "Review of Particle Physics", Phys. Rev. D, vol. 66, (**2002**).

[15] Barger V., Kneller J.P., Lee H.S., Marfatia D., Steigman G., "Effective number of neutrinos and baryon asymmetry from BBN and WMAP", Phys. Rev. Lett. B, vol. 566, p. 8, (**2003**), [arXiv:hep-ph/0305075].

[16] Stix M., "The Sun", Springer–Verlag, Berlin & Heidelberg, (**1991**).

[17] Eddington A.S., Observatory, vol. 43, p. 341, (**1920**).

[18] Atkinson R.d'E., Houtermans F.G., Z. Phys, vol. 54, p. 656, (**1929**).

[19] Gamow G., Phys. Rev. vol. 53, p. 595, (**1938**).

[20] Bethe H.A., Phys. Rev., vol. 55, p. 434, (**1939**).

[21] Bahcall J.N. Home Page: http://apollo.sns.ias.edu/ jnb/

[22] Bahcall J.N., Pinsonneault M.H., "What do we (not) know theoretically about solar neutrino fluxes?", Phys. Rev. Lett., vol. 92, 121301, (**2004**), [arXiv:astro-ph/0402114].

[23] Bahcall J.N., Serenelli A.M., "How Do Uncertainties in the Surface Chemical Composition of the Sun Affect the Predicted Solar Neutrino Fluxes", Astrophys. J., vol. 626, p. 530, (**2005**), [arXiv:astro-ph/0412096].

[24] Bahcall J.N., Serenelli A.M., Basu S., "New solar opacities, abundances, helioseismology and neutrino fluxes", Astrophys. J., vol. 621, p. L85, (**2005**), [arXiv:astro-ph/0412440].

[25] Bahcall J.N., "The luminosity constraint on solar neutrino fluxes", Phys. Rev. C, vol. 65, 025801, (**2002**), [arXiv:hep-ph/0108148].

[26] Gravesse N., Sauval A.J., Space Sci. Rev., vol. 85, p. 161, (**1998**).

[27] Asplund M., Gravesse N., Sauval A.J., "Cosmic Abundances as Records of Stellar Evolution and Nucleosynthesis", ASP Conference Series, eds. F.N. Bash & T.G. Barnes, (**2005**), [arXiv:astro-ph/0410214].

[28] Adelberger E.G. et al., "Solar Fusion Cross-Sections", Rev. Mod. Phys., vol. 70, p. 1265, (**1998**), [arXiv:astro-ph/9805121].

[29] Haxton W.C., Parker P.D., Rolfs C.E., "Solar Hydrogen Burning and Neutrinos", [arXiv:nucl-th/0501020].

[30] Casella C. et al., Nucl. Phys. A, vol. 706, p. 203, (**2002**).

[31] Bonetti R. et al., Phys. Rev. Lett., vol. 82, p. 5205, (**1999**), [arXiv:nucl-ex/9902004].

[32] Bahcall J.N., Moeller C.P., Astr. Phys. Journ., vol. 155, p. 511, (**1969**).

[33] Junghans A.R. et al., Phys. Rev. Lett., vol. 88, 041101, (**2002**); Phys. Rev. C, vol. 68, 065803, (**2003**).

[34] Formicola A. et al., "Astrophysical S-factor of $^{14}N(p,\gamma)^{15}O$", Phys. Lett. B, vol. 591, p. 61-68, (**2004**), [arXiv:nucl-ex/0312015].

[35] Michaud G., Vauclair S., "Element Separation by Atomic Diffusion in Solar Interior and Atmosphere", Cox A.N., Livingston W.C., Matthews M.S. Editors, The University of Arizona Press, Tucson, (**1991**).

[36] Turck-Chieze S. et al., "New Solar Seismic Models and the neutrino puzzle", subm. to Astrophys. J., (**2002**), [arXiv:astro-ph/0203107].

[37] Turck-Chieze S. et al., "Surprising Sun", Phys. Rev. Lett., vol. 93, p. 211102, (**2004**), [arXiv:astro-ph/0407176].

[38] Kirsten T.A., "Solar neutrino experiments: results and implications", Rev. Mod. Phys., vol. 71, p. 1213-1232, (**1999**).

[39] Bahcall J.N., "Neutrino Astrophysics", Cambridge University Press, Cambridge, (**1989**).

[40] 't Hooft G., Phys. Lett. B, vol. 37, p. 195, (**1971**).

[41] Pontecorvo B., Chalk River Report, PD205, (**1946**).

[42] Davis R.J., Harmer D.S., Hoffman K.C., "Search for neutrinos from the sun", Phys. Rev. Lett., vol. 20, p. 1205-1209, (**1968**).

[43] Davis R.J. et al., "Measurement of the solar electron neutrino flux with the Homestake Chlorine Detector", Astroph. J., vol. 496, p. 505-526, (**1998**).

[44] Kamiokande Collaboration, "Solar Neutrino Data Covering Solar Cycle 22", Phys. Rev. Lett., vol. 77, p. 1683, (**1996**).

[45] Kuzmin V.A., Sov. Phys. JETP vol. 22, p. 1051, (**1966**).

[46] Bahcall J.N., Davis R. et al., Phys. Rev. Lett., vol. 40, p. 1351, (**1978**).

[47] Gallex Collaboration, "Gallex Solar Neutrino Observations: Results for Gallex IV", Phys. Lett. B, vol. 447, p. 127-133, (**1999**).

[48] Gallex Collaboration, Phys. Lett. B, vol. 420, p. 114, (**1998**); Phys. Lett. B, vol. 436, p. 158, (**1998**).

[49] GNO Collaboration, "Complete results for five years of GNO solar neutrino observations", Phys. Lett. B, vol. 616, p. 174, (**2005**), [arXiv:hep-ex/0504037].

[50] Gavrin V.N. for the SAGE Collaboration, "The Baksan Gallium Solar Neutrino Experiment", Nucl. Phys. Proc. Suppl., vol. 16, p. 483-484, (**1990**).

[51] Gavrin V.N. for the SAGE Collaboration, "Measurement of the solar Neutrino Capture rate in SAGE and the value of the pp-neutrino flux at the earth.", Nucl. Phys. Proc. Suppl., vol. 138, p. 87-90, (**2005**).

[52] Cattadori C., Ferrari N., Pandola L., "Results from radiochemical experiments with main emphasis on the gallium ones", Nucl. Phys. Proc. Suppl., vol. 143, p. 3-12, (**2005**).

[53] Bahcall J.N., Pinsonneault M.H., Basu S., Christensen-Dalsgaard J., "Are Standard Solar Models reliable?", Phys. Rev. Lett., vol. 78, p. 171-174, (**1997**), [arXiv:astro-ph/9610250].

[54] Bahcall J.N., Bethe H.A., "A solution of the Solar Neutrino Problem", Phys. Rev. Lett., vol. 65, p. 2233, (**1990**).

[55] Bahcall J.N., "Solar Neutrinos: where we are, what we need", Nucl. Phys. A, vol. 631, p. 29c-41c, (**1998**), [arXiv:nucl-th/9802050].

[56] Halzen F., Martin A.D., "Quarks & Leptons: An introductory Course in Modern Particle Physics.", John Wiley & Sons, (**1984**).

[57] Gelmini G., Roulet E., "Neutrino masses", Rept. Prog. Phys., vol. 58, p. 1207-1266, (**1995**), [arXiv:hep-ph/9412278].

[58] Peccei R.D., "Neutrino Physics", AIP Conf. Proc., vol. 490, p. 80-124, (**1989**), [arXiv:hep-ph/9906509].

[59] Pontecorvo B., ZhETP, vol. 33, p. 549, (**1957**).

[60] Wolfenstein L., "Phys. Rev. D", vol. 17, p. 2369, (**1978**).

[61] Mikheyev S.P., Smirnov A.Y., Il Nuovo Cimento, vol. 9C, p. 17, (**1986**).

[62] Lobashev V.M. et al., Nucl. Phys. Proc. Suppl., vol. 91, p. 280-286, (**2001**).

[63] Bonn J. et al., Nucl. Phys. Proc. Suppl., vol. 91, p. 273, (**2001**).

[64] Assamagan et al., Phys. Rev. D, vol. 53, p. 6065, (**1996**).

[65] ALEPH Collaboration, Eur. Phys. J. C, vol. 2, p. 395, (**1998**).

[66] Pirro S., "Prospects in Double Beta Decay searches", subm. to Eur. Phys. J., (**2005**).

[67] Klapdor-Kleingrothaus H.V. et al., "Latest results from the Heidelberg-Moscow double beta decay experiment" Eur. Phys. J. A, vol. 12, p. 147-154, (**2001**), [arXiv:hep-ph/0103062].

[68] Klapdor-Kleingrothaus H.V. et al., "Evidence for Neutrinoless Double Beta Decay", Mod. Phys. Lett. A, vol. 16, p. 2409-2420, (**2001**), [arXiv:hep-ph/0201231].

[69] Aalseth C.E. et al., "Comment on evidence for neutrinoless double beta decay", Mod.Phys.Lett.A, vol. 17, p. 1475-1478, (**2002**), [arXiv:hep-ex/0202018].

[70] Feruglio F., Strumia A., Vissani F., "Neutrino oscillations and signals in beta and 0nu2beta experiments", Nucl. Phys. B, vol. 637, p. 345-377, (**2002**), addendum vol. 659, p. 359-362, (**2003**). [arXiv:hep-ph/0201291].

[71] Klapdor-Kleingrothaus H.V. et al., "Search for neutrinoless double beta decay with enriched ^{76}Ge in Gran Sasso 1990-2003", Phys. Lett. B, vol. 586, p. 198-212, (**2004**), [arXiv:hep-ph/0404088].

[72] CUORE Collaboration, "A new limit on the neutrinoless beta beta decay of Te-130", [arXiv:hep-ex/0501034].

[73] Mather J.C. et al., "Measurement of the cosmic microwave background spectrum by the COBE FIRAS instrument", Astroph. J., vol. 420, p. 439, (**1994**).

[74] WMAP Collaboration, "First Year Wilkinson Microwave Anisotropy Probe (WMAP) observations: determination of cosmological parameters.", Astrophys. J. Suppl., vol. 148, p. 175, (**2003**), [arXiv:astro-ph/0302209].

[75] Barger V., Marfatia D., Tregre A., "Neutrino mass limits from SDSS, 2dFGRS and WMAP", Phys. Lett. B, vol. 595, p. 55, (**2004**), [arXiv:hep-ph/0312065].

[76] Kamiokande Collaboration, "Observation of a small atmospheric muon-neutrino / electron-neutrino ratio in Kamiokande.", Phys. Lett. B., vol. 280, p. 146-152, (**1992**).

[77] Super-Kamiokande Collaboration, "Evidence for oscillation of atmospheric neutrinos", Phys. Rev. Lett., vol. 81, p. 1562-1567, (**1998**).

[78] Super-Kamiokande Collaboration, "Tau neutrinos favored over sterile neutrinos in atmospheric muon neutrino oscillations", Phys. Rev. Lett., vol. 81, p. 1562-1567, (**2000**), [arXiv:hep-ex/0009001].

[79] Super-Kamiokande Collaboration, "Evidence for an oscillatory signature in atmospheric neutrino oscillation", Phys. Rev. Lett., vol. 85, p. 3999-4003, (**2004**), [arXiv:hep-ex/0404034].

[80] Super-Kamiokande Collaboration, "A Measurement of Atmospheric Neutrino Oscillation Parameters by Super-Kamiokande I", subm. to Phys. Rev. D, (**2005**), [arXiv:hep-ex/0501064].

[81] SOUDAN-2 Collaboration, "Measurement of the L/E distribution of atmospheric neutrinos in Soudan 2 and their interpretation as neutrino oscillations", Phys. Rev. D, vol. 68, 113004, (**2003**), [arXiv:hep-ex/0307069].

[82] MACRO Collaboration, "Measurements of the atmospheric muon neutrino oscillations, global analysis of the data collected with MACRO detector", Eur. Phys. J. C, vol. 36, p. 323-339, (**2004**).

[83] SuperKamiokande Home Page: http://www-sk.icrr.u-tokyo.ac.jp/sk/

[84] Super-Kamiokande Collaboration, "The Super-Kamiokande Detector", Nucl. Instrum. Meth. A, vol. 501, p. 418-462, (**2003**).

[85] Super-Kamiokande Collaboration, "Determination of Solar Neutrino Oscillation Parameters using 1496 Days of Super-Kamiokande-I Data", Phys. Lett. B, vol. 539, p. 179-187, (**2002**), [arXiv:hep-ex/0205075].

[86] SNO Home Page: http://www.sno.phy.queensu.ca/

[87] SNO Collaboration, "The Sudbury Neutrino Observatory", Nucl. Instrum. Meth. A, vol. 449, p. 172-207, (**2000**).

[88] SNO Collaboration, "Measurement of charged current interactions produced by ^8B solar neutrinos at the Sudbury Neutrino Observatory", Phys. Rev. Lett., vol. 87, 071301, (**2001**).

[89] SNO Collaboration, "Direct Evidence for Neutrino Flavor Transformation from Neutral-Current Interactions in the Sudbury Neutrino Observatory", Phys. Rev. Lett., vol. 89, No. 1, 011302, (**2002**).

[90] SNO Collaboration, "Measurement of the Total Active ^8B Solar Neutrino Flux at the Sudbury Neutrino Observatory with Enhanced Neutral Current Sensitivity", Phys. Rev. Lett., vol. 92, 181301 (**2003**).

[91] SNO Collaboration, "Electron Energy Spectra, Fluxes, and Day-Night Asymmetries of ^8B Solar Neutrinos from the 391-Day Salt Phase SNO data Set", subm. to Phys. Rev. C, (**2005**).

[92] J.N. Bahcall, P.I. Krastev, A.Yu. Smirnov, "Where do we stand with solar neutrino oscillations?", Phys. Rev. D, vol. 58, 096016, (**1998**), [arXiv:hep-ph/9807216].

[93] J.N. Bahcall, P.I. Krastev, A.Yu. Smirnov, "Solar neutrinos: global analysis and implications for SNO", JHEP, vol. 0105, p. 015, (**2001**), [arXiv:hep-ph/0103179].

[94] Bahcall J.N., Gonzalez-Garcia M.C., Peña-Garay C., "Gloabl Analysis of solar neutrino oscillations including SNO CC measurement", JHEP, vol. 0108, p. 014, (**2001**), [arXiv:hep-ph/0106258].

[95] Bahcall J.N., Gonzalez-Garcia M.C., Peña-Garay C., "Before and After: How has the SNO neutral current measurement changed things?", JHEP, vol. 0207, p. 054, (**2002**), [arXiv:hep-hp/0204314].

[96] Bahcall J.N., Gonzalez-Garcia M.C., Peña-Garay C., "Solar Neutrinos Before and After KamLAND", JHEP, vol. 0302, p. 009, (**2003**), [arXiv:hep-hp/0212147].

[97] Bahcall J.N., Gonzalez-Garcia M.C., Peña-Garay C., "Solar Neutrinos Before and After Neutrino 2004", JHEP, vol. 0408, p. 016, (**2004**), [arXiv:hep-hp/0406294].

[98] Bohem F., "Studies of Neutrino Oscillations at Reactors" in "Current Aspects of Neutrino Physics", David O. Caldwell (Ed.), Springer, (**2001**).

[99] Boehm F. et al., "Final results from the Palo Verde neutrino oscillation experiment", Phys. Rev. D, vol. 64, 112001, (**2001**), [arXiv:hep-ex/0107009].

[100] Chooz Collaboration, "Limits on neutrino oscillations from the Chooz experiment", Phys. Lett. B, vol. 466, p. 415-430, (**1999**), [arXiv:hep-ex/9907037].

[101] KamLAND web page: http://www.awa.tohoku.ac.jp/KamLAND/

[102] KamLAND Collaboration, "KamLAND: a reactor neutrino experiment testing the solar neutrino anomaly", Nucl. Phys. Proc. Suppl., vol. 91, p. 99-104, (**2001**).

[103] KamLAND Collaboration, "First Results from KamLAND: Evidence for reactor Anti-Neutrino Disappearance", Phys. Rev. Lett., vol. 90, 021802, (**2003**), [arXiv:hep-ex/0212021].

[104] KamLAND Collaboration, "Measurement of Neutrino Oscillation with KamLAND: Evidence of Spectral Distortion", Phys. Rev. Lett., vol. 94, 081801, (**2005**), [arXiv:hep-ex/0406035].

[105] Caldwell D.O., "Studies of Neutrino Oscillations at Accelerators" in "Current Aspects of Neutrino Physics", David O. Caldwell (Ed.), Springer, (**2001**).

[106] LSND Collaboration, "Evidence for neutrino oscillations from the observation of anti-neutrino(electron) appearence in a anti-neutrino(muon) beam", Phys. Rev. D, vol. 63, 112001, (**2001**).

[107] KARMEN Collaboration, "Upper limits for neutrino oscillations muon anti-neutrino → electron anti-neutrino from muon decay at rest", Phys. Rev. D, vol. 65, 112001, (**2002**), [arXiv:hep-ex/0203021].

[108] Brice S.J. for the MiniBooNE Collaboration, "MiniBooNE", Nucl. Phys. Proc. Suppl., vol. 143, p. 115-120, (**2005**).

[109] Nomad Collaboration, "Search for nu(mu) → nu(e) oscillations in the NOMAD experiment.", Phys. Lett. B, vol. 507, p. 19-31, (**2003**), [arXiv:hep-ex/0306037].

[110] K2K Collaboration, "Evidence for muon neutrino oscillation in an accelerator-based experiment", Phys. Rev. Lett., vol. 94, 081802, (**2005**), [arXiv:hep-ex/0411038].

[111] Thomson M.A. for the MINOS Collaboration, "Status of the MINOS experiment", Nucl. Phys. Proc. Suppl., vol. 143, p. 249-256, (**2005**).

[112] Bueno A. for the ICARUS Collaboration, "The ICARUS Project", Nucl. Phys. Proc. Suppl., vol. 143, p. 262-265, (**2005**).

[113] Autiero D. for the OPERA Collaboration, "Status of the OPERA experiment (CNGS1)", Nucl. Phys. Proc. Suppl., vol. 143, p. 257-261, (**2005**).

[114] Halzen F., "High Energy Neutrino Astronomy: Towards Kilometer-Scale Detectors", in "Current Aspects of Neutrino Physics", David O. Caldwell (Ed.), Springer, (**2001**).

[115] NESTOR Collaboration, "Nestor deep sea neutrino telescope: deployment and results", Nucl. Phys. Proc. Suppl., vol. 151, p. 279-286, (**2006**).

[116] Brunner J. for the ANTARES Collaboration, "Status of the Antares project", Nucl. Phys. Proc. Suppl., vol. 145, p. 323-326, (**2005**).

[117] Sapienza P., "A km3 detector in the mediterranean: status of nemo", Nucl. Phys. Proc. Suppl., vol. 145, p. 331-334, (**2005**).

[118] AMANDA Collaboration, "New results from the Amanda neutrino telescope", Nucl. Phys. Proc. Suppl., vol. 145, p. 319-322, (**2005**).

[119] IceCube Collaboration, "Sensitivity of the IceCube detector to astrophysical sources of high energy muon neutrinos", Astropart. Phys., vol. 20, p. 507-532, (**2004**), [arXiv:astro-ph/0305196].

[120] Zalewska A., "Topical questions in the experimental neutrino physics", Acta Phys. Polon. B, vol. 34, p. 5365-5383, (**2003**).

[121] Oberauer L., "Low-energy neutrino physics after SNO and KamLAND", Mod. Phys. Lett. A, vol. 19, p. 337-348, (**2004**), [arXiv:hep-ph/0402162].

[122] Friedland A., Lunardini C., Peña-Garay C., "Solar neutrinos as probes of neutrino matter interactions", Phys. Lett. B, vol. 594, p. 347, (**2004**), [arXiv:hep-ph/0402266].

[123] Miranda O.G., Tortola M.A., Valle J.W.F., "Are solar neutrino oscillations robust?", [arXiv:hep-ph/0406280].

[124] Barger V., Huber P., Marfatia D., "Solar Mass-Varying neutrino oscillations", [arXiv:hep-ph/0502196].

[125] Anderson K. et al., "White paper report on using nuclear reactors to search for a value of theta(13)", FERMILAB-PUB-04-180, (**2004**), [arXiv:hep-ex/0402041].

[126] Oberauer L., "Search for θ_{13} with Reactor Experiments", talk at "Neutrino 2004", Paris, France, Nucl. Phys. Proc. Suppl., vol. 143, p. 277-281, (**2005**).

[127] Lindner M., "Future precision neutrino oscillation experiments and theoretical implications", [arXiv:hep-ph/0503101].

[128] NOνA Collaboration, "NOνA: proposal to build a 30kton off-axis detector tu study nu(mu) $\rightarrow$ nu(e) oscillations in the NuMI beamline", (**2004**), [arXiv:hep-ex/0503053].

[129] Hayato Y. for the T2K Collaboration, "T2K at J-PARC", Nucl. Phys. Proc. Suppl., vol. 143, p. 269-276, (**2005**).

[130] Hobayashi T., "Super Beams", Nucl. Phys. Proc. Suppl., vol. 143, p. 303-308, (**2005**).

[131] Nakamura K., "Hyper-Kamiokande: A next generation water Čerenkov detector", Int. J. Mod. Phys. A, vol. 18, p. 4053-4063, (**2003**).

[132] Jung C.K., "Feasibility of a next generation underground water Čerenkov detector: UNO", [arXiv:hep-ex/0005046].

[133] Buchmüller W., "Baryon asymmetry and thermal leptogenesis", Nucl. Phys. Proc. Suppl., vol. 143, p. 462-469, (**2005**).

[134] KATRIN Collaboration, "KATRIN: Direct measurement of a sub-eV neutrino mass", Nucl. Phys. Proc. Suppl., vol. 145, p. 263-267, (**2005**).

[135] Lattanzi M., Ruffini R., Vereshchagin G., "On the possible role of massive neutrinos in cosmological structure formation", AIP Conf. Proc., vol. 668, p. 263-287, (**2003**), [arXiv:astro-ph/0305035].

[136] Strumia A., Vissani F., "Implications of neutrino data circa 2005", Nucl. Phys. B, vol. 726, p. 294-316, (**2005**), [arXiv:hep-ph/0503246].

[137] Avignone F.T., "Strategies for Next Generation Neutrinoless Double-Beta Decay Experiments", Nucl. Phys. Proc. Suppl., vol. 143, p. 233-239, (**2005**).

[138] GERDA Collaboration "The germanium detector array (GERDA) for the search of neutrinoless beta beta decay of Ge-76 at LNGS", Nucl. Phys. Proc. Suppl., vol. 145, p. 242-245, (**2005**).

[139] CUORE Collaboration, "CUORE: A Cryogenic Underground Observatory for Rare Events", Nucl. Instrum. Meth. A, vol. 518, p. 775-798, (**2004**), [arXiv:hep-ex/0212053].

[140] Bahcall J.N., Murayama H., Peña-Garay C., "What can we learn from neutrinoless double beta decay experiments?", Phys. Rev. D, vol. 70, 033012, (**2004**), [arXiv:hep-ph/0403167].

[141] Wong T., "Neutrino Magnetic Moments: Status and Prospects", Nucl. Phys. Proc. Suppl., vol. 143, p. 205-210, (**2005**).

[142] Beacom J.F., Vogel P., "Neutrino magnetic moment, flavor mixing, and the SuperKamiokande solar data", Phys. Rev. Lett., vol. 83, p. 5222, (**1999**), [arXiv:hep-ph/9907383].

[143] MUNU Collaboration, "Final results on the neutrino magnetic moment from the MUNU experiment", Phys. Lett. B, vol. 615, p. 153-159, (**2005**), [arXiv:hep-ex/0502037].

[144] KamLAND Collaboration, "A high sensitivity search for anti-nu(e)'s from the sun and other sources at KamLAND", Phys. Rev. Lett., vol. 92, 071301, (**2004**), [arXiv:hep-ex/0310047].

[145] SNO Collaboration, "Electron Antineutrino Search at the Sudbury Neutrino Observatory", Phys. Rev. D, vol. 70, 093014, (**2004**), [arXiv:hep-ex/0407029].

[146] Yilmaz D., Yilmazer A.U., "Global analysis of solar neutrinos (assumed to be Majorana particles) together with the new KamLAND data in the RSFP framework", J.Phys.G, vol. 31, p. 1123-1131, (**2005**).

[147] Bahcall J.N., Peña-Garay C., "A road map to solar neutrino fluxes, neutrino oscillation parameters and tests for new physics", JHEP, vol. 0311, p. 004, (**2003**), [arXiv:hep-ph/0305159].

[148] Bahcall J.N., Gonzalez-Garcia M.C., Peña-Garay C., "Does the Sun Shine by *pp* or CNO Fusion Reactions?", Phy. Rev. Lett., vol. 90, 131301, (**2003**), [arXiv:astro-ph/0212331].

[149] The Hubble Heritage Project: http://heritage.stsci.edu/

[150] Janka T. et al., "Explosion mechanisms of massive stars", [arXiv:astro-ph/0212314]

[151] Schramm D.N., "Neutrinos from Supernova 1987A", Comm. Nucl. Part. Phys., vol. 17, p. 239, (**1987**).

[152] Kamiokande Collaboration, "Observation of a neutrino burst from the supernova SN1987A", Phys. Rev. Lett., vol. 58, p. 1490-1493, (**1987**).

[153] IMB Collaboration, "Angular distribution of events from SN1987A", Phys. Rev. D, vol. 37, p. 3361, (**1988**).

[154] Dighe A., Keil M., Raffelt G., "Identifying Earth matter effects on supernova neutrinos at single detector", JCAP, vol. 0306, p. 006, (**2003**), [arXiv:hep-ph/0304150].

[155] Mantovani F., Carmignani L., Fiorentini G., Lissia M., "Anti-neutrinos from the earth: the reference model and its uncertainties.", Phys. Rev. D, vol. 69, 013001, (**2004**), [arXiv:hep-ph/0309013].

[156] Raghavan R.S. et al., "Measuring the Global Radioactivity in the Earth by Multidetector Antineutrino Spectroscopy", Phys. Rev. Lett., vol. 80, p. 635, (**1998**).

[157] KamLAND Collaboration, "Experimental investigation of geologically produced antineutrinos with KamLAND", Nature, vol. 436, p. 499-503, 28 July (**2005**).

[158] Fiorentini G., Lissia M., Mantovani F., Ricci B., "KamLAND results and the radiogenic terrestrial heat", Phys. Lett. B, vol. 629, p. 77-82, (**2005**), [arXiv:hep-ph/0508048].

[159] Herndon M.J., Edgerley D.A., "Background for Terrestrial Antineutrino Investigations: Radionuclide Distribution, Georeactor Fission Events and Boundary Conditions on Fission Power Production", subm. to Proc.Roy.Soc.Lond.A Math.Phys.EngSci., (**2005**), [arXiv:hep-ph/0501216].

[160] Raghavan R.S., "Detecting a nuclear fission reactor at the center of the earth", (**2002**), [arXiv:hep-ex/0208038].

[161] Lanou R.E., "Update on HERON", Nucl.Phys.Proc.Suppl., vol. 138, p. 98-101, (**2005**).

[162] McKinsey D.N., Coakley K.J., "Neutrino detection with CLEAN", "Astropart. Phys.", vol. 22, p. 355-368, (**2005**), [arXiv:astro-ph/0402007].

[163] Suzuki Y., "Future solar neutrino experiments", Nucl. Phys. Proc. Suppl., vol. 143, p. 27-34, (**2005**).

[164] MOON Collaboration "Double Beta decays and Solar neutrinos with Mo-100", Czech. J. Phys., vol. 54, p. B317-B325, (**2004**).

[165] Kopylov A. et al., "Lithium experiment on solar neutrino to weigh the CNO cycle", Phys. Atom. Nucl., vol. 67, p. 1182-1187, (**2004**), [arXiv:hep-ph/0310163].

[166] Raghavan R.S., "Inverse beta Decay of $^{115}In \rightarrow {}^{115}Se^{*}$: a new possibility for detecting solar neutrinos from the proton-proton reaction", Phys. Rev. Lett., vol. 37, p. 259, (**1976**).

[167] Raghavan R.S., "pp solar neutrino spectroscopy: return of the indium detector", subm. to Phys. Rev. Lett., (**2001**), [arXiv:hep-ex/0106054].

[168] LENS Collaboration, "The LENS Project: Low Energy Neutrino Spectroscopy", Prog. Part. Nucl. Phys., vol. 48, p. 231-232, (**2002**).

[169] Back H. et al., "LENS-Sol: A detector for measuring the neutrino luminosity of the sun", publ. in *Tokyo 2004, Neutrino oscillations and their origin*, p. 50-58, (**2004**).

[170] Chen M., "The SNO liquid scintillator project", Nucl. Phys. Proc. Suppl., vol. 145, p. 65-68, (**2005**).

[171] LENA Home Page: http://www.e15.physik.tu-muenchen.de/research/lena.html

[172] Oberauer L., von Feilitzsch F. , Potzel W., "A large liquid scintillator detector for low-energy neutrino astronomy", talk at "TAUP 2003", Seattle, Washington, USA, Nucl. Phys. Proc. Suppl., vol. 138, p. 108-111, (**2005**).

[173] Marrodan T. et al., "Search For The Proton Decay P → K+ Anti-Nu In The Large Liquid Scintillator Low Energy Neutrino Astronomy Detector Lena", Phys. Rev. D, vol. 72, 075014, (**2005**), [arXiv:hep-ph/0511230].

Chapter 2

[174] LNGS Home Page: http://www.lngs.infn.it/

[175] BOREXino Home Page: https://borex.lngs.infn.it/

[176] Raghavan R.S. et al., "New tools for solving the solar neutrino problem", Phys. Rev. Lett., vol. 57, p. 1801-1804, (**1986**).

[177] BOREXino Collaboration, "Measurement of the C-14 abundance in a low-background liquid scintillator", Phys. Lett. B, vol. 422, p. 349-358, (**1998**).

[178] BOREXino Collaboration, "Light propagation in a large volume liquid scintillator", Nucl. Intrum. Meth. A, vol. 440, p. 360, (**2000**).

[179] BOREXino Collaboration, "Science and technology of BOREXino: a realtime detector for low energy solar neutrinos", Astropart. Phys. , vol. 16, p. 205-234, (**2002**), [arXiv:hep-ex/0012030].

[180] BOREXino Collaboration, "Measurements of extremely low radioactivity levels in BOREXino.", Astropart. Phys., vol. 18, p. 1-25, (**2002**), [arXiv:hep-ex/0109031].

[181] Knoll G.F., "Radiation Detection and Measurements", John Wiley & Sons, New York, (**1989**).

[182] Birks J.B., "The Theory and Practice of Scintillation Counting", Pergamon Press, (**1964**).

[183] Ianni A., Montanino D., Villante F.L., "How to observe ^8B solar neutrinos in liquid scintillator detectors.", Phys. Lett. B, vol. 627, p. 38-48, (**2005**), [arXiv:physics/0506171].

[184] Cadonati L., Calaprice F.P., Chen M.C., "Supernova neutrino detection in BOREXino", Astropart. Phys., vol. 16, p. 361-372, (**2002**), [arXiv:hep-ph/0012082].

[185] Benziger J. et al., "A scintillator purification system for a large scale solar neutrino experiment", Nucl. Instrum. Meth. A, vol. 47, p. 278, (**1998**).

Chapter 3

[186] Gaisser T.K., "Cosmic Rays and Particle physics", Cambridge University Press, (**1990**).

[187] MACRO Collaboration, "Vertical muon intensity measured with MACRO at the Gran Sasso Laboratory", Phys. Rev. D, vol. 52, p. 3793, (**1995**).

[188] MACRO Collaboration, "Measurement of the energy spectrum of underground muons at Gran Sasso with a transition radiation detector", Astropart. Phys., vol. 10, p. 10, (**1999**), [arXiv:hep-ex/9807009].

[189] LVD Collaboration, "Study of single muons with the Large Volume Detector at Gran Sasso laboratory", Phys. Atom. Nucl., vol. 66, p. 123, (**2003**), [arXiv:hep-ex/0202006].

[190] Jackson J. D., "Classical Electrodynamics", John Wiley & Sons Inc. (New York), 3rd ed., (**1999**).

[191] Particle Data Group, "Review of particle physics", Eur. Phys. J. C, vol. 3, p. 1-794, (**1998**).

[192] Dossi R., Ianni A., Ranucci G., Smirnov O.Yu., "Methods for precise photoelectron counting with photomultipliers", Nucl. Instrum. Meth. A, vol. 451, p. 263, (**2000**).

[193] ETL Home Page: http://www.electrontubes.com/

[194] Emmolo D., Orlando P., "Technique account for BOREXino's photomultipliers survey", technical report, (**2005**).

Chapter 4

[195] Lagomarsino V., Testera G., "A gateless charge intergrator for BOREXino energy measurement", Nucl. Intrum. Meth. A, vol. 430, p. 435, (**1999**).

[196] Gatti F. for the BOREXino Collaboration, "DAQ electronics for BOREXino experiment", Nucl. Phys. Proc. Suppl., vol. 78, p. 111-114, (**1999**).

[197] Peterson W., "VMEbus Handbook", 4th Edition, VITA publications, (**1997**), http://www.vita.com

Chapter 5

[198] Paubert G. "Tundra Universe driver".

[199] Mitchell M., Oldham J., Samuel A., "Advanced Linux Programming", 1st Edition, New Riders Publishing, June 2001, available online at http://www.advancedlinuxprogramming.com/

[200] Rubini A., Corbet J., "Linux Device Drivers", 2nd Edition, O'Reilly, June 2001, available online at http://www.xml.com/ldd/chapter/book/

[201] CORBA Home Page: http://www.omg.org/corba/

[202] Razeto A., private communication, (**2002**).

Chapter 7

[203] Echidna Home Page: http://bxweb.lngs.infn.it/echidna/ (restricted access).

[204] D'Angelo D., Razeto A., "Echidna documentation", http://bxweb.lngs.infn.it/echidna/docs/

[205] D'Angelo D., "Echidna Programmer's guide", http://bxweb.lngs.infn.it/echidna/docs/

[206] D'Angelo D., "Echidna: the ROOT file for users", http://bxweb.lngs.infn.it/echidna/docs/

[207] The CVS System Home Page: https://www.cvshome.org/

[208] Kernighan B.W., Ritchie D.M., "The C programming language", 2nd ed., Prentice Hall Inc., (**1989**).

[209] Stroustroup B., "The C++ programming Language", 3rd ed., Addison-Wesley, (**1997**).

[210] Gamma E., Helm R., Johnson R., Vlissides J., "Design Patterns. Elements of reusable Object Oriented Software", 1st edition, Addison-Wesley Professional, January (**1995**).

[211] The ROOT System Home Page: http://root.cern.ch/

[212] Brun R., Canal P., private communications (**2004**).

Chapter 8

[213] Sabelnikov A., private comunication, (**2003**).

[214] Jänner K., "VME PMT-Pulser LENS_Fiber2: Anwender - Kurzbeschreibung und Information", technical manual (in German), MPIK-HD Electronic Department, (**2002**).

Chapter 9

[215] BOREXino Collaboration, "A large-scale low background liquid scintillator detector: the counting test facility at Gran Sasso", Nucl. Instrum. Meth. A, vol. 406, p. 411, (**1998**).

[216] BOREXino Collaboration, "Ultra-low Background Measurements in a Large Volume Underground Detector", Astropart. Phys., vol. 8, p. 141-157, (**1998**).

[217] BOREXino Collaboration, "Search for electron decay mode $e \to \gamma + \nu$ with prototype of BOREXino detector.", Phys. Lett. B, vol. 525, p. 29-40, (**2002**).

[218] BOREXino Collaboration, "New limits on nucleon decays into invisible channels with the BOREXINO counting test facility", Phys. Lett. B, vol. 563, p. 23-34, (**2003**), [arXiv:hep-ex/0302002].

[219] BOREXino Collaboration, "Study of the neutrino electromagnetic properties with prototype of BOREXino detector", Phys. Lett. B, vol. 563, p. 35-47, (**2003**).

[220] BOREXino Collaboration, "New Experimental limits on heavy neutrino mixing in B-8 decay obtained with the BOREXino Counting Test Facility", JETP Lett., vol. 78, p. 261-266, (**2003**).

[221] BOREXino Collaboration, "New experimental limits on violations of the Pauli Excusion Principle obtained with the BOREXino Counting Test Facility", Eur. Phys. J. C, vol. 37, p. 412-431, (**2004**), [arXiv:hep-ph/0406252].

[222] BOREXino Collaboration, "Phenylxylyethane (PXE): a high-density, high-flashpoint organic liquid scintillator foar applications in low-energy particle and astrophysics experiments", subm. to Nucl. Instrum. Meth. A, (**2004**), [arXiv:physics/0408032].

[223] BOREXino Collaboration, "Search for electron antineutrinos with the BOREXino prototype at the Gran Sasso underground laboratory", subm. to Eur. Phys. J. C, (**2006**), [arXiv:hep-ex/0602027].

[224] BOREXino Collaboration, "CNO and pep neutrino spectroscopy in BOREXino: measurement of the cosmogenic ^{11}C background with the Counting Test Facility" subm. to Phys. Rev. D, (**2006**), [arXiv:hep-ex/0601035].

[225] Niedermeier L., Grieb C., D'Angelo D., Korschinek G., Oberauer L., Feilitzsch F., "Scintillator Purification by Silica Gel Chromatography in the context of Low Counting Rate Experiments", prepared for 8th International Conference ICATPP 2003, Como, Italy, 6-10 Oct (**2003**).

[226] Gatti E., De Martini F., "A new linear method of discrimination between elementary particles in scintillation counters", IAEA Wien p. 265-276, (**1962**).

[227] http://www.e15.physik.tu-muenchen.de/borexino/memo.htm.

[228] CTF analysis web page. http://pcdavide.mi.infn.it/cgi-bin/index.cgi (restricted access).

[229] James F., "MINUIT: Function Minimization and Error Analysis. Reference Manual" Computing and Networks Division, CERN Geneva, Switzerland. http://wwwasdoc.web.cern.ch/wwwasdoc/minuit/minmain.html

Chapter 10

[230] Hagner T., von Hentig R., Heisinger B., Oberauer L., Schönert S., Von Feilitzsch F., Nolte E., "Muon induced Production of Radioactive Isotopes in Scintillation Detectors", Astropart. Phys., vol. 14, p. 33, (**2000**).

[231] Galbiati C., Pocar A., Franco D., Ianni A., Cadonati L., Schönert S., "Cosmogenic ^{11}C production and sensitivity of organic scintillator detectors to pep and CNO neutrinos", Phys. Rev. C, vol. 71, 055805, (**2005**), [arXiv:hep-ph/0411002].

[232] Franco D. for the BOREXino Collaboration, "C-11 measurement and CNO and pep fluxes at BOREXino", Nucl. Phys. Proc. Suppl., vol. 145, p. 29-32, (**2005**).

[233] Franco D., private communication, (**2005**).

[234] LVD Collaboration, "Measurement of the neutron flux produced by cosmic-ray muons with LVD at Gran Sasso", (**1999**), [arXiv:hep-ex/9905047].

[235] FLUKA Home Page: http://www.fluka.org/

[236] Deutsch M., "Proposal for a Cosmic Ray Detection System for the BOREXino Solar Neutrino Experiment", Massachusetts Institute of Technology, (**1996**).

Theses

[237] D'Angelo D., "Metodologie per la caratterizzazione ed il riconoscimento di diverse tipologie di eventi nel rivelatore CTF, prototipo dell'esperimento BOREXino", Tesi di Laurea (in Italian), Università degli Studi di Milano, (**2001**).

[238] Franco D., "The BOREXino Experiment: Test of the Purification Systems and Data Analysis in the Counting Test Facility", Ph.D. Thesis, Università degli Studi di Milano, (**2005**).

[239] Galbiati C., "Data taking and analysis of the Counting Test Facility of BOREXino", Ph.D. Thesis, Università degli Studi di Milano, (**1999**).

[240] Grieb C., "Future Neutrino Detectors and their Impact on Particle- and Astrophysics", Ph.D. Thesis, Technische Universität München, (**2004**).

[241] Lendvai C., "Identification of Muon-Induced Signals in the Deep Underground Neutrino-Scintillation-Detector BOREXINO", Ph.D. Thesis, Technische Universität München, (**2005**).

[242] Manuzio D., "Towards the detection of subMeV solar neutrinos in BOREXino: data reconstruction and analysis tools", Ph.D. Thesis, Università degli studi di Genova, (**2004**).

[243] Monzani M.E., "Characterization and calibration of the BOREXino detector for solar and supernova neutrinos", Ph.D. Thesis, Università degli Studi di Milano, (**2005**).

[244] Niedermeier L., "High Efficiency Purification of Liquid Scintillators for the Solar Neutrino Experiment BOREXino", Ph.D. Thesis, Technische Universität München, (**2005**).

[245] Peiffer P., "Das Kalibrationssystem für den Äusseren Detektor des BOREXino Experiments", Diplomarbeit (in German), MPIK-HD, (**2003**).

[246] Razeto A., "Events Readout for a Real-Time Neutrino Detector", Ph.D. Thesis, Università degli Studi di Genova, (**2002**).

Acknowledgements

My first acknowledgement goes to Prof. von Feilitzsch for the great chance he offered me with this Ph.D. His trust gave me the freedom to bring ahead the project independently and maturing (I hope!) a deal of experience, but at the same time his support was always present at the right moments.

My gratitude goes just the same to Lothar (Prof. Oberauer), who guided me through this work, being at the same time a well of knowledge, a solid reference point and a friend. He even managed to read and correct this thesis (but don't blame him for the remaining mistakes!).

I'm in debt to Ludwig for his beamer. Ok, yes, also for home, patience, Wurst, 2 years of sharing joys and sorrows under the same roof, Bier, marsala, police on our back, a true relationship (non-gay), but does all this really compare ... to his beamer?!

I'm grateful to Christian L., who shared this work with me in the lucky and the unlucky times, fighting and partying, and being just good friends. May his new American life be truly happy.

What should I say about a team like E15? In random order, I want to thank Michi W. für "Schlittschuhlaufen", Patrick for being my espresso-mate, Chiara for being someone so special, Teresa für die Heizung, Jean-Come for just being Jean-Come, Marianne for the courage to read my thesis, Walter and Wolfang R. für die Hinweise and all the others, Kathrin, Tobi, Christian G., Michi S., Walter, Wolfgang W., Emanuel, Christian I., Christian C., Sebastian, Vitali, Georg, Alexandra and those I'm forgetting, for being the most pleasant group of friends one could want to work and have fun with. The idea of departing already leaves me "lost in translation"...

A special mention deserves Beatrice: she can sound terrible when she wants, but actually she's just terribly ...sweet! and caring. and a guide-light. and a friend.

I also wish to say I will not forget the kindness of Prof. Nolte who left us too soon.

I owe a lot to my Italian friends in Munich as well: Alessandro T., Leonardo and all the group "Italians", especially Daniela G., who corrected my broken english, prepared a delicious tiramisù for the party and ...ok, the rest she knows ...

Die Niedermeiers werde ich immer erinnern, die gar keine Vermieter gewesen sind, sondern eine echte zweite Familie für fast drei Jahre.

Ok, so far it sounds like I had a great family here in Munich, right? but the fact is that I had two, the other one being at Gran Sasso and being just as great.

This includes the wonderful team that shared with me the joy and despair of running the detector through numerous air runs, accidents and excitements: Marco P., il "ciccione", who has followed all my work at Gran Sasso, Daniela M."braccia-di-fata", whose flap-flap of the eyes can do magic, Alessandro R. in arte "huge" and his (literally) intruding ferret, Andrew, Olivier and "dulcis im fundo" Maria Elena.

I keep in my heart Alba and Stefano, who made me feel at home in their “casetta” (ok, maybe sometimes I felt a little bit *too much* at home), Paolo and Marta who won’t do the same mistake, Maria the real reason for coming to the lab and the rest of the crew: George (and his sister), Laszlo, Heide, Federica C., Henning, Burkhard (farewell!), Peppino Dr. Di Pietro, Augusto, Stefano G., Yuri and Elena with whom I shared a beautiful summer of cats and blackberries in the lab.

I’d like to thank Aldo and the fellows in Milan, Emanuela, Barbara and Davide F., for the always pleasant cooperation.

Dei tanti esseri umani sparsi per il mondo che condividono questa vita con me e che porto sempre dentro, menziono solo mamma e papà, senza i quali nulla sarebbe possibile, nè saprei cos’è l’amore.